THÈSE / UNIVERSITÉ DE BRETAGNE OCCIDENTALE

sous le sceau de l'Université européenne de Bretagne

pour obtenir le titre de

DOCTEUR DE L'UNIVERSITÉ DE BRETAGNE OCCIDENTALE

Mention : électronique

École Doctorale : Santé, Information-Communications, Mathématiques, Matière (ED 373)

présentée par

Andreas ARNOLD-BOS

Préparée au laboratoire E^3I^2 - Extraction et Exploitation de l'Information en Environnement Incertains (EA 3876)

École Nationale Supérieure des Ingénieurs des Études des Techniques d'Armement (ENSIETA)

Marine surveillance with bistatic radar : theory, simulation, contribution to computer-aided ship wakes detection

Thèse soutenue le 2 février 2010

devant le jury composé de :

Christian BROSSEAU, président du jury
Professeur, Université de Bretagne Occidentale

Joseph SAILLARD, rapporteur
Professeur, École Polytechnique de l'Université de Nantes

Marc SAILLARD, rapporteur
Professeur, Université du Sud, Toulon-Var

Marc ACHEROY, examinateur
Professeur, École Royale Militaire, Bruxelles

Philippe COURMONTAGNE, examinateur
Enseignant-chercheur, ISEN, Toulon

Ali KHENCHAF, examinateur, directeur de thèse
Professeur, ENSIETA, Brest

Arnaud MARTIN, examinateur, co-encadrant
Enseignant-chercheur ENSIETA, Brest

Sylvain COLSON, invité
Responsable métier Direction Électromagnétique, Direction Générale de l'Armement

François LE CHEVALIER, invité
Directeur scientifique, Thales, Division Aéronautique

THÈSE / UNIVERSITÉ DE BRETAGNE OCCIDENTALE

sous le sceau de l'Université européenne de Bretagne

pour obtenir le titre de

DOCTEUR DE L'UNIVERSITÉ DE BRETAGNE OCCIDENTALE

Mention : électronique

École Doctorale : Santé, Information-Communications, Mathématiques, Matière (ED 373)

présentée par

Andreas ARNOLD-BOS

Préparée au laboratoire E^3I^2 - Extraction et Exploitation de l'Information en Environnement Incertains (EA 3876)

École Nationale Supérieure des Ingénieurs des Études des Techniques d'Armement (ENSIETA)

La surveillance maritime en imagerie radar bistatique : théorie, simulation, contribution à la détection automatique du sillage des navires

Thèse soutenue le 2 février 2010

devant le jury composé de :

Christian BROSSEAU, président du jury
Professeur, Université de Bretagne Occidentale

Joseph SAILLARD, rapporteur
Professeur, École Polytechnique de l'Université de Nantes

Marc SAILLARD, rapporteur
Professeur, Université du Sud, Toulon-Var

Marc ACHEROY, examinateur
Professeur, École Royale Militaire, Bruxelles

Philippe COURMONTAGNE, examinateur
Enseignant-chercheur, ISEN, Toulon

Ali KHENCHAF, examinateur, directeur de thèse
Professeur, ENSIETA, Brest

Arnaud MARTIN, examinateur, co-encadrant
Enseignant-chercheur ENSIETA, Brest

Sylvain COLSON, invité
Responsable métier Direction Électromagnétique, Direction Générale de l'Armement

François LE CHEVALIER, invité
Directeur scientifique, Thales, Division Aéronautique

How to cite this document:

Andreas Arnold-Bos, *Marine surveillance with bistatic radar: theory, simulation, contribution to computer-aided ship wakes detection* (translation of the original in French: *La surveillance maritime en imagerie radar bistatique: théorie, simulation, contribution à la détection automatique du sillage des navires*), PhD thesis, École Doctorale Santé, Information-Communications, Mathématiques, Matière (ED 373), Université de Bretagne Occidentale, defended on February 2nd, 2010.

```
@phdthesis{arnold:2010,
    title        = {Marine surveillance with bistatic radar: theory,
simulation, contribution to computer-aided ship wakes detection
(translation of the original in French: La surveillance maritime
en imagerie radar bistatique: th\'eorie, simulation, contribution
\`a la d\'etection automatique du sillage des navires)},
    author       = {Arnold-Bos, Andreas},
    year         = 2010,
    month        = {February},
    address      = {Brest, France},
    school       = {Universit\'e de Bretagne Occidentale},
    type         = {PhD thesis}
}
```

This document was compiled on February 6, 2024.

Note to international readers

This is a translation of my PhD thesis originally published in 2010 in French under the title "*La surveillance maritime en imagerie radar bistatique: théorie, simulation, contribution à la détection automatique du sillage des navires*". This translation has no official value, with respect to the university where this thesis was defended. French policy is that dissertations must be published in French[1]. Naturally, I feel that some elements, not published in the journal papers associated to this thesis, are interesting enough to be shared with the international community where English is the *de facto* scientific language. The document should be of interest especially for newcomers to the field of Radar imaging: indeed I tried to write this dissertation in such a way that it is as self-sufficient as possible when demonstrating the base equations.

I undertook this translation project between June 2022 and February 2024, meaning that things have since more or less evolved since 2010. However, most of the time, I chose the translation to faithfully match how the thesis was originally written, meaning there are no significant updates in the state of the art. Due to the size of the document, and because writing is not the only thing I do in my life, I admit to having used machine translation extensively to cut on translation time. Automated translation has today reached a point where it is fairly efficient, especially for technical publications. I only revised the translation here and there to correct very specific, technical translations or very clumsy expressions, where I noticed them. I apologize in advance if you spot a few inconsistencies left; there surely are some. As for the style, which might be somewhat old-fashioned and very formal for an English reader, it is a rather faithful reflection of the original style, due in part to the French academic way of writing, and my own idiosyncrasies. This is an editing choice! I tried to avoid, however, the use of the royal "we", a very French thing, while still acknowledging the input of my advisors (who are also, indirectly, addressed by the use of the "we" pronoun!).

–Andreas Arnold

[1] This is increasingly changing. However, at the time when I wrote my thesis, it was still enforced extensively.

Acknowledgments

The work presented in this thesis was carried out at the E^3I^2 laboratory (Extraction et Exploitation de l'Information en Environnements Incertains[2]), EA3876, directed by Professor Ali Khenchaf and hosted by ENSIETA (École Nationale Supérieure des Ingénieurs des Études et Techniques d'Armement[3]), in Brest. It was funded by a scholarship granted by the Brittany region.

First and foremost, I would like to thank Ali Khenchaf for welcoming me into the laboratory and supervising my thesis. I appreciate his immense patience, trust, and valuable guidance that allowed me to conduct my work under favorable conditions. I also thank Arnaud Martin [4] for co-supervising my thesis, providing advice, and introducing me to teaching and student supervision.

I express my deep gratitude to Arnaud Coatanhay and Michel Legris for their availability and keen interest in my work. The highly insightful discussions we had were crucial for the progress of my thesis. It was also in discussions with Michel that I discovered the world of underwater acoustics, a field in which I am currently working in. I would also like to thank Yann Doutreleau and the staff of the Laboratory of Naval Structures Mechanics for their valuable advice in hydrodynamics and naval mechanics.

I extend my gratitude to the members of the jury for agreeing to evaluate my work under the presidency of Christian Brosseau. Thanks to Joseph Saillard and Marc Saillard for their interest in my work and for accepting to be the rapporteurs of this thesis. Marc Acheroy, Philippe Courmontagne, Sylvain Colson, and François Le Chevalier also agreed to be part of my jury, and I am very grateful to them.

I sincerely thank all the members of the General Sonar Studies department at Thales Underwater Systems[5] for welcoming me into their team since June 2007 and for encouraging me during moments of doubt in my writing: without them, I wouldn't have made it. But

[2]Extraction and Exploitation of Information in Uncertain Environments.

[3]Note when translating: ENSIETA was renamed ENSTA Bretagne in December, 2010. ENSTA stands for École Nationale Supérieure de Techniques Avancées. Along with a similarly named school near Paris, these two establishments are engineering schools educating civilian students, but also military cadet officers headed for a career in the French defense procurement agency. By 2025, these two schools are due to merge into a single establishment.

[4]Arnaud passed away much too young, at the age of 49, in August 2023. I dedicate this translation to him *in memoriam*.

[5]Note at translation: Thales Underwater Systems is now Thales DMS France.

the support was not only moral: I also want to thank Daniel Cano and Olivier Le Comte for allowing a temporary adjustment of my schedule to help me with my writing.

The working environment at ENSIETA has been very pleasant, so I want to thank all the school staff and especially the documentation service and Annick Billon-Coat for their efficient assistance. I also thank Luc Jaulin for our numerous scientific discussions. I particularly thank all the PhD students from the E^3I^2, SHI, MSN, and DTN laboratories for their good spirits. Thanks to Laurent and Arunas for the good times in the D219 office; to Gustavo, with whom I had great pleasure collaborating; to Cécile as well. Thanks to Vincent for the long philosophical discussions and for broadening my musical horizons. Finally, a more special thanks to Isabelle, who, among other things, introduced me to photography and Finistère –thanks to her, I am now the "happy manservant" of two cats!

My thanks also go to my other friends: on one hand, to Pierre (*I.S.P.V.*!) and his family, and on the other hand, André, Colette, Kristen, Rebecca, and other MOO members (*you guys made it possible!*), for the unforgettable moments we spent together.

Lastly, I cannot conclude without thanking my family for their support and encouragement throughout my years of study, and more generally for enabling me to reach this point.

Table of contents

Glossary and acronyms

Acronyms used throughout this dissertation are listed in the following table, with the French translation whenever available.

BiSAR	*Bistatic Synthetic Aperture Radar*	Radar à synthèse d'ouverture bistatique
BSA	*Backscattering Alignment*	Convention d'alignement "rétrodiffusion"
CPU	*Central Processing Unit*	Processeur
DORIS	*Doppler Orbitography and Radiopositioning Integrated by Satellite*	Détermination d'Orbite et Radiopositionnement Intégré par Satellite
PSD	Power Spectral Density	Densité spectrale de puissance
DTMB	*David Taylor Model Basin*	(a proper name, a U.S. hull testing basin)
EBCM	*Extended Boundary Condition Method*	A method to compute the RCS of a rough surface (Franceschetti *et al.* [71, 70])
Envisat	*Environmental Satellite*	(Proper name, an European remote sensing satellite)
ERS	*European Radar Satellite*	(Proper name, an European remote sensing satellite)
ESA	*European Space Agency*	Agence spatiale européenne
FFBP	*Fast Factorised Back Projection*	(A synthetic aperture focusing algorithm, Ulander *et al.* [178])
FFSW	*Far Field Ship Wave*	(A ship wake elevation prediction code, Keramidas *et al.* [101])
FFT	*Fast Fourier Transform*	Transformée de Fourier rapide
FFTW	*Fastest Fourier Transform in the West*	(A fast Fourier transform computer library, [75])
FPGA	*Field-Programmable Gate Array*	Réseau logique programmable
FSA	*Forward Scattering Alignment*	Convention d'alignement "diffusion avant"
FT	Fourier Transform	Transformée de Fourier
GLONASS	*GLObal'naya NAvigatsionnaya Sputnikovaya Sistema*	Russian global navigation system using satellites
GLSL	*Graphics Library Shading Language*	A *shader* programming language associated with the OpenGL library
GNSS	*Global Navigation System using Satellites*	Système de positionnement mondial par satellite

GPU	*Graphical Processing Unit*	
GRT	Generalized Radon Transform	Transformée de Radon Généralisée
GSM	*Global System for Mobile Communications*	A global wireless phone standard initiated by the French "Groupe Spécial Mobile" normalization group
HLSL	*High Level Shading Language*	(A *shader* programming language associated to Microsoft's DirectX library)
H-TSM	*Hybrid Two-Scales Model*	Modèle des deux échelles hybride
IEEE	*Institute of Electrical and Electronics Engineers*	(An U.S. learned society)
ISAR	*Inverse Synthetic Aperture Radar*	Radar à ouverture synthétique inverse
JONSWAP	Joint North Sea Wave Analysis Project	Projet conjoint d'analyse des vagues et de l'atmosphère en mer du Nord
KA	Kirchhoff Approximation	Approximation de Kirchhoff
LFM	Linear Frequency Modulation	Modulation linéaire en fréquence
MaRS	*Marine Radar Simulator*	(Proper noun; a radar simulator program, presented in this dissertation)
MTI	*Moving Target Indicator*	Caractérisation des cibles mobiles
NASA	*National Air and Space Administration*	(An U.S. space agency)
NOAA	*National Oceanic and Atmospheric Administration*	(An U.S. agency)
OpenGL	*Open Graphics Languge*	(A standard 3D programming library)
NATO	North Atlantic Treaty Organization	Organisation du Traité de l'Atlantique Nord
PRF	*Pulse Repetition Frequency*	Période de répétition des impulsions
RAM	*Random Access Memory*	Mémoire vive
RAR	*Real Aperture Radar*	Radar à ouverture réelle
RCS	Radar Cross-Section	*Surface Équivalente Radar*
ROC	Receiver Operating Characteristic	Caractéristique Opérationnelle du Récepteur
RT	Radon Transform	Transformée de Radon
SAR	*Synthetic Aperture Radar*	Radar à ouverture synthétique
shader	(Small computer program executed by a GPU at rendering time.)	
SIR	*Space Imaging Radar*	(U.S. space radar missions: SIR-A, SIR-B and SIR-C)
SMF	Stochastic Matched Filter	Filtrage Adapté Stochastique
SPECAN	*SPEctral ANalysis*	(Algorithme d'intégration en antenne syntétique par analyse spectrale, Vidal *et al.* [181])
SPM	*Small Perturbations Method*	Méthode des petites perturbations
SPOT	Satellite Pour l'Observation de la Terre	(Proper noun meaning "Satellite for the Observation of Earth", a French family of optical remote sensing satellites)
SSA	*Small Slopes Approximation*	Approximation des faibles pentes
SWPE	*Sea Wave Pattern Evaluation*	
HT	Hough Transform	Transformée de Hough
TSM	*Two-Scales Model*	Modèle des deux échelles
psu	Practical Salinity Unit	Unité pratique de salinité
USGS	*United States Geological Survey*	(Agence gouvernementale américaine consacrée aux sciences de la Terre)
WiFi	*Wireless Fidelity*	"Haute fidélité sans fil" (wireless computer data transmission as defined in norm IEEE 802.11 and extensions).

Nomenclature

These are the main notations as used in the different chapters of this document. Associated frames are described in appendix A.

General conventions

- Frames are written in calligraphic style (exemple: $\mathcal{R}$). The only exception to this convention is for spectra: the swell power spectral density $\mathcal{S}$, and swell energy spectral density $\mathcal{E}$. Frames are defined in A.
- Points are written in capital roman letters: A. Distance to point A to point B is denoted by $\parallel$ AB $\parallel$.
- Scalars are denoted in italics. If a scalar and a vector share the same notation, except for absence or presence of bold, then we consider the vector (when written in boldface) and the norm of this vector (absence of boldface). The only exception concerns powers and energies, denoted in sans serif fonts (for example, P), as well as the couple $\mathbf{H}/H$ (magnetic field vector / height of a wave) and $\mathbf{B}/B$ (magnetic induction field / sea state).
- Vectors are written in bold: $\mathbf{v}$. Unit vectors have a circumflex accent: $\hat{\mathbf{v}}$. The coordinates of vector $\mathbf{v}$ in coordinate system $\mathcal{R}$ are denoted by $\{\mathbf{v}\}_{\mathcal{R}}$; this is a triplet of scalar coordinates on which one can perform a matrix operation (which only makes sense once these coordinates are specified).
- Matrices are written in "typewriter" font: `M`.
- Tensors are written in blackboard boldface: $\mathbb{T}$
- $\angle(\mathbf{a}, \mathbf{b})$ is the oriented angle formed by vectors $\mathbf{a}$ and $\mathbf{b}$. Notation $\breve{a}$ is an algebraic rotation angle around vector $\mathbf{a}$. In particular, if a frame $\mathcal{R}(\mathrm{O}, \hat{\mathbf{a}}, \hat{\mathbf{b}}, \hat{\mathbf{c}})$ is being considered, then $\breve{c}$ denotes the bearing and $\breve{b}$ the elevation of a point relatively to $\mathcal{R}$.

Notations

These are the notations used in this dissertation. Vectors defining the frames are given in appendix A.

Scalars

Lower case letters

a_1, a_2, a_3, a_4	Generic constants ("local variables")	
b_1, b_2, b_3, b_4	Generic constants ("local variables")	
c_0	Celerity of light in void, equal to 299 792 458 m/s	[m/s]
$c(K)$	Phase velocity of a wave having wave number K	[m/s]
$c_g(K)$	Group velocity of a wave having wave number K	[m/s]
c_m	Phase velocity of a wave having wave number K_m	[m/s]
c_p	Phase velocity of a wave having wave number K_p	[m/s]
c_{ij}	Coefficients of Cox and Munk's probability function	
$c_{\text{Anis.}}$	Control function (for anisotropic filtering)	
d	Depth of the ocean channel	[m]
d_{FFT}	Dimension of a FFT	
d_y, d_z	Dimensions of an antenna	[m]
d_y^{SAR}	Length of the equivalent synthetic aperture antenna	[m]
dr	Range resolution	[m]
dr_{sol}	Range resolution on ground	[m]
$dr_{\text{az.}}$	Azimuth (cross-range) resolution	[m]
dt_X	Time difference of propagation time due to Doppler effect for a signal transmitted at t_X	[s]
$dr_{\text{ele}}, dr_{\text{az}}$	Resolution on the elevation and azimuthal axis	[m]
f_0	Transmitted signal carrier frequency	[Hz]
$f(t)$	Instantaneous frequency	[Hz]
f_{CM}	Cox et Munk's asymetry function	
$f_{\text{RAR}}(t_X, s)$	RAR raw image	[V]
$f_{\text{SAR}}(t_X, s)$	SAR image	[V]
f_D	Doppler frequency	[Hz]
g_0	Acceleration of gravity	[m/s^2]
$g_{V_b,\theta_b}(K_x, K_y)$	Fonction describing the support of a wake's spectrum	
h	Height of the transmitting antenna, relatively to the ground	[m]
i, j	Generic notation for array indices in image matrices: i is the row index, j is the column index (usual Fortran conventions)	
k_k	Von Kármán's constant, circa 0,4	
m	Number of pulses	
m_0, m_1	Parameters for the Filon integration of P and Q (chapter 3)	
n	Number of pixels in an image	[pixels]

$n_x \times n_y$	Number of pixels in an image, for rows and columne	[pixels]
m	Number of pixels in a window	[pixels]
$n_\rho \times n_\theta$	Number of pixels in a Radon transofrm	[pixels]
n_t	Number of time iterations (anisotropic filtering)	
p	Water pressure	[Pa]
p_{FL}	Exponent of Fung and Lee's capillary spectrum, $p_{\mathrm{FL}} = 3 - \log U_0$ with U_0 in m/s	
p_0	Atmospheric pressure	[Pa]
r_0	Transmitter-to-target distance at distance of closest approach	[m]
r'_0	Receiver-to-target distance at distance of closest approach	[m]
r_J	Exponent for the JONSWAP spectrum	
$r_{\min}$	Minimum transmitter-target-receiver distance	[m]
s	Time corresponding to an arrival time on the range axis in radar imaging ("short time")	[s]
s_d	Detection threshold	
s_L	Exponent of the Longuet-Higgins directional spectrum	
t	Generic time	[s]
t_X	Time at which a pulse atom starts being transmitted	[s]
t_P	Time at which the pulse atom reaches the target	[s]
t_R	Time at which the pulse atom is received	[s]

Capital letters

A	Area of the sea surface	[m^2]
$A_c(z)$	Solution of the continuity equation	[m^2/s]
$A_{V_b,Y}(\theta)$	Kochin's function for a ship of hull Y going at speed V_b	[m]
B	Beaufort sea state	
B_l, B_h	Low and high frequency components of Elfouhaily's spectrum	
B_b	Ship beam	[m]
C_r	"Wavelet correlation" of Kuo and Chen	
D	Fictious antenna displacement length	[m]
D_b	Ship draft	[m]
D_x, D_r	Scalar directivity for antennas, at transmission and reception	
$D_{x,\text{ max. Hertz.}}$	Maximum directivity for a Hertz dipole	
Dp_b	Ship displacement	[kT]
D_j^h, D_j^v et D_j^d	Horizontal, vertical, diagonal detail images at scale j of a wavelets decomposition	

E_0	Amplitude of transmitted signal	[V]
$E_n(t)$	Noise at reception (additive, white, gaussian)	[V]
$E_{n'}(t)$	Noise at reception (additive, white, gaussian) after pulse compression	[V]
E_R	Generic received signal	[V]
E_X	Generic transmitted signal	[V]
$E^{\text{sin, } f_0}$	Truncated sine signal, transmitted at frequency f_0	[V]
$E^{\text{chirp, } f_0, \Delta f}$	Linear *chirped* transmitted signal of carrier f_0 of bandwidth Δf	[V]
$E^{\text{c'}, f_0, \Delta f}$	Linear *chirped* transmitted signal of carrier f_0 of bandwidth Δf, with infinite pulse repetition rate.	[V]
E_X	Average energy of transmitted signal	[J]
E_R	Average energy of received signal	[J]
$\mathsf{E}_{\text{swell}}$	Mechanical energy of swell	[J]
$\mathcal{E}$	Spectrum of the mechanical energy of swell	[J/rad/m] or [J/rad/s]
$F(x, \theta)$	Integral appearing in Kochin's function	
F_J	*Fetch*	[m]
F_p, F_m	Components of Elfouhaily's spectrum	
Fr	Froude number: Fr$=V_b/\sqrt{(g_0 L_b)}$	
G	Green function of the Helmholtz equation	
H	Height of a wave, can be dependent on the wave number K: $H(K)$	[m]
$H_{1/3}$, H_{m_0}	Two definitions of the significant wave height	[m]
H_{flou}	Modulation transfer function, between an ideal Radon transform, and a blurred Radon transform	
H_{MTF}	Modulation transfer function, between the wave elevation map and the image as observed by a radar or optical sensor	
I	Generic image of size $n_x \times n_y$	
$\bar{K}$	Ratio between the wave number K of a wave, with the wave number at gravity-capillarity transition K_m	
K_b	Wave number of the Kelvin wake in the ship's direction of travel	[rad/m]
K_p	Wave number at the maximum of a gravity wave spectrum	[rad/m]
K_m	Wave number at gravity-capillarity transition: $K_m = 363$ rad/m	[rad/m]
K_{max}	Maximum indicative value of the wave numbers K when generating a discrete sea surface map	[rad/m]
$K_{\text{-3 dB, 1}}, K_{\text{-3 dB, 1}}$	Limits of the bandwidth of a gravity wave spectrum	[rad/m]
L	Width of an imaged sea surface area	[m]
L_b	Length of a ship	[m]
L_{min}	Minimum width of a surface area to generate so as to properly capture the wave energy	[m]

L_{PM}	Pierson-Moskowitz spectrum	
L_j^i	Legth of the $i-$th ship of class j	[m]
M	Image blurred by local averaging (low pass filtering)	
M_j	Module of the three detail images of a wavelet decomposition at scale j	
$M_w(x,y)$	Mask, between 0 et 1, to attenuate the spectrum of a synthetic Kelvin wake	
P	Generic point in space (the target)	
P'	Generic point at the surface of the antenna	
N	Noise image	
N_x	Number of points in direction x when discretizing ship hull Y	
N_z	Number of points in direction z when discretizing ship hull Y	
N_θ	Number of points in direction θ when discretizing Kochin's integral	
$P(\theta)$	Integral appearing when computing Kochin's function	
P	Generic power	[W]
P_X	Instantaneous power of transmitted signal	[W]
P_R	Instantaneous power of received signal	[W]
$\mathsf{P}_{\text{totale, 1d}}$	Total power of a 1D sea spectrum	[m^2/rad/m] or [m^2/rad/s]
$Q(\theta)$	Integral appearing when computing Kochin's function	
R	Position of the receiver	
R	A Radon-transformed image: $R = \mathcal{R}I$	
R'	Ideal Radon transform image where spikes are Dirac functions	
R_f	Total reflectance function	
R_a	Reflectance function, ambient component	
R_d	Reflectance function, diffuse component	
R_s	Reflectance function, specular component	
$\hat{R}'$	Estimate of an ideal Radon transform through Wiener filtering	
S, S'	Generic surface, and, abusing the notation, its area	[m^2]
S_w, S_nl, S_t et S_v	Source terms when computing the dead-water wake	[J/rad/m/s]
S_X	Surface of the transmitting antenna, and, abusing the notation, its area	[m^2]
S_{x_0,y_0}	Sine function of equation $x_0\cos\theta + y_0\sin\theta = \rho$	
[S]	Salinity	[g/kg] or [ppm] ou [pss]
[Cl]	Chlorinity	[g/kg]
$\mathcal{S}$	Generic notation for a sea spectrum	[m^2/rad/m]
$\mathcal{S}_{\text{1d}}$	Generic notation for a 1D sea spectrum	[m^2/rad/m] or [m^2/rad/s]
$\mathcal{S}_{\text{2d}}$	Generic notation for a 2D sea spectrum	[m^2/rad/m] or [m^2/rad/s]
$\mathcal{S}_{\text{omni}}$	Generic notation for an omnidirectional sea spectrum	[m^2/rad/m] or [m^2/rad/s]

T	Surface temperature of water	[°C]
T_I	Pulse repetition interval	[s]
T_X	Pulse duration	[s]
T'_X	Pulse duration after pulse compression	[s]
U_0	Wind friction speed	[m/s]
U_{mn}	Polarimetric coefficients of the Kirchhoff approximation	
U_{ref}	Reference wind speed	[m/s]
U_z	Wind speed at altitude z counted in centimetres.	[m/s]
Ur	Ursell number: Ur$=H\Lambda^2/d^3$	
X	Position of the transmitter ("*X-mitter*")	
V_b	Speed of a ship	[m/s]
V_j^i	Speed of the $i-$th ship of class j	[m/s]
$Y(x,z)$	Function describing the shape of a ship's hull	[m]
V_j^i	Hull of the $i-$th ship of class j	
Z_u, Z_c	Slope of the sea surface in the *upwind* and *crosswind* directions	

Lowercase Greek letters

α_c	Half angle at the top of the dead water wake	[rad]
α_{FL}	Philips constant of the Fung and Lee spectrum, $2{,}810^{-3}$	
α_J	Philips constant of the JONSWAP spectrum: $5/4$	
α_m	Philips-Kitaigorodskii generalized equilibrium parameter	
α_{pq}	Polarimetric coefficients of the small perturbation model	
α_{PM}	Philips constant of the Pierson-Moskowitz spectrum, $8{,}110^{-3}$	
β	Half angle at the generic vertex with respect to the axis of the nacire and counted from its bow (chapter 3)	[rad]
β_c	Half angle at the top of the cone of the Kelvin wake: $\beta_c = \arcsin 1/3 \approx 19{,}471°$at sea of infinite depth	[rad]
β_D	Donelan directional spectrum shape parameter	
β_{FL}	Fung and Lee spectrum parameter: 0.74	
β_J	JONSWAP spectrum parameter	
β_{PM}	Pierson-Moskowitz spectrum parameter: 0.74	
γ_b	Angle between the local normal of a facet, and the bisector (Δ_b) of the angle $\widehat{XPR}$	[deg]
γ_c	Dimension parameter characterizing the value of β_c	
γ_s	Shininess term (Phong model)	
γ_J	JONSWAP Improvement Factor Parameter	
ϵ	Arbitrarily small positive quantity	

ϵ_0	Dielectric constant of vacuum: $\epsilon_0 = 8{,}85410^{-12}$ F/m	[F/m]
ϵ_r	Relative dielectric constant of water	[F/m]
$\epsilon_r\text{inf}$	High frequency limit of ϵ_s, approximately 4.9 F/m	[F/m]
ϵ_s	Static permittivity of seawater	[F/m]
ϵ_{EM}	Generic Permittivity	[F/m]
$\zeta(x, y, t)$	Sea surface elevation function	[m]
$\zeta_t(x, y)$	Sea surface elevation function for date t	[m]
$\zeta_t(x, y, t)$	Surface elevation function for an elementary wave	[m]
$\zeta_w(x, y)$	Wake elevation function	[m]
η_0	Vacuum Impedance: $\eta_0 = 119.9169832\mathcal{F} \approx 376.7303\ \Omega$	[Ω]
η, ξ	By definition: $\eta = Z_u/\sigma_u$ and $\xi = Z_c/\sigma_c$	
θ	Direction of propagation of a wake wave (chapter 3)	[rad]
λ_0	Electromagnetic wavelength corresponding to the carrier	[m]
λ_i	Own value associated with the i-th stochastic adapted filter	
$\lambda_{\text{Anis.}}$	Scattering constant (anisotropic filtering)	
κ	Transmission loss term	
κ_1	Weighting term when calculating the Kochin integral (Chapter 3): κ_1 is between about 0.025 and 0.1	
κ_{FFT}	Attenuation constant of the FFT used during the generation of the sea surface	
κ_p, κ_m	Polarization and wind dependency terms in Ward and Wicks' form factor of speckle model	
ν	1) Bearing angle of target (SAR integration); 2) form factor of the K distribution	1) [rad], 2) [-]
$\xi_{\text{el}}, \xi_{\text{az}}$	Angular aperture terms (elevation, azimuth) at -3 dB, such as $\Phi_{\text{el}} = \xi_{\text{el}}$ and $\Phi_{\text{az}} = \xi_{\text{az}}$	
ρ	Seawater density	[kg/m^3]
ρ_0	Air density	[kg/m^3]
ρ_a	Ambient reflectivity parameter	
ρ_d	Diffuse reflectivity parameter	
ρ_s	Specular reflectivity parameter	
ρ_{Doppler}	"Doppler" compression ratio	
ρ_{EM}	Generic electric charge density	[C/m^3]
$\rho_{EM,m}$	Generic magnetic charge density	
$\rho_{EM,ms}$	Generic surface magnetic charge density	
$\sigma(\hat{\mathbf{r}}_x, -\hat{\mathbf{r}}_r)$	"Radar cross section" function	[m^2]
σ	Standard deviation of an image (chapters 6 and 7)	
σ_J	JONSWPAP spectrum parameter	
σ_n	Standard deviation of $n(t)$	
σ'_n	Standard deviation of $n'(t)$	
σ_s	Static conductivity of seawater	[S.m^{-1}]

σ_u, σ_c	Standard deviation of sea slopes in *upwind* and *crosswind* directions	[m]
σ_x, σ_r	"Equivalent area" function of transmitting and receiving antenna	[m^2]
σ_ζ	Standard deviation of function ζ	[m]
θ_1, θ_2	Angles giving a stationary phase when calculating the Kochin integral	[rad]
$\theta_!+$	Special value of the angle θ when calculating the Kochin integral	[rad]
θ_i	Generic angle of incidence	[rad]
θ_s	Generic angle of emergence	[rad]
θ_i^l	Local angle of incidence in P	[rad]
θ_s^l	Local emergence angle in P	[rad]
θ_i^v	Angle of incidence in the wind frame relative to mean sea level	[rad]
θ_s^v	Angle of emergence in the wind frame relative to mean sea level	[rad]
$\underline{\sigma}_x$, $\underline{\sigma}_r$	Normalized "equivalent area" function of the transmitting and receiving antenna: $\underline{\sigma}_x = S_x\sigma_x$	[m^2]
τ	Period of a wave	[s]
τ_r	Surface relaxation time	[s]
τ_s	Water Surface Tension	[N/m]
$\phi(\theta)$	Kochin function phase	[rad]
ϕ_s	Generic angle formed by the direction of the radio wave reflected by the surface, with the x-axis of the current coordinate system	[rad]
ϕ_s^l	Same meaning as ϕ_s, relative to the local facet coordinate system	[rad]
ϕ_s^v	Same meaning as ϕ_s, relative to the global wind frame relative to mean sea level)	[rad]
ϕ_{rb}	Radar trajectory to ship's trajectory angle	[rad]
$\phi_{\mathrm{SAR}}(t)$	Phase history of a point during SAR integration	[rad]
ψ	Direction of a wave relative to the direction of the wind	[rad]
ψ_0	Wind direction relative to the x axis in the world frame	[rad]
ψ'	Direction of a wave relative to the x axis in the world frame	[rad]
ω	Pulsation of electromagnetic wave	[rad/s]
ω_0	Pulsation of electromagnetic carrier	[rad/s]
$\omega_i, i = 0..N_z$	Weight for Filon quadrature when computing F (chapter 3)	
$\omega'_i, i = 0..N_x$	Poids for Filon quadrature when computing P and Q (chapter 3)	

Uppercase Greek letters

Δ	Asymmetry ratio "*upwind/crosswind*" of Elfouhaily *et al.*	
(Δ_b)	Bisector of angle $\widehat{XPR}$	
$\Delta d_{\text{az.}}$	Antenna width in azimuth at target	[s]
Δf	Transmitted signal bandwidth	[Hz]
Δf_D	Doppler frequency shift such as $\Delta f_D = f_D - f_0$	[Hz]
ΔK	Discretization step of wavenumbers	[rad/m]
Δt	Transceiver-target time of flight	[s]
$\Delta t_{\text{illum.}}$	Duration of illumination of a target	[s]
ΔT	Temperature difference	[°c]
Δx	Discretization step of an image in width	[pixels]
Δy	Discretization step of an image in height	[pixels]
$\Delta\theta_d$	Discretization step of a Radon transform for angles	[rad]
$\Delta\rho_d$	Discretization step of a Radon transform for distance	[pixel]
Z_w	Fourier transform of ζ_w	
Λ	Wavelength of an ocean wave	[m]
Λ'	Wavelength of an ocean wave at Bragg resonance length	[m]
Λ_b	Wavelength of a ship wake wave on the ship longitudinal axis	[m]
Φ	Pressure potential function for swell	[m^2/s]
Φ_e	Elementary pressure potential function for a 2D wave	[m^2/s]
Φ_{az}, Φ_{el}	Angular aperture in azimuth, elevation	[rad]
Ω	Pulsation of a wave	[rad/s]
Ω_p	Peak pulsation for a wave spectrum	[rad/s]
Ω_{wa}	Inverse wave age	

Vectors

Lowercase letters

$\mathbf{f}$	Generic force	[N]
$\mathbf{h}_i$	i-th stochastic matched filter, associated with eigenvalue λ_i	
$\mathbf{j}$	Electric current density	[A/m^2]
$\mathbf{j}_m$	Magnetic current density	[V/m^2]
$\mathbf{j}_s$	Surface electric current density	[A/m^2]
$\mathbf{j}_m s$	Surface electric current density	[A/m^2]
$\hat{\mathbf{d}}$	Specular direction given by Snell-Descartes' law	
$\hat{\mathbf{l}}$	Vector from the target pointing to the light source	
$\hat{\mathbf{n}}$	Normal to a surface	
$\hat{\mathbf{p}}_x = (0, \hat{p}_y, \hat{p}_z)$	Polarimetric vector of the transmitting antenna	
$\hat{\mathbf{p}}_r$	Polarimetric vector of the receiving antenna	

$\mathbf{q}$	Vector parallel to the bisector of the angle formed by the incident radio wave at the surface and the reflected wave; components $\{[q_u, q_c, q_\zeta]\}_{\mathcal{V}}$	
$\mathbf{r}$	Transmitter-target vector; $r = \|\|\mathbf{r}\|\|$ is the origin-target distance of the surface (in Chapter 3); $\mathbf{r}$ is the origin-target vector (appendix C)	[m]
r	Target-receptor vector (general case); vector origin-target point of the surface (appendix C)	[m]
$\mathbf{s}$	Hydrodynamic current vector	[m/s]
$\hat{\mathbf{v}}$	Vector starting from the target and pointing to the camera	
$\mathbf{w}$	Fenêtre de signal	
$\mathbf{z}$	Observation vector	
$\omega = [\omega_x, \omega_x]$	Pulsation vector of an electromagnetic wave, or an arbitrary signal (depending on the context)	[rad/s]

Capital letters

$\mathbf{B}$	Total magnetic induction field vector	[Wb/m^2]
$\mathbf{D}$	Total magnetic induction field vector	[C/m^2]
$\mathbf{E}$	Total electric field vector	[V/m]
$\mathbf{E}^i$	Incident electric field vector	[V/m]
$\mathbf{E}^r$	Reflected electric field vector	[V/m]
$\mathbf{E}_X$	Electric field vector on the surface of the transmitting antenna	[V/m]
$\mathbf{E}_R$	Electric field vector on the surface of the receiving antenna	[V/m]
$\mathbf{F_E}$	Diffracted electric field vector	[V/m]
$\mathbf{H}$	Total magnetic field vector	[A/m^2]
$\mathbf{K} = [K_x, K_y]$	Wave vector of a wave	[rad/m]
$\mathbf{K'}$	Wave vector of a wave at the Bragg frequency	[rad/m]
$\mathbf{V}$	Velocity vector of a particle of water, of components $[u(x,y,z,t), v(x,y,z,t), z(x,y,z,t)]$	[m/s]
$\mathbf{V_X}$, $\mathbf{V_R}$	Transmitter and receiver speed (bistatic case)	[m/s]

Matrices, tensors

$\mathtt{B}$	Matrix to go from *forward scattering* convention to *backscattering* convention	
$\mathtt{D}_x, \mathtt{D}_r$	Polarimetric directivities of transmitting and receiving antennas	
$\mathtt{N}$	Complex Gaussian white noise matrix of zero mean and unit standard deviation, dimension $n \times n$	
$\mathtt{P}$	Signal variance-covariance matrix	

$\mathtt{P}_x$	Polarimetric matrix of the transmitting antenna	
$\mathtt{P}_r$	Polarimetric matrix of the receiving antenna	
$\mathtt{Q}$	Noise variance-covariance matrix	
$\mathtt{R}_{\theta_d}$	Rotation matrix of angle θ_d	
$\mathtt{S} = [s_{pq}]$	Normalized amplitude polarimetric scattering matrix (complex)	$[\mathrm{m}^2]$
$\mathtt{S}_{2d}$	Matrix of dimension $n \times n$ containing the spectrum of the simulated surface	
$\mathtt{S}^0 = [s^0_{pq}]$	Normalized amplitude polarimetric scattering matrix (complex)	
$\mathtt{\Sigma} = [\sigma_{pq}]$	Non-normalized polarimetric radar cross section matrix (complex)	$[\mathrm{m}^2]$
$\mathtt{\Sigma}^0 = [\sigma^0_{pq}]$	Normalized polarimetric radar cross section matrix (complex)	
$\mathtt{V}$	Intrinsic matrix of a camera	
$\mathtt{z}_{t=0}$	Matrix representing the sea surface at $t = 0$, size $n \times n$, surface width: L meters	
$\mathtt{Z}_{t=0}$	Fourier transform of the matrix representing the elevations, $\mathtt{z}_{t=0}$, at t =0.	
$\mathbb{T}$	Viscous stress tensor	[N.m]
$\mathbb{O}$	Zero tensor	[N.m]

Functions, operators and miscellaneous symbols

$\jmath$	Imaginary number: $\jmath^2 = -1$
$\star$	Hermitian operator (transpose conjugate)
$x \mapsto \mathrm{sinc}$	Cardinal sine ($\mathrm{sinc}(x) = \sin(x)/x$)
$t \mapsto \wedge(t)$	Triangle function (defined at eq. 1.5)
$\langle \bullet, \bullet \rangle$	Cross-correlation operator
amb($\bullet$,$\bullet$)	Ambiguity function
$\mathcal{F}[\bullet]$	Fourier transform operator
$\mathcal{H}[\bullet]$	Hough transform operator
$\mathcal{R}[\bullet]$	Radon transform operator

Introduction

Behold, the sea itself,
And on its limitless, heaving breast, the ships;
See, where their white sails, bellying in the wind,
speckle the green and blue,
See, the steamers coming and going, steaming in
or out of port,
See, dusky and undulating, the long pennants of
smoke.
Behold, the sea itself,
And on its limitless, heaving breast, the ships.

– Walt Whitman

This thesis was started in 2004. That year marked the hundredth anniversary of the direct ancestor of the current radar, the *Telemobiloskop*, invented in the German Empire by Christian Hülsmeyer [65]. However, like any invention, radar is not the brain child of a single person: it follows from a long chain of discoveries that is impossible to summarize in a few pages but for which it is still necessary to give a brief outline. It is possible to place –somewhat arbitrarily– the formal beginning of the work on electromagnetic waves in 1861, when James Clerk Maxwell published his seminal article *On Physical Lines of Force* where the laws of electricity and magnetism discovered previously by Gauss, Ampère and Faraday were unified; and which were later put in their final vector form, by Heaviside, in 1884 [20].

Then began the long series of technical innovations, often made up of trial and error and fortuitous discoveries, which marked the beginning of the history of radar and radio.

It was therefore in 1904 that Hülsmeyer filed a patent for his *telemobiloskop*, a device designed to, on the first hand, detect the presence of ships in absence of visibility by using the reflection of electromagnetic waves on metallic surfaces and to second, to give an indication of the direction of arrival by adjusting the orientation of the radio antenna. It was a relatively rustic device, since it did not measure the distance. The signal was a burst generated using a spark; and this signal was transmitted using a primitive antenna resembling what is today called a Yagi antenna. Prospects were lukewarm, and Hülsemeyer's invention ended with commercial failure.

The potential of such an instrument for aerial surveillance was not yet perceived, prob-

ably because it was not yet developed. During the First World War and the post-war period, anti-aircraft early warning was essentially based on a network of human lookouts, and it was only fortuitously that it was discovered, in various parts of the world, that the passage of an aircraft in the direct travel line between a radio transmitter and a receiver could disrupt the transmission. These phenomena were then studied, then exploited for the purpose of detection, by crisscrossing the land with a mesh of transmitters and receivers, emitting in continuous wave, and detecting the passage of an aircraft by the beats caused by interference of the emitted wave with the reflected wave [29]; these are the so-called *radio fences*, a technology still used today for some anti-intrusion applications.

It was during the 1930s that radar began to acquire its final form, with work carried out in particular in the United States, France, the United Kingdom, Japan and Germany [29, 83, 190]. Thus, it was just on the eve of the Second World War that radar was born. The war made it possible to carry out its first operational use, to refine the doctrine of use, and to observe some defects and some new unexpected uses.

In the aftermath of the war, radar found new civilian uses, from air traffic control to meteorology, imagery of the Earth's surface and that of other planets. It also regained the first function for which it had been developed: maritime surveillance. It was also during the 1950s that the concept of synthetic aperture imaging was formulated: indeed, it was in 1951 that Carl Wiley, an engineer at Goodyear, formulated its theory [80]. The first experimental tests were carried out as early as 1952 using optical techniques to perform the Fourier transform, because the computing power needed to carry out the algorithms numerically was not available at the time. It was also necessary to wait for the rediscovery of the fast Fourier transform algorithm by Cooley and Tukey in 1965 [45] to be able to envisage a digital application in real time. Indeed this algorithm plays an essential role for signal processing.

It was in 1978 that Seasat made its flight. This satellite was the first to be put into orbit with a synthetic aperture radar on board. In addition, it was specifically designed to image the sea. The mission was a success: it highlighted the high visibility of ocean waves on the radar, but also of the wakes of ships or internal waves generated by what appeared to be submarines [166], thus opening the possibility of maritime surveillance applications from space. This unexpected result –because the visibility of the wake is significantly lower in traditional coastal radar or on-board radar configurations, due to the lower shaving angle– has prompted ambivalent comments from the Pentagon. The satellite stopped working after three months, officially due to a failure [206]; but in fact, many proponents of the "conspiracy theory" suggest that this breakdown was only a cover-up story mounted by the US intelligence services to prevent the publication of the images [33]. Since then, the mastery of high-resolution radar systems in orbit has been a jealously guarded technology, which offers great possibilities for maritime surveillance, for civilian or military purposes. The major interest of a radar in orbit comes in particular from their great swath, which makes it possible to scan a large area quickly: of the order of several hundred kilometers. In addition, unlike optical sensors, the radar makes it possible to see through clouds. The disadvantages of a such a system are however a very important cost as well as the short revisit period above a point on the globe, preventing for example from imaging the same ship on two successive passes and to follow its trajectory as finely as a coastal radar would. To compensate for the small revist period, it is possible to use satellite constellations, which has an impact on costs. Still, satellite radar is a very fashionable field in the scientific literature, judging by the impressive number of publications in this field alone.

With the rise of unmanned aircraft (drones) since the late 1990s, we can however design an interesting alternative to satellites in the form of a group of drones monitoring a surface

using optical sensors, infra-red or radar. The advantage of such systems is that their cost is much weaker than a satellite, as they require constraints weaker techniques and can make use of components available off the shelf. Even more economical alternatives in the form of airships have also been considered (e.g. by the United States, with the JLENS cruise missile defense program – *Joint Land Attack Cruise Missile Defense Elevated Netted Sensor System*). An advantage of airborne systems is that they are of better resolution than a radar mounted on a satellite: their sensors therefore make it possible to see things that would be impossible to discern from space. In addition, an aircraft is much more responsive and less expensive to reposition on a specific area, than a satellite.

Bistatic and monostatic systems

There are two types of radar configurations (Skolnik [158]): on the one hand, monostatic configurations, where the transmitter and receiver are located in the same place, often sharing the same antenna; and on the other hand bistatic systems, where the transmitter and receiver are located in different locations. The vast majority of radars today are monostatic, but bistatic systems were historically used first, before this technique was abandoned. Back then, the technology did not allow to use the same antenna in transmission and reception: it was necessary to wait for the invention of the *duplexer* to allow to switch the radar in two modes, one capable of transmitting at high power, and the other capable of processing the incoming low power signals; on the other hand, the technology of continuous wave "radio fences" was fundamentally bistatic. Nevertheless, the principle of bistatic radar has since experienced several resurgences [193] (pp. 35-57): the first one was in the 1950s, when the first missiles were developed. Indeed, the technology did not allow to put a radar transmitter on board a missile; the missile was only equipped with a receiving antenna, and processed the radar signals emitted by the aircraft that had launched the missile and which reflected on the opposing target. The last resurgence began in the 1980s and continues to this day. It is partly explained by the democratization of powerful computing means (FPGA, "software-defined radio") and on the other hand by the need to improve the performance of current radars, especially against stealth or very small targets.

The context of marine surveillance

Function The function of a maritime surveillance radar is to detect targets on the surface of the water: ships, submarine on the surface; or to image the sea in search of man-made manifestations: ship wakes, oil trails left following illegal degassing at sea or oil spills, *etc.* Historically, maritime surveillance has always been aimed at securing transit areas with high traffic, such as the Ushant (Ouessant) rail in France, but also to prevent overexploitation of fishing zones, to monitor the exclusive economic zone of States. The current geopolitical context means that maritime surveillance is also becoming crucial to limit illegal immigration, as well as piracy. In this context, it is generally small fast boats ("*go-fast crafts*") that must be detected [204], or even semi-submersibles, a technology that is currently beginning to be used by cartels for drug trafficking [26].

Means In maritime surveillance, commonly used sensors are mainly coastal radars (typically mounted on semaphores) or mounted on patrol ships. The advantage of such systems is the cost of operation, relatively small (for coastal stations), coverage excellent schedule, and good availability. The spatial coverage is by against reduced to an area of a few tens of kilometers radius, which does not changes not over time, and that is strongly related

to the local geography. Indeed, the coast can partially hide certain areas and the altitude of the radar influences its maximum range. Optical and infrared monitoring also plays an important role in the military field. Earth observation satellites are set to play an increasing role in maritime surveillance, provided they have a processing chain ranging from an adequate sensor, to a field response team, appropriate algorithms and a chain of command and transmission. The journalist Nicolas-Jean Brehon, in an article in Le Monde (6 June 2000), summed up the importance of this channel by recounting the following facts: an illegal degassing by an oil tanker sailing outside an authorized area was spotted by ERS-1 as early as 1991 (the year of its launch), but: "*due to lack of coordination and responsiveness, the image of the double offence was not exploited*". Fortunately, the situation has changed a little by the time Brehon wrote his paper, without being perfect yet: "*In 1996, ERS 1 acquired an image showing an illegal degassing. Local authorities reacted, took samples in the sea and in the ship tank. Penalties exceeded one million dollars and thirteen months of jail time.*"

Operational requirements Here I break down ten major objectives to be achieved for a surveillance system; these can be thought of as the "ten commandments" to abide by, to make it a useful system from an operational point of view:

1. **maximizing spatial coverage**, expressed in square kilometres: the largest possible area should be monitored;

2. **maximize hourly coverage**: the same area should ideally be monitored constantly, which is not possible with an airborne system or satellite, which is mobile by design. In this case we then want to maximize the *recurrence period*, the length of time that separates two passages of the vector, within the range of the point to be monitored;

3. **maximize availability**: as a complementary concept of hourly coverage, availability expresses the ability of the system to function at all times and not to be, by example, weather-dependent (due to, for instance, bad weather preventing an aircraft to fly, or clouds masking the scene for an optical sensor), or dependent upon technical constraints preventing the system to work: breakdowns, refueling, maintenance.

4. **have a good detection rate**: the system should as far as possible avoid missing a target in the area to be monitored;

5. **have a low false alarms rate**: ideally, we do not want to provide false detections, which would have the effect of overload operators or actors who have to decide on an intervention following a detection;

6. **have a low reaction time**: in case the vessels are fast, it is important that the delay between the acquisition of the signal by the sensor, the processing of this signal, as well as the reaction of an intervention team be as small as possible. This period may vary depending on the type of target to be detected. For a large cargo-type vessel, the speed of is of the order of twenty knots and the heading is nearly constant, which means that if the time between acquisition and reaction is of the order of half an hour, the ship will have moved 39 km with an easily predictable trajectory and it will be possible to reacquire the target, for example by redirecting a patrol ship or aircraft equipped with radar. In the case of a small, fast target, the delay should be decreased sharply or the information would become outdated. The need for an adequate processing chain is especially crucial for the use of satellite signals.

7. **have a low cost**, both during design and installation (launch costs for a satellite, for example) but also for the operation (carrier fuel, staff salary, etc.) and for maintenance. Here we touch on the notions of *total cost of ownership*, which is often neglected. Pedersen *et al.* [140] claim that the average implementation costs per square kilometre being monitored, for a satellite or an aircraft, are more or less the same (about 0.08 euros), but it should also be mentioned that the choice ought also to be made on the complementarity of the two solutions. In addition, mass production also makes it possible to significantly reduce costs; thus satellite ERS-2, based essentially on the same elements as ERS-1, was developed at a cost 60% less than ERS-1 [61], which was itself based on the SPOT platform. The average annual operating cost is estimated at 5.4 million euros [50][6] while the overall cost of the ENVISAT programme, the successor to ERS, is estimated at 2.9 billion euros (same source, after inflation correction).

8. **have a long service life**: the guaranteed service life is usually the order of only a few years for a satellite, the duration of additional operation is not contractually guaranteed. For example, the effective lifespan of the ERS-1 satellite was almost nine years, for a three-year contractual life; ERS-2, launched in 1995, is still in flight, although increasingly affected by failures.

9. **be discreet** (in military applications). It is easily shown that the decrease in the power received, in an active monostatic configuration, is in $1/r^4$ (where r is the radar-target distance). In a passive ("listening") situation, the attenuation is in $1/r^2$ only, which means that at the same received power level, the radar is detected from much further by the target than the radar detection range. Solutions have been proposed to limit the probability of radar emission detection, such as frequency agility techniques.

10. **have a low vulnerability** (in military applications). Vulnerability is inversely proportional to discretion. Two kinds of vulnerabilities can be distinguished. The first is a "hard" vulnerability that results in the possibility of the destruction of the radar by an anti-radar missile that guides itself on its emissions. A bistatic radar is less subject to this kind of threat. The second vulnerability is of the "soft" kind, it is related to the sensitivity to interference. For a bistatic radar, the receiver can optionally be repositioned to limit the influence of a jammer. For a monostatic system, it is not necessarily possible to reposition the sensor, but it is sometimes possible to dynamically reconfigure the antenna diagram, in the case of an active antenna, so as to limit the influence of the jammer.

As part of this thesis, I shall try to keep these ten requirements in mind. While it goes without saying that I will try to optimize the rate of good detections and minimize the rate of false alarms, I will as much as possible transfer the constraint of reaction time onto the calculation time, which must be low and ideally achievable on an embedded platform. Similarly, the coverage and cost requirements will be used to determine a configuration that can be used in a practical way, in the last chapter.

Objectives, approach and contributions of my work

The objective of my work is to see if it is possible to contribute to the improvement of maritime surveillance through the use of bistatic systems. Among all the detectable

[6] After conversion into euros of the 30 million francs (year 2000) given in the report and correction of inflation (17.9 %) between June 2000 and December 2009.

elements in the image, I was interested in the wakes generated by ships: I intentionally ignored the problem of detecting the ship itself, because this problem is already very widely covered in the literature. Crisp [49] summarizes the reasons why ship detection is now preferred to wake detection: on the one hand, the ship's reflectivity is independent of the sea state, on the other hand, stationary ships do not have a wake; the wake is often not very visible at wide angles of incidence; and finally, wake detection is computationally intensive. Nevertheless, several arguments can go in favor of wake detection. On the one hand, the wakes are often visible over great distances, several tens of kilometers. On the other hand, a wake provides a large amount of information about a ship: first of all its heading and an indication of presence, but also its speed, as well as potentially its dimensions and the shape of its hull. Finally, if it is possible for a ship to have a "stealth" shape, it will be more difficult for it to hide its wake[7].

In my work, I have taken a two-step approach. The first step concerns a modeling of the received signal depending on the physical parameters describing the scene: the ship, and its environment. The second step aims to explore the possibility of going back from the received signal to the scene, namely to detect the wake and to retrieve the parameters describing the motion of the ship (ship velocity and heading). It is therefore quite natural that the dissertation was divided into two parts. The approach I have implemented is illustrated in the figure 1.

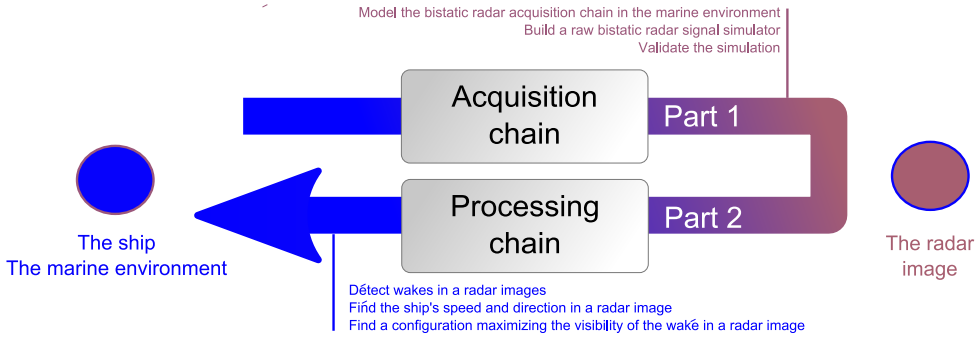

Figure 1: *The two-steps approach of this dissertation*

First part I start by modeling the entire radar acquisition chain, the elements of which are shown in figure 2. The chain as a whole is discussed in chapter 1, then I focused on the modeling of the maritime surface in the chapter 2, the wake (chapter 3) as well as the reflection of radar waves on the sea surface (chapter 4). In the chapter 5, the various elements described in the previous chapters are unified as part of the presentation of a simulator of raw bistatic radar signals. With this simulator, I have obtained what seems to us to be the first series of bistatic synthetic antenna radar images in the maritime environment, since no similar image has yet been published in the literature to the best of my knowledge. I then validated this simulation against experimental data gleaned from the literature in the monostatic case, especially from the point of view of speckle noise. Since the scene is represented by a map of wave heights cut into facets, I also discussed the problem of choosing good discretization steps: this is a recurring problem in the context, but often treated only very lightly in the literature.

[7]However, when designing a ship, resistance to advancement is optimized, which has the collateral effect of limiting the amplitude of wake waves. The optimization of the ship can only be done for a small range of precise speeds, so there are still speeds where the ship has a more visible wake. That said, the nominal cruising speed –the one that the ship will use the most– is that where resistance, and ship wake amplitude, is smallest...

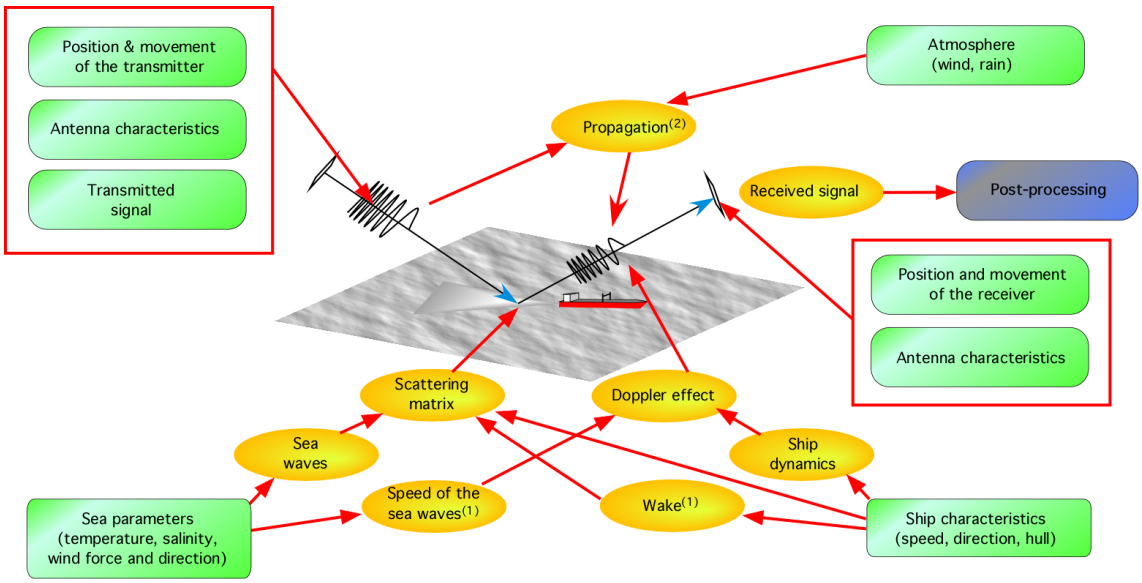

Figure 2: *The bistatic radar acquisition chain described, modeled and simulated in the first part. (1) linear model only, (2) straight line propagation without atmospheric absorption. The green boxes represent the parameters, the yellow ellipses represent the phenomena, and the red arrows represent the dependency relationships.*

Second part In the second part of the dissertation, I try to find the information of the presence of a ship in a radar image from its wake, as well as its heading and speed, if possible. Initially (chapter 6), I was interested in the detection of the so-called "dead water" wake in satellite radar images. This wake presents itself as a dark line in the images. After a state of the art, I implemented and tested four typical algorithms on synthetic data in order to evaluate them comparatively. In a second step (chapter 7), I considered the problem of detecting Kelvin wakes in high-resolution images. I started by identifying a number of criteria for choosing the best imaging configuration *a priori*; this configuration being possibly bistatic. Then, I proposed an algorithm for detecting and analyzing the wake of Kelvin, to find the direction of movement of the ship, as well as its speed. This algorithm is based on the location properties of the wake spectrum in the Fourier transform of images. It also makes use of a relatively recent[8] extension of the notion of matched filtering: the *stochastic matched filtering* (Cavassilas and Xerri [37], Courmontagne [47]). The algorithm also works for spatial images acquired in the optical field and it is on such images that a first validation was done.

[8]Note at translation time (2022): I recently found that these methods are actually dating back to (at least) the early 1970s and are known under various names depending on the scientific community; this is discussed in the appendix dedicated to Stochastic Matched Filtering.

Part I

Simulation of bistatic, polarimetric synthetic aperture radar images of marine scenes

Chapter

1 Modeling the acquisition chain

Contents

In this chapter, the various elements of the bistatic radar acquisition chain are reviewed, following the figure 2 of the Introduction. This figure naturally serves as a guide for the outline of this chapter, and more generally for the first part of this work.

In order, I consider the transmitted signals (section 1.1), with a discussion on the choice of frequency bands, as well as an introduction to the notion of pulse compression. Then antennas are briefly discussed (section 1.2), describing the shape of the field emitted by an antenna as part of polarimetric radar, as well as the case of reception. We discuss in a third step (section 1.3) the interaction of the emitted wave with the atmosphere as well as the imaged surface. Since this discussion requires modeling the surface, as well as discussing electromagnetic models, this part serves only as an introduction to the problem, and will be further developed in chapters 2, 3 and 4. Once these points 1.1, 1.2 and 1.3 are covered, they are unified in the equation of the polarimetric bistatic radar, established

in the section 1.4. This equation is the mathematical counterpart of the figure 2 of the introduction. Finally, in section 1.7, I conclude by explaining the concept of synthetic aperture, which I briefly present in the monostatic case as well as in the bistatic case, with an application in a simple bistatic case. The calculation code used in this demonstration is the one that was developed as part of this work to process the signals simulated in chapter 5. It corresponds to the "post-processing" box in figure 2.

Some of the elements presented in this chapter were published in the journal paper "Bistatic radar imaging of the marine environment. Part I: theoretical background" [9].

1.1 The transmitted signal

Depending on the application, the transmitted signal can vary significantly. These signals are generally modulated over a fairly narrow bandwidth Δf centered around carrier frequency f_0, which corresponding wave length is denoted by λ_0.

1.1.1 Choosing the carrier frequency

Several considerations have an influence on the choice of the carrier frequency. Here are listed the most important factors coming into play:

Target visibility The target is visible from the moment where the wavelength is significantly smaller than the typical size of the structures of the target. If, on the contrary, the wavelength is much larger than the structures of the target, then the scattering of the wave by the target is done through the Rayleigh scattering mechanism. The reflectivity of the target, in the Rayleigh zone, is in λ_0^{-4} and is rapidly decreasing towards zero. Concretely this means that the structures much smaller than the wavelength are invisible (transparent). For instance, a very long-wave airborne radar used to image a forest will only see the surface of the ground and not the trees; at intermediate frequencies, it will see the trunks and branches, but not the leaves; while at very high frequencies, it will only see the canopy.

Size of the transmitter and receiver To be effective, antennas must have a size that is at least of the order of magnitude of the wavelength of the signal to be transmitted. If the antenna must be small, it will have to use small wavelengths. Mechanical considerations (like resistance to wind, maximum torque for the motor rotating the antenna) can also affect the size of the antenna.

Maximum range of the radar Generally speaking, a large wavelength (HF bands) will allow to take advantage of propagation and reflection on the ionosphere, which makes it possible to have ranges reaching thousands of kilometers (over-the-horizon radars). The high frequencies are more sensitive to atmospheric absorption, which limit the range.

Law The use of radio frequency bands is subject to approval by States, which in turn are subject to deliberations within the International Telecommunication Union. Thus it is impossible to choose an arbitrary frequency and very hard to have access to a frequency near the "ideal" frequency needed for a pratical application, due to the pressure of competition and lobbying. Appendix B, which presents the characteristics of several current radars, clearly shows that frequencies and transmission bands are standardised. In this work, I will therefore use these frequencies in the simulations.

1.1.2 Common frequency bands

The frequency bands follow a conventional classification set up during World War II by the Allies to categorize their own systems and those of the Germans. This classification has since been used by the IEEE learned society (IEEE 521-1984 standard) and the International Telecommunication Union. Table 1.1 shows some of these bands, as commonly used in radar. Higher and lower frequency bands do exist, but they are not mentioned because they are not needed in this work.

Band	f_0	λ_0	Comment
HF	3-30 MHz	10-100 m	*High frequency.* Used by over-the-horizon radars
P	<300 MHz	>1 m	For "*Previous*", used *a posteriori* to name the early English radars of the *Chain Home* system.
VHF	50-330 MHz	0,9-6 m	*Very High frequency.* Very long range radars, or ground penetrating radars.
UHF	300-1000 MHz	0,3-1 m	*Ultra High frequency.* Long range radars, used also for ground penetration or to see through foliage.
L	1-2 GHz	15-30 cm	For "*Long*" wavelengths. Used for Seasat, and for GNSS, WiFi, cell phones.
S	2-4 GHz	7,5-15 cm	For "*Short*" wavelengths.
C	4-8 GHz	3,75-7,5 cm	For "*Compromise*", a compromise between S and X bands for satellite transponders and weather radars; also used experimentally for marine radar imaging.
X	8-12 GHz	1,67 2,5 cm	During World War II, used for anti-aircraft artillery (X for "*crosshair*"). The band most often used for marine radars.
Ku	12-18 GHz	1,67-2,5 cm	Band under K-band (subscript "u" meaning *under*), for high resolution imaging, satellite downlinks.
K	18-27 GHz	1,11-1,67 cm	From German "*Kurz*", short. Often used for weather radars since it is sensitive to droplets of water suspended in clouds.
Ka	27-40 GHz	0,75-1,11 cm	Band above K-band (subscript "a" meaning *above*). Used for short range speed measurement "radar guns", and automobile collision avoidance radars.

Table 1.1: *Conventional naming of radio and radar bands. In this work we use L-band to K-band, with a focus on X-band, which is very used for marine surveillance.*

1.1.3 The shape of the transmitted signal

We denote by $E_X(t)$, the signal emitted as a function of time. First of all, let us distinguish between continuous wave radars and pulse radars.

Continuous wave radars These radars typically work by emitting a carrier frequency signal f_0 frequency modulated by a sinusoidal signal over a band Δf. This emitted signal is superimposed on the signal reflected by the target. The period of the beat between the transmitted signal and the received signal then makes it possible to go back to the distance. This principle is used on most radio altimeters as well as on some radars guns used by the police to monitor traffic.

Pulse radars They make up the majority of radar systems. They periodically transmit pulses separated by a period of silence. Each pulse has a duration T_X and is transmitted at *pulse repetition rate* T_I, which inverse is known as the *pulse repetition frequency* (PRF).

The simplest signal a pulse radar can transmit is arguably a sinusoidal pulse of carrier frequency f_0 and amplitude E_0:

$$E_X^{\sin,\, f_0}(t) = \begin{cases} E_0 e^{\jmath 2\pi f_0 t} \text{ if } kT_I \leq t < kT_I + T_X, k \in \mathbb{N} \\ 0\text{else} \end{cases} \tag{1.1}$$

However today, other waveforms are used, that offer better performance.

1.1.4 Resolution and pulse compression

This paragraph explains why other waveforms are preferred today[1]. For every transmitted signal $E_X(t)$, the received signal can always be written:

$$E_R(t) = \kappa E_X(t - \Delta t) + E_n(t) \tag{1.2}$$

where Δt is the transmitter-target-receiver time of flight[2] and κ is an attenuation factor. The received signal is corrupted by an additive noise $E_n(t)$ considered as white and Gaussian, with standard deviation σ_n and zero mean. This noise is for instance thermal noise in the transmitting and receiving chain. It can be shown[3] that the filter maximizing the signal-to-noise ratio at reception is the matched filter, obtained by intercorrelating the received signal with the transmitted signal or, equivalently, by convoluting the conjugate and time-reversed transmitted signal with the received signal:

$$\langle E_X, E_R \rangle(t) = \int_{t=0}^{+\infty} E_X^\star(t') E_R(t + t') dt' \tag{1.3}$$

This can be done using either a digital or an analog (optical) computer[4].

Matched filtering for truncated sine pulses Assuming the pulse repetition frequency is infinite (which does not change the end result but simplifies the equations greatly), it comes:

$$\langle E_X^{\sin,\, f_0}, E_R^{\sin,\, f_0} \rangle(t) = \kappa E_0^2 \wedge \left(\frac{t - \Delta t}{T_X} \right) e^{\jmath 2\pi f_0 (t - \Delta t)} + E_{n'}(t) \tag{1.4}$$

In this expression, $\wedge$ is the triangle function:

$$\wedge(x) = \begin{cases} 0 \text{ if } x \in]-\infty, -1/2[\cup]-1/2, +\infty[\\ 1 + x/2 \text{ if } x \in [-1/2, 0] \\ 1 - x/2 \text{ if } x \in]0, 1/2] \end{cases} \tag{1.5}$$

and $E_{n'}(t)$ is a centered additive white Gaussian noise of standard deviation $\sigma_{n'} = \sigma_n E_0 \sqrt{T_X}$.

[1] This paragraph is very close to the "*Pulse compression*" article in Wikipdia, for which I contributed the initial version on December 14, 2006 and which I still regularly curate.

[2] See paragraph 1.5.2 for the computation of Δt.

[3] In appendix D, in a more general case.

[4] Note added when translating: intercorrelation can be done in the Fourier plane. Yet, it is possible to perform the Fourier transform using a lens: if a transmissive object illuminated by coherent light is placed one focal length in front of a convergent lens, then its Fourier transform is formed one focal length behind the lens. Optical correlation is done using several kinds of optical setups, the earliest being known as the Vander-Lugt correlator (1963). The data is printed or etched onto a translucent medium (like photographic film), known as a spatial light modulator (SLM) where the amplitude and sometimes the phase is controlled; the SLM is then lighted by a laser, the image fed into the correlator, and the result captured by a camera. Today, there exist computer-controlled SLMs behaving as small screens with HDMI input. This can be used also to design computer-controlled optical "phased arrays" or holographic systems. There are still technical challenges to solve before these become mainstream devices.

If two pulses come back (nearly) at the same time, the intercorrelation is equal to the sum of the intercorrelations of the two elementary signals. To distinguish one "triangular" envelope from that of the other pulse, it is clearly visible that the times of arrival of the two pulses must be separated by at least T_X so that the maxima of both pulses can be separated. If this condition is not met, both triangles will be mixed together and impossible to separate. The logical conclusion is that, *to increase the resolution, it is necessary to decrease the duration of the pulse.*

The instantaneous transmitted power is:

$$\mathsf{P}_X(t) = \frac{1}{2\eta_0}|E_X|^2(t) \tag{1.6}$$

This power is written in Watts, and η_0 is the impedance of void. The average transmitted energy is:

$$\mathsf{E}_X = \int_0^T \mathsf{P}_X(t)dt = \frac{1}{2\eta_0}E_0^2 T_X \tag{1.7}$$

Similarly the energy of the received signal is $\mathsf{E}_R = \kappa\frac{1}{2\eta_0}E_0^2 T_X$. The signal-to-noise ratio at reception is then:

$$\rho'_{\text{sin}} = \frac{\mathsf{E}_r^2}{\frac{1}{2\eta_0}\sigma_{n'}^2} = \frac{\kappa^2 E_0^2 T_X}{\sigma_n^2} \tag{1.8}$$

The signal-to-noise ratio increases with the length of the pulse (all other parameters being equal). For the signal to remain exploitable, the pulse must therefore stay long enough, which is the opposite of what is needed for resolution.

Matched filtering with a linearly frequency-modulated signal The idea is to get to transmit a signal combining the two following properties: on the one hand having a long duration to minimize the peak power; on the other hand having an autocorrelation function that is as narrow as possible (at the -3 db cutoff frequencies) so as to have the best resolution as possible.

One type of signal allowing this, is the *linear frequency modulation* (LFM) or *chirp*). This is a signal which instantaneous frequency varies between $f_0 - \Delta f/2$ and $f_0 + \Delta f/2$ on the duration of the pulse. Instantaneous frequency is related to the instantaneous phase ϕ by the relationship:

$$f(t) = \frac{1}{2\pi}\left[\frac{d\phi}{dt}\right]_t \tag{1.9}$$

For a LFM ramp transmitted between $t = 0$ and $t = T_X$ it comes that:

$$f(t) = f_0 - \frac{\Delta f}{2} + \frac{\Delta f}{T_X}t \tag{1.10}$$

The instantaneous phase is obtained by integrating over t:

$$\phi(t) = 2\pi\left[\left(f_0 - \frac{\Delta f}{2}\right)t + \frac{\Delta f}{2T_X}t^2\right] \tag{1.11}$$

A *chirp* transmitted periodically is then written thusly:

$$E_X^{\text{chirp, } f_0,\Delta f}(t) = \begin{cases} E_0 e^{\jmath 2\pi\left[(f_0 - \frac{\Delta f}{2})t + \frac{\Delta f}{2T_X}t^2\right]} & \text{if } kT_I \leq t < k/T_I + T_X, k \in \mathbb{N} \\ 0 & \text{else} \end{cases} \tag{1.12}$$

It is of course possible to use descending ramps instead of rising ramps. Writting the formulas is immediate and the properties exposed below will remain the same.

As with the "truncated sinusoidal" pulse, let us now calculate the intercorrelation function between the emitted signal and the received signal. To simplify the calculation, we also consider the *chirp* is written not as above, but in the following simplified form (the final result will remain the same), also considering that the PRF zero:

$$E_X^{c'}(t) = \begin{cases} E_0 e^{j2\pi\left(f_0 + \frac{\Delta f}{2T_X}t\right)t} & \text{if } -T_X/2 \leq t < T_X/2 \\ 0 & \text{else} \end{cases} \tag{1.13}$$

Given that this autocorrelation is equal (barring a translation and a constant attenuation factor κ) to the autocorrelation of $E_X^{c'}$, we use the latter:

$$\langle E_X^{c'}, E_X^{c'} \rangle(t) = \int_{-\infty}^{+\infty} {s^{c'}}^{\star}(-t') E_X^{c'}(t-t')dt' \tag{1.14}$$

It can be show [92][5] that the autocorrelation function of $E_X^{c'}$ is:

$$\langle E_X^{c'}, E_X^{c'} \rangle(t) = T_X \Lambda\left(\frac{t}{T_X}\right) \text{sinc}\left(\pi \Delta f t \Lambda\left(\frac{t}{T_X}\right)\right) e^{i2\pi f_0 t} \tag{1.15}$$

The maximum of the autocorrelation function $E_X^{c'}$ is reached at 0 and around this point, this function varies as the cardinal sine term. The temporal width of this cardinal sine at -3 dB cutoff is close to $T'_X = \frac{1}{\Delta f}$. Everything happens as if after pulse compression, we had the resolution of a truncated sinusoidal pulse of duration T'_X which, for common choices of Δf, is smaller than T_X, hence the name "pulse compression". The range resolution after pulse compression is therefore:

$$dr = \frac{c_0}{2\Delta f} \tag{1.16}$$

There is also a gain on the signal-to-noise ratio after pulse compression compared to what we had before compression. Indeed, the signal maximum after compression is $T_X \kappa E_0$ and the new standard deviation of the noise after compression is:

$$\rho'_{\text{chirp}} = T\left(\frac{\kappa E_0}{\sigma_n}\right)^2 \tag{1.17}$$

By injecting relation 1.8 in the case of the sinusoidal signal, taking for the duration of the sinusoidal signal the equivalent duration $T'_X \frac{1}{\Delta f}$, we observe that:

$$\rho'_{\text{chirp}} = \frac{T_X}{T'_X}\rho'_{\text{sin}} = \Delta f T_X \rho'_{\text{sin}} \tag{1.18}$$

This means that, compared to a truncated sinusoidal signal of duration T_X, a *chirp* of the same duration T_X but modulated on a band Δf will give a signal-to-noise ratio $\Delta f T_X$ times higher, after pulse compression. This gain $\Delta f T_X$ can be factored into the radio link budget: everything happens as if the transmitter had an even higher transmission power.

We have seen that the compressed signal, in the case of an *chirp*, gives a signal strongly resembling a cardinal sine. To the extent that the cardinal sine may have secondary lobes with a rather large amplitude, it is customary to apodize the signal by convoluting the result of the matched filtering with an apodizing window, such as a Chebychev, Hamming

[5] Pages 38 to 44. A very rigorous demonstration of the autocorrelation of a *chirp* signal and its properties. The authors work with a real-valued signal, meaning their result is divided by a factor 2 compared to what we have here in the complex-valued case.

or Hann[6] function; in practice, this step can be done at the same time as the matched filtering by multiplying the reference *chirp* by the apodizing window before correlation. Apodization results in a small widening of the main peak of correlation, thus a small loss of resolution; but in return the secondary lobes are much more attenuated, which improves the image quality overall.

Generalization The results obtained here with a linear frequency-modulated signal generalize to any signal of duration T_X occupying a bandwidth of width Δf. In equation 1.18, it should be noted that the special case of the classical truncated complex sinusoidal pulse is consistent with this generalization. Indeed, it can be shown that the amplitude spectrum of a truncated sinusoidal signal of duration T_X and carrier frequency Δf, is a cardinal sine centered at f_0 with a bandwidth at -3 dB, equal to $\Delta f = 1/T_X$. Thus, apart from linear *chirp*, other modulations are commonly used in radar: Barker codes [88], *chirps* hyperbolic, discrete frequency hopping emission, *etc.*. In our work, we only used linear frequency modulated (LFM) *chirps*.

1.2 Antennas

1.2.1 General considerations

An antenna is a transducer: it transforms an electrical signal, into a radio-electric wave, composed of a magnetic field and an electric field $\mathbf{E}$ propagating in space. The radiated power per unit area is equal to:

$$\frac{d\mathrm{P}}{dS} = \frac{1}{2\eta_0}|\mathbf{E}(\mathrm{P},t)|^2 \ [\mathrm{W/m^2}] \tag{1.19}$$

The transformation can also be done in the opposite direction when the antenna is operating in reception mode: the radio-electric wave is transformed into an electrical signal. The radar antennas commonly used today in maritime surveillance often use the *slotted arrays* technology, in the form of a waveguide pierced with regularly spaced slits to directly transmit or receive the waves. Another technology currently in use is that of *patch antenna*, consisting of a conductive surface, affixed to one side of a dielectric smooth surface; on the other side is a conductive reflector: this antenna therefore resembles a printed circuit board, thus lending itself to easy industrial production and the use over curved surfaces, that is, flush to the surface of another object (the side of an aircraft, for example). Other older types of antennas consist of networks of wired strands, such as the Yagi-Uda antenna (the classical "TV aerial"), or aperture antenna, which are made of a typically parabolic reflector, lighted by a waveguide ending in a horn.

The operation of an antenna is generally governed by the laws of electromagnetism, in particular the Stratton and Chu equation, a proof of which is given in appendix C. The mechanisms involved are those of diffraction and are qualitatively the same as in Optics.

The choice of an antenna is linked to several considerations. First of all, there is the size: a large antenna offers a greater resistance to wind (an important consideration for radars mounted on a ship) or weighs heavier (another important parameter, especially if the antenna is mechanically steered). A second important parameter is the yield, typically between 0.6 or 0.7, which is taken here equal to one to simplify. A third parameter that is sometimes important is the cost of manufacturing. And finally, the last parameter, and the most important for performance, is its directivity. Indeed, as we will see below, the

[6]Note at translation time: many texts mistakenly spell that as the "Hanning" window (as "Hamming"); but the name is actually that of Austrian meteorologist Julius von Hann (1839-1921).

dimensions of the antenna influence its gain and angular resolution, that is to say its ability to transmit or receive in a privileged direction.

1.2.2 The simple case of the aperture antenna

In order to understand the physical phenomena at work for an antenna, we consider the canonical case of the aperture antenna. On this type of antenna, the electromagnetic wave generated by the magnetron or the klystron is led to the antenna via a waveguide. This waveguide ends with a horn that illuminates the surface of a plate or wire mesh of large dimensions that act as a reflector. The electric field $\mathbf{E}_X$ that forms on the surface of the reflector in turn gives birth to an electromagnetic wave that will propagate in space. Note that this $\mathbf{E}_X$ field has no reason for being constant over the entire reflective surface.

Often the reflector has a parabolic shape on one or more of its dimensions, with the horn at the focal point of this parabola. This arrangement allows to reflect the waves towards infinity by minimizing the angular dispersion of the waves, in the same way as headlights on a car. However, unlike a headlight, this phenomenon of angular dispersion cannot be so well minimized. Indeed, the Radar antenna reflector size is relatively small in front the size of the radio wavelength, and one cannot neglect diffraction. Each point P′ of the surface[7] of the antenna S_X will then radiate as a punctual source, and the total scattered field at one point P of the space is the coherent sum of all infinitesimal fields created by the points P′ of S_X. The way this works is, with minimal differences, how other types of antenna work, which makes it possible to generalize the concepts developed in this paragraph. Let us now calculate the electric field generated by an idealized plane antenna at any point P of space.

1.2.2.1 Frames and hypotheses

We start in the transmitting antenna frame $\mathcal{X}(\mathrm{X}, \hat{\mathbf{x}}_x, \hat{\mathbf{y}}_x, \hat{\mathbf{z}}_x)$. Point X is on the surface of the antenna and is taken, if possible, at the center of symmetry of the surface. In the remainder of this section, the following assumptions are taken:

1. The reflector is considered to be flat, with dimensions d_y and d_z and area S_X. This simplifies equations; on the other hand, for a non-planar reflector, it is always possible to consider a virtual flat surface as a reference, even if it means changing the distribution of the electric field on this surface.

2. The reflector is assumed to be perfectly conductive.

3. We also consider that we are in the far field of so that Fraunhofer conditions hold (see appendix C, page 239):
$$r > \frac{2\max(d_y, d_z)^2}{\lambda_0} \tag{1.20}$$
where r is the XP distance and λ_0 is the electromagnetic wavelength.

4. Finally, we consider that the electric field on the surface of the antenna is constant in space. The surface field at one point P′ of S_X can then be written:
$$\mathbf{E}_X(\mathrm{P}', t) = E_X(t)\hat{\mathbf{p}}_x \tag{1.21}$$
Vector $\hat{\mathbf{p}}_x$ is the *polarization vector* of the transmitting antenna. Coordinates for $\hat{\mathbf{p}}_x$ in the $\mathcal{X}$ frame are denoted $(0, \hat{p}_y, \hat{p}_z)^t$. If $\hat{p}_z = 0$ the antenna is said to be polarized horizontally, and if $\hat{p}_z$ =1, it is vertically polarized.

Figure 1.1 illustrates the notations that have been introduced here.

[7] In the following, S_X will denote both the physical surface of the antenna and the area of that surface.

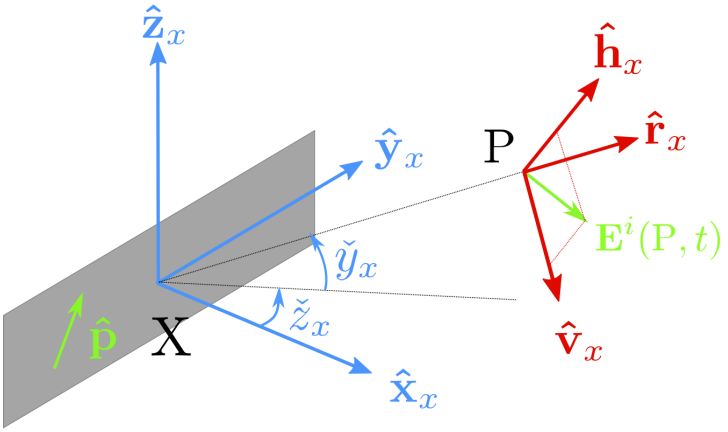

Figure 1.1: *Geometric configration to compute the radiated field at a point P.*

1.2.2.2 Radiated field at a point P

The expression of the electric field $\mathbf{E}^i(\mathrm{P},t)$ generated by the antenna at a point P of space[8], is given by the vector expression of the Fraunhofer diffraction ([1], see also in appendix for a demonstration of the result, stated in the equation C.84 of the appendix C):

$$\mathbf{E}^i(\mathrm{P},t) = \frac{\jmath k_0 e^{-\jmath k_0 r}}{2\pi r}(\hat{\mathbf{n}} \times \mathbf{F}_\mathbf{E}) \times \hat{\mathbf{r}}_x \tag{1.22}$$

where[9]:

$$\mathbf{F}_\mathbf{E}(\mathrm{P},t) = \iint_{S_X} \mathbf{E}_X(\mathbf{XP}',t) e^{jk_0 \mathbf{XP}.\mathbf{XP}'} dS' \tag{1.23}$$

with:

- $\hat{\mathbf{n}} = \hat{\mathbf{x}}_x$, a unit vector normal to the surface S_X of the antenna;
- P' is a point on the surface of S_X that contributes to the integral;
- $\mathbf{E}_X(\mathrm{P}')$ is the field on the surface of the antenna.

Under these conditions, and using the assumption that the electric field is constant at the antenna surface, we can evaluate $\mathbf{F}_\mathbf{E}$ and we can make the following simplification:

$$\mathbf{F}_\mathbf{E}(\mathrm{P},t) = E_X(t)\sigma_x(\hat{\mathbf{r}}_x)\hat{\mathbf{p}} \tag{1.24}$$

The magnitude σ_x, homogeneous to a surface – we shall see later why – makes it possible to obtain the amplitude of the wave diffracted by the aperture in direction $\hat{\mathbf{r}}_x$, parameterized in elevation by $\angle y_x$ and in azimuth by angle $\angle z_x$ in the antenna coordinate system.

We now introduce $\hat{\mathbf{E}}^i = (\hat{\mathbf{n}} \times \hat{\mathbf{p}}) \times \hat{\mathbf{r}}_x$; given we assume to be in the far field, $\hat{\mathbf{E}}^i$ is (almost) in a plan. In the coordinate system associated with the emitted wave $\mathcal{P}_x(\mathrm{P}, \hat{\mathbf{v}}_x, \hat{\mathbf{h}}_x, \hat{\mathbf{r}}_x)$, $\hat{\mathbf{E}}^i$ is entirely defined by both components $\hat{E}^i_h$ and $\hat{E}^i_v$ while the third is always zero. Also there is a linear relationship between the two non-zero coordinates of $\hat{\mathbf{p}}_x$ in the $\mathcal{X}$ coordinate system: $(\hat{p}_y, \hat{p}_z)$, and the two non-zero coordinates of $\hat{\mathbf{E}}^i$ in $\mathcal{P}_x$. This relationship is written[10] using the following matrix equation:

$$\begin{bmatrix} \hat{E}^i_v \\ \hat{E}^i_h \end{bmatrix}_{\mathcal{P}_x} = E_X(t)\sigma_x(\hat{\mathbf{r}}_x)\frac{\jmath k_0 e^{-\jmath k_0 r}}{2\pi r} \underbrace{\begin{bmatrix} -\cos \breve{z}_x & 0 \\ \sin \breve{y}_x \sin \breve{z}_x & \cos \breve{y}_x \end{bmatrix}}_{\mathtt{P}_x} \begin{bmatrix} \hat{p}_z \\ \hat{p}_y \end{bmatrix}_{\mathcal{X}} \tag{1.25}$$

[8] The notation $\mathbf{E}^i$ corresponds to the incident electric field on the surface illuminated by the antenna.
[9] The meaning of the "prime" notation in the integral is explained at page 236.
[10] The fact of putting the $\hat{E}^i_v$ component first is customary in the community.

The matrix $\mathtt{P}_x$ is therefore used to describe the polarization of the wave emitted in P, given the polarization vector $\hat{\mathbf{p}}_x$ of the wave on the antenna. In the end, the signal emitted at a point P can be calculated as follows:

$$\left\{\mathbf{E}^i\right\}_{\mathcal{P}_X}(t) = E_X(t)\sigma_x(\check{z}_r, \check{y}_r)\frac{\jmath k_0 e^{-\jmath k_0 r}}{2\pi r}\mathtt{P}_x\left\{\hat{\mathbf{p}}_x\right\}_{\mathcal{X}} \tag{1.26}$$

1.2.2.3 Antenna directivity and gain

Definition It can be seen from the equation 1.24 that this is the function σ_x which differs from one antenna to another since it alone depends on its shape. It is this function that characterizes the antenna. In fact, we usually use an expression derived from σ_x to characterize the antenna: this is directivity. We define as the *directivity* of the transmitting antenna $D_x(\hat{\mathbf{r}}_x)$, the ratio of the power density emitted by the antenna in a given direction, on the average power radiated per unit area on a sphere of radius $4\pi r^2$. We also consider the gain $G_x(\hat{\mathbf{r}}_x)$, which is the product of directivity by yield. We assume here that the yield is worth one, so we will sometimes confuse the two notions.

Calculation The total power emitted at the antenna is given by the flux of the square of the Poynting vector through the antenna surface S_X:

$$\mathsf{P}^i_{\text{tot}} = \iint_{S_X}\frac{1}{2\eta_0}||\mathbf{E}^i(\mathbf{P'}, t)||^2 dS' \tag{1.27}$$

with P' on the antenna surface. The radiated power in a given direction is given by the relation (1.19), which gives after injecting the equation 1.22:

$$\frac{d\mathsf{P}^i}{dS}(\mathrm{P}, t) = \frac{1}{2\eta_0 r^2\lambda_0^2}||\left(\hat{\mathbf{n}}\times\iint_{S_X}\mathbf{E}(\mathbf{XP'})e^{-\jmath\mathbf{k}_0\mathbf{XP}.\mathbf{XP'}}dS'\right)\times\hat{\mathbf{r}}_x||^2 \tag{1.28}$$

Given the definition above:

$$D_x(\hat{\mathbf{r}}_x) = \frac{\frac{d\mathsf{P}^i}{dS}}{\mathsf{P}_{\text{tot}}/(4\pi r^2)} \tag{1.29}$$

which yields

$$D_x(\hat{\mathbf{e}}_r) = \frac{4\pi}{\lambda_0^2}\frac{\parallel\left(\hat{\mathbf{n}}\times\iint_{S_X}\mathbf{E}_X(\mathrm{P'}, t)e^{-\jmath\mathbf{k}_0.\mathbf{XP'}}dS'\right)\times\hat{\mathbf{r}}_x\parallel^2}{\iint_{S_X}\parallel\mathbf{E}_X(\mathrm{P'})\parallel^2 dS'} \tag{1.30}$$

Maximum directivity The maximum radiation is obtained when all points on the antenna surface radiate in phase. In the case where the surface is perfectly flat, the maximum radiation is reached in the normal direction on the surface. The maximum gain of the antenna is calculated using this information (which translates mathematically to $\hat{\mathbf{r}} = \hat{\mathbf{n}}$) which simplifies the expression of the electric field in the normal direction. We have indeed:

$$\frac{d\mathsf{P}^i}{dS}(\mathrm{P}, t) = \frac{1}{2\eta_0\lambda_0^2}||\mathbf{E}^i(\mathrm{P}, t)||^2 \tag{1.31}$$

$$= \frac{1}{2\eta_0\lambda_0^2}||\left(\hat{\mathbf{n}}\times\mathbf{F}_{\mathbf{E}}\right)\times\hat{\mathbf{r}}_x||^2 \tag{1.32}$$

$$\frac{d\mathsf{P}^i}{dS}(\mathbf{r}_x) = \frac{1}{2\eta\lambda^2}||\mathbf{F}_{\mathbf{E}}||^2 \tag{1.33}$$

wher $\mathbf{F_E}$ simplifies in:

$$\mathbf{F_E} = \iint_{S_X} \mathbf{E}_X(\mathrm{P}')dS' \tag{1.34}$$

given the phase term, $\exp(\mathbf{r}'.\hat{\mathbf{r}})$ is equal to one (as per our hypothesis). The maximum directivity is then:

$$D_{\mathrm{x,\ max}} = \frac{4\pi}{\lambda_0^2} \frac{||\iint_{S_X} \mathbf{E}_X(\mathrm{P}')dS'||^2}{\iint_{S_X} ||\mathbf{E}_X(\mathrm{P}')||^2 dS'} \tag{1.35}$$

Normalization of directivity We often consider an imaginary antenna that would have a constant directivity equal to 1 in all directions. Yet:

$$\forall \hat{\mathbf{r}}_x, D_x(\hat{\mathbf{r}}_x) = 1 \Rightarrow \underbrace{\frac{||\left(\hat{\mathbf{n}} \times \iint_{S_X} \mathbf{E}_X(\mathrm{P}')e^{j\mathbf{k}_0.\mathbf{XP}'}dS'\right) \times \hat{\mathbf{r}}_x||^2}{\iint_{S_X} ||\mathbf{E}_X(P')||^2 dS'}}_{\text{homogeneous to an area}} = \frac{\lambda_0^2}{4\pi} \tag{1.36}$$

This term is homogeneous to an area, which is assimilated to the area of the isotropic antenna. We can therefore see the antenna gain as a ratio of areas. Everything happens as if the power radiated by the actual antenna in the direction $\hat{\mathbf{r}}_x$ was the one emitted a isotropic antenna whose surface area would have been multiplied by the directivity:

$$D_x(\hat{\mathbf{r}}_x) = \frac{4\pi}{\lambda_0^2}\mathrm{surface}(\hat{\mathbf{r}}_x) \tag{1.37}$$

The isotropic antenna being a view of mind, directivity is sometimes normalized with respect to the *Hertzian dipole*. The Hertzian dipole consists of a wire of length very small in front of the electromagnetic wavelength, and a simple calculation shows that the theoretical maximum directivity that can be expected of such an antenna is:

$$D_{x,\ \mathrm{max.\ Hertz.}} = \frac{4\pi}{\lambda_0^2}\frac{3}{8\pi}\lambda_0^2 = \frac{3}{2} \tag{1.38}$$

So there is a difference of a factor of 3/2 between the two normalizations, about +1.76 dB. This is the "isotropic antenna" convention that is usually taken in the radar community.

Vector form Directivity and gain can be considered in a vector form when polarization is involved:

$$\mathtt{D}_x = D_x(\hat{\mathbf{r}}_x)\mathtt{P}_x \tag{1.39}$$

$$\mathtt{G}_x = G_x(\hat{\mathbf{r}}_x)\mathtt{P}_x \tag{1.40}$$

1.2.2.4 Directivity and angular apertures of usual antennas

For a real antenna, the directivity is most often determined experimentally[11], using a suitably calibrated receiver placed away from the antenna whose directivity is to be determined. It is, however, possible to make an exact calculation for common simple antennas: rectangular and elliptical, which we have used in our work.

[11]Note at translation time: it can also be determined beforehand using finite element methods where the Maxwell equations are solved numerically.

Antenna directivity for a rectangular aperture Consider a rectangular antenna of size d_y in the $\hat{\mathbf{y}}_x$ direction and d_z in the $\hat{\mathbf{z}}_x$ direction. It is easy to show that function σ_x is of the form $\sigma_x = S_X \underline{\sigma}_x$ with $S_X = d_y \times d_z$ and:

$$\underline{\sigma}_x(\check{z}_x, \check{y}_x) = \text{sinc}\left(\pi \frac{d_y}{\lambda_0} \sin\check{z}_x \cos\check{y}_x\right) \text{sinc}\left(\pi \frac{d_z}{\lambda_0} \sin\check{y}_x\right) \tag{1.41}$$

where $\text{sinc}(x) = \sin(x)/x$. The directivity of such an antenna is then:

$$D_{\text{x, rect}}(\check{z}_x, \check{y}_x) = \frac{4\pi}{\lambda_0^2} \frac{||\iint_{S_X} \mathbf{E}_X(\text{P}')dS'||^2}{\iint_{S_X} ||\mathbf{E}_X(\text{P}')||^2 dS'} = \frac{4\pi}{\lambda_0^2} \frac{(S_X)^2 \underline{\sigma}_x^2(\check{z}_x, \check{y}_x)}{S_X} = \frac{4\pi}{\lambda_0^2} S_X \underline{\sigma}_x(\check{z}_x, \check{y}_x).^2 \tag{1.42}$$

Antenna directivity for elliptical aperture If the aperture is elliptic, of major axis d_y in direction $\hat{\mathbf{y}}_x$ and minor axis d_z in direction $\hat{\mathbf{z}}_x$, then the integral of the diffraction is solved with the Bessel function of the first kind of order 1, denoted by J_1 [103]. Area S_X is worth $2\pi ab$ and function $\underline{\sigma}_x$ is:

$$\underline{\sigma}_x(\check{z}_x, \check{y}_x) = \frac{J_1(\text{arg})}{\text{arg}} \tag{1.43}$$

The arg argument of the Bessel function is:

$$\text{arg} = k_0 d_y \sqrt{(\cos\check{y}_x \sin\check{z}_x)^2 + \left(\frac{d_z}{d_y} \sin\check{y}_x\right)^2} \tag{1.44}$$

This formula easily adapts to the case of a circular antenna.

Notion of angular aperture *Angular aperture* is used to characterize the dimensions of the cone in which the antenna radiates or receives the best. It is characterized either by the angular domain where the directivity loss is less than -3 dB relative to the maximum directivity, or by the angular sector separating the first minima around the maximum. Of the two definitions, the first is the most common. In general, the angular aperture is calculated at elevation Φ_{site} (for a zero azimuth), and the azimuthal aperture at angle Φ_{azimuth} (for a zero elevation). The angular aperture in the horizontal plane (azimuth) is:

$$\Phi_{\text{az}} = 2\check{z}_x^0 \text{ such that } D_x(\check{z}_x^0, 0) = \frac{1}{2} D_x(\check{z}_x = 0, \check{y}_x = 0) \tag{1.45}$$

And similarly, the angular aperture in the vertical (elevation) plane is:

$$\Phi_{\text{el}} = 2\check{y}_x^0 \text{ such that } D_x(0, \check{y}_x^0) = \frac{1}{2} D_x(\check{z}_x = 0, \check{y}_x = 0) \tag{1.46}$$

In general, the value of the $\Phi_{\text{el}}, \Phi_{\text{az}}$ terms can only be found by a numerical approach. For a rectangular antenna, assuming for instance $\check{y}_x = 0$, we have:

$$\underline{\sigma}_x(\check{z}_x, 0) = \text{sinc}\left(\pi \frac{d_y}{\lambda_0} \sin\check{z}_x\right) \tag{1.47}$$

and solving numerically for $\check{z}_x$ when:

$$\underline{\sigma}_x(\check{z}_x, 0) = \frac{1}{\sqrt{2}} \tag{1.48}$$

yields $\Phi_{\text{el}} \approx 0.886\lambda_0/d_z$. For similar considerations, $\Phi_{\text{az}} \approx 0.886\lambda_0/d_y$. For the circular antenna, we will find an aperture of respectively $1.02\lambda_0/d_y$ and $1.02\lambda_0/d_z$, in the vertical plane (elevation) and in the horizontal plane (azimuth).

It should be noted that for these formulas, we made the assumption that apertures are small, so that simplifying approximations can be made, such as a limited development. The notion of antenna aperture is important, because it is it that makes it possible to determine the ability of the antenna to discriminate the direction of arrival of radio waves,

In both cases, it appears that to decrease the angular aperture, it is necessary either to increase the size of the antenna, or decrease the wavelength λ_0. This result is valid for any antenna, regardless of its technology. Figure 1.2 shows the gain diagram for a rectangular and elliptical antenna of the same dimensions; this diagram shows the characteristic pattern composed of a main lobe (for a zero elevation and azimuth) and secondary lobes. The appendix B gives some antenna dimensions as found from the open literature. Since the dimensions of the antenna of the figure 1.2 are not realistic for a radar, we show in the figure 1.3 the main lobe of a rectangular antenna of length d_y =1.22 m and width d_z =0.38 cm. It can be noted that the lobe is much narrower, which is due to the fact that dimensions are larger; similarly, the lobe is much more narrow in azimuth than in elevation, which is due to the fact that the antenna is wider in the horizontal direction. A narrow lobe in azimuth is a desirable thing, insofar as it allows to reduce angular ambiguity about the location of the target. In counterpart, having a wider lobe allows, when the antenna is mounted on the mast of a boat, to have a certain robustness on ship pitch variations, regardless of the state of the sea (which allows to avoid a servo system to keep the antenna aimed at the horizon).

The length taken for the figure 1.3 corresponds to the length of a Furuno FAR 2855 on-board radar antenna (4 feet); the width at 3 dB of the lobe is here about 1.32°in azimuth. The datasheet announces an azimuthal aperture of 1.8°in X-band, which gives a good agreement between theory and reality despite the fact that the real antenna is not rectangular but a slotted array.

1.2.3 Receiving antennas

Because of the reciprocity of the Stratton and Chu equations, it is possible to calculate the field created on the surface of the antenna from the field originating from a point P of space. This field is obtained by a relationship similar to that of the emission case. The components of the received electric field $\mathbf{E}_R$ at the antenna are written in a form analogous to equation 1.26:

$$\{\mathbf{E}_R\}_{\mathcal{R}}(t) = \jmath k_0 \frac{e^{-\jmath k_0 r'}}{2\pi r'} \sigma_r(\hat{\mathbf{r}}') \{\hat{\mathbf{p}}_r\}^t_{\mathcal{R}} \mathtt{P}_r \{\mathbf{E}^s\}_{\mathcal{P}_R} \tag{1.49}$$

where σ_r is the analog of σ_x but for reception (same form), r' the distance $||$ RP$||$, $\hat{\mathbf{p}}_r$ is the polarization vector of the receiving antenna, and $\mathtt{P}_r$ the matrix equivalent to $\mathtt{P}_x$ but written in the coordinate system $\mathcal{R}$ described in figure 1.4. It is possible to reuse all the concepts developed for the antennas used for transmission (angular aperture, gain, *etc.*).

1.2.3.1 Antenna lobe footprint on the ground

When imaging a somewhat flat surface (such as the sea surface), it is interesting to know the dimensions of the area on the sea surface, that is illuminated by the antenna lobe. These dimensions have a double interest:

- the illuminated area will directly influence the link budget given by the radar equation, which we will see later in the 1.4 section;
- the parameters of this area will also have some importance when considering the mechanism of integration into synthetic antenna, because we will see that the larger

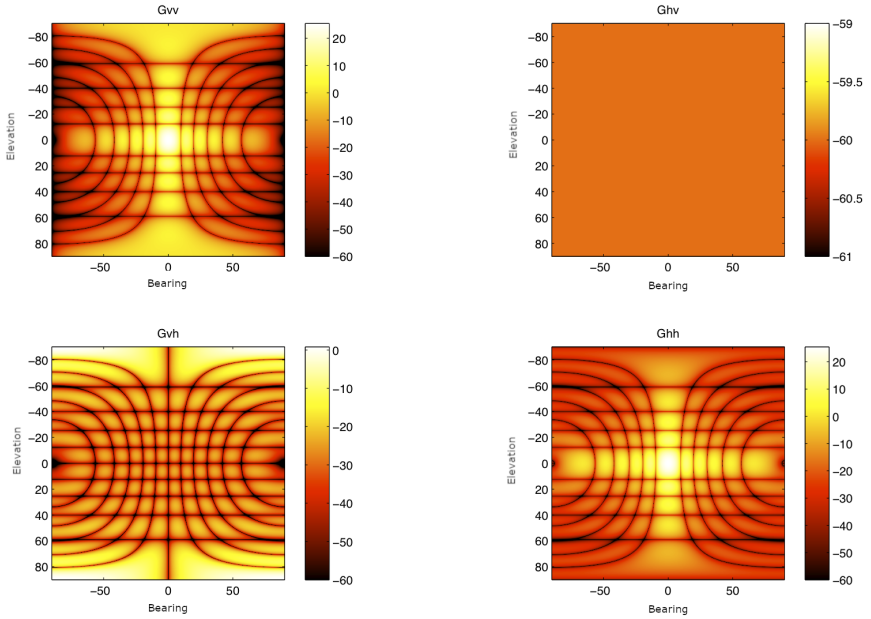

(a) Rectangular antenna

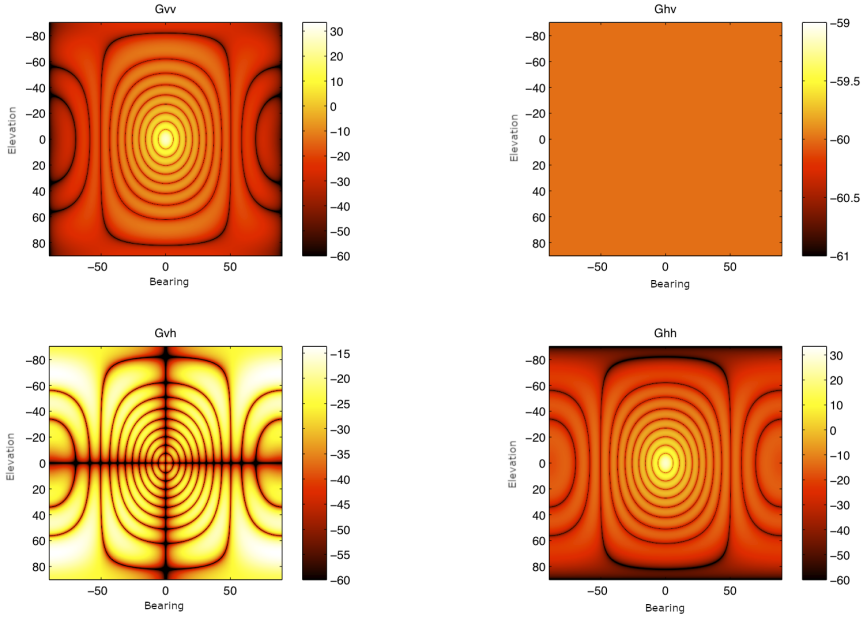

(b) Elliptic antenna

Figure 1.2: *Gain matrix* $\mathbf{G}_{\mathbf{x}}(\hat{\mathbf{r}}_{\mathbf{x}})$ *at a 10 GHz frequency, for an antenna of 18 cm (length) by 14 cm (width), far a rectangular aperture (a) and elliptic aperture (b).*

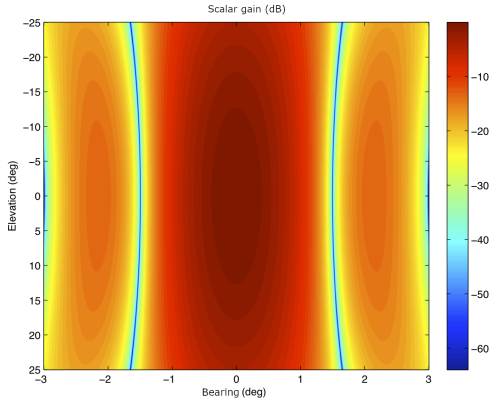

Figure 1.3: $\underline{\sigma}_x$ *function (in dB),* $\lambda = 3.10^{-2}$ *m,* $d_z = 3,8$ *cm,* $d_y = 1,22$ *m (4 ft).*

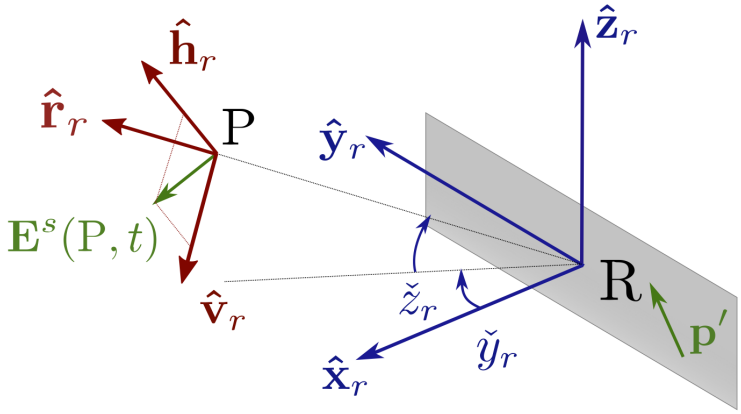

Figure 1.4: *Geometric configuration used to compute the received electromagnetic field on an antenna.*

the illuminated surface, the longer this integration will be (see section 1.7, and more particularly paragraph 1.7.3.2).

In emission, this size corresponds more or less to the total illuminated surface. In reception, it is the points on the surface located on the footprint of the receiving antenna lobe that contribute to the received signal. The notations we use are those given in figure 1.5. We want to determine the lengths Δd (*swath on the ground*) and Δd_{az} (*width of the footprint, in azimuth*). We work here with the transmitting antenna placed in X but we can make an analogous calculation in reception. It is assumed that the antenna is aimed at point C on the mean surface of the sea, with an incidence angle θ_i. An arbitrary point M of the mean surface of the sea is being considered. In the world coordinate system $\mathcal{W} = (\mathrm{O}, \hat{\mathbf{x}}, \hat{\mathbf{y}}, \hat{\mathbf{y}})$, points X, C and M have the following coordinates:

$$\{\mathrm{X}\}_{\mathcal{W}} = [0, 0, h]^t \tag{1.50}$$
$$\{\mathrm{C}\}_{\mathcal{W}} = [h \tan\theta_i, 0, 0]^t \tag{1.51}$$
$$\{\mathrm{M}\}_{\mathcal{W}} = [x_M, y_M, 0]^t \tag{1.52}$$

Point M has coordinates, in the antenna frame $\mathcal{X}$:

$$\{\mathrm{M}\}_{\mathcal{X}} = \begin{bmatrix} \sin\theta_i & 0 & -\cos\theta_i \\ 0 & 1 & 0 \\ \cos\theta_i & 0 & \sin_i\theta \end{bmatrix} \begin{bmatrix} x_M \\ y_M \\ 0 \end{bmatrix} - \begin{bmatrix} 0 \\ 0 \\ h \end{bmatrix} = \begin{bmatrix} x_M \sin\theta_i + h\cos\theta_i \\ y_M \\ x_M \cos\theta_i - h\sin\theta_i \end{bmatrix} \tag{1.53}$$

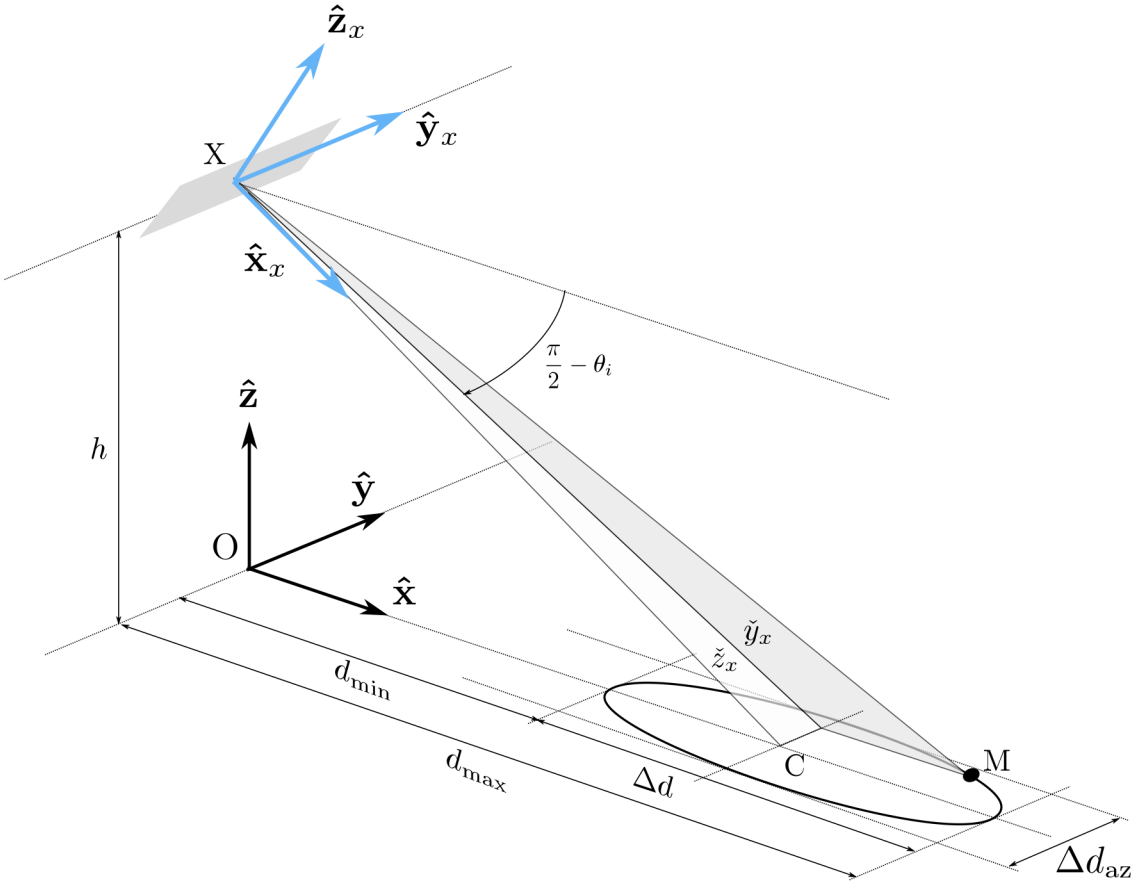

Figure 1.5: *Acquisition geometry.*

The elevation and bearing of M in the antenna frame is thus:

$$\check{z}_x = \operatorname{atan}\frac{y_M}{x_M \sin\theta_i + h\cos\theta_i} \tag{1.54}$$

$$\check{y}_x = \operatorname{atan}\frac{x_M \cos\theta_i - h\sin\theta}{\sqrt{(x_M \sin\theta_i + h\cos\theta_i)^2 + y_M^2}} \tag{1.55}$$

Consider the size of the footprint of the portion of the antenna lobe where the gain is greater than the maximum gain removed of 3 dB. The scalar gain function of the antenna is assumed to be known; it is usually expressed as a function of the azimuth and elevation angle as described above. It is therefore sufficient to determine the angle for which the gain loss is less than 3 dB. For a rectangular antenna of dimensions $d_y \times d_z$:

$$\sigma_x(\alpha_y, \alpha_z) = S_X \operatorname{sinc}\left(\pi \frac{d_z}{\lambda_0} k_y\right) \operatorname{sinc}\left(\pi \frac{d_y}{\lambda_0} k_z\right) \tag{1.56}$$

avec:

$$k_x = \cos\check{y}_x \cos\check{z}_x \tag{1.57}$$

$$k_y = \cos\check{y}_x \sin\check{z}_x \tag{1.58}$$

$$k_z = \cos\check{y}_x \sin\check{z}_x \tag{1.59}$$

In a given direction (bearing or elevation), we saw that the gain drops by 3 dB as soon as the argument x_0 of the cardinal sine is such that $x_0 = 0.442946471\pi = \pm\xi\pi$. In azimuth,

we have:

$$x_0^a = \pi \frac{d_y}{\lambda_0} \sin \check{y}_x \tag{1.60}$$

while on the elevation axis:

$$x_0^s = \pi \frac{d_z}{\lambda_0} \cos \check{y}_x \sin \check{z}_x \tag{1.61}$$

By calculating the corresponding values for $\check{y}_x$ and $\check{z}_x$, and injecting them into 1.55, we can find that:

$$\Delta d = 2h\xi\lambda_0 \frac{\sqrt{d_y^2 - \lambda_0^2\xi^2}}{(d_y \cos\theta_i)^2 - \lambda_0^2\xi^2} \tag{1.62}$$

and:

$$\Delta d_{\text{az}} = 2h\xi\lambda_0 \sqrt{\frac{1 + \tan\theta_i^2}{d_z^2 - \xi^2\lambda^2}} \tag{1.63}$$

1.3 Target and clutter: wave/environment interactions

Generally speaking, the waves produced by the transmitting module can reach the receiver either through a direct path that does not meet any targets, or by being reflected by elements of the scene: the atmosphere, the sea, or a ship. For a solid target, we generally use the notion of radar cross section (RCS), denoted σ. The RCS can be defined as the apparent surface that would be needed for a target, to reflect a power P' in the direction $-\hat{\mathbf{r}}_r$, while it is subjected to an incident wave propagating in the direction $\mathbf{r}_x$ with a surface power density given by equation 1.19:

$$\mathsf{P}'(-\hat{\mathbf{r}}_x) = \frac{d\mathsf{P}}{dS}(\hat{\mathbf{r}}_x) \times \sigma(\hat{\mathbf{r}}_x, -\hat{\mathbf{r}}_r) \tag{1.64}$$

It is important to see that the RCS is not the physical surface of the object, but an apparent surface that fluctuates according to the direction $\mathbf{r}_x$ of arrival of the incident wave and the direction $-\hat{\mathbf{r}}_r$ of the reflected wave.

The notion of RCS can be put in vector form, in order to represent the polarization effects: we then consider matrix $\Sigma = [\sigma_{pq}]$ where p and q are the polarizations at transmission and reception, respectively. We then consider the incident field $\mathbf{E}^i$, and the reflected field $\mathbf{E}^s$; to be able to make sense of the Σ matrix, these vectors must be expressed in specific coordinate systems; we therefore use the "incident wave" polarimetric coordinate system $\mathcal{P}_I$ and the "reflected wave" polarimetric coordinate system in the so-called *forward scattering alignment* convention $\mathcal{P}_S^F$ (see figure 1.6 or appendix A for the definition of these frames:

$$\left\{\mathbf{E}^s\right\}_{\mathcal{P}_S^F} = \Sigma \left\{\mathbf{E}^i\right\}_{\mathcal{P}_I} \tag{1.65}$$

In the case of an infinite surface, the normalized radar cross section $\Sigma^0 = [\sigma_{pq}^0]$ is used, which involves the actual illuminated surface A, and the surface of the wavefront $4\pi r^2$:

$$\Sigma^0 = \frac{4\pi r^2}{A}\Sigma \tag{1.66}$$

We can also consider an amplitude scattering matrix, $\mathbb{S} = [S_{pq}]$, such that $\sigma_{pq} = S_{pq}S_{pq}^*$. In the case of the atmosphere, we do not consider a RCS but rather volume attenuation and scattering.

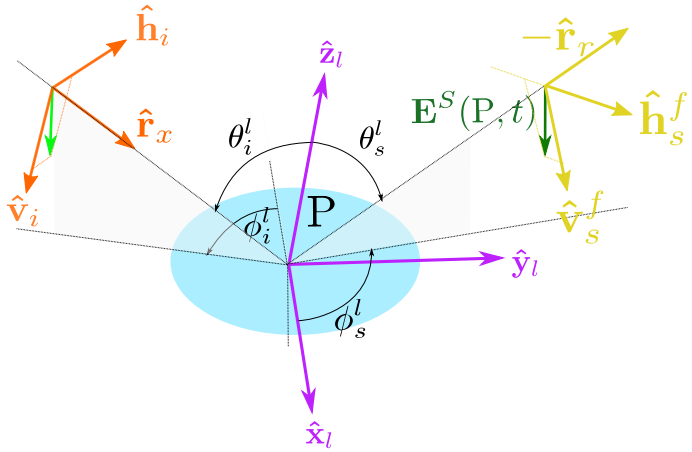

Figure 1.6: *Frames used to express the incident field and the reflected field on the surface. The incident wave coordinate system is* $\mathcal{P}_I(\mathrm{P}, \hat{\mathbf{v}}_i, \hat{\mathbf{h}}_i, \hat{\mathbf{r}}_x)$ *while the reflected wave coordinate system in forward scattering alignment convention is* $\mathcal{P}_S^F(\mathrm{P}, \hat{\mathbf{v}}_s^f, \hat{\mathbf{h}}_s^f, \hat{\mathbf{r}}_s^f)$.

1.3.1 Atmospheric interactions with radio waves

1.3.1.1 Absorption and scattering

The interaction between the radio wave and the air molecules, or the elements that are suspended in the atmosphere (water droplets, dust, ...) can be described by two phenomena: absorption and scattering.

Absorption is characterized by the excitation of electrons of atoms in the path of the radio wave, these electrons gaining an energy equal to that of the photon absorbed according to the laws of quantum mechanics. Absorption increases with the density of atoms in the medium in which the radio waves travel. Assuming that the atoms are evenly distributed, it can be considered that a certain fraction $a.dz$ of the photons are absorbed in a slice of thickness dz of medium crossed; thus the intensity of the wave loses a quantity $d\mathsf{P} = -a\mathsf{P}dz$ when crossing this slice, which makes it possible to arrive at the differential equation:

$$\frac{d\mathsf{P}}{dz} = -a\mathsf{P} \tag{1.67}$$

whose solution is of the form $\mathsf{P}_0 \exp(-az)$: the wave therefore undergoes an exponential decay. This decay or attenuation is especially present in case of rain or fog and reaches a few decibels per kilometer in X band. In optics, attenuation is the cause of a decrease in contrast for sources located far from the emitter, typically visible on foggy days for objects on the horizon: the visibility range decreases. This phenomenon is also true in radar.

The scattering of radio waves in the atmosphere is characterized by the random deviation $d\theta$ of the waves (assumed to be planar), according to its initial direction of propagation θ, which we assume to be zero to simplify. The probability density of the deviation angle is called the *scattering function*. This function is theoretically parameterized according to two angles (analogous to a bearing and elevation) but since it generally presents an axial symmetry related to the isotropy of the medium it is possible to parameter the function using only one angle. The typical shape of a scattering function is shown in figure 1.7: propagation is maximum around the initial direction of propagation, but there is a possibility for the wave to be deviated around a direction θ. Two cases occur: if $d\theta < \pi/2$ then the wave continues to propagate forward, this is called *forward scattering*; or the deviation $d\theta$ is greater than $\pi/2$, in which case the wave goes back to the transmitter: this is called *backscattering*. By abuse of language, we also speak of a "*forward scattering*"

configuration when the transmitter and receiver point in the same direction but in the opposite direction, as well as a "*backscattering*" configuration when the transmitter and receiver point in the same direction. In Optics, forward scattering explains why the image of punctual sources located far from the receiver are blurred in a misty environment. The width of the point spread function increases with the distance between the source and the receiver. Still in Optics, if the receiver "looks" in the same direction as the source, then backscattering will be at the origin of a so-called "glow veil" superimposed over the image of the scene. This is caused by the light reflected by the diffusing medium. A typical example is when a car is driven in the fog: the driver sees the fog reflect the light from the headlights of their car. The same phenomena are valid in radar, although it goes without saying that the shape of the scattering function varies with the frequency and the characteristing of the scattering medial.

Scattering is caused by the interaction between the radio wave and particles which size is less than or equal to the wavelength (as an order of magnitude). Depending on the regime, we then speak of Rayleigh scattering or Mie difusion (whose modern formulation is provided by Stratton [167], 9.25, p. 564). Semi-empirical scatterering functions have been created to better model the scattering of a wave in a medium, such as the Henyey-Greenstein function [94] (which is configurable and generic); others are purely experimental. As a rule, the veiling and blurring effect caused by scattering impairs the correct imaging of a point target and decreases the effective range of a system using electromagnetic waves; this is true both in the optical field, as for example in underwater optics where these phenomena are particularly troublesome [60] or in the field of radar imaging. In a context other than weather radar, the signal returned from the atmosphere is undesirable and considered as noise masking the scene; this noise is named *clutter*.

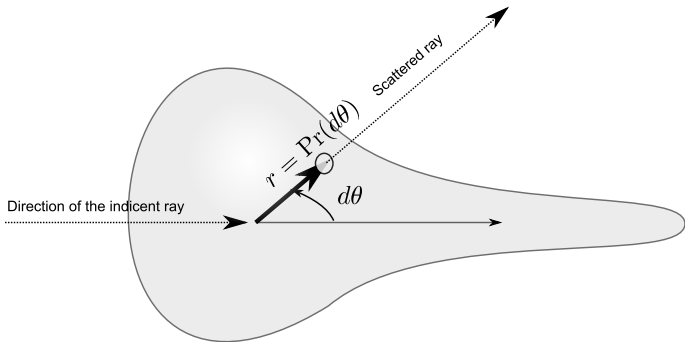

Figure 1.7: *Shape of a typical scattering function. The probability of scattering Pr in direction $d\theta$ is proportional to the radial distance r from the surface of the scattering function to the origin; the volume enclosed by this surface is one to normalize the total probability. The shape has an axial symmetry around the initial direction of propagation.*

1.3.1.2 Atomspheric propagation ducts (*ducts*). Ionospheric interactions.

The variation of the refractive index in the atmosphere, depending on the point where one is, can cause the rays to deviate, which means that they no longer propagate in a straight line. In the optical field, this phenomenon is known as mirage. The index variation is related to pressure, temperature and the presence of water vapour [159]. In our case, however, we will hypothesize straight-line propagation, which makes sense for relatively short range X-band airborne applications.

On the other hand, the ionosphere, divided into several layers of variable index, can

reflect radio waves towards the ground. These reflected waves can in turn reflect off the ground to return to the ionosphere, and so on, allowing for long-range propagation. Nevertheless, the influence of the ionosphere is especially important at low frequencies (HF bands) and negligible for centimeter waves, which is the field in which we work.

1.3.2 Surface interaction

To simplify our point, we call here "surface interaction", any interaction between the radio wave and something other than the atmosphere. The modeling of the reflection of a radio wave by a surface being a complex field, we will not seek in this chapter to make a complete state of the art but only to present the main phenomena. Specific aspects of wave scattering on the sea surface will be discussed later, in chapter 4.

1.3.2.1 Complex wave/target interaction

The interaction of a wave with a complex target is difficult to model analytically. The determination of the RCS can be done experimentally on a model, using an anechoic chamber; or numerically, using approximate methods (approximation by geometric optics, by the general theory of diffraction, by solving Maxwell's equations by the method of finite differences, *etc.*). Each method has a different degree of realism, simplicity and computation time.

To get an idea of the RCS of a ship, there are empirical formulas. Skolnik [158] gives such a formula, valid for non-stealth targets, in monostatic configuration, for resolutions larger than the ship, and for small grazing angles, with unspecified polarization. This empirical formula is as follows:

$$\sigma = 52 f_0^{1/2} \mathrm{Dp}_b^{3/2} \tag{1.68}$$

where f_0 is the radar frequency in MHz and Dp_b the ship's displacement in thousands of tons. The formula has been validated for λ_0 wavelengths of 3.25, 10.7 and 23 cm and displacements of 2 to 17 kilotons. The radar cross section is of the order of 10^4 m^2 for a freighter. For resolutions smaller than the ship, finer models should be used: this is what happens for this dissertation.

1.3.2.2 Interaction with an infinite rough surface

Since this point deserves more development than mere generalities, it is dealt with in more detail in chapter 4 in the context of a maritime surface. Qualitatively, an infinite rough surface will also reflect the wave. Two types of reflection are possible. If the surface is very weakly rough compared to the wavelength, that is, if the variations in height of the surface are small in front of this wavelength, then the reflection will tend to be specular: the surface behaves like a mirror by reflecting the wave (mainly) in the direction respecting the Snell-Descartes law of reflection. If, on the contrary, the variations in height are no longer negligible in relation to the wavelength, then there will also be diffuse reflection, meaning the waves will also be reflected in directions other than the specular direction. This reflected energy will be able to return to the radar. It is, in particular, diffuse reflection that allows a monostatic radar to build an image of the maritime surface. In the context of maritime surveillance where the ship is considered to be the target, the energy contributed by the ocean surface is perceived as undesirable noise that is also called *clutter*.

1.4 Writing the bistatic radar equation

The bistatic polarimetric radar equation in amplitude, is obtained by putting together all the elements of the acquisition chain, in order to obtain an expression of the electric field at the receiving antenna, as a function of the electric field on the transmitting antenna. For this we use equations 1.26 at emission, 1.65 for the surface, and 1.49 at reception. However, care must be taken to properly address the sequence of frame changes between the transmitting antenna and the receiving antenna, as illustrated in figure A.2, page 223, in Annex A. We end up with [1, 104, 13, 9]:

$$\{\mathbf{E}_R\}_{\mathcal{R}}(\mathrm{R},t) = C.\{\hat{\mathbf{p}}_r\}'_{\mathcal{R}}\,\mathtt{P}_r\mathtt{R}_{\mathcal{P}^{\mathcal{B}}_{\mathcal{S}}\to\mathcal{P}_{\mathcal{R}}}\mathtt{B}\Sigma\mathtt{R}_{\mathcal{P}_{\mathcal{X}}\to\mathcal{P}_{\mathcal{I}}}\mathtt{P}_x\,\{\hat{\mathbf{p}}_x\}_{\mathcal{X}} \tag{1.69}$$

with:

$$C = -k_0^2\frac{e^{-\jmath k_0(r+r')}}{4\pi^2 rr'}\sigma_r(\check{z}_r,\check{y}_r)\sigma_x(\check{z}_x,\check{y}_x)E_X(t) \tag{1.70}$$

This equation shows rotation matrices $\mathtt{R}_{\mathcal{P}_{\mathcal{X}}\to\mathcal{P}_{\mathcal{I}}}$ and $\mathtt{R}_{\mathcal{P}^{\mathcal{B}}_{\mathcal{S}}\to\mathcal{P}_{\mathcal{R}}}$, as well as the frame change matrix from the front scattering alignment convention to the backscattering alignment convention:

$$\mathtt{B} = \begin{bmatrix} 1*0 \\ 0*-1 \end{bmatrix} \tag{1.71}$$

This backscattering alignment convention makes it possible to use in reception, the same coordinate system as the transmitting antenna, in the specific case of monostatic configuration.

1.5 Received signal and the Doppler effect

1.5.1 Expression of the received signal, in the narrowband approximation

Starting from expression of the scalar signal from equation 1.2 of the paragraph 1.1.4, assuming that there is no noise:

$$E_R(t) = \kappa E_X(t-\Delta t) \tag{1.72}$$

Using the narrowband approximation, it is further assumed that:

$$E_X(t) = \mu(t)e^{\jmath 2\pi f_0 t} \tag{1.73}$$

where $\mu(t)$ is a (possibly complex), frequency modulating function Δf that has a small amplitude in front of the carrier frequency f_0. The received signal is then ([88], page 27):

$$E_R(t) = \kappa\mu(t-\Delta t)e^{\jmath 2\pi f_0(t-\Delta t)} \tag{1.74}$$

1.5.2 Computing the total time of flight Δt

Given the previous equation, it is therefore necessary to know the total time of flight Δt on the path between the transmitter, the target and the receiver. This is equivalent to calculating the total distance $r + r'$ traveled by the electromagnetic wave between the transmitter, target, and receiver, since $\Delta t = (r + r')/c_0$. This distance $r + r'$ intervenes both in the calculation of attenuation losses and for the Doppler effect. It varies over time due to the movement of objects.

Following Airiau and Khenchaf [1] and Arnold-Bos, Khenchaf and Martin [9], we assume straight line propagation, and also assume to know the respective position of the transmitter, target, and receiver at a reference time t_0: $\mathbf{T}(t_0)$, $\mathbf{P}(t_0)$ and $\mathbf{R}(t_0)$ and their (assumed constant) speed vectors $\mathbf{V_X}$, $\mathbf{V_P}$ and $\mathbf{V_R}$.

We are now interested in a small signal "atom" emitted between dates t_X and $t_X + dt_X$, where t_X is not necessarily equal to t_0. Our problem is to know $t_R(t_X)$, the date of arrival of the signal and travel time $\Delta t = t_R - t_X$. This travel time is a function t_X, the position of the objects and their speed. If we note t_P, the date when the signal atom reaches the target, then:

$$\begin{aligned} r &= c_0 \times (t_P - t_X) && (1.75)\\ r &= ||\mathbf{P}(t_P) - \mathbf{X}(t_X)|| && (1.76)\\ &= ||\mathbf{XP}(t_X) + \mathbf{V_P}(t_P - t_X)|| && (1.77) \end{aligned}$$

with:

$$\mathbf{XP}(t_X) = \mathbf{XP}(t_0) + (\mathbf{V_P} - \mathbf{V_X})(t_X - t_0) \quad (1.78)$$

By equating (1.75) and (1.77), squaring the result, and solving for $t_P - t_X$, it comes:

$$t_P - t_X = \frac{\mathbf{XP}(t_X).\mathbf{V_P} + \sqrt{\Delta_1}}{c_0^2 - V_P^2} \quad (1.79)$$

where

$$\Delta_1 = ||\mathbf{XP}(t_X).\mathbf{V_P}||^2 + (c_0^2 - V_P^2)||\mathbf{XP}(t_X)||^2 \quad (1.80)$$

Similarly:

$$\begin{aligned} r' &= c_0 \times (t_R - t_P) && (1.81)\\ r' &= ||\mathbf{R}(t_R) - \mathbf{P}(t_P)|| && (1.82)\\ &= ||\mathbf{PR}(t_P) + (t_R - t_P)\mathbf{V_X}|| && (1.83) \end{aligned}$$

which yields:

$$t_R - t_P = \frac{\mathbf{PR}(t_P).\mathbf{V_R} + \sqrt{\Delta_2}}{c_0^2 - V_R^2} \quad (1.84)$$

with

$$\Delta_2 = ||\mathbf{PR}(t_P).\mathbf{V_R}||^2 + (c_0^2 - V_R^2)||\mathbf{PR}(t_P)||^2 \quad (1.85)$$

and:

$$\mathbf{PR}(t_P) = \mathbf{PR}(t_X) + (\mathbf{V_R} - \mathbf{V_P})(t_P - t_X) \quad (1.86)$$

1.5.3 The Doppler effect

The Doppler effect, named after its main discoverer Christian Doppler (1803-1853), is characterized by the frequency shift of a signal emitted or reflected by a moving object, relatively to the frequency of the signal which would have been obtained were said object non-moving.

1.5.3.1 The Doppler effect at the first order

The time of flight Δt between X, P and R changes with the date of emission t_X due to the movement of the objects. We can evaluate the derivative of the travel time Δt at $t = t_X$ as:

$$\left[\frac{d\Delta t}{dt}\right]_{t=t_X} = \frac{1}{c_0}\left\{\left[\frac{dr}{dt}\right]_{t=t_X} + \left[\frac{dr'}{dt}\right]_{t=t_X}\right\} \quad (1.87)$$

In the monostatic case, we simply have:

$$\left[\frac{d\Delta t}{dt}\right]_{t=t_X} = 2\frac{\mathbf{V_P}.\mathbf{XP}}{c_0} \quad (1.88)$$

This term is negative if the target approaches the radar. At reception, the variation of the time of flight will have a double effect. On the one hand, a pulse train emitted regularly will arrive at increasingly closer intervals (if the target gets closer) and reciprocally. On the other hand, there will be a "compression" of the duration of the received pulse, if the time of flight decreases; conversely there is a temporal expansion if the time of flight increases. Indeed:

- The time of flight of a signal atom transmitted at t_X is $\Delta t(t_X)$
- The time of flight of a signal atom transmitted at $t_X + dt_X$ is $\Delta t(t_X + dt_X) = \Delta t(t_X) + dt_X \left[\frac{d\Delta t}{dt}\right]_{t_X}$
- the time of flight difference is therefore: $dt_X \left[\frac{d\Delta t}{dt}\right]_{t_X}$, which is a local compression/expansion of the pulse duration being proportional to:

$$\rho_{\text{Doppler}}(t_X) \approx 1 + \left[\frac{d\Delta t}{dt}\right]_{t=t_X} \tag{1.89}$$

This term $\rho_{\text{Doppler}}(t_X)$ can be thought of as the "Doppler compression coefficient". If velocities are constant over the duration of the transmitted pulse, this coefficient will be constant at the first order: $\rho_{\text{Doppler}}(t_X) = \text{constant} = \rho_{\text{Doppler}}(t_X)$. It is also possible to compute $\rho^{-1}_{\text{Doppler}}$, and after Taylor expansion at the first order:

$$\rho^{-1}_{\text{Doppler}}(t_X) \approx 1 - \left[\frac{d\Delta t}{dt}\right]_{t=t_X} \tag{1.90}$$

The received signal will have a duration $\rho_{\text{Doppler}} T_X$. It will be centered around frequency $f_0/\rho_{\text{Doppler}} = f_0 + f_D$ where f_D is the *Doppler shift*. The received pulse will have a bandwidth $\Delta f/\rho_{\text{Doppler}}$. Figure 1.8 illustrates this point.

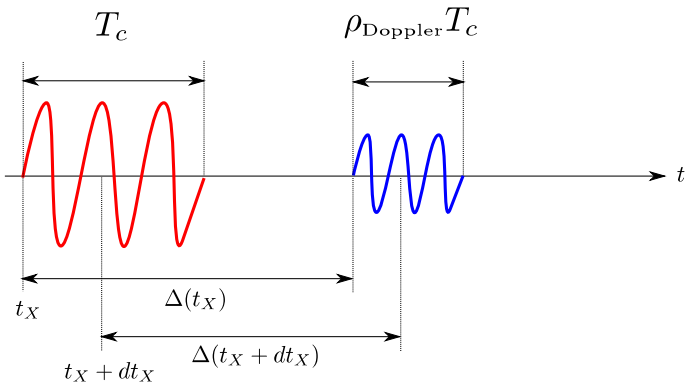

Figure 1.8: *Doppler effect using the notations introduced in this chapter. The transmitted signal is shown in red, the received signal in blue, distance $r + r'$ is assumed to decrease. Compression effects are visually exagerated.*

1.5.3.2 Influence of the Doppler effect on the received signal in the narrowband hypothesis

The equations written above are general. We are now working in the case of narrowband and short-duration signals. In this case, the compression/dilatation of the pulse by Doppler effect is not appreciable because, when the received signal is sampled (usually after a

baseband frequency shift), the variation in pulse duration is generally much less than the temporal or spatial sampling step on the range axis, meaning the "pixels" (range bins) occuped by the pulse will be the same whatever the Doppler shift. Similarly, if we consider the echoes of several consecutive pulses for the same moving target, the distance variation over time is often too small to result in an appreciable shift at the *range bins*. However the Doppler effect can still be perceived by a phase shift of the sampled signal. All this is due to the fact that the factor ρ_{Doppler} is very close to one. To illustrate this point, consider this toy problem. A stationary monostatic radar with a 10 GHz carrier, transmitting on a 60 MHz band and a target approaching 800 km/h. We have:

$$\left[\frac{d\Delta t}{dt}\right]_{t=t_X} \approx 3,7 10^{-7} \tag{1.91}$$

meaning the Doppler shift (for the carrier frequency) is 3,7 kHz, the bandwidth augmenting by 22 Hz! This, in practice, in the narrow band hypothesis, it can be assumed that in modulation function $\mu\left(t - \Delta t(t)\right)$, term Δt is constant ([88], page 28). Then:

$$\begin{aligned} E_R(t) &= \kappa\mu(t - \Delta t(t_X))e^{\jmath 2\pi f_0(t-\Delta t(t))} &(1.92)\\ &= \kappa\mu(t - \Delta t(t_X))e^{\jmath 2\pi(f_0+f_D)t-\jmath 2\pi\Delta t(t_X)} &(1.93)\end{aligned}$$

so, in the end:

$$E_R(t) = \kappa E_X(t - \Delta t(t_X))e^{\jmath 2\pi f_D t-\jmath 2\pi\Delta t(t_X)} \tag{1.94}$$

This means that the signal received with Doppler effect simply undergoes a carrier shift equal to f_D, the other effects being negligible. Term $2\pi\Delta t(t_X)$ is a phase difference that one would have had anyway, with or without Doppler effect. Under the same assumptions, and if we want to get rid of the formalism of the Doppler frequency, we can adapt the initial definition of the received signal (from the equation 1.74):

$$E_R(t) = \kappa E_X(t - \Delta t(t_X))e^{-\jmath 2\pi f_0\Delta t(t)} \tag{1.95}$$

1.5.3.3 The ambiguity function

The ambiguity function describes the result of the matched filtering (or pulse compression) of the received signal shifted in Doppler frequency, relative to the signal that was emitted (Le Chevalier [116], pp. 53-59). This is a generalization of the function given to the equation 1.3, which is now written (under the narrowband hypothesis):

$$\text{amb}(E_X, E_R)(t, f_D) = \int_{t=0}^{+\infty} E_X^\star(t')E_X(t + t')\exp^{\jmath 2\pi f_D t}\, dt' \tag{1.96}$$

Figure 1.9 shows the ambiguity function in the case of a LFM *chirp* signal. We see that the support of this function is a straight line. This result is explained by the fact that in the case of the LFM *chirp* function, the correlation of said LFM *chirp* with its Doppler-shifted version, is the original LFM *chirp*, shifted in time compared to the non-Doppler shifted chirp. For other functions, the ambiguity function may differ significantly.

The ambiguity function proves important when writing synthetic aperture radar integration equations, at the end of this chapter. We shall come back to that later on.

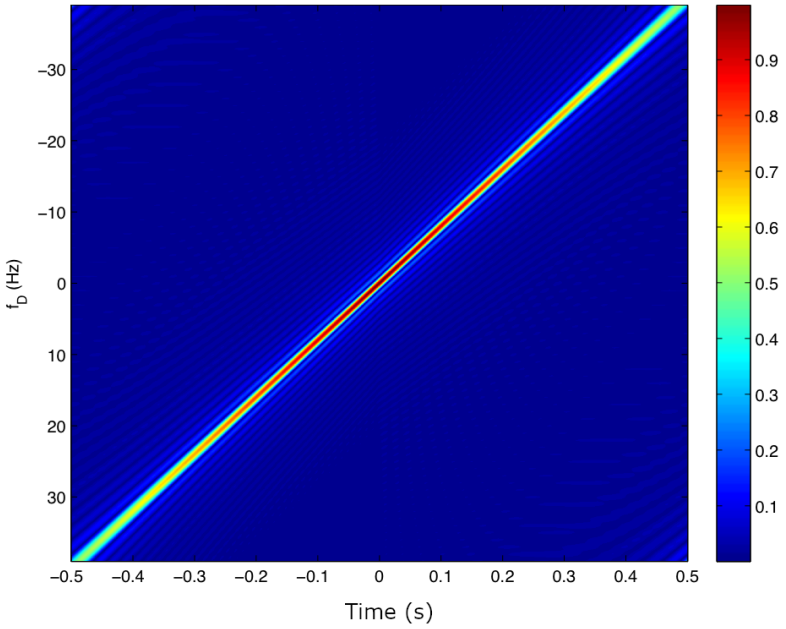

Figure 1.9: *Ambiguity function for a LFM* chirp *de porteuse* $f_0 = 0$ *Hz, de durée* $T = 1$ *s, modulé sur* $\Delta f = 80$ *Hz.*

1.6 Bistatic geometrical configuration and ground resolution

1.6.1 The Fresnel ellipsoid

The locus of points P such that the sum of distances $r = ||\mathbf{XP}||$ and $r' = ||\mathbf{PR}||$ is equal to a given constant r_0, is by definition an ellipsoid, called the *Fresnel ellipsoid*. The transmitter and receiver are the foci of this ellipsoid. In the monostatic case, this ellipsoid obviously becomes a sphere. The intersection of the Fresnel ellipsoid with a plane is either the empty set, a point, or an ellipse. The geometric characteristics of this ellipse are provided in appendix A, paragraph A.4. By an abuse of language, we will call this ellipse, if it exists, the *fresnel ellipse*.

1.6.2 Slant range and ground range resolution

There are two types of resolution that can be considered: on the one hand, the physical resolution of the instrument, i.e. the ability to distinguish a point reflector from another, neighbor, for a given parameter (distance or angle); on the other hand the sampling resolution. The first is related only to the instrument; the second is related to the recorded signal, regardless of the hardware. Increasing the sampling resolution infinitely will never allow to distinguish between two point reflectors, if they have been imaged with too low an instrumental resolution. We are interested here in the first kind of resolution, namely instrumental resolution.

Slant range resolution Slant range resolution is the radial range betwen the target and the radar[12]. This is the resolution on the "total path length", which is linked to the total

[12]The "slant range" name comes from the fact that this is the length of the hypotenuse of the radar-

time of flight $t_X + t_R$. After pulse compression, the typical time width of the pulse is $1/\Delta f$ where Δf is the bandwidth over which the pulse has been modulated[13]. Resolution on the range axis is then given by ([82], p. 54):

$$dr = \frac{1/\Delta f}{||\,\mathbf{grad}\ \Delta t||} = \frac{c_0}{\Delta f||\hat{\mathbf{r}}_x(\mathrm{P}) + \hat{\mathbf{r}}_r(\mathrm{P})||} \tag{1.97}$$

which can be rewritten as:

$$dr = \frac{c_0}{\sqrt{2}\Delta f\sqrt{1+\cos^2\vartheta(\mathrm{P})}} \tag{1.98}$$

with $\vartheta(\mathrm{P})$ the angle $\widehat{\mathrm{XPR}}$. In the monostatic case, we come back to the relationship already established at equation 1.16:

$$dr = \frac{c_0}{2\Delta f} \tag{1.99}$$

It is worth noting that the monostatic configuration will always give a better slant range configuration, compared to all other (bistatic) configuration.

Range resolution on the ground

Assume the radar to image a plane surface of equation $z = 0$. The ground range resolution is obtained by projecting vectors $\hat{\mathbf{r}}_x$ and $\hat{\mathbf{r}}_r$ on the ground plane, meaning only their x and y components are kept. Denoting by $\hat{\mathbf{r}}_x^s$ and $\hat{\mathbf{r}}_r^s$ the projections of $\hat{\mathbf{r}}_x$ et $\hat{\mathbf{r}}_r$, we get [82]:

$$dr = \frac{1/\Delta f}{||\,\mathbf{grad}\ \Delta t||} = \frac{c_0}{\Delta f||\hat{\mathbf{r}}_x^s(\mathrm{P}) + \hat{\mathbf{r}}_r^s(\mathrm{P})||} \tag{1.100}$$

In the monostatic case, the range resolution on the ground can be easily and explicitely written as:

$$dr_{\mathrm{sol}} = \frac{c_0}{2\Delta f\sin\theta_i(\mathrm{P})} \tag{1.101}$$

where $\theta_i(\mathrm{P})$ is the incident angle at target point P. The ground range resolution has no meaning when $\theta_i = 0$, when the wavefront is parallel to the surface (at nadir). There is a notion of bistatic nadir which is dependent upon point P; the direction of the bistatic nadir is obtained when $\hat{\mathbf{r}}_x(\mathrm{P}) + \hat{\mathbf{r}}_r(\mathrm{P})$ is zero, or said otherwise, when vector $\hat{\mathbf{r}}_x(\mathrm{P}) + \hat{\mathbf{r}}_r(\mathrm{P})$ is orthogonal to plane $z = 0$.

1.7 Synthetic aperture imaging

1.7.1 Overall view

Synthetic aperture radar (SAR) is a technique to increase the resolution of a target in the azimuth axis on the sole condition that the radar-target distance varies over time. In other words, it is assumed that the Doppler frequency of the target varies over time. The idea is then to coherently sum the signal corresponding to the target over several successive pulses, so as to increase the resolution of the image along the azimuthal direction.

In monostatic radar imaging, two configurations are possible: either the radar is in motion, most often in a straight line, and the target is immobile: this is called synthetic antenna imaging; if, on the other hand, the radar is fixed and the target is mobile, we speak of reverse synthetic antenna imaging (but the approach implemented is the same). Several sub-configurations may exist in the case of SAR imaging:

target-nadir triangle in the monostatic case, assuming the target to be on the ground, and assuming the ground to be flat.

[13] Doppler shift is typically totally negligible at this point.

1. *strip mode*: the antenna is oriented in a direction that is essentially orthogonal to its trajectory, which is essentially a straight line;

2. *squint mode*: the antenna is oriented at an angle different from $\pi/2$ with respected to the trajectory, which is essentially a straight line as in the strip mode;

3. *spotbeam/spotlight mode*: the antenna is continously steered at the position of a specific object of the scene, so that it remains in the line of sight, which allows to gain in azimuth resolution, at the cost of smaller imaged region;

4. *scanSAR* mode, where the elevation pattern of the array is steered electronically very quickly in order to increase the swath, at the cost of a lower temporal coverage of each object, *i.e.* of a degraded resolution.

In bistatic radar imaging, there are several additional degrees of freedom: the target can be mobile and both antennas stationary; one of the antennas can be mobile, or both can be mobile. In addition, the trajectory of the transmitter and receiver is not necessarily in the same direction.

1.7.2 Monostatic SAR imaging

1.7.2.1 Configuration

The monostatic case is here considered in strip map mode, as shown in figure 1.10(a). Suppose the antenna is aimed at a P point of $(x_P.y_P.0)$ coordinates. The radar R follows a straight trajectory, so that $\mathrm{R}(t) = [0.V_X t.h]'$. We now write $r(t) = ||\mathbf{PR}(t)||$. Then:

$$r(t) = \sqrt{x_P^2 + (y_P - V_X t)^2 + h^2} \tag{1.102}$$

It is always possible to write $r(t)$ in the following manner:

$$r(t) = \sqrt{(V_X t)^2 + r_0^2} \tag{1.103}$$

where r_0 is the distance between P and point R_0 which minimizes $r(t)$ (called *point of closest approach*, PCA), *i.e.* the orthogonal projection of P on the trajectory of R. The *distance of closest approach* is written r_0). It is also assumed, for simplicity, that the origin of times is taken when R is at R_0.

1.7.2.2 Expressing the received signal

Assume the radar to emit a pulse every T_I seconds. Note $t_X = nT_I$, the date when the n-th pulse is transmitted. It is always possible to write $t = t_X + s$. It is now assumed that the durations T_I, t, s are small, or that $V_X t_X \ll 1$, which is perfectly true in practice. Now let us write the signal received for the n-th pulse emitted. We start from the equation 1.95, which allows us to write:

$$E_R(t_X + s) = \kappa E_X(t_X + s - \Delta t(t_X)) \exp\left\{-\jmath \frac{4\pi}{\lambda_0} r(t_X)\right\} \tag{1.104}$$

By performing a Taylor development of order 2 of the term $r(t_X)$ for t_X around zero, we find:

$$r(t_X) = r_0 + \frac{1}{2}\frac{V_X^2 t_X^2}{r_0} + o(t_X^2) \tag{1.105}$$

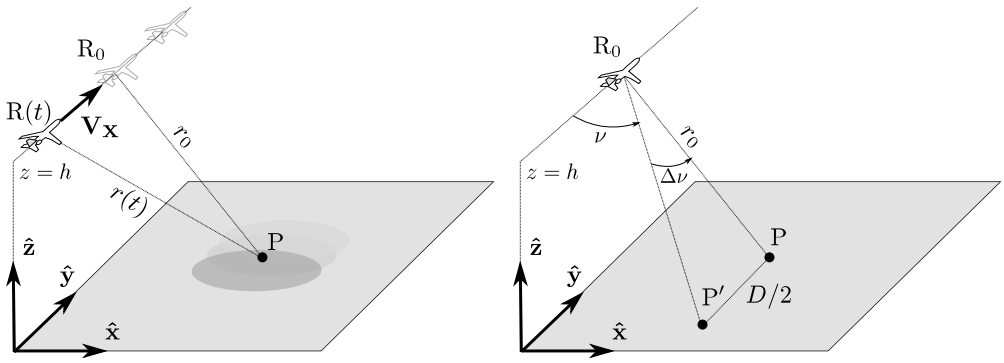

(a) Notations of aragraphs 1.7.2.1, 1.7.2.2, and 1.7.2.3.

(b) Notations of pararaphs 1.7.2.4.

Figure 1.10: *Geometric configuration of a scene observed by a monostatic synthetic antenna radar in strip map mode.*

Under this approximation, the signal received for the n-th pulse is of the form:

$$E_R(t_X + s) = \kappa E_X(t_X + s - 2r(t_X)/c_0) \exp\left\{-\jmath\left(\frac{2\pi}{\lambda_0}\frac{V_X^2 t_X^2}{r_0} - \frac{4\pi}{\lambda_0} r_0\right)\right\} \tag{1.106}$$

Since we have a time-range relationship $r_0 = 2c_0 s$, it is possible to write:

$$E_R(t_X + s) = \kappa E_X(t_X + s - 2c_0 r(t_X)) \exp\left\{-\jmath\frac{2\pi}{\lambda_0}\frac{V_X^2 t_X^2}{2c_0 s} - \jmath\frac{8\pi}{\lambda_0} c_0 s\right\} \tag{1.107}$$

We write:

$$\phi_{\text{SAR}}(t) = \frac{2\pi}{\lambda_0}\frac{V_X^2 t_X^2}{2c_0 s} \tag{1.108}$$

Figure 1.11 graphically shows the evolution of $\phi_{\text{SAR}}(t)$ over time, as well as the form of $\exp\{-\jmath\phi_{\text{SAR}}(t)\}$, in the case of monostatic SAR. We see that the beats follow a LFM *chirp*.

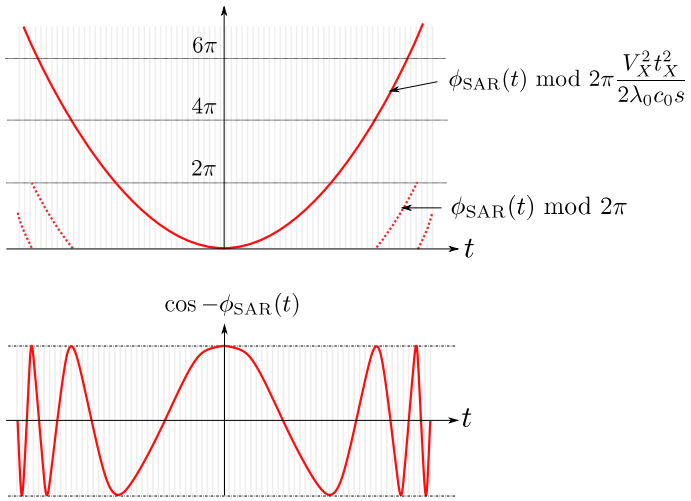

Figure 1.11: *Time evolution of $\phi_{SAR}(t)$ and $\cos -\phi_{SAR}(t)$ during synthetic aperture radar integration (adapted from [95]).*

1.7.2.3 SAR integration in practice

The received radar signal given by equation 1.107 can be written not as a one-dimensional function of $t_X + s$, but as a two-dimensional function of t_X and s:

$$f_{\mathrm{RAR}}(t_X, s) = \kappa E_X(t_X + s - 2c_0 r(t_X)) \exp\left\{-\jmath\frac{2\pi}{\lambda_0}\frac{V_X^2 t_X^2}{2c_0 s} - \jmath\frac{8\pi}{\lambda_0}c_0 s\right\} \tag{1.109}$$

A graphical representation of f_{RAR} can be found in figure 1.12. The t_X axis is commonly called the *azimuthal axis*: this name is due to the fact that fixed radars with mechanical scanning are generally rotating, each pulse being emitted in a different direction. The s axis is called the (slant) *range axis*; thus, $f_{\mathrm{RAR}}(t_X, s)$ contains the signal received on a date s after the emission of the n-th pulse, at t_X.

Negligible range migration If during the illumination time of point P, the difference in the times of flight for each pulse is less than the resolution $1/\Delta f$ of the signal on the time axis, we can consider that the migration in distance of the point P is negligible. This means that all received pulses for the target start and end at the same range bin on the sampled range axis, whatever the pulse. In this case, the processing of the SAR signal is done according to two steps that we will detail: distance compression, and azimuthal compression.

Range compression is done by matched filtering on $f_{\mathrm{RAR}}(t_X, s)$, at a fixed t_X, as described in paragraph 1.1.4. Once this processing is done, the signal undergoes another matched filtering in the azimuthal direction to increase the resolution of the signal: this is azimuth compression. If the scene contains only one point P whose distance to the radar trajectory is r_0, the synthetic antenna integration consists in summing coherently, for all t_X where the signal received from the point P is not negligible, the signal received by compensating the phase. Assuming here that P is permanently visible:

$$f_{\mathrm{SAR}}(t_X, s) = \int_{-\infty}^{+\infty} f(u, s) e^{\jmath\phi_{\mathrm{SAR}}(u)} du \tag{1.110}$$

If we now generalize the integration for a scene with several points, we must realize the integration for all the points having a distance of minimum approach r_0. In general, the distance r_0 is not reached at t =0. The formula 1.110 therefore generalizes as the intercorrelation of $f_{\mathrm{RAR}}(t_X, s)$, with $\exp \jmath\phi_{\mathrm{SAR}}(t)$ (for a fixed s parameter):

$$f_{\mathrm{SAR}}(t_X, s) = \int_{-\infty}^{+\infty} f_{\mathrm{RAR}}(t_X + u, s) e^{\jmath\phi_{\mathrm{SAR}}(u)} du \tag{1.111}$$

Staying in line with paragraph 1.1.4, this can be construed as an azimuth pulse compression. This pulse compression can be effiently performed in the Fourer plane, as is done for range compression.

General case: non negligible range migration In the more general case where the range migration is no longer negligible, it is then necessary to use an algorithm that explicitly takes into account this migration. Various approaches exist to perform the SAR integration operation in all its generality. The best known algorithm is the Range-Doppler algorithm (for example, we can refer to [92] for an introduction to most SAR integration algorithms, including this one). The method we have just described above in case of negligible range migration is none other than the Range-Doppler algorithm without a step known as *range cell migration correction*). The migration correction is done simply, before azimuth compression. We work in Fourier space in the azimuthal direction, that is to say in

the space of Doppler frequencies, while remaining in the space of time or distances for the axial direction of the antenna; this is what is at the origin of the name of the method. The distance-Doppler signal is then reinterpunted so that the place of the Doppler spectrum of the points associated with a reference distance r_0, is brought back to a line located entirely on the Axis of Doppler frequencies, as shown in figure 1.12. Azimuthal compression can then be performed directly in the Fourier domain (see figure 1.12). Indeed, an interesting property of the signal is that, for a pulse emitted at t_X, the contribution received from two distinct and fixed points P_1 and P_2 will differ in the Doppler component, even if the signal of the two points arrives at the same time. Also the algorithm used to integrate the image for a single point is the same for a scene composed of many points. Indeed, it can be shown that the location of the spectral components of the contributions of all points having the same minimum distance to the radar r_0, is the same.

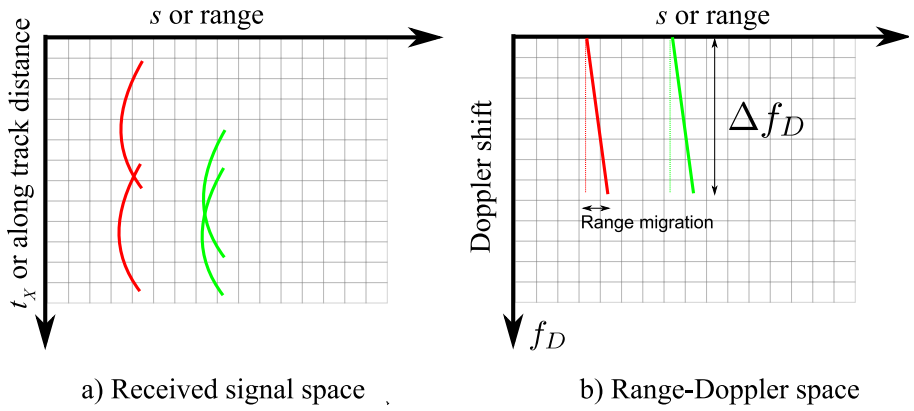

Figure 1.12: *Received signal space $f_{RAR}(t_X, s)$ and range-Doppler space. The locus of the contribution of all the points having the same closest point of approach, is the same for all these points.*

Other algorithms are also used. The *Chirp Scaling Algorithm* [148, 52] gets rid of the interpolation step by modifying directly the azimutal chirp to compensate the range migration. The $\omega - k$ algorithm allows doing the pulse compression in both the range and azimuth axes by using the Stolt method [192]. The *Fast Factorised Back Projection* (FFBP) [178], and the *SPECtral ANalysis* (SPECAN) algorithms [181] are fast approaches for SAR integration. In this thesis, only the Range-Doppler algorithm was used.

Note on the hypotheses we used We also note that during the integration a hypothesis is made on the trajectory of the vehicle (as well as the target). In reality, the trajectory of the vehicle is only imperfectly known. Also it is important to have robust algorithms and an approximation of the trajectory at an accuracy greater than the wavelength of the signal, which is often difficult! For this purpose, specific instruments can be used:

- for airborne SAR, an excellent inertial navigation system, which is a significant additional cost – several tens of thousands of euros;
- for spaceborne SAR, a precise orbitography, for example carried out with the French DORIS system (Determination of Orbit and Integrated Radiopositioning by Satellite), which makes it possible to know the position of a satellite with centimetric precision;

It is also possible (for airborne SAR) for the aircraft to fly high (possibly out of the troposphere), to try and limit turbulence – which also increases the swath. Finally, we can

try to use the signal received by radar to try to estimate the trajectory, hybridizating the estimation with inertial means: for example a correlation of the received signal over two consecutive pulses provides an indication of the transverse displacement [27]. In practice, however, in radar, these precision problems are somewhat less felt than in the case of synthetic antenna sonar, where these hybridization techniques are used.

When targets are moving, we refer to the ambiguity function of the emitted signal. In the case of a linear frequency ramp, we saw above that the Doppler effect would shift the measured arrival moment of the signal coming from a moving target after pulse compression. This results in a translation in the image. This result remains relevant in SAR imaging: if the target is mobile, then its image will be perfectly focused, but not where it should be if it were immobile. For instance, the image of a car would not necessarily be over the image of the road. The measurement of this offset makes it possible to go back to the target-radar relative speed. This is a process called Moving Target Indication (MTI).

1.7.2.4 Azimuthal resolution after SAR integration

In practice, a coherent sum cannot be computed for $t_X \in]-\infty, +\infty[$, unless the antenna rotates so as to always aim at target P. Otherwise, point P will only be illuminated for a limited duration $\Delta t_{\text{illum.}}$ depending on the speed V_X of the radar carrier, and the width $\Delta d_{\text{az}}(\text{P})$ of the antenna lobe in azimuth at point P (this width can be calculated according to the formulas in paragraph 1.2.3.1):

$$\Delta t_{\text{illum.}} = \Delta d_{\text{az}} / V_X \tag{1.112}$$

(strictly speaking, the amplitude of the received signal also varies with the variation in reflectivity due to the variation of viewing direction, but this variation is small if the width of the transmitting antenna lobe is large). Similarly, since function $t \mapsto \exp \jmath\phi(t)$ is discretized at times t_X, it will be necessary to ensure that the inverse of the pulse repetition period T_I is greater than the maximum frequency reached by the azimuthal *chirp* azimutal during the illumination time of the target. This is nothing else than a Shannon-Nyquist condition.

The following development owes largely to Hovanessian [95] (pp. 18-19 et p. 22). Resolution after azimuthal integration is linked to the bandwidth of the azimuthal *chirp*. Let us consider a point P' of coordinates $[x_P, y_P + D/2, 0]^t$. Parametrizing the points as a function of angle ν, as shown in figure 1.10(b), the Doppler frequency at points P and P' can be computed as follows:

$$f_D(P) = \frac{2V_X \cos\nu}{\lambda_0} \tag{1.113}$$

$$f_D(P') = \frac{2V_X \cos(\nu + \Delta\nu)}{\lambda_0} \tag{1.114}$$

Assuming $\Delta t \ll 1$ it comes:

$$\Delta f_D = f_D(P') - f_D(P) = \frac{2V_X}{\lambda_0} \Delta\nu \sin\nu \tag{1.115}$$

Angle $\Delta\nu$ can be approximated by $D/2r_0$, yielding:

$$\Delta f_D = \frac{V_X D}{\lambda r_0} \sin\nu \tag{1.116}$$

Hence the azimuth resolution:

$$dr_{\text{az.}} = \frac{D}{2} = \frac{\lambda_0 r_0 \Delta f_D}{2V_X \sin\theta} \tag{1.117}$$

This equation is special: it does not depend on the antenna aperture, contrarily to the resolution for a real aperture radar (paragraph 1.2.2.4). Recall that synthetic aperture integration is a specific case of pulse compression for a *chirp*; the duration of illumination $\Delta t_{\text{illum.}}$ must then be equal to $1/\Delta f_D$, meaning the carrier flies over a distance $d_y^{\text{SAR}} = V_X \Delta t_{\text{illum.}}$. Then:

$$d_y^{\text{SAR}} = V_X \Delta t_{\text{illum.}} = \frac{V_X}{\Delta f_D} = \frac{\lambda_0 r_0}{D \sin \nu} \tag{1.118}$$

By manipulating the equations it comes that:

$$dr_{\text{az.}} = \frac{\lambda_0 r_0}{2 d_y^{\text{SAR}} \sin \nu} \tag{1.119}$$

This is an equivalent equation for the azimuth resolution at a range r_0 for an array of length d_y. Quantity d_y^{SAR} can be seen as the length of the synthetic aperture radar antenna, as necessary to get resolution $dr_{\text{az.}}$. The real antenna length can be used to get a lower bound for resolution $dr_{\text{az.}}$. Assuming that the target is illuminated during a time greather than $1/\Delta f_D$, since the illumination time is linked to the real aperture, itself linked to the physical length of the transmitting array d_y:

$$\frac{r_0 \lambda}{d_y} \geq d_y^{\text{SAR}} = \frac{\lambda_0 r_0}{D \sin \nu} \tag{1.120}$$

Noting that $\nu \approx \pi/2$ (maximum illumination), then the resolution is equal to $D/2$, meaning that:

$$dr_{\text{az.}} \geq \frac{d_y}{2} \tag{1.121}$$

This value is a theoretical limit used to judge the quality of the integration. Indeed as the duration of illumination increases, we substantially meet the hypothesis $u \approx \pi/2$ and then the resolution goes towards the maximum limit. This shows an interesting effect: the azimuthal resolution will then no longer depend on the distance to the antenna.

1.7.3 Generalizing to the bistatic case

1.7.3.1 The general case

In the bistatic case, the principles for synthetic aperture integration are the same as in the monostatic case. First a pulse compression is carried out on the range axis. Then an azimuthal synthetic aperture integration is performed; this reduces to a pseudo pulse compression on the azimuth axis. We consider the notations in figure 1.13, which only generalize those of the monostatic case. We take the origin of time when the distance $r(t) + r'(t)$ is minimal and denoted by $r_{\min}$. Note that the instant $t = 0$ is not necessarily when the distance is $r_0 + r'_0$. In fact, this distance is not necessarily reached because of the speeds of the transmitter and the receiver do not necessarily match. As in the monostatic case, the signal received for the n-th transmitted pulse takes the form:

$$E_R(t_X + s) = E_X(t_X + s - \Delta t(t_X)) e^{-\jmath\left(\phi_{\text{SAR}}(t) - \frac{2\pi}{\lambda_0} r_{\min}\right)} \tag{1.122}$$

with:

$$\phi_{\text{SAR}}(t) = \frac{2\pi}{\lambda_0}[r(t) + r'(t) - r_{\min}] \tag{1.123}$$

Following [44], and being inspired by the monostatic case, a Taylor development at the second order of $r(t)$ et $r'(t)$ around $t = 0$, yields:

$$\phi_{\text{SAR}}(t) = -\frac{2\pi}{\lambda_0}\left(\frac{V_X^2 t^2}{2 r_0} + \frac{V_R^2 t^2}{2 r'_0}\right) \tag{1.124}$$

It is this term that is used to make the synthetic aperture integration: instead of a *chirp* in the form of a linear frequency ramp, we have a *chirp* whose instantaneous frequency is given by the derivative of $\phi_{\text{SAR}}(t)$. The rest of the processing is then essentially the same as in monostatic. And in fact, monostatic algorithms have mostly been adapted to the bistatic case (see Ben Kassem [25] for a simple parallel case addressed by the Range-Doppler method and by integration into the time domain; see Yew *et al.* [198] for a generalization of the Range-Doppler algorithm, and Wong *et al.* for a generalization of the Chirp Scaling Algorithm [194]).

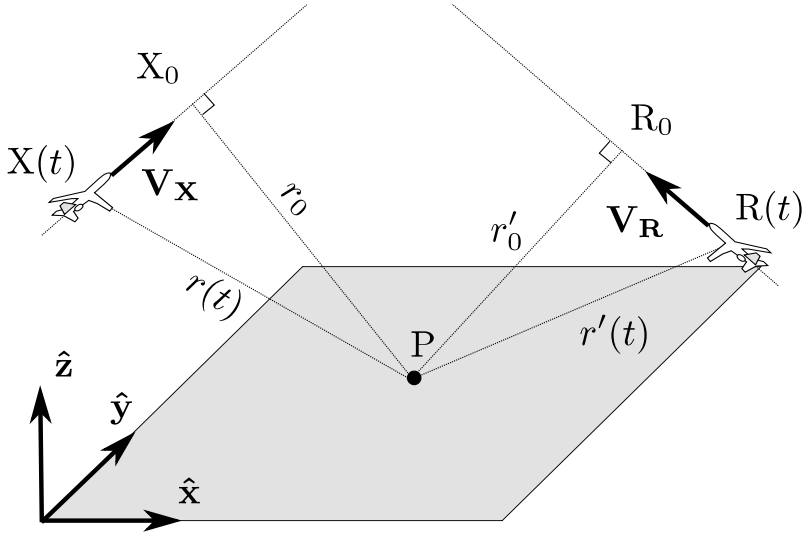

Figure 1.13: *Configuration and notations for bistatic synthetic aperture imaging*

1.7.3.2 Parallel BiSAR configuration where the carriers have the same constant velocity vector

Equation 1.124 has a limitation: there is no explicit dependency between the parameters of $\phi(t)$ and the time s used on the range axis. Indeed, we have:

$$s = \frac{r_{\min}}{c_0} \tag{1.125}$$

but the denominators of the terms of f_D are r_0 and r'_0. In practice, it is necessary to use a "trick" to come back to parameterization depending on s. For this a hypothesis is needed concerning the location of the points for which one calculates the phase history. To illustrate this point, we consider here the special case where the transmitter and the receiver have the same velocity vector: $\mathbf{V}_X = \mathbf{V}_R$. This configuration is shown in 1.14. The advantage of this configuration is that the phase history of the points associated with a minimum approach distance $r_{\min}$, will not change over time. We can therefore calculate, for each $r_{\min}$, this story, and perform the pulse compression for the whole dataset at the same time using the same equation; this is very efficiently done using a Fourier transform as is done in the monostatic case.

However, for a given bistatic configuration, one of the antennas must be steered so that it aims at the same point T of plane $z = 0$, as the other antenna. This makes it possible to ensure an optimal power budget since the antenna lobes will overlap; if they do not, the budget would be poor. Synchronizing the antennas between two carriers so that they aim at the same point is a complex issue in practice.

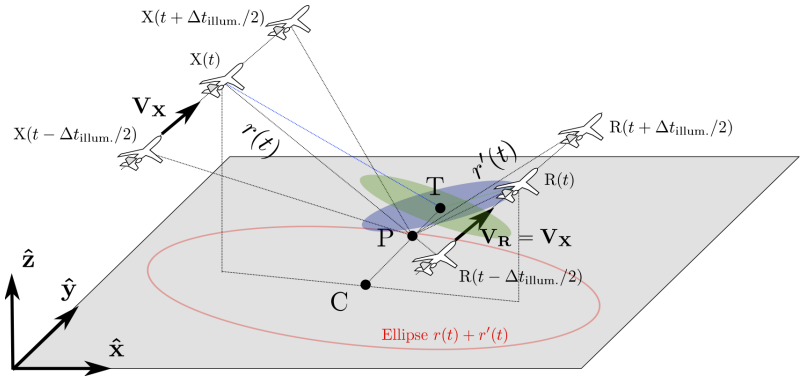

Figure 1.14: *Parallel BiSAR configration. The two carriers do not necessarily fly at the same altitude; their antenna is not necessarily pointing 90° sideways.).*

To perform the azimuthal pulse compression, it is necessary to calculate the history of the phases around the date when a given target is illuminated at best. It is important to note that this date is not necessarily when the transmitter-target-receiver range is shortest. This does not change the formulas but only the time window where the function $\phi(t)$ is calculated: it is no longer centered at $t = 0$. This is nothing but the bistatic counterpart of the monostatic "squint" mode.

To find this date when a given target is illuminated at best, we have to make a hypothesis on the position of the target on the Fresnel ellipse. To do this, we consider the history of the points located on the half-line [CT), where C is the center of the Fresnel ellipses and T the point where the two antennas aim at. These points are indeed well lit by the antennas. We could have taken any other half-line, as long as the points on that half-line would be well lit.

The approach is then as follows:

1. In a fixed coordinate system with respect to the transmitter and receiver, for a given distance $r_{\min}$ (or a date $s = r_{\min}/c_0$), calculate the parameters of the Fresnel ellipse intersecting the ground and associated with this distance $r_{\min}$;

2. Determine the coordinates of the point P belonging to both this ellipse, and the half-line [CT);

3. Assuming a fixed target P and mobile antennas, calculate the distance $r(t) + r'(t)$ for t ranging from $-\Delta t_{\text{illum.}}/2$ to $+\Delta t_{\text{illum.}}/2$;

4. Calculate the minimum distance of approach $r_{\min}$, this is done numerically using an optimization algorithm (dichotomy, gradient descent, *etc.*);

5. The phase function associated with s is then $\phi_{\text{SAR}}(t) = 2\pi/\lambda_0(r(t) + r'(t) - r_{\min})$

Once the phase function is known, integration over the azimuth axis is done exactly as in the monostatic case.

1.7.3.3 Illustrations of a specific "parallel track" BiSAR case

Given a configuration (see the table 1.2) for a simulated radar, an example of bistatic synthetic aperture integration is shown in figure 1.15. At the beginning of the simulation, the transmitter is at $\text{X}(0) = [-6000; 0; 3000]$ while the receiver is at $\text{R}(0) = [-3000; 0; 3000]$; this configuration will be repeated in chapter 5 and is illustrated in figure 5.4(d). The

Variable	Valeur
True (ground) speed of the aircraft	$V_X = 222$ m/s (800 km/h)
Carrier frequency	$f_0 = 10{,}0$ GHz ($\lambda_0 \approx 3$ cm)
Modulation	$\Delta f = 60$ MHz (linear frequency ramp, rising)
PRF	222 Hz
Pulse duration	$T_X = 0{,}333$ μs
Peak power	1 W
Losses	none
Antennas	rectangular, uniformly lit, 4 m$\times$ 5 cm

Table 1.2: *Parameters of the simulated bistatic radar*

transmitter aims at the ground with an incidence of 45 degrees, and the receiver with an incidence of 63.4 degrees. The configuration of the diffusers is given in figure 1.15(a); they are ideal isotropic diffusers of SER unit. The range history $r(t) + r'(t)$ is shown in figure 1.15(c). Figure 1.15(b) shows the baseband received signal; we can clearly see the phase beats caused by the range variation history. Figure 1.15(d) shows the result of pulse compression on the range axis. Figure 1.15(f) shows the image after compression over the range and azimuth axis. Finally, the azimuth cross-section of the integrated signal for the target located at (0.0) is given in the figure 1.15(e). We measure a resolution of 2.25 m, which is close to the ideal 2 m that would be obtained in the equivalent monostatic configuration (given that the antenna is 4 m long). The simulation presented here has the advantage of providing a first validation of the bistatic syntethic aperture integration algorithm in a non-trivial geometric configuration. This configuration is the same as one implemented in chapter 5, dedicated to the simulation of radar images in the marine environment.

1.8 Conclusion of this chapter

This chapter is essentially a detailed treatment of the bistatic radar equation. It thus made it possible to process the different components of the radar acquisition chain: the transmitted and received signal, the antennas, the target. It also included a treatment of the Doppler effect in bistatic configuration. This development was followed by a brief introduction to the problem of monostatic and bistatic synthetic aperture integration. This problem is not the main contribution of our work so it has been dealt with quickly, nevertheless trying to illustrate the problem in a simple bistatic case. This is rarely done in the literature, as it focuses mainly on the monostatic case.

The next three chapters of this manuscript will essentially be a deepening of the modeling of the reflection of a radar wave on a rough surface, in this case the ocean surface with wakes. Chapter 5 will follow very closely the framework of chapter 1, since it will deal with the implementation of the various components of the chain exposed in this chapter. The goal being a raw radar signal simulation, it will show the results obtained on these signals after bistatic synthetic aperture integration.

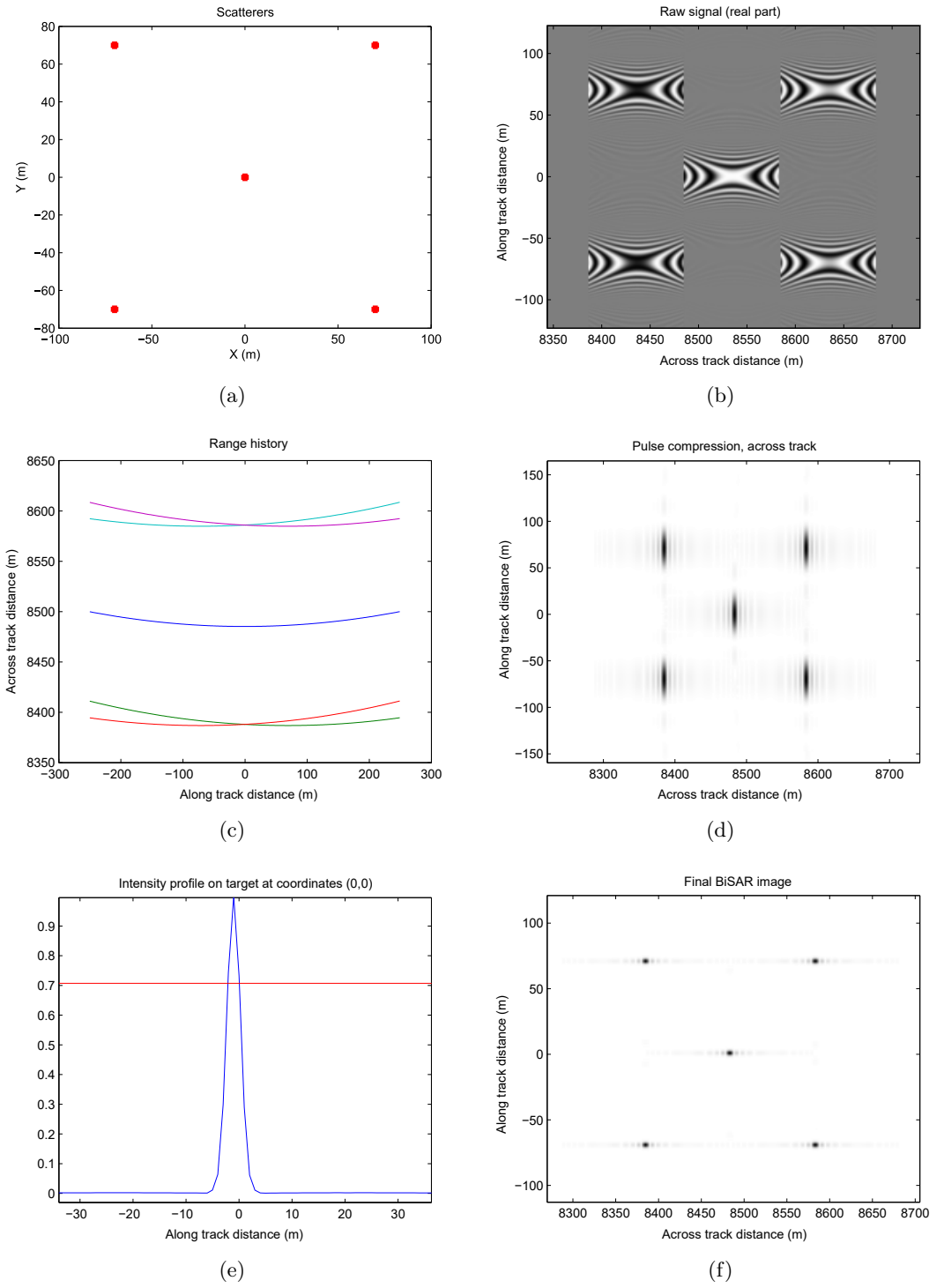

Figure 1.15: *BiSAR integration using the Range-Doppler method (without range migration compensation) for a set of point targets with unit RCS.*

Chapter

2 Describing and modelling the marine surface

Contents

This chapter does not pretend to replace a good text on oceanography. However, the simulation of the radar signal reflected by the sea requires to know a number of models with their area of validity as well as their limits. In a first part (section 2.1), we will first explore some of the physical characteristics of the sea, such as temperature and salinity. These two parameters have an influence on the electrical permittivity of the surface. In a second part (2.2), we focus on the geometric characteristics of the surface, which will also have an influence on the aspect of the sea in radar images. These geometric features can be described in several ways; we present three main families of approaches. We start by studying the Navier-Stokes equations (section 2.2.2) and their solutions at several levels of approximation, with a particular focus on the linear approximation. This study will also be an opportunity to demonstrate a number of relationships that will be fundamental in the rest of the manuscript (including the wave dispersion relationship, the phase and group speed of the wave components, *etc.*). A second approach considers the sea as a statistical 2D signal (section 2.2.4) whose probability density of heights can be studied from a spectral point of view, depending on the various parameters influencing the creation of waves: mainly the direction and speed of the wind. The last approach, probabilistic (section 2.2.6), models the probability of wave slopes as a function of wind. The last two approaches outlined above are those used in the electromagnetic models, as exposed in chapter 4.

2.1 Physical characteristics of the marine environment

2.1.1 Temperature

The temperature of the sea varies according to the season, the position on the globe, and depth. As part of the radar signal modeling, only surface temperature matters really. Indeed, it influences the dielectric constant of water on the surface, as we will see in paragraph 2.1.3.2. Temperature maps can be obtained either by buoys, or by remote sensing. The figure 2.1 gives the average sea surface temperature for year 2005. In the following, the temperature will be noted T and will be expressed in degrees Celsius.

2.1.2 Salinity

Since seawater is a good solvent, it is an environment in which a large number of substances can dissolve and enter into relationship. The sea contains an average of 34.7 g of salts per kilogram of water sea. However, salinity varies according to the seas. Historically, salinity [S] was deducted from chlorinity [Cl], that is, the quantity in g/kg or parts per million of chlorine, bromine and iodine present in seawater and precipitated by silver nitrate titration [8]. This relationship between [S] and [Cl] is linear:

$$[\mathrm{S}] = 0.03 + 1.805[\mathrm{Cl}] \text{ [g/kg] or [ppm]} \tag{2.1}$$

Since 1978, the salinity of the ocean has been defined by the conductivity of seawater, which directly depends on the amount of dissolved salts in the water. The practical salinity scale is used; it is defined in practical salinity units (psu). This unit is totally dimensionless because it is defined as a function of the ratio K_s between the electrical conductivity of the water of sea at 15° C and 1013.15 hPa, and that of a standard solution (at the same pressure and temperature conditions) of potassium chloride wherein the mass fraction of potassium chloride is 0.0324356. The equation of the practical salinity then connects K_s to [S] using this relation [8]:

$$[\mathrm{S}] = 0.0080 - 0.1692K_s^{1/2} + 25.3851K_s + 14.0941K_s^{3/2} - 7.0261K_s^2 + 2.7081K_s^{5/2} \text{ [psu]} \tag{2.2}$$

The practical salinity scale is defined in such a way that [S] = 35 ups when ratio K_s is 1, so that similar (but not identical) values to to the former scale are obtained. Figure 2.2 is a global map of average salinity in ocean waters. The usual value for salinity in the rest of the dissertation is taken to be [S] = 35 psu$\approx$ 35 ppm.

2.1.3 Electromagnetic characteristics of seawater

2.1.3.1 General considerations

From the electromagnetic point of view, the sea can be described by two quantities: the relative electrical permittivity and the relative magnetic permeability. Since seawater is a non-magnetic medium, its magnetic permeability is close to one: $\mu \approx 1$, and so we will take it equal to one. Seawater is therefore only described by its constant dielectric. The relative dielectric constant ϵ_r is the ratio of the dielectric constant of the medium ϵ_d to the dielectric constant of the vacuum ϵ_0. It is a complex number which real part and imaginary part are without units.

2.1.3.2 Model for the relative dielectric constant of sea water

In the case of seawater, the relative dielectric constant ϵ_r depends on the salinity, temperature, and the frequency of the incident radio wave. A number of semi-empirical consider-

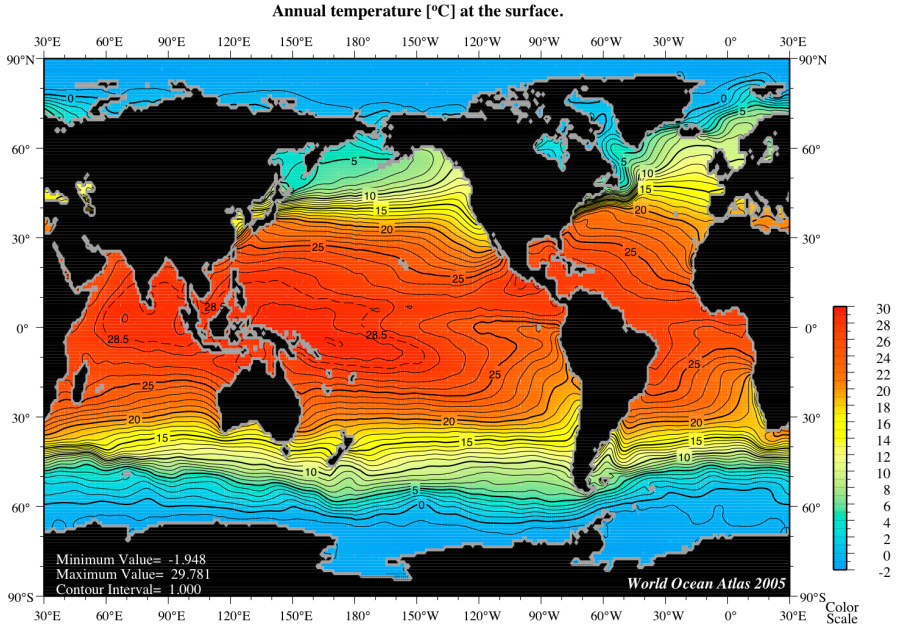

Figure 2.1: *Average surface temperatures in year 2005 (data courtesy of NOAA/National Oceanographic Data Center, [120]).*

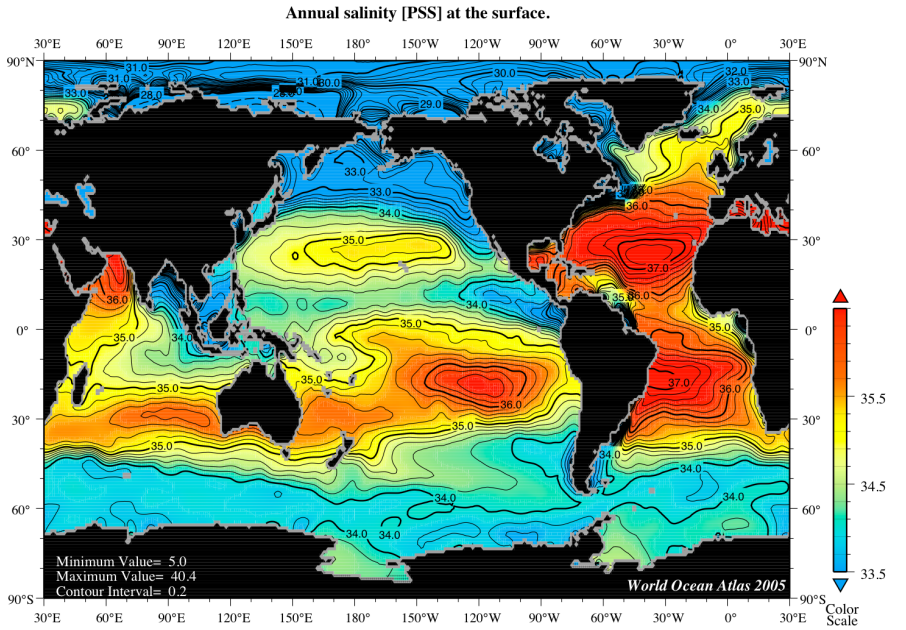

Figure 2.2: *Average surface salinity (PSU) in 2005 (data courtesy of NOAA/National Oceanographic Data Center, [7]).*

ations yield the following model, which is only one among many [107, 51]:

$$\epsilon_r = \epsilon_{r\,\inf} + \frac{\epsilon_s - \epsilon_{r\,\inf}}{1 + (\omega\tau_r)^2} - \jmath\left[\frac{(\epsilon_s - \epsilon_{r\,\inf})\omega\tau_r}{1 + (\omega\tau_r)^2} + \frac{\sigma_s}{\omega\epsilon_0}\right] \tag{2.3}$$

where:

- $\epsilon_0 = 8.854 \times 10^{-12}$ F/m is the vacuum permittivity;
- $\omega = 2\pi f$ is the pulsation of the incoming radio wave rad/s;
- ϵ_s is the static dielectric constant in F/m; it is obtained thanks to this semi-empirical equation:

$$\begin{aligned}\epsilon_s &= (87.134 - 1.949\text{10}^{-1}T - 1.276\text{10}^{-2}T^2 + 2.491\text{10}^{-4}T^3)\ldots \\ &\quad \times(1 + 1.613\text{10}^{-5}T[\mathrm{S}] - 3.656\text{10}^{-3}[\mathrm{S}] + 3.210\text{10}^{-5}[\mathrm{S}]^2 - 4.232\text{10}^{-7}[\mathrm{S}]^3)\end{aligned} \tag{2.4}$$

- σ_s is the static conductivity of salt water, which is given by:

$$\sigma_s = \sigma_s^0 \exp(-g(T)) \tag{2.5}$$

$$\sigma_s^0 = 0.18252[\mathrm{S}] - 1.461\text{9}10^{-3}[\mathrm{S}]^2 + 2.093\text{10}^{-5}[\mathrm{S}]^3 - 1.282\text{10}^{-7}[\mathrm{S}]^4 \tag{2.6}$$

$$\begin{aligned}g(T) &= 2.033\text{10}^{-2}\Delta T + 1.266\text{10}^{-4}\Delta T^2 + 2.464\text{10}^{-6}\Delta T^3\ldots \\ &\quad -(1.849\text{10}^{-5} - 2.551\text{10}^{-7}\Delta T + 2.551\text{10}^{-8}\Delta T^2)[\mathrm{S}]\Delta T\end{aligned} \tag{2.7}$$

$$\Delta T = 25 - T \tag{2.8}$$

- τ_r is the relaxation time of the surface in seconds; physically, if an excess of free charges is added in a conductive medium, this excess will decay exponentially with a time constant τ_r. For seawater, the time of relaxation is obtained by this semi-empirical relation:

$$\begin{aligned}\tau_r &= f \times \left(1.110\text{9}10^{-10} - 3.824\text{10}^{-12}T + 6.938\text{10}^{-14}T^2 - 5.096\text{10}^{-16}T^3\right) \\ &\quad \times \left(1 + 2.282\text{10}^{-5}T[\mathrm{S}] - 7.638\text{10}^{-4}[\mathrm{S}] - 7.760\text{10}^{-6}[\mathrm{S}]^2 + 1.105\text{10}^{-8}[\mathrm{S}]^3\right)\end{aligned} \tag{2.9}$$

- $\epsilon_{r\,\inf}$ is the high frequency limit of ϵ_s; it is generally equal to 4,9.

2.1.3.3 Limits of the model

The model was validated for a certain range of salinities and temperatures. It is necessary to use realistic temperatures (between 1 and 40 degrees Celsius); the salinity can go from 4 g/kg up to 35 g/kg, or even 37 g/kg.

2.1.4 Wind

Wind is the primary cause of swell. As the shape of the swell will directly influence the roughness of the sea and therefore the reflected radar signal, the wind is a very important parameter in the modeling of the radio signal reflected by the sea surface. Low altitude tropospheric winds are of specific interest, since they are the ones who interact directly with the surface of the sea. Boundary layer phenomena in the vicinity of the surface will slow down the air speed so that, at the limit where the altitude z tends towards zero, the wind speed is only of the order of a few centimeters per second: this is the friction speed which will be denoted by U_0. The wind speed increases rapidly with altitude and reaches

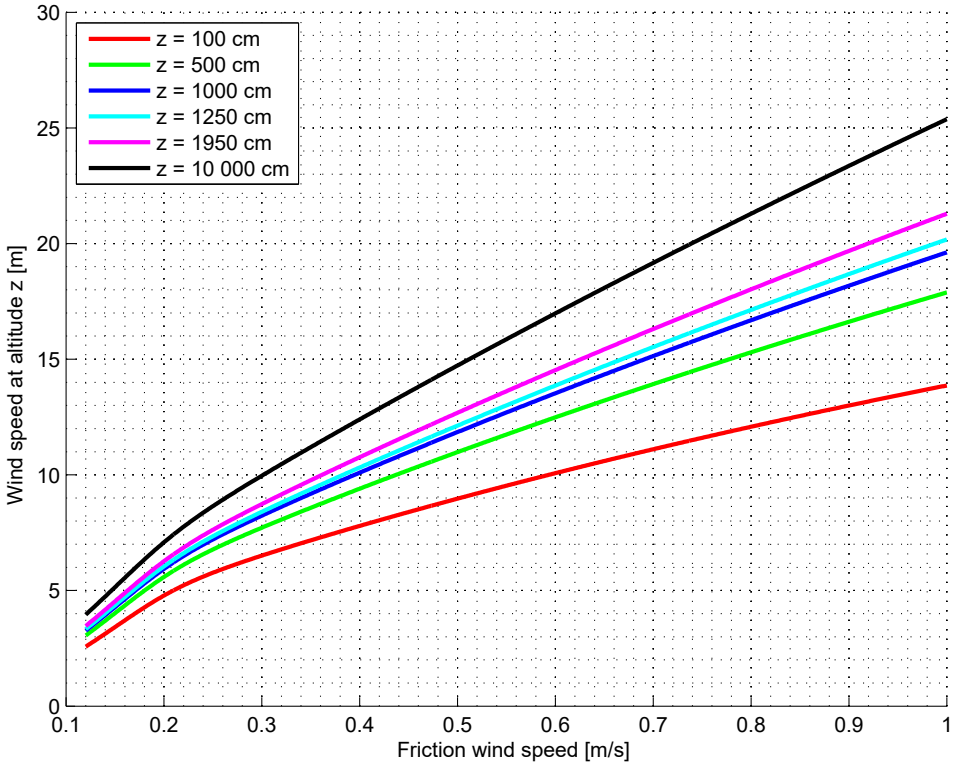

Figure 2.3: *Wind speed in m/s as a function of the friction speed, for several altitudes z (in centimeters).*

an asymptotic limit denoted by U. This limit is of course a simplification. In the following, we will note U_z the wind speed in m/s at altitude z, expressed in centimeters.

A commonly used speed/altitude model for wind in the maritime environment, is the following [78]:

$$U_z = (U_0/k_k)\ln(z/z_0) \text{ [m/s]} \tag{2.10}$$

with k_k the Von Kármán constant (about 0.4); z is in centimeters, U_0 in m/s and:

$$z_0 = 6.8410^{-3}/U_0 + 4.2810^{-1}U_0^2 - 0.0443 \text{ [cm]} \tag{2.11}$$

This model has been experimentally validated for friction speeds over 0.12 m/s. The abacus given at figure 2.3 can be used to get the wind speed U_z in m/s from the friction velocity U_0 for several standard altitudes z in centimeters.

The force of the wind can be characterized by the Beaufort scale, which describes by a number B (integer), a range of wind speeds and typical effects on the sea and on the ground. The formulation of this scale has evolved over the years; the one presented here is used internationally since 1946 (resolution 9 of the International Meteorological Committee, in Paris). The Beaufort scale is related to wind speed by the empirical formula [24]:

$$U_{1000} = 0,836B^{3/2} \text{ [m/s]} \tag{2.12}$$

Table 2.1 describes the Beaufort scale in more detail. The sea state is characterized by another scale, the Douglas scale, also standardized by the World Meteorological Organization ([3], table 3700). This scale is given in table 2.2. The Douglas scale, in the case of

a fully developed, offshore sea, is conceptually equivalent to the Beaufort scale, because it involves the height of the swell, which can be linked to the force of the wind as we shall see in the paragraph 2.2.4. In the remainder of the manuscript, the Beaufort scale is used.

2.2 Geometrical characteristics of the ocean: sea waves

This section addresses the geometry of the sea surface and its temporal evolution. Modeling of the maritime surface has historically been one of the great applications of hydrodynamics, insofar as the knowledge of the shape of waves and wake has many applications in naval architecture and offshore engineering: prediction of the amplitude of waves to size a structure, calculation of forces, resistance to advance, *etc.* In general, the simplest categorization of waves can be done from their wavelength Λ (see figure 2.5). Depending on the wavelengths, the physical mechanisms at the origin of the waves are not the same. For our application, three regimes are of interest: *i)* very small wavelengths, the domain of capillary waves dominated by surface tension forces, *ii)* gravity waves, dominated by inertial forces, and *iii)* waves of intermediate wavelength. These are the regimes that are observable with radar. Figure 2.4 gives a classification of the different types of waves that can be observed according to the forces at work, their origin, and their wavelength.

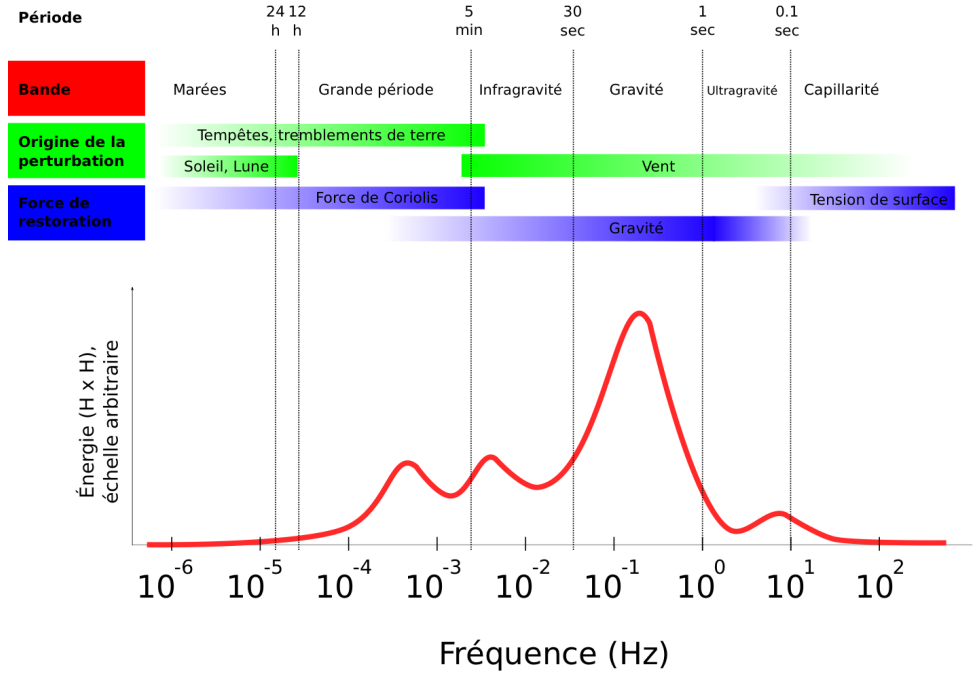

Figure 2.4: *Classification of waves depending on their period and the forces creating them; adapted from Kinsman [105].*

Modeling these waves can be done within the most general framework possible, namely the Navier-Stokes equations, but the direct resolution of these equations is usually impossible. Approximations are generally used, depending on the type of phenomenon to model: the swell or the capillary waves. Here we begin by presenting the Navier-Stokes equations, as well as three approximate models common to solve these equations in an approximate way: the Airy model, Gerstner's model, and Stokes' model. Airy's model and Gerstner's are treated in more detail because they are the basis of many of the results used in the rest of this manuscript; we will only mention the most important results of Stokes' theory. We will not deal with the other more specific models of ocean waves (cnoidal theory, Boussinesq

B	Name	U_{1000}			H_{m_0} [1]	Description
		kt	km/h	m/s		
0	Calm	0	0	0	0-0,2	See like a mirror.
1	Light air	1-3	1-6	0,3-1,5	0,1	Ripples with appearance of scales are formed, without foam crests.
2	Light breeze	4-6	7-11	1,6-3,3	0,2	Small wavelets still short but more pronounced; crests have a glassy appearance but do not break.
3	Gentle breeze	7-10	12-19	3,4-5,4	0,6	Large wavelets; crests begin to break; foam of glassy appearance; perhaps scattered white horses.
4	Moderate breeze	11-15	20-29	5,5-7,9	1	Small waves becoming longer; fairly frequent white horses.
5	Fresh breeze	16-21	30-39	8,0-10,7	2	Moderate waves (l=1,2 m) taking a more pronounced long form; many white horses are formed, chance of some spray.
6	Strong breeze	22-27	40-50	10,8-13,8	3	Large waves begin to form; the white foam crests are more extensive everywhere; probably some spray.
7	High wind	28-33	51-62	13,9-17,1	4	Sea heaps up and white foam from breaking waves begins to be blown in streaks along the direction of the wind; spindrift begins to be seen.
8	Gale	34-40	63-75	17,2-20,7	5,5	Moderately high waves of greater length; edges of crests break into spindrift; foam is blown in well-marked streaks along the direction of the wind
9	Strong gale	41-47	76-87	20,8-24,4	7	High waves; dense streaks of foam along the direction of the wind; sea begins to roll; spray affects visibility.
10	Storm	48-55	88-102	24,5-28,4	9	Very high waves with long overhanging crests; resulting foam in great patches is blown in dense white streaks along the direction of the wind; on the whole the surface of the sea takes on a white appearance; rolling of the sea becomes heavy; visibility affected.
11	Violent storm	56-63	103-117	28,5-32,6	11,5	Exceptionally high waves; small- and medium-sized ships might be for a long time lost to view behind the waves; sea is covered with long white patches of foam; everywhere the edges of the wave crests are blown into foam; visibility affected.
12	Hurricane	>64	>117	>32,7	>14	The air is filled with foam and spray; sea is completely white with driving spray; visibility very seriously affected.

Table 2.1: *Wind force according to the Beaufort scale ([154], page 415).* *(1): H_{m_0} is the significant wave height in meters, offshore, see page 77, equation 2.111.*

Force	H_{m_0} [m]	Description
0	0	Calm (glassy)
1	0 - 0,1	Calm (rippled)
2	0,1 - 0,5	Smooth
3	0,5 - 1,25	Slight
4	1,25 - 2,5	Moderate
5	2,5 - 4	Rough
6	4 - 6	Very rough
7	6 - 9	High
8	9 - 14	Very high
9	>14	Phenomenal

Table 2.2: *Douglas sea state.*

theory, Korteweg-De Vries theory, *etc.*), nor with the theory of solitons: we are interested only in the "nominal" case in deep waters. Similarly, the results related to capillary waves will only be summarized. Last but not least, breaking waves are not detailed here, we refer the reader elsewhere (for example, some elements can be found in [125]).

D'autres approches complémentaires existent pour modéliser la surface de l'eau. Plus empiriques, elles modélisent l'apparence de la surface sans chercher nécessairement à la relier à des bilans mécaniques. Ces approches sont: *i)* l'approche probabiliste, où l'on modélise la probabilité d'apparition d'une vague de hauteur H, *ii)* l'approche spectrale, qui est complémentaire de l'approche probabiliste, et *iii)* une seconde approche probabiliste, qui cherche à déterminer la densité de probabilité de l'apparition d'une pente donnée à la surface de l'eau. Ces trois approches, complémentaires de celles découlant des équations de Navier-Stokes, servent également lors de la modélisation des interactions d'une onde radio avec la surface de la mer.

Other complementary approaches exist to model the water surface. These empirically model the appearance of the surface without necessarily trying to link it to mechanical forces at play. These approaches are: *i)* the probabilistic approach, where the probability of occurrence of a wave of height H is modeled, *ii)* the spectral approach, which is complementary to the probabilistic approach, and *iii)* a second probabilistic approach, which seeks to determine the probability density of the appearance of a given slope on the surface of the water. These three approaches, which are complementary to those derived from the Navier-Stokes equations, are also used when modeling the interactions of a radio wave with the sea surface.

2.2.1 Geometrical configuration of a 1D sea surface

The space is provided with a direct orthogonal coordinate system: $\mathcal{W}(\mathrm{O}, \hat{\mathbf{x}}, \hat{\mathbf{y}}, \hat{\mathbf{z}})$, such as the mean plane of the sea surface is described by the plane of equation $z = 0$ (z is positive uwpards). The sea bottom is assumed flat; it is at a depth d. The wind direction is given by the unit vector $\hat{\mathbf{u}}$ that is collinear to the mean plane of the sea. In this framework, we describes the sea as a surface ζ, which is a function with two spatial variables x and y and a time variable t. This description assumes that the sea is a "2D1/2" surface, i.e. that there is no roller waves. Function ζ_t, depending on x and y, is the surface described by the sea at the instant t; it is a snapshot, that is to say it is only described by spatial variables. Similarly, the notation $\zeta_{x,y}$ corresponds to the elevation, as a function of time, at a point of coordinates (x, y). The configuration is shown in figure 2.5.

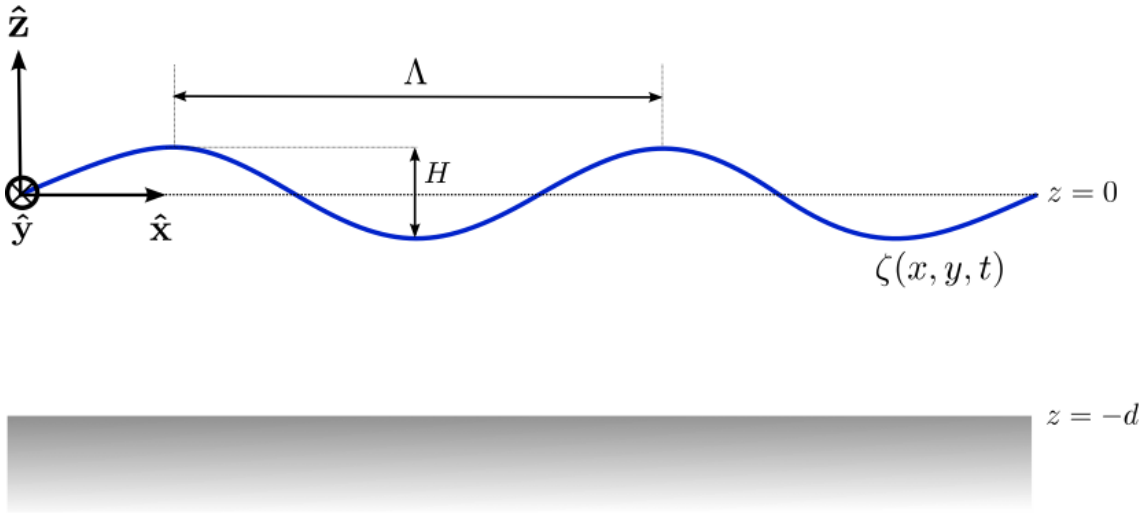

Figure 2.5: *Geometrical configuration and notations used in this paragraph.*

2.2.2 Navier-Stokes equations

Navier-Stokes equations are named after Henri Navier (1785-1836) and Sir George Gabriel Stokes (1819-1903). They describe the movement of fluid substances such as liquids and gases in the continuum mechanics approximation. They describe the fact that variations in the momentum of infinitesimal volumes of fluids are the result of the action of dissipating viscous forces (similar to friction), pressure changes, as well as other internal or external forces (such as gravity). There are several forms for these equations; here is given a useful form adapted to a simplified model of the ocean. Since the equations of Navier-Stokes are differential, these only make sense in a well-defined domain with precise boundary conditions.

The Navier-Stokes equation describes the conservation of momentum. It corresponds to the application of Newton's second law to the volume of fluid in a Galilean reference frame. This principle can be written for a small water volume element centered in (x, y, z), of density ρ, and dimensions dx, dy, dz (Stewart [165], section 7.6):

$$\rho \frac{D\mathbf{V}}{Dt} = \mathbf{f} \tag{2.13}$$

where $\mathbf{V}(x, y, z, t) = [u(t), v(t), w(t)]^t$ is the velocity vector of a small vector volume, D/Dt is the total derivative, and $\mathbf{f}$ is the resulting force from all volumic forces having an effect on this infinitesimal volume. This total derivative can be explicited:

$$\rho \frac{D\mathbf{V}}{Dt} = \mathbf{f} \tag{2.14}$$

$$\Leftrightarrow \quad \rho \left(\frac{\partial \mathbf{V}}{\partial t} + \frac{\partial \mathbf{V}}{\partial x}\frac{dx}{dt} + \frac{\partial \mathbf{V}}{\partial y}\frac{dy}{dt} + \frac{\partial \mathbf{V}}{\partial z}\frac{dz}{dt} \right) = \mathbf{f} \tag{2.15}$$

$$\Leftrightarrow \quad \rho \left(\frac{\partial \mathbf{V}}{\partial t} + u\frac{\partial \mathbf{V}}{\partial x} + v\frac{\partial \mathbf{V}}{\partial y} + w\frac{\partial \mathbf{V}}{\partial z} \right) = \mathbf{f} \tag{2.16}$$

$$\Leftrightarrow \quad \rho \left(\frac{\partial \mathbf{V}}{\partial t} + \mathbf{V} \cdot \mathbf{grad}\ \mathbf{V} \right) = \mathbf{f} \tag{2.17}$$

For most of the problems, the resulting force from all volumic forces can be written:

$$\mathbf{f} = -\mathbf{grad}\ p + \mathbf{div}\mathbb{T} - \rho g_0 \hat{\mathbf{z}} + \mathbf{f}' \tag{2.18}$$

where:

- **grad** p is the pressure gradient;
- $\mathbb{T}$ is the viscous constraint tensor;
- $-\rho g_0 \hat{\mathbf{z}}$ is the volumic weight;
- $\mathbf{f}'$ corresponds to other forces.

The Navier-Stokes equation alone does not describe the fluid on its own. It must be added a certain number of conservation equations: conservation of mass, conservation of energy, or an equation of state (Stewart [165], section 7.1). The equation of conservation of mass is almost always necessary; it is also sufficient in our case, *modulo* a number of additional hypotheses. This equation corresponds to the fact that the mass variation in volume $dxdydz$ during dt, caused by a flow of liquid particles moving at the speed $\mathbf{V}$, is equal to the mass of fluid entering the volume, from which is subtracted the outgoing mass:

$$\frac{\partial \rho}{\partial t} + div(\rho \mathbf{V}) = 0 \tag{2.19}$$

where ρ is the volumic density of the water

2.2.2.1 Writing the Navier-Stokes equations for ocean waves

2.2.2.1.1 Hypotheses

To model the waves, five additional hypotheses can be added, as a first approximation:

2D motion hypothesis Movement is considered to be in the $x - z$ plan only. This hypothesis makes it possible to simplify the equations. The generalization to the 3D case is immediate by rotation around the z axis.

Incompressible water Sea water is assumed to be incompressible (it is really of about 4 % for every 1000 bar), and that density is invariant in space and time[2]: ρ is written as a constant. The mass conservation equation 2.19 then becomes:

$$div\, \mathbf{V} = 0 \tag{2.20}$$

No additional forces All other forces than gravity and pressure are neglected:

$$\mathbf{f} = -\,\mathbf{grad}\ \ p - \rho g_0 \hat{\mathbf{z}} = -\,\mathbf{grad}\ \ (p + \rho g_0 z) \tag{2.21}$$

With this hypothesis, Coriolis forces and surface tensions are discarded, which simplifies our model.

Non-viscous fluid The fluid is assumed to be non-viscous, that is, that its viscous constraints tensor is null: $\mathbb{T} = \mathbb{O}$. In particular, surface tensions are null. This is valid for swell but not for capillary waves, having a smaller wavelength.

Irrotational fluid The fluid is assumed to be irrotational: ($\mathbf{rot}\ \ \mathbf{V} = \mathbf{0}$). Physically, this means that the local angular velocity of the fluid is zero; this goes hand in hand with the

[2] In reality, ρ depends on pressure, temperature and salinity, which in turn vary with depth, position, and seasons.

absence of viscosity. This means that the velocity vector field comes from a scalar potential Φ:

$$\mathbf{V} = \mathbf{grad}\ \Phi \tag{2.22}$$

So equation 2.20 becomes:

$$\Delta\Phi = 0 \tag{2.23}$$

The momentum conservation equation becomes:

$$\mathbf{grad}\ \left(\frac{\partial\Phi}{\partial t} + \frac{1}{2}\left(\mathbf{grad}\ \Phi\right)^2\right) = \mathbf{f} \tag{2.24}$$

Given that variable Φ is for the moment an unknown, nothing prevents us by swapping the variable for another one: $\Phi \leftarrow \Phi/\rho$. With the way $\mathbf{f}$ was previously written in equation 2.21, we get:

$$\mathbf{grad}\ \left(\frac{\partial\Phi}{\partial t} + \frac{1}{2}\left(\mathbf{grad}\ \Phi\right)^2 + \frac{p}{\rho} + g_0 z\right) = \mathbf{0} \tag{2.25}$$

thus:

$$\frac{\partial\Phi}{\partial t} + \frac{1}{2}\left(\mathbf{grad}\ \Phi\right)^2 + \frac{p}{\rho} + g_0 z = C(t) \tag{2.26}$$

where $C(t)$ is only a function of time. Since Φ is only defined up to a constant, this constant being only a function of time, it is possible to choose this constant as the atmospheric pressure p_0, so that 2.26 becomes:

$$p = \underbrace{(p_0 - \rho g_0 z)}_{(1)} - \underbrace{\rho\left(\frac{\partial\Phi}{\partial t} + \frac{1}{2}\left(\mathbf{grad}\ \Phi\right)^2\right)}_{(2)} \tag{2.27}$$

where term (1) is the hydrostatic pressure (with p_0 the atmospheric pressure) and term (2) is the so-called dynamic pressure.

2.2.2.1.2 Boundary conditions

So that the problem may be solved, it is necessary to add a definition domain and also boundary conditions to equations 2.23 and 2.27 (Dean et Dalrymple [53] section 3.2.2).

Definition domain Consider the fluid between $z = \zeta$ and $z = -d$, for $-\infty < x < +\infty$.

Kinematic condition at the free surface The velocity of the fluid at $z = \zeta$ is equal to the velocity of the free surface, that is, the water-air interface:

$$\underbrace{\frac{D\zeta}{Dt} = \frac{\partial\zeta}{\partial t} + u\frac{\partial\zeta}{\partial x}}_{\text{velocity of the free surface}} \quad \approx \quad \underbrace{w = \frac{\partial\Phi}{\partial z}}_{\text{velocity of the fluid}} \tag{2.28}$$

hence:

$$\left[\frac{\partial\zeta}{\partial t} + \frac{\partial\Phi}{\partial x}\frac{\partial\zeta}{\partial x} - \frac{\partial\Phi}{\partial z}\right]_{z=\zeta} = 0 \tag{2.29}$$

Dynamic condition at the free surface The forces acting on the fluid at free surface should be in equilibrium, *i.e.* the momentum is conserved at the free surface. The pressure

at the free surface must match the atmospheric pressure p_0. Equation 2.27 giving the motion at the surface, becomes:

$$\left[\frac{\partial\Phi}{\partial t}+\frac{1}{2}\left(\left(\frac{\partial\Phi}{\partial x}\right)^2+\left(\frac{\partial\Phi}{\partial z}\right)^2\right)+g_0\zeta\right]_{z=\zeta}=0 \tag{2.30}$$

Free surface relation Derivating 2.30 with respect to time, gives the derivative of ζ with respect to t, which can be injected into 2.29:

$$\left[\frac{\partial^2\Phi}{\partial t^2}+g_0\frac{\partial\Phi}{\partial z}\right]_{z=\zeta}=\left[-\frac{1}{2}\frac{\partial}{\partial t}\left(\left(\frac{\partial\Phi}{\partial x}\right)^2+\left(\frac{\partial\Phi}{\partial z}\right)^2\right)+g_0\frac{\partial\Phi}{\partial x}\frac{\zeta}{\partial x}\right]_{z=\zeta} \tag{2.31}$$

Kinematic condition at the sea bottom The sea bottom is impermeable, so at a depth $-d$ the vertical component of the velocity must be zero:

$$\left[\frac{\partial\Phi}{\partial z}\right]_{z=-d}=0 \tag{2.32}$$

2.2.2.2 Solving the equations

The problem to solve is made of the following equations: 2.23, 2.27, 2.29, 2.30, 2.31 and 2.32. This is a system of equations where potential Φ is the unknown.

2.2.2.2.1 Airy's linear model

Airy proposed in 1845 an approximate solution to this system by linearizing the equations. This means that $\mathbf{V}^2$ is negligible with respect to the other components. As we shall see, this corresponds to small amplitude waves.

Airy began by noting that ζ is unknown; the definition domain of the equations is thus unknown. Assuming as a first approximation that ζ is very small compared to the channel depth d and wavelength Λ. The potential function is thus defined for $-d<z<0$. The dynamic condition at $z=0$ (eq. 2.30) becomes:

$$\left[g_0\zeta+\frac{\partial\Phi}{\partial t}\right]_{z=0}=0 \tag{2.33}$$

The free surface relation 2.31 is also simplified and becomes the so-called *Poisson's relation*:

$$\left[\frac{\partial\Phi^2}{\partial t^2}+g_0\frac{\partial\Phi}{\partial z}\right]_{z=0}=0 \tag{2.34}$$

Elementary solution Using the *variable separation method* (Dean et Dalrymple [53] section 3.4.1 or Le Méhauté [125], 16-2.1.3) assuming that an elementary solution Φ_e is of the form:

$$\Phi_e(x,z,t)=A_c(z)\cos(Kx-\Omega t)=\Re\left(A_c(z)e^{\jmath Kx-\jmath\Omega t}\right) \tag{2.35}$$

With this solution[3], K is the wavenumber and Ω is the time pulsation. By inserting this expression for Φ in the equations, it comes:

[3]It is also possible to use a sine instead of a cosine, and the general form of the equation does not change.

Continuity equation 2.23	$\rightarrow$	$-K^2 A_c(z) + \frac{d^2 A_c}{dz^2} = 0$
Non-penetration condition at sea bottom 2.32	$\rightarrow$	$\left[\frac{dA_c}{dz}\right]_{z=-d} = 0$
Poisson's relation 2.34	$\rightarrow$	$-\Omega^2 A_c(z=0) = -g_0 \left[\frac{\partial A_c}{\partial z}\right]_{z=0}$

The possible solutions for the continuity equation are of the form:

$$A_c(z) = a_1 e^{Kz} + b_1 e^{-Kz} \tag{2.36}$$

or, equivalently:

$$A_c(z) = a_2 \cosh(Kz) + b_2 \sinh(Kz) \tag{2.37}$$

In these equations, a_1, b_1, a_2, b_2 are arbitrary conditions. The second form, once inserted into the other equations, gives the following system:

$$\begin{cases} -a_2 K \sinh(Kd) + b_2 K \cosh(Kd) = 0 \\ -a_2 \Omega^2 + b_2 g_0 K = 0 \end{cases} \tag{2.38}$$

So that this system may be solved for a_2 and b_2, its determinant must be zero. Then:

$$\Omega^2 = g_0 K \tanh(Kd) \tag{2.39}$$

This is the *dispersion relation* because it links the spatial wavenumber to the temporal pulsation. This is a fundamental equation which is used many times in the rest of this dissertation. Now if $d \rightarrow \infty$, the dispersion relation becomes:

$$\Omega^2 = g_0 K \tag{2.40}$$

Similarly, the phase and group velocity for the ocean waves may be computed. We recall that the phase velocity is the velocity of a wavefront of a monochromatic wave, while the group velocity is the velocity of the envelope of a group of at least two monochromatic waves of close wavelength (this is also the propagation speed of the energy of a wave packet). Phase velocity c is by definition:

$$c(K) = \frac{\Omega}{K} = \sqrt{\frac{g_0}{K} \tanh Kd} \tag{2.41}$$

while group velocity is by definition:

$$c_g(K) = \frac{d\Omega}{dK} = \frac{\frac{dg_0}{K} \operatorname{sech}(Kd)^2 - \frac{g_0}{K^2} \tanh(Kd)}{2\sqrt{\frac{g_0}{K} \tanh(Kd)}} \tag{2.42}$$

When the channel depth becomes infinite, then the group velocity of ocean waves becomes half the phase velocity:

$$c_g(K) = \frac{1}{2}\sqrt{\frac{g_0}{K}} = \frac{1}{2} c(K) \tag{2.43}$$

This result will be useful in the next chapter (section 3.1.1.1) to explain the shape of the Kelvin wake of a ship.

Knowing the dispersion relation, constant A_c becomes:

$$A_c(z) = \gamma \frac{\cosh\left(K(z+d)\right)}{\cosh(Kd)} \tag{2.44}$$

with γ an arbitrary constant. The potential equation Φ is then:

$$\Phi(x,z,t) = \gamma \frac{\cosh\left(K(z+d)\right)}{\cosh(Kd)} \cos(Kx - \Omega t) \tag{2.45}$$

To get the elevation function ζ_e coming from Φ_e, we use the dynamic condition at the free surface 2.33:

$$\zeta_e(x,t) = -\gamma\Omega \sin(Kx - \Omega t) \tag{2.46}$$

If H is the total height (crest-to-through) of the wave, we get:

$$\zeta_e(x,t) = -\frac{H}{2} \sin(Kx - \Omega t) \tag{2.47}$$

The 3D elementary solution is a sinusoidal wave propagating in the direction given by a wave vector $\mathbf{K} = [K_x, K_y]^t$:

$$\zeta_e(x,y,t) = -\frac{H}{2} \sin\left(\mathbf{K}.\mathbf{x} - \Omega t\right) \tag{2.48}$$

with $\mathbf{x} = [x, y]^t$.

General solution The general 2D solution (Le Méhauté [125], 16-3) is obtained using the fact that the differential equations are linear, and that the conditions put on Φ could have been obtained using a sine instead of a cosine in equation 2.35. The general solution has the form:

$$\zeta(\mathbf{x},t) = \int_{K\in\mathbb{R}} -\frac{H(K)}{2} \sin\left(\mathbf{K}.\mathbf{x} - \Omega(K)t + \phi_0(K)\right) dK \tag{2.49}$$

where $\phi_0(K)$ is the phase at origin and H is the wave height, which is a function of K. Pulsation Ω is always linked with K using 2.39. The general 3D solution is obtained by summing independent 2D waves each propagating in their own vertical plane; it is thus:

$$\zeta(\mathbf{x},t) = \iint_{K_x,K_y\in\mathbb{R}^2} -\frac{H(\mathbf{K})}{2} \sin\left(\mathbf{K}.\mathbf{x} - \Omega(K)t + \phi_0(\mathbf{K})\right) d\mathbf{K} \tag{2.50}$$

The idea behind this solution is illustrated by figure 2.6.

Velocity of water particles under the Airy model The local velocity vector is obtained by taking the gradient of the potential 2.22 (Dean et Dalrymple [53] section 4.1, Le Méhauté [125], 16-3.3, Gelpi et Norris [81]):

$$\begin{cases} u = \frac{\partial\Phi}{\partial x} \\ w = \frac{\partial\Phi}{\partial z} \end{cases} \tag{2.51}$$

Using the expression obtained at 2.45, it comes, for the 2D wave:

$$\begin{cases} u(x,z,t) = -\frac{H}{2}\frac{g_0 K}{\Omega}\frac{\cosh(K(z+d))}{\cosh(Kd)} \sin(Kx - \Omega t) \\ w(x,z,t) = \frac{H}{2}\frac{g_0 K}{\Omega}\frac{\sinh(K(z+d))}{\sinh(Kd)} \cos(Kx - \Omega t) \end{cases} \tag{2.52}$$

If the water is deep, meaning $Kd > \pi$, then the hyperbolic terms converge to one. Also, using the deep water dispersion relation 2.40, the equations can be rewritten further, yielding:

$$\begin{cases} u(x,t) = -\frac{H}{2}\Omega \sin(Kx - \Omega t) \\ w(x,t) = \frac{H}{2}\Omega \cos(Kx - \Omega t) \end{cases} \tag{2.53}$$

In 3D, considering the elementary solution 2.50, the velocity of an elementary monochromatic wave is given by:

$$\mathbf{V}_e(x,y,t) = \frac{H}{2}\Omega \left(-\sin(Kx - \Omega t)\frac{\mathbf{K}}{K} + \cos(Kx - \Omega t)\hat{\mathbf{z}} \right) \tag{2.54}$$

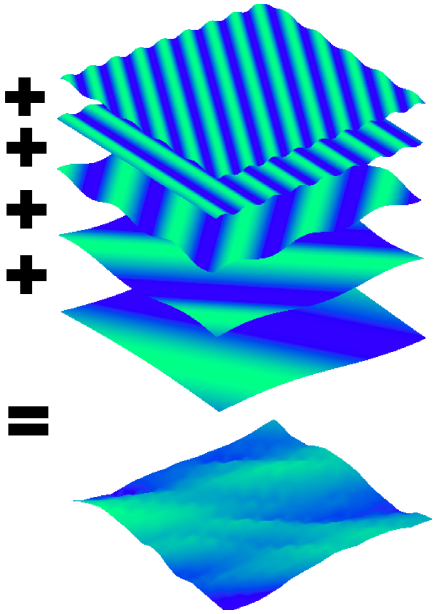

Figure 2.6: *Decomposing the sea surface elevation as a sum of individual sinusoidal waves, after [79].*

Given the linearity of equation 2.22, the 3D velocity field associated to 2.50 is:

$$\mathbf{V}(x,y,t) = -\frac{\mathbf{K}}{K} \times \iint_{K_x,K_y\in\mathbb{R}^2} \frac{H(K)}{2}\Omega(K)\sin(\mathbf{K}.\mathbf{x} - \Omega(K)t + \phi_0(K))d\mathbf{K} \quad (2.55)$$

$$\ldots + \hat{\mathbf{z}} \times \iint_{K_x,K_y\in\mathbb{R}^2} \frac{H(K)}{2}\Omega(K)\cos(\mathbf{K}.\mathbf{x} - \Omega(K)t + \phi_0(K))d\mathbf{K} \quad (2.56)$$

This expression for the velocity vector of water particles is useful when computing the Doppler shift of radio waves hitting the sea surface (Gelpi et Norris [81]); to do this, use the equations in chapter 1, paragraph 1.5.3. A possible justification that it is the water particles that are responsible for the Doppler shift, and not the free surface of the ocean, is provided at chapter 5, when commenting figure 5.12(b) (page 143).

Trajectory of elementary water particles in the Airy approximation Consider the elementary 2D solution 2.47 and write $x_e(x,z,t)$ and $z_e(x,z,t)$ the position of a water particle at time t. We have: $u = dx_e/dt$ and $v = dy_e/dt$. The position of an elementary particle is obtained, up to an additive constant, by integrating the velocity vector with respect to time. Using the expressions of u and w found at 2.52, it is immediate to see that the relation for $x_e(t)$ and $y_e(t)$ (Le Méhauté [125], 16-4.2.2) is:

$$\frac{x_e(t)^2}{r_a^2} + \frac{y_e(t)^2}{r_b^2} = 1 \quad (2.57)$$

with:

$$r_a = \left(\frac{H}{2}\right)\frac{\cosh(K(z+d))}{\sinh(kd)} \quad (2.58)$$

$$r_b = \left(\frac{H}{2}\right)\frac{\sinh(K(z+d))}{\sinh(kd)} \quad (2.59)$$

This means that the trajectory of the particles is a closed ellipse. For deep waters ($dK > \pi$), $\sinh(Kd) \approx \cosh(Kd) \approx \exp(Kd/2)$ and similarly: $\sinh(K(z+d)) \approx \cosh(K(z+d)) \approx \exp(K(z+d)/2)$. It comes:

$$r_a = r_b = \left(\frac{H}{2}\right) e^{\frac{Kz}{2}} \tag{2.60}$$

The motion is then circular. The radius of the circules decreases exponentially with z. A similar study can be made for shallow waters. In the general case, the trajectory of a particle is a linear combination of circular trajectories with varying amplitudes and pulsations.

2.2.2.2.2 Gerstner's trochoidal model

Airy's theory establishes the trajectory of a small volume of water $dxdydz$ centered on a fixed point (Euler approach). But, it is also possible to use a Lagrangian approach, where a single particle is followed through time, so that the motion of the free surface may be reconstructed. Gerstner's theory is an example of this approach, where it is assumed, on an *a priori* basis, that the motion of all particles is circular (Le Méhauté [125], 17-1.4): this is equivalent to following Airy's result and to go back to the original surface.

For a monochromatic wave, in the 2D case, at a date t and for a particle $P(x,t)$ considered at date t and rotating around a point of abscissa x and zero elevation, Gerstner's hypotheses yield coordinates:

$$\left\{ \begin{array}{rcl} x_P(x,t) & = & x + \frac{H}{2}\sin(Kx - \Omega t - \phi_0) \\ z_P(x,t) & = & -\frac{H}{2}\cos(Kx - \Omega t - \phi_0) \end{array} \right. \tag{2.61}$$

où:

- $H/2$ is the radius of the circular motion;
- K et Ω are linked by the *ad hoc* dispersion relation, for instance 2.40;
- ϕ_0 is an arbitrary phase term.

Figure 2.7 illustrates the space-time evolution of such a wave and compares it to Airy's sinusoidal wave.

Agreement condition between Gerstner's and Airy's models If $H \ll 1$, then, at order 2, equations 2.61 give:

$$\left\{ \begin{array}{rcl} x_P(x,t) & = & x \\ z_P(x,t) & = & -\frac{HK}{2} - \frac{H}{2}\frac{(Kx-\Omega t-\phi_0)^2}{2} \end{array} \right. \tag{2.62}$$

This development at order 2 is the same as the following parametric curve:

$$\left\{ \begin{array}{rcl} x_P(x,t) & = & x \\ z_P(x,t) & = & -\frac{H}{2}\cos(Kx - \Omega t - \phi_0) \end{array} \right. \tag{2.63}$$

This corresponds to a sinusoidal free surface, as in Airy's model. Thus, if $H \ll 1$, Gerstner's waves and Airy's wave are the same up to order 2 and are rigorously equal only at the limit where H goes toward 0. This configuration is illustrated at figure 2.8(a).

Studying Gerstner's waves at a fixed time t Curve ζ_t which is the graphical representation of $x \to P(x,t)$ at a fixed time t, is parametrized by abscissa x. This is a trochoid. It is easy[4] to see that, if:

[4]For instance, by studying the derivatives.

- $HK/2 < 1$: the curve never crosses itself. The surface is physically acceptable but its throughs have a larger radius of curvature than the sinusoidal wave, and the crests are more peaky (*cf.* fig. 2.8(b));
- $HK/2 = 1$: the curve has cusp points at $x = 2k\pi, k \in \mathbb{Z}$, this is the limit where the surface becomes physically acceptable (*cf.* fig. 2.8(c));
- $HK/2 > 1$: the curve crosses itself, which is not physically acceptable (*cf.* fig. 2.8(d)). In reality, the waves would have broken long before this situation.

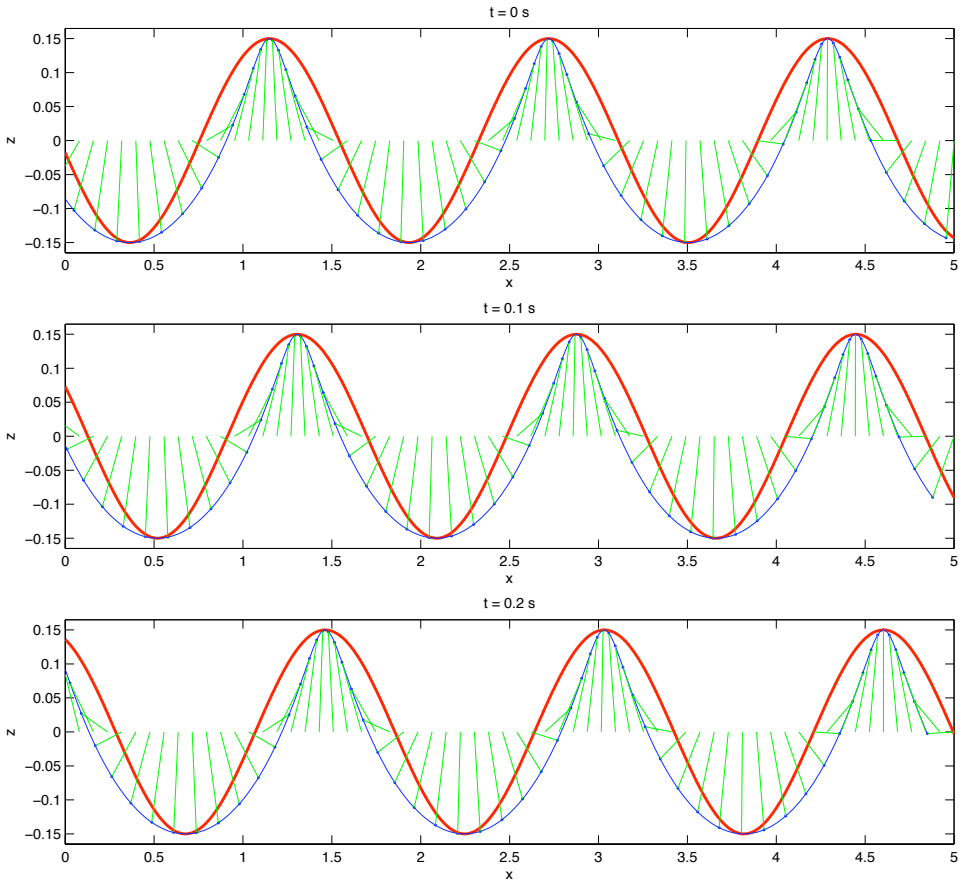

Figure 2.7: *Simulation of the evolution of a Gerstner wave with a single wavenumber ($K = 4$ rad/m et $H = 0,3$ m). The blue points represent a water particle; the green lines link the water particles to their rotation center; the red curve corresponds to a sinusoidal wave of amplitude H and wavenumber K. The particles turn clockwise if the wave propagates to the right, as is the case here.*

General case for Gerstner's waves The general situation is obtained with particles following a trajectory that is a linear combination of circular motions.

Why Gerstner's model is interesting As we have seen, Gerstner's approach goes in the opposite direction to that of Airy since we have a Lagrangian and not Eulerian approach. This is very useful, because it is understood that it would be desirable that both approaches give the same result. Under Airy's assumptions, and after solving the Navier-Stokes equations, we found that the particles have a circular motion in the vicinity of the surface, this

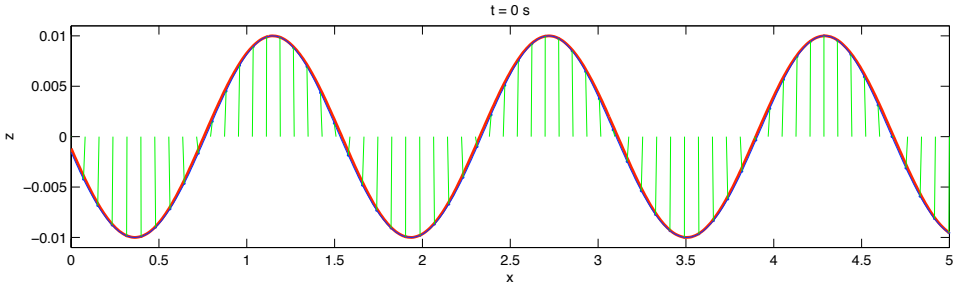

(a) Case $H \ll 1$: Gerstner's and Airy's models give the same result (here $K = 4$ rad/m and $H = 0,02$ m; beware that scales are not the same x and z-wise).

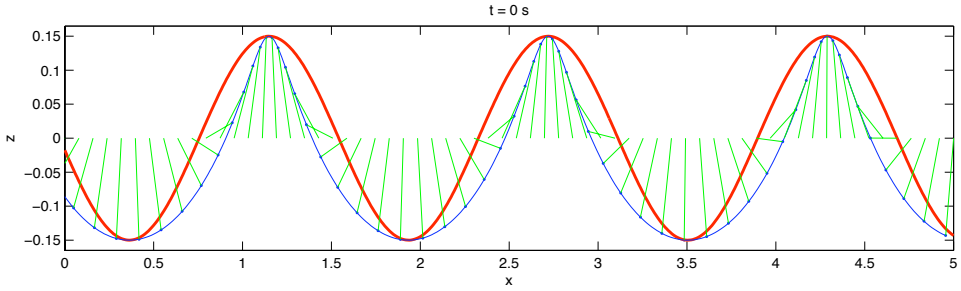

(b) Case $HK/2 < 1$: the wave is realistic-looking but more peaky than a sinusoidal wave (here $K = 4$ rad/m and $H = 0,30$ m).

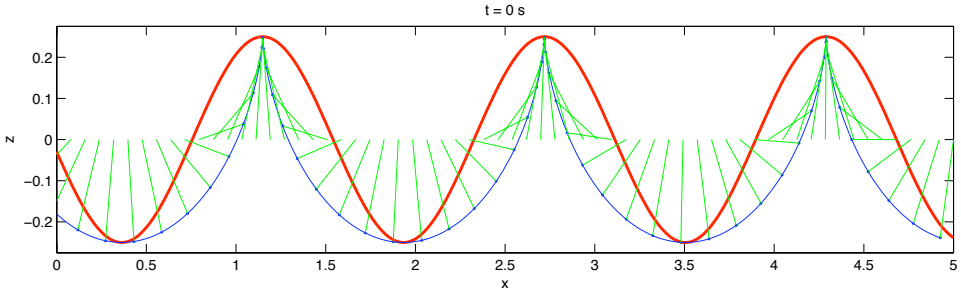

(c) Case $HK/2 = 1$: the wave is nearly breaking, the curve is a cycloid (here $K = 4$ rad/m and $H = 0,50$ m).

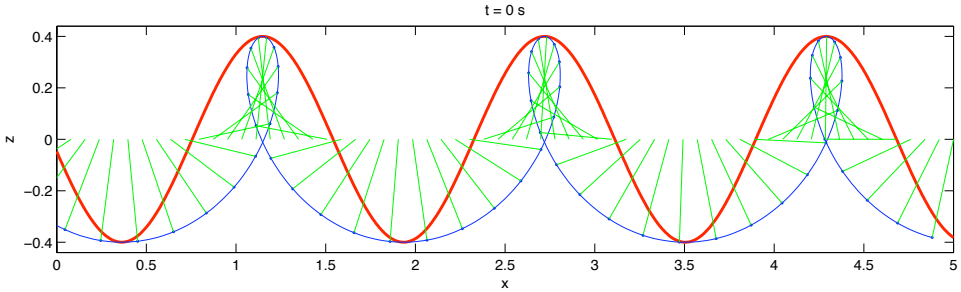

(d) Case $HK/2 > 1$: the curve crosses itself and is thus not physical (here $K = 4$ rad/m and $H = 0,80$ m).

Figure 2.8: *Some remarkable configurations for Gerstner's waves, using the same notations as fig. 2.7.*

which is the starting point of Gerstner's model. We can use Gerstner's model to test the extent to which Airy's assumptions on wave amplitude must be verified and what type of error is made if these assumptions are not not respected.

Airy's assumptions established that the ζ elevation of the surface of the water had to be very small in front of the depth and the wavelength of waves. The development of equation 2.62 shows that this amplitude must above all be small in front of the unit length so that the model of Airy and that of Gerstner coincide. If this is not the case, there is a difference between Airy's model, giving sinusoidal waves, and Gerstner's model, giving trochoidal waves. This has an influence on the shape of the free surface elevation, as we have seen above (the trochoid is more peaky than the sinusoid). This mainly has an influence on the calculation of the velocity vector field. Indeed:

1. Les équations 2.53 donnent le vecteur vitesse d'une particule d'eau en un point d'abscisse x. Ce point est supposé être sur la surface d'Airy, qui est sinusoïdale. En intégrant par rapport au temps, on trouve une trajectoire circulaire par rapport à un centre fixe au cours du temps, comme indiqué à l'équation 2.57 modifiée pour une mer de grande profondeur.

2. The equations 2.53 give the velocity vector of a particle of water at a point of abscissa x. This point is supposed to be on Airy's surface, which is sinusoidal. Integrating with respect to time, this gives a circular trajectory with a fixed centre in time, as shown by equation 2.57 modified for a sea of large depth.

3. Or si l'on applique l'hypothèse des centres de rotation fixes au cours du temps, on aboutit naturellement au modèle de Gerstner. On constate que sauf pour le cas limite $H \to 0$, la surface de Gerstner et la surface d'Airy ne coïncident pas.

4. Or if we apply the assumption of fixed centers of rotation to the over time, we naturally arrive at Gerstner's model. One finds that except for the limit case $H \to 0$, the shape of Gerstner and Airy's surface do not coincide.

So we also commit a positioning error equal to Δx on the velocity vector field. This positioning error of is periodic and bounded by $H/2$. This error is present when, in the simulations, we shall try to estimate the local field of Doppler velocities of water particles.

2.2.2.2.3 Stoke's model

Contraily to Airy's model, Stokes' model accounts for non-linear components (Le Méhauté [125], 17-2). The approach uses a limited development series parameterized by ϵ, which is small. Parameter ϵ depends on the curvature of the waves: $\epsilon = HK/(2\pi)$. So:

$$\Phi = \epsilon\Phi_1 + \epsilon^2\Phi_2 + \ldots + \epsilon^n\Phi_n + \ldots \quad (2.64)$$

$$\zeta = \epsilon\zeta_1 + \epsilon^2\zeta_2 + \ldots + \epsilon^n\zeta_n + \ldots \quad (2.65)$$

The terms Φ_i and ζ_i in the development can be isolated. They can be separatedly inserted into the Navier-Stokes equations and solved as if terms of lesser order $j \neq i$ were zero.

Since the analytical results of the Stokes waves have not been used in the thesis, only qualitative results are given here. Some of them are worth noting. First of all, we can show that if we truncate the development of Stokes to order one, we find the solutions of the Airy model. The higher-order terms are those that introduce nonlinearities; In particular, the trajectory of the particles will no longer be closed, and when the order becomes higher, the shape of the surface will tend to resemble a cycloid (without really being one), insofar as the waves are no longer symmetrical with respect to the level $\zeta = 0$. However, we keep

a symmetry with respect to the vertical line passing through the crest of the waves. In general, the higher orders of development are used for shallow seas, especially at order five; Demirbilek and Vincent state in the Coastal Engineers Manual ([54], page II-1-32) that this development remains fast enough to calculate and contains asymptotic expressions for both the "deep sea" and "shallow sea" domains that give results that correspond better to observations than many other models.

A final important result is a limit beyond which the wave must break. This paragraph is a summary of elements from the Coastal Engineers Manual ([54], page II-1-35): Stokes predicted that, theoretically, the wave can only remain stable if the velocity of the water particles at the crest of the waves is less than the speed of the wave or phase velocity; this criterion then limits the angle of the waves at the crest to 120 degrees (figure 2.9). Michell gave a criterion according to which the amplitude to wavelength ratio cannot exceed $(H/\Lambda)_{\max} = 1/7$ in deep water, *i.e.* at this limit the height of the wave is 14 % of the wavelength. Miche in 1944 generalized this relationship to waters of varying depth, by the relation:

$$\left(\frac{H}{\Lambda}\right)_{\max} = \frac{1}{7}\tanh\left(\frac{2\pi d}{\Lambda}\right) \tag{2.66}$$

On peut comparer ce résultat à celui obtenu pour la houle de Gerstner (figure 2.8), qui donne une limite $HK/2 = 1$ soit $(H/\Lambda)_{\max} = 1/\pi$: la cambrure maximale autorisée par le modèle de Gerstner est beaucoup plus importante que dans le modèle de Stokes, et physiquement irréaliste. Cependant, le critère de Stokes généralisé par Miche semble lui aussi surévaluer la limite de déferlement, puisque expériementalement, on a observé en laboratoire du déferlement, en condition d'eau profonde, lorsque la hauteur n'était que de 6 % de la longueur d'onde [189].

This result can be compared to that obtained for Gerstner's waves (figure 2.8), which gives a limit $HK/2 = 1$ or $(H/\Lambda)_{\max} = 1/\pi$. However, the Stokes criterion generalized by Miche also seems to overestimate the breaking wave limit. Indeed, experimentally, it was observed in a laboratory setting, that for deep waters, waves break as soon as the height exceeds only 6% of the wavelength [189].

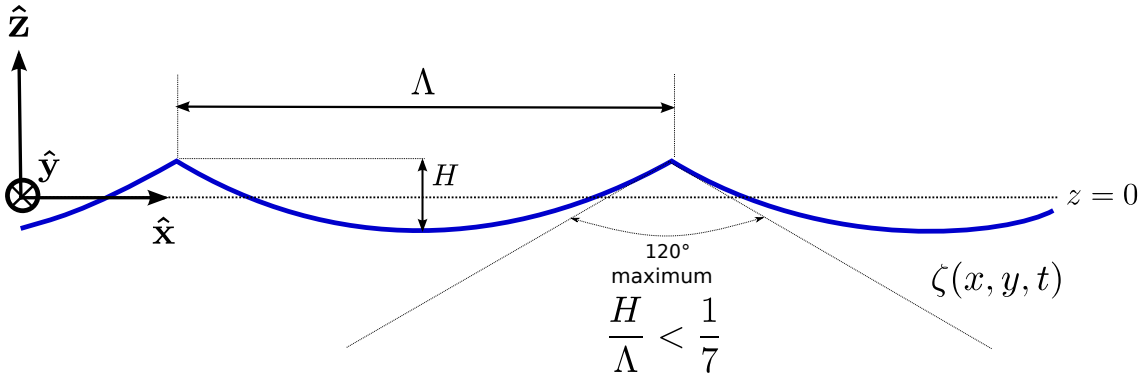

Figure 2.9: *Typical shape of a Stokes wave for a high order at the limit of breaking, in a sea of infinite depth.*

2.2.2.3 Validity domain for the various models

Since the linear model is particularly interesting, it is important to know the limits of the model's applicability. Ursell [179] proposed in 1953 a dimensionless number, the Ursell number denoted Ur, which makes it possible to quantify the degree of nonlinearity of the

theory necessary to model a wave:

$$\mathrm{Ur} = \frac{H\Lambda^2}{d^3} \tag{2.67}$$

Le Méhauté ([125], p. 204) considers that the linear theory is valid for waves having a small Ursell number $\mathrm{Ur} \ll 1$ with long wavelengths ($\Lambda \gg d$). This author continues with a more general categorization of the various theories, based on the value of the two dimensionless numbers $d/(g_0\tau^2)$ and $H/(g_0\tau^2)$, where τ is the wave period. This categorization is made in the form of an abacus shown at figure 2.10. The term $H/d \approx 0.8$ is a breaking wave limit. We do not address breaking waves in this thesis. Nevertheless, the interested reader may wish to consult the work of Tulin and Landrini [175] for an introduction to the topic of breaking waves for the sea alone and in the presence of a ship.

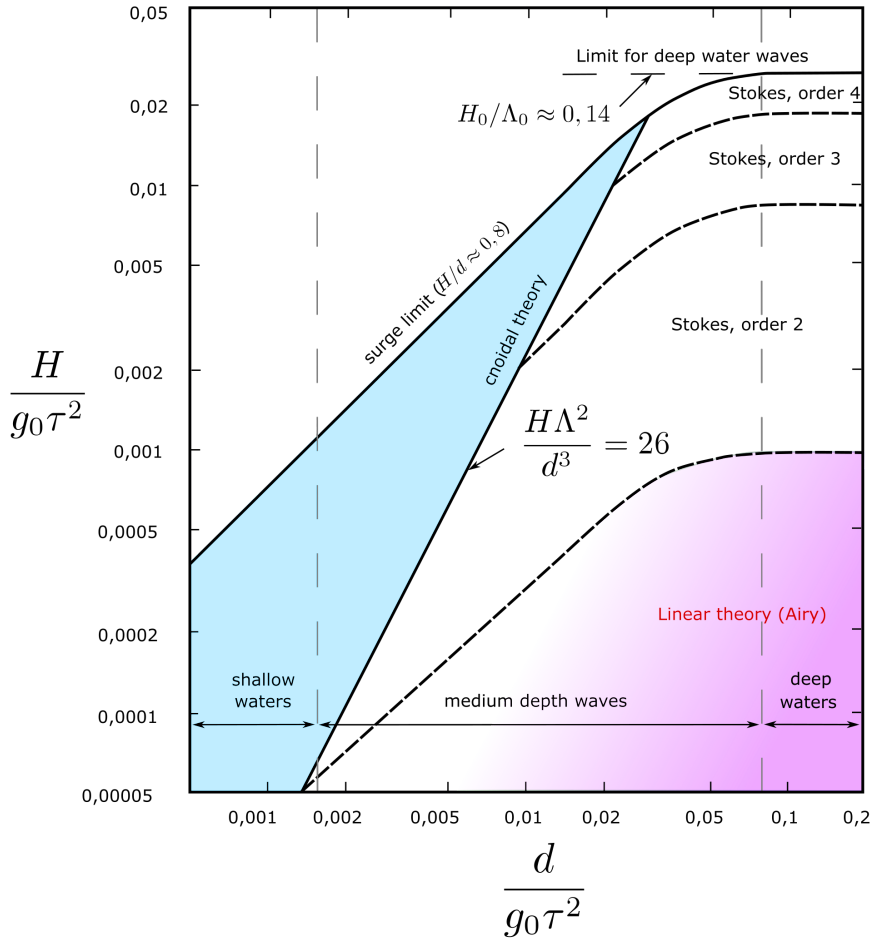

Figure 2.10: *Categorizing various theories for wave modeling, after Le Méhauté [125].*

2.2.3 Modeling capillary waves

Capillary waves are waves present on the surface of the water, whose dynamics are dominated by surface tensions that we have neglected when previously solving the Navier-Stokes equations. These waves are of smaller wavelength, on the order of a centimeter. There are so-called gravity-capillary waves whose dynamics are also influenced by gravity, and whose

wavelength is intermediate between those of pure capillary waves, and that of swell. The modeling of capillary waves has been known at least since the work of Sir Horace Lamb (1849-1934) [115]. The description of these waves requires more detailed modeling of the interface between water and air. We start with an energy balance, which involves three potential energies:

- the potential energy of gravity, the value of which is obtained by integrating the potential energy density due to gravity; for this purpose, the assumption of incompressibility used for the wave, with regard to water, as well as the invariability of the acceleration of gravity is retained;
- the energy related to the surface tension τ_s; to facilitate the calculation of surface tension, it is assumed, as for the wave, that the variations in the height of the surface are small;
- the kinetic energy, for which we consider that the velocity results from a potential (irrotational fluid hypothesis, which was also made for the swell).

We then arrive at an equation on the potential which is the Laplace equation, which we solve with the relevant boundary conditions: the velocity becomes zero far from the water/air interface, and the vertical component of the velocity at the interface corresponds to the movement of the interface. It is also shown that the regime is dispersive, with the following dispersion relation:

$$\Omega^2 = ||\mathbf{K}|| \left(\frac{\rho - \rho_0}{\rho + \rho_0} g_0 + \frac{\tau_s}{\rho + \rho_0} \mathbf{K}^2 \right) \tag{2.68}$$

where ρ is the sea water density, ρ_0 that of air, and τ_s the surface tension.

2.2.4 Spectral modelling of the sea surface

2.2.4.1 Definitions and properties

Let $\zeta_t(x, y)$ denote the elevation function giving the height of the sea at the point of position (x, y) represented in the world coordinate system $\mathcal{W}(\mathrm{O}, \hat{\mathbf{x}}, \hat{\mathbf{y}}, \hat{\mathbf{z}})$ (*cf.* Annex §A.2.1). For a given sea surface, it is possible to regard this function as a particular realization of a 2D random signal. This random signal is characterized by its *power spectral density* function (PSD), a term to be taken in the sense of "Fourier transform of the autocorrelation function of ζ_t" and not in the sense of mechanical power density. By abuse of language, we call a *wave spectrum* or *sea spectrum*, the DSP of a sea surface.

Spectrum for a 1D sea surface Assume the wind blows in the direction of increasing x values. Recall that the PSD of a random signal is the expected value of the Fourier transform of the autocorrelation of the signal. Assuming hypotheses of stationarity and ergodicity are valid, the autocorrelation of the elevation function is defined as:

$$\langle \zeta_t, \zeta_t \rangle(u) = \lim_{u \to \infty} \frac{1}{u} \int_{-u/2}^{+u/2} \zeta_t(x + u) \zeta_t^\star(x) dx \tag{2.69}$$

The autocorrelation is an even function, since the elevations are real values. The PSD is the Fourier transform of this expression [5]:

$$\mathcal{S}_{1d}(K) = \frac{1}{2\pi} \int_{u \in \mathbb{R}} \langle \zeta_t, \zeta_t \rangle(u) e^{-\jmath K u} du \tag{2.70}$$

[5] The Fourier transform is here with respect to the wave number K; the transform is scaled by a factor $1/2\pi$, and the inverse transform is done without scaling the integral by $1/2\pi$. See chapter 5, paragraph 5.2.1.

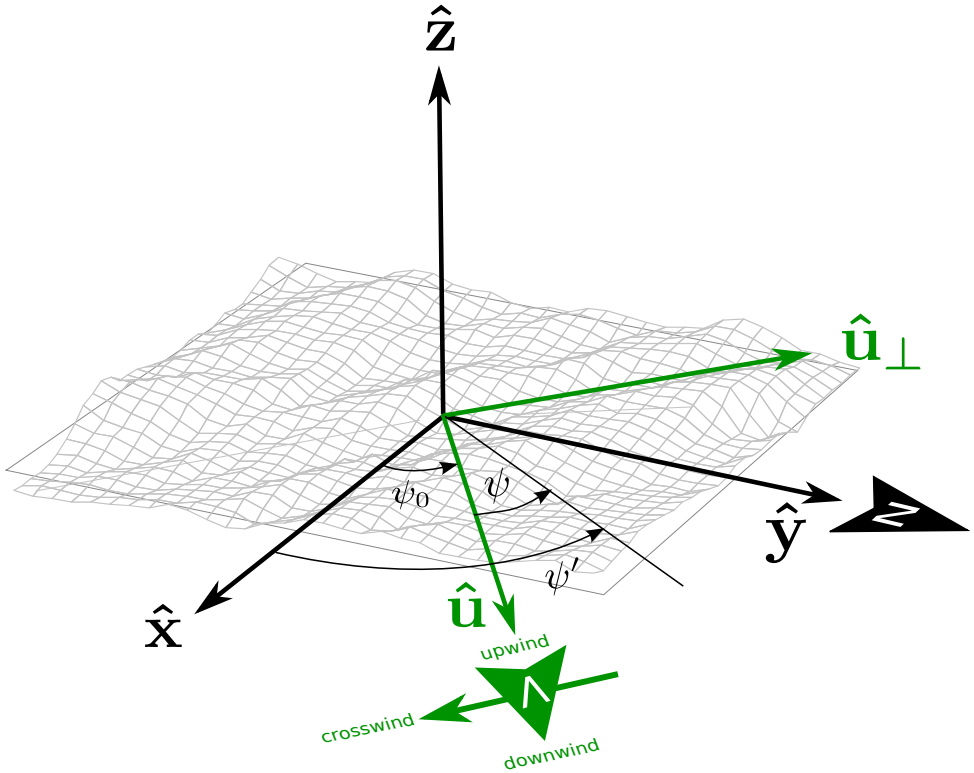

Figure 2.11: *Frames used in paragraphs 2.2.4 et 2.2.6, see also appendix A. The green arrow gives the direction in which the wind blows.*

An alternative, but equivalent definition of the spectrum allows working directly with surfaces ζ_t [2]:

$$\mathcal{S}_{1d}(K) = \lim_{u\to\infty} \frac{1}{2\pi} E\left(\frac{1}{u}\left|\int_{-u/2}^{+u/2} \zeta_t(x) e^{-\jmath Kx} dx\right|^2\right) \tag{2.71}$$

where E is the expectation operator, over all possible ζ_t realizations of the sea elevations.The PSD is expressed in $[\mathrm{m}^2/(\mathrm{rad.m}^{-1})]$. This is the amount of power[6] (proportional to a squared amplitude), in the wave number interval dK (expressed in $\mathrm{rad.m}^{-1}$). The total power expressed by all the waves is then:

$$\mathsf{P}_{\text{totale, 1d}} = \int_o^{+\infty} \mathcal{S}_{1d}(K) dK \tag{2.72}$$

It is possible to re-write this spectrum as a function of the time pulsation of the waves; the spectrum is then written $\mathcal{S}_{1d,\Omega}$. To do that, express the fact that the spectrum, expressed as a function of K and the spectrum, expressed as a function of Ω, must conserve the total power of the sea, $\mathcal{P}_{\text{totale, 1d}}$, after a change of variables [78, 63]. It comes:

$$\mathcal{S}_{1d,\Omega}(\Omega) d\Omega = \mathcal{S}_{1d}(K) dK \tag{2.73}$$

or equivalently:

$$\mathcal{S}_{1d,\Omega}(\Omega) = \mathcal{S}_{1d}(K) \frac{dK}{d\Omega} \tag{2.74}$$

[6]This expression should be construed in the "signal processing" meaning of the term, and not the "mechanical" meaning. The mechanical energy density, given below at equation 2.113, is proportional to $\mathcal{S}_{1d}(K)$.

and reciprocally. The derivative $dK/d\Omega$ can be computed using the adequate dispersion relation, for instance equation 2.40 for the swell. Expressed that way, the PSD has units $[\mathrm{m}^2/(\mathrm{rad.s}^{-1})]$. The spectrum is then the PSD of the $\zeta_x(t)$ function for a fixed x abscissa. The correspondance between the two variables (pulsation and wave number) is crucial. Indeed, $\zeta_x(t)$ can be easily measured at a single point using a buoy equipped with a positioning system (such as a GNSS receiver) and an accelerometer to measure the variations of height through time. This has long been the most used system to derive experimental spectra.

Spectrum for a 2D sea surface It is possible to generalize the equations to a 2D surface. Still assuming that the stationarity and ergodicity hypotheses hold, the autocorrelation becomes:

$$\langle \zeta_t, \zeta_t \rangle(u,v) = \lim_{u,v\to\infty} \frac{1}{uv} \int_{-u/2}^{+u/2} \int_{-v/2}^{+v/2} \zeta_t(x+u, y+v)\zeta_t(x,y)dxdy \tag{2.75}$$

and the 2D power spectral density:

$$\mathcal{S}_{2d}(K_x, K_y) = \frac{1}{4\pi^2} \int_{u,v\in\mathbb{R}} \langle \zeta_t, \zeta_t \rangle(u,v) e^{-\jmath(K_x u + K_y v)} dudv \tag{2.76}$$

where $K = \sqrt{K_x^2 + K_y^2}$ is the wave number of a wave propagating in a direction $\psi' \in]-\pi, \pi]$ relatively to the x axis, that is:

$$K_x = K\cos\psi' \tag{2.77}$$
$$K_y = K\sin\psi' \tag{2.78}$$

The two-dimensional power spectral density has the two following properties:

1. $\forall \psi' \in]-\pi, \pi], \mathcal{S}_{2d}(K, \psi') = \mathcal{S}_{2d}(K, \psi' + \pi)$: the function is even, because ζ_t has real values;
2. $\forall \psi' \in]-\pi, \pi], \mathcal{S}_{2d}(K, \psi_0 - \psi') = \mathcal{S}_{2d}(K, \psi_0 + \psi')$: symmetry with respect to a priviliedged direction ψ_0 which is the direction into which the wind blows; this is imposed by experimental conditions. Variable $\psi = \psi' - \psi_0$ is now used throughout the chapter.

An important notion, is that of an *omnidirectional sea spectrum*, that is, a power spectral density that is only a function of K and which is expressed in $[\mathrm{m}^2/(\mathrm{rad.m}^{-1})]$:

$$\mathcal{S}_{\mathrm{omni}}(K) = \int_{-\pi}^{+\pi} \mathcal{S}_{2d}(K, \psi') K d\psi' \tag{2.79}$$

The 2D spectrum can then be decomposed into a radial part and an angular part under the following form [63]:

$$\mathcal{S}_{2\mathrm{d}}(K, \psi') = \frac{1}{K} \mathcal{S}_{\mathrm{omni}}(K) \mathcal{S}_{\mathrm{dir}}(\psi', \ldots) \tag{2.80}$$

Term $\mathcal{S}_{\mathrm{omni}}$ corresponds to a 1D spectrum as defined previously. Term $\mathcal{S}_{\mathrm{dir}}$ is the *angular repartition function* or the so-called *directional wave spectrum* . The additional $1/K$ factor allows to re-create the energy diminution of the 2D sea spectrum over all directions, as circles of radii K have a perimeter increasing with K. Depending on the models, $\mathcal{S}_{\mathrm{dir}}$ depends on other parameters than ψ_0. This function has the same properties as $\mathcal{S}_{2\mathrm{d}}$ (it

is even and has a central symmetry). Besides, it is normalized such that its integral over $\psi' \in]-\pi, \pi]$ is 1.

Which spectrum is the best? There is plenty of literature about sea spectra and it is probably impossible to list all the spectra proposed to date. In general, spectra are derived from experimental data (time series, radar measurements) on which semi-empirical models are adapted. It was found that there is no universal semi-empirical model, in the sense that there is no particular spectrum that can characterize any sea or ocean in the world, because of local specificities concerning the weather, currents, and bathymetry. However, some spectra are more commonly used than others. In the following, we will present some usual omnidirectional and directional spectra. A review of some common spectra can be found in an article by Elfouhaily and Chapron [62].

2.2.4.2 Some omnidirectional spectra

2.2.4.2.1 Pierson and Moskowitz

Assuming the wind blew over the same area with a constant speed for a sufficiently long time on a sufficiently large surface, it can be assumed that the waves will enter into statistical equilibrium with the wind: we arrive at the idealized concept of a *fully developed sea*. Pierson and Moskowitz proposed in 1964 [143] an idealized spectrum for such a sea:

$$\mathcal{S}_{1\mathrm{d},\ \mathrm{PM},\ \Omega_p}(\Omega) = \frac{\alpha_{\mathrm{PM}} g_0^2}{\Omega^5} \exp\left[-\beta_{\mathrm{PM}} \left(\frac{\Omega_p}{\Omega}\right)^4\right] \tag{2.81}$$

où:

- α_{PM} is the Philips' constant (dimensionless) taken as $8{,}1 10^{-3}$ for the Pierson and Moskowitz spectrum;
- β_{PM} is a dimensionless constant taken experimentally as 0,74 for the Pierson and Moskowitz spectrum;
- $\Omega_p = g_0/U_{1950}$ is the peak pulsation (that is the pulsation where the spectrum is maximum).

Expressed using wave numbers using equation 2.74 with dispersion relation 2.40, this spectrum becomes:

$$\mathcal{S}_{1\mathrm{d},\ \mathrm{PM}}(\Omega) = \frac{\alpha_{\mathrm{PM}}/2}{K^3} \exp\left[-\beta_{\mathrm{PM}} \left(\frac{K_p^2}{K^2}\right)\right] \tag{2.82}$$

with K_p the wave number associated to pulsation Ω_p:

$$K_p = \Omega_p^2/g_0 = g_0/U_{1950}^2 \tag{2.83}$$

The Pierson and Moskowitz spectrum is adequate for swell only. Other spectra are needed for smaller, capillary waves.

2.2.4.2.2 The JONSWAP spectrum

The JONSWAP (Joint North Sea Wave Project) spectrum was developed in 1973 to dimension the resistance of North Sea oil rigs (Hasselmann *et al.* [90]). Observing their experimental data, *et al.* understood that the fully developed sea hypothesis is rarely verified in practice. In reality, the fully developed sea formation process is realized by

complex non-linear interactions over a large distance. To model this, Hasselmann *et al.* incorporated the notion of *fetch* into their model. *Fetch* F_J corresponds the distance, in meters, over which the wind blew with a constant direction and speed. It is then possible to modify the Pierson-Moskowitz spectrum by adding a factor $\gamma_J^{r_J}$ modifying the shape of the spectrum depending on the *fetch*:

$$\mathcal{S}_{\text{1d, J, }\Omega_p}(\Omega) = \frac{\alpha_{\text{J}} g_0^2}{\Omega^5} \exp\left[-\beta_{\text{J}} \left(\frac{\Omega_p}{\Omega}\right)^4\right] \gamma_J^{r_J} \tag{2.84}$$

The exponent r_J is chosen as follows

$$r_J = \exp\left[-\frac{(\Omega - \Omega_p)^2}{2\sigma_J^2 \Omega_p^2}\right] \tag{2.85}$$

For $\gamma_J = 1$, a similar equation to Pierson-Moskowitz is obtained. But in reality, the experimental JONSWAP data led to the following constants ([165], section 16.4):

- $\alpha_{\text{J}} = 0,076 \left(\frac{U_{1000}^2}{F_J g_0}\right)^{0,22}$
- $\beta_{\text{J}} = 5/4$
- $\Omega_p = 22 \left(\frac{g_0}{U_{10000} F_J}\right)^{1/3}$
- $\gamma_J = 3,3$
- $\sigma_J = \begin{cases} 0,07 \text{ if } \Omega \leq \Omega_p \\ 0,09 \text{ if } \Omega > \Omega_p \end{cases}$

where the *fetch* F_J is in meters, the wind speed at an altitude of 10 metres U_{1000} is in m/s and the pulsation Ω is in radians per seconds.

2.2.4.2.3 The Fung and Lee spectrum

Fung et Lee [78] defined an unified spectrum allowing to represent gravity waves and capillary waves. The spectrum is defined over two intervals:

$$\mathcal{S}_{\text{1d, FL}} = \begin{cases} \mathcal{S}_{\text{1d, FL, gravity}}(K) & \text{if } K \leq 4 \text{ rad/m} \\ \mathcal{S}_{\text{1d, FL, capillary}}(K) & \text{if } K > 4 \text{ rad/m} \end{cases} \tag{2.86}$$

where:

- $\mathcal{S}_{\text{1d, FL, gravity}}$ is a gravity wave spectrum inspired by the Pierson-Moskowitz spectrum:

$$\mathcal{S}_{\text{1d, FL, gravity}}(K) = \frac{\alpha_{\text{FL}}/2}{K^3} \exp\left[-\beta_{\text{FL}} \frac{K_p^2}{K^2}\right] \tag{2.87}$$

  with a Philips' constant $\alpha_{\text{FL}} = 2,810^{-3}$ and $\beta_{\text{FL}} = 0,74$, and K_p defined by equation 2.83;

- $\mathcal{S}_{\text{1d, FL, capillary}}$ is a modified Philips spectrum for capillary waves:

$$\mathcal{S}_{\text{1d, FL, capillary}}(K) = a_0(1 + 3\bar{K}^2) \left[K(1 + \bar{K}^2)\right]^{-(p_{\text{FL}}+1)/2} \tag{2.88}$$

  with K in radians/metres, $a_0 = 0,87510^{-4}(2\pi)^{p_{\text{FL}}-1} g_0^{(1-p_{\text{FL}})/2}$; $p_{\text{FL}} = 3 - \log_{10}(U_0)$ with U_0 in m/s; and $\bar{K} = K/K_m$ avec K in radians/metres. Constant K_m is equal to $\sqrt{g_0\rho/\tau}$, where ρ is the density of sea water and τ_s the surface tension; K_m is the so-called "gravity-capillary peak", its computed value is 363 rad/m.

2.2.4.2.4 Spectre d'Elfouhaily

The Elfouhaily spectrum [63] is one of the most recent spectra. It generalizes the JONSWAP model and, once incorporated into electromagnetic wave scattering models (*cf.* chapter 4), it is reputed to give results having a good consistency with experimental electromagnetic measurements. Unlike the JONSWAP spectrum, the Elfouhaily spectrum is provided in 2D, so there is an omnidirectional spectrum and a directional spectrum, itself being dependent on the wavelength of the waves (*cf.* paragraph 2.2.4.3.4). Like the Fung and Lee spectrum, one of the main interests of the Elfouhaily spectrum is to unify two spectra adapted respectively to low and high frequencies, within the same model:

$$\mathcal{S}_{\text{1d, Elf., }\Omega_{wa}}(K) = \frac{(B_l + B_h)}{K^3} \tag{2.89}$$

where l and h correspond respectively to low and high frequencies. These two spectra are parameterized by Ω_{wa}, the *non-dimensional inverse wave age*, which is an input, under the constraint: $0,84 \leq \Omega_{wa} \leq 5$, value 0.84 corresponding to a fully developed sea. The two components B_l et B_h are given below.

Low frequency part The low frequency part is given by equation:

$$B_l = \frac{1}{2}\alpha_p \frac{c_p}{c(K)} F_p \tag{2.90}$$

where:

- α_p is the generalized Philips-Kitaigorodskii equilibrium parameter, chosen as $6,010^{-3}\sqrt{\Omega}_{wa}$;
- $c(K)$ is the phase velocity of a wave of wave number K:

$$c(K) = \sqrt{\frac{g_0}{K}\left(1 + \left(\frac{K}{K_m}\right)^2\right)} \tag{2.91}$$

- $K_m = 363$ rad/m is the "gravity-capillary" peak wave number, as for the Fung and Lee spectrum;
- $c_p = c(K_p) = U_{1000}/\Omega_{wa}$ is the phase velocity of waves having a wave number K_p corresponding to the maximum of the spectrum:

$$K_p = \frac{g_0}{U_{1000}^2}\Omega_{wa}^2 \tag{2.92}$$

- F_p is a function describing gravity waves:

$$F_p = L_{\text{PM}}\gamma_J^{r_J} \exp\left\{-\frac{\Omega_{wa}}{\sqrt{10}}\left(\sqrt{\frac{K}{K_P}} - 1\right)\right\} \tag{2.93}$$

- L_{PM} is a spectrum following the form of the Pierson-Moskowitz spectrum:

$$L_{\text{PM}} = \exp\left(-\frac{5}{4}\frac{K_p^2}{K^2}\right) \tag{2.94}$$

- $\gamma_J^{r_J}$ is the amelioration factor proposed by Hasselmann *et al.* in the JONSWAP spectrum but with a modified value:

- $\gamma_J = 1,7$ if $0,84 < \Omega_{wa} < 1$ or $\gamma_J = 1,7 + 6 \log \Omega_{wa}$ if $1 \leq \Omega_{wa} < 5$;
- $r_J = \exp\left\{-\frac{\left(\sqrt{\frac{K}{K_p}}-1\right)^2}{2\sigma_J^2}\right\}$
- $\sigma_J = 0,08(1 + 4\Omega_{wa}^{-3})$

High frequency part The high frequency part is given by relation:

$$B_h = \frac{1}{2}\alpha_m \frac{c_m}{c} F_m \tag{2.95}$$

where:

- α_m is the generalized Philips-Kitaigorodskii equilibrium parameter, chosen as $0,14U_0/c_m$ (linear model) or $[1 + a\ln(U_0/c_m)]10^{-2}$, with $a = 1$ if $U_0 < c_m$ and 3 otherwise (non-linear model, which is the one used in this thesis);
- c_m is the phase velocity of the gravity-capillary peak waves, with wave number K_m: $c_m = \sqrt{2g_0/K_m}$, that is 0,23 m/s;
- F_m is a function describing capillary waves:

$$F_m = \exp\left\{-\frac{1}{4}\left(\frac{K}{K_m} - 1\right)^2\right\} \tag{2.96}$$

2.2.4.2.5 Comparaison of the spectra

The figure 2.12 provides a comparison between the Fung and Lee spectrum for its gravity part: $\mathcal{S}_{1d,\,FL,\,gravity}$, that is the one taken from the Pierson spectrum ((figure 2.12, left); the complete Fung and Lee spectrum $\mathcal{S}_{1d,\,FL}$ (figure 2.12, center), and the Elfouhaily spectrum $\mathcal{S}_{1d,\,Elf.}$ with the age of the inverse waves corresponding to a fully developed sea so that the comparison is valid with the spectrum of Fung and Lee (figure 2.12, right). These spectra are the ones we actually used in our work.

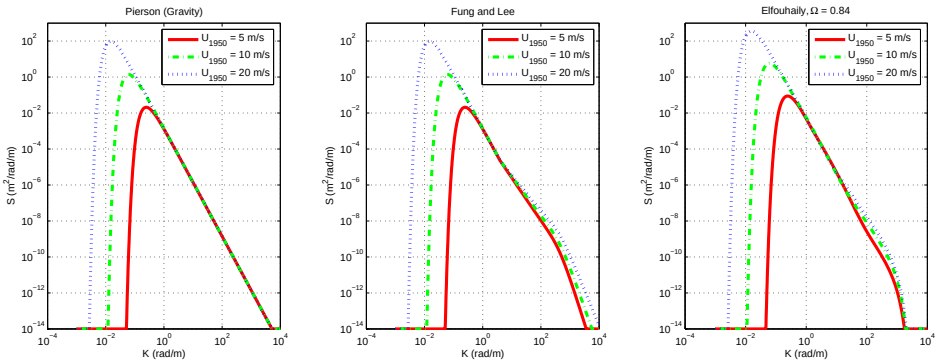

Figure 2.12: *Comparaison of the Pierson-Moskowitz spectrum (gravity waves part), with the Fung and Lee spectrum, and the Elfouhaily spectrum*

It can be noted that the spectrum of Fung and Lee provides more energy for the capillarity spectrum, but also that the decay is faster, compared to the gravity part of the Pierson spectrum. The spectrum of Elfouhaily has the same appearance, with an even

faster decay, and even more energy in the capillarity part. For all these spectra, as the wind increases, the spectrum becomes wider (in non-logarithmic units), which is why the waves become higher. It is also interesting to observe, for the purely gravity part of the Fung and Lee spectrum, that if the wind increases, the curve of the spectrum is simply translated along an asymptote (in the logarithmic domain): the curves retain an identical shape regardless of the wind speed. This is a phenomenon of self-similarity noted by Kitaigorodskii [106], and which we will exploit in the chapter 5 when determining how to best discretize a spectrum to perform oceanic radar image simulation.

2.2.4.3 Some directional spectra

Since the 2D spectrum must have symmetry with respect to the wind propagation axis, the Fourier series decomposition of the directional spectrum can only have even terms [86]. It is therefore of the form:

$$\mathcal{S}_{\text{dir}}(\mathbf{K},\psi) = \frac{1}{2\pi}\left[1 + \sum_{n=1}^{+\infty} a_{2n}\cos(2n\psi)\right] \tag{2.97}$$

Elfouhaily, Chapron and Katsaros [63] further proposed a categorization of directional spectra based on an asymmetry ratio "*updwind / crosswind*", which is equal to the coefficient of the second term of the Fourier series:

$$\Delta(K) = a_2 = \frac{\mathcal{S}_{\text{dir}}(\mathbf{K},0) - \mathcal{S}_{\text{dir}}(\mathbf{K},\frac{\pi}{2})}{\mathcal{S}_{\text{dir}}(\mathbf{K},0) + \mathcal{S}_{\text{dir}}(\mathbf{K},\frac{\pi}{2})} \tag{2.98}$$

Elfouhaily *et al.* then showed that for most directional spectra, the ratio $\Delta(K)$ was in the form:

$$\Delta(K) = \tanh f(K_p/K) \tag{2.99}$$

With f, a *ad hoc* function. Here we follow the work of Elfouhaily, Chapron and Katsaros in [63] to present some usual directional spectra.

2.2.4.3.1 The Longuet-Higgins directional spectrum

The simplest directional spectrum used to model a large class of rough surfaces, including the sea, was proposed by Longuet-Higgins *et al.* in 1963 [124]:

$$\mathcal{S}_{\text{dir, LH}}(\mathbf{K},\psi) = \left(\frac{2^{s_L-1}}{\pi}\right)\frac{\Gamma^2(s_L+1)}{\Gamma(2s_L+1)}\cos^{2s_L}\left(\frac{\psi}{2}\right) \tag{2.100}$$

where Γ is Euler's gamma function and $s_L \geq 2$ is an integer parameter. The dependence is therefore in cosine, the multiplicative factor being used only for normalization purposes. The ratio $\Delta(K)$ is in the form:

$$\Delta(K) = \tanh\left(\frac{\ln 2}{2}s_L\right) \tag{2.101}$$

We see that in this spectrum, there is no dependence on the wavelength of the waves. This is what makes this model so simple, and explains its success, despite its simplified description of reality.

2.2.4.3.2 The Mitsuyasu directional spectrum

In their paper, Mitsuyasu *et al.* [130] took up and modify the Longuet-Higgins spectrum to introduce a wavenumber dependence in the exponent s_L:

$$s_L = 11.5 \left(\frac{c(K)}{U_{1000}} \right)^{2.5}, \; K > K_p \tag{2.102}$$

which gives:

$$\Delta(K) = \tanh \left(\left(3,98 \frac{c(K)}{U_{1000}} \right)^{2.5} \right) \tag{2.103}$$

2.2.4.3.3 The Donelan directional spectrum

Donelan *et al.* found that a hyperbolic secant directional spectrum described even better the data obtained during tests conducted on Lake Ontario [56, 108], and therefore proposed[7]:

$$\mathcal{S}_{\text{dir, Donelan, }\Omega}(\mathbf{K}, \psi) = \frac{K \beta_D(K)}{2} \operatorname{sech}^2 (\beta(K)\psi) \tag{2.104}$$

with:

$$\beta_D(K) = \begin{cases} 2,61(K/K_p)^{2.6} \text{ if } \sqrt{0.56} < (K/K_p) < \sqrt{0.95} \\ 2,28(K/K_p)^{-2.6} \text{ if } \sqrt{0.95} < (K/K_p) < \sqrt{1.6} \\ 1.24 \text{ otherwise} \end{cases} \tag{2.105}$$

The ratio ΔK of Elfouhaily is then equal to:

$$\Delta(K) = \frac{1 - \operatorname{sech}^2 \left(\beta_D(K) \frac{\pi}{2} \right))}{1 + \operatorname{sech}^2 \left(\beta_D(K) \frac{\pi}{2} \right))} \tag{2.106}$$

2.2.4.3.4 The Elfouhaily directional spectrum

As mentioned above, the paper by Elfouhaily *et al.* [63] also provides a directional spectrum, which has the particularity of depending on the wavelength of the waves. The spectrum is defined as:

$$\mathcal{S}_{\text{dir, Elf.}}(K, \psi) = \frac{1}{2\pi} \left(1 + \Delta(K) \cos(2\psi) \right) \tag{2.107}$$

where $\Delta(K)$ is the ratio "*updwind / crosswind*" introduced above, which re-uses the parameters introduced in the low and high frequency omnidirectional Elfouhaily spectra:

$$\Delta(K) = \tanh \left(a_0 + a_p (c/c_p)^{2.5} + a_m (c/c_m)^{2.5} \right); \tag{2.108}$$

Here, a_0 is a constant equal to $(\ln 2)/4$, a_p is 4; a_m is $0.13 U_0/c_m$, and c_p, c_m are as defined above in equation 2.95. The figure 2.14 shows the behavior of the spectrum; it is possible to see that the distribution at K_p (peak wave number) does not depend upon the wind speed, whereas it depends on said wind speeds for other wave numbers.

[7] Once made the transformation for a wavenumber spectrum, the original being given in pulsation.

2.2.5 Probability of wave heights. Energy density spectrum.

Experimental observations widely represented in the literature have shown that the wave height distribution follows a Rayleigh distribution quite closely. This becomes especially true when wave energy is concentrated in a small frequency band. Then the distribution follows the form ([54], p. II-1-74):

$$\Pr(H) = \frac{2H}{\sigma_\zeta^2} \exp\left(-\frac{H^2}{2\sigma_\zeta^2}\right) \tag{2.109}$$

The standard deviation σ_ζ of the heights of the surface generated over the entire spectrum, is:

$$\sigma_\zeta = \sqrt{\int_0^{+\infty} \mathcal{S}_{1\mathrm{d}}(K) dK} \tag{2.110}$$

An alternative definition, which is that of the *significant wave height*, denoted by H_{m_0}. This significant wave height is:

$$H_{m_0} = 4\sigma_\zeta \tag{2.111}$$

Note that in older texts, another definition of significant height is used: it corresponds to the mean wave height (trough to crest) of the highest third of the waves. This definition was proposed by Sverdrup and Munk in 1947 following studies that were initially used to prepare for the Allied landing in Normandy during World War II; It corresponds quite well to the empirical observations made by sailors. This significant height was noted $H_{1/3}$. Qualitatively, $H_{1/3}$ is close to H_{m_0}. Indeed, it is shown that the probability density of sea wave heights is close to a Rayleigh distribution; yet, for such a distribution, $H_{1/3}$ is exactly equal to H_{m_0} [54].

The graph in the figure 2.13 shows the plot of H_{m_0} as a function of Beaufort Sea state (or, alternatively, wind speed U_{1950}). The values of H_{m_0} are calculated by integration on logarithmic steps between 10^{-4} and 10^4 (8192 samples) from the spectrum of Elfouhaily, Fung and Lee, or the "gravity" part of the spectrum of Fung and Lee given by Pierson. The descriptive sea heights associated with the Beaufort scale (given in the table 2.1) are added for reference. On the one hand, Fung and Lee's spectrum seems to slightly underestimate the height of the waves, compared to other spectra. More importantly, there is a divergence of the curves corresponding to the predictions obtained through the spectra, with the descriptive heights, as soon as the sea states become high (about $B > 5$). This divergence is explained by a different asymptotic behaviour between the theoretical curves given by spectrum integration, and the experimental reference data. Physically, this difference can be interpreted by the failure to take breaking waves into account in the spectral approach, or by the fact that the model has not been adapted by regression to high sea states. In any case, it seems that the spectral approach gives a wrong description of the surface since B >5; This remark will be important in chapter 5 when it comes to simulating radar signals reflected by an oceanic surface.

Energy of a wave For a sinusoidal wave of small height H, the mechanical energy is equal to:

$$\mathsf{E}_{\mathrm{swell}} = \frac{1}{8}\rho g_0 H(K)^2 \tag{2.112}$$

We can also define the average energy density by introducing H_{m_0}: it is $\bar{\mathsf{E}}_{\mathrm{swell}} = \rho g_0 \sigma_\zeta^2$ or $1/16\rho g_0 H_{m_0}^2$. It is then possible to define a spectrum of energy density, in the form:

$$\mathcal{E}(K) = \rho g_0 \mathcal{S}_{1\mathrm{d}}(K) \tag{2.113}$$

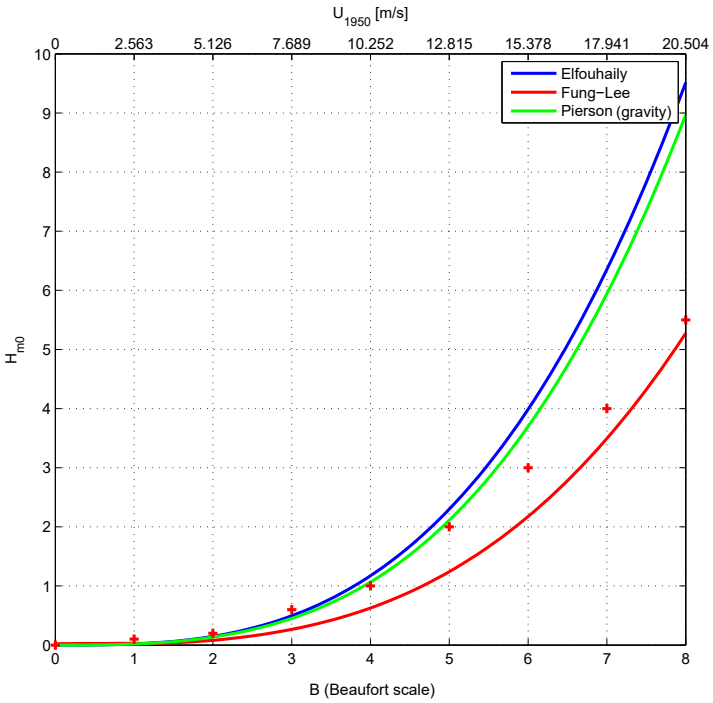

Figure 2.13: *Significant height in meters depending on Beaufort condition B (or wind speed at 19.5 m altitude), for several sea spectra. Crosses correspond to the heights of the table 2.1.*

2.2.6 Wave slope probability: the model of Cox and Munk

Apart from the spectral approach, another approach to characterizing the water surface is to determine the probability density function of the slopes of the waves of the water surface. Cox and Munk [48] determined in 1954 such a statistic, empirical, from aerial photographs to visualize the reflection specular of the sun. The slopes Z_u and Z_c correspond respectively to the slope from the elevation function ζ in the opposite direction to that of the wind (*i.e.* $-\hat{\mathbf{u}}$ if the wind blows in the direction given by the vector $\hat{\mathbf{u}}$: this is the direction called *upwind* in the Anglo-Saxon literature) and to the slope in the direction orthogonal to the wind (direction *crosswind*, according to $-\hat{\mathbf{u}}_\perp$). Please refer to the figure 2.11 for an illustration of these concepts.

As a first approximation, the slope distribution is roughly Gaussian; however, because of the asymmetry of the swell, that the front of the wave is steeper than the back. This asymmetry is accentuated for high winds. The slope distribution is therefore also asymmetrical. Therefore, Cox and Munk suggested using a Gram-Charlier distribution, which corresponds to a normal distribution distorted by a function f_{CM} to introduce non-zero higher order moments. They thus set $\xi = Z_c/\sigma_c$ and $\eta = Z_u/\sigma_u$, and then:

$$\Pr_{\text{Cox \& Munk}}(\xi,\eta) = \frac{1}{2\pi\sqrt{\sigma_u\sigma_c}} \exp\left\{-\frac{1}{2}(\xi^2+\eta^2)\right\} f_{CM}(\xi,\eta) \tag{2.114}$$

In this equation, σ_u and σ_c are the standard deviations of slopes in the two main directions *upwind* and *crosswind*; they are linearly dependent on measured wind speed U_{1250} expressed in m/s at an altitude of 41 feet (about 1250 cm). The deformation function f_{CM}

is of the form [48]:

$$f_{CM}(\xi,\eta) = 1 - \frac{c_{21}}{2}(\xi^2-1)\eta - \frac{c_{03}}{6}(\eta^3-3\eta) + \frac{c_{40}}{24}(\xi^4-6\xi^2+3) \quad (2.115)$$

$$+\frac{c22}{4}(\xi^2-1)(\eta^2-1) + \frac{c_{04}}{24}(\eta^4-6\eta^2+3) \quad (2.116)$$

Two measurement campaigns were carried out by Cox and Munk's team: the first was carried out on a "clean" sea, *i.e.* a natural unpolluted sea (*clean sea*), while the second was carried out on a *slick sea* where oil was intentionally spilt over the sea to mitigate capillary waves and keep only the gravity waves. Figure 2.15 shows the distribution of slopes for a "clean" sea. Note that the maximum density is not located at zero, but is shifted for negative Z_u, corresponding to the front of the wave. The wind blows from right to left. There is no asymmetry in the *crosswind* direction.

After regression on experimental data, the coefficients c_{ij} for the clean sea were determined as follows [48]:

$$\sigma_u^2 = 0,000 + 3,1610^{-3} \times U_{1250} \pm 0,002 \quad (2.117)$$

$$\sigma_c^2 = 0,003 + 1,9210^{-3} \times U_{1250} \pm 0,004 \quad (2.118)$$

$$\sigma_u^2 + \sigma_c^2 = 0,003 + 5,1210^{-3} \times U_{1250} \pm 0,004 \quad (2.119)$$

$$c_{21} = 0,01 - 0,0086U_{1250} \pm 0,03 \quad (2.120)$$

$$c_{03} = 0,04 - 0,033U_{1250} \pm 0,12 \quad (2.121)$$

$$c_{40} = 0,40 \pm 0,23 \quad (2.122)$$

$$c_{22} = 0,12 \pm 0,06 \quad (2.123)$$

$$c_{04} = 0,23 \pm 0,41 \quad (2.124)$$

while, for the slick sea, they are [48]:

$$\sigma_u^2 = 0,005 + 0,7810^{-3} \times U_{1250} \pm 0,002 \quad (2.125)$$

$$\sigma_c^2 = 0,003 + 0,8410^{-3} \times U_{1250} \pm 0,002 \quad (2.126)$$

$$\sigma_u^2 + \sigma_c^2 = 0,008 + 1,5610^{-3} \times U_{1250} \pm 0,004 \quad (2.127)$$

$$c_{21} = 0,00 \pm 0,02 \quad (2.128)$$

$$c_{03} = 0,02 \pm 0,05 \quad (2.129)$$

$$c_{40} = 0,36 \pm 0,24 \quad (2.130)$$

$$c_{22} = 0,10 \pm 0,05 \quad (2.131)$$

$$c_{04} = 0,26 \pm 0,31 \quad (2.132)$$

The mathematical form of the Cox and Munk probability distribution is such that the probability of having significant slopes can only increase with sea state. This means that the effects of wave breaking are not taken into account by Cox and Munk's model.

2.3 Conclusion of this chapter

This chapter highlighted a number of parameters and models that can be used for modeling the sea in View of the simulation of its radar image. The input parameters of these models are temperature, salinity, and wind speed, respectively. The temperature and salinity have a direct influence on the dielectric constant of seawater (relation 2.3). Wind speed directly affects the shape of the surface.

A large part of the chapter has been devoted to the study of this surface. This highlighted a dual modeling approach for the wave heights: either analytical – by a model resulting

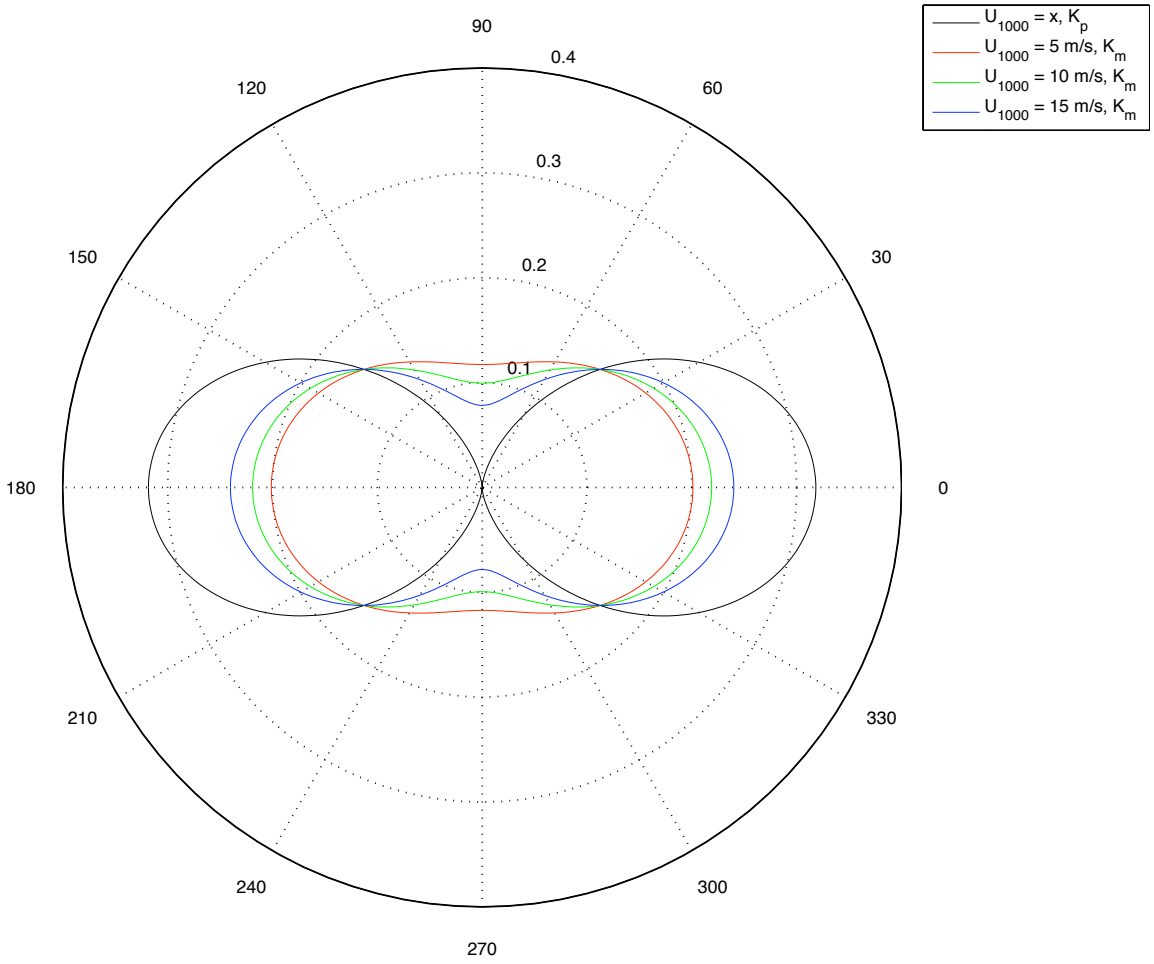

Figure 2.14: *Values of the Elfouhaily* et al. *directional spectrum, for varying wavelengths and wind speeds.*

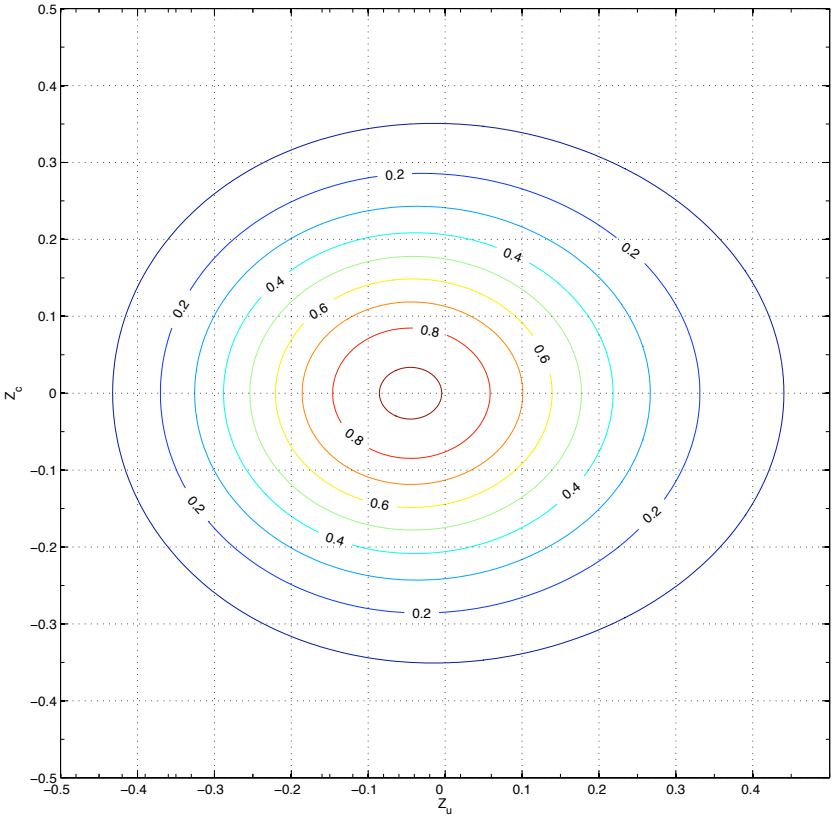

Figure 2.15: *Wave slope probability according to Cox and Munk ($U_{1250} = 15$ m/s, "clean" distribution). Wind blows towards negative Z_u values.*

from the approximate resolution of the Navier-Stokes equations – or probabilistic, which is divided into three sub-approaches: height probabilities, power spectral density approach, and slope probabilities. This chapter mainly illustrated the linear framework, most notably by using the Airy and Gerstner swell model. Those are at the heart of the electromagnetic models used in the following chapters of this thesis. By reasoning on the correspondance between wave heights as obtained through spectra, and those obtained in practice, it is possible to give a limit stating that the sea state must not go beyond Beaufort state 5, unless the wave heights be overrated as compared to reality. Now, the only thing remaining is how to model ship wakes: this is the topic of the next chapter.

Chapter

3 Ship wakes: models and phenomenology

Contents

In a sufficiently resolved radar image, ship wakes are among the most visible signs of the presence of a vessel. Since wakes can persist for several hours, they can extend for kilometers. The radar echo of the wake is often more prominent (on the surface) than that of the boat itself and can frequently be seen from space. Moreover, the wake is also visible in radar or optical images acquired from an airborne platform.

In this chapter, we focus on the appearance of the wake in radar. It can be demonstrated that the wake can be decomposed into several components: the Kelvin wake, related to non-viscous hydrodynamic phenomena, the turbulent wake, originating from viscosity forces, and the dead water wake that can extend over several tens of kilometers. Other phenomena related to the wake are also visible on radar. They are associated with the presence of internal waves in environments where the volume of water is stratified into layers of different density.

The main goal of the chapter is to model the map of water surface heights in the presence of a wake and to relate this map to the physical parameters responsible for the wake: the shape of the boat's hull and its speed. Throughout the chapter, a fundamental assumption is made that the drift is zero, so the ship's course and heading are identical. We will initially consider the wake in its generality to briefly categorize the various phenomena known under the very general term "wake," and then explore how these phenomena manifest in a radar image. Subsequently, we delve into the modeling and simulation of the Kelvin wake height map.

3.1 Ship wakes and their radar image: general overview

Figure 3.1 is a high-resolution optical image of a ship off the coast of Boston. This image well illustrates various phenomena referred to as wakes. Firstly, there is a V-shaped structure formed by a set of divergent and transverse waves propagating within a cone, with its apex at the front of the ship and symmetric with respect to the ship's axis. This is the Kelvin wake. Immediately behind the ship, as well as along the hull, the white foam is a

manifestation of turbulent phenomena near the vessel. There is also a dark trail behind the ship: this trail has a width close to that of the ship and is aligned with the trajectory. This is the dead water wake, which appears approximately one ship length behind the vessel and extends over a considerable distance: several tens of kilometers.

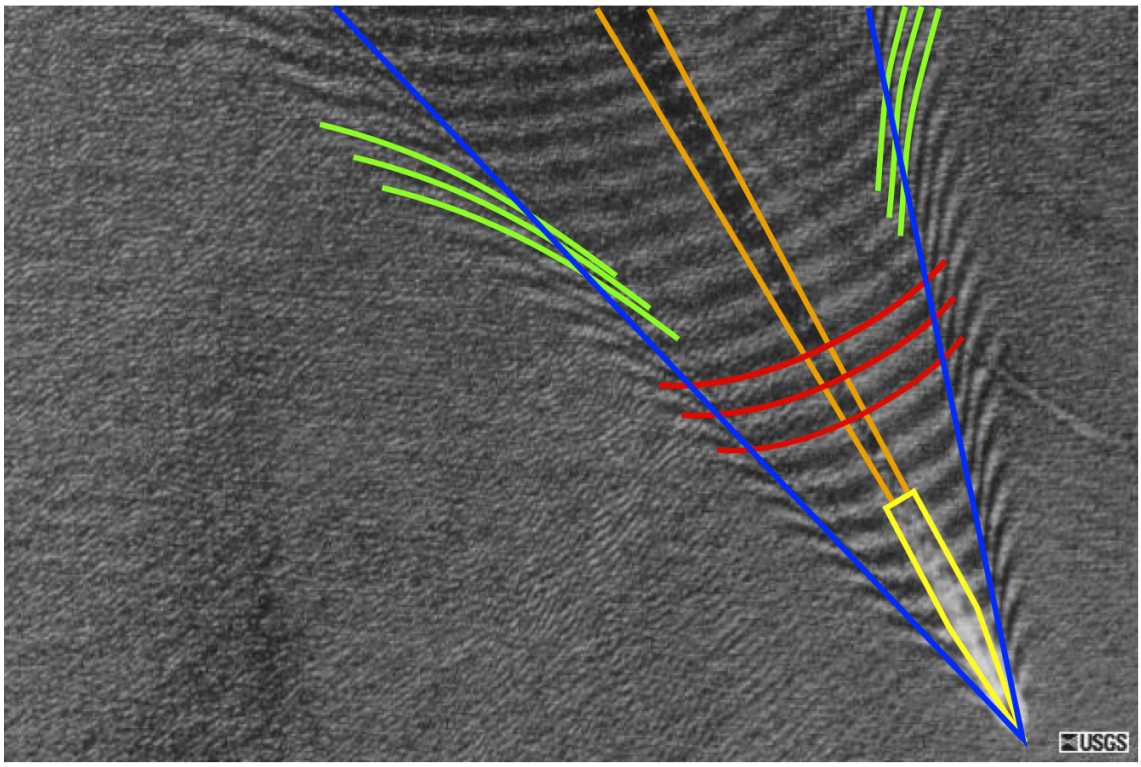

Figure 3.1: *Divergent Kelvin waves (in green) and transverse waves (in red) existing within the Kelvin cone (in blue). The turbulent wake is in yellow, and the dead water wake is in orange. Image from USGS, in the public domain.*

3.1.1 Kelvin wakes

We begin this section by focusing on the Kelvin wake. The theoretical study of the non-turbulent wake started with the foundational work of William Thomson, Baron Kelvin, in the late 19th century. These contributions had a significant impact on naval architecture as the forces required to displace water in the wake are directly related to the resistance forces against the ship's movement. The Kelvin wake was later examined in more detail by Ursell, Wehausen, Laitone, and numerous other authors throughout the 20th century. The equations of the Kelvin wake can be derived within the framework of the Navier-Stokes equations, under the assumptions of non-viscosity, allowing the velocity field of water to be derived from a potential, and modeling the hull as a set of source terms (a demonstration of these equations can be found, for example, in [137]).

3.1.1.1 Geometric characterization of the Kelvin wake

Independent of the derivation of the Navier-Stokes equations for the wake problem, numerous properties of the Kelvin wake can be deduced from purely geometric and straightforward considerations. The geometric interpretation presented here has been known since at least the work of Lighthill [119] (p. 273). We start by assuming working in the far field,

ensuring that wave fronts are straight lines. We then assert that the wake wave fronts do not move in the ship's reference frame, a observation drawn from empirical evidence. Consider a wake wave propagating in the direction θ with the ship's axis of symmetry. Referring to Figure 3.2, let A be the position of the ship at a given time t_0, and B(t) be the position of the ship at a time $t_0 + t$. Define C(t) as the position of the common wavefront to $B(t)$, such that $\widehat{\mathrm{BAC}} = \theta$, making (AC) the direction of wave propagation. If C(t) is on the same wavefront as B(t), necessarily (AC) is perpendicular to (BC). The fact that the wake is stationary means that, concerning the axis (AB), the phase velocity of the wave must be equal to the speed V_b of the ship. This also implies that the ship's speed projected onto (AC) is equal to the phase velocity of the wake wave propagating in the direction (AC):

$$c(K) = V_b \cos\theta \tag{3.1}$$

Assuming an infinitely deep sea, we have (see Equation 2.41 in Chapter 2):

$$\sqrt{\frac{g_0}{K}} = V_b \cos\theta \tag{3.2}$$

which leads to:

$$K = \frac{g_0}{V_b^2 \cos^2\theta} = K_b \sec^2\theta \tag{3.3}$$

where $K_b = g_0/V_b^2$ is the wave number associated with the ship or the wake waves traveling in the direction of the ship's route, and $\sec x = 1/\cos x$ (secant function). This relation characterizes the spectral locus of the wake.

Now consider a second wake wave propagating in a direction $\theta + d\theta$. It is also assumed to be emitted at A and will also follow the relation 3.3. Let $\mathbf{K} + d\mathbf{K}$ be the wave vector of this second wave in its propagation direction $\theta + d\theta$; its norm is:

$$K + dK = \frac{K_b}{\cos^2(\theta + d\theta)} \approx K \tag{3.4}$$

Then, the norm of the projection of $\mathbf{K}+d\mathbf{K}$ onto the direction θ of the first wave will also be very close to K. The energy of the signal propagating in the direction θ is then carried by a packet of waves interfering with each other, with a wavelength close to $K = K_b/\cos^2\theta$. This energy propagates at the group velocity $c_g(K)$. Recall that the group velocity is twice the phase velocity (still in an infinitely deep sea), as shown in Equation 2.42 of Chapter 2. It follows that the energy of the wave packet propagating in the direction (AC) is mostly located between A and D(t), a point such that $\mathbf{AD}(t) = \frac{1}{2}\mathbf{AC}(t)$. Considering all possible positions of D as a function of θ, it is observed that D lies on a circle of radius $r = 1/4||\mathbf{AB}||$. The maximum deviation of D from (AB) is equal to the radius r of this circle. Denote $D_{\max}(t)$ as this position. One can then calculate the angle $\beta_c = \widehat{\mathrm{D_{max}BA}}$, corresponding to the opening of the cone. It is given by:

$$\beta_c = \arcsin\left(\frac{r}{3r}\right) = \arcsin\frac{1}{3} \approx 19.471 \tag{3.5}$$

This relation holds regardless of the duration t of the ship's movement. Therefore, it is concluded that the envelope of Kelvin waves is a cone with an opening angle of $2\beta_c$, approximately 39 degrees. The crucial result to remember is that this cone depends neither on the ship's speed nor the shape of its hull but only on the depth of the ocean, assumed to be infinite here.

A similar reasoning can be made by considering the finite-depth dispersion relation d provided in Chapter 2. It can be rigorously shown that the depth dependence is defined by the dimensionless factor γ_c, such that:

$$\gamma_c^2 = \frac{V_b^2}{g_0 d} \tag{3.6}$$

For example, in [144], where γ_c is calculated analytically, it is shown that if $\gamma_c^2 < 0.2$, then one can consider being in "infinite depth," and the angle of the wake β_c is indeed 19.471 degrees. If, on the other hand, γ_c^2 is 1, then β_c is 90 degrees, and beyond this, the system of transverse waves disappears, leaving only divergent waves with a specific form.

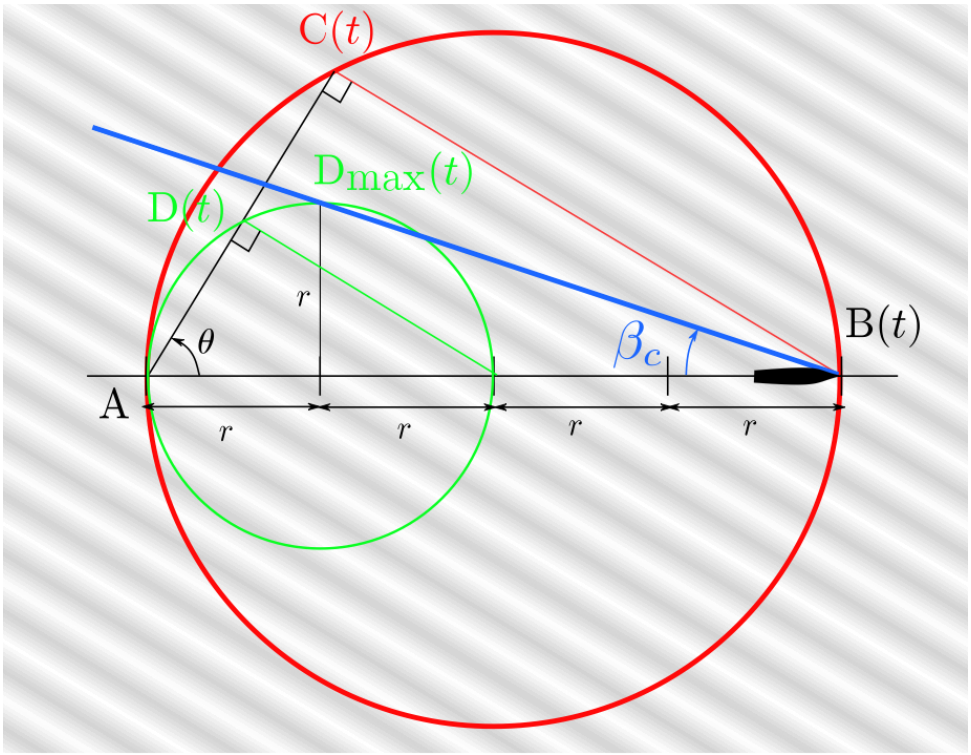

Figure 3.2: *Geometric principle for calculating parameters of the Kelvin wake. Only a single monochromatic wave, traveling in the direction θ, is considered here.*

3.1.1.2 The Kelvin wake in radar observations

The Kelvin wake has been observed using synthetic aperture radar (SAR). The study of such wakes observed by radar began after the Seasat flight in 1978. Seasat, the first satellite equipped with synthetic aperture radar (in L-band), was also the first to demonstrate that ship wakes, including the Kelvin wake, could be observed by radar. On monostatic radar satellite images, the Kelvin wake is characterized by one or two bright lines with an opening angle of β_c, as shown in Figure 3.3. The system of divergent and transverse waves is rarely visible in radar images because it requires a wavelength of wake waves compatible with the radar resolution and a very calm sea (such conditions exist but are rare, as seen in Figure 5.12(b) on page 144 in Chapter 5, acquired by Seasat). However, the observation frequency of the Kelvin wake by spaceborne radar is much lower than that of observing the dead water wake. Melsheimer *et al.* reported in [128] that, out of 400 ERS 1 and 2 images showing a wake, only 17

In practice, the visibility of the Kelvin wake arms depends significantly on the orientation of the satellite's orbit relative to the ship's direction. It is essential to note that caution is needed when comparing Seasat measurements with measurements from ERS satellites because Seasat operated in HH polarization, while ERS data are in VV polarization. Generally, turbulent wakes are more visible in VV images, whereas Kelvin wakes are more visible in HH polarization [93, 98]. This is why statements in the literature often claim that the wake is "more visible in VV than in HH polarization" (see, for example, [84, 49]) without specifying that it refers only to the dead water wake. Most articles focus on the visibility of the wake in satellite imagery, especially ERS-1/2, where only the dead water wake is of major interest.

3.1.2 Phenomena caused by viscosity

The turbulent wake has multiple origins [149]: firstly, there are viscosity effects that give rise to turbulent currents along the hull, the vortices generated by ship propellers, or the waves created by the ship's bow and stern, which, in practice, may break even though it is not considered in the Kelvin elevation model. The turbulent wake is practically the primary cause of the disturbed area near the ship, which is manifested, for example, by the presence of visible foam or bubbles. In practice, near-field turbulence is extremely challenging to model, especially since these turbulences exist not only on the surface but also within the volume of water.

However, based on radar images and high-resolution optical images taken from space or an aircraft, it has been observed that there are large-scale phenomena in the far field, with an extension of several tens or even a hundred kilometers. These phenomena are characterized by systems of dark or bright lines existing inside the Kelvin cone, and their origin has long been debated.

3.1.2.1 Dead water wakes

The dead water wake is characterized on monostatic radar by a dark streak directly in the ship's axis, at a sufficient distance for the foam from near-field turbulent wake to disappear. The dark color indicates low roughness due to the absence of gravity waves in this area, which does not favor radar wave backscattering on the water surface. This dark band can be seen, for example, in the images in Figure 5.12 in Chapter 5. This band is also visible in optical bands.

Origin of the Dead Water Wake The origin of this streak was the subject of debates during the 1980s. The initial hypothesis was that the vortices generated by ship propellers break the dynamics of gravity waves. Swean in 1987 [168] (cited by Griffin *et al.* [85] and Reed *et al.* [149]) conducted studies on a numerical model of a destroyer with two propellers and showed that the lifetime of these vortices is not long enough to explain the dead water wake alone. Griffin, reported in [85], a plausible hypothesis supported by real-world experiments: the persistence of the dead water wake is caused by a redistribution, due to the passage of the boat, of the surfactants naturally present on the water surface. The effect of surfactants is enhanced in case of human-induced pollution, namely various hydrocarbons.

3.1.2.2 Width of the dead water wake

It has been shown semi-empirically that the width of the turbulent and dead water wakes, as a function of the distance x from the stern, follows a law of $x^{1/a}$, with a being a constant whose value ranges from 4 [34] to 5 [28] (Chapter 14). Ziloh and Milman [202] proposed

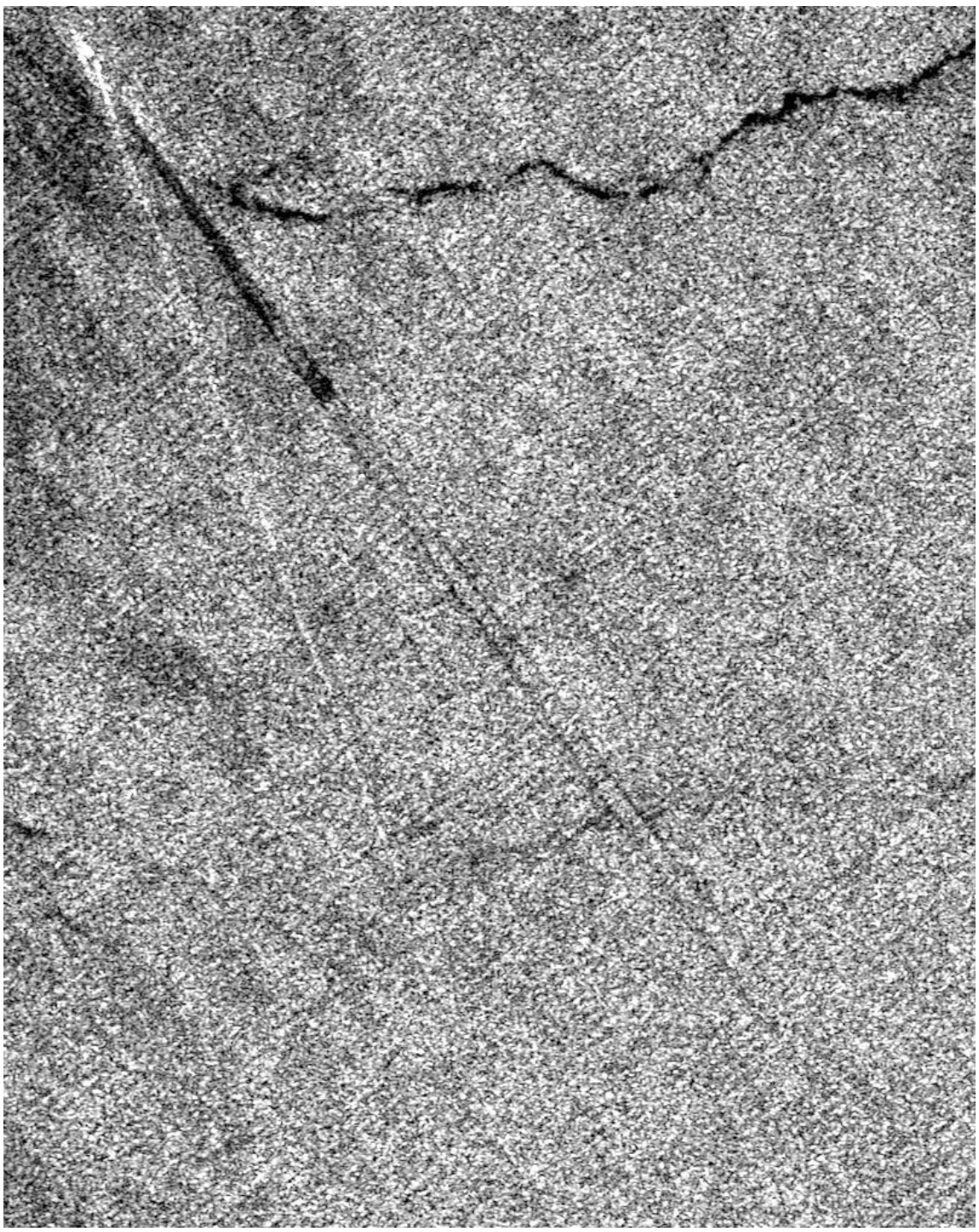

Figure 3.3: *Ship off the coast of the Malacca Strait (ERS-1 image, acquired on May 4, 1996, at 15:59 UTC). The wake extends for about 12 kilometers (source: ESA).*

in 2004 an empirical formula based on the compilation of several previous studies, giving the width of the dead water wake by specifying the hidden constants:

$$W(x) = \frac{\bar{w_0}}{\left(\frac{\bar{x_0} L_b}{B_b}\right)^{1/a}} B_b^{a-1} x^{1/a} \tag{3.7}$$

where B_b is the width of the ship, L_b is its length, $\bar{x_0} \approx 4$, and $\bar{w_0} \approx 4$. As mentioned above, theoretically a is 5, but in practice, it varies from 4 to 5 in equation 3.7.

Characteristics of the Dead Water Surface Equation 3.7 only describes the location of the dead water wake but not its surface characteristics, for example, in terms of the wave spectrum. For this, other models exist. One can refer to Reed and Milgram [149], who provide a generic formulation of the energy balance on sea surface waves in the dead water wake region. They start from the equation relating the spectral energy density of waves $\mathcal{E}$ (defined in Equation 2.113 in Chapter 2) to the wave vector $\mathbf{K}$ and time t, with $c_g(\mathbf{K})$ being the group velocity (defined in Equation 2.42):

$$\frac{\partial \mathcal{E}(\mathbf{K})}{\partial t} + \mathbf{c}g(\mathbf{K}) \, \mathbf{grad} \;\; \mathcal{E}(\mathbf{K}) = 0 \tag{3.8}$$

They then modify this equation 3.8 by introducing source terms:

$$\frac{\partial \mathcal{E}(\mathbf{K})}{\partial t} + \mathbf{c}g(\mathbf{K}) \, \mathbf{grad} \;\; \mathcal{E}(\mathbf{K}) = S_w(\mathbf{K}) + Snl(\mathbf{K}) - S_t(\mathbf{K}) - S_v(\mathbf{K}) \tag{3.9}$$

The equation consists of terms with the following meanings:

- S_w is a source term for short-wavelength waves, related to the wind;
- Snl is a source term related to non-linear interactions between capillary waves and gravity waves;
- S_t is the attenuation term for short-wavelength waves due to turbulence;
- S_v is the viscous attenuation term.

This differential equation needs to be integrated to find the value of the spectrum modified by the wake for each wave $\mathbf{K}$, depending on time. Reed and Milgram propose the initial condition $\mathcal{E}(\mathbf{K}) = 0$ at the beginning of the dead water wake, *i.e.*, a ship length behind the stern. They work in the ship's reference frame, so time can be related to position using the relationship $x = V_b t$, where V_b is the ship's speed. Reed and Milgram then provide a formulation for these source terms, some of which depend on experimental measurements that we will not replicate here, as we have not implemented the method.

Griffin *et al.* [85] propose a method assuming that at the center of the wake, there is a current that, in a first approximation, in the far field and in the turbulent wake, takes the form $\mathbf{s}(x, y, z) = s(y)\hat{\mathbf{x}}_b$ (see Figure 3.4). Starting from the modified Equation 3.8 to bring out the current $\mathbf{s}$:

$$\frac{\partial \mathcal{E}(\mathbf{K})}{\partial t} + (\mathbf{s} + \mathbf{c}g(\mathbf{K})) \, \mathbf{grad} \;\; \mathcal{E}(\mathbf{K}) = 0 \tag{3.10}$$

they show that the spectrum of the dead water wake $\mathcal{S}(K, \psi)$ can be written in terms of the spectrum of the unmodified ocean $\mathcal{S}\infty(K_\infty, \psi_\infty)$ through the relationship:

$$\mathcal{S}(K, \psi) = \left[\frac{1 - \sqrt{1 - 4s\sqrt{K/g_0}\sin\theta_\infty}}{2} \right]^3 \mathcal{S}_\infty(K_\infty, \psi_\infty) \tag{3.11}$$

In this equation, the spectrum of the dead water wake for a wave with wavenumber K and direction ψ relative to the wind is considered. It is related to the wake at infinity for a wave initially arriving with direction ψ_∞ and wavenumber direction K_∞, being linked by the relation $K \sin\psi = K_\infty \sin\psi_\infty$.

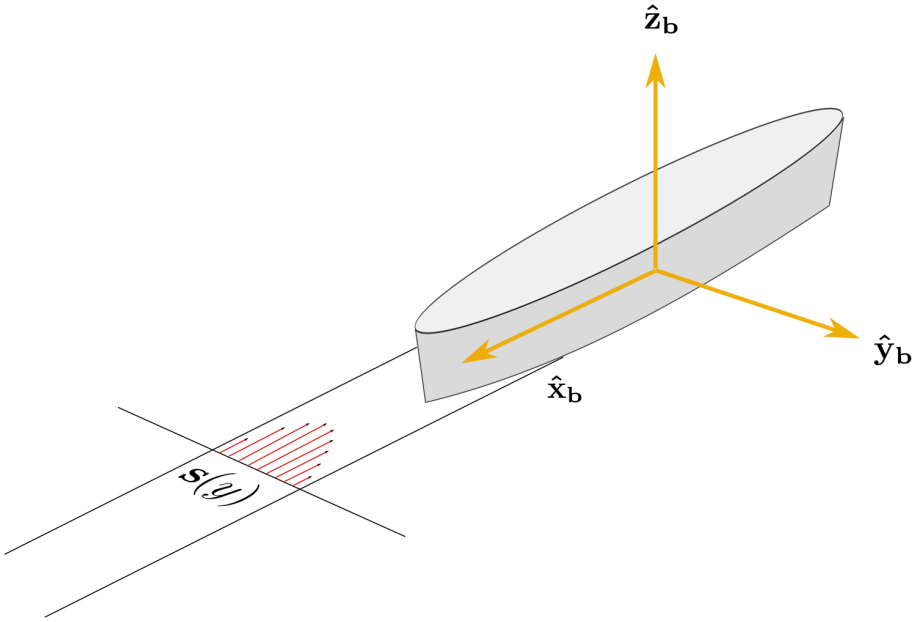

Figure 3.4: *Surface current in the dead water region (Griffin* et al. *hypothesis [85]); diagram inspired by Oumansour [137].*

3.1.2.3 The "Bright V" wakes

The term "Bright V wake" refers to a set of bright lines forming a V or semi-V cone, whose opening angle is not consistent with the Kelvin wake angle β_c. This type of bright lines is common in many radar images. In Seasat images, the opening angle typically ranges from 14 to 17 degrees and can extend to a range of 1 to 7 degrees [85]. Various hypotheses have been proposed to explain this phenomenon. All these hypotheses are based on the same mechanism concerning the radar-scene interaction: the scattering of electromagnetic waves in diffuse regime is created by Bragg scattering [180] (also see Chapter 4, page 109): waves with approximately the same wavelength as the incident radio wave will diffract the wave, causing constructive interference in the direction of the receiver, leading to an increase in received energy and, consequently, bright lines.

Interrupted Kelvin Wake (IKW) Hypothesis The Interrupted Kelvin Wake (IKW) hypothesis is based solely on the Kelvin wake and does not involve a "turbulent" mechanism. It starts from the observation that the wavenumber of Kelvin wake waves, as given in Equation 3.3, increases towards infinity as one approaches the direction orthogonal to that of the ship. In this case, these are divergent waves. This means *a contrario* that the wavelength of these divergent waves tends to zero, passing through the Bragg wavelength. It can be assumed that the bright V wake is caused by Kelvin wake waves in Bragg configuration. This hypothesis was first proposed by Lyden *et al.* in 1985. Supporting elements were provided by Munk in 1987 [133], after analyzing SIR-B radar data from a space shuttle *Challenger* mission. By taking the wavenumber K' of the Bragg waves as input, which depends on the acquisition geometry (see Chapter 4, Equation 4.4), and using

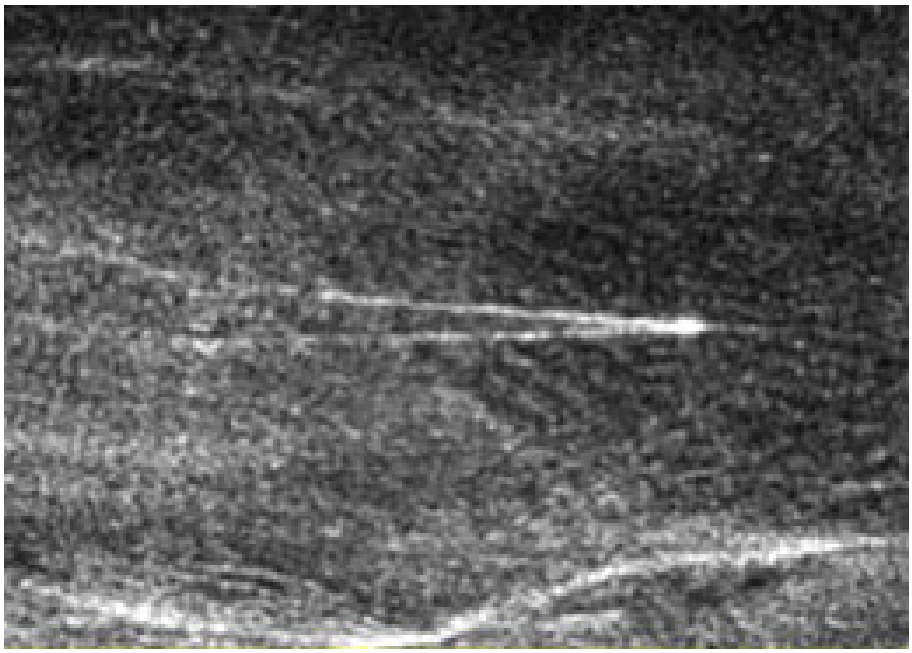

Figure 3.5: *Bright V wake observed by Seasat [149].*

considerations from Section 3.1.1.1, especially the phase velocity for K', the theoretical half-angle α_c of the bright V wake can be determined (in monostatic configuration) as [123]:

$$\alpha_c = \arctan\left(\frac{c_g(K')}{V_b}\cos\phi_{rb}\right) \tag{3.12}$$

where ϕ_{rb} is the radar trajectory angle relative to the ship trajectory, and V_b is the ship's speed. Zilman and Miloh [201, 200] conducted a theoretical study in 1996 on the appearance of the "Bright V" under the assumption of the interrupted Kelvin wake by calculating the Kelvin wake for a simple hull and introducing the influence of surfactants, which also seems to corroborate data published earlier by Shemdin in 1990 [155].

Modified Kelvin Wake by Surface Current Hypothesis This hypothesis is a continuation of the approach by Griffin *et al.* mentioned above [85]. It posits that, in the far field, at the center of the wake, a current $\mathbf{s}(y)$ (see Figure 3.4) disrupts Kelvin wake waves. Griffin *et al.* modify the developed model to integrate the refraction of wake waves inside the current zone. They then show that the constant phase lines of the Kelvin wake, as well as the wavelengths and potentially the slopes, are modified near the dead water wake zone.

Influence of Internal Waves The mechanism of internal waves is a separate phenomenon. In all circumstances, the ship generates wake waves not only on the surface but throughout the entire volume of water. These waves normally have little effect on the surface. However, in the presence of strongly stratified water in salinity or density (which is equivalent), these internal waves can modulate the surface waves in a way that makes a bright wake appear if the surface waves are at the Bragg frequency (see the example in Figure 3.6). In 1997, Stapleton [164] conducted a study on series of SAR images at several frequencies and for boats of various sizes (three fishing vessels and a larger high-sea tug, the Olmeda, see Figure 3.7). He observed that the theoretical angle predicted by the IKW theory did not correspond to the observed angle for Olmeda, but it matched well for the wakes of smaller

vessels. This suggests that the internal wave mechanism predominates for bright V wakes created by larger ships, without being able to draw definitive conclusions due to the small experimental basis.

Other Hypotheses Stapleton [164] notes that the hypotheses listed above work well for low wind speeds, less than 5 m/s for the IKW hypothesis, also noting that turbulent wakes are not very visible beyond 10 m/s. Therefore, there are other mechanisms to study to explain the visibility of turbulent wakes for slightly higher wind speeds.

3.2 Calculation of wave amplitudes in the Kelvin wake

We now focus on the analytical calculation of the elevation map of a Kelvin wake. Throughout this section, we work in the ship coordinate system $\mathcal{B}$ described in Appendix A (see also Figure 3.8), oriented such that the x-axis is positive in the direction of the stern. Thus, if θ is positive, the wave moves towards the port side.

3.2.1 Ship modeling

To model the Kelvin wake, we assume that the ship's hull can be described by an equation of the form $y = Y(x, z)$ in the ship frame, as shown in Figure 3.8. Note that a completely wet body can be perfectly modeled by this representation, assuming y is zero wherever the hull "does not exist." Analytic representations for the hull can be obtained in simple cases, such as the Wigley hull, cosine-sine hull, *etc.* (see, for example, Wu [197], p. 83-84):

Wigley Hull The Wigley hull is given by the following equation:

$$Y(x,y) = \frac{B_b}{2}\left(1-\left(\frac{2x}{L_b}\right)^2\right)\left(1-\left(\frac{z}{D_b}\right)^2\right) \quad x \in [-L_b/2, L_b/2], z = [-D_b, 0] \tag{3.13}$$

where B_b is the beam of the ship, L_b is its length, and D_b is its draft.

Cosine-Sine Hull This hull is given by the following equation:

$$Y(x,y) = \frac{B_b}{2}\left(1+\cos\left(\frac{2\pi z}{L_b}\right)\right)\left(1+\sin\left(\frac{\pi x}{2D_b}\right)\right) \quad x \in [-L_b/2, L_b/2], z = [-D_b, 0] \tag{3.14}$$

General Case In a real case, representing the ship's hull analytically is impractical. A discretized representation of the surface is used instead. In our approach, we use a series of $N_x \times N_z$ points $Y(x_i, z_i)$, where $\{x_i\}$ and $\{z_i\}$ are sampled at a constant step size Δx and Δz, respectively, yielding N_x segments (or $n_x + 1$ points) in x and N_z segments in depth. It is understood that only the wet (immersed) part of the hull needs being discretized. The origin of the coordinates is arbitrary, but since we assume that the hull has a symmetry plane, it is convenient to place the origin of the frame on the ship's symmetry axis.

3.2.2 Obtaining surface heights: the Kochin integral

Within the framework of linear theory of inviscid fluids, it can be shown that the disturbance generated by a hull is a sum of sinusoidal waves, each propagating in a direction θ with a given amplitude and wave number following the relation 3.3. In a simplified manner, we proceed by calculating the Kelvin wake system generated by a single pressure point on the water surface, and we generalize it to an entire hull by considering that the wake system

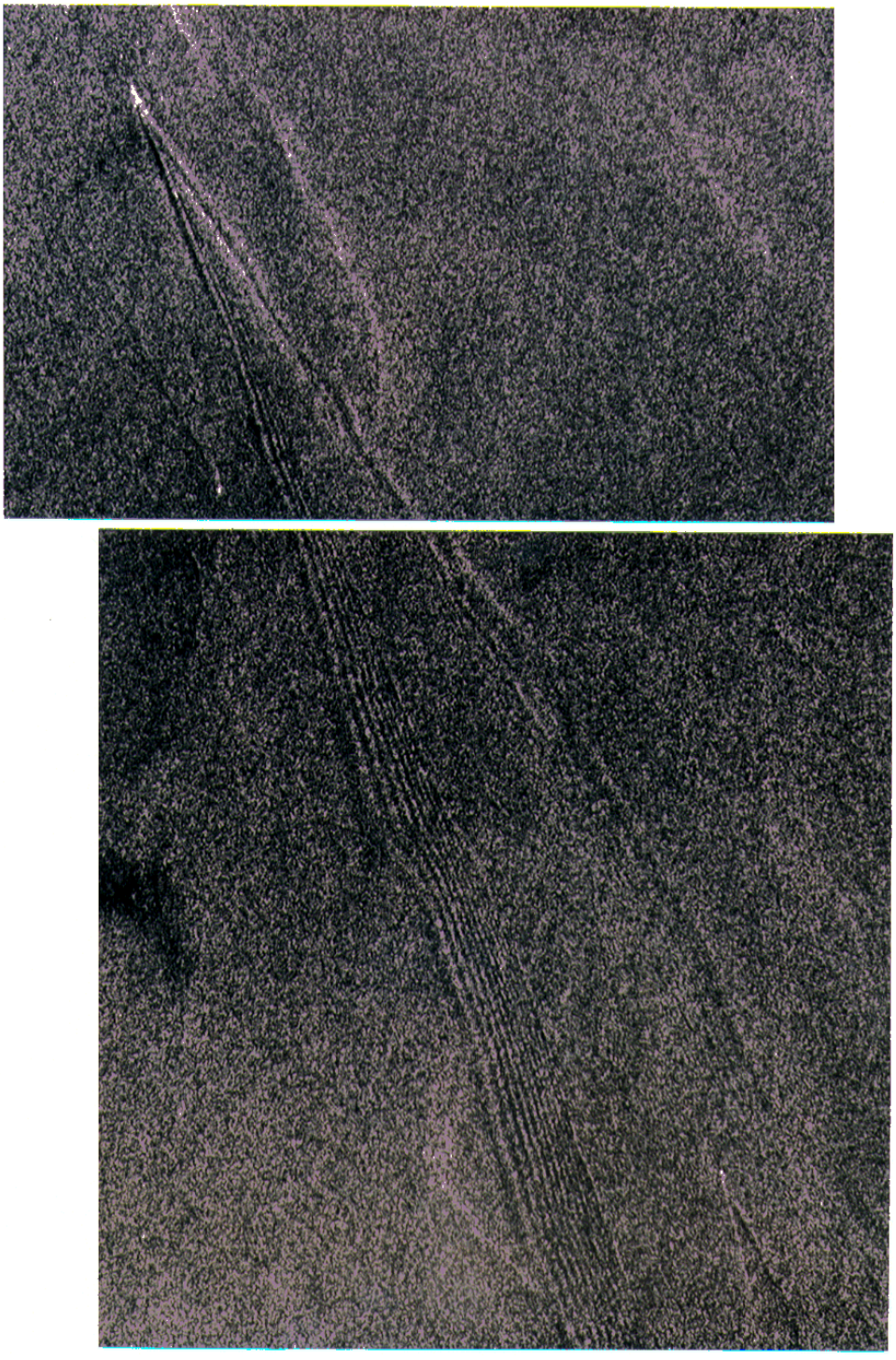

Figure 3.6: *Internal wake observed by ERS 1 in C-band off the coast of Sweden in 1991. The wake extends over nearly 40 km (Image: ESA/EURIMAGE/Spacetec, from [66]).*

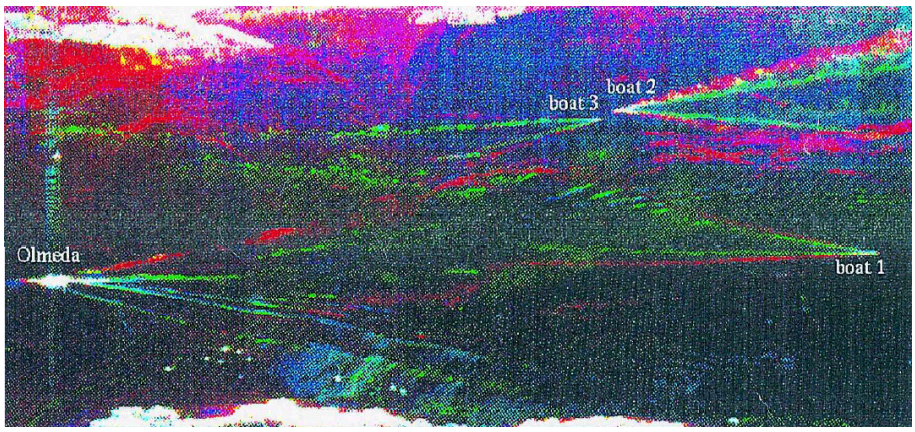

Figure 3.7: *Bright V wakes observed at several frequencies (hence the color composite image) by Stapleton [164].*

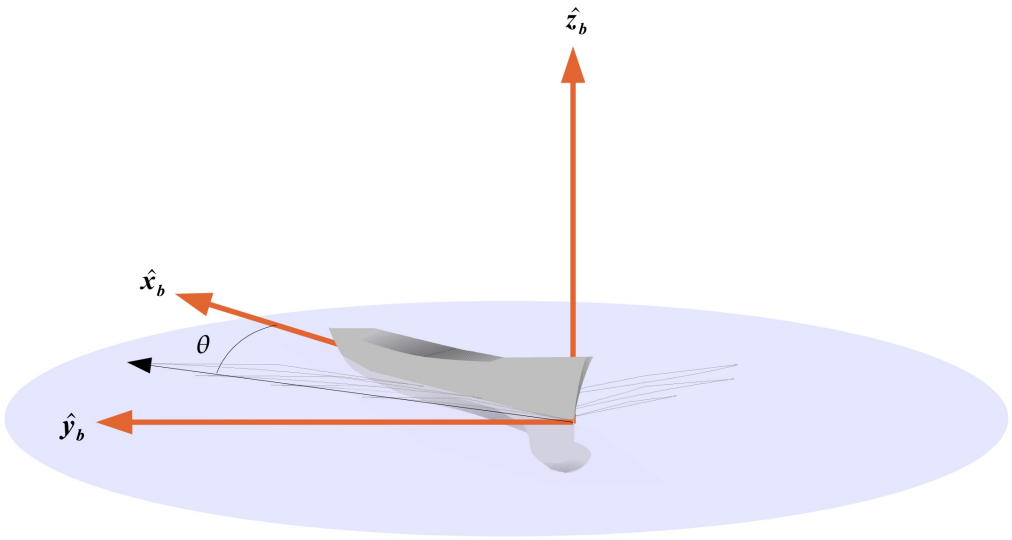

Figure 3.8: *Notations used for the "wet body" frame, in this case, the DTMB 5415 hull.*

for a single point is the Green's function of the differential problem describing the wake. One can refer to K. Oumansour's thesis [137] for a more comprehensive presentation of the calculation of this Green's function from the Navier-Stokes equations. Nevertheless, after using the Green's function, an integral representation of the elevation map is obtained, called the *Kochin Integral*:

$$\zeta_w(x,y) = \Re \int_{-\frac{\pi}{2}}^{+\frac{\pi}{2}} A_{V_b,Y}(\theta) e^{-\jmath\phi(\theta)} d\theta \tag{3.15}$$

where:

$$\phi(\theta) = K(\theta)[x\cos\theta + y\sin\theta] \tag{3.16}$$

and $K(\theta)$ is given by Equation 3.3. In this integral, $A_{V_b,Y}(\theta)$ is a function solely of θ and parameterized by the hull shape Y and the ship speed V_b, both provided as input. We will call $A_{V_b,Y}$ the *amplitude function*; it is also known as the *Kochin function*. It is a closed analytical form that can be used to calculate the elevation map as well as the resistance

to the advancement of the hull. Indeed, it is for this latter problem, more critical in naval architecture than the height of the wake waves, that the theory was developed.

Moreover, the components of the fluid velocity vector $[u(x,y,z), v(x,y,z), w(x,y,z)]$ in the $\mathcal{B}$ frame are given by [174]:

$$u(x,y,z) = -\frac{g_0}{V_b}\Re\int_{-\frac{\pi}{2}}^{+\frac{\pi}{2}} A_{V_b,Y}(\theta)e^{K_b z\sec^2\theta}e^{-\jmath\phi(\theta)}d\theta \tag{3.17}$$

$$v(x,y,z) = -\frac{g_0}{V_b}\Re\int_{-\frac{\pi}{2}}^{+\frac{\pi}{2}} A_{V_b,Y}(\theta)e^{K_b z\sec^2\theta}e^{-\jmath\phi(\theta)}\tan\theta d\theta \tag{3.18}$$

$$w(x,y,z) = -\frac{g_0}{V_b}\Re\jmath\int_{-\frac{\pi}{2}}^{+\frac{\pi}{2}} A_{V_b,Y}(\theta)e^{K_b z\sec^2\theta}e^{-\jmath\phi(\theta)}\sec\theta d\theta \tag{3.19}$$

Depending on the approximations made, several more or less approximate forms of $A_{V_b,Y}$ can be obtained for a given hull shape. In the following paragraph 3.2, up to section 3.2.3.4 (not included), we will describe a technique proposed by Tuck, Lazauskas, and Scullen from the University of Adelaide in a series of seven technical reports describing their computational code *Sea Wave Pattern Evaluation* (SWPE). We will specifically focus on their first report [174], as well as an earlier reference by Tuck [173]. The approach followed by Tuck, Lazauskas, and Scullen was to formulate the Kochin integral within the framework of Michell's slender ship theory (proposed in 1898: [129]), which assumes that the ship's beam B_b is small compared to its length or, more precisely, that the derivative of the function Y with respect to x is small. Indeed, this assumption greatly simplifies the calculations. This choice was reinforced by the fact that, over time, it has been observed in the community that the Michell approximation, despite the significant simplifications it introduces, often yields results of similar order of magnitude to much more complex and sophisticated computational codes, at a much lower computational cost [172].

Tuck, Lazauskas, and Scullen then simplified the amplitude function $A_{V_b,Y}$ resulting from the Michell approximation using several simplifying assumptions, which have also been lifted in the later reports of the series. However, in the implementation used in this manuscript, these assumptions have been retained. They are as follows:

1. The assumption of an infinitely deep sea;
2. The far-field assumption: wave elevations are only calculated for points (x,y) located at least two ship lengths away;
3. There is no transom stern: that is, the function $Y : (x,z) \mapsto Y(x,z)$ decreases continuously to 0 at the front and rear of the ship;
4. The assumption of a hull admitting a symmetry plane: this simplifies calculations; moreover, this assumption is not very restrictive in practice because most ships are symmetric anyway.

Under these assumptions, the amplitude function can be written as:

$$A_{V_b,Y}(\theta) = -\frac{2\jmath}{\pi}K_b^2\sec^4(\theta)[P(\theta)+\jmath Q(\theta)] \tag{3.20}$$

with:

$$P(\theta) = \int F(x_b,\theta)\cos(K_b x_b\sec\theta)dx_b \tag{3.21}$$

The integral Q is similar to P, but uses a sin() function instead of cos(). The function F itself is an integral:

$$F(x,\theta) = \int Y(x,z_b)\exp(K_b z_b\sec^2\theta)dz_b \tag{3.22}$$

3.2.3 Integration scheme for the Kochin integral

In the literature, the calculation of the above integrals is often done in the case of hulls defined by a mathematical formula, as described in paragraph 3.2.1, for which analytical formulas can be found. However, in the general case, such formulas do not exist, and numerical integration is necessary. However, the choice of the integration scheme is very delicate due to the nature of the integrals, as the integrand can oscillate rapidly due to terms like $\exp(\jmath \sec\theta)$. Standard integration schemes cannot be used. Tuck *et al.* propose clever integration schemes for each sub-integral that are well-suited to the problem, derived from Tuck's earlier work.

3.2.3.1 Calculation of F

To calculate F, Tuck *et al.* suggest using an integration method inspired by the Filon scheme, which handles integrands that oscillate rapidly and provides precision equivalent to a trapezoidal rule integration scheme:

$$F(x,\theta) = \sum_{j=0}^{N_x} \omega_j Y(x,z_j) \exp(K_b z_j \sec^2\theta)\Delta z \tag{3.23}$$

The weights ω_i are given by the following equations:

$$\omega_0 = (e^{m_0} - 1 - m_0)/{m_0}^2 \tag{3.24}$$
$$\omega_{N_z} = (e^{-m_0} - 1 + m_0)/{m_0}^2 \tag{3.25}$$
$$\tag{3.26}$$

For other values of j:

$$\omega_j = (e^{m_0} + e^{-m_0} - 2)/{m_0}^2 \tag{3.27}$$

where $m_0 = K_b \sec^2\theta\Delta z$. Here too, if m_0 tends to zero, it is important to hard-code the limit values of ω_j to avoid numerical divergence:

$$\lim_{m_0\to 0} \omega_0 = 1/2 \tag{3.28}$$
$$\lim_{m_0\to 0} \omega_j = 1 \text{ if } j \neq 0, N_z \tag{3.29}$$
$$\lim_{m_0\to 0} \omega_{N_z} = 1/2 \tag{3.30}$$

3.2.3.2 Calculation of P and Q

The calculation of integrals P and Q (equation 3.21) is done simultaneously to consolidate the computation of $F(x,\theta)$. Here too, a Filon scheme is used, this time exact. By assuming that Y tends to zero at the ends of the hull, the scheme can be written as:

$$P(\theta) \approx \sum_{i=1}^{i=N_x-1} \omega_i' F(x,\theta)\cos(K_b x_i \sec\theta)\Delta x \tag{3.31}$$

Where we define the weights ω_i' for i different from 0 and $N_x - 1$. In the case where i is even, the weight is given by:

$$\omega_i' = (3m_1 + m_1\cos 2m_1 - 2\sin 2m_1)/m_1^3 \tag{3.32}$$

And, if i is odd:

$$\omega' i = 4(\sin m_1 - m_1 \sin m_1)/m_1^3 \tag{3.33}$$

With $m_1 = K_b \sec\theta \Delta x$. Different weights are assigned for $i = N_x$ if there is a transom stern; however, in our case, we assume this is not the case, so the weights at the ends are zero. Note that if m_1 tends to zero, care must be taken: in implementation, the limit transition for $\omega' i$ cannot be straightforward. Therefore, the limit values of ω_i need to be hard-coded as soon as $m1$ is below a threshold ϵ (for example, 10^{-5}). These limits are $2/3$ and $4/3$ for even and odd i, respectively. It is observed that these weights then correspond to the standard Simpson's integration method. Once P and Q are calculated, the value of $AV_b, Y(\theta)$ can be obtained immediately.

3.2.3.3 Calculation of the Kochin integral

The calculation of the Kochin integral is much more delicate. As mentioned earlier, the issue arises due to the presence of secant terms in θ, a term whose oscillation frequency tends to infinity as $|\theta|$ approaches $\pi/2$. Tuck, Collins, and Wells propose, in [173], an approach inspired by the method of stationary phase. The stationary phase method is commonly used in analysis to evaluate an integral where the integrand is a rapidly oscillating term around zero, and its envelope varies slowly. It is then possible to consider that where the integral oscillates rapidly, positive terms are compensated by negative terms, resulting in a net integral of zero. The only contribution to the integral comes from intervals where the integrand oscillates slowly, in other words, where the phase $\phi(\theta)$ (whose expression is given by equation 3.16) evolves very gently or where the derivative of the phase vanishes. The integral is then approximated by the sum of the function values at these points where the phase has a vanishing derivative. A first approximation of the wave height can be obtained by considering only the contribution of points where the phase is stationary (Oumansour [137]). However, it is not possible to calculate the height outside the Kelvin cone, even if small amplitude waves do indeed exist in this area.

In the method proposed by Tuck in the article [173], which predates the reports describing SWPE, not only are the points of stationary phase used, but also intervals centered around these points with appropriately calculated widths. More importantly, the function is attenuated at the edges of the intervals around the points of stationary phase by weighting it with a half-Gaussian. This allows working outside the Kelvin cone.

It is shown [173, 137] that the number of points where the phase is stationary in the Kochin integral depends on the position relative to the Kelvin wake cone defined in section 3.1.1.1. The position of the point (x, y) where the wake height is to be calculated is defined by the following polar coordinates, relative to the front of the ship:

$$r = \sqrt{x^2 + y^2} \tag{3.34}$$

$$\beta = \arctan\left(\frac{y}{x}\right) \tag{3.35}$$

Which are then compared to the critical angle β_c defining the opening of the cone, itself defined earlier.

Integration strictly within the cone When $|\beta| < \beta_c$, there is no particular problem. The integrand has two stationary points obtained when $d\phi/d\theta = 0$, which are given by the relations:

$$\theta_{2,1} = \arctan\left[\frac{-1 \pm \sqrt{1 - 8\tan^2\beta}}{4\tan\beta}\right] \tag{3.36}$$

Integration is carried out around these points by weighting the values of the integrand with a Gaussian factor that depends on the frequency of oscillations. More specifically, denoting $\Delta\theta$ as the discrete integration step:

1. Start from one of the stationary points θ_i and either increase or decrease θ by $\pm\Delta\theta$. Here, we assume that θ increases.

2. As long as $\phi(\theta) - \phi(\theta_i) < 0.6$, count the integrand with a unit weighting (this value of 0.6 has been empirically chosen by Tuck *et al.*).

3. If, for a given θ, denoted θ_i^+, such that $\phi(\theta_i^+) - \phi(\theta_i) \leq 0.6$, and $\phi(\theta_i^+ - \Delta\theta) - \phi(\theta_i) < 0.6$, then for all $\theta \leq \theta_i^+$, weight the integrand by a factor ν_w calculated as follows:

$$\nu_w(\theta) = \exp\left[-\kappa_1(\phi(\theta) - \phi(\theta_i^+))^2\right] \tag{3.37}$$

   where κ_1 is between 0.025 and 0.10, with the exact value not having much influence on the integral.

A similar result is obtained in the other direction by starting the integration at θ_i^-. However, it should be noted that there may be a problem in the region $\theta_1 < \theta < \theta_2$. Indeed, if the phase variation between θ_1 and θ_2 is not excessive, a unit weighting will be maintained in this region. Otherwise, attenuation will be applied. Tuck *et al.* propose conducting a test at the value $\theta_f = (3\theta_1 + \theta_2)/4$, an approximate value of the inflection point of $\phi(\theta)$ inside the cone. If $|\phi(\theta_2) - \phi(\theta_f)| < \pi/2$, a unit weighting is applied between θ_1 and θ_2. Otherwise, a Gaussian weighting is used as indicated above.

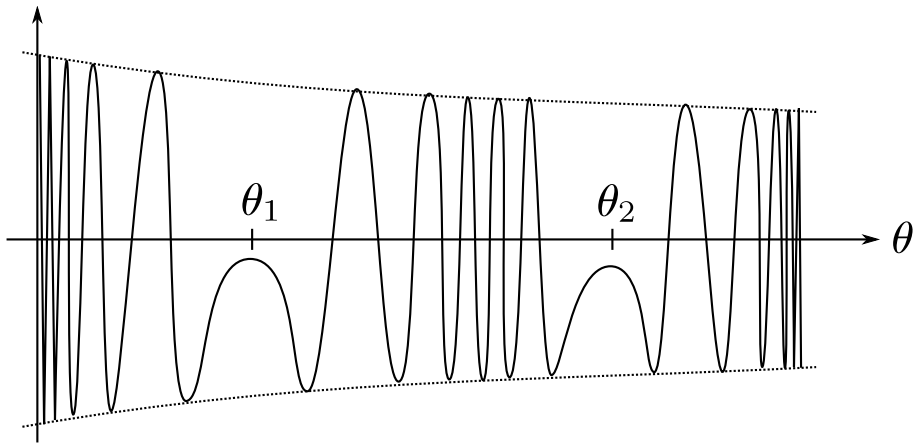

Figure 3.9: *Shape of the integrand of the function ζ_w (eq. 3.15) inside the Kelvin cone (inspired by [173]).*

Integration outside the cone When outside the cone, there are no stationary points. In this case, the elevation tends exponentially toward zero as r approaches infinity. However, the heights are not entirely zero when close to the cone boundary. Tuck *et al.* observe that these non-zero heights contribute during integration in the intervals where the integrand of the Kochin integral oscillates at the lowest frequencies, *i.e.*, at the inflection point where $d^2\phi/d\theta^2$ is zero. This point is given by:

$$-\tan\beta = \frac{1 + \sin^2\theta}{(\tan\theta)(5 + \sin^2\theta)} \tag{3.38}$$

Since the equation giving θ cannot be solved analytically, it must be solved numerically without requiring too much precision.

We have adopted a different approach. Noting that the absolute value of the frequency only increases, we integrate as long as the instantaneous frequency of the integrand is

compatible with the Shannon-Nyquist frequency defined by the value $1/(2\Delta\theta)$. In practice, we use unit weighting as long as the instantaneous frequency is far from the Shannon frequency, and then we weight it with a decreasing exponential so that the weighting is 0 when the integrand oscillates at the Shannon-Nyquist frequency.

3.2.3.4 Improving calculation robustness

To ensure better calculation robustness, we have taken the following additional measures compared to the elements provided in [174] and [173]. On the one hand, we know that the wake waves have zero height for angles $\beta \gg \beta_c$ and for $x < 0$. To guarantee this result and guard against the ever-present numerical noise, we multiply the numerical result of the integral $\zeta_w(x, y)$ by the following mask function M_w:

$$M_w(x,y) = \begin{cases} \exp -\kappa_2(\beta - \beta_c)^2 \text{ if } |\beta| > \beta_c, x \leq 0 \\ 1 \text{ if } |\beta| \leq \beta_c, x \leq 0 \\ 0 \text{ if } x < 0 \end{cases} \tag{3.39}$$

This mask function imposes a square exponential decay when the absolute value of the angle β is significantly greater than β_c. This result may not be absolutely physical but allows preserving the orders of magnitude, which is most important. We have chosen $\kappa_2 = 1/9$ (for β measured in degrees), corresponding to a standard deviation of approximately 2.12 degrees. This choice is empirical.

On the other hand, we observed another numerical noise resembling a spectrum folding issue: by directly implementing the scheme proposed by Tuck, Lazauskas, and Scullen, the wake map $\zeta_w(x, y)$, once transformed into the 2D Fourier domain, exhibits spectrum replicas that corrupt the signal by introducing waves with unrealistic directions. Furthermore, these replicas disturb the wave height value. To address this problem, the adopted solution was to apply a mask around the location of the theoretical frequencies of the spectrum, as provided by Equation 3.3. This binary mask, with a width of one pixel around the theoretical location, is then weighted by a Gaussian with a typical width of three pixels to minimize the Gibbs phenomenon before performing the filtering itself.

In the simulations presented in this manuscript, we often used the standard DTMB 5415 hull, which has the significant advantage of being extensively studied in the literature (see, for example, [149]), and its numerical model is freely available on the Internet (see Figure 3.10). The calculation is performed by scaling the hull, so that its overall length is one hundred meters; thus, its width is 13.25 meters.

Figure 3.11 illustrates the distribution of wake waves generated by the hull at two typical speeds. For the lower speed, the divergent waves tend to be more visible than at the higher speed. This behavior is typical.

3.2.4 Validation and limits of the computation

We now turn our attention to the validation of these wave height maps. In the literature, the hull length used may not necessarily match that in our calculation code. This is not an issue because the characteristic equations of the wake exhibit a fundamental property, which is a scaling relation with respect to the Froude number. The Froude number is a dimensionless characteristic number of the flow, indicating the relative importance of forces related to velocity and gravitational force. It is defined as follows:

$$\mathrm{Fr} = \frac{V_b}{\sqrt{g_0 L_b}} \tag{3.40}$$

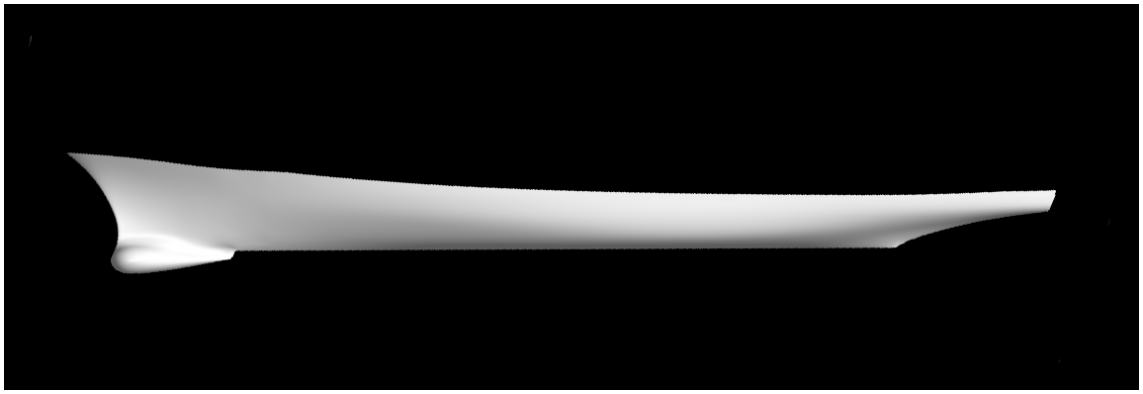

Figure 3.10: *The David Taylor Model Basin (DTMB) 5415 hull.*

Here, V_b is the ship's speed, and L_b is its length. It is then shown that the characteristics of the wake (the amplitudes, the wavelengths) are homothetic by a factor of L_b when the flow occurs at equal Froude numbers. This property is used here and will play a crucial role in Chapter 7.

We perform the first series of comparisons on measurements conducted in a basin and reported in [149], reproduced in Figure 3.12, alongside the results obtained with our implementation of SWPE. The measurements are taken around the hull, indicating that the operating regime is that of the near field. However, as mentioned earlier, the formulas we implemented are only valid at large distances from the ship (at least two ship lengths behind it) and for ships without a transom stern. The formulas exist in the general case, but their calculation requires more computation time, which is not justified in our case. Nevertheless, it is observed that the shape of the waves remains close to the experimentally obtained one. Only the amplitude is somewhat different. However, the obtained heights remain acceptable in terms of order of magnitude, even if they are not rigorously exact.

The second comparison is made in the far field between our results and those reported in a paper by Griffin et al. [85], for a simulation performed with another calculation code using slender ship theory: the FFSW code developed by Keramidas et al. [101]. Figure 3.13 reproduces the results from [85] and shows our results in the same configuration, using the same units to facilitate comparison. It is observed that the general shape of the waves is reproduced (though divergent waves are challenging to observe in Griffin et al.'s published figure, even though they are present). More importantly, good agreement is found in terms of the maximum wave height. Specifically, the maximum height calculated by FFSW is 6.41 feet, while our SWPE implementation yields a height of 6.61 feet, representing a difference on the order of 3

3.3 Conclusions of this chapter

This chapter provided an overview of various phenomena collectively referred to as "wake," while discussing how these phenomena are perceived by a synthetic aperture radar (SAR) system. Two categories of phenomena were defined. On the one hand, there are non-viscous phenomena, resulting in the Kelvin wake, which is deterministic and relatively well-known. The second category corresponds to phenomena originating from turbulence. These phenomena interact with the Kelvin wake in a complex and still poorly understood way, thus generating typical signatures like the "bright V" characteristic of a ship's wake. Finally, wave interactions in the water volume are also responsible for phenomena visible to radar.

The last part of the chapter explained a relatively fast numerical evaluation technique to obtain an elevation map and a velocity field map for the Kelvin wake. This technique was based on the description of the SWPE calculation code proposed by Tuck, Lazauskas, and Scullen [174]. Although the calculation code is published in the form of an executable (*Michlet*), we re-implemented the code ourselves for several reasons: a better understanding of the phenomena, the fact that only an executable is available without the source code, limiting flexibility in use and modification, *etc.* The results obtained with our implementation were compared with some data available in the open literature, showing satisfactory agreement. We limited the implementation to the far field and the case of ships without a transom stern. Leo Lazauskas, in a personal communication, emphasized that these simplifying assumptions cannot ensure, if attempted, correct inversion of the Kochin integral to retrieve hull parameters, and that the complete formulation in the near field is then indispensable[1]. This inversion is indeed a possible perspective of our work, which is also in line with a previous thesis [197], but this point should be taken into account if one wishes to attempt it.

The results of this second part will then be reused in Chapter 5 dedicated to ship wake simulation. The theoretical elevation model will also be important in Chapter 7, dedicated to the detection of the Kelvin wake in a radar image or an optical image.

[1]Email from Leo Lazauskas (December 2007, excerpt): "*There is also a very subtle mathematical matter to do with Fourier inversion of the ship-wave integral that was the subject of much heated debate back in the 1960's and 1970's. (Apparently. I'm old, but not old enough to have been an eye witness!) Mathematically, the correct inverse can only be obtained by including the near-field as well as the far-field. This is probably not a problem for your work, but you should be aware of it if you want to investigate the subtle maths involved in the process*".

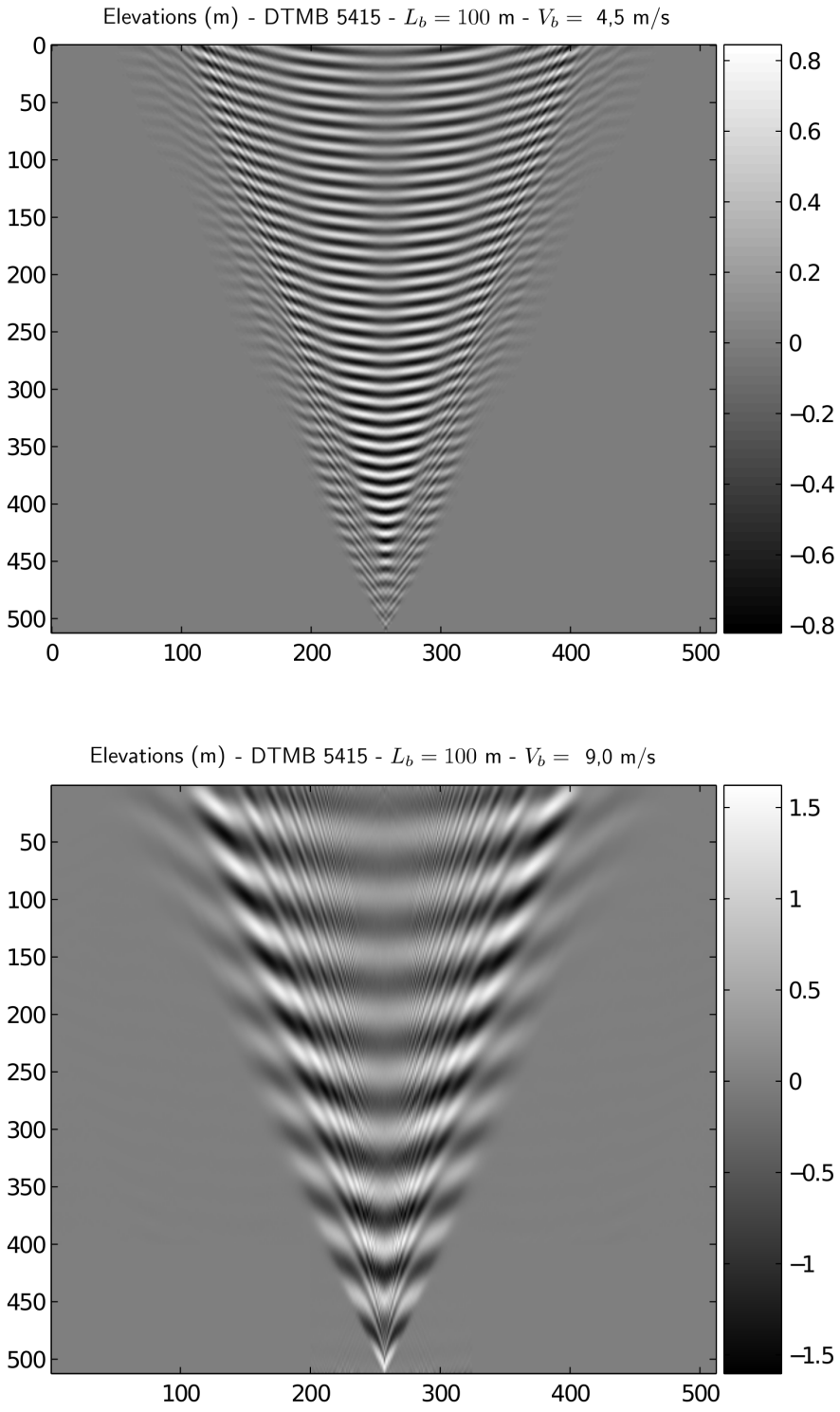

Figure 3.11: *Wake waves generated by the DTMB 5415 hull, scaled to a length of 100 m; the ship speed is 4.5 m/s (8.7 knots, Fr = 0.143) in the first case and 9 m/s (17.5 knots, Fr = 0.287) in the second case.. All dimensions are given in meters.*

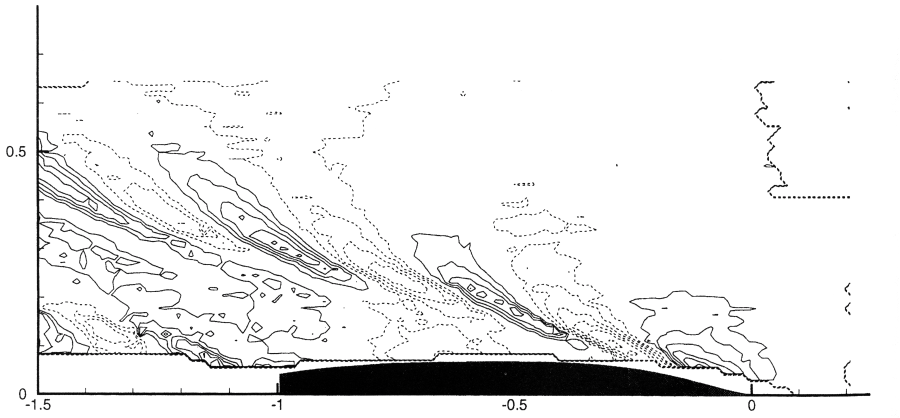

(a) Experimental basin measurements. Dashed lines: negative levels; full lines: positive values.

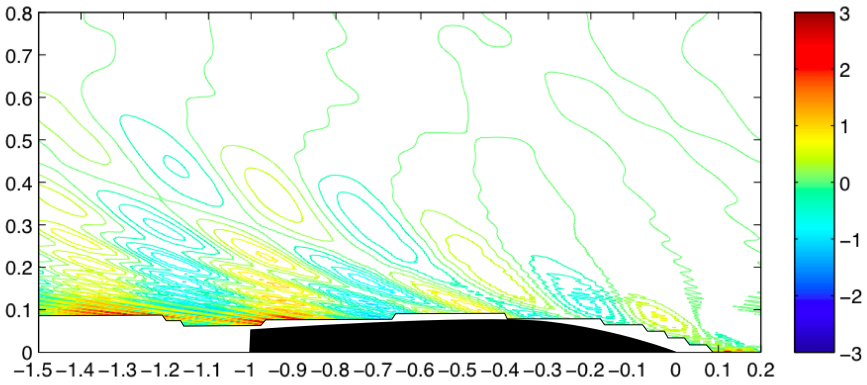

(b) Our SWPE implementation

Figure 3.12: *Comparison between the calculated height map with our SWPE implementation and basin measurements (from [149]) for a DTMB 5415 hull at* $Fr = 0.2755$. *Scale for the* x, y *axis in ship lengths* L_b. *Contour lines:* $0.002L_b$. *Color scale: one unit corresponds to* $0.01L_b$.

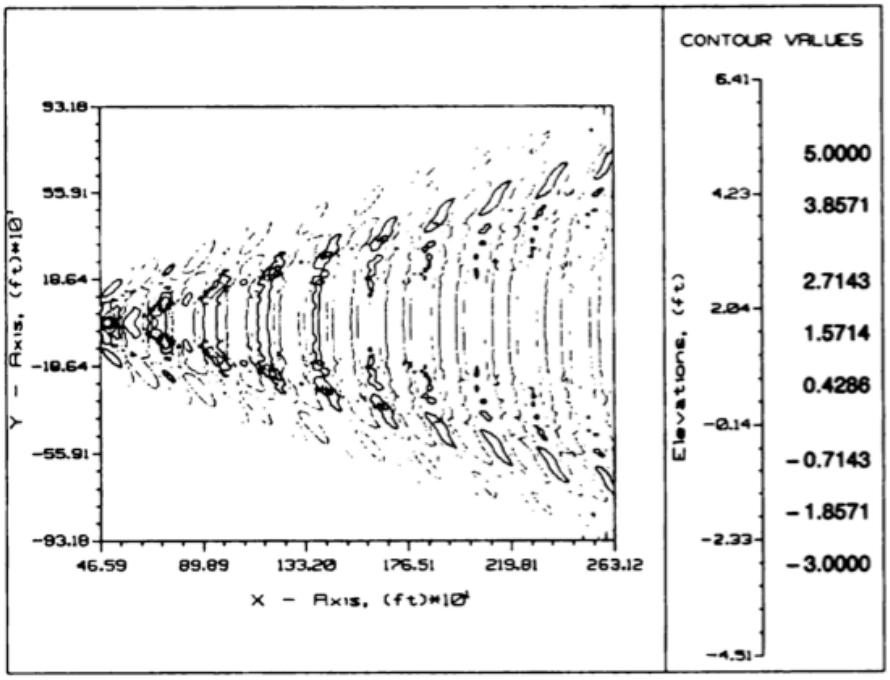

(a) Far-field simulation with the FFSW calculation code [101], according to Griffin *et al.* [85]

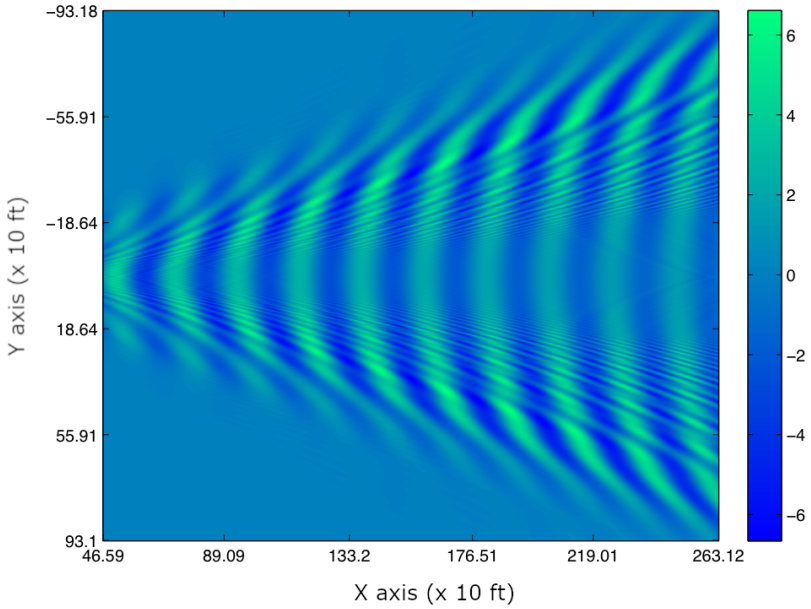

(b) Our SWPE Implementation – heights between -6.66 feet and 6.61 feet

Figure 3.13: *Comparison between the calculated height map with our SWPE implementation and the result of the FFSW far-field wake calculation code (according to [85]) for a DTMB 5415 hull with length L_b = 465.9 feet (142 m) at 20 knots (12.28 m/s). Heights are in feet. The Froude number is identical to that in Figure 3.12.*

Chapter

4 Reflection of Electromagnetic Waves on the Maritime Surface

Contents

Chapter 1 established the radar equation, which governs the link budget between the transmitter, the target, and the receiver. In particular, in Section 1.3 of Chapter 1, we introduced the concept of the *radar cross-section*, which is involved in the calculation of the reflectivity of an object to radio waves. In this chapter, we will further develop these concepts, focusing on the particular case where the object is the sea surface. We consider the power-normalized polarimetric scattering matrix $\mathbf{\Sigma}^0 = [\sigma^0_{pq}]$ for an infinite rough surface. This matrix describes how an incident wave $\mathbf{E}^i$ emitted from a source located at a distance r from a surface is reflected by that surface, forming a reflected wave $\mathbf{E}^s$.

In this chapter, after a brief literature review, we explain the approach taken to calculate the power-normalized polarimetric scattering matrix in the case where the considered surface is the sea. These explanations will be followed by cross-validation with other models and real data published in the literature, particularly in the case of a monostatic configuration.

In general, calculating the power-normalized scattering matrix requires going back to the Maxwell equations, which must be solved, taking into account the boundary conditions specific to the surface. There are methods that numerically integrate these equations: notable examples include the method of moments (one recent implementation, among others, can be found in Soriano and Saillard [161, 162]). These approaches are generally numerically accurate and theoretically tend toward the exact solution of the integral electromagnetic equations derived from Maxwell's equations, but they are slow and memory-intensive. It is also worth noting that these methods work on a deterministic surface, perfectly known; this surface can also be a given and fixed realization of a stochastic process. The major drawback of these methods for our application is the slowness of the calculation, so we will prefer asymptotic, approximate solutions, which are generally faster. In this chapter, we develop several such asymptotic methods suitable for calculating the power-normalized polarimetric scattering matrix for a rough surface, particularly the sea surface. These methods do not require a deterministic sea surface as input but only a statistical description of the surface: spectral density, slope probability density, *etc.* These asymptotic

methods return the average radar cross-section. After a brief literature review, we will focus more specifically on the development of two methods: the Kirchhoff approximation and the Small Perturbations method. Most of this chapter was published in the paper "Bistatic Radar Imaging of the Marine Environment. Part I: theoretical background" [9].

4.1 Obtaining the electromagnetic scattering matrix of an ocean surface

4.1.1 General overview

In general, as explained in Chapter 1, there are two categories of reflection phenomena to consider and simulate: *specular* reflection and *diffuse* reflection [180]. Specular reflection is the way in which an electromagnetic wave reflects off a very smooth surface: at the extreme limit where this surface is perfectly smooth, it behaves like a mirror, hence the name "specular." On the sea, specular reflection is caused by waves of large wavelength. Waves that are not in a specular configuration are also visible but reflect less energy, following a mechanism called "diffuse reflection." On the water, diffuse reflection is caused by ripples, which, having roughly the same wavelength as the incident radio wave, will diffract the wave by making it interfere constructively in the direction of the receiver: this is the *Bragg diffraction* phenomenon, which we will revisit in Section 4.1.3. Figure 4.1 visually illustrates the concepts of specular reflection and diffuse reflection in the case of an optical link over the sea.

(a) Optical image in forward scattering configuration ($\phi_i = \phi_s = 0$).

(b) Paths of light rays: direct path in white, atmospheric diffusion in red, specular reflection on the sea in yellow, diffuse reflection on the sea in gray, non-illuminated areas in black. The image was manually segmented.

Figure 4.1: *Optical vision is a typical case of bistatic configuration. This sunrise behind the island of Porquerolles (Var, France) clearly illustrates the various paths of light from the source to the camera lens and its interactions with the environment (photo by Andreas Arnold, 2008).*

The calculation of the scattering matrix requires taking both phenomena into account. This can be done either by calculating their contributions separately and then attempt-

ing to combine them, or by considering them simultaneously. Before describing the implemented method, we will establish a brief state of the art regarding the methods for evaluating the scattering matrix of waves on rough surfaces. The adopted geometric configuration and notations are described in Figure 4.2.

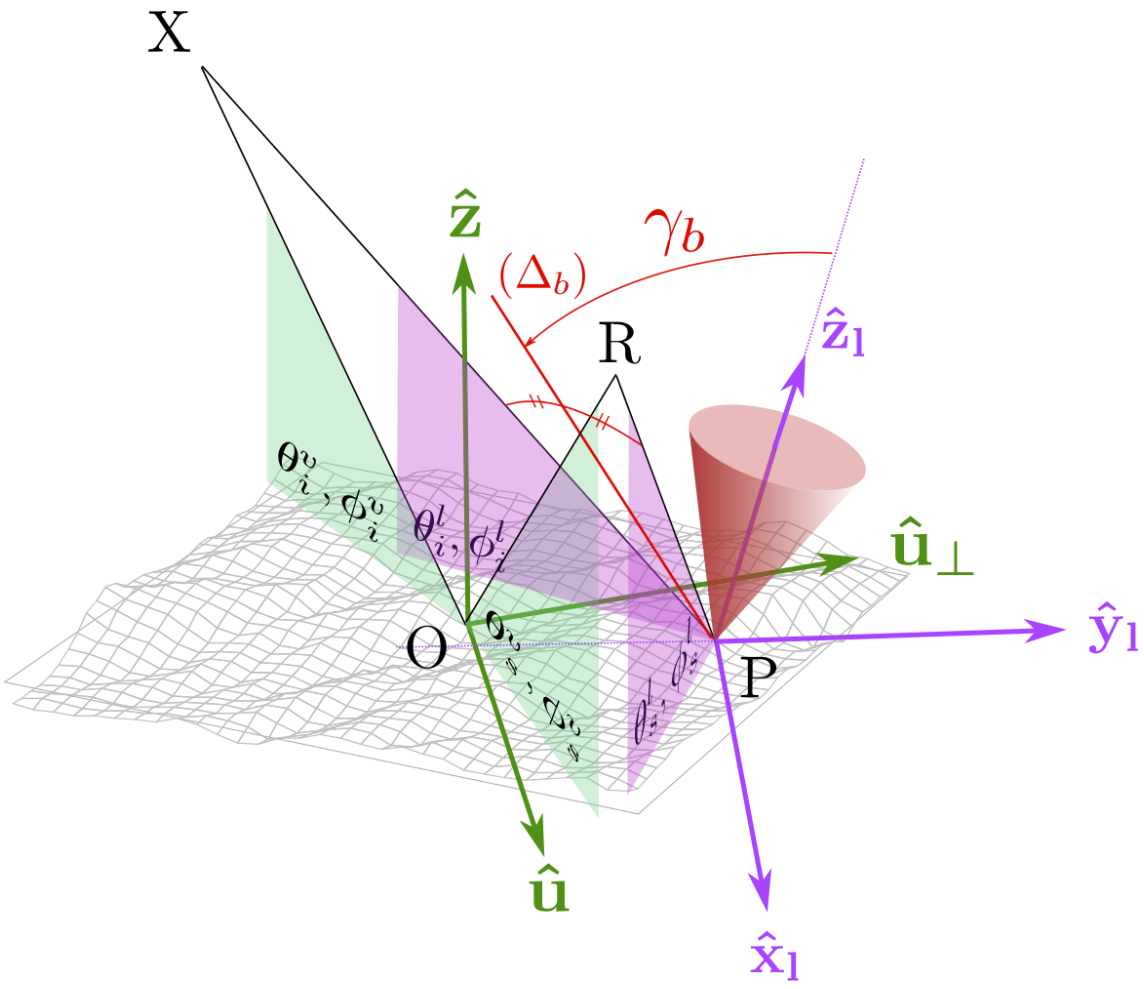

Figure 4.2: *Wind frame $\mathcal{V}$ (in green) versus local frame $\mathcal{L}$. The "wind" frame is defined with respect to the mean sea level and its vertical, and the wind direction, by vectors $\hat{\mathbf{u}}$ (downwind direction), $\hat{\mathbf{u}}_\perp$, $\hat{\mathbf{z}}_g$, and the "global bistatic angles" $(\theta_i^v, \theta_s^v, \phi_i^v, \phi_s^v)$. A "local frame" is defined by vectors $\hat{\mathbf{x}}_l$, $\hat{\mathbf{y}}_l$, $\hat{\mathbf{z}}_l$, and the bistatic angles $(\theta_i, \theta_s, \phi_i, \phi_s)$. The local frame coincides with the wind frame if the facet coincides with the mean sea level. The transmitter is placed at X and the receiver at R. The line (Δ_b) is the bisector of the angle $\widehat{\mathrm{XPR}}$. Inside the red cone, reflection is specular.*

4.1.2 The Kirchhoff approximation

The Kirchhoff Approximation (KA) is a commonly used approach to calculate the contribution of specular reflection. This method was proposed by Brekovskikh in 1952 [31, 32], described in general terms, for example, in the work of Beckmann and Spizzichino [23], Ulaby [177], also in an article by Fung [77], and adapted to the bistatic case by Barrick [21].

The Kirchhoff Approximation involves making a simplifying assumption to facilitate this

evaluation. Specifically, it is assumed that the curvature radius of the sea waves is much larger than the wavelength of the electromagnetic waves, so that the surface can be locally approximated by its tangent plane. For high electromagnetic frequencies, geometric optics approximations can be used. The validity of the Kirchhoff Approximation increases as the working frequency increases and becomes reasonable above the gigahertz range for the water surface. This means that we do not consider frequencies below gigahertz in the scope of the work presented here. In any case, the Kirchhoff approximation amounts to considering that only the specular points on the sea surface will contribute to the reflected signal. One can also work in the framework of physical optics [177]. In this case, surfaces with slightly greater curvature relative to the electromagnetic wavelength are tolerated; however, only the first approach has been implemented in our work, so only that one will be developed.

In the framework of geometric optics, in the far-field, it is observed that the diffusion coefficients are then proportional to the probability of finding such specular points given the transmitter-receiver configuration:

$$\sigma_{pq} = \frac{\pi k_0^2 ||\mathbf{q}||^2}{q_\zeta^4} |U_{mn}|^2 \mathrm{Pr}(Z_u, Z_c) \tag{4.1}$$

where $\mathbf{q} = k_0(\hat{\mathbf{r}}_s^f - \hat{\mathbf{r}}_x)$, a vector whose coordinates in the wind frame $\mathcal{V}$ (defined in Appendix A) are given by the triplet $[q_u, q_c, q_\zeta]$; and $\mathrm{Pr}(Z_u, Z_c)$ is the probability of determining a slope $Z_u = -\partial\zeta/\partial x = -q_u/q_\zeta$ and $Z_c = -\partial\zeta/\partial y = -q_c/q_\zeta$ on the sea surface, in the upwind and crosswind directions, respectively[1]. One can use the probability density of slopes given by Cox and Munk [48], as described in Chapter 2, section 2.2.6. Finally, U_{mn} is a polarimetric coefficient that depends on the bistatic angles $(\theta_i^v, \phi_i^v, \theta_s^v, \phi_s^v)$ determined in the wind frame $\mathcal{V}$ and the Fresnel coefficients [177]. The complete calculation of coefficients in the bistatic case is presented in Appendix C, page 243.

The AK approach is suitable for calculating the average specular contribution of gravity waves on an infinite sea surface. Gravity waves are those satisfying the large curvature radius criterion. It has been found that the method gives good agreement with experimental results when close to the specular direction, *i.e.*, that given by Snell's law; however, it underestimates reflection in other directions. Numerically, the difference begins to be noticeable beyond ±20 degrees from the specular direction.

4.1.3 The Small-Perturbations Method

The Small-Perturbations Method (SPM) is well suited for describing the diffuse component. It was first described for radio waves by Rice [151]. The method is also well developed theoretically in Ishimaru's work [97]. In the case of water, it has been shown that the method is in agreement with experiments conducted in a pool and outdoors [196, 195].

The derivation of the Small-Perturbations Method equations begins with the fact that the total electric field $\mathbf{E}$ in the vicinity of the surface can be written as the sum of the electric field of the incident wave, the electric field of the reflected wave (specular and diffuse), and the transmitted field. A boundary condition is then introduced. In the case where the surface is perfectly conductive, this condition is that the tangential component of the electric field is zero at the surface. This tangential component can be written as:

$$\mathbf{E_t} = \mathbf{E} - (\mathbf{E}.\hat{\mathbf{z}}_l)\hat{\mathbf{z}}_l \tag{4.2}$$

where $\hat{\mathbf{z}}_l$ is the local normal to the surface. This vector $\hat{\mathbf{z}}_l$ is then expressed as a power series of a small quantity ϵ, such as the height of the surface or the local slope. Indeed, for

[1]Here the function ζ is assumed to be given in the wind frame $\mathcal{V}$.

the development to make sense, both quantities must be small, meaning that the surface is almost flat.

This power series, injected into the equation above, also allows expressing the incident, transmitted, and reflected electromagnetic waves as a power series of ϵ. At zero order, the reflected wave simply corresponds to the specular component reflected by a flat surface. The Small-Perturbations Method corresponds, in the literature, to what is obtained by truncating the development at the first order (as in our work), second order (as proposed, for example, by Tsang and Kong [171]), or higher: this introduces a certain amount of diffusion. It goes without saying that the higher the order, the longer the calculation time.

Let's go back to ϵ. Since this quantity is small, it amounts to assuming that the typical height of the waves is also small compared to the wavelength of the electromagnetic waves. If one wishes to work with a maritime surface, it will, therefore, be possible to represent only a somewhat unrealistic sea, composed of capillary waves and otherwise flat on a large scale.

It can then be shown that the waves on the surface contributing to the majority of the reflected radioelectric energy, at the first order of the surface power series, are the waves that diffract the incident waves in such a way that these waves interfere constructively. This is a mechanism called "Bragg scattering", so named by analogy with the phenomenon of the same name discovered in the field of crystallography by Bragg father and son in 1915 (Valenzuela [180]). In the monostatic case, this relationship can be found through simple geometric considerations, as shown in Figure 4.3. Consider a monochromatic surface with a wavelength Λ. Two points P and P$'$ separated by Λ can reflect an incident wave with a wavelength λ_0 arriving at the angle of incidence θ_i if the path difference of the reflected ray at point P and the reflected ray at point P$'$ satisfies the relation:

$$\Lambda = \Lambda' \tag{4.3}$$

where the Bragg wavelength Λ' is defined by:

$$\Lambda' = \frac{n\lambda_0}{2\sin\theta_i} \tag{4.4}$$

where n is a non-zero integer.

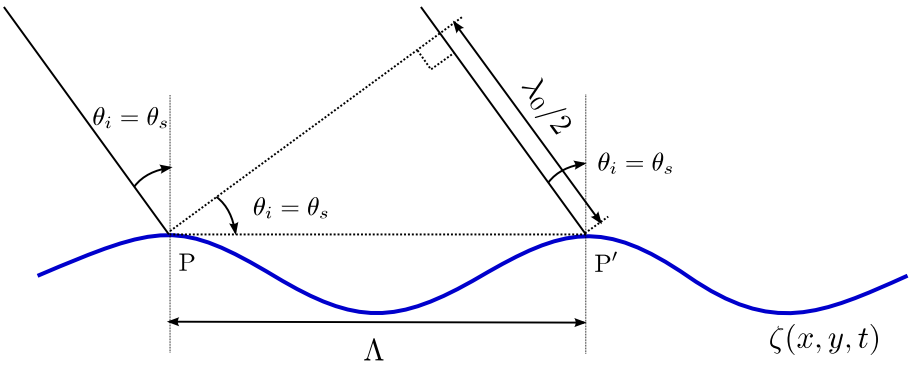

Figure 4.3: *Principle of the calculation of the Bragg configuration criterion in a monostatic configuration ($\theta_i = \theta_s$, $\phi_i = 0$, $\phi_s = \pi$).*

In this case, the amplitude of the reflected electric wave at λ_0 is proportional to the amplitude of the waves with wavelength Λ' as well as the Fresnel coefficients. There is often an abuse of language referring to *Bragg waves* for the waves responsible for Bragg

diffraction in the considered radar configuration. In the bistatic case, the above criterion is generalized. The components of the scattering matrix are given by:

$$\sigma_{mn} = 8k_0^4 \cos^2(\theta_i)\cos^2(\theta_s)|\alpha_{pq}|^2 \mathcal{S}(||\mathbf{K'}||, \angle(\mathbf{K'}, \hat{\mathbf{u}})) \tag{4.5}$$

where α_{pq} is a polarimetric coefficient depending on the bistatic angles and the permittivity of the sea [97, 40], provided in the bistatic case in Appendix C, page 246; and $\hat{\mathbf{u}}$ is the vector defining the wind direction. The wave vector $\mathbf{K'}$ corresponds to the Bragg bistatic configuration, and it is defined as follows:

$$\mathbf{K'} = \begin{bmatrix} k_0 \sin(\theta_s)\cos(\phi_s - \phi_i) - k_0 \sin(\theta_i) \\ k_0 \sin(\theta_s)\sin(\phi_s - \phi_i) \end{bmatrix} \tag{4.6}$$

This relation generalizes Equation 4.4 in the bistatic case. The bistatic angles are taken for a flat average surface; depending on the intended use of the method, either $(\theta_i, \phi_i, \theta_s, \phi_s)$ will be equal to $(\theta_i^v, \phi_s^v, \theta_s^v, \phi_s^v)$ or $(\theta_i^l, \phi_i^l, \theta_s^l, \phi_s^l)$. Numerically, it can be observed that this method is suitable for estimating the diffuse component but is invalid in the specular region, where it diverges and yields values that are much too high in certain configurations. The key takeaway regarding the Bragg diffraction phenomenon modeled by the Small-Perturbations Method, whether in monostatic or bistatic configuration, is that the wavelength order of the waves in the Bragg configuration is the same as that of the electromagnetic wave λ_0. The validity domain of the method is achieved for angles γ_b greater than 20 degrees (roughly outside the specular region) and less than 60 or 70 degrees because beyond that, shadowing phenomena must be considered, and the observed returns are lower than those predicted by the small-perturbation model.

4.1.4 Composite models

4.1.4.1 Two Scales Model

The Two Scales Model (TSM) was proposed later as an evolution of the Small-Perturbations Model (see, for example, Bass and Fuks [22]) and applied to maritime surfaces by Valenzuela [180] or Chan and Fung [38]. The Two Scales Model has been recently extended to both bistatic and maritime surface cases by Khenchaf and Airiau [104, 102]. This model postulates that the sea can be seen as the superposition of two categories of waves: gravity waves with a large radius of curvature and capillary waves. In reality, of course, the transition between gravity waves and capillary waves is continuous, and this assumption is only a first approximation. In fact, there are studies showing that a three-scale model would probably be more appropriate; see, for example, [184]. However, this would complicate the models and make them slower in their evaluation. One argument in favor of the two-scale model is to increase the validity domain of the results compared to the Small-Perturbations Model. The idea behind the Two Scales Model is that the waves contributing to the Bragg diffraction process are locally tilted by the waves with a larger wavelength. The scattering coefficients are then calculated using the SPM approach for all possible combinations of "local" bistatic angles $(\theta_i^l, \theta_s^l, \phi_i^l, \phi_s^l)$. A weighted average of all these coefficients is then performed to obtain the estimate of the sea scattering coefficient. The weighting is obtained through the slope distribution.

Interestingly, the few combinations of local bistatic angles that are rather specular in nature do not corrupt the weighted average because the associated weighting tends to be small. This also means that the Two Scales Model tends to underestimate specular reflection. This problem can be addressed simply by adding coefficients obtained from the AK model [180]. This is the context in which one can speak of a composite model.

4.1.4.2 Other methods

There are other methods that attempt to unify diffuse reflection and specular reflection into a single theory. Elfouhaily and Guérin published a relatively exhaustive categorization of these methods in [64]. One of these methods is the Small-Slope Approximation (SSA), presented by Voronovich. Like the SPM approach, the SSA approach proceeds with a series expansion of the reflected wave and can be written at several orders. Interested readers can refer to (for example) [182] for the first-order approximation (SSA-1) and [183] for the second-order approximation (SSA-2), which is slightly more accurate. SSA-1 has been recently compared to the Two Scales Model in the bistatic case by Awada [15]; the conclusions of this article are that the Two Scales Model gives results close to SSA-1, while being more robust because SSA-1 mathematically degenerates in certain specific bistatic configurations where the Two Scales Model performs well. Additionally, SSA is a slower method to compute than the Two Scales Model. One can assume that SSA at the second order probably gives more accurate results but at a necessarily higher computational cost. In the following, we compare our own results to results obtained with SSA in a monostatic configuration. Other methods have been proposed. For instance, the Extended Boundary Condition Method (EBCM) has been proposed and implemented by Franceschetti et al. [71, 70]; it has been tried, in particular, in the case of the sea by Guo and Wu [87]. These authors have shown that the EBCM approach gives results similar to the methods mentioned above, but it does not make assumptions about a division of the wave spectrum as, for example, the Two Scales Model. However, this method has been tried in the case of a fractal model of the sea surface. The drawback of fractal methods is that there is no simple link between the model parameters and physical parameters such as wind speed and direction. Finally, another composite method called Weighted Curve Approximation has been proposed by Elfouhaily *et al.*, but we will not discuss it here.

4.2 A novel approximation of the scattering matrix using a hybrid Model

4.2.1 Motivation

All the methods mentioned above are approximations, *i.e.*, statistical. The surface is described by its roughness, that is, by quantities such as the standard deviation of surface heights or slopes, the power spectral density, or the probability density of slopes. In the case of the sea, these quantities depend on the speed and direction of the wind. To perform the calculation, bistatic angles are given with respect to the mean sea level: $(\theta_i^v, \theta_s^v, \phi_i^v, \phi_s^v)$, as shown in Figure 4.2. These angles have been referred to as "global" bistatic angles in our work. Once the configuration is defined, the polarimetric scattering coefficients obtained by these methods, which we call "approximate," are an average over an infinite sea surface of the true scattering coefficient (which is actually of a local nature). This average takes into account both gravity waves and capillary waves. The advantage is that the sea does not need to be described locally, meaning that no height map is needed. These approximate methods are therefore particularly well-suited for quickly calculating a link budget. However, they have several major disadvantages. On the one hand, even if the average sea backscattering cross-section (SER) is known, we know nothing about how this SER fluctuates around its mean when the point on the sea where one is located varies. On the other hand, when deterministic and/or local structures are present on the sea surface (*e.g.*, wakes or oil slicks), it is evident that the SER will change at that location. Moreover, the phenomenon of glint is not taken into account by this approach.

To simulate such scenes, a detailed description of the sea taking into account local variations is required. For this purpose, it is more appropriate to use a description by height map and segmentation of the surface into small facets (which allows local variation of surface parameters). This approach is recurrent in the simulation field; the next chapter provides an extended state of the art on this subject. The sea surface is represented as a sheet of triangles, each vertex of the triangle being a point on the sea whose altitude is read from a matrix of dimensions $n \times n$. The triangles have equal ground area, with the value denoted as dS. The sheet is discretized so that gravity waves are well represented, and subpixel-sized structures are considered statistically using an approximate model. The electromagnetic signature of each triangle is then calculated using an approximate diffusion model suitable for low roughness waves (small-perturbations model, SSA, *etc.*), using local bistatic angles at the facet (recall that it is inclined relative to the mean sea level). As these models presuppose an infinite sea, the scattering coefficient is brought back to the surface dS. Thus, we proceed by emulating the two-scales model, using not a probabilistic slope model (for gravity waves) but the specific realization of the sea that was used to build the elevation map.

In simulations using this approach, the focus is often on diffuse reflection [73, 72, 138, 43]. This can be understood, as these articles consider monostatic side-looking radars with intermediate incidences – a classic case for satellite-based radars. In these configurations, diffuse reflection largely dominates. In essence, the approach implemented in these articles consists of emulating the two-scales method. An elevation map of the sea is generated, with the sea surface divided into sufficiently small facets to represent gravity waves. The reflection is then calculated for each facet with the small-perturbations model, bringing the contribution to the surface of this facet, and using local bistatic angles at this facet. The problem is that the way these authors handle the few facets in specular configuration is very unclear from our point of view. In [138] and [43], only diffuse reflection is treated using the small-perturbations model; in [73] and [72], we understand that the same approach has been used. However, in more "exotic" configurations, such as those encountered in bistatic radar, local specular reflections can have a greater influence.

From here on, we will focus on describing in more detail an approach based on facets but taking specular reflections into account. We then compare this method with other numerical approaches and experimental data collected in the literature to validate it.

4.2.2 Description

First, we generate a height map of the sea surface. This map is represented as a matrix of size $n \times n$. The ground projection of the facets represented by this matrix all have a ground area dS. We obtain the scattering coefficients for each point on the surface by calculating the local bistatic angles with respect to the local normals. We then use the AK model and the small perturbations method assuming that the facets are, in fact, of infinite size. We then obtain, for each facet, a scattering matrix Σ_0 (corresponding to this infinite sea), which is multiplied by the surface dS to obtain the actual contribution of the facet.

This approach is somewhat similar to the two-scales method, with one significant difference. Here, as a small sea surface is generated, the proportion of points in specular configuration can be significant enough that the false but very high values given by the SPM approach in these configurations can significantly distort the average contribution of the surfaces. Indeed, the coefficients provided by the SPM approach are sometimes of the same order of magnitude as those provided by the AK model (around +10 dB), sometimes even much higher (+90 dB!). The conclusion is as follows: one can simply add the contribution of the AK model to those provided by the two-scales model, but one cannot add

the contributions of the AK model to those of the small perturbations model.

Therefore, it is necessary to choose only the coefficients of the AK model in nearly specular directions and choose those given by the SPM model in directions corresponding to diffuse reflections. The specular zone is approximately located in a cone with a 20° opening around the local normal $\hat{\mathbf{z}}_l$. More formally, if P is a facet, and γ_b is the angle formed by the bisector of the angle $\widehat{XPR}$ and the local normal to the surface $\hat{\mathbf{z}}_l$ at P, the reflection is specular when γ_b is approximately less than 20° (see Figure 4.2).

That being said, the transition between the specular and diffuse zones must be smooth. Drawing inspiration from the approach proposed at the Applied Physics Laboratory by Jackson to model the reflection of acoustic waves on the seabed [205], we chose to calculate, for each possible configuration, a weighted average of the coefficients obtained by the AK approach and the SPM approach. The weights we used are as follows:

- for co-polarizations:

$$\sigma_{nn} = (1 - w_1)\delta_{\text{SP}}\sigma_{nn,\ \text{SP}} + w_1\delta_{\text{AK}}\sigma_{nn,\ \text{K}} \tag{4.7}$$

- for cross-polarizations:

$$\sigma_{nm} = (1 - w_2)\delta_{\text{SP}}\sigma_{nm,\ \text{SP}} + w_2\delta_{\text{AK}}\sigma_{nm,\ \text{K}} \tag{4.8}$$

with:

$$\log_{10} w_1(\gamma_b) = -\left(\frac{\gamma_b}{6\pi}\right)^8 \tag{4.9}$$

$$\log_{10} w_2(\gamma_b) = -\left(\frac{\gamma_b}{20\pi}\right)^{1.5} \tag{4.10}$$

The weighting functions w_1 and w_2 were chosen semi-empirically. They are polynomial in the logarithmic space, allowing for relatively easy manual adjustment. The selected coefficients were chosen by hand to try to minimize any abrupt changes in the slope of the curves at the specular/diffuse transition. Good results are observed for all combinations of local bistatic angles $(\theta_i^l, \theta_s^l, \phi_i^l, \phi_s^l)$.

Figure 4.4 shows the value of the diffusion coefficients for fixed values of θ_i^l, θ_s^l, ϕ_i^l, and varying ϕ_s. As stated earlier, it is clear that the AK model underestimates diffuse reflection (which occurs here when ϕ_s is between 20 and 160°), compared to the values obtained with the small perturbations model. Conversely, the SPM model does not perform well in the specular zone. The weighted average yields better results.

In equations (4.7) and (4.8), two factors appear: δ_{SP} and δ_{AK}. These are boolean visibility factors. Their meanings are as follows:

- δ_{AK} is a "macroscopic" visibility factor that affects specular reflection. For a given facet, $\delta_{\text{AK}} = 1$ if and only if the facet is visible to both the transmitter and the receiver without being occluded by another facet. This visibility factor is calculated using a standard ray-tracing or Z-buffer procedure.

- Diffuse reflection has a local nature, and the occlusion of one facet by another does not play a significant role. However, it may happen that the inclination of certain facets, in the bistatic configuration, causes the radio wave to "penetrate" the facet to reach the receiver. This behavior is not physical. Only facets such that $\hat{\mathbf{n}}_i^l.\hat{\mathbf{z}}^l < 0$ and $\hat{\mathbf{n}}_s^l.\hat{\mathbf{z}}^l > 0$ can contribute to the diffuse reflection process. This condition is represented by the boolean δ_{SP}, which is a "local" visibility factor.

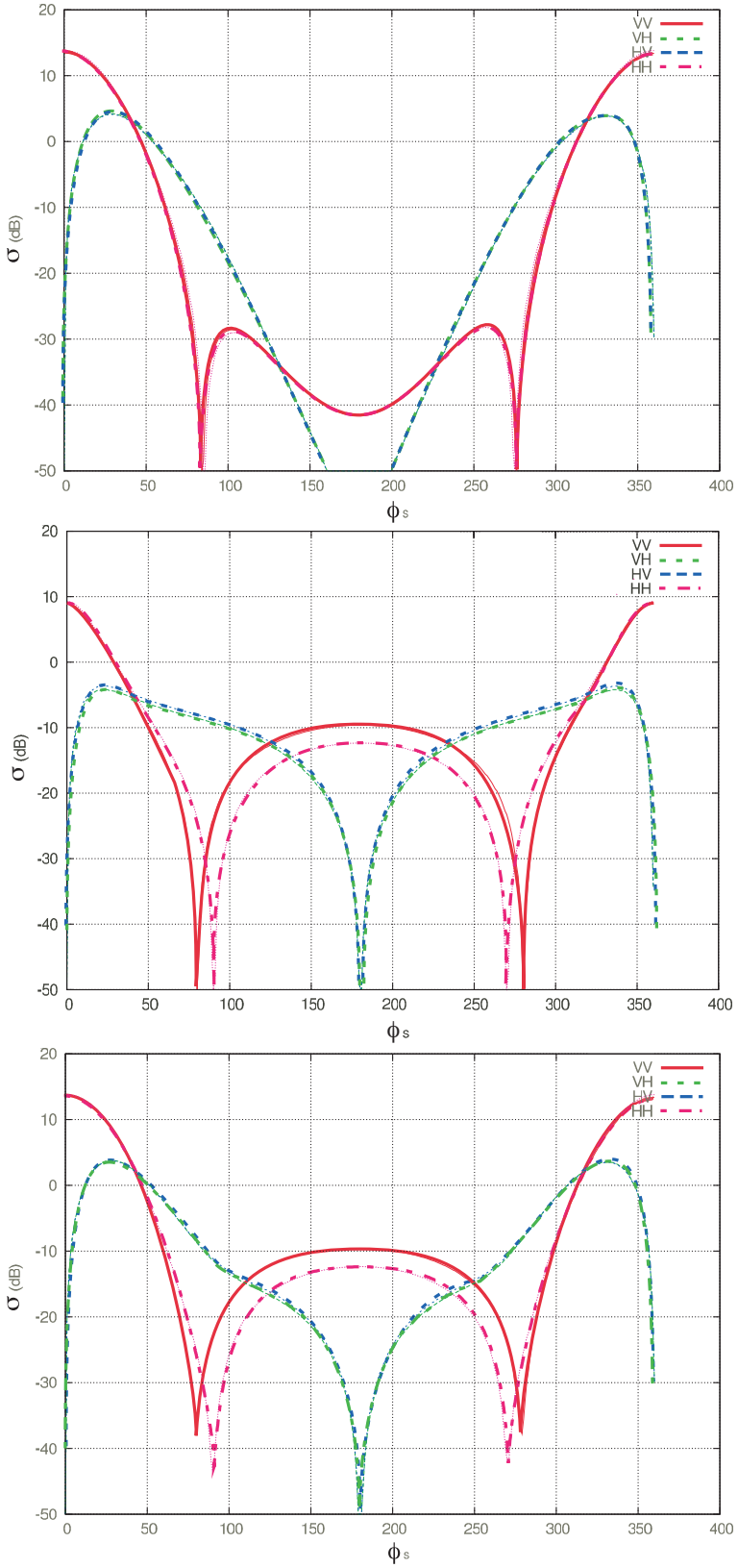

Figure 4.4: *Normalized local reflection coefficients for* $\theta_i^l = 20$, $\theta_s^l = 30$, $\phi_i^l = 0$, *and various* ϕ_s^l. $U_{1950} = 4.53m/s$, f_0=*10 GHz. Top: Kirchhoff approximation, middle: Small Perturbations, bottom: weighted average of AK and SPM by an angle-dependent function* γ_b.

Visibility factors do not play the same role everywhere. When the angles θ_i^v and θ_s^v are not excessive (say below 65), all facets are visible, and the macroscopic visibility factor is 1 everywhere. Therefore, its calculation can be skipped. Conversely, if θ_i^v and θ_s^v are close to 90°, as in coastal radar conditions, then the macroscopic visibility factor is zero everywhere, and its calculation can also be skipped. However, in the critical zone ranging from approximately 65 to 85 for the incidence angle, some facets may be visible, and others may not; in this interval, it is imperative to calculate the macroscopic visibility factor.

4.2.3 Validation

If we place the transmitter and receiver very far from the surface (here, 10^5 m) and average the contribution of facets over a large sea surface, we should intuitively retrieve the results of conventional approximate methods (two-scale method, SSA model, *etc.*). Here, we consider a surface of 512×512 facets with a resolution of one meter (experimentally, the average does not depend much on the discretization step). We find an excellent agreement between our results and those obtained by Voronovich and Zavorotni [183] in an article where they compared the use of SSA-2 with experimental data reproduced here (see Figure 4.5). For graphs established at a wind speed of 15 m/s, we are at a Beaufort sea state equal to 5, just at the limit stated in Chapter 2; nevertheless, we still maintain good agreement between the model and reality. The choice of the sea spectrum may have a small influence on the SER, as seen here. The use of the Fung and Lee spectrum gives lower reflectivity than that of the Elfouhaily spectrum. This can be explained by the fact that the energy of the capillary spectrum is lower in the case of the Fung and Lee spectrum, as noted in Chapter 2. Figure 4.6 shows the dependence of the diffusion coefficient on the wind direction and reproduces experimental measurements published by Moore and Fung [131] under the same conditions. The agreement is less evident but still acceptable, as it is known that the SER can fluctuate rapidly and significantly around its average. Long [121] (Chapter 6, p. 353) reminds us that in the context of radar imaging of the sea, the average radar cross-section of the sea can vary by an amplitude of up to 10 dB within a one-minute interval[2]. Keeping this in mind, one may legitimately wonder if the choice of the spectrum has such a great importance concerning the calculation of the sea SER. However, the spectrum plays a fundamental role in the texture of the surface; it is, in fact, the directional spectrum that plays the most significant role in this aspect. The influence of the wind direction is reflected in Figure 4.6: there is a difference in reflectivity between the *upwind* and *crosswind* directions (0 and 180) since real waves tend to have steeper slopes on the front. The linear superposition model of waves cannot model this, which explains why the electromagnetic model predicts identical returns in both directions.

Finally, our method yields very similar results to those obtained with the two-scale model and SSA-1 under more general bistatic conditions as presented in [15], but we omit them here for brevity.

4.3 Conclusion of this chapter

This chapter presented several methods for calculating the components of the polarimetric scattering matrix (in power). All existing methods have been categorized into three groups: exact methods, approximate methods, and hybrid methods; these methods are compared in Table 4.1.

The last approach was chosen for radar image simulation, as it provides a good compromise between computation speed and representativity of the obtained coefficients. Most

[2]Original quote: *"The 'average' radar cross-section can change as much as 10 dB in a 1-minute interval."*

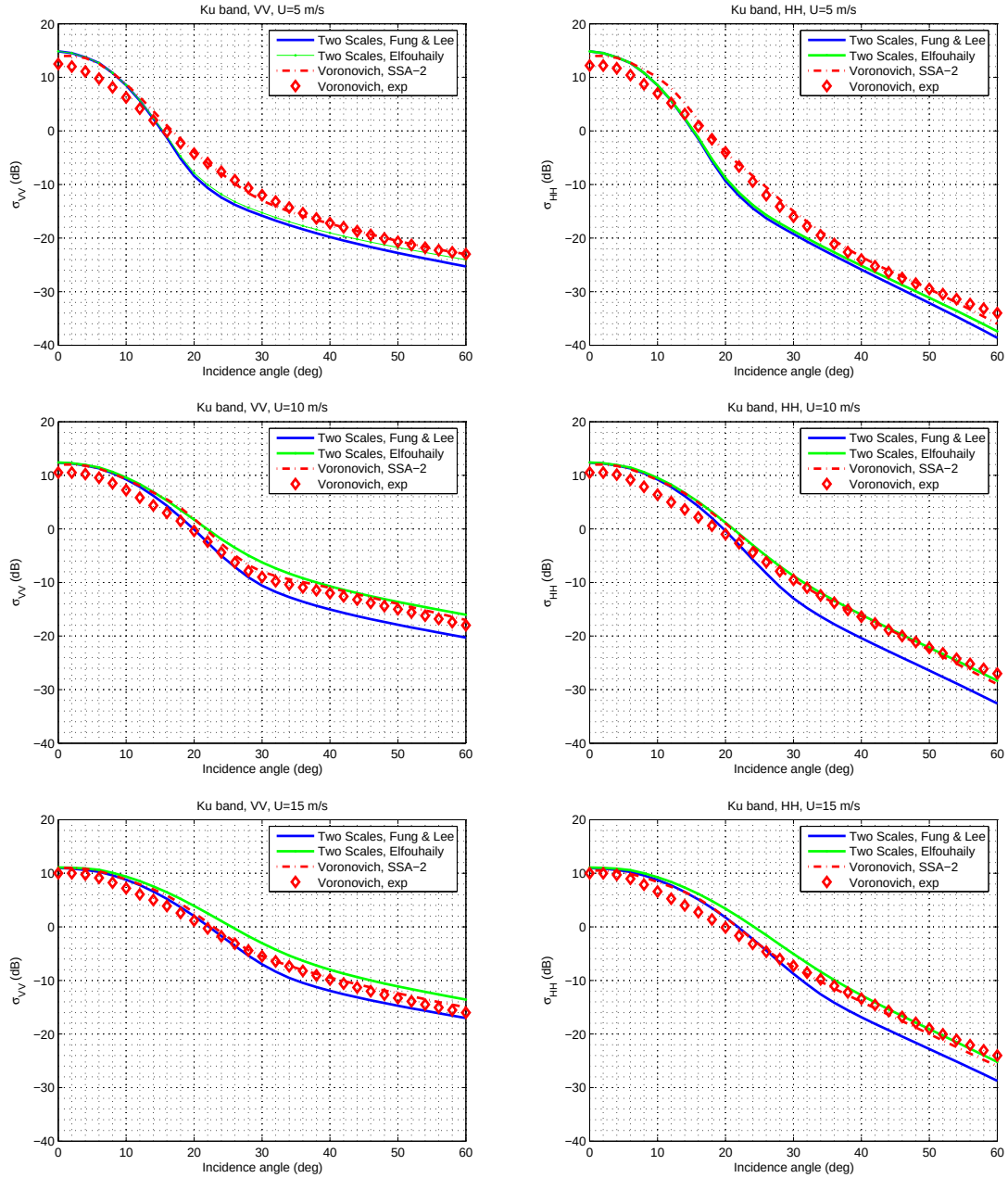

Figure 4.5: *Comparison between the hybrid two-scale method presented here (Fung and Lee spectrum [78] and Elfouhaily spectrum [63]) and SSA-2 (values cited from Voronovich [183]), where the Elfouhaily spectrum was used. Experimental data from the same article [183] are also represented. Wind speed is indicated at $z = 10$ m, and the working frequency is 14 GHz. The left column is in VV polarization, and the right column is in HH polarization. H-TSM: our hybrid two-scale approach.*

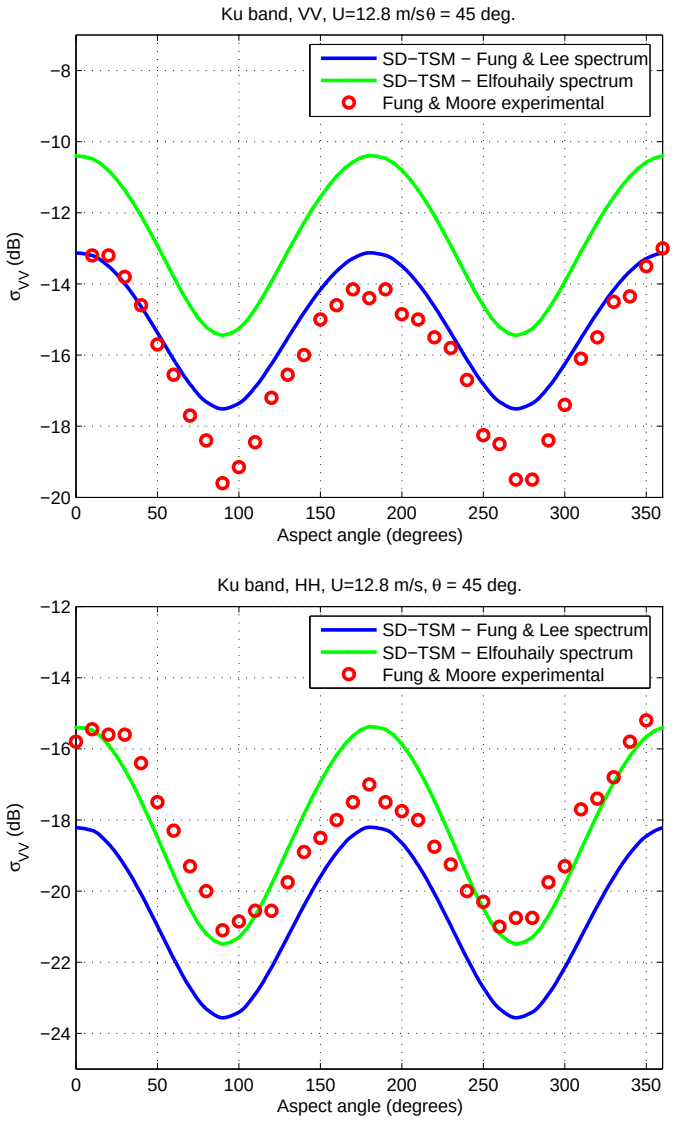

Figure 4.6: *Comparison between our hybrid two-scale method (H-TSM) using the Fung and Lee spectrum [78] or the Elfouhaily spectrum [63] and experimental values published in [131] at 13.9 GHz. Wind speed is given at z =1950 cm. H-TSM: our hybrid two-scale approach.*

Methods	Example methods	Advantages	Disadvantages
Exact	Method of Moments Finite Difference Method	(Quasi-)exact for the surface (deterministic) considered	Very slow Memory-intensive Complex
Approximate (asymptotic)	**Specular reflection**: AK **Diffuse reflection**: SPM, TSM **Composite methods**: SSA, WCA AK+SPM, AK+TSM...	Very fast (AK, SPM) Fast (other methods) Relatively simple	Only average coefficient for an infinite surface
Approximate with large-scale surface deterministic	Weighting AK/SPM in a local coordinate system associated with a facet	Quite fast	Not rigorously exact

Table 4.1: *Comparison of existing methods for calculating the radar cross-section of a rough surface.*

existing radar simulators only use diffuse reflection coefficients, which we demonstrated is not viable in general bistatic configurations. The method we used is based on a facet approach: the diffusion coefficient associated with this facet is the weighted average between the coefficient derived from the Kirchhoff Approximation and the coefficient derived from the Small Perturbation Method, taken in the local frame of the facet. This approach allows us to account for both specular and diffuse reflection. While this method is not new, to our knowledge, no convincing validation has been proposed in the literature. Therefore, we demonstrated that our hybrid approach yields similar results to the small slope approximation and real data when considering the average diffusion coefficient for a large surface. This validation was done in the monostatic case, the only case where data is readily available in the literature.

Chapter

5 Simulation of Bistatic Radar in the Maritime Environment in the Presence of Wakes

Contents

Simulators for radars in maritime environments are already a well-established trend in the literature. These tools are useful for validating radar imaging models. Since writing a simulator requires prior knowledge of the phenomenon's modeling, simulation allows for model validation by comparing results with real data. There are other potential uses for a simulator. For instance, a raw radar data simulator can test beamforming, focusing, and synthetic aperture integration algorithms with perfect knowledge of the scene: a pseudo-ground truth. With such pseudo-truth, one can also test inversion algorithms to retrieve scene parameters (wind speed and direction, wave height maps, *etc.*) and verify the accuracy of the obtained results.

Given the current interest in bistatic radars, there is a need for simulators adapted to such configurations. To our knowledge, while there are numerous simulators for monostatic

radars, none are known for bistatic radar, especially in the maritime environment, except for the work of Wang et al. [185] proposed in 2007. However, these works simulate radar images, not radar signals, as we will distinguish between these two elements shortly.

To develop such a tool, it is essential to understand the theory that models each element of the acquisition chain in the bistatic case. These various elements have been developed in the previous chapters, and we reuse them here to describe the implementation of a bistatic polarimetric radar simulator operating in the maritime environment, including the modeling of the ocean and wakes. This simulator has been named “MaRS” for Marine Radar Simulator. This chapter is structured as follows. First, we provide a state-of-the-art overview of radar image simulation, justifying the choices made. Next, we describe the overall operation of the simulation. Section 5.2 covers in detail aspects related to the terrain elevation map. In particular, considerations about the choice of the scene discretization step are presented in subsection 5.2.5. The last part is dedicated to the analysis of simulation results and algorithmic complexity costs. Most of this chapter served as the basis for the journal paper “Bistatic radar imaging of the marine environment. Part 2: simulations and results analysis” [12] and the conference paper "Investigating Possible Bistatic Configurations For Ship Wake Imaging Through Simulation" [10].

5.1 A brief typology of radar signal simulators

In a very general sense, various categories of simulators can be distinguished (for an initial review and comparison, one can refer to [203]).

5.1.1 Clutter maps

Firstly, there are tools for simulating clutter in a radar image. These are primarily advanced statistical models of speckle noise [6], with the scene generally considered flat. However, since we know that a scene is spatially correlated, there will inevitably be spatial correlation in the speckle noise that needs to be considered and simulated [145]. In the end, a 2D image is obtained, where each pixel is a particular realization of the adopted speckle noise statistic (potentially with spatial correlation ad hoc). These maps are useful, for example, in developing detection and tracking algorithms in a noisy environment, but they are not strictly radar simulators since they only seek to statistically model the appearance of the final image.

5.1.2 Facet-based radar image modeling with a transfer function

Many publications focus on modeling radar images, especially those from side-looking radar, often with synthetic aperture antennas. The images captured by such radars are often of high resolution and cover a large area, making them operationally important for detecting ship wakes, oil slicks resulting from an oil spill, or detecting illegal discharges [150, 113, 46]. Since the goal is to simulate large-area images at a low algorithmic cost, these tools do not necessarily emulate all the steps of the acquisition chain. Here again, various levels of complexity can be adopted. The canonical approach for such simulations was presented by Franceschetti [74]. Here’s what he proposes: first, model the scene as a set of triangular or quadrangular facets. Calculate the reflectivity for each of these facets for the incident angle under which they are located, taking into account shadows and, for more advanced models, multiple reflections. Convolve the reflectivity map with a transfer function modulation that considers the antenna gain (possibly synthetic). Introduce random phase shifts of the wave at the level of each facet to simulate speckle noise. Convolution can be efficiently done in

the frequency domain using the Fourier transform. The case of the marine environment has also been explored by Franceschetti and his team, either for a non-polluted sea [73] or with oil [72].

In the maritime case, the situation is more complicated because the scene, *i.e.*, the water surface, is in motion. However, there is an explicit expression for the transfer function linking the water height function to the "radar image" function, which is not the case with an arbitrary surface [5, 91]. This transfer function is divided into several parts. The first, which dominates, simulates the modulation of the radar cross-section by the variation in wave slopes. The second is used to model non-linear hydrodynamic interactions, while the third, the so-called *velocity bunching* process, only occurs in SAR imaging.

- The *velocity bunching* mechanism exclusively manifests itself in synthetic aperture radar (SAR) imaging: it results in the formation of patterns similar to waves in the radar image even in the absence of reflectivity variation caused by a slope change (this phenomenon is known as *tilt modulation* in the Anglo-Saxon literature). This phenomenon occurs because SAR positions a reflector on the range axis through the Doppler effect, and the orbital motion of particles will modify this positioning. Waves moving in the direction orthogonal to the radar trajectory (in monostatic configuration) will move across the SAR image. As water particles have different orbital velocities, but spatially slightly correlated, these movements will differ, shifting the position of reflectors in a wave-like pattern.

- The non-linear hydrodynamic interaction mechanism is caused by a local variation in the balance of forces acting on capillary waves when they are driven by the movement of gravity waves. In particular, the centrifugal acceleration created by the orbital motion of particles must be taken into account. Since this acceleration does not have the same direction everywhere, it will cause a periodic modulation of the wavelength of capillary waves [4]. This effect is visible in radar (with real or synthetic aperture) because, through modulation, the wavelength of capillary waves may locally correspond to the Bragg wavelength, making the wave very visible to the radar.

Nevertheless, the transfer function approach is very effective in simulation because it links the spectrum of the radar image to simulate to the sea spectrum through a simple Fourier transform, which is very fast to compute. Moreover, the transfer function model raises the hope of model inversion to recover the water height from the radar image. The issue is that, most often, a perfect movement of the radar antenna is considered (a straight line), but atmospheric turbulence can cause the aircraft to move and thus defocus the image. It is challenging to introduce such movements into the "transfer function"-based approach. However, a solution has recently been proposed by Franceschetti and his team for ground imaging with weakly disturbed motion [68, 69].

It is essential to note that, in all cases, this approach is an image radar simulation but not a radar simulator since the lower-level steps (pulse compression, SAR image formation, *etc.*) are not actually performed; only their effects are emulated.

5.1.3 Simplified facet-based approach

In this approach, similar to the previous one, the scene is initially modeled as a set of triangles. The visibility and reflectivity for these triangles are calculated, considering local angles of incidence and possibly secondary reflections. However, it is assumed that we are working at radar resolution, and the antenna's directivity function is a Dirac delta function (no secondary lobes). Additionally, speckle noise is simulated by term-wise multiplication of the reflectivities of different facets, with a specific realization of the speckle noise law

(assuming the multiplicative law). Timo Balz demonstrated in his 2007 thesis [18] that it is now possible to simulate all these steps directly on graphics cards by programming in the shading language of the graphics library used (GLSL for OpenGL, HLSL for DirectX). The graphics card can calculate shadows and reflectivity, and speckle noise law realizations are loaded into the card through an image texture matrix. This approach allows for near real-time simulation of radar images. Balz notably incorporated multiple reflections and bistatic configurations. In a less recent study, Tunaley [176] (1991) addressed ship wakes by considering purely diffuse reflection in the monostatic case on a realistic Kelvin wake and a simulated sea with a Pierson-Moskowitz spectrum. The simulation also accounted for turbulent wakes and *velocity bunching* phenomena resulting from the Doppler effect of the radio wave interacting with water particles in orbital motion. Oumansour [138] conducted a similar study in his thesis, simplifying the Kelvin wake by limiting its contribution to the bow and stern of the boat, not integrating over the entire hull, and assuming the wake is zero outside the Kelvin cone, introducing a discontinuity at the cone's boundary. Additionally, the scene was assumed to be stationary.

5.1.4 Radar signal simulators in the time domain

This category aims to emulate all elements of the acquisition chain explicitly, yielding a "raw" signal as obtained by a real synthetic aperture radar (SAR) after baseband demodulation. This simulated signal can then be processed as if it were acquired by an actual radar. The advantage of such simulation is that the sensor's position can freely evolve over time, allowing, for example, the simulation of the abrupt yaw effect of an aircraft due to turbulence. The periodic transmission of the impulse is simulated, with the impulse shape being a system parameter. The scene is described as a list of facets, and the position of these facets is updated each time an impulse is emitted. For each facet, the radar equation is solved; then, the contribution of each facet (a suitably attenuated, phased, and Doppler-shifted chirp) is added to a buffer representing the received raw signal. This is why it is referred to as a radar signal simulator in the time domain. The major drawback of a raw radar simulator is the computational time cost, which explains why it has only recently gained attention [132]. Nevertheless, these calculations are highly parallelizable, and by utilizing the capabilities of computer clusters, multi-core processors, and adding the power of graphics cards, significant performance gains can be achieved in the context of raw radar signal simulation [100].

In our case, we aim to simulate bistatic configurations, where the transmitter and receiver are not necessarily in the same location. Unlike monostatic radars, bistatic radars can be used in much more diverse configurations. One can imagine a scenario where a coastal radar illuminates a scene, and the receiver is on board an aircraft. Alternatively, the transmitter could be on board a satellite, and the receiver on board an aircraft. Another scenario might involve two aircraft, one with the transmitter and the other with the receiver, flying on parallel trajectories [44]. In fact, the possible configurations are too numerous to be enumerated. This diversity contradicts efficiency. Simulators using an optimized approach based on transfer functions in certain bistatic cases could be envisioned, and this approach was indeed proposed in 2007 by Wang et al. [185]. A radar simulator in the time domain is very general and can handle all possible configurations, additionally providing the ability to test algorithms working on raw signals, which image radar simulators do not allow. Therefore, this is the approach we have adopted. In the end, we demonstrate that it is entirely feasible to simulate acquisitions on well-resolved scenes (on the order of meters in resolution) and sufficiently large (500×500 m) for these pseudo-acquisitions to serve a useful purpose.

5.1.5 General description of the simulation

The main elements interacting in the image formation process are illustrated in Figure 5.1. Note the presence of ship wakes, as they are prominent in SAR images [164, 149]. However, we will not cover the simulation of the radar image of a ship or sea-vessel interactions. The main steps of the simulation are presented in Table 5.1. Next to each step, we indicate the chapters and paragraphs where we discuss the steps in more detail.

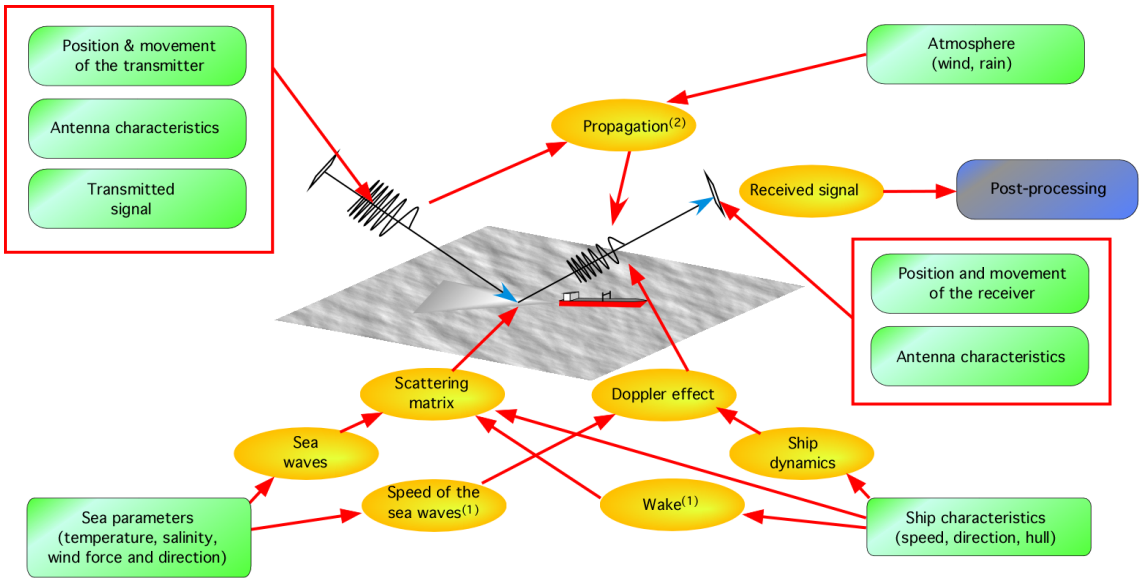

Figure 5.1: *Simulated configuration. Red arrows indicate dependency relationships (some omitted for clarity). (1): partially simulated, nonlinear interactions not considered, first approximation only for turbulent wake; (2) not simulated. Green elements are input parameters, blue elements are outputs, yellow elements are phenomena to be modeled.*

As can be seen, the simulation closely follows the main steps of the acquisition chain as presented in Chapter 1 (sections 1.1 to 1.5), with various modules developed in Chapters 2, 3, and 4. Notably, the elevation map is introduced, a crucial aspect of the simulation as it allows local influence on the scene's representation to incorporate a wake. Introducing a wake requires a map if we want to approach the problem realistically. The antennas are modeled either analytically for canonical apertures (rectangular, circular, elliptical) or numerically by reading from a disk file.

5.2 Generating the height map

Describing the scene as a height map raises several questions, such as *i)* how to generate this surface, *ii)* how to evolve it over time, and *iii)* more crucially, how to choose the discretization steps and the size of the scene, a recurring but rarely addressed question in the literature. This last point is very important because too large a discretization step will yield results that are not representative of reality; on the other hand, a too fine mesh will increase computational costs. We particularly show that the minimum size of the scene evolves as a function of the square of the wind speed.

INITIALIZATION	
· initialize the transmitter and receiver	
· choose discretization steps	paragraph 5.2.5,
· generate the wave height map at $t = 0$	paragraph 5.2.1,
· generate the Kelvin wake height map at $t = 0$	chapter 3
· save maps for future reuse	
SIMULATION	
for each t **from** t_0 **to** t_{fin} **step** 1/PRF**:**	
update wave map	paragraph 5.2.3
translate wake map by interpolation	paragraph 5.2.2
surface map ← wave map + Kelvin wake map	paragraph 5.2.2
change spectrum in turbulent wake zone	paragraph 5.2.2
move transmitter and receiver	
for each facet **of** surface map**:**	
calculate gains & losses,	chapter 1
...especially antenna gains	paragraph 1.2
...and scattering coefficients	chapter 4
calculate propagation time	paragraph 1.5.3
add received signal to reception buffer	paragraph 5.2.4
end for	
save reception buffer to disk	
end for	
POST-PROCESSING (OUTSIDE SIMULATION)	
· Synthetic Aperture Radar (SAR) processing (if desired), detection, *etc.*	

Table 5.1: *Simulation steps in pseudo-code form.*

5.2.1 Sea surface generation

At the beginning of the simulation ($t = 0$), a random surface is generated based on a sea spectrum, as described in Chapter 2. The approach followed is classical and well-established in the literature, at least since Mastin et al. in 1987 [127]. Here's how it works. We know the 2D power spectral density (PSD) of the sea surface (denoted $\mathcal{S}$); it is a function of the 2D wave vector $\mathbf{K}$ and physical parameters like wind speed and direction. A common practice is then to generate a map of wave heights for $t = 0$ by filtering white noise [127, 176, 170]. The algorithm is as follows. First, we generate a matrix $\mathtt{N}$ of size $n \times n$ of complex numbers where the real and imaginary parts are distributed according to a normal distribution with zero mean and unit variance; the size of the matrix is equal to the dimension of the map. We then construct a matrix $\mathtt{S}_{2d}$ containing the values of the spectrum $\mathcal{S}$ for wave wave vectors $\mathbf{K}$, such that the amplitudes of $\mathbf{K}$ range from $-\pi n/L$ to $+\pi n/L$ with a step $\Delta K = 2\pi/L$; L represents the physical width of the surface in meters. The rules for correctly choosing ΔK and n will be discussed in paragraph 5.2.5. Once $\mathtt{S}_{2d}$ is calculated, we multiply its square root term by term by $\mathtt{N}$:

$$\mathtt{Z}_{t=0} = \sqrt{\mathtt{S}_{2d}}\mathtt{N} \tag{5.1}$$

After inverse Fourier transform, we obtain the height map at $t = 0$:

$$\mathtt{z}_{t=0}(x, y) = \kappa_{\mathrm{FFT}} \mathcal{F}^{-1}\left[\mathtt{Z}_{t=0}\right](x, y) \tag{5.2}$$

The constant κ_{FFT} is a normalization factor depending on the implementation of the fast Fourier transform[1]. For example, with the FFTW library [75], $\kappa_{\mathrm{FFT}} = \sqrt{(}\Delta K^{d_{\mathrm{FFT}}})$ where ΔK is the spatial wave number discretization for the sea, and d_{FFT} is the dimension of the transform (for example, $d_{\mathrm{FFT}} = 2$ for a 2D sea). Nonlinearities are left out of the model here, but approaches based on Fourier transform that take into account certain nonlinear phenomena have been proposed, for example, by Toporkov [170] and Saillard et al. [153].

5.2.2 Generating the wake

Kelvin's Wake It is generated following the procedure described in Chapter 3, paragraph 3.2. This calculation provides a map of heights as well as a map of the velocity field of the wake waves. The first is used for reflectivity calculations, and the second is used for Doppler calculations. We work in the linear domain, and therefore the map of the "sea + wake" surfaces is simply obtained by adding the components taken separately; the same goes for the velocity field. If the illumination time is long enough, care should be taken to translate the wake. Rather than regenerating the map, which is time-consuming – between forty seconds and a minute, typically – it is better to reinterpolate the map from known points in a reference Kelvin wake map. This is possible because, as a reminder, the wake is stationary in the ship's frame.

Simulation of Dead Water Wake Since turbulence has the effect of attenuating capillary waves at the back of the ship, it is necessary to decrease the energy put into the capillary part of the spectrum. We used a simple and qualitative way to achieve this by acting as if the wind was blowing less in the area of the map corresponding to the dead water wake. In other words, without changing the height map, we calculated the reflectivity of

[1] Some implementations often multiply the value of the harmonics by the surface in pixels of the signal matrix, which speeds up the calculation; therefore, this additional factor needs to be taken into account, but it is not a general case.

points in the dead water wake in the same way as presented earlier, using the Kirchhoff approximation (for the specular part, with a slope probability corresponding to a smooth sea, such as that provided by Cox and Munk), and the small perturbation model for the diffuse part. It is then assumed that the wake is taking a lower wind speed, for example by halving it, compared to the rest of the map. This approach is certainly only a first approximation, but it is robust and provides visually convincing results, as shown in the simulated radar images provided in Section 5.3. Strictly speaking, it would be necessary to calculate the spectrum more precisely, for example, using one of the energy formulations presented in Chapter 3, in paragraph 3.1.2.1, which still involves integrating a differential equation and redefining a spectrum for every point in the dead water wake. An alternative and much more suitable approach for simulation would be to develop a semi-empirical model of the spectrum in the dead water zone, depending on the wind speed, ship speed, distance to the ship, and possibly surface tension. However, such a spectrum has not yet been published in explicit form in the literature to our knowledge.

Simulation of the bright V-Wake The mechanism of the bright V-wake as described in Chapter 3 has *not* been simulated. Looking ahead a bit to the rest of the chapter, we see that the discretization step of the height map does not go below a meter. Therefore, waves with shorter wavelengths will not be represented by this height map. They will need to be statistically modeled through a spectral approach. For the Kelvin wake, the wavelength of the dominant waves depends on where we are relative to the ship and the median axis of the wake. The bright V-wake is caused by waves at the Bragg frequency (relative to the emitter-receiver configuration), so it would be necessary to find the location of these waves in order to then calculate their height and thus find the reflected intensity. For this, two theoretically possible approaches would be:

1. determine, for each point inside the Kelvin cone, the wave vector corresponding to the Bragg configuration, and look for the amplitude of the Kelvin wake waves associated with that wavelength. For this, it is ideal to have an explicit analytical formula for the wake elevation function ζ_w. Such formulas exist for simple hulls, and expressions can be found, for example, in the case of a Wigley hull or a parabolic hull in Wu [197], p. 83-85.

2. calculate, a priori, what the opening of the bright V-wake is using the generalized relationship 3.12 (page 91) in the bistatic case; then determine the amplitude of the components only on these points.

The drawback of the first method is to be slower than the second; but in return, the second method in a way imposes *a priori* the image that one wants to receive, which eliminates any predictive use of the simulator.

5.2.3 Temporal evolution of the elevation map

Once the map $\mathsf{z}_{t=0}$ is known, the map at any date t can be deduced from $\mathsf{z}_{t=0}$ by element-wise multiplying its Fourier transform $\mathsf{Z}_{t=0}$ by a phase factor $\exp(-j\Omega t)$. Assuming the sea depth is infinite, the temporal pulsation Ω of an individual wave is related to the spatial wave vector's magnitude K by the following dispersion relation ([169], see also Chapter 2, equation 2.40):

$$\Omega^2 = g_0 K \tag{5.3}$$

The table containing the Ω values only needs to be calculated once, as well as the transform $\mathsf{Z}_{t=0}$.

5.2.4 Writing the received signal in the "received signal" buffer. Managing the Doppler effect.

Assuming the pulse is emitted at t_X, the received signal function $E_R(t)$, which for a polarimetric radar is a two-dimensional vector (horizontal channel and vertical channel), is stored in a table $\mathtt{E}_R$. For simplicity, in the rest of the paragraph, we assume that the radar is not polarimetric. The table $\mathtt{E}_R$ is dimensioned to store samples arriving for dates between $t_X + s_{\min}$ and $t_X + s_{\max}$. The chosen discretization step δ_t obeys the Shannon-Nyquist criterion[2], corresponding to the bandwidth of the emitted signal modulation. In fact, we work in baseband, omitting any reference to the carrier frequency outside the Doppler coefficient calculation $\rho_{\text{Doppler}}(t_X)$ as given in Chapter 1 in Section 1.5.3. This significantly reduces the discretization step, saving on the size of the table and speeding up the calculation time. Thus, the i-th entry of $\mathtt{E}_R$ corresponds to the arrival time interval $[s_{\min} + i\delta t, s_{\min} + (i+1)\delta t]$.

The table $\mathtt{E}_R$ is initially filled with zeros. The following work is done for each facet of the scene. For the n-th facet, we perform the link budget, introducing a gain factor K_n, calculate the travel time $\Delta t(t_X)$ between the emitter, the facet, and the receiver for the signal "atom" emitted at the beginning of the pulse (at date t_X), as well as the calculation of $\rho_{\text{Doppler}}(t_X)$. This last calculation requires knowledge of the facet's speed, or more precisely, the orbital speed of water particles within these facets, as it is this speed that causes the Doppler effect (Gelpi and Norris [81]). These orbital speeds can be efficiently calculated by Fourier transform using the relation 2.52 demonstrated in Chapter 2 (for sea alone) or by using the *ad hoc* relation for the Kelvin wake, provided in Chapter 3 (equations 3.17, 3.18, and 3.19). The total speed of the particles is then the sum of the components of the sea-alone waves and the wake waves. To be more rigorous, it would be necessary to take into account the effects of non-linearity of the ocean surface in the calculation of the Doppler frequency. A reasoning in the 1D case taking into account these nonlinearities was proposed by Gelpi and Norris in 2003 [81]. Having all the elements in hand, we now write the signal into $\mathtt{s}$, using the considerations from paragraph 1.5.3.2 of Chapter 1.

5.2.5 Choosing surface sampling steps

Let L be the width of the sea surface we are simulating and n the number of facets per side (for simplicity, we consider only square surfaces). The choice of these parameters is crucial. A large number of facets will increase the simulation duration, and randomly chosen values for L and n can lead to non-physical results. The sampling of the elevation map is directly related to the sampling of the sea spectrum by the relations

$$\Delta K = \frac{2\pi}{L} \tag{5.4}$$

$$K_{\max} = \pi\frac{n}{L} \tag{5.5}$$

where ΔK is the sampling step of spatial wave numbers, and $K_{\max}$ is the maximum wave number represented in the frequency domain: for wave numbers higher than $K_{\max}$, the map is represented statistically and non-deterministically. In this part, we will determine indicative values for the minimal value of L (denoted as $L_{\min}$) and the value of $K_{\max}$.

[2]It is worth noting that since the received signal is complex, the sampling frequency can go down to the maximum frequency of the baseband signal and does not have to be at least twice as high, as is the case for a real signal.

5.2.5.1 Minimal sampling step ΔK of the Spectrum

The low-frequency peak corresponding to the dominant wave frequency extends over a small range of wave numbers. The energy in this range must be sufficiently well "captured" when generating the sea map; otherwise, the resulting elevation map would not correspond to a sufficiently rough sea. There are several possibilities to achieve this:

- Use a fixed step ΔK with an approximation of the power spectral density (PSD) by steps (*i.e.*, when generating the sea, capture the energy of the spectrum by simple rectangle integration). This approach is easy, but the size of the rectangles must be adapted to the spectrum variations, or else a large portion of the energy would be lost.
- Use variable-step integration while keeping rectangle interpolation. Implementing this with a fast Fourier transform is more challenging.
- Use a constant sampling step but allocate, for each frequency interval, the average value of the spectrum in that interval. Numerically integrating the spectrum is required for this. However, if the sea sampling step is too small, it will result in an almost monochromatic sea, which may not be acceptable depending on the simulation goals.

The first solution is often usable if ΔK is chosen carefully, as we will demonstrate. Indeed, in Chapter 2 (paragraph 2.2.4.2), we have shown that most gravity spectra (Pierson, JONSWAP, Elfouhaily) have the form

$$f(K,U) = \frac{a_1/2}{K^3} \exp\left(-\frac{b_1 g_0^2}{K^2 U^4}\right) \tag{5.6}$$

where a_3 and a_4 are scalars whose exact values depend on the considered spectrum. The function f has the following property:

$$\forall a, K, U > 0, f(Ka^2, U) = f(K, aU)/a^6 \tag{5.7}$$

which means that if the wind speed changes, the bandwidth in the logarithmic scale of the spectrum does not change. If the wind speed U is multiplied by a factor a, the logarithmic curve of the spectrum is simply translated along its asymptote at $+\infty$ by a vector with coordinates $[-2\log a; 6\log a]$. This result is a manifestation of the self-similarity theory of the spectrum noticed by Kitaigorodskii [106]. This self-similarity can be observed in Figure 2.12 in Chapter 2. It can also be seen in Figure 5.2, which also shows the notations used here. Suppose we know the -3 dB bandwidth $[K_{\text{-3 dB},1}(U_{\text{ref}}), K_{\text{-3 dB},2}(U_{\text{ref}})]$ for a reference wind speed U_{ref}. A consequence of self-similarity is that we can then deduce the -3 dB bandwidth $[K_{\text{-3 dB},1}(U), K_{\text{-3 dB},2}(U)]$ for any wind speed U:

$$K_{\text{-3 dB},1}(U) = K_{\text{-3 dB},1}(U_{\text{ref}}) \frac{K_p(U)}{K_p(U_{\text{ref}})} \tag{5.8}$$

$$K_{\text{-3 dB},2}(U) = K_{\text{-3 dB},2}(U_{\text{ref}}) \frac{K_p(U)}{K_p(U_{\text{ref}})} \tag{5.9}$$

where $K_p(U)$ is the wave number corresponding to the maximum of the spectrum. To capture the energy contained in the low-frequency peak, the sampling step ΔK can be chosen to be smaller than, say, α percent of the -3 dB bandwidth of the spectrum:

$$\Delta K = \alpha \times (K_{\text{-3 dB},2}(U) - K_{\text{-3 dB},1}(U)) \tag{5.10}$$

Then, using, for example, Equation (5.4) and injecting the value of ΔK given in Equation 5.10, we obtain:

$$L_{\min} = \alpha \frac{2\pi}{K_{\text{-3 dB},2}(U_{\text{ref}}) - K_{\text{-3 dB},1}(U_{\text{ref}})} \left(\frac{U}{U_{\text{ref}}}\right)^2 \tag{5.11}$$

The interpretation of Equation 5.11 is as follows: *the width L_{min} of the surface to be generated follows only a dependence on the wind speed U, and this dependence is quadratic.* In particular, the width $L_{\min}$ does not directly depend on the number of facets n per side of the discretized surface. To get an idea of the order of magnitude of $L_{\min}$, we use the gravity spectrum of Fung and Lee (see paragraph 2.2.4.2.3 in Chapter 2); this choice is explained by the fact that we will also use the capillary spectrum of Fung and Lee a little later. By numerical resolution (zeroing the derivative), we find that the peak of the Fung and Lee spectrum is at:

$$K_p(U) = 0.702 g_0/U^2 \text{ [rad/m]} \tag{5.12}$$

If we arbitrarily take the reference speed U_{ref} at 10.0 m/s, we find numerically:

$$K_{\text{-3 dB},1}(10) = 4.5510^{-2} \text{ rad/m} \tag{5.13}$$

$$K_{\text{-3 dB},2}(10) = 1.2210^{-1} \text{ rad/m} \tag{5.14}$$

Finally, if $\alpha = 25.0\%$ (which is a good compromise), we have:

$$L_{\min} = 3.28U^2 \tag{5.15}$$

This gives values of 82.1, 328, and 739 meters for $L_{\min}$ with wind speeds equal to 5, 10, and 15 m/s (at 19.5 m altitude), respectively. A similar numerical result should be obtained with the other spectra. These dimensions are perfectly acceptable in terms of computation time for most configurations, except perhaps for the highest wind speeds where, in any case, the linear model reaches its limits. It is important to note that these values for $L_{\min}$ are indicative, not mandatory.

5.2.5.2 Maximum wave number $K_{\max}$

The maximum value of the wave number $K_{\max}$ directly influences the facet density, n/L. Ideally, we would like to perform a coherent sum of the contributions from each facet because it would be more rigorous. For this to be possible, the statistically represented structures (capillary waves) must have a typical height H such that the phase difference of the waves reflected by two points on the surface is small compared to 2π. If we use the Rayleigh criterion, we accept a maximum phase difference of $\pi/2$, which means that:

$$H < \frac{\lambda_0}{8\cos\theta_i^g} \tag{5.16}$$

...where θ_i^v is the angle of incidence relative to the mean plane of the surface. We write this relation in the monostatic case because it is not necessary to consider more here. We note $H_{\text{Rayleigh}} = \lambda/8$. Using the definition of the significant wave height, which is one definition among others, the typical height developed by waves with a wave number greater than K is:

$$H_{>K}(K) = 4\sqrt{\int_K^{+\infty} \mathcal{S}_{1\text{d}}(K').dK'} \tag{5.17}$$

It is possible to invert this relation analytically or numerically, that is, to obtain a relation that allows obtaining K from $H_{>K}(K)$ and in particular K_{Rayleigh} from $h(K_{\text{Rayleigh}})$. So,

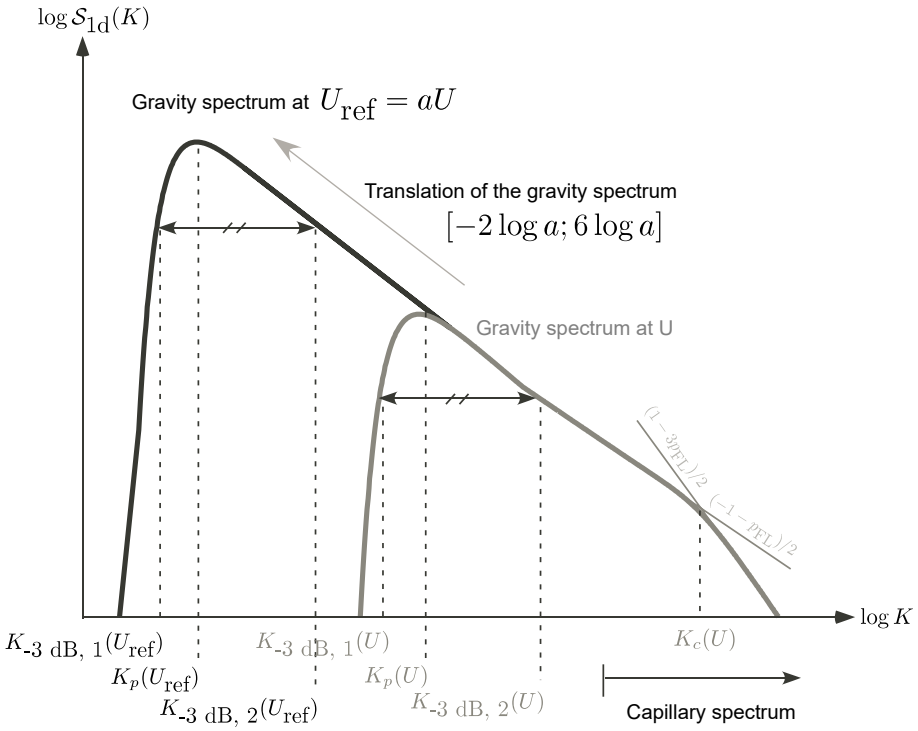

Figure 5.2: *Notations and parameters used in this section for wave numbers. The Fung and Lee spectrum is shown with its asymptotes.*

if waves with a wave number smaller than K_{Rayleigh} are to be represented deterministically in the height map, Equation (5.5) can be used to obtain the facet density in facets/meter.

Here, any spectrum could be used, but since we only need an order of magnitude, we choose an analytical approach with a simple spectrum for capillary waves, namely the Phillips spectrum modified by Fung and Lee (Equation 2.88 in Chapter 2), which we recall here:

$$\mathcal{S}_{1d,\ FL,\ capillarity}(K) \quad = \quad a_0(1+3\bar{K}^2)\left[K(1+\bar{K}^2)\right]^{-(p_{FL}+1)/2} \tag{5.18}$$

where $a_0 = 0.87510^{-4}(2\pi)^{{p_{FL}}^{-1}} g_0^{(1-p_{FL})/2}$, K in radians per meter, $\bar{K} = K/K_m$, $K_m = 363$ [rad/m], and $p_{FL} = 3 - \log_{10}(U_0)$, with U_0 being the wind friction speed in m/s. It is not trivial to integrate this function analytically according to Equation (5.17). However, it is easy to see that in the logarithmic domain, this function is practically piecewise linear. It can be shown that:

$$\mathcal{S}_{1d}(K) \quad \approx \quad a_0 K^{-\frac{p_{FL}+1}{2}} \text{ if } K < K_c \tag{5.19}$$

$$\mathcal{S}_{1d}(K) \quad \approx \quad 3a_0 K_m^{{p_{FL}}^{-1}} K^{\frac{1-3p_{FL}}{2}} \text{ if } K \geq K_c \tag{5.20}$$

where K_c is the wave number where the two approximating straight lines will intersect in the logarithmic domain:

$$K_c = K_m \times 3^{\frac{1}{{p_{FL}}^{-1}}} \tag{5.21}$$

It is much easier to integrate this approximation, and, aside from the difference between

the true spectrum and the approximation (which is negligible), we obtain after integration:

$$H_{>K}(K) = 4\sqrt{\frac{2a_0}{p_{\mathrm{FL}}-1}\left(K^{\frac{1-p_{\mathrm{FL}}}{2}} - \frac{2\sqrt{3}}{9}K_m^{\frac{1-p_{\mathrm{FL}}}{2}}\right)} \text{ if } K < K_c \tag{5.22}$$

$$H_{>K}(K) = 4\sqrt{\frac{2a_0}{p_{\mathrm{FL}}-1}K_m^{p_{\mathrm{FL}}-1}K^{\frac{3}{2}(1-p_{\mathrm{FL}})}} \text{ if } K \geq K_c \tag{5.23}$$

If $K = K_c$, then the height is equal to:

$$H_{>K}(K_c) = 4\sqrt{\frac{2\sqrt{3}}{9}\frac{a_0}{p_{\mathrm{FL}}-1}K_m^{\frac{1-p_{\mathrm{FL}}}{2}}} \tag{5.24}$$

If we equate these expressions to H_{Rayleigh}, we then obtain:

$$K_{\mathrm{Rayleigh}} = \left(\frac{(p_{\mathrm{FL}}-1)H_{\mathrm{Rayleigh}}^2}{32a_0K_m^{p_{\mathrm{FL}}-1}}\right)^{\frac{2}{3(1-p_{\mathrm{FL}})}} \text{ if } H_{\mathrm{Rayleigh}} \leq H_{>K}(K_c) \tag{5.25}$$

$$K_{\mathrm{Rayleigh}} = \left(\frac{(p_{\mathrm{FL}}-1)H_{\mathrm{Rayleigh}}^2}{32a_0} + \frac{2}{9}\sqrt{3}K_m^{\frac{1-p_{\mathrm{FL}}}{2}}\right)^{\frac{2}{1-p_{\mathrm{FL}}}} \text{ otherwise} \tag{5.26}$$

Numerically, we obtain the results given in Figure 5.3, where the Rayleigh height is obtained at zero incidence angle[3]:

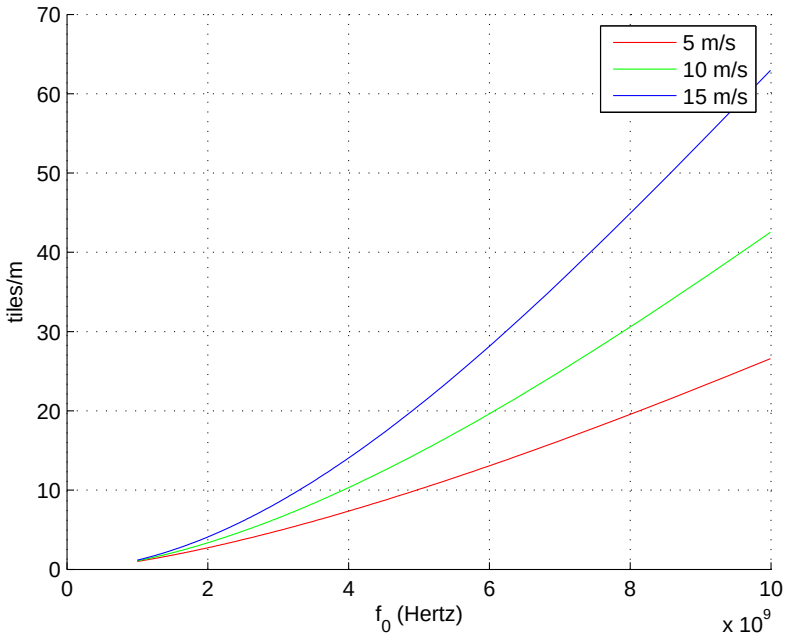

Figure 5.3: *Facet density [facets/m] as a function of the carrier frequency f_0 [Hz] of the radar, such that waves with a wavelength smaller than a facet develop a height lower than $H_{Rayleigh}$, for various wind speeds at 19.5 m altitude. The asymptotic form of the Fung and Lee spectrum [78] is used.*

In the case of sea spectra, it appears that the typical width of a facet such that the Rayleigh criterion is satisfied is of the same order of magnitude as the carrier wavelength.

[3]This is the lower bound of all possible Rayleigh heights with constant wavelength λ_0.

It is therefore highly doubtful that using the small perturbation model on a small facet would give a very physical result (*quid*, for example, of diffraction?), since this method was developed for infinitely large surfaces, or at least very large compared to the electromagnetic wavelength.

For this reason, it is preferable to use lower facet densities and to use incoherent summation. Using the notations of Equation (1.69), the complex amplitude scattering matrix $\mathbf{S}$ is approximated by taking the square root term by term of the power scattering matrix $\mathbf{\Sigma}^0$. Then, since the sum is incoherent, a random phase $\phi(x, y)$, uniformly distributed between 0 and 2π, is added to the signal reflected by the facet at (x, y). Note that the sum is spatially incoherent, but there is necessarily some degree of temporal coherence, at least over short durations, otherwise it would not be possible to perform the integration of the signal in synthetic aperture radar over the sea. In our simulation, we assumed $\phi(x, y)$ to be constant in time since the typical illumination duration of a facet is less than 0.5 s. Nevertheless, $\phi(x, y)$ has no *a priori* reason not to depend on time.

However, one cannot increase the size of the facets arbitrarily. In order to observe the local variation in reflectivity due to the inclination of the waves, the facet density must be higher than the final image resolution (which may eventually result from synthetic aperture integration). This resolution depends on the choice of radar parameters; in the case of synthetic aperture radar, it is the resolution of the synthetic aperture that matters. Furthermore, the facet density will influence the nature of speckle noise: a sufficient number of facets per resolution cell is needed for the speckle noise to begin to develop. It is easy to verify that if the complex signals from six scatterers with the same average amplitude but with random phase are summed, then the amplitude of the resulting signal already follows the Rayleigh distribution. This is a good indicative value for the facet density one should have. Tunaley [176], however, went up to 16 facets per resolution cell.

5.3 Simulations and results

In this section, we will first show some monostatic and bistatic images simulated by MaRS and then integrated into synthetic aperture by the algorithm described in Section 1.7 of Chapter 1. We then compare the speckle noise of the images synthesized by MaRS with models and experimental data obtained in configurations that we have simulated (Section 5.3.2); this comparison allows us to discuss the validity of the appearance of the images from a quantitative point of view. In Section 5.3.3, we qualitatively compare the appearance of the wake in the simulated images with that of some real images gathered from the literature.

5.3.1 Monostatic and bistatic SAR images

5.3.1.1 Configurations

In this section, we present four of the configurations that we have simulated (see Figure 5.4). These are two airborne monostatic configurations, one with an incidence angle of 45 and the other with 63.4; and two bistatic synthetic aperture radar (BiSAR) configurations. The first bistatic configuration is a compromise between the two monostatic configurations mentioned earlier, with two carriers flying in concert on a parallel trajectory. This type of configuration was experimented with during a joint experiment between ONERA and DLR (Deutsches Zentrum für Luft- und Raumfahrt) in 2004 [58], with slightly different radars than those in our simulation and over land only. The second bistatic configuration is a coordination between an airborne radar and a coastal-type radar: the airborne carrier flies in a straight line with a side-looking radar, and the ground radar points in the direction

where the airborne antenna points so that the antenna lobes are always overlapped as best as possible. This latter configuration is at the limits of the validity of the simulation because the reflection at low grazing angles is not modeled rigorously accurately; nevertheless, it will highlight many qualitative aspects.

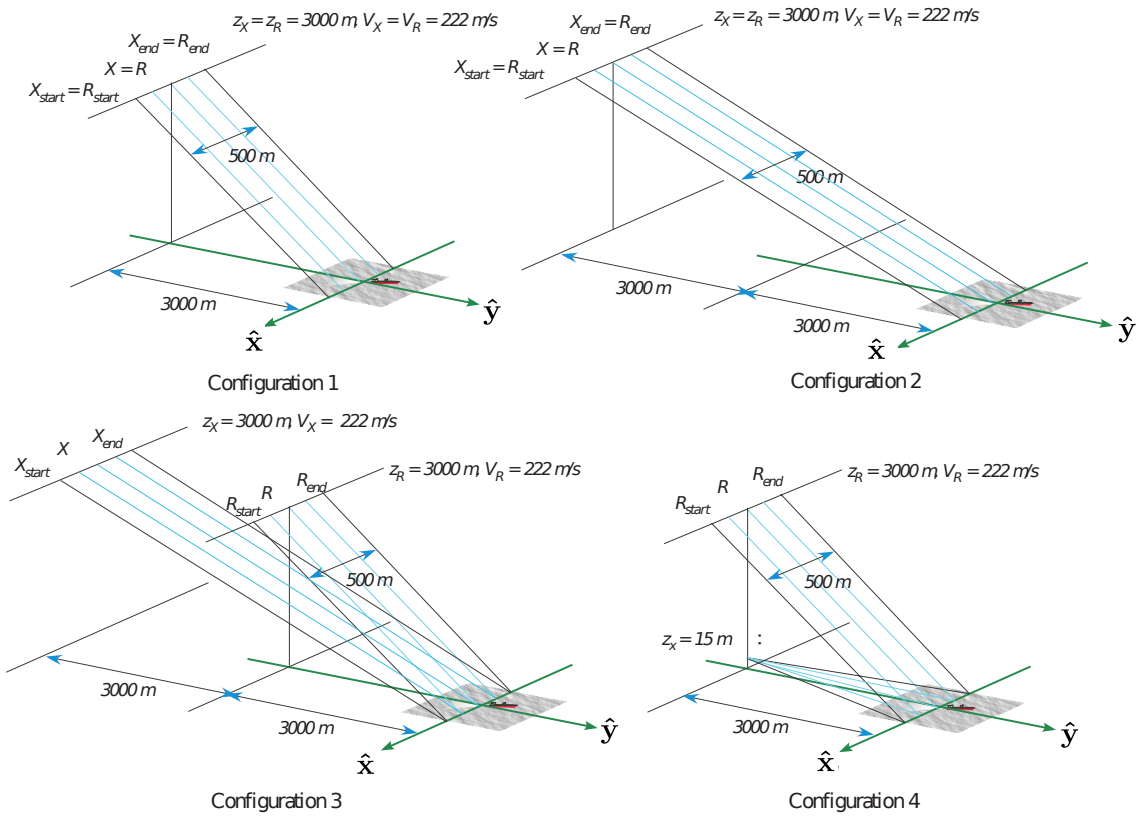

Figure 5.4: *Configurations simulated in this section. 1) Monostatic SAR, $\theta_i = 45$, 2) Monostatic SAR, $\theta_i = 63.4$, 3) "ONERA-DLR"-like Bistatic BiSAR, 4) "airborne-coastal" Bistatic BiSAR*

The characteristics used to simulate the sensors and the environment are summarized in Tables 5.2 and 5.3; it is noted that for the radar, the parameters presented in the first chapter are reused. In this case, the radar characteristics were more or less inspired by the Furuno FAR 28x7 series of coastal radars with the short-range setting (except for the pulse repetition frequency). The wake is created by the hull of a fast destroyer type DTMB 5415 scaled so that its length is one hundred meters; the ship travels at a speed of 4.5 m/s to create clearly visible transverse waves. The elevation map obtained at $t = 0$ is shown in Figure 5.5.

5.3.1.2 Results of the simulation

Figure 5.6 shows the contribution of each facet of the map to the bistatic radar equation as defined in the bistatic radar equation (1.69) of Chapter 1. Since the transmitter has a very low grazing angle, many facets are hidden and do not contribute to the reflection. The superposition of the lobes of the transmitting antenna with the receiving antenna is clearly visible here, as well as the sidelobes, which do not overlap perfectly since the two antennas are separated. Once the signal is obtained, it is transmitted to a post-processing chain to obtain a synthetic aperture integrated image. Given the configuration we have here, a simple Range-Doppler algorithm is sufficient for synthetic aperture integration, as

Variable	Value
True airspeed	$V = 222$ m/s (800 km/h)
Carrier frequency	$f_0 = 10.0$ GHz ($\lambda_0 \approx 3$ cm)
Modulation	$\Delta f = 60$ MHz (linear up-ramp)
PRF	222 Hz
Pulse duration	$T_X = 0.333$ μs
Peak power	1 W
Losses	none
Antennas	rectangular, uniformly illuminated, 4 m $\times$ 5 cm

Table 5.2: *Characteristics of the simulated bistatic radar equipment*

Variable	Value
Temperature	20°C
Salinity	35 ups
Ocean depth	$d = \infty$
Wind speed	$U_0 = 36$ cm/s, $U_{1950} \approx 10$ m/s (5 Beaufort)
Wind direction	$\psi_0 = 30°$
Spectrum:	Elfouhaily, $\Omega_{wa} = 0.84$ (omnidirectional)
	and Fung & Lee (directional)

Table 5.3: *Simulated characteristics for the environment*

we saw in Chapter 1 (Section 1.7.3.3). The integration was done for targets considered as fixed. The histogram of the image intensities was then truncated so that the intensity corresponding to the 98^{th} percentile becomes the new maximum.

The images obtained in the monostatic configurations are shown in Figures 5.7(a) and 5.7(b). The appearance of the wake in these images is compared to real images in Section 5.3.3 in the HH case; as for images in HV and VH polarization, a comparison is impossible: most sensors being co-polarized, images of wakes in cross-polarization are very rare and to our knowledge, not found in the literature. The simulation suggests that excellent contrast can be obtained with images acquired in cross-polarization, but this remains to be compared with real measurements when they become available. Moreover, since the reflectivity in the diffuse region is most significant in VV polarization, this configuration is probably the worst for imaging Kelvin wakes: the returns from the wake waves are lost in those from the rest of the sea, leaving only the reduced reflectivity of the turbulent wake to make it visible in the VV configuration. Judging by other simulations not presented here, we found that these conclusions are generally valid for any configuration (bistatic or monostatic), any carrier frequency, and any sea state.

The image obtained in configuration 3 is shown in Figure 5.8(a) and does not differ too qualitatively from the images obtained in monostatic configurations 1 and 2. In fact, in a sense, configuration 3 is only weakly bistatic since the transmitter and receiver are not very far apart. The received image is therefore a compromise between the two monostatic images and does not provide additional information about the scene. On the other hand, configuration 4 can be considered as being "truly" bistatic. The use of the coastal radar implies that the reflection is completely diffuse (since the angle of incidence is large for the airborne receiver). Unlike configurations 1, 2, and 3, the back of the waves is not visible from the transmitter, making them less reflective. The contrast thus obtained between the front and back of the waves makes them much more visible, regardless of polarization. In

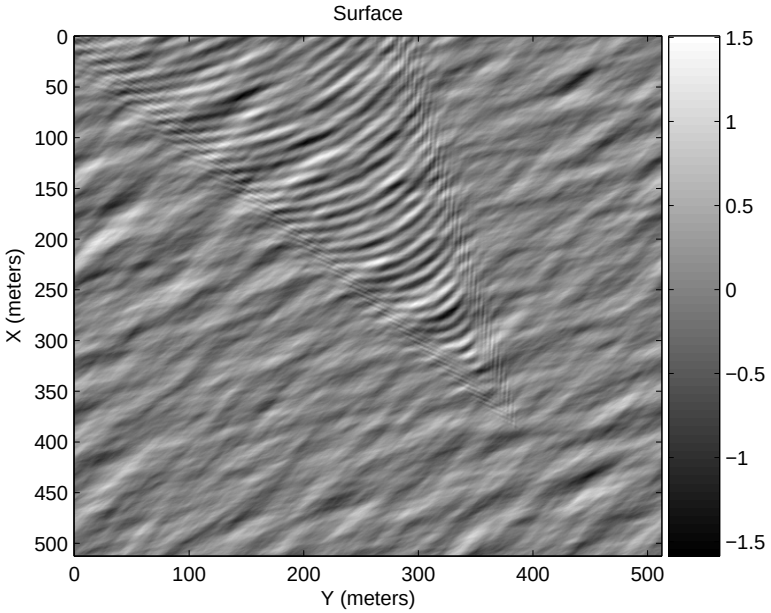

Figure 5.5: *Elevation map (in meters) used in the simulations (512×512 facets with a width of 1 m). The ship has a length of 100 m and a slow speed (4.5 m/s or 8.7 knots). The ship itself is not simulated.*

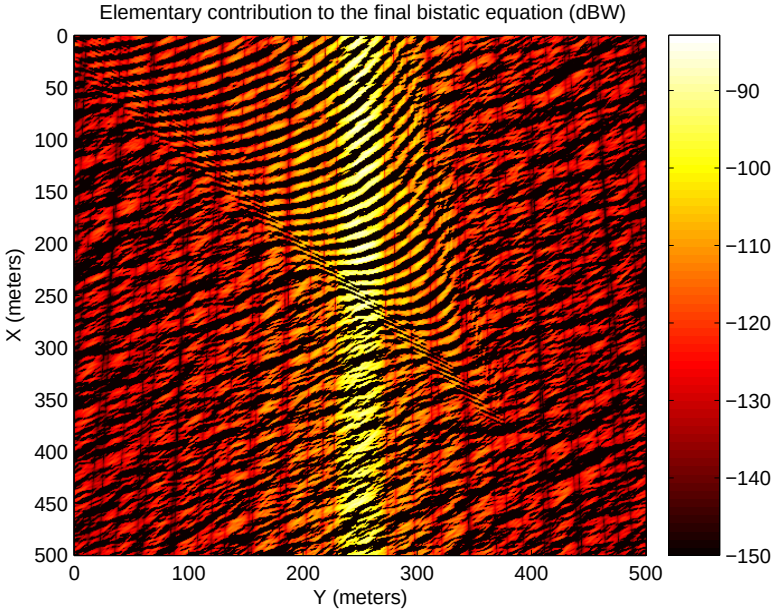

Figure 5.6: *Elementary contribution of the scatterers in the bistatic radar equation (power equation 1.69 of Chapter 1) for configuration 4, when the two antennas are in the same vertical plane. Antenna lobes and hidden facets are clearly visible.*

fact, this fourth configuration shows one of the theoretical advantages of bistatic radar: using an airplane to retrieve the signal allows bistatic synthetic aperture integration and therefore increases the image resolution compared to what would have been obtained with only the coastal radar (about 2.25 m at the center of the image compared to 27.5 m). At the same time, the excellent contrast obtained at low grazing angles is preserved. The drawback is that the antenna of the coastal radar must be slaved to the antenna of the plane, which is a highly non-trivial technological problem that also excludes, at least initially, applications where the plane does not cooperate with the ground receiver.

5.3.2 Analysis of speckle noise

5.3.2.1 Speckle noise distributions

It is interesting to analyze the characteristics of the speckle noise obtained in the simulated images to test the limits of the simulation. Traditional models of speckle noise in marine radar images traditionally include the Rayleigh distribution, the Weibull distribution, and the K distribution [186]; a good review of these models can be found in the reference work by Ward, Tough, and Watts [188], as well as in [6] and [57]. Of these laws, only the Rayleigh and K laws have a "physical" basis. The first results from the coherent sum of waves reflected by a large number of independent scatterers in the same resolution cell, each wave having the same average amplitude as the others but a random phase. The K law results from the composition of a gamma-type law, which reflects low-frequency spatio-temporal variations in reflectivity directly related to gravity waves, and a rapidly varying component modeled by a Rayleigh distribution. This model is particularly well-suited to the marine environment and has therefore received a lot of attention in the community. The probability density distribution of the amplitude z of a pixel under the assumption of the K law is given by:

$$\Pr(z) = \frac{2b}{\Gamma(\nu)} \left(\frac{bz}{2}\right)^{\nu} K_{\nu-1}(bz) \tag{5.27}$$

where b is a scale factor, ν controls the shape of the distribution, and $K_{\nu-1}$ is the modified Bessel function of the second kind of order $\nu - 1$. When ν is large (>10), the law quickly converges to a Rayleigh distribution; when, on the contrary, ν is small (<2), the distribution becomes much sharper, meaning that the image has almost uniform amplitude, except for a few very bright pixels.

5.3.2.2 Comparison with theoretical speckle distributions, at high incidences

To conclude, let's make a very important remark: the model for electromagnetic wave scattering used in the simulator has not been formally validated for high angles of incidence, so we should be cautious about drawing too hasty conclusions. Nevertheless, we will show that the major trends known in the literature are reflected in the simulation.

We calculated the histogram of the amplitude distribution of images in the absence of a wake, and for each reference distribution (Rayleigh, K, or Weibull), we estimated the parameters of that distribution using a 2-d optimization algorithm that seeks to minimize the mean squared difference between the measured histogram and the reference law. Then, we test whether the law is acceptable using the Kolmogorov-Smirnov test. It turned out that the K law was the most appropriate model for modeling speckle noise in simulated images, as it consistently passes the test with an error probability less than 10^{-5}. For each simulation, the shape parameter ν is systematically smaller for HH polarization and larger for VV polarization, meaning that HH radar images are more "spiky" than VV images. This observation is consistent with the literature [6, 57].

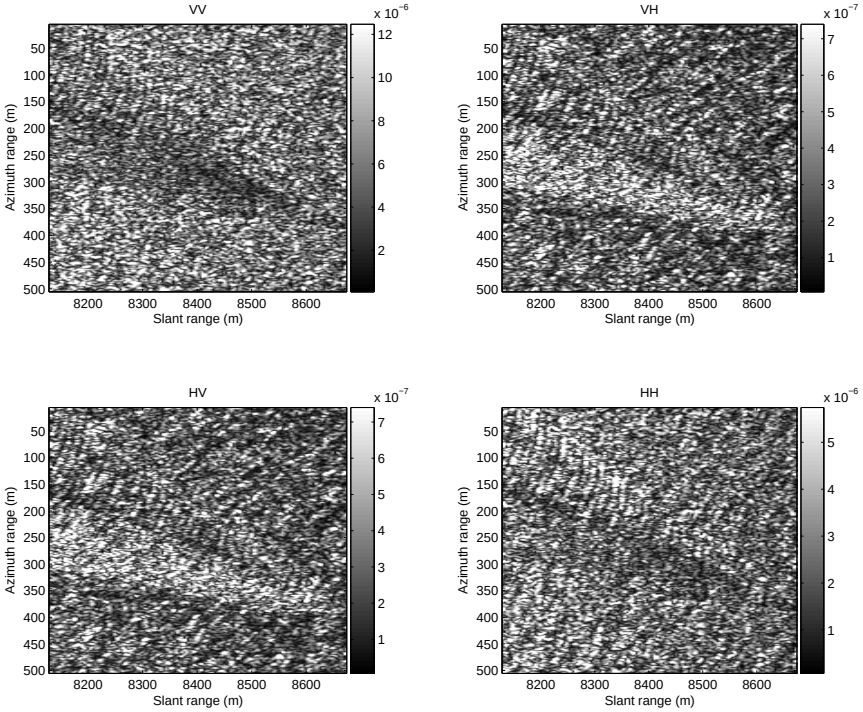

(a) Configuration 1: Monostatic SAR, $\theta_i = 45$

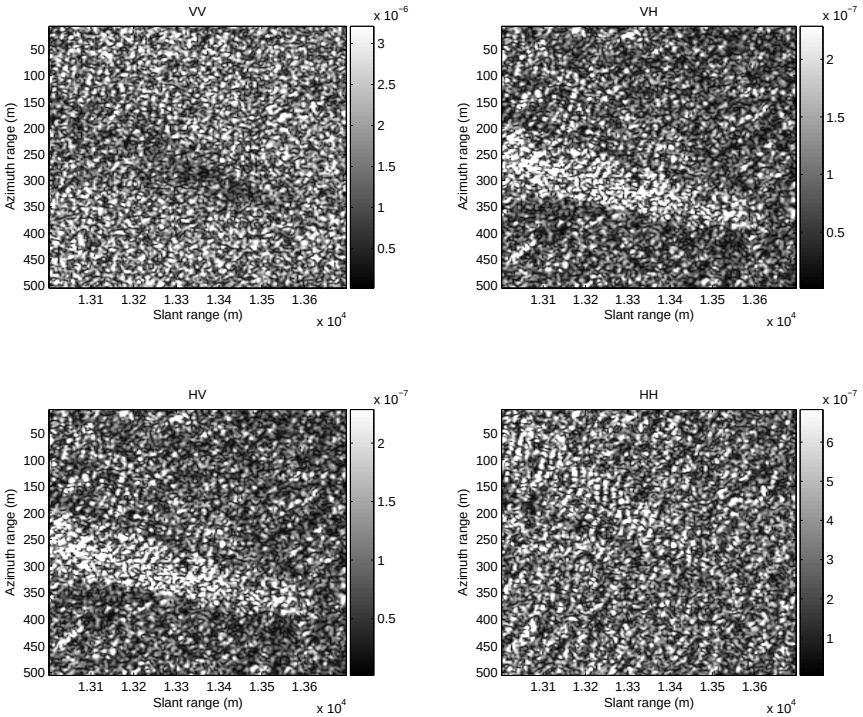

(b) Configuration 2: Monostatic SAR, $\theta_i = 63{,}4$

Figure 5.7: *Simulation results for configurations 1 and 2 defined in Figure 5.4*

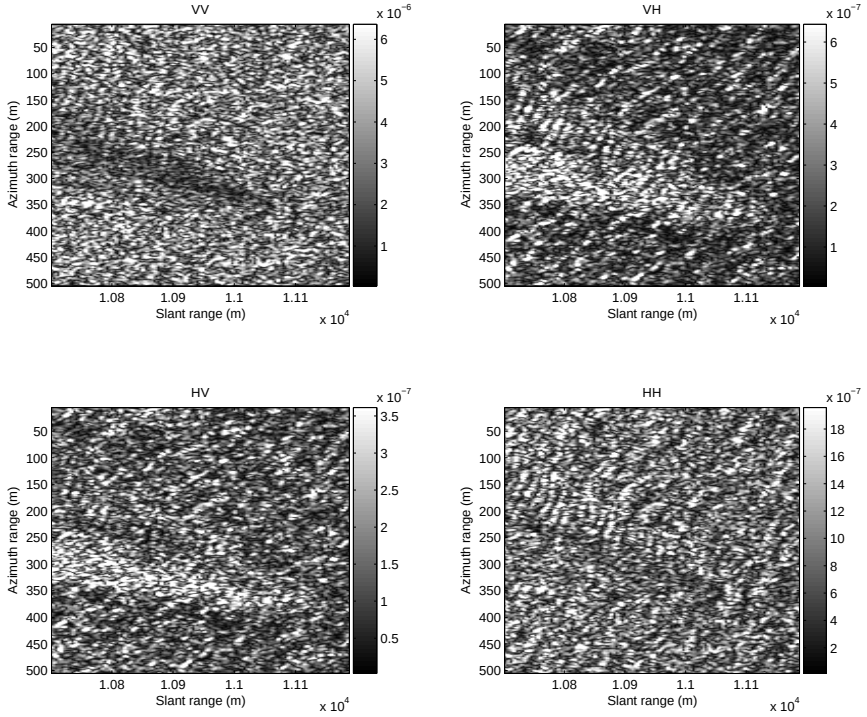

(a) Configuration 3: Bistatic SAR, parallel trajectory of carriers,

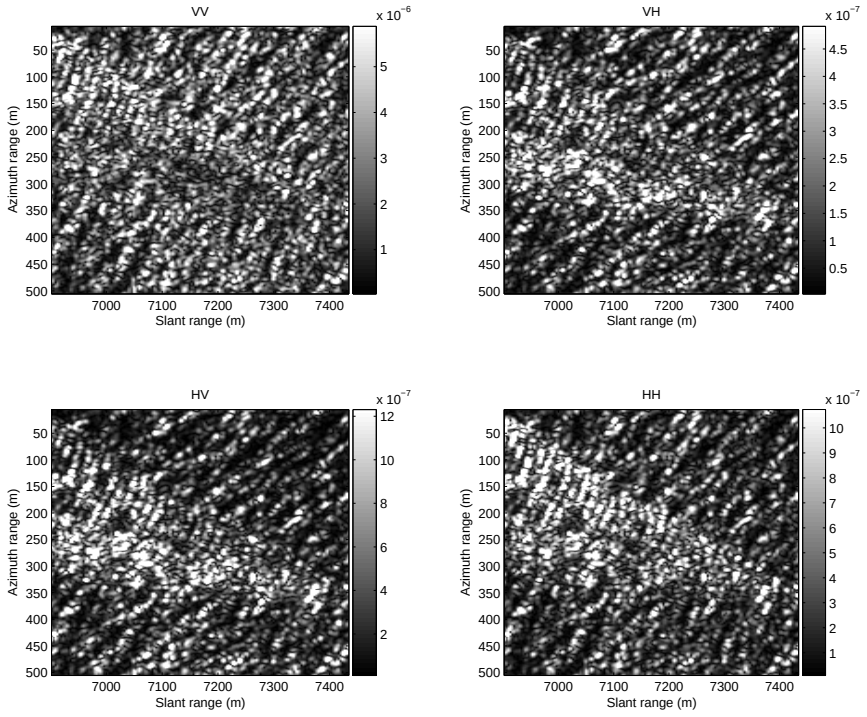

(b) Configuration 4: Bistatic SAR with coastal/airborne antenna cooperation. Note the high contrast and resolution, two advantages of this configuration.

Figure 5.8: *Simulation results for configurations 3 and 4 defined in Figure 5.4*

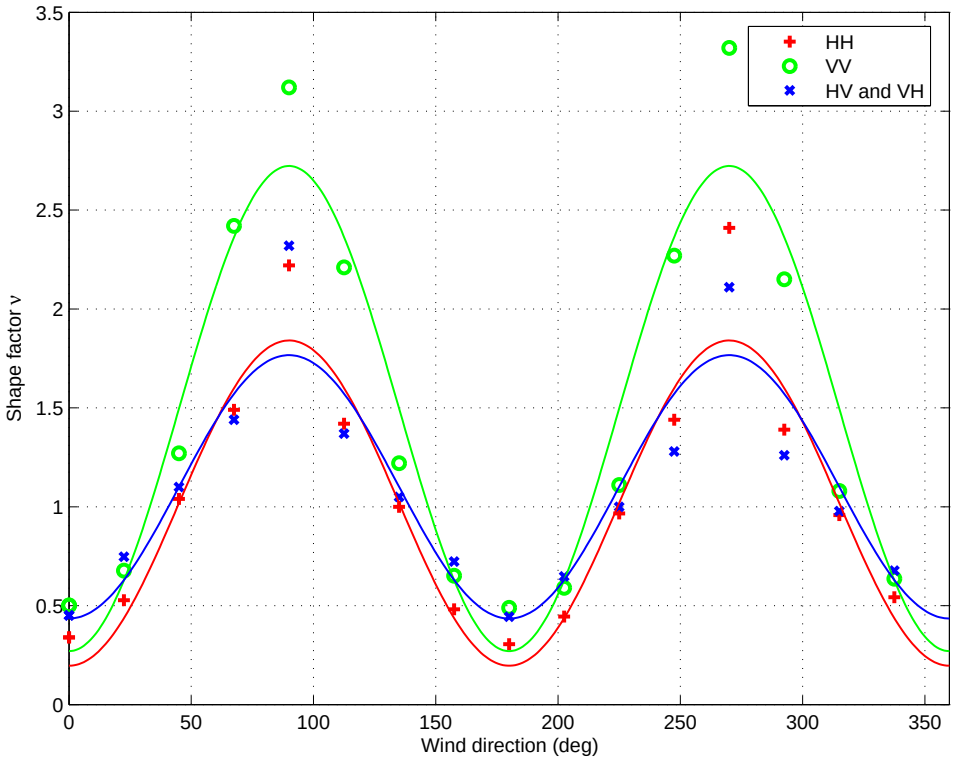

Figure 5.9: *Shape parameter of the K distribution "ν" as a function of wind direction for a grazing angle of one degree (monostatic case). The regression to a cosine curve was done by least squares.*

We show in Figure 5.9 the values of ν calculated for surfaces of 500×1500 pixels (ground resolution of 1 m in azimuth and 0.75 m in range) at 10 GHz, and an incidence angle θ_i^g of 89, which emulates the working conditions of a coastal radar (we use a hypothetical SAR-like configuration here only to have a uniform line of sight over a large surface, which is not the case for a coastal radar that rotates on itself). There is an average of 3.1 facets per resolution cell after synthetic aperture integration, and it has been verified that the results do not change significantly for higher facet densities. The environmental conditions are still those in Table 5.3.

This configuration was chosen to compare our results with the empirical model developed by Ward, Baker, and Watts [187] for monostatic configurations:

$$\log \nu = \frac{2}{3} \log(90 - \theta_i^g) + \frac{5}{8} \log \left(\frac{dr_{\text{az.}} dr}{4.2} - \kappa_m - \kappa_p \right) \tag{5.28}$$

where θ_i^g is the incidence angle in degrees (from 80 to 89.1), dr and $dr_{\text{az.}}$ are the range and azimuthal resolutions (in meters), $\kappa_p = 1$ for VV polarization and 1.7 for HH polarization; κ_m is a wind-dependent term that Watts and Wicks [191] modeled with a sine wave based on their measurements:

$$\kappa_m = \frac{1}{3} \cos(2\psi) \tag{5.29}$$

where ψ is the wind direction relative to the radar line of sight (0 is the downwind direction, 180 is the upwind direction). The average level of ν is slightly higher than predicted by

the model ($\nu = 0{,}0657 \pm 0{,}0423$ in HH, $\nu = 0{,}1324 \pm 0{,}0851$ in VV); this means that the sea clutter is slightly more like a Rayleigh distribution than expected, especially in VV polarization. The difference between the simulation and the experiment is probably due to one of the approximations made in the simulation (linearity of the model, no breaking waves, no foam) or the limit of one of the approaches (poor modeling of reflectivity at the considered incidences, possible challenge to the simulation of speckle noise by the sum of terms with random phase, *etc.*). However, the evolution of the term ν with respect to the wind direction is consistent with the model proposed by Watts and Wicks. It is interesting to relate this evolution to that of the sea reflectivity with the wind direction, as this evolution also follows a sinusoidal law in the linear framework, see, for example, Figure 4.6 in Chapter 4. In general, the wind dependence remains the same for smaller incidence angles, clutter in the VV channel increasingly following a Rayleigh law as the incidence angle decreases.

5.3.2.3 Comparison with real data in the monostatic case – Average Incidences

The behaviors mentioned in the previous paragraph seem to be found also in field experiments. We compared results from an experiment conducted in Australia (Stacy *et al.* [163]). In this experiment, data were acquired with an airborne radar (the Ingara platform) that imaged the sea surface at constant incidence while rotating around the same point. Data were acquired at a resolution of 1 m at a frequency of 10 GHz for several polarizations. Data were acquired over several days, and measured wind speeds varied between 6.1 m/s and 13.2 m/s. Figure 5.10 reproduces results published by Stacy *et al.* (wind speed is not specified in [163], we assume it is approximately 10 m/s).

As before, we simulated a series of synthetic aperture radar images (one image per wind direction) at a meter-scale ground resolution and a carrier frequency of 10 GHz, with wind set at 10 m/s, which is a good average of the observed speeds during the field experiment. The results are shown in Figure 5.11. We also present results obtained for other carrier frequencies.

It is noted that the predicted shape factor at an incidence of 60 degrees is very large and tends to infinity in VV, which means that the simulation predicts a Rayleigh-type clutter at these incidences, while the experiment tends to suggest that the clutter remains more like a K distribution. There is also a discrepancy in the clutter shape in cross-polarization, as its shape factor is generally the lowest in the simulator, while it should be the highest according to the experiments. However, it should be noted that the validation was done with experimental data where the sea state was already very high, enough to question the validity of the models used.

However, we also observe that the relationship between ν and the wind direction is correlated with the reflectivity/wind direction dependence, meaning that reflectivity is highest when looking in the direction from which the wind is coming. In simulations under conditions equivalent to those of Stacy *et al.*, the shape factor for simulations is once again overestimated compared to experimental data, and when ν was too large, it is better to use the Weibull model on these simulated data. However, we still find the dependence of the shape factor on incidence: speckle noise becomes more "Rayleigh" or "Weibull" type as the incidence decreases or the wind speed increases. So, even if the numerical result is slightly different between simulation and reality, we qualitatively find the expected behavior.

Comparing simulation and experiments in bistatic cases is very difficult, as few experimental measurements have been published in the literature. However, some trends can already be seen in the two bistatic configurations mentioned above. In Configuration 3 (BiSAR with parallel trajectories), the speckle noise characteristics are numerically and

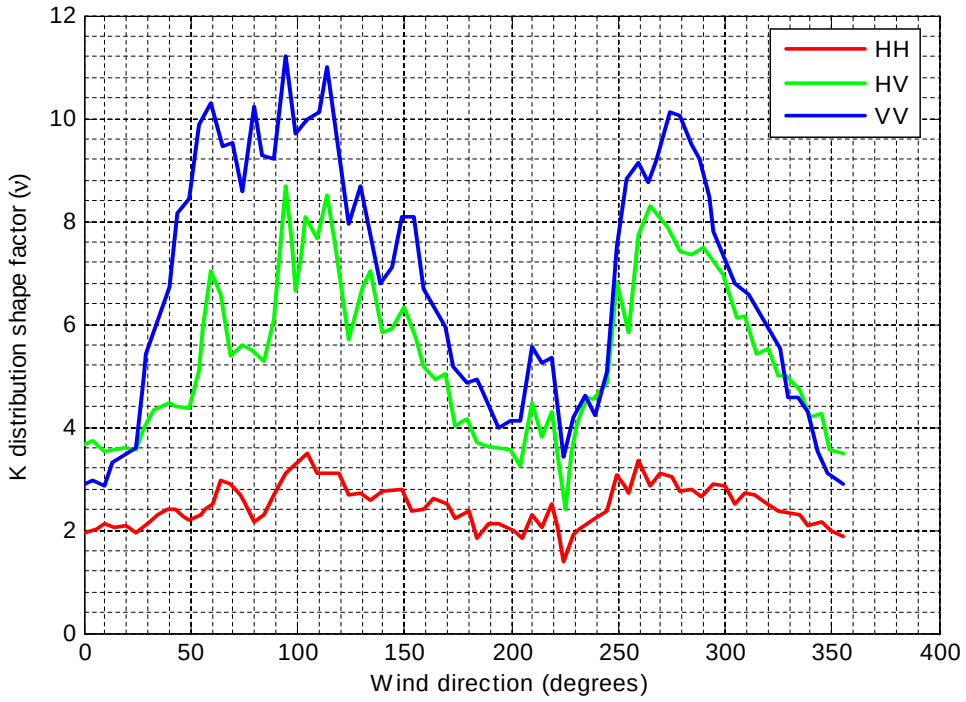

Figure 5.10: *Shape factor of the K distribution obtained during the Stacy* et al. *experiment [163] over the sea (incidences 55 to 65 degrees, f_0 = 10 GHz).*

qualitatively comparable to the results obtained in monostatic Configurations 1 and 2. Configuration 4 (Hybrid Coastal/Airborne BiSAR) has characteristics that are numerically comparable to those obtained with a monostatic coastal radar configuration, which is in line with intuition.

5.3.3 Appearance of the Kelvin wake in simulated radar images

Let's now discuss the appearance of the Kelvin wake in simulated images. For comparison, we refer to data available in the literature, which unfortunately are not widely distributed. The two images in Figure 5.12 are among the few radar images published in the literature where the Kelvin wake is seen in its entirety, showing the system of transverse and divergent waves rather than just the "bright" and "dark" lines typically visible in satellite radar images.

The scarcity of such images is probably explained by several factors. Firstly, it is understandable that, for most ships, visibility of the Kelvin wake requires high resolution, which is currently only available aboard airborne synthetic aperture radars (SARs). See Chapter 7, Section 7.1 for a discussion on these requirements. Unfortunately, data from airborne radars are less widely distributed than data from satellite radars. Satellite radar data, with a recognized role in environmental study and protection, are widely disseminated to many government agencies and research institutes worldwide at a low cost. In contrast, airborne radar data, primarily intended for military applications, are not systematically made available to the scientific public but only during trial campaigns. There is a clear bias in favor of studying wakes in satellite images rather than airborne images [49].

The image in Figure 5.12(a) was acquired during a 1985 trial campaign using an L-band

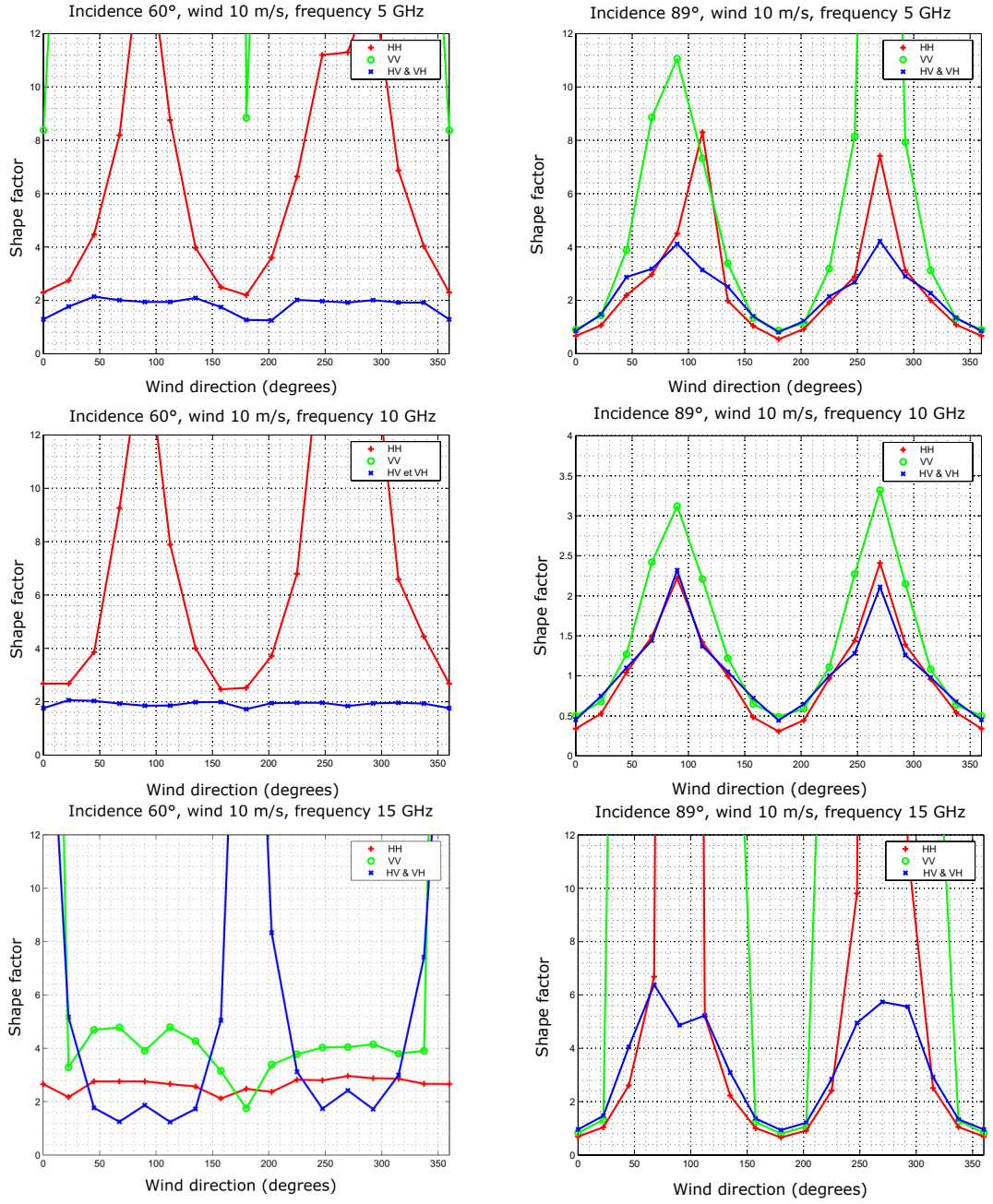

Figure 5.11: *Shape factor of the K distribution obtained with MaRS for different frequencies and several incidences.*

synthetic aperture radar (likely in HH polarization to obtain Seasat-like images). The ship involved was cooperative and well-known, the USS Quapaw, a high-sea tug with a hull length of 59.4 m. At the time of imaging, the ship was operating at 16.5 knots (Fr = 0.352) [149]. The divergent system is clearly visible in this image as an alternation of light and dark lines. The turbulent wake is also clearly visible, forming a dark line dividing the wake into two nearly symmetrical parts. The Kelvin wake is visible in its entirety, with the "canonical" cone of 39 degrees opening.

The second image in Figure 5.12(b) was acquired by the Seasat satellite. It is interesting because it clearly shows a shift between the ship's echo and the Kelvin wake. This phenomenon can occur in synthetic aperture radar images. This image is interesting because it shows that even though the Kelvin wake is fixed in the ship's reference frame, it is not the surface front responsible for the Doppler shift of the radio wave, but each water particle. Indeed, if the surface were the source of the Doppler shift, then the image of the Kelvin wake would be "glued" to the ship's echo because the wake travels at the same speed as the ship in the longitudinal direction. However, this is not the case. Water particles in motion, interacting with the radio wave, move at the orbital speed of the waves, which is significantly slower than the ship's speed. For example, for a ship traveling at 4.5 m/s (or 8.7 knots), the maximum orbital speed of the wake waves is 1.53 m/s. It is evident that this shift can be used as a means of estimating the ship's speed, and this technique is widely used in the literature.

The images obtained through simulation (Figures 5.7(a), 5.7(b), 5.8(a), 5.8(b)) were generated in the X-band. Simulated images in the L-band, which are not presented here, share a significant resemblance in appearance with the simulated X-band images; hence, we have excluded them. One might argue that simulated images in HH polarization bear a resemblance to the images in Figure 5.12, but the reverse is also plausible. Here, the absence of real data is acutely felt, preventing definitive conclusions due to insufficient data for statistical observations.

5.4 Implementing the simulator

The question of the simulator's implementation is, strictly speaking, beyond the diagram presented in Figure 5.1 at the beginning of this chapter. Nevertheless, delving into it is interesting as various considerations, such as computational speed, influence the choice of a simulation method similar to what we have developed. In this section, we discuss potential future directions for creating a simulator akin to MaRS with an even more efficient implementation.

5.4.1 Implementation constraints and architecture

Computational time is a significant concern when designing a simulator, and there is typically a trade-off between computation time and the accuracy of models used. To optimize performance, the primary functions of MaRS have been coded in C++. However, they are invoked by a scripting language (a Lua language interpreter is included in the software). Using a scripting language imparts crucial modularity to MaRS, facilitating the writing of unit tests and regression tests. Additionally, simulation parameter files are directly scripted in Lua and dynamically loaded by the interpreter, offering a considerable advantage in terms of time efficiency.

The notable modularity of the MaRS implementation is worth emphasizing. The application accommodates various spectra, surface characteristics (permittivity, roughness, *etc.*), and scattering matrix calculation models. MaRS fully utilizes the object-oriented

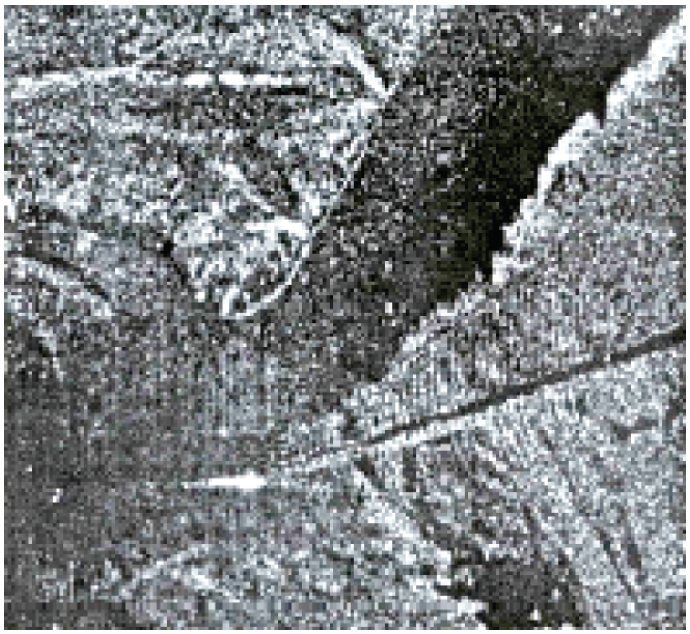

(a) Image 1, from Lyden *et al.* [123].

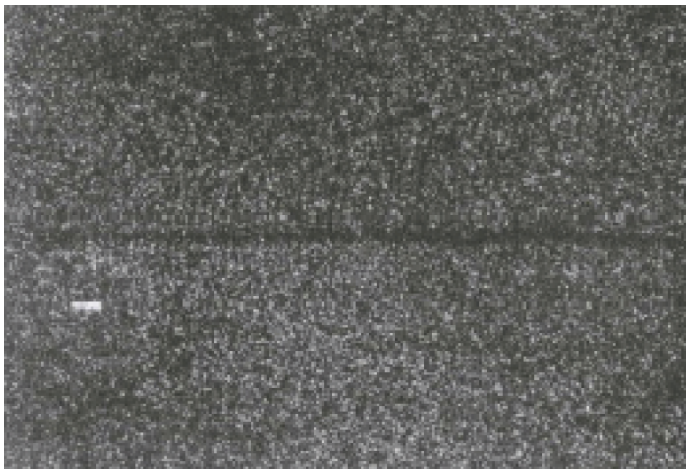

(b) Image 2, from Case *et al.*, [36]

Figure 5.12: *Kelvin wake images seen in high-resolution synthetic aperture radar..*

approach provided by the C++ language: the surface designated for simulation is divided into facets, with each facet associated with an abstract class for reflectivity calculation. Implementations of these classes are provided for various models (Kirchhoff's Approximation, Small Perturbation methods, weighted average of the two previous approaches). This allows the immediate use of different models for each facet, meaning that, for example, within the wake, a different electromagnetic calculation model could be applied compared to the rest of the sea. The same flexibility applies to surface properties (roughness, permittivity, salinity, temperature, *etc.*), which can also vary from one facet to another. Other types of simulations beyond those envisioned here can be imagined, such as locally polluted maritime surfaces with oil, provided the appropriate models and permittivities are available (see, for example, [16] for such models). In any case, this object-oriented approach combined with the use of a scripting language makes the simulator highly adaptable to various applications.

5.4.2 Portability

The code is portable to all environments compatible with the POSIX standard. It has been successfully tested on Windows 2000 and XP (using the Cygwin environment), GNU/Linux (ENSIETA computing cluster), DEC ULTRIX (IFREMER's "*Nymphéa*[4]" computing cluster), and MacOS X.

5.4.3 Computational time considerations

The computation times are well below what was initially envisioned at the project's outset, although they are not negligible. In this paragraph, we first aim to determine the theoretical algorithmic complexity of various calculation steps and then provide the observed computation times in practice. We then discuss potential avenues for improvement.

5.4.3.1 Theoretical algorithmic complexity and practical results

For a typical session, the following steps are executed. Firstly, we generate a surface map for a matrix of n facets; the complexity of the calculation is theoretically dominated by that of the fast Fourier transform, which is $\mathcal{O}(n \log n)$. However, it turned out that the hidden constant behind the n calls to the function calculating the spectrum also plays a significant role in practice. We then calculate an elevation map for the wake following the procedure described in Chapter 3. Reusing the notations from this chapter, the internal integrals P and Q of the elevation function (equation 3.21 from Chapter 3) are precalculated on the ship's hull, which is discretized into $N_x \times N_z$ points. The integrals are calculated for N_θ values of θ between 0 and $\pi/2.0$. Then the elevation is evaluated for the n facets of the map. This process is essentially $\mathcal{O}(N_\theta)$ and remains quite fast (approximately 40s to 45s). The elevation map of the wake is calculated only once since it is static relative to its origin. However, it will need to be reinterpolated to simulate the ship's movement in the world reference frame, which is also a linear process. Finally, as many impulses as necessary are emitted on the surface. For each of the m emitted impulses, the contribution of the n facets must be calculated. This is typically the step that requires significant optimization, as it is where the majority of the computation time is spent. It was found that trigonometric functions accounted for approximately 30% of the computation time, and tabulating them resulted in an optimization factor of 8 for the innermost calculation loop in the simulator. The computation times for a single CPU are summarized in Table 5.4.

[4] "Water lily", in French.

Operation	Complexity
Generation of the sea map	$\mathcal{O}(n \log n)$
Spatial phase shifting of the sea map	$\mathcal{O}(n \log n)$
Wake map: P & Q for all θ	$\mathcal{O}(N_\theta N_x N_z)$
Wake map: elevation calculation	$\mathcal{O}(nN_\theta)$
Sending an impulse	$\mathcal{O}(n)$

Operation	Time (s)	Values
Generation of the sea map	5	$n^2 = 512 \times 512$
Spatial phase shifting of the sea map	0.13	$n^2 = 512 \times 512$
Wake map: P & Q for all θ	0.2	$N_\theta = 300$, $N_x = 50$, $N_z \leq 28$
Wake map: elevation calculation	45	$n^2 = 512 \times 512$, $N_\theta = 300$
Sending an impulse	6.6	$n^2 = 512 \times 512$
TOTAL for m impulses	3497	$m = 500$

Table 5.4: *Algorithmic complexities (in array access) and typical computation times on a 3 GHz single-core Pentium 4, under Cygwin, measurements using the* `gprof` *utility. The code is written in C++.*

5.4.3.2 Further ways to improve the computation time

It is clear that if the width of the map increases by a factor a, the computation time increases by a factor a^2, making simulations in the time domain unsuitable for calculations on very large surfaces. In the context of our work, the approaches used to make the calculation faster were as follows: firstly, precalculating data as much as possible, especially with function tables; secondly, weak parallelization of calculations (simultaneous calculation of multiple configurations and/or polarizations on a computing cluster).

However, there are several strategies to decrease the computation time of a radar signal simulator: parallelization and the use of graphics cards. These two strategies of parallelization and the use of graphics cards are in line with current trends in the evolution of computer hardware. Moreover, the state of the art conducted at the beginning of this chapter shows that they are also very well suited to the radar domain, as demonstrated by the works of Kalkuhl *et al.* [100] and Balz [18] (respectively for parallelization and the use of graphics cards).

Indeed, the problem of simulating raw radar signals is highly separable, both in time and space. In other words, the calculation result corresponding to the surface at a date $t + \Delta t$ does not depend on the calculation done at date t since the linear model allows for calculating the positions and characteristics of the two scenes directly from the elements at date $t = 0$. It is possible to parallelize the calculations corresponding to separate instants on two distinct processors. Furthermore, the signal returned by one facet does not depend on the signal returned by a neighboring facet. It is therefore possible to partition the space of the scene at a given instant into small zones that can be simulated by different processors; in this case, only access to the memory where the received signal is stored needs to be shared. Programming on a parallel architecture is well-known and standardized; it can be done, for example, either by directly using the POSIX standard or using other open standards to distribute the computational load among several nodes in a computing cluster (MPI[5] standard from Stanford), or several cores of the same processor (OpenMP[6] standard or Apple's open-source Grand Central dispatch technology).

[5]MPI: Message Passing Interface
[6]OpenMP: Open Multi-Processing

Regarding recent developments in computer hardware, it appears that Moore's Law[7] seems to be reaching its limits for generic processors[8]. This explains why the improvement of computational performance is currently achieved by increasing the number of processors (so-called "multi-core" architectures). However, the performance of graphics processors –called Graphics Processing Unit (GPU)– is currently experiencing less stagnation than that of general-purpose processors (Figure 5.13), as they are more specialized processors and therefore more easily optimizable. Moreover, the video game industry provides an extremely important incentive for performance improvement. A GPU performs highly vectorized operations that can be repurposed for other applications, with high performance gains in the case of calculations that lend themselves well to parallelization (like our problem): this is known as General Purpose programming on Graphics Processing Units (GPGPU), a term that, according to `gpgpu.org`, was first proposed by Mark Harris in 2002 during his doctoral thesis work on real-time cloud simulation [89]. In the case of simulating radar signals, there is also a great similarity with the simulation of 3D optical images in the operations to be performed, such as calculating normals, reflection angles, *etc.*

5.4.4 Limitations of the GPGPU approach

There is a limitation to this approach, which is related to the fact that the discipline of GPGPU is relatively new and so far, no standard has been genuinely available. Also, scientific computation on a graphics card was, until now, a "craft" activity due to the lack of standardization of programming interfaces or graphics card architectures. This situation is expected to change in the near future, for example, with the CUDA (Compute Unified Device Architecture) standard from NVIDIA (whose first implementation was made public in February 2007), or with the emergence of the OpenCL standard, proposed by an industrial consortium including Apple, NVIDIA, and Intel. This standard should allow for the rapid and simple development of very general-purpose computing applications with an abstraction of the hardware layer, seamlessly supporting multi-core architectures and graphics cards. The first implementation of OpenCL is available on OS X 10.6 "Snow Leopard," released on August 28, 2009. Nevertheless, this field remains highly specialized and not necessarily accessible to the entire scientific community.

5.5 Conclusion of this chapter

The simulation techniques implemented are not new: as indicated in the introduction, the most similar approach to ours was already proposed in 1991 by Tunaley [176]. However, the simulation presented here has the merit of showing what is probably the first series of simulated images in a maritime environment with bistatic configurations. The simulation also takes into account specular reflection, allowing for work in arbitrary bistatic configurations. Additionally, the chapter provides an in-depth discussion of the problem of discretizing surfaces in the case of a radar image simulation based on facets.

5.5.1 Towards an answer to the discretization problem

The problem of discretization is recurrent and arises for most simulation approaches feasible in our problem (and not just for the chosen approach). However, it turns out that in the

[7] Moore's Law is a conjecture stating that the average number of transistors in processors available on the market doubles every eighteen months.

[8] By "generic processor," we mean a processor not specialized in any particular computation, *i.e.*, the Central Processing Unit (CPU).

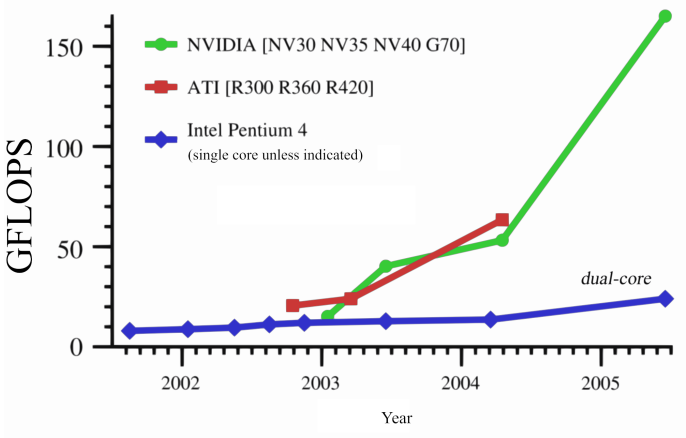

Figure 5.13: *Evolution of computing power in billions of floating-point operations per second (GFLOPS) for some GPUs, compared to that of the Intel Pentium 4 processor (adapted from Luebke [122]).*

literature, this point is often ignored. The conclusion that can be drawn from the discussion is as follows: the dimensions of the surface to be simulated must increase quadratically with the wind speed, and the density of facets must increase with the working frequency (which is intuitive) but also with the wind speed, following an analytical relationship that we have outlined in a simplified case just enough to provide an easily usable form for the relationship.

5.5.2 Simulation possibilities

Recent advances in computer processing speeds now make it possible to simulate raw radar signals in a time frame that is becoming acceptable for various applications. This enables control over every parameter in the acquisition chain with fewer approximations. The simulated signal can then be transmitted to post-processing chains, such as synthetic aperture radar (SAR) integration algorithms or data exploitation chains (detection and localization of targets, for example). The simulator can be easily specialized to represent coastal, airborne, or satellite-based radars, or a combination of these configurations. The consideration of specular effects has allowed for the implementation of simulation in the specific case of transmitting a GPS signal received near the sea surface (Coatanhay, Arnold-Bos, and Khenchaf [42, 41]). The simulation has demonstrated a clear dependence between the impulse response of the maritime surface and sea state (Figure 5.14), offering the possibility of studying inversion schemes to retrieve wind speed (as proposed by Zavorotny *et al.* [199]) using controlled simulation. This simulation would not have been possible with a SAR image simulator or a raw data simulator considering only diffuse reflections, as the configuration used is highly specular (refer to Chapter 4, Section 4.2 for a discussion on this point).

However, even if simulation is feasible in terms of computation time, it is by no means instantaneous and cannot be used to quickly generate a large image database. Thus, simulation remains more of a study tool (for configurations, acquisition strategies) than an image production tool, for example, to serve as a learning base for a recognition algorithm. There remains a clear niche for fast image simulators, either based on the modulation transfer function linking the height map and radar image or relying on harnessing the computing power of graphics cards. The latter approach is probably the most convincing today and seems promising for the future. Unfortunately, there is still a marked boundary

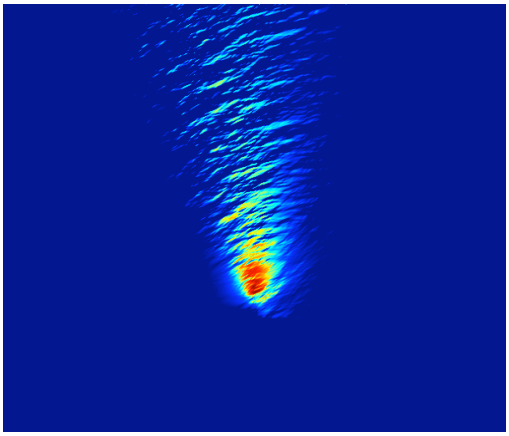

(a) Shape of elementary contributions from facets (natural values) for a receiver at 10 m altitude, with the satellite aiming downward at an incidence of 45 degrees. Specular reflection clearly dominates (in red).

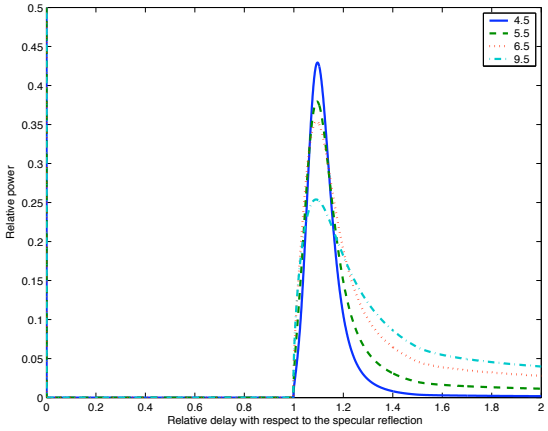

(b) Envelope of the impulse response, depending on sea state

Figure 5.14: *Reflection of a GPS wave above a maritime surface (excerpt from Coatanhay, Arnold-Bos, and Khenchaf [42]).*

between the radar-related scientific community, *i.e.*, qualified in the field of Physics, and the 3D programming community, mainly associated with the video game industry. GPGPU is a highly specialized and rapidly evolving discipline for which scientists are not trained. One could imagine recruiting expert personnel more capable of creating such code, or outsourcing, with a double problem: firstly, the issue of vocabulary, which may not be exactly the same between the two communities, and secondly, the problem of human resources, meaning low remuneration in the scientific field, making it difficult to attract graphics programming experts, who are primarily drawn to the video game industry. In the end, one could envision a situation where only a few laboratories worldwide will be able to produce fast and efficient calculation code using these technologies. This could lead to a monopolistic situation that would be problematic if the code were not distributed within the community.

5.5.3 Validation and limits of the simulation

Regarding the realism of the simulation, validation was conducted at three points. First, there was the validation of the different stages of the simulation taken separately, in the early chapters. The main validation concerns that of the reflection model on the rough surface. The test conducted in Chapter 4, Section 4.2.3, showed that the average reflection on a discretized surface corresponds well to the average predicted by classical statistical models. This leads to the validation of the average power link budget. The actual validation of the simulation was done on the speckle noise shape parameter and also on the visual aspect.

Speckle noise corresponds to power fluctuations around the mean. The behavior of speckle noise could not be exactly matched with a model or experimental data. Only the general sinusoidal shape of the wind direction dependence function of the speckle noise shape parameter was found, but quantitative numerical agreement was not achieved. The disagreement could be explained either by the absence of accounting for nonlinearities or the breaking of waves or the presence of foam, or perhaps because the validation was

performed for incidences and sea states at the limit of the simulation's validity.

The last validation, finally, concerned the visual aspect of the images compared to real wake data. This last point is not satisfactory since few wake images under equivalent conditions (high-resolution radar images) with a well-visible Kelvin wake are available for comparison. The lack of data also arises in bistatic configurations, whether the wake is present or not: there simply are no available data to validate the visual aspect of the simulation. The inability to fully validate this visual aspect, coupled with difficulties in obtaining convincing speckle noise, casts doubt on the predictive capability of the simulation proposed in this chapter. Thus, there is a need to improve the models and simulation approaches for radar signals reflected by the ocean surface. There are also other aspects to improve in the simulation presented here, including the simulation of turbulent wakes or the "V-shaped" bright spot, as well as the consideration of nonlinearities in the sea surface model. Aside from its importance in obtaining reliable data, this dual effort to improve models and validate them can also open up major prospects concerning inversion, namely, the ability to retrieve the physical parameters of the scene from the radar image.

The theoretical limits of the simulator result from the concatenation of the limits of various implemented models. In strict terms, the simulated maritime surface can range from state 1 to state 2 because the linear model must be valid, and there should be no foam on the sea surface; however, the transition between "validity" and "non-validity" is not abrupt, and by violating the model, it is possible to obtain images that remain reasonably accurate up to sea states 3 to 4. The incidences were formally validated up to 60 degrees in Chapter 4, but we considered facet masking, which allows us to extend the validity of the model to around 70 to 80 degrees; nevertheless, in this chapter, we presented results in very shallow configurations to compare them with a theoretical speckle noise model. Regarding the carrier frequency, the low-frequency limit is given by the validity of the Kirchhoff approximation, which is reasonably true only from the gigahertz range. The very high-frequency limit of the models has not been formally studied; therefore, we estimate that the diffusion model should remain reasonably valid up to 20 or 30 gigahertz.

5.5.4 The final word

In any case, MaRS is a first step towards answering two major questions concerning bistatic radar.

The first question concerns the operational benefits brought by bistatic configurations. The fact that the receiver is passive is already interesting in itself, but other arguments in favor of bistatic configurations have been put forward, such as their reduced cost (provided the transmitter is not provided), potentially better images in certain cases, although the meaning of "better" and "in certain cases" remains sketchy, subjective, and highly dependent on applications at best. The answer to these questions requires at the very least some images to form an intuition and, at best, metrics that can only be truly developed when ground truth is available (or a pseudo-ground truth provided by a simulator). In both cases, configurations where bistatic radar is not interesting should quickly become apparent, and vice versa.

The second question concerns the operational requirements and technical problems to be solved when bistatic imaging is performed. Simulation allows us to see which parameters are important and what orders of magnitude are acceptable or not. To illustrate, the kinds of questions that could be asked are:

- How would the image be affected if continuous waves were used instead of well-controlled pulses?

- What is the influence of the accuracy of sensor localization on the quality of the final image?
- How to improve image quality in cases of poor localization?
- *etc.*

These uncertainties and limits can now be simulated and help designers devise viable configurations and develop algorithms that attempt to push the boundaries of these configurations.

Part II

Contribution to automatic detection and analysis of ship wakes

Introduction

In the systems currently proposed in the literature or even operational ones, few seek to detect the wake, and none rely exclusively on the wake to detect ships. This absence is not due to the laziness of designers! The wake is a radar-visible phenomenon, but its visibility is not guaranteed and, in any case, much lower than that of the ships. Moreover, ship detection uses constant false alarm rate detection schemes, which are fast and robust in implementation, making them suitable for the analysis of a large amount of data, such as a raw satellite image with a size routinely reaching 4000×4000 pixels. However, as we will see, wake detection is much more algorithmically complex, requiring heavy computational power. Currently, to our knowledge, the only company offering wake detection in satellite radar maritime surveillance products is Kongsberg Satellite Services, with a useful processing time (one hour from acquisition to alert) but using a computing farm for processing.

Generally, wake detection occurs in a small image surrounding a ship detected by a dedicated algorithm. If at that moment the wake is detected, then one can consider using the additional information for information fusion. This additional information is obtained occasionally, with high uncertainties, which has led experts in the field, like Tunaley, to label it as "low grade."

Despite these preliminary remarks, it remains that the wake provides a significant amount of additional information that would be a shame not to consider when possible. If the wake is detected, it provides valuable additional information about the ship that caused it. Here are the kinds of information theoretically derivable from the wake:

1. **Confirmation of the presence of a ship:** A ship does not always create a visible wake, but if it does, the probability of a ship being present is stronger.

2. **Ship heading:** The direction of the wake provides information about the ship's heading, which can be provided to a target tracking chain.

3. **Ship width:** Zilman and Miloh [202] showed that the width of the dark wake at a given distance from the ship's stern is a direct function of the ship's width (equation 3.7 in Chapter 3). Therefore, if it is possible to segment the wake and find the width of the dark wake, it is theoretically possible to estimate the ship's width.

4. **Ship speed:** The Kelvin wake spectrum provides information about the ship's speed. If it can be analyzed (i.e., if it is visible in the image, requiring sufficient resolution), it is possible to deduce the ship's speed and also obtain confirmation of the heading.

Zilman's method mentioned in the previous point also allows the retrieval of the speed, theoretically. Additionally, the offset of the ship's position to the wake in the radar image (due to Doppler shift) also allows for estimating its speed.

5. **Ship location:** The wake consists of waves with low speed and practically no Doppler shift in the image (unlike the ship). Therefore, the wake's tip provides a better indication of the ship's position.

6. **Identification of the hull:** Through a more in-depth analysis of the Kelvin wake, it is theoretically possible to identify the ship's hull [197].

Another interesting aspect concerns the dead water wake –the dark trail behind the ship– which is visible from space using synthetic aperture radar. Indeed, besides detecting the ship and providing its heading, there is also the fact that its radar image is strongly similar to what is observed when a ship leaves an oil or petroleum trail in its wake, for example due to illegal degassing. Therefore, detecting a dark wake or detecting illegal degassing is more or less using the same algorithms, which should be optimized.

Formally, one can consider that the second part of this manuscript is dedicated to the inverse operation of the one described in the first part. Indeed, the first part was dedicated to the modeling and simulation of a wake radar image in polarimetric (possibly bistatic) radar imaging from the characteristics of an input scene. This second part, on the other hand, focuses on the issue of retrieving the parameters of the scene (i.e., the ship) from a radar image.

Apart from simply being interested in wake detection, there is also the visibility issue of the wake that needs to be solved: the wake is used sparingly because, until now, its visibility is more due to "luck" than a real intention to image it. Therefore, it is conceivable that optimizing the wake visibility should be prioritized before using it in a detection application. This optimization should allow evaluating the best acquisition geometry, the best frequency, the best antenna, in short, all the elements of the acquisition chain described in Chapter 1. The process of finding a good configuration is actually an optimization process, which requires a metric consistent with the intended use of the wake: detection. It is entirely possible to consider using elements such as the detection probability (to maximize) or the false alarm probability (to minimize) as elements of the desired metric. In summary, a three-step work program is established:

1. Develop a good wake detection and characterization algorithm; "good" is to be understood in the sense of the ten "commandments" detailed in the general introduction of the manuscript and can be broken down into specific sub-goals. This step can be broken down into two sub-steps:

   (a) Design one or more algorithms.

   (b) Test on a restricted basis to evaluate the algorithm and choose the best.

2. Apply this detector in several configurations (typically simulated) to find the configuration for which it could work best: in this step, the detector is considered fixed and perfect, and the configuration is optimized.

3. Once the best configuration is found, validate it under experimental conditions if it is deemed sufficiently valuable.

This approach justifies the attempt made in this second part, which covers only the first step of the program and attempts to partially address the second through theoretical

reflection and not through tests. These limitations (search for the best configuration, testing on bases) arise from the limitations of the simulation tool developed during the first part. Indeed, on the one hand, the validation of the model could only be done in specific configurations that are just a subset of the exploratory configurations; there is therefore a veil of doubt cast on its "prediction" capacity, which in any case can hardly replace experience. On the other hand, the computation time for a single image is still very long in practice, even if the times obtained were better than those initially predicted: this prevents generating a vast image database. Additionally, all wake-related phenomena have not been taken into account (especially turbulent wake, limiting the application of the simulation to high-resolution configurations where this wake is not predominant). Finally, the parameter space characterizing an acquisition configuration is too large to explore. The third step of the work program (experimental validation) is beyond the scope of this manuscript.

To summarize, the second part of this manuscript is entirely dedicated to the problem of wake detection and analysis. It is subdivided into two chapters: Chapter 6 and Chapter 7. The first chapter is devoted to the study of turbulent wake detection in satellite radar images. It provides a brief overview of the domain and presents a theoretical and numerical comparison (using simulated data) of four classical wake detection algorithms. The following chapter is dedicated to the characterization of the Kelvin wake in high-resolution images, including optical and radar images. It begins with a brief reflection on the optimal geometric configuration to better detect the Kelvin wake in high-resolution radar images. Subsequently, it presents a method for analyzing the Kelvin wake to retrieve the ship's speed and heading.

Chapter

6 Detection of Dead Water Wake in Satellite Radar Images

Contents

In Chapter 3, we observed that in relatively low-resolution radar images, such as those acquired by a satellite, the dead water wake appears as a dark line possibly attached to a bright line corresponding to the "bright V," which itself is the region where Kelvin waves are at the Bragg frequency of the radar's radio wave. The rest of the Kelvin system is not visible, except possibly for the edge of the cone, which appears as another bright line. Nevertheless, it is then possible to use line detection algorithms to highlight these elements. In better-resolved images, the dead water wake takes on the appearance of a wider dark band. However, in this chapter, we will only consider the case of low-resolution satellite radar imagery. The wake detection process follows a generic pattern that is common to most computer vision detection problems. This pattern is described in Figure 6.1.

For the detection of dead water wake, the content of each "box" in Figure 6.1 is as follows:

Preprocessing: This step aims to reduce the amount of speckle noise while preserving, or even improving, the visibility of the wake. This step is optional if the following steps are sufficient to discriminate the wake from the noise.

Simplification: Secondly, we perform an image transformation to reduce the dimension of the problem. We choose another parameterization to represent a line: instead of describing it as a collection of pixels, we prefer an analytical representation. Lines are then represented by the reduced equation: $\rho_d = x \cos\theta_d + y \sin\theta_d$, where $\rho_d \in \mathbb{R}$ is the distance from the line to the origin of the image and $\theta_d \in [0; \pi[$ is the angle between the normal to

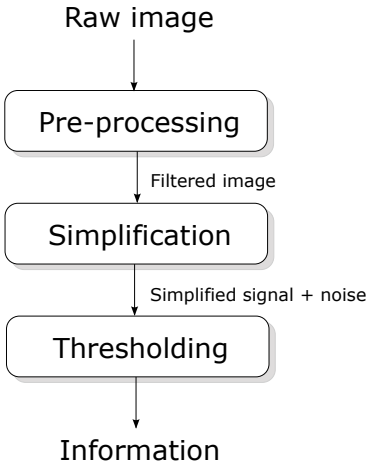

Figure 6.1: *General principle of a computer vision detection system*

the line and the x-axis. The line is thus represented by a pair (ρ_d, θ_d), namely, a unique point in an angle-distance space, and not as a collection of pixels. It should be noted that in practice, the angle-distance plane will be discretized with a step of $\Delta\theta_d \times \Delta\rho_d$. The problem is then to find a method to switch from the original Cartesian plane (x, y) to the representation in the angle-distance plane (ρ_d, θ_d). Two methods are commonly used: the Radon transform (RT) and the Hough transform (HT) .

Thresholding: Whether using one or the other of the transforms, the angle-distance plane will then need to be thresholded to isolate the few points (ρ, θ) that actually correspond to a line in the original image. These points result in a peak. If the signal-to-noise ratio is not good, then several false alarms may be detected in the image. To increase the signal-to-noise ratio in the transform, the thresholding is often preceded by another denoising step. One can also use a clustering algorithm to merge the peaks in the image that are too close together.

At the end of the day, the algorithm outputs the equation of the wake line. This line equation provides the ship's direction (through the parameter θ). However, this direction results in two possible headings: $\theta_b = \theta + \pi/2$ or $\theta_b + \theta + 3\pi/2$. The wake is generally a straight line segment starting from the ship. It is possible to detect the ship and/or the interruption of the segment. However, the wake will also be interrupted when the waves have dissipated the turbulent zone, at a great distance from the ship. Therefore, the interruption of the segment is a risky criterion. If we rely on ship detection by its echo, it is possible that it is absent from the image or sub-image we are processing. To simplify, we will consider that we are only looking for the direction of the ship's movement and not the heading.

In this chapter, we will provide an overview of existing methods for each of the detailed steps mentioned above, corresponding naturally to three paragraphs (6.1: dimensionality reduction, 6.2: preprocessing, and 6.3: thresholding). Dimensionality reduction is presented first because ideally it can do without preprocessing and because it is at the heart of the problem. We will then focus (section 6.4) on four processing chains in particular, as these approaches are highly representative of the overall methods available to date, which we will compare theoretically as well as with numerical results. The chapter will conclude on the possibility of using these methods in an operational maritime surveillance context. An outline of this chapter was published at the Caractérisation du Milieu Marin 2006 conference [11].

6.1 Dimensionality reduction

6.1.1 Radon transform

6.1.1.1 Definition and basic properties

It was in 1917 that Johann Radon proposed the transform that bears his name [146, 147], a transform that is now fundamentally used, especially in the field of medical imaging [99]. In general, the Radon transform of a real 2D function $I : (x, y) \mapsto I(x, y)$ is defined in such a way that the value of the transform at (ρ_d, θ_d) is equal to the integral of the function I along the line with the equation $\rho_d = x \cos\theta_d + y \sin\theta_d$. In this case, ρ_d is the distance from the line to the origin of the $(x = 0, y = 0)$ coordinate system, and θ_d is the angle between the x-axis and a normal to the line. Mathematically, this can be written in the form:

$$\mathcal{R}[I](\rho_d, \theta_d) = \iint_{x,y} I(x, y)\delta_0(x \cos\theta_d + y \sin\theta_d - \rho_d)dxdy \tag{6.1}$$

The rigorous hypotheses guaranteeing the existence of this integral are provided in Radon's articles [146, 147]:

- The function I is continuous at every point.
- The integral $\iint |I(x, y)|/\sqrt{x^2 + y^2}dxdy$ taken over the entire plane converges.
- For every point P(x,y) and every $\rho \geq 0$, the function $\bar{I}_P(\rho) = \frac{1}{2\pi}\int_0^{2\pi} I(x + \rho cos\theta, y + \rho \sin\theta)d\theta$ is such that $\lim_{\rho\to\infty} \bar{I}_P(\rho) = 0$.

In this case, $\mathcal{R}[I]$ exists almost everywhere. In practice, in image processing, these assumptions are violated - for example, in the presence of contours, I is discontinuous - but the results stated in this paragraph remain usable in practice.

Linearity The linearity of integral 6.1 also implies the linearity of the Radon transform, *i.e.*, that:

$$\mathcal{R}[aI_1 + bI_2] = a\mathcal{R}[I_1] + b\mathcal{R}[I_2] \tag{6.2}$$

for any functions I_1 and I_2 (from $\mathbb{R}$ to $\mathbb{R}$) and any real constants a and b.

Naive Calculation Algorithm in the Discrete Case The Radon transform can also be seen in another way, which allows us to deduce a first computer implementation of the algorithm. Assume that the function is zero everywhere except at one point with coordinates (x_0, y_0), where it is equal to 1. An infinite number of lines pass through this point, which will have the equation:

$$S_{x_0,y_0}(\rho, \theta) : x_0 \cos\theta + y_0 \sin\theta = \rho \tag{6.3}$$

The integral over the function I along each of these lines will necessarily be 1, meaning that *the Radon transform of a Dirac spike $\delta(x_0, y_0)$ is the sinusoid S_{x_0,y_0} with equation (6.3).* The linearity of the transform allows us to deduce that the Radon transform is the superposition (by linear combination) of all the sinusoids $S_{x,y}$ for all couples (x, y), with each sinusoid weighted by the value of the function I at the point (x, y). The reciprocal of the transform can also be deduced. If x and y are fixed, the integral along the sinusoid $S_{x,y}(\rho, \theta)$ in the angle-distance plane, divided by the length of that sinusoid, allows us to retrieve the value of the function I at the point (x, y).

The remark made in the previous paragraph allows us to describe a first algorithm for numerical computation of the Radon transform. Suppose that the function I is discretized on $n_x \times n_y$ elements (on a grid with steps $\Delta x \times \Delta y$).

1. **Initialization** Create a matrix $\mathtt{T}$ of dimensions $n_\rho \times n_\theta$ initially filled with zeros, representing the discretized angle-distance plane with a step of $\Delta\theta \times \Delta\rho$. This matrix is necessarily of finite size since the angles are in $[0; 2\pi[$ and the distances from the lines to the origin are bounded by the length of the image diagonal.

2. **Calculation** For each point with discrete coordinates $(i, j), i \in [1..n_y], j \in [1..n_x]$ of the function to transform, increment the matrix $\mathtt{T}$ by a value of $I(i, j)$ for all the cells on the (discretized) sinusoid $S_{i,j}$. The coordinates of these cells are calculated by sweeping the interval $[0, \pi[$ with a step $\Delta\theta$ for the variable θ.

3. **Result** In the end, $\mathtt{T}$ will contain the discretized Radon transform of the function I.

Invertibility It is possible to invert the Radon transform, *i.e.*, to retrieve a function equal to I from $\mathcal{R}[I]$. This possibility was also proven by Radon [146, 147]. Numerically, the naive inverse transform algorithm is similar to the direct transform. In both cases, the algorithm's complexity in terms of array access is $\mathcal{O}(n_x n_y n_\theta)$, which is very costly. It should be noted that the periodicity of trigonometric functions implies that the Radon transform is periodic (with a period of 2π) for the angular variable. Moreover, it is trivial to show that a rotation by an angle θ_d of I around the origin results in a translation of θ_d in the Radon transform in the angle-distance plane.

6.1.1.2 Link between the Radon transform and the Fourier transform

Let's consider the Fourier transform of a function I with two variables $\mathbf{x} = (x, y)^t$:

$$\mathcal{F}[I](\nu)) = \int_{-\infty}^{\infty}\!\!\int I(\mathbf{x}) e^{-\jmath 2\pi \mathbf{x}^t.\nu}\, d\mathbf{x} \tag{6.4}$$

with $\nu = (\nu_x, \nu_y)$ the spatial frequency vector.

Rotation of the Fourier Plane Suppose we consider I', the function obtained after rotating the plane of variables by an angle θ_d around the origin. This rotation can be represented by the matrix:

$$\mathtt{R}_{\theta_d} = \begin{bmatrix} \cos\theta_d & \sin\theta_d \\ -\sin\theta_d & \cos\theta_d \end{bmatrix} \tag{6.5}$$

such that $\mathbf{x}' = \mathtt{R}_{\theta_d}\mathbf{x}$, where $\mathbf{x}'$ represents the variables of I'. $\mathtt{R}^t_{\theta_d}$ denotes the transpose of $\mathtt{R}_{\theta_d}$, which is also its inverse. The very definition of I' states that:

$$I'(\mathbf{x}') = I(\mathbf{x}) = I(\mathtt{R}^{\mathtt{t}}_{\theta_\mathtt{d}}\mathbf{x}') \tag{6.6}$$

The Fourier transform of I' is:

$$\mathcal{F}[I'](\nu')) = \int_{-\infty}^{\infty}\!\!\int I'(\mathbf{x}') e^{-\jmath 2\pi \mathbf{x}'^t.\nu'}\, d\mathbf{x}' \tag{6.7}$$

The phase term here is:

$$\mathbf{x}'^t.\nu' = (\mathtt{R}_{\theta_d}\mathbf{x})^t.\nu' = \mathbf{x}^t.\mathtt{R}^t_{\theta_d}.\nu' \tag{6.8}$$

and thus, it follows:

$$\mathcal{F}[I'](\nu') = \mathcal{F}[I](\mathtt{R}^t_{\theta_d}.\nu') \tag{6.9}$$

This means that *"the Fourier transform of I' is derived from that of I by rotating the frequency pulsations around the origin."*

The "*Fourier Slice Theorem*" Let's now consider the Fourier transform along the line with equation $\nu_y = 0$. We have:

$$\mathcal{F}[I](\nu_x, 0) = \int_{-\infty}^{\infty} \int_{-\infty}^{\infty} I(x,y) e^{-\jmath 2\pi x \nu_x} \, dx \, dy \tag{6.10}$$

As the phase term no longer depends on y, it is possible to write:

$$\mathcal{F}[I](\nu_x, 0) = \int_{-\infty}^{\infty} \left[\int_{-\infty}^{\infty} I(x,y) \, dy \right] e^{-\jmath 2\pi x \nu_x} \, dx \tag{6.11}$$

The Radon transform of the image I corresponding to the set of lines with equations:

$$x \cos 0 + y \sin 0 = \rho \Leftrightarrow x = \rho = \text{cte} \tag{6.12}$$

is given by:

$$\mathcal{R}[I](\rho, 0) = \int_{-\infty}^{\infty} I(x,y) \, dy \tag{6.13}$$

and we have:

$$\mathcal{F}[I](\nu_x, 0) = \int_{-\infty}^{\infty} \mathcal{R}[I](\rho, 0) \, e^{-\jmath 2\pi x \nu_x} \, dx \tag{6.14}$$

In other words, the 2-D Fourier transform of I along the $\nu_y = 0$ axis is the 1-D Fourier transform of the Radon transform of I for the set of lines parameterized by $\theta = 0$.

By applying the preliminary remark on the rotation of the Fourier plane, it is possible to generalize this result to lines parameterized by a non-zero angle θ_d. The result becomes: *the 1-D Fourier transform, along the line $\theta = \theta_d$, of the Radon transform of I, is the 2-D Fourier transform of I read along the line passing through the origin of frequencies and with slope θ_d* :

$$\mathcal{F}[I](\nu_x, \nu_y) = \int_{-\infty}^{\infty} \mathcal{R}[I](\rho, \theta) \, e^{-\jmath 2\pi (x\nu_x + y\nu_y)} \, dx \, dy \tag{6.15}$$

with:

$$\left\{ \begin{array}{rcl} \nu_x & = & \rho \cos \theta_d \\ \nu_y & = & \rho \sin \theta_d \end{array} \right. \tag{6.16}$$

This property is known in the Anglo-Saxon world as the *"Fourier Slice Theorem"*. Refer to Kak and Slaney [99] (Chapter 4, p. 56) for an explanation similar to ours of this property. The *Fourier Slice Theorem* is important because it provides a fast method for calculating the Radon transform:

1. Compute the 2D Fast Fourier Transform of the function (complexity in $\mathcal{O}(n \log n)$ where n is the typical width or height of the image).

2. Retrieve the value of the 2D Fourier transform along n lines in frequency space, passing through the origin of frequencies, with the i-th line forming an angle $\theta = \pi i / n$ with the ν_x axis (number of array accesses proportional to the number of pixels in the image).

3. Perform the inverse Fourier transform along each of these lines.

In the end, the algorithmic complexity of calculating the Radon transform is of the same order as that of the fast Fourier transform, which is an important result when considering computation speed. We will reuse this result later when we discuss the algorithmic complexity of our algorithms.

6.1.1.3 Using the Radon Transform for wake detection

The Radon transform is well suited for detecting wake lines because they are either very bright or very dark. Intuitively, if all the pixels in a given line are bright, and the others have low values, then the Radon transform of the image will give a significant sum for the parameter set (ρ, θ) corresponding to the line, and moderate values elsewhere. In other words, a peak appears in the Radon transform for parameter sets corresponding to the lines to be detected in the image. Similarly, a very dark line will give a strong negative peak. On the contrary, due to the summation process, speckle noise becomes Gaussian, by applying the law of large numbers, although this is true only for (ρ, θ) corresponding to lines of sufficient length in the image.

6.1.2 The Hough transform

The Hough transform was patented in 1962 by Paul Hough (U.S. Patent 3,069,654) and also uses a parametric representation of lines. In his patent, Hough suggested using the representation $y = ax+b$, which poses an obvious problem when the line is vertical because a becomes infinite. Duda and Hart [59] suggested using the same representation as the Radon transform, and this is how the Hough transform is most commonly known today. The Hough transform can be generalized to any curve that can be expressed in the form of an implicit equation $f(\mathbf{u}) = 0$, where $\mathbf{u}$ is a parameter vector of dimension n to be estimated [17].

The calculation of the Hough transform generally begins with the use of a contour detection algorithm on the image, which can be seen as a specific case of preprocessing if one wishes to stay within the framework outlined at the beginning of the section since contour detection is already a useful signal filtering process. After this step, a binary image is obtained: a pixel with coordinates (x_0, y_0) has a value of one if it is on a contour, and zero everywhere else.

This pixel (x_0, y_0) can belong to an infinite number of lines with an equation of the form: $\rho = x_0 \cos\theta + y_0 \sin\theta$, which is a sine wave in the $\rho - \theta$ space. As with the Radon transform, the $\rho - \theta$ space is represented by a discretized array with steps $\Delta\rho \times \Delta\theta$. Each cell in the array (initially zero) that intersects the sine wave is incremented by one during a process known as "voting." In practice, it is often possible to obtain the orientation θ' of a local contour with a certain precision $\Delta\theta$ from the direction of the local gradient (which is orthogonal to the contour). Therefore, voting only needs to be performed on the portion of the sine wave between $[\theta' - \Delta\theta/2; \theta' + \Delta\theta/2]$, which significantly speeds up the calculation time and increases the signal-to-noise ratio in the final transform (O'Gorman and Clowes [135]). In the end, if many pixels are located in the image space on a line with equation $\rho_d = x\cos\theta_d + y\sin\theta_d$, the cell corresponding to (ρ_d, θ_d) will have a large number of votes compared to other cells. After a thresholding process, it is possible to identify this cell and obtain the parameters of the line from its coordinates. Unlike the Radon transform, the Hough transform is clearly not invertible.

The algorithmic complexity of the naive calculation, in practice, does not result in prohibitive computation time. O'Gorman and Clowes' method reduces calculation time by

restricting the interval of votes through the estimation of the local contour direction using the gradient. In practice, the gradient estimation is not very accurate, and cells also need to be incremented in a certain neighborhood (typically ± 20 degrees around the estimated angle). In the case of maritime radar images, care must be taken because the presence of noise strongly disrupts the estimation of the gradient direction. O'Gorman and Clowes' variant has not been used for this reason in our work.

6.2 Image preprocessing before transformation

The presence of speckle noise makes radar images more challenging to process because the wake signature can be hidden in noise. If one wishes to use the Hough transform or the Radon transform, noise elimination is even more critical as contours must be particularly well detectable, and noise should not be considered as noise. For this reason, this section provides a brief overview of existing methods for preprocessing a radar image for contour detection. This overview is relatively general, presenting methods actually used in the literature for wake detection as well as methods that may not have been specifically implemented for this application but have been proposed in the literature for globally similar preprocessing problems, and we consider them representative. In the context of wake detection, preprocessing depends on the subsequent processing: Radon transform or Hough transform.

In the case of the Radon transform, the input signal is a grayscale image. Although the Radon transform has some robustness to noise due to its inherent design (summing pixels along lines to reduce the influence of noise through averaging), this robustness is not perfect. Noise removal before the Radon transform can be beneficial. The goal is to reduce the influence of speckle noise and increase the visibility of the useful signal, which is achieved through filtering.

Now consider the case of the Hough transform. The input to this algorithm is a binary image resulting from thresholding (typically, the output of a contour detector). This contour detection should reveal the contours of the signal and try, as much as possible, to eliminate spurious contours due to noise. One can conceptualize this contour detection in two ways: either denoise the image as for the Radon transform before applying a contour detector, or design a contour detector with an "integrated robustness" to noise, explicitly taking noise into account. Alternatively, one can perform contour detection followed by filtering of the output of the contour detector.

6.2.1 Linear edge detection filters

Classic edge detectors focus on detecting points in the image where the local intensity gradient is strong, as this visually translates to the presence of an edge. The simplest filters (Prewitt, Sobel) only calculate the gradient, while more advanced filters, such as the Canny-Deriche filter [55] or the Shen and Castan filter [156], perform image smoothing by applying a filter close to a Gaussian in the direction orthogonal to which the gradient is calculated. This simultaneous smoothing and edge detection aim to denoise the image. However, since these filters are based on linear filtering, they uniformly apply the same amount of smoothing across the entire image. A contour, like wake lines, is locally characterized by a strong intensity gradient compared to the background, which corresponds to the sea. Applying smoothing tends to attenuate this gradient, preventing the proper detection of the wake. Therefore, pushing the smoothing too far would erase the useful signal. Conversely, if the noise is too strong, insufficient cleaning of the image will continue to hide the wake amidst the noise. Filtering can be performed in the spatial or frequency domain; in the

former case, the complexity is $\mathcal{O}(nm)$ where n is the number of points in the signal, and m is the size of the window used for the linear filter. In the frequency domain, the calculation complexity is dominated by the Fourier transform (thus being $\mathcal{O}(n \log n)$), which is better than computing in the spatial domain when m is large (typically $m > 64$ today).

6.2.2 Anisotropic filtering using partial differential equations

The anisotropic filtering approach by solving partial differential equations was introduced by Perona and Malik [141] to address the drawbacks of isotropic linear filtering, particularly its non-preservation of the signal in areas of strong variations. It is based on the following principle: we know that the solution at time t of the heat equation on a distribution of known sources at $t_0 = 0$ is the convolution of the initial distribution of sources with a Gaussian whose width is proportional to $|t - t_0|$ (meaning the Gaussian functions are the Green's functions for the heat equation partial derivative equation). In image processing, each pixel of the raw image can be seen as a source term at t_0, and we can effectively obtain the result of a 2D Gaussian blur by solving the 2D heat equation. However, it is possible to intervene on the diffusion constant to make it zero where the gradient is strong (*i.e.*, where edges are present) or, conversely, strong in areas of weak gradient, where the image is nearly uniform, and only noise is present. This can be achieved using a control function $c_{\text{Anis.}}$ (with values between 0 and 1) multiplying the diffusion constant $\lambda_{\text{Anis.}}$:

$$\begin{cases} \frac{\partial I}{\partial t} = \lambda_{\text{Anis.}}\, div\left(c_{\text{Anis.}}(|\,\mathbf{grad}\;\; I|^2)\,\mathbf{grad}\;\; I\right) \\ I(t=0,x,y) = I_0(x,y) \end{cases} \tag{6.17}$$

In this equation, I_0 represents the original noisy image, and $I(t)$ is the image at iteration t. Smoothing increases with time t and the diffusion constant $\lambda_{\text{Anis.}}$. Various forms have been proposed for the control function $c_{\text{Anis.}}$. We tested the function proposed by Sochen, Kimmel, and Malladi [160] because it optimizes the compromise between weak diffusion in the gradient direction and good diffusion in the tangential direction:

$$c_{\text{Anis.}}(|\,\mathbf{grad}\;\; I|) = \frac{1}{\sqrt{1 + |\,\mathbf{grad}\;\; I|^2}} \tag{6.18}$$

Filtering is performed by iteratively solving the differential equation using a finite difference scheme over time. If the parameters are well-tuned, the convergence of these methods is fast. The downside of the method is adapting the number of iterations (and thus the amount of filtering) and the parameter $\lambda_{\text{Anis.}}$. This adaptation is done through trial and error. The result on speckle noise images may not be the best compared to other methods. The computation time is $\mathcal{O}(n \times n_t)$, where n is the number of points in the image, and n_t is the number of temporal iterations.

6.2.3 Classic anisotropic speckle noise filters

Several speckle noise filters have been developed over the years, roughly around the time when synthetic aperture radar signals became available, and computer processing power began to be sufficient. Among the well-known filters are the Lee filter [117], the Frost filter *et al.* [76], and the Kuan filter *et al.* [112]. These filters are described in the spatial domain by their impulse response, which varies depending on the position of the filtered pixel. This implies that these filters are nonlinear. Let:

- (x, y) be the coordinates of the pixel to be filtered in the image,
- (x', y') be the coordinates of pixels in a coordinate system centered on the pixel to be filtered (x, y),

- $I(x, y)$ be the intensity at (x, y),
- $M_{\mathbf{w}}(x, y)$ be the mean of pixels in the window $\mathbf{w}$ centered at (x, y),
- $\Sigma_{\mathbf{w}}(x, y)$ be the standard deviation of pixels in the window,
- $I_f(x, y)$ be the intensity of the pixel after filtering.

In SAR images, it is generally assumed that the noise is multiplicative. In the case of developed speckle noise, the distribution of amplitudes follows a Rayleigh distribution. If, furthermore, all pixels in the window are independently drawn according to a Rayleigh distribution with the same parameter, then $M_{\mathbf{w}}$ and $\Sigma_{\mathbf{w}}$ are related by the following equation:

$$M_{\mathbf{w}} = \Sigma_{\mathbf{w}} \sqrt{\frac{\pi}{2}} \tag{6.19}$$

If, on the other hand, the central pixel of the window has a significantly different reflectivity, because it is a bright point, then $\eta_{Anis.} = \Sigma_{\mathbf{w}}/M_{\mathbf{w}}$ will be larger. This ratio will also tend to be larger in areas where the image has rapid transitions (echoes/shadows or edges) that one wishes to preserve. Thus, if the ratio $\eta_{Anis.}$ is large, the impulse response of the filter must approach a Dirac peak.

Lee Filter This is a simplified initial approach to the problem that approximates the linear model. Then the criterion of minimizing the mean square error between the filtered signal and the true signal is applied, resulting in an expression where the filtered pixel is a weighted average between the original pixel and the mean of intensities in the window $M_{\mathbf{w}}(x, y)$:

$$I_f(x, y) = \lambda_{\text{Lee}}(x, y) I(x, y) + (1 - \lambda_{\text{Lee}}(x, y)) M_{\mathbf{w}}(x, y) \tag{6.20}$$

The weight $\lambda_{\text{Lee}}(x, y)$ depends on the number of views N_v used to construct the image to be denoised and the ratio $\eta_{Anis.}(x, y)$:

$$\lambda_{\text{Lee}}(x, y) = 1 - \left[\frac{\nu_{Anis.}}{\eta_{Anis.}}\right]^2 \tag{6.21}$$

with $\nu_{Anis.} = \sqrt{\frac{1}{N_v}}$. If $\eta_{Anis.}(x, y)$ is large, $\lambda_{\text{Lee}}(x, y)$ tends to 1, and $I(x, y)$ is favored. Similarly, if the number of views N_v is significant, the image will naturally tend to be smoothed, and areas of rapid variations will be more meaningful, *i.e.*, the presence of rapidly varying signal, not noise.

Frost Filter This filter has a 2D impulse response $f_{x,y}^{\text{Frost}}(x', y')$ that is a 2D exponential, equal to 1 at (x', y') and decreasing as one moves away from this point. The typical attenuation distance varies depending on the ratio between the mean $M_{\mathbf{w}}(x', y')$ of pixels in the filter window and the standard deviation $\Sigma_{\mathbf{w}}(x', y')$ of intensities in the window.

$$f_{x,y}^{\text{Frost}}(x', y') = \exp\left(-\sqrt{x'^2 + y'^2} \frac{s(x, y)^2/m(x, y)^2}{\tau_{\text{Frost}}}\right) \tag{6.22}$$

In equation 6.22, τ_{Frost} is an attenuation constant typically adjusted through trial and error. Here also, the larger $\eta_{Anis.}$ is, the smaller the filter width becomes, making it similar to a Dirac peak.

Kuan Filter This filter can be seen as a variant of the Lee filter, as it also performs a weighted average between the central pixel and the window mean following 6.20. However,

the weight formulation is different as it results from a local additive model, *i.e.*, it depends on the signal. In Kuan's formulation, the weight becomes:

$$\lambda_{\text{Kuan}} = \frac{1 - \nu^2_{Anis.}/\eta^2_{Anis.}}{1 + \nu^2_{Anis.}} \tag{6.23}$$

6.2.4 Wavelet-based methods

Another category of adaptive filters is based on the application of wavelet theory, which is now classic in image processing, and which we will not elaborate on. However, there are several possible approaches involving wavelets at one point or another in the algorithm.

6.2.4.1 Wavelet filters for speckle noise filtering

The principle of these methods is to apply a wavelet transform to the image, then threshold the transform coefficients before reconstructing the image. Approaches based on wavelets have also been tried on images with speckle noise. Depending on the chosen wavelet, the results are more or less better, with some wavelets performing better in certain circumstances and less well in others. A recently proposed approach is to perform a simultaneous decomposition on multiple bases and locally choose the best of these bases: this is the principle of the Discrete Wavelet Transform with Enriched Diversity (DWEDWT), which gives good results on sonar images [96]. Once the image is denoised, a linear derivative filter

6.2.4.2 Intra-scale wavelet correlation

Kuo and Chen [113] proposed a criterion based on what they call "intra-scale correlation" of an orthogonal wavelet decomposition of the image to improve the visibility of linear elements present in radar wake images before applying a Radon transform. The idea is to compute a discrete wavelet transform of the image at n scales, typically using the Mallat algorithm, providing four sub-images per scale: an approximation image A_j and three detail images D^h_j, D^v_j, and D^d_j (horizontal, vertical, and diagonal details). The side effect is that the dimension of sub-images at scale j is reduced by a factor of 2^{-j} compared to the initial size of the image. Then, the module of the detail image M_j is calculated at each scale j (operations are element-wise):

$$M_j = \sqrt{|D^h_j|^2 + |D^v_j|^2 + |D^d_j|^2} \tag{6.24}$$

The "wavelet correlation" r at position (x, y) is calculated by multiplying, over all scales, all the modules M_j calculated from wavelet decomposition coefficients for which the point at coordinates (x, y) has contributed. This requires resampling the module sub-images M_j, $j > 1$, so that they have the same size as M_1 (this operation is symbolized by the operator $[\uparrow 2^x]$):

$$r = \prod_{j=1}^{n} [\uparrow 2^{j-1}] M_j \tag{6.25}$$

This intra-scale correlation can then be (in theory) thresholded on high values to reveal only the wake contours. Figure 6.3 shows the result of Kuo and Chen's processing on an ERS-1 image, while Figure 6.2 shows a result on a high-resolution SAR image, closer to the configuration illustrated in their article, where only the high-resolution case was addressed. It can be observed that in the satellite case, the dead water wake is not highlighted, unlike the ship, which is well distinguished from the background. Therefore, the method is more

of a "ship detector" than a "wake detector"! This behavior can be explained by the fact that wavelets are a theory originally developed for the one-dimensional case to detect singularities in the signal (discontinuities, etc.). Once "immersed" in 2D space, wavelets will not be able to detect all 2D singularities (lines and contours) and will be effective only on points [35]. Hence, better ship detection. In the case of the simulated high-resolution image, the entire Kelvin system is highlighted as a set of "remarkable points," but the dead water wake is not highlighted, even though the Kelvin wake/Dead water wake contrast is significant and could have suggested good detection. The use of a Radon transform is not improved after Kuo and Chen's processing.

6.2.4.3 Other approaches using adapted wavelets

Other approaches adapting wavelets and specifically dedicated to 2D image processing have been proposed in the literature, such as the *ridgelets* –from *ridge* ("mountain ridge") and *wavelet*– introduced by Candès and Donoho [35]. The calculation of *ridgelets* is done very simply by applying the Radon transform to images and then applying a 1D wavelet transform along the axes θ = constant. This way, the wavelets are applied not to lines in the image but to the peaks corresponding to these lines in the Radon transform, which constitute point singularities where wavelets are effective in detection. The potential interest of methods based on *ridgelets* and *curvelets* is twofold. Firstly, they aim to preserve lines, which are one of the "signatures" of wakes in low-resolution spatial radar images. Secondly, they are applied after calculating a Radon transform, an operation we already use.

6.3 Thresholding in the $\rho - \theta$ space

After applying the Radon or Hough transform, it is necessary to detect the peaks corresponding to wake lines. This can be done in various ways; we enumerate some of them here. We will focus more specifically on the Radon transform, but it is easy to adapt the methods to the Hough transform.

6.3.1 $k \times \sigma$ thresholding

This very simple approach is the most commonly used for detecting dead water wakes in a satellite image (Rey *et al.* [150]). The local average M of the Radon transform[1] R is calculated over a typical window size of 3×3, before subtracting it from R. In other words, a high-pass filtering is performed. This highlights the peaks and eliminates variations in the mean level of the transform. Then, the standard deviation σ of the image $R - M$ is calculated. Each pixel in $R - M$ with a magnitude greater than $k \times \sigma$ ($k \approx 3 - 4$) is considered to be a peak and corresponds to a line in the original image.

6.3.2 Wiener Filter thresholding

Given that *i*) the Radon transform is calculated, in practice, on a discretized space with step $\Delta\rho \times \Delta\theta$, and *ii*) wake lines have a width that is not necessarily infinitely thin, the peak corresponding to a wake line is not necessarily a Dirac peak: it can spill over into neighboring cells. Rey *et al.* [150] suggest imagining that the Radon transform (whose Fourier transform is denoted by $\mathcal{F}[R]$ and the average power spectral density by $|\mathcal{F}[\bar{R}]|^2$) is a blurred version of an ideal Radon transform (with Fourier transform $\mathcal{F}[R']$) where the

[1] Or the Hough transform...

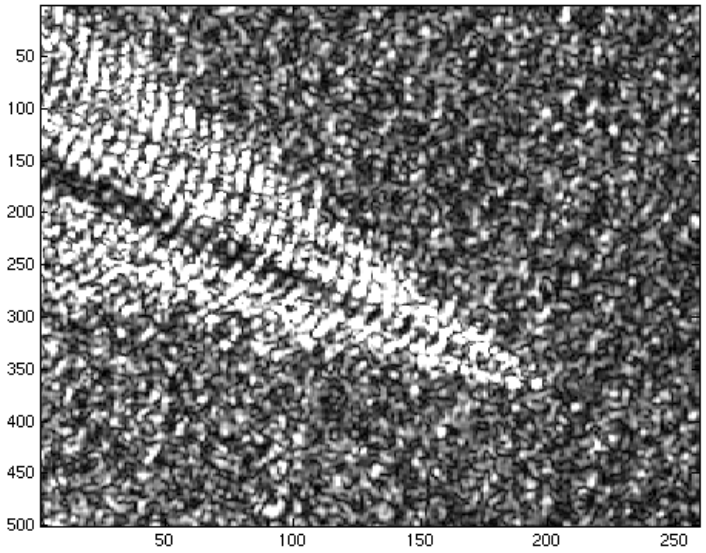

(a) Simulated SAR image with MaRS, resolution $\approx 2 \times 2$ m, sea state 2

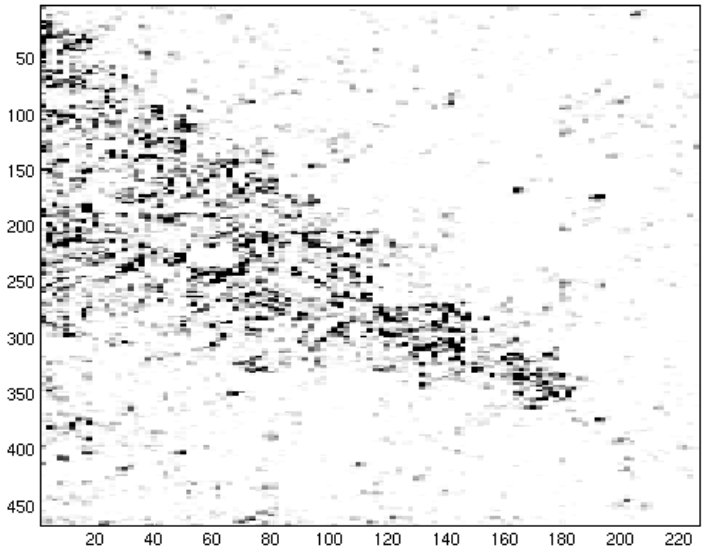

(b) Result of wavelet correlation on five scales.

Figure 6.2: *Multi-scale wavelet correlation on a high-resolution SAR image. Darker areas indicate stronger correlation.*

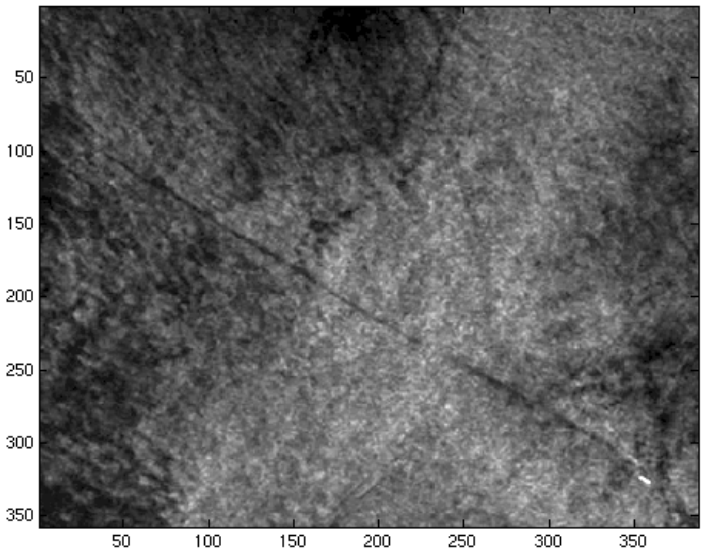

(a) ERS-1 Image (Strait of Messina). An oil tanker leaves an oil slick in its wake (© ESA).

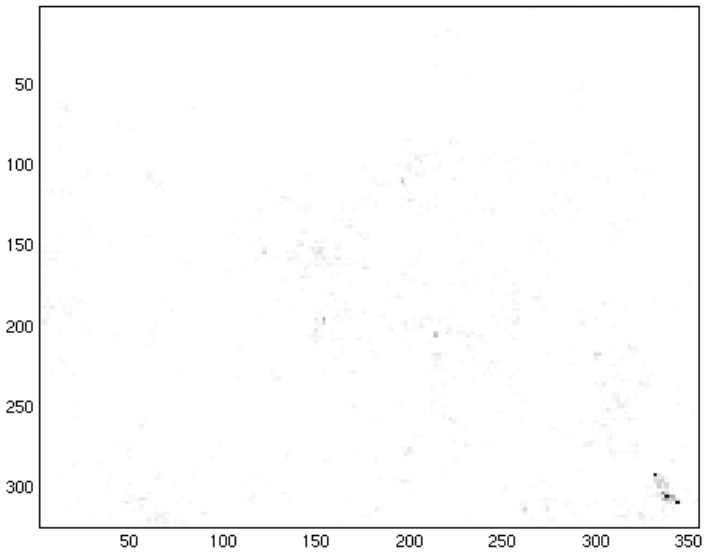

(b) Multi-scale Daubechies wavelet correlation on four scales. Darker areas indicate stronger correlation. Only the ship is highlighted by the processing (bottom, right).

Figure 6.3: *Multi-scale wavelet correlation on a satellite SAR image.*

peaks corresponding to the wake are Dirac peaks. The blur is created by convolving the ideal Radon transform with a transfer function that is modeled *a priori* (Fourier transform: $\mathcal{F}[H_{\text{blur}}]$). The rest of the Radon transform, *i.e.*, the part not corresponding to the peaks, is modeled as noise (Fourier transform denoted by $\mathcal{F}[N]$, average power spectral density denoted by $|\mathcal{F}[\bar{N}|^2]$). Thus, we have:

$$\mathcal{F}[R] = \mathcal{F}[H_{\text{blur}}]\mathcal{F}[R'] + \mathcal{F}[N] \tag{6.26}$$

Under this assumption, Rey *et al.* [150] use Wiener deconvolution to recover the estimate of the original peak. The interest of Wiener deconvolution, compared to naive deconvolution, is as follows. Naive deconvolution works by inversion:

$$\mathcal{F}[\hat{R}'] = \frac{\mathcal{F}[R]}{\mathcal{F}[H_{\text{blur}}]} \tag{6.27}$$

where $\mathcal{F}[\hat{R}]$ represents the Fourier transform of the estimate of R' and where the operations are to be performed term by term in the frequency domain. However, it can be seen that this filter is equivalent to:

$$\mathcal{F}[\hat{R}'] = \mathcal{F}[R'] + \frac{\mathcal{F}[N]}{\mathcal{F}[H_{\text{blur}}]} \tag{6.28}$$

... so that in frequencies where $\mathcal{F}[H_{\text{blur}}]$ tends to zero, the noise will be amplified. The use of the Wiener filter aims to reverse the blur process without (too much) increasing the noise level during inversion by attenuating frequencies where the noise predominates. The obtained expression, optimal in terms of least squares, is as follows ([152], eq. 6.13, page 383; a good introduction to Wiener theory can also be found in [114], Chapter VIII):

$$\mathcal{F}[\hat{R}'] = \frac{1}{\mathcal{F}[H_{\text{blur}}]} \frac{(\mathcal{F}[H_{\text{blur}}])^\star}{|\mathcal{F}[H_{\text{blur}}]|^2 + \frac{|\mathcal{F}[\bar{N}]|^2}{|\mathcal{F}[\bar{R}]|^2}} \mathcal{F}[R] \tag{6.29}$$

where $\star$ denotes the conjugate transpose. It can be observed that the denominator introduces the inverse of the mean signal-to-noise ratio[2] $|\mathcal{F}[\bar{R}]|^2/|\mathcal{F}[\bar{N}]|^2$. When this signal-to-noise ratio tends to zero, Equation 6.29 is equivalent to Equation 6.27. Conversely, if this signal-to-noise ratio increases, $\hat{R}'$ tends toward R, so that the noise is not amplified.

Concretely, in our situation, the filter H_{blur} is taken as a Gaussian with a standard deviation similar to that of the observed peak in the Radon transform (we took 0.5 pixels, with the filter support taken over 5 pixels; Rey *et al.* used 7 pixels). In Rey's original article, Wiener filtering was only applied to windows centered around peaks of R passing a wake $k \times \sigma$ with k equal to 4.5

6.4 A comparison of four methods

We implemented four distinct chains, as shown in Figure 6.4, utilizing the methods developed above in a consistent and representative manner. However, it should be kept in mind that some steps can be exchanged between two algorithms, which would increase the number of algorithms to be tested. For this reason, we limit ourselves to four chains. Section 6.4.1 provides a more detailed description of the algorithms, illustrating them on a real image (Figure 3.3 from Chapter 3, showing a wake off the Strait of Malacca). The following paragraphs summarize various points of comparison of the algorithms and the results on simulated data.

[2] In practice, this signal-to-noise ratio is often assumed to be constant over the entire spectrum, which is correct if the noise is white. The exact value of the signal-to-noise ratio is often determined empirically, *i.e.*, based on a visual criterion.

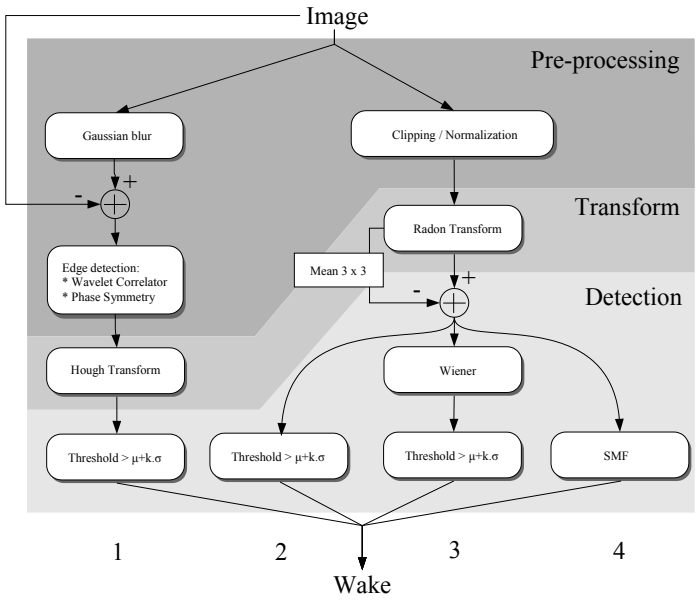

Figure 6.4: *Flowchart of the four chains {1, 2, 3, 4} presented here.*

6.4.1 Description of the four reference chains

6.4.1.1 Chain 1: Hough Transform (TH)

This chain aims to test the Hough transform. It starts with the calculation of the phase symmetry indicator as described by Kovesi in [109]. This indicator is followed by a morphological operation (a top-hat with a circular structuring element of radius 2, adjustable parameter). This treatment maximizes the visibility of the wake and minimizes noise. The result is then thresholded (not shown in the diagram), taking the top 10% of the highest values; the choice of this percentage can be adjusted. The thresholded image is then processed by another morphological operation, an opening with a structuring element of one-pixel radius, to fill in continuity gaps in the wake line caused by thresholding. Then, a classic Hough transform is applied with the parametrization (ρ, θ) by Duda and Hart. The peak in the Hough transform is then detected by "$k \times \sigma$" thresholding, where only the values above k times the standard deviation $\times$ of the data is kept. Figure 6.5 shows the Hough transform of the reference image, the final result, and the pre-processing result.

6.4.1.2 Chain 2: Classic Radon Transform (TR)

This chain aims to test the Radon transform. It is the simplest and most classical approach, without post-processing of the Radon transform. It starts with a histogram processing to make the best use of the available dynamic range (truncation of the highest percentiles of the original histogram, stretching). At this stage, it is possible to consider a histogram transformation to bring speckle noise to a reference distribution, such as the Rayleigh distribution. Then, the Radon transform is performed, followed by a high-pass filtering, calculated by subtracting the local mean over a 3×3 window (for example) from the Radon transform. This high-pass filtering allows keeping only the variations around the local mean of the Radon transform, which strongly depends on the length of the straight segment on which the image sum was performed. This highlights the peaks corresponding to the wake. The chain ends with "$k \times \sigma$" thresholding. This method is directly inspired

by the description given by Rey *et al.* [150]. Figure 6.6 shows the Radon transform of the reference image, with the thresholding result leading to wake detection.

6.4.1.3 Chain 3: Radon Transform + Wiener Filter

This third chain is derived from the second and adds post-processing of the Radon transform by a Wiener filter, following the proposal of Rey *et al.* [150] to improve the classical approach (Chain 2). Figure 6.7 shows the result of deconvolution on a small window centered around the peak of the Radon transform obtained at the end of Chain 2.

6.4.1.4 Chain 4: Radon Transform + Stochastic Matched Filtering (SMF)

The fourth chain substitutes the Wiener filter with a stochastic matched filter, following Courmontagne [46] (see Appendix D). As indicated in this article, the result of the stochastic adaptive filtering can then be thresholded, taking into account the likelihood ratio of the two hypotheses {presence of noise alone, presence of signal and noise}. This operation is described in Appendix D, Section D.6. To compare the result of this chain with that of the other chains, we will simply perform "$k \times \sigma$" thresholding. In the tests we conducted, we assumed that the peak corresponding to the wake had a size of 9×9. The stochastic adaptive filter has not been tested on real images.

6.4.2 Algorithmic complexity of the four processing chains

All filtering operations are performed using fast Fourier transform (FFT). Therefore, the complexity of the Fourier transform dominates. For an image of size $N \times N$, this results in an array access complexity of $\mathcal{O}(N \log N)$. However, this metric leaves out the "hidden constant" that allows us to compare algorithms among themselves.

The phase symmetry is calculated by a Gabor wavelet decomposition, and this decomposition is done using as many Fourier transforms as the product of the number of scales and the number of orientations (typically 6×6).

The Hough transform cannot be calculated by FFT, giving it a complexity of $\mathcal{O}(N^2 M)$ (M: the number of intervals used to discretize the set of angles). However, since a small number of image points actually belong to a contour, the hidden constant is low, making the algorithm fast and equivalent in computation time to the optimized Radon transform. That said, the Hough transform requires a preprocessing step, which, as we have just seen, is very costly, unlike the chains using the Radon transform.

A particular case is the stochastic adaptive filtering (FAS). Using the notations from Appendix D, it is noted that even though the FAS is calculated using a series of fast Fourier transforms (one for each filter $\mathbf{h}_i$), the preparation phase itself takes more time. In the applied examples below, the filter is applied to a 9×9 window, requiring the calculation of two correlation matrices of size $9^2 \times 9^2$. For these matrices to be representative, it is necessary to simulate the appearance of a large number of line signatures in the Radon plane, requiring as many Radon transforms (in our case, at least more than $9^2 = 81$, because otherwise, the covariance matrix would be nearly singular, and some eigenvalues would tend towards zero or an undefined value from a computational perspective).

6.4.3 Computation time

The computation times of the algorithms themselves were determined using Matlab, with an Intel Core Duo processor at 2 GHz, without specific optimization. They are given in Table 6.1. The computation time of Algorithm 1 based on the Hough transform is the longest and by far. However, the majority of the computation time is spent on calculating

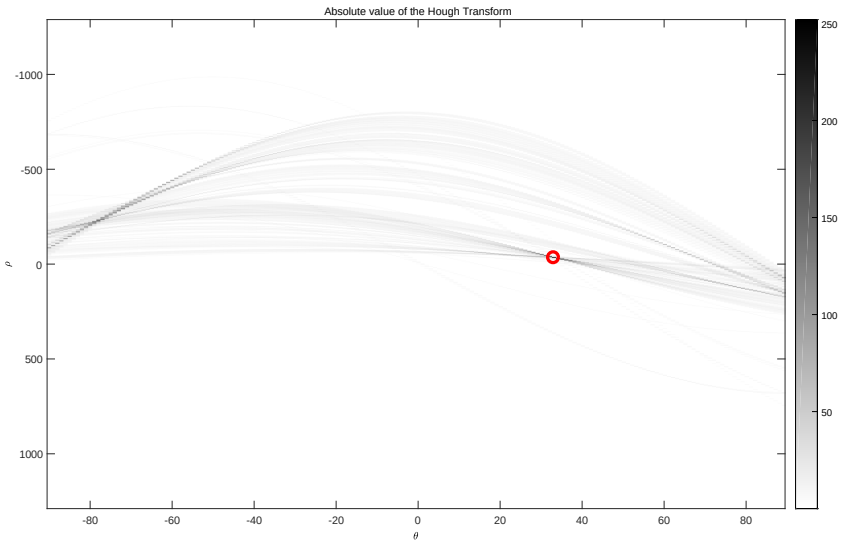

(a) Hough Transform, the maximum is indicated by the red circle

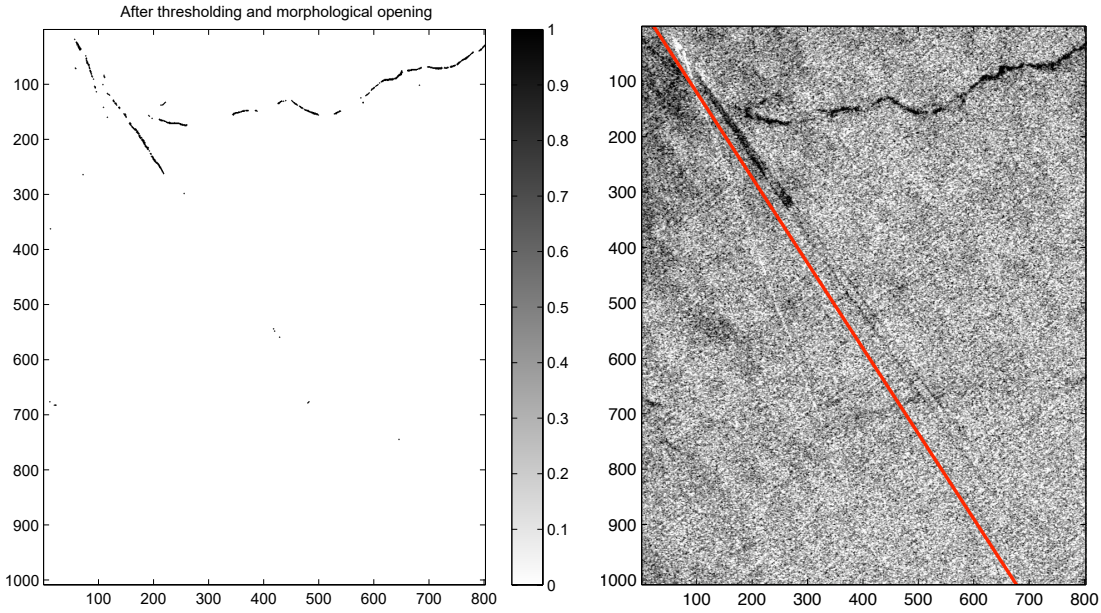

(b) Preprocessing result

(c) Input image and detected line

Figure 6.5: *Test of Chain 1: Hough Transform*

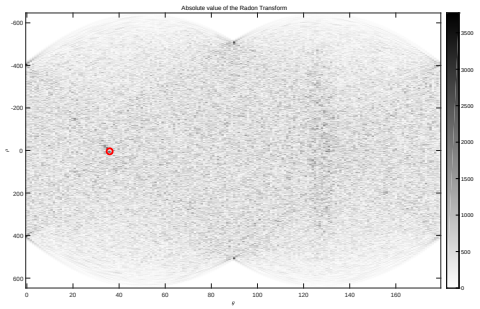

(a) Absolute value of the Radon transform after 3×3 high-pass filtering. The maximum is indicated by the red circle.

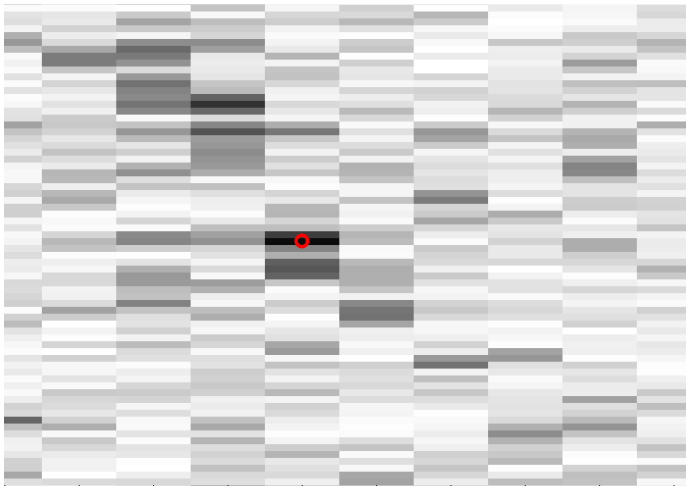

(b) Zoomed-in view of the maximum

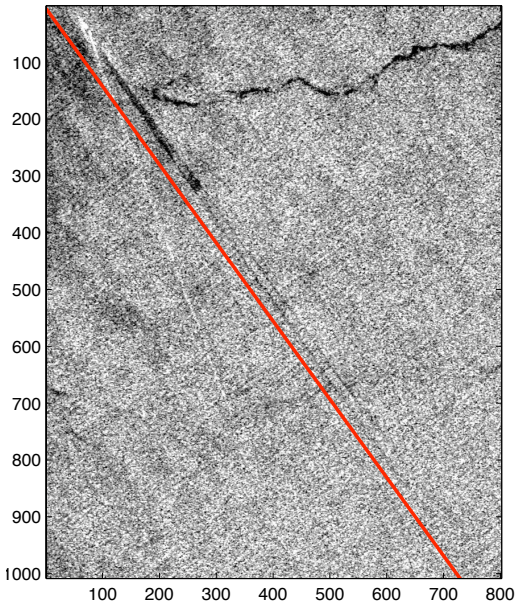

(c) Input image and resulting line (corresponding to the maximum of the transform)

Figure 6.6: *Test of Chain 2: Radon Transform*

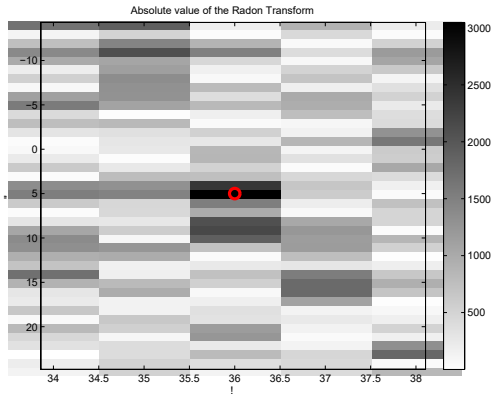

Figure 6.7: *Zoomed-in view of the Wiener filtering result (Chain 3) after deconvolution with a Gaussian filter of standard deviation 0.5 pixels. The input image is the same as for the other chains.*

Algorithm	Average Computation Time (s)
1	34.77
2	3.68
3	5.75
4	3.92

Table 6.1: *Computation times for the four dead water wake detection algorithms (measured on an Intel Core Duo computer, MacOS X 10.5 + Matlab 7.5).*

the phase symmetry (32.35 seconds on average). This time includes the calculation of the 36 Gabor wavelets (6 orientations, 6 scales), which can be precalculated in practice. Algorithm 4 (Radon transform and stochastic adaptive filtering with a filter) is not much longer than the basic filtering because the stochastic adaptive filter is calculated offline. The computation time of the stochastic adaptive filter is directly related to the quantity of reference images that are simulated. The computation times of the signal and noise covariance matrices used to obtain the filters are negligible. The calculation of matrix `P` takes about 1500 s for 1000 trials (and as many Radon transforms). The calculation of matrix `Q` takes only one to two minutes because only one Radon transform is calculated, namely that of the image to be filtered, from which the noise information is extracted.

However, it is clear that the processing time (about three seconds per image at best) remains very significant. In practice, a large image, several thousand pixels wide, needs to be scanned. Scanning cannot be done with a sliding window for obvious reasons of computation time. Therefore, we work on blocks of sub-images, but it will be necessary to take into account a certain overlap between blocks to handle the case where a wake falls between two blocks. It is also realized that another solution could consist of a preliminary detection of the ship, followed by wake detection in a window centered around the boat's position.

6.4.4 Comparison on simulated images

In addition to the comparison on real images, a more in-depth comparison was carried out on synthetic wake images that were generated to provide the necessary *a priori* data to construct the stochastic adaptive filter used in reference chain 4. The noise is assumed

to be multiplicative, following the Rayleigh distribution, generated by taking the norm of a complex Gaussian noise with unit standard deviation. It is assumed that the dead water wake appears as a line a few pixels wide, adjacent to a bright line, randomly placed immediately to the left or right (equiprobable). The wake is assumed to be always present in the image. For each set of parameters, a large number n_{bt} of images ($n_{\text{bt}} = 1000$ in our case) are generated by randomly varying the noise, as well as the position and orientation of the wake. The parameters used are summarized in Table 6.2.

(a) Parameters not varying across the test databases

Parameter	Meaning	Value
a_c	Clutter amplitude	1
W_s	Width of the dark line (in pixels)	3
W_b	Width of the bright line (in pixels)	2

(b) Parameters varying for each test database

Parameter	Meaning	Value
N	Side of the image (square) in pixels	128 or 256
$\rho_{\max}$	Maximum value of ρ	$\lfloor N/2 \rfloor$
C_b	Bright wake/clutter contrast (dB)	0.5 dB; 1 dB; 2 dB; 3 dB; 6 dB
a_b	Amplitude of the bright line without noise	$a_b = 10^{\frac{C_b}{20}}$
C_s	Dark line contrast on clutter (dB)	$C_s = C_b$
a_s	Amplitude of the dark line without noise	$a_s = 10^{\frac{C_s}{20}}$

(c) Parameters varying for each of the n_{bt} images in a test database. The variables u_1 and u_2 are independent random variables whose realization changes for each image and are drawn from a uniform distribution between 0 and 1.

Parameter	Meaning	Value
θ	Angle of the x-axis to the wake normal	$u_1 \times \pi$
ρ	Distance from the line to the origin of the coordinate system	$u_2 \times \rho_{\max}$

Table 6.2: *Parameters used for generating synthetic images.*

The four reference chains are then tested by varying the signal-to-noise ratio, *i.e.*, the contrast of the wake lines compared to the clutter level, at four levels: 0.5 dB, 1 dB, 2 dB, 3 dB, and 6 dB. The size N of the image is also varied, testing two sizes (128 and 256 pixels wide, respectively). This allows testing the influence of the length of the wake lines on the integration performed during the Radon transform and, to some extent, in the Hough transform. To conduct the test, a certain number of statistics are compiled in terms of detection or false alarms.

Here's how detections are counted. At the end of each chain, the processing is completed with a thresholding by setting the threshold to $s_d = k \times \sigma$. We consider s_d as a parameter that can be varied. For a given value of s_d, we only keep the value pairs (ρ, θ) passing the thresholding. We then determine whether each of these value pairs is correctly detected or not. A detection is considered good if:

- a wake is visible in the image (an always true assumption in our case);
- the detected line is sufficiently close to the actual line, as indicated in the test image database for the considered image. For this, a tolerance margin of 10 pixels for ρ and 3 degrees for θ is considered. The tolerance for θ is taken modulo π.

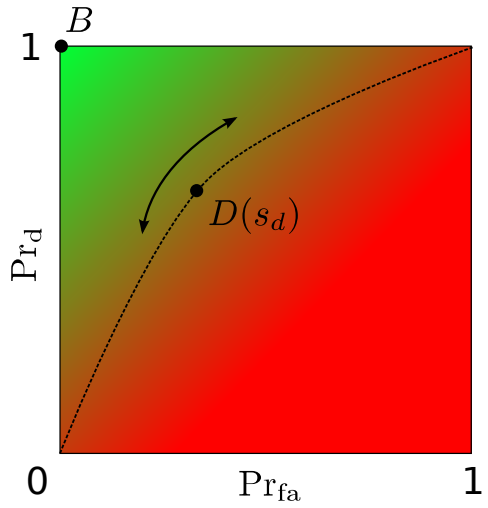

Figure 6.8: *Interpretation of a ROC curve: the operating point D moves along a curve, the curvilinear abscissa depending on the threshold s. We want to maximize the detection probability Pr_d while minimizing the false alarm probability Pr_{fa},* i.e.*, finding a threshold s such that D is as far as possible from the optimal operating point B,* i.e.*, in the light green area.*

On the contrary, a detection is counted as false if:

- it is returned when no wake is present in the image;
- the parameters (ρ, θ) are outside the allowed tolerance range for the parameters of the wake actually present in the image.

We then compile, for a given value of s_d of the threshold, the number of good detections and the number of false detections for all images in the database, which allows us to calculate the wake detection probability Pr_d and the false alarm probability Pr_{fa} as functions of the threshold $k \times \sigma$:

$$\mathrm{Pr_d}(s_d) = \frac{n_{\mathrm{bd}}(s_d)}{n_{\mathrm{bt}}(s_d)} \tag{6.30}$$

$$\mathrm{Pr_{fa}}(s_d) = \frac{n_{\mathrm{fa}}(s_d)}{n_{\mathrm{det}}(s_d)} \tag{6.31}$$

where n_{bd} is the number of good detections counted on the test database, n_{fa} is the number of false alarms, and n_{det} is the total number of wakes detected (rightly or wrongly). The Receiver Operating Characteristic (ROC) curves of each algorithm are then represented, allowing them to be compared. Figure 6.8 recalls how to interpret such a curve. The actual ROC curves are given for the four algorithms as a function of the wake contrast, for an image size of 256 pixels (Figures 6.9 to 6.13) and 128 pixels (Figures 6.14 to 6.18).

The clear ranking of algorithms that emerges from the comparison of ROC curves is as follows:

1. Chain 4: Radon Transform + Stochastic Matched Filtering
2. Chain 2: Radon Transform alone
3. Chain 1: Hough Transform

4. Chain 3: Radon Transform + Wiener Filtering

It is observed that stochastic matched filtering slightly improves robustness compared to the classical algorithm where only the Radon Transform is performed. However, for a contrast below 2 dB, it becomes challenging to achieve a good trade-off between detection probability and false alarm probability, even for Chain 4. Beyond 3 dB, the trade-off becomes excellent. One notably observes the poor performance of Wiener filtering in enhancing the visibility of the wake. In fact, if the filter is poorly adapted, it will also amplify the noise. This adaptation is very challenging because, in the Radon plane after high-pass filtering, the noise also consists of significant peaks, which will also be made stronger by deconvolution (one can start to convince oneself by comparing Figure 6.6(b) with Figure 6.7). If there is a perfect adaptation of the deconvolution filter (i.e., using a filter closer to reality rather than a Gaussian), it tends towards the concept of a matched filter. This explains the superiority of Chain 4 over Chain 3. Finally, it should be noted that the image size has some influence on the detection rate, as rates at equivalent contrast levels are better for 256×256 images; however, for the strongest contrasts, the difference in terms of detection probability remains minimal.

6.5 Conclusion of this chapter

This chapter has provided an overview of wake detection methods, followed by a comparison of four reference chains implementing several classical approaches. It has also presented an overview of filtering methods, allowing the removal of speckle noise in a radar image and improving wake visibility.

The result of our comparison reveals that stochastic matched filtering is the most promising detection algorithm among those tested, but the detection improvement comes at a cost: the signal must be modeled *a priori* through simulation. However, this can be done offline before the actual detection, at the expense of modeling the wake and determining representative signal parameters. In our evaluation, the most commonly used wake detection algorithm (Algorithm 2) takes the second place; it has the merit of being simple and fast. The Hough transform is unsuitable for wake detection as it requires a preprocessing step that is too costly to be truly interesting, even if it works for sufficiently large contrasts. A comparison has also been made from the perspective of algorithmic complexity, placing the classic chain number two in the first place, while stochastic matched filtering takes the second place (for online processing, assuming the filters are precomputed). However, the computation time remains too high to perform processing on a sliding window. It is imperative to work on image blocks with careful overlap management to avoid working on a truncated wake. It should be noted that the *a priori* provided by ship detection (not addressed here) can make a big difference: detecting the wake in a window centered on the ship detection is often sufficient.

One point to improve is the evaluation of algorithms. Only an initial evaluation has been conducted here on a battery of simulated images. It would be beneficial to complement this evaluation with tests on real data (assuming it can be acquired). In this situation, the algorithms would be evaluated against the result of manual segmentation. Two points should be noted: firstly, we do not have such an image bank, and secondly, there is a need for a metric to compare automatic results with manual segmentation. A possible approach for this task was proposed by Martin, Laanya, and Arnold-Bos [126]; it involves manually annotating images by human operators, then merging the annotations, taking into account the level of detail or uncertainty of the annotations, to arrive at a reference annotation that can be compared to the outputs of the algorithms to be tested.

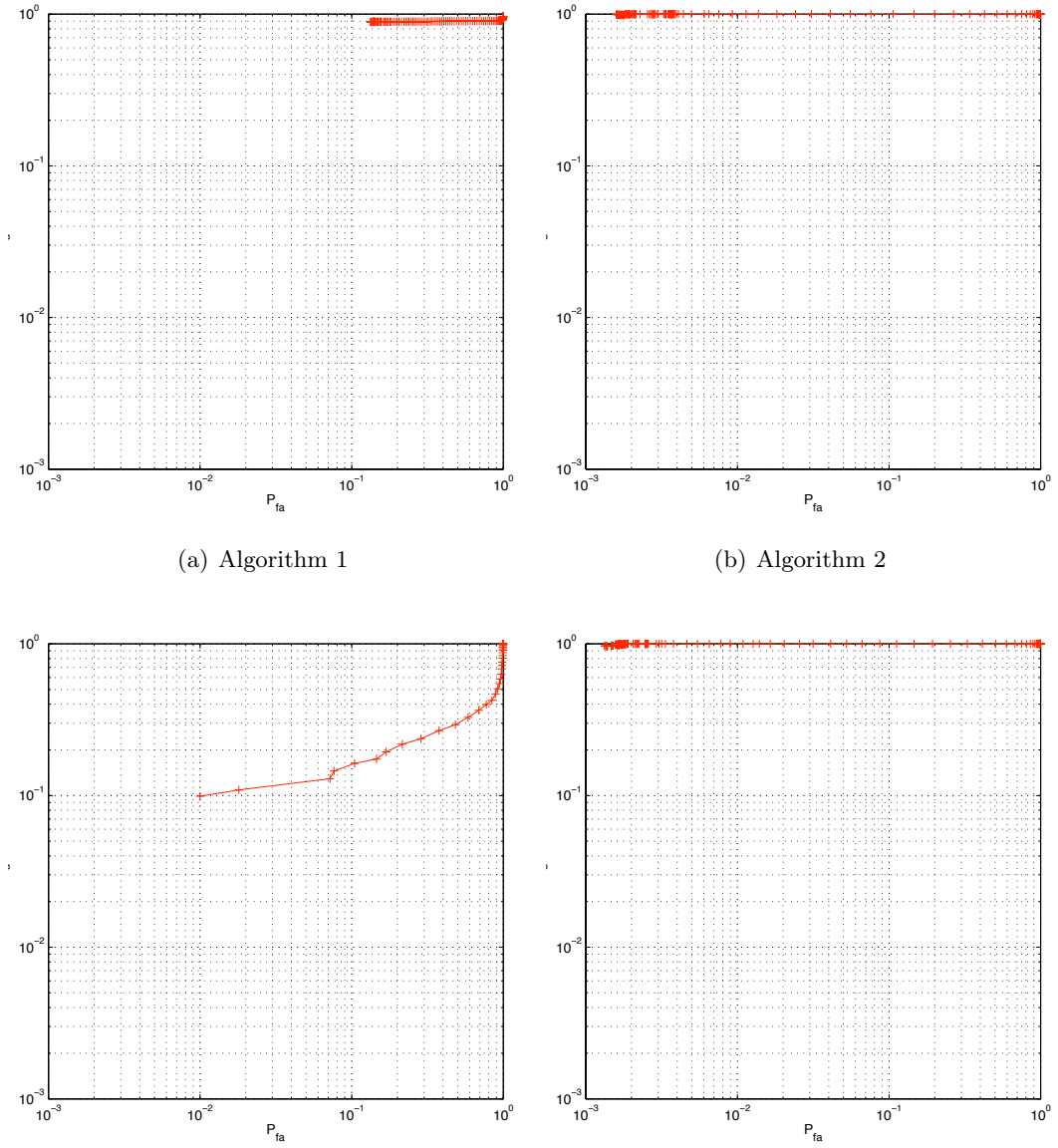

(a) Algorithm 1

(b) Algorithm 2

(c) Algorithm 3

(d) Algorithm 4

Figure 6.9: *Results for images of size 256×256, contrast equal to 6 dB*

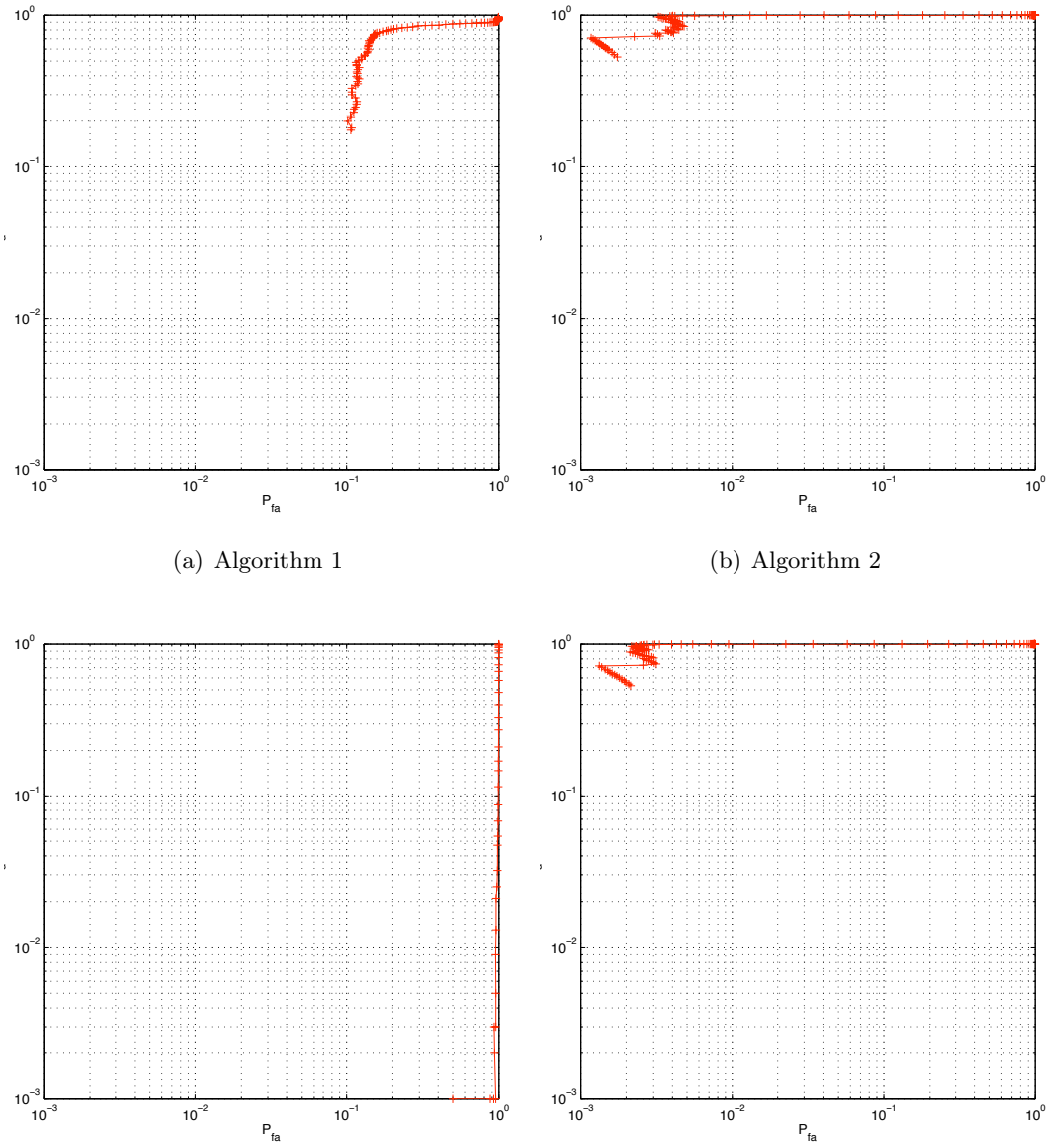

(a) Algorithm 1

(b) Algorithm 2

(c) Algorithm 3

(d) Algorithm 4

Figure 6.10: *Result for images of size 256×256, contrast equal to 3 dB*

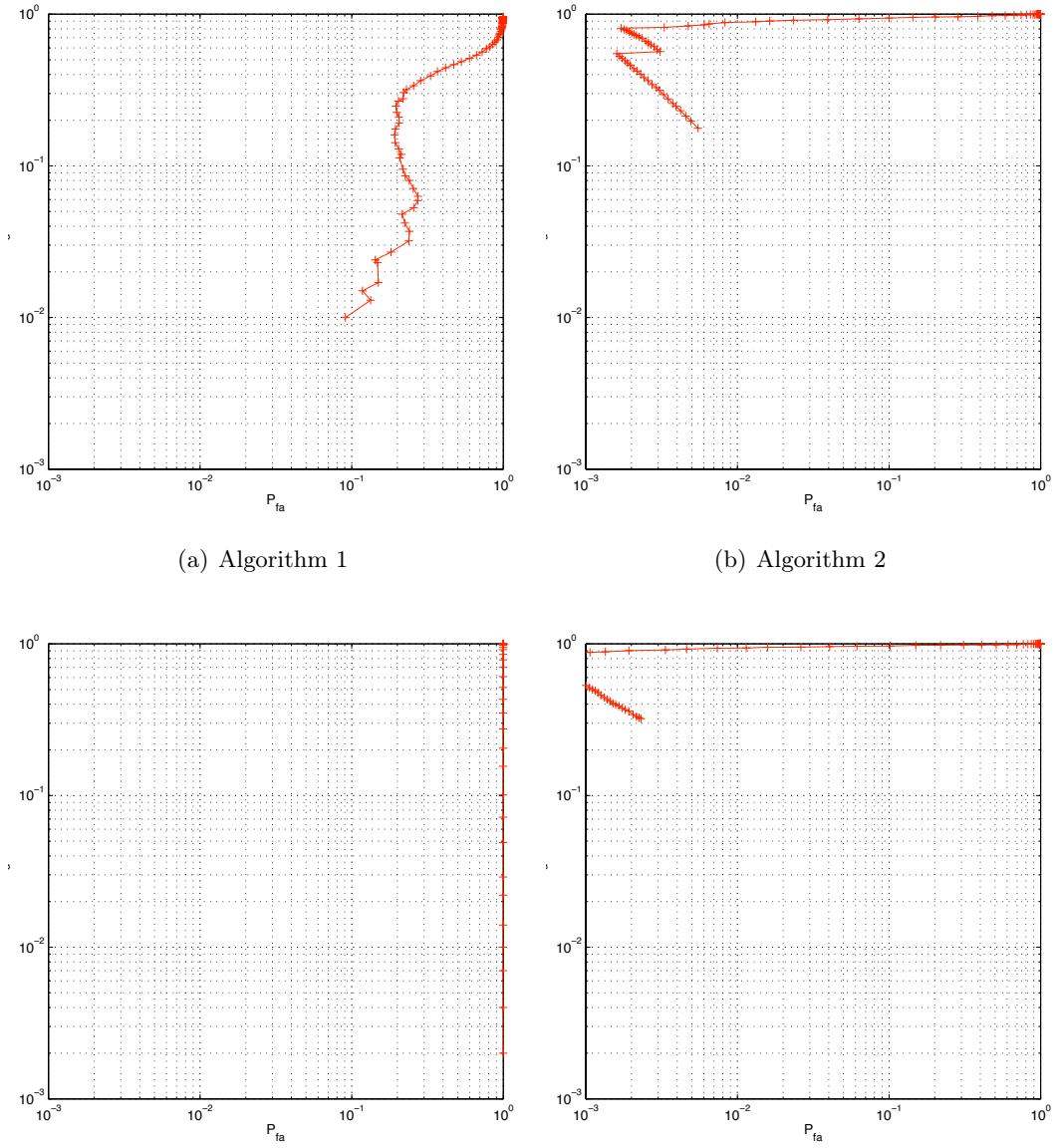

(a) Algorithm 1

(b) Algorithm 2

(c) Algorithm 3

(d) Algorithm 4

Figure 6.11: *Result for images of size 256×256, contrast equal to 2 dB*

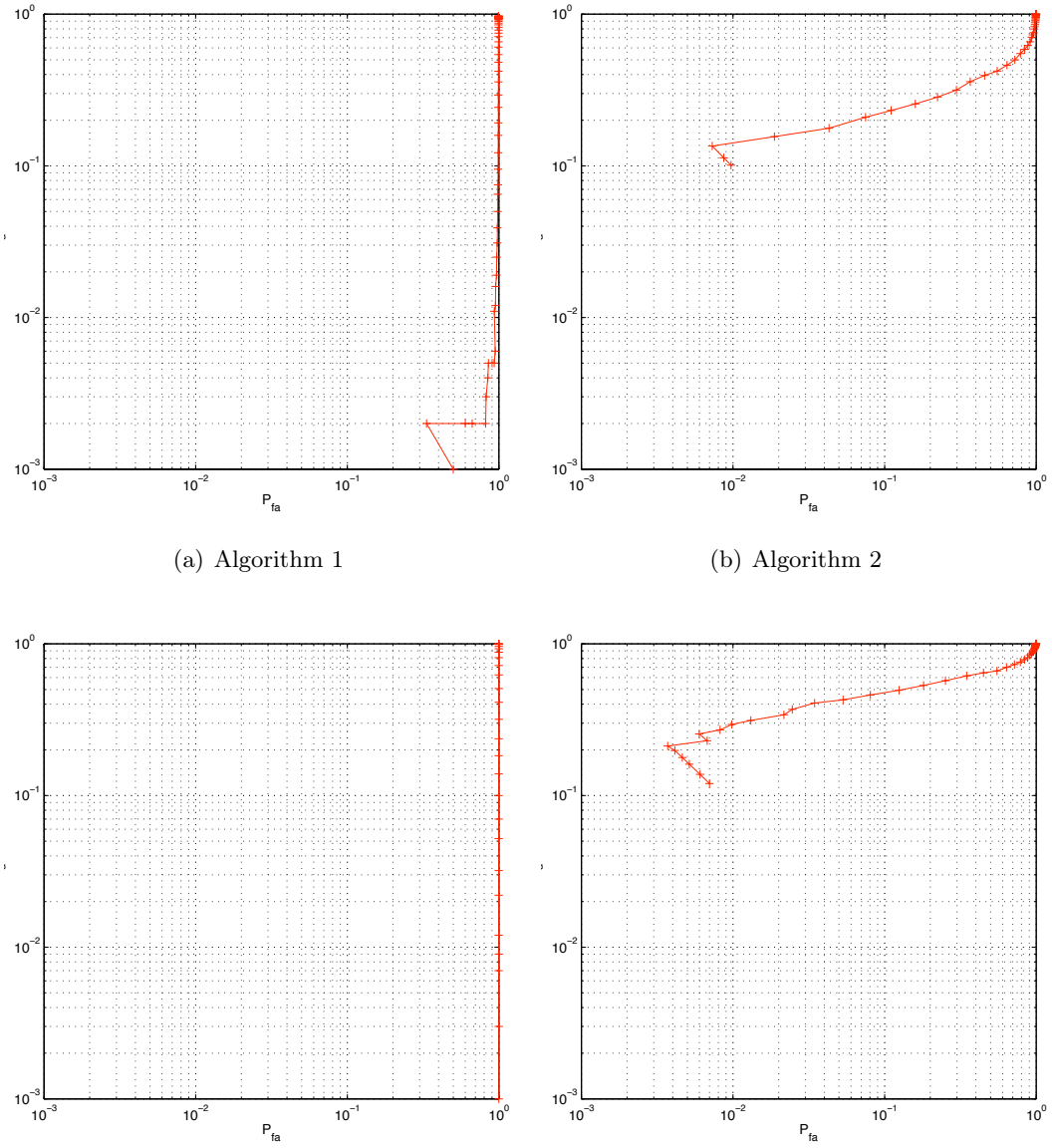

(a) Algorithm 1

(b) Algorithm 2

(c) Algorithm 3

(d) Algorithm 4

Figure 6.12: *Result for images of size 256×256, contrast equal to 1 dB*

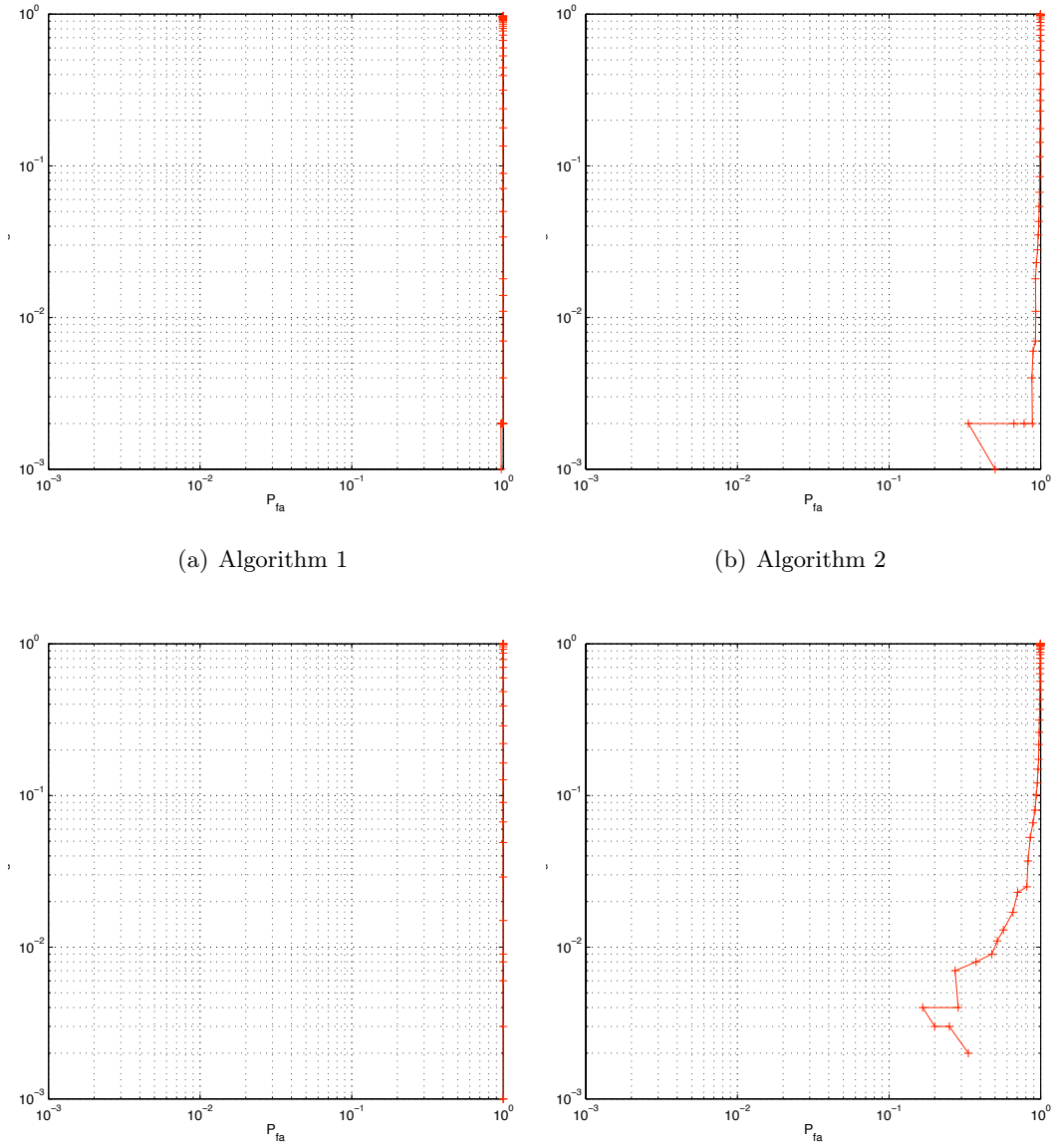

(a) Algorithm 1

(b) Algorithm 2

(c) Algorithm 3

(d) Algorithm 4

Figure 6.13: *Result for images of size 256×256, contrast equal to 0,5 dB*

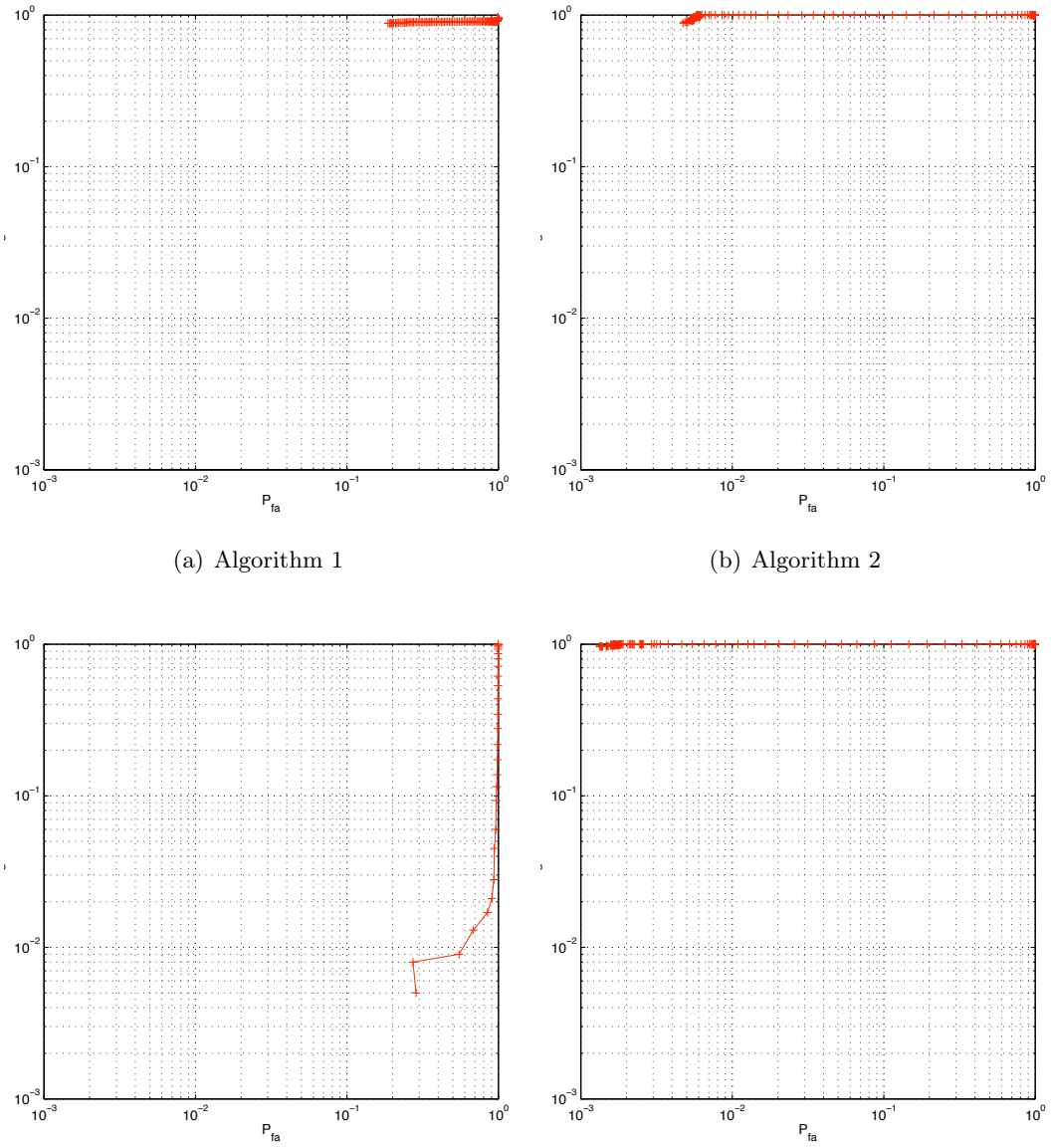

(a) Algorithm 1

(b) Algorithm 2

(c) Algorithm 3

(d) Algorithm 4

Figure 6.14: *Result for images of size 128×128, contrast equal to 6 dB*

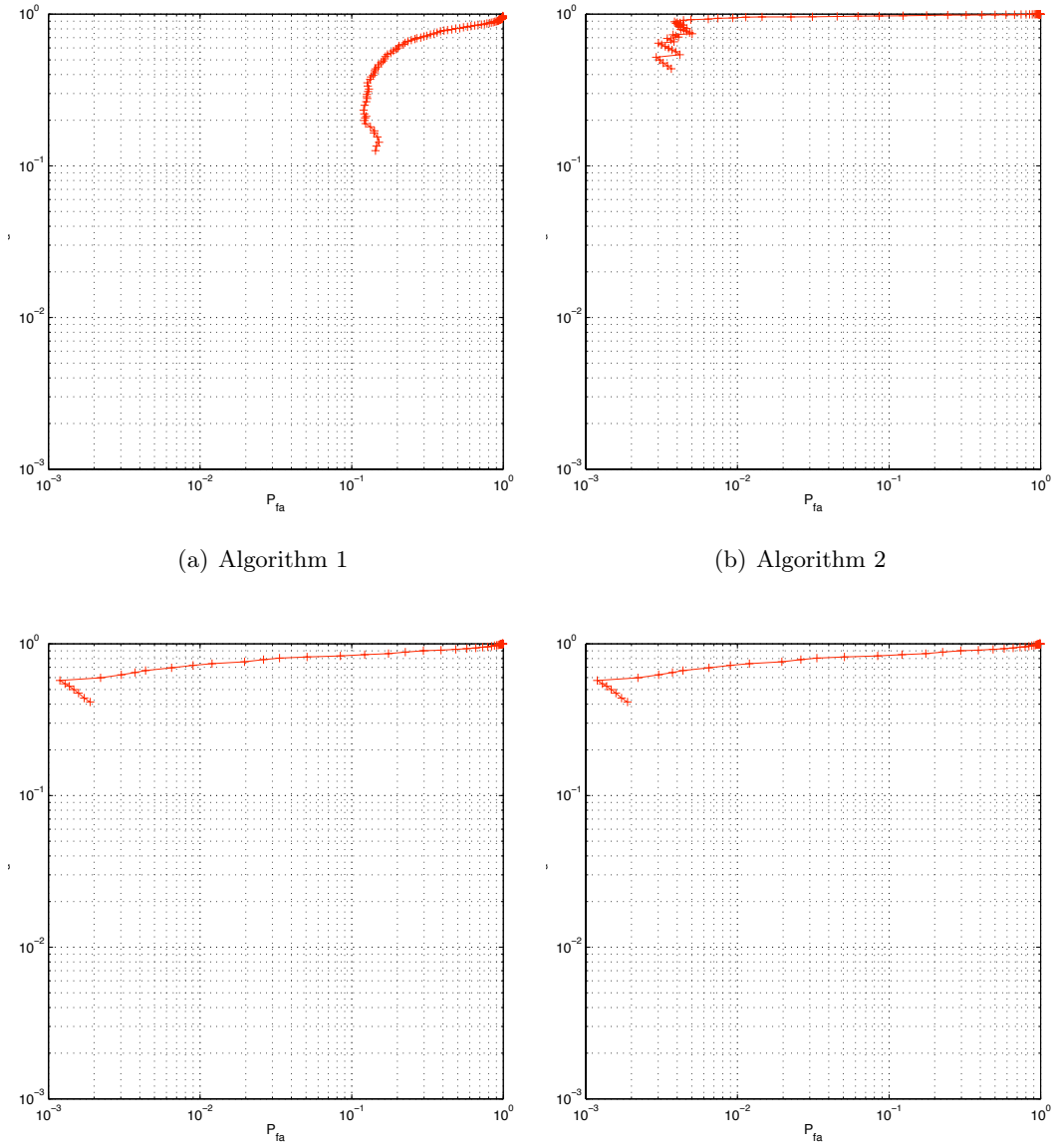

(a) Algorithm 1

(b) Algorithm 2

(c) Algorithm 3

(d) Algorithm 4

Figure 6.15: *Result for images of size 128×128, contrast equal to 3 dB*

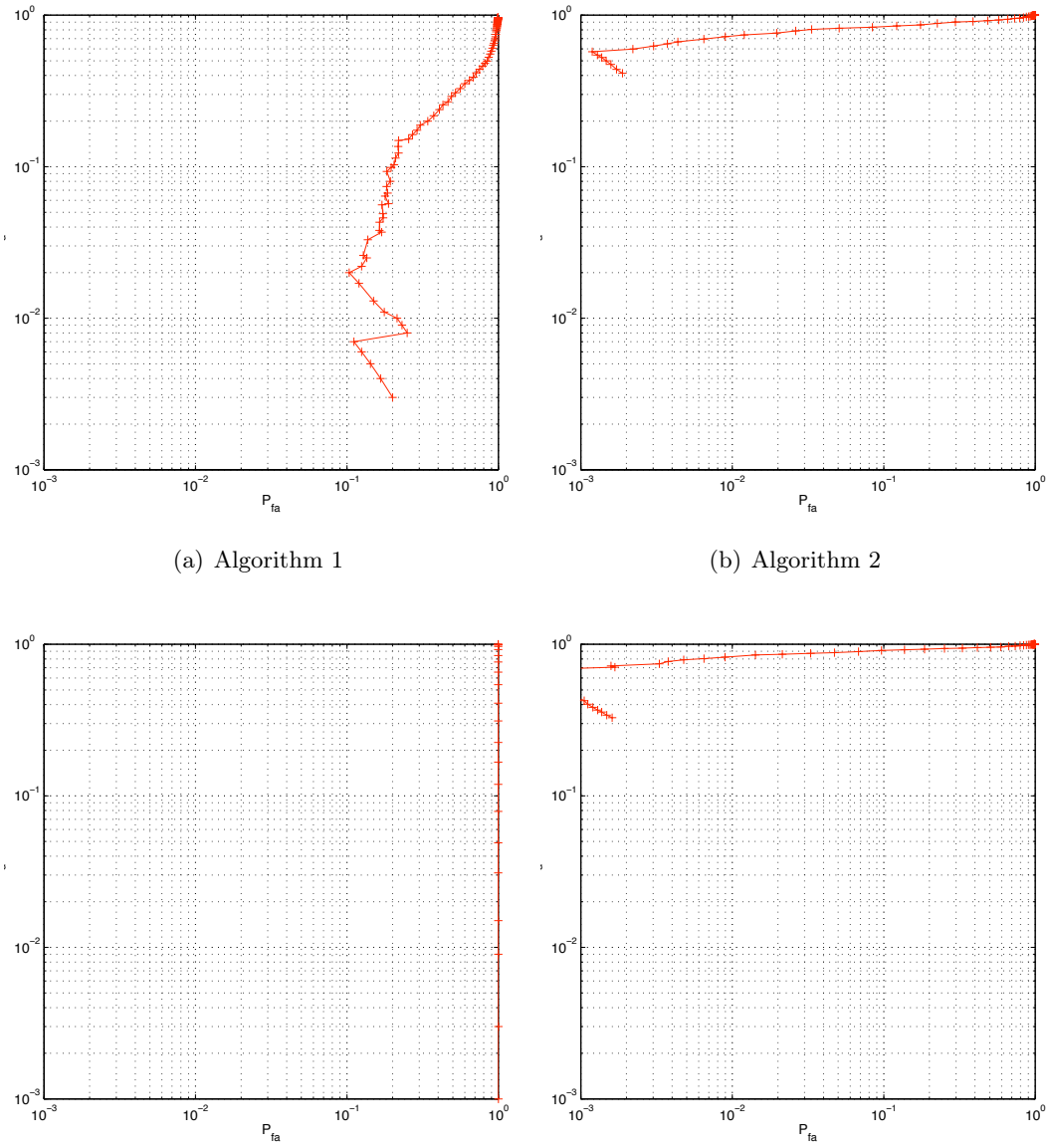

(a) Algorithm 1

(b) Algorithm 2

(c) Algorithm 3

(d) Algorithm 4

Figure 6.16: *Result for images of size 128×128, contrast equal to 2 dB*

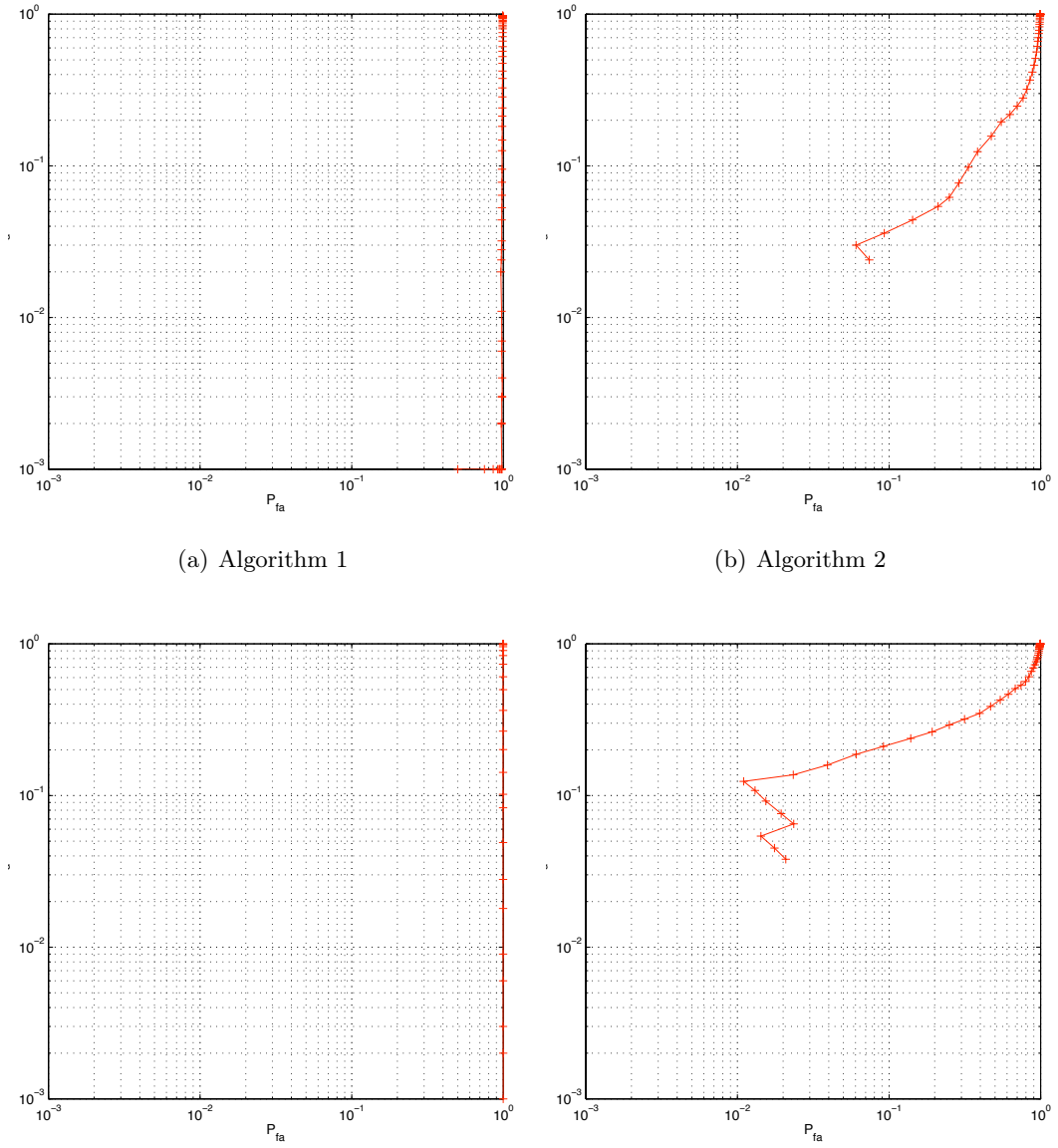

(a) Algorithm 1

(b) Algorithm 2

(c) Algorithm 3

(d) Algorithm 4

Figure 6.17: *Result for images of size 128×128, contrast equal to 1 dB*

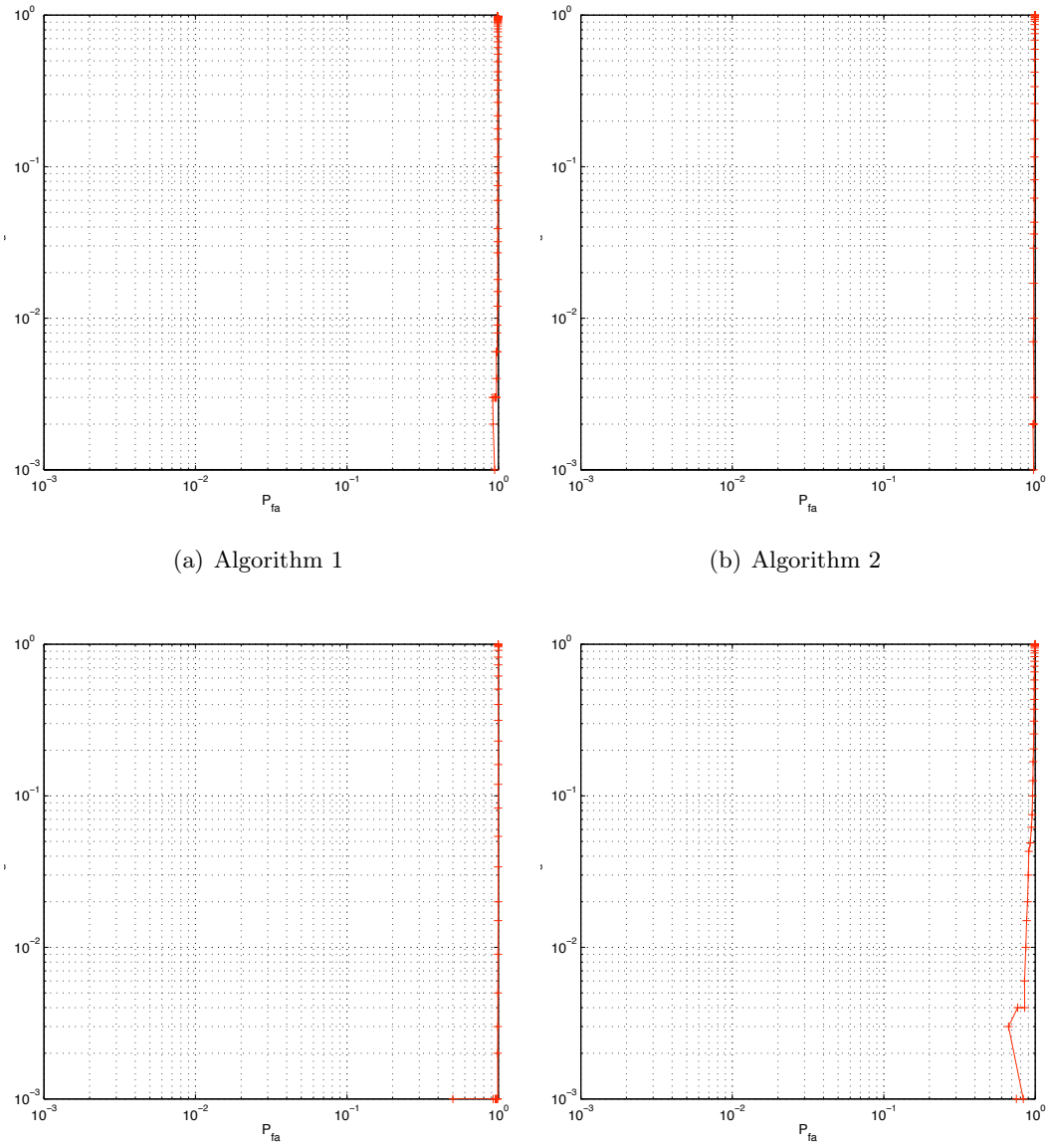

(a) Algorithm 1

(b) Algorithm 2

(c) Algorithm 3

(d) Algorithm 4

Figure 6.18: *Result for images of size 128×128, contrast equal to 0,5 dB*

Chapter

7 Detection of Kelvin Wake in High-Resolution Radar and Optical Images

Contents

As discussed in Chapter 3, wakes are highly visible elements in radar images. In low-resolution radar images obtained by observation satellites, it is possible to see wakes extending over several kilometers behind the ship. This wake appears as straight lines. Initially, a dark line is observed in the direction of the ship's travel, possibly framed by one or two bright lines: this is the turbulent wake. One can also see one, sometimes two bright lines extending on either side of the turbulent wake to form a cone typically with a 39 opening, with its apex at the stern of the ship: this is the radar image of the Kelvin wake. The previous chapter shows that line detection algorithms, supported by appropriate preprocessing and post-processing, can detect these lines, providing information about the presence of a ship, as well as its position and heading.

However, in low-resolution images, the Kelvin wake wave system inside the cone is not visible. These waves are only visible with higher-resolution side-looking radars, typically airborne. Detecting internal waves is interesting because it allows retrieving the wake spectrum, which is known to depend only on the ship's speed. The ship's speed is an additional element that can potentially be used to estimate the parameters of the ship's motion model to predict its trajectory.

In this chapter, which follows the previous one, we attempt to answer the question of detecting and analyzing the Kelvin wake waves in high-resolution radar images (as well as in high-resolution optical images since the method presented in this chapter is also valid for these data). Initially, we focus on the acquisition conditions of images to maximize the visibility of these waves (Section 7.1); the reflections presented in this section were published in our article "Investigating Possible Bistatic Configurations For Ship Wake Imaging

Through Simulation" [10] during the IEE Radar 2007 conference. Subsequently (Sections 7.2 to 7.4), we present an algorithm to recover the ship's speed parameters from raw radar or optical images. This algorithm uses a preprocessing step based on the generalized Radon transform of the wake, which is then thresholded using stochastic matched filtering. This algorithm was proposed in "Obtaining a Ship's Speed and Direction From Its Kelvin Wake Spectrum Using Stochastic Matched Filtering" [12], which we presented at the IGARSS 2007 conference. Additional reflections on this work are provided at the end of the chapter.

7.1 Choice of *a priori* design to enhance Kelvin wake visibility in radar imagery

The size of the variable space influencing the quality of the received image is very large, and we will not go into detail, as these elements are explained in the early chapters of this manuscript. It is, therefore, extremely difficult, if not unrealistic, to choose the "brutal" approach of testing each parameter individually. It is better to start with some simple *a priori* considerations to select certain configurations, then validate these configurations through more detailed simulation and sea trials, if possible. The rest of this section details the important parameters that will influence the quality of the final image.

7.1.1 Radar design choices

There are radar hardware design choices that will directly affect the visibility of desirable elements in the image, such as carrier frequency, polarization, modulation, and antenna (which influence resolution), *etc.* These elements are fixed before measurements are taken, *i.e.*, during the design of the equipment, and do not depend on the platform or acquisition geometry. When imaging the sea, the ability to directly measure heights by a variation in the distance traveled by the wave is often of lesser importance compared to the ability to distinguish waves using shadows and/or contrast differences between one side and the other of the waves. Indeed, these contrast differences create a visible periodicity effect, for example, in a Fourier transform. For this reason, we propose contrast as the first criterion to optimize. The choice of parameters is made based on this criterion.

7.1.1.1 Polarization

Some polarizations are better than others in maritime surface imaging. For monostatic radars, as discussed in Chapter 3 (Section 3.1.1.2), the HH polarization is considered better for imaging the Kelvin wake than the VV polarization, as HH polarization provides better contrast between the specular and diffuse zones, or between steeper and more moderate slopes. This allows for a better view of Kelvin wake waves. In fact, specular returns will tend to be comparatively more significant than diffuse returns. HH polarization also favors the visibility of ships. In contrast, VV polarization is considered better for the visibility of dead water wakes and hydrocarbon slicks. Cross-polarization is not yet widely used in consumer radars, although it is beginning to be available in satellite products as it provides even better contrast for medium incidence angles. The MaRS simulator confirms this in the monostatic case and suggests that bistatic cases yield similar results.

7.1.1.2 Frequency

The X-band is the most frequently used frequency band in maritime radar. Still, it has been shown that the L-band, with lower frequencies, can highlight several elements of the Kelvin wake, in the form of bright lines forming a cone of about 12 degrees around the

ship's direction of motion (see Chapter 3). This is because at these frequencies, the waves from that part of the wake resonate with radio waves. Additionally, this band is also used by positioning satellites (GPS, Galileo, *etc.*), even though the resolution of a bistatic radar using these opportunistic transmitters will be very low since the emission has a low bandwidth (about one megahertz), much less than a dedicated radar system. Another advantage is that diffuse reflection tends to decrease with frequency, further maximizing the contrast between the specular and diffuse zones.

7.1.1.3 Resolution requirement

Depending on what you want to observe, resolution requirements differ. With the resolutions currently available with radar satellites (about 30 m, as multiview imagery is generally used to reduce speckle noise), turbulent wakes and the transition between the wake and the undisturbed area in front of the Kelvin cone can be seen well, although less frequently than the turbulent wake. However, Kelvin wake waves, *i.e.*, those "inside" the cone, are not visible. To have a chance of seeing these waves, the ground resolution must be compatible with the wavelength of the Kelvin wake. For example, a ship traveling at a speed $V_b = 10$ knots generates transverse waves in the ship's direction with a wavelength equal to $2\pi V_b^2/g_0 = 17.2$ m, which means that the ground resolution must be at least 8.5 to 9 m for the image to be sampled respecting the Shannon-Nyquist criterion. This ground resolution criterion will affect both the distance axis resolution (and signal modulation) and the azimuth modulation (and antenna size).

7.1.2 Operational choices

Operational choices are those that will influence the observation configuration, *i.e.*, both the position of the transmitter and the receiver, the angle of incidence, the distance to the target, *etc.*, to maximize the visibility of the elements one wishes to observe.

7.1.2.1 Resolution

In monostatic configuration, the ground resolution in distance increases with the incidence angle θ according to the well-known relationship:

$$dr_{\text{sol}} = \frac{dr}{\sin\theta} \tag{7.1}$$

where dr is the resolution on the distal axis (in the bistatic case, the expression is given in Chapter 1, Section 1.6.2). This suggests, at least in monostatic configuration, the use of large incidence angles (or, in other words, shallow grazing angles) to maximize resolution. Moreover, the slope of the waves will influence their reflectivity. This slope will vary with the wind speed (for the sea in general) and the shape of the ship's hull in the wake zone. If one wishes to maximize wave contrast, a very shallow incidence is also desirable because the backs of the waves will tend to appear darker while the visible faces will be brighter. Once this contrast is maximized, it will allow for a better estimation of the spatial frequency of the waves.

7.1.2.2 Platform altitude

A low grazing angle is more easily obtained for a platform flying at low altitude. However, in the case of an aircraft, atmospheric turbulence in the troposphere must be taken into account, which could blur the images due to sudden movements in the pointing direction of the antenna. In the case of a satellite, flying at a low altitude (*e.g.*, 200 km) is costly

because residual atmospheric friction tends to slow down the satellite: a significant amount of fuel will be needed to keep the satellite in place. This results in a shorter lifespan than a satellite flying at a higher altitude. Additionally, to power the radar system, it is preferable to use solar panels continuously rather than a battery, imposing a heliosynchronous orbit at an altitude of approximately 800 km. Annex B shows that most Earth observation radar satellites use a heliosynchronous polar orbit.

7.1.2.3 Minimizing sea clutter based on position

The last point to address concerns the limitation of sea clutter. Simulations in Chapter 5 and experimental data show a strong dependence between the sea clutter shape and the incidence angle (on the one hand) and the angle between the radar's line of sight and the wind direction (on the other hand). As seen in Section 5.3.2.2, sea clutter tends more toward a Rayleigh distribution as the incidence decreases, and as the radar looks in the direction of wave propagation, resulting in much less dispersion of pixel intensity in the image.

7.1.2.4 Swath and time on target

For a practical application, one wants to maximize the observed area. The largest swath is obtained either for orbiting radars (up to 500 kilometers, but with low resolution – typically 100 meters) or for trans-horizon radars emitting in the HF band (but again, with low resolution). Since the resolution requirement is strongest for wake detection applications, one will have to settle for a limited swath.

Nevertheless, it is possible to find a good compromise between swath and resolution on an airborne SAR system at high altitude. To give an idea with a current system, the American high-altitude, long-endurance drone RQ-4A *Global Hawk* is reportedly capable of covering 40,000 square nautical miles per day, around 137,000 km^2, roughly a quarter of metropolitan France, at a resolution of 6×6 meters in scanning mode, and even more in *spotlight* mode (see Annex B for more detailed characteristics). The balance is therefore not so negative.

As for current radar satellites, flying in a heliosynchronous orbit also has an impact on the time spent over the target area. The heliosynchronous polar orbit allows imaging the entire Earth: with each orbit, which lasts about 100 minutes, the Earth will have rotated a bit on itself (about 2800 km at the equator), and the satellite's ground track will be different. The satellite will pass directly above the same point after a cycle whose order of magnitude is about 30 days and will return to the vicinity (within a few kilometers) of that point after a sub-cycle of about three days. This granularity is very low and does not allow imaging the same area continuously with a single satellite. Moreover, the date and time of passage of these satellites over a zone are well known, allowing for a reaction in case one seeks to avoid detection by these satellites.

7.1.2.5 Operational requirements for bistatic cases

Bistatic configurations could be chosen for two reasons: firstly, to optimize wake visibility, and secondly, for cost reasons – in the hope of using only an opportunistic transmitter – or for reasons of discretion.

Use of Opportunistic Transmitters If an opportunistic transmitter is used, well-known and continuously available emissions should be favored to maximize the bistatic system's usage time. One could think of GPS emissions or public radio, television, or GSM relay stations. Moreover, these emissions are usually omnidirectional, allowing the receiver to be

placed anywhere as long as the link budget remains good. Unfortunately, these emissions are often of very narrow bandwidth, for spectrum congestion minimization reasons:

- GPS: the band is of the order of megahertz, giving a ground resolution of less than 150 m after compression;
- terrestrial digital television: the European standard DVB-T allows emissions on channels of 5, 6, 7, or 8 MHz wide, *i.e.*, less than 30 m to 18.75 m in distance resolution.
- GSM stations: 25 MHz of bandwidth, subdivided into 125 channels of 200 kHz;
- FM radio stations: about 200 kHz of bandwidth at best;

The fact that these modulations are often continuous complicates things. Moreover, it should be remembered that these emissions are only available close to the coast (except for GPS). In the end, bistatic experiments using these opportunistic sources have had mixed results in applications with a strong resolution requirement.

Use of Cooperative Transmitters in the Atmospheric Domain The use of cooperative sources significantly simplifies the implementation of the bistatic radar system. To choose the ideal configuration, one can start by studying resolution. In bistatic configuration, resolution degrades with the angle between the pointing axes of the transmitter and the receiver antennas (see Chapter 1, Section 1.6). This observation tends to favor, in the bistatic case, configurations where the pointing axes of the antennas are in the same plane (configurations 3 and 4 in Chapter 5). Non-parallel BiSAR configurations (such as the one illustrated in Figure 1.13 in Chapter 1) assume that the antennas of the transmitter and the receiver are steered to illuminate the same spot, which is a challenging technical problem. This type of configuration also favors working in *spotlight* mode (both antennas point to a fixed point in the scene), which improves resolution and flexibility but limits the swath.

Moreover, in the case where two carriers fly in parallel, the obtained images are qualitatively similar to the monostatic case, as shown in Chapter 5 when comparing Configuration 3 with SAR Configurations 1 and 2. Since, in general, it will not be feasible to fly two aircraft in concert to image an area, it seems logical to settle for the monostatic SAR configuration to do the job.

Use of Spaceborne Transmitters The availability time of the satellite on the ground for bistatic applications is related to the orbits of the satellites. In heliosynchronous polar orbit, this time is of short duration with low time repetitiveness (every three days). However, this repetitiveness increases with the number of satellites in orbit. It is also possible to imagine placing transmitters in geostationary orbit to illuminate a larger area, but the power budget will be lower. Only a small number of such transmitters, three or four, is needed to illuminate most of the Earth (except at the poles), as the Earth is seen at an angle of about 17 degrees from geostationary orbit, allowing 42% of the planet to be visible. Dedicated radar satellites (*i.e.*, emitting a wideband pulsed signal) are not currently in orbit. However, BiSAR applications with geostationary relay satellites have been recently tested [118].

Conclusion In the context of Kelvin wake imaging, airborne SAR imaging seems ideal from an operational standpoint. If one wishes to use a bistatic system, the only bistatic configuration that seems to have some operational interest for wake imaging at first glance is Configuration 4 in Chapter 5: a ground-based transmitter, an airborne receiver, or vice

versa. This configuration also has the advantage of clearly highlighting the wake waves through the alternation of well-illuminated and non-illuminated slopes, making it easy to detect them and calculate their period. On the downside, antenna steering is required, necessitating a dedicated communication link between the transmitter and the receiver. This link does not exist today. Indeed, given the implementation difficulties, the gain provided by a bistatic configuration seems to be *extremely marginal* for a Kelvin wake imaging application.

7.2 The problem of Kelvin wake detection and analysis

In the following, it is assumed that one wishes to detect and analyze the Kelvin wake of a ship in a sufficiently well-resolved image, acquired by radar or an optical sensor. The principle of the method we are going to develop is, with a few adaptations, the same in the case of radar imaging (possibly bistatic) and in the optical case.

7.2.1 Kelvin wake height map in the world coordinate system

Theory shows that the elevation function ζ_w of the sea surface at point (x, y) can be described as the superposition of sinusoidal waves, each with a certain direction θ, a certain amplitude, and a certain phase $\phi(\theta)$. In the case of a perfectly flat sea in the presence of only the Kelvin wake, Chapter 3, page 94, equation 3.15 established that in the ship's frame of reference $\mathcal{B}$:

$$\zeta_w(x_b, y_b) = \mathfrak{R} \int_{-\frac{\pi}{2}}^{+\frac{\pi}{2}} A_{V_b,Y}(\theta) e^{-\jmath\phi(\theta)} d\theta \tag{7.2}$$

with:

$$\phi(\theta) = \frac{g_0}{(V_b \cos\theta)^2} [x_b \cos\theta + y_b \sin\theta] \tag{7.3}$$

where $A_{V_b,Y}$ is the Kochin function, parametrized by the ship speed V_b and the hull shape function Y. In the world frame $\mathcal{W}$, calling θ_b the ship heading, we can always write:

$$\begin{cases} \zeta_w(x, y) = \mathfrak{R} \int_{-\pi/2}^{\pi/2} A_{V_b,Y}(\theta) \exp(-\phi(\theta)) d\theta \\ \phi(\theta) = \jmath K_{V,\theta_b}(\theta) [x \cos(\theta - \theta_b) + y \sin(\theta - \theta_b)] \end{cases} \tag{7.4}$$

Here, $K_{V_b,\theta_b}(\theta)$ is the wave number of the waves traveling in the direction θ in the ship frame:

$$K_{V_b,\theta_b}(\theta) = \frac{K_b}{\cos(\theta - \theta_b)^2} \tag{7.5}$$

where $K_b = g_0/V_b^2$ is the wave number associated with the ship and g_0 is the acceleration due to gravity. It is useful to consider the *analytic representation* $\tilde{\zeta}_w$ of ζ_w:

$$\tilde{\zeta}_w(x, y) = \zeta_w(x, y) + \jmath \check{\zeta}_w(x, y) \tag{7.6}$$

where $\check{\zeta}_w$ is obtained by the Hilbert transform of ζ_w [197]. Then we have:

$$\tilde{\zeta}_w(x, y) = \int_{-\pi/2}^{\pi/2} A^{\star}_{V_b,Y}(\theta) \exp(-\phi(\theta)) d\theta \tag{7.7}$$

where $\star$ denotes the conjugate. It is then shown that the Fourier transform $\tilde{Z}_w$ of ζ_w, using (K_x, K_y) as coordinates in the Fourier plane, is:

$$\tilde{Z}_w(K_x, K_y) = \int_{-\pi/2}^{+\pi/2} A^{\star}_{V_b,Y}(\theta)\delta(g_{V_b,\theta_b}(K_x, K_y))d\theta \tag{7.8}$$

where δ is the Dirac distribution and the function g_{V,θ_b} defines the locus (k, θ) of the wake spectrum; this function must satisfy the equation (7.5), thus:

$$g_{V_b,\theta_b}(K_x, K_y) = 0 \overset{\triangle}{\Leftrightarrow} \sqrt{K_x^2 + K_y^2} - \frac{K_b}{\cos^2(\arctan(K_y/K_x) - \theta_b)} = 0 \tag{7.9}$$

This spectrum lives in the half-plane defined by the inequality:

$$K_x \cos\theta_b + K_y \sin\theta_b \geq 0 \tag{7.10}$$

It is then possible to go back to the Fourier transform Z_w of ζ_w. Indeed both transforms are linked by a key property of the Hilbert transform: for any function s of analytic representation $\tilde{s} = s + \jmath\check{s}$, its Fourier transform is:

$$\tilde{S} = S + \jmath\check{S} \tag{7.11}$$

where:

$$\tilde{S}(f) = [1 + \mathrm{sgn}(f)]S(f) \tag{7.12}$$
$$\check{S}(f) = -\jmath\,\mathrm{sgn}(f)S(f) \tag{7.13}$$

This relation (7.11) can be extended to 2D using the following set of equations [197]:

- for K_x, K_y such that $K_x \cos\theta_b + K_y \sin\theta_b > 0$:

$$\check{Z}_w(K_x, K_y) = -\jmath Z_w(K_x, K_y) \tag{7.14}$$
$$\tilde{Z}_w(K_x, K_y) = 2Z_w(K_x, K_y) \tag{7.15}$$
$$Z_w(K_x, K_y) = \frac{1}{2}Z_w(K_x, K_y) \tag{7.16}$$

- for K_x, K_y such that $K_x \cos\theta_b + K_y \sin\theta_b > 0$:

$$\check{Z}_w(K_x, K_y) = 0 \tag{7.17}$$
$$\tilde{Z}_w(K_x, K_y) = Z_w(K_x, K_y) \tag{7.18}$$

- for K_x, K_y such that $K_x \cos\theta_b + K_y \sin\theta_b < 0$:

$$\check{Z}_w(K_x, K_y) = \jmath Z_w(-K_x, -K_y) \tag{7.19}$$
$$\tilde{Z}_w(K_x, K_y) = 0 \tag{7.20}$$
$$Z_w(K_x, K_y) = \frac{1}{2}Z_w(-K_x, -K_y) \tag{7.21}$$

Figure 7.1(b) illustrates this result by showing the Fourier transform of Figure 7.1(a), with the locus of the spectrum satisfying equation (7.9).

7.2.2 Modulation transfer function linking the height map to the received image

In remote sensing, only an image $I(i,j)$ of the surface defined by $z = \zeta(x,y)$ is known; this image is acquired by a camera or radar. The coordinates i,j are pixel coordinates in the image at the acquisition resolution. The Kelvin wake height map $\zeta_w(x,y)$ is not known. In SAR imaging, however, it is possible to relate the spectrum of I to the spectrum of ζ_w through a modulation transfer function $\mathcal{F}[H_{\mathrm{MTF}}]$ [5, 91]; the same can be done with optical images. In all cases, we have:

$$\mathcal{F}\left[I\right](\kappa_i,\kappa_j) = \mathcal{F}[H_{\mathrm{MTF}}](K_x,K_y)\mathcal{F}\left[\zeta\right](K_x,K_y) \tag{7.22}$$

In equation 7.22, the left term is a Fourier transform in the spatial frequency plane of the image κ_i and κ_j; and the right term is a Fourier transform in the frequency plane of the elevation map.

To illustrate the concept of the modulation transfer function, we have mainly developed the theory in the context of Optics. The functions involved in Optics are simpler than in Radar, making it easier to grasp the ideas, while knowing that the results we need in the following are qualitatively the same in both domains. However, to stay focused on our main exposition, this work is relegated to Appendix E. Moreover, the problem of the transfer function has probably been more extensively studied in the literature in the Radar domain than in the Optics domain. Interested readers can refer, for example, to Hasselmann and Hasselmann [91] or Krogstad [110, 111] for the modulation transfer function theory in monostatic radar, and to Wang *et al.* [185] for computational aspects in the bistatic case. One of the advantages of this digression into the Optics domain is to show that the work presented in the rest of this chapter can be used for both optical and radar images. Another advantage is that it is also very easy to obtain a large quantity of real optical images to validate our approach, which is not the case for radar images.

7.3 An algorithm for Kelvin wake detection in optical and radar images

7.3.1 Problem

If we assume that the modulation transfer function $\mathcal{F}[H_{\mathrm{MTF}}]$ is nearly linear – which is the case in both Optics and Radar – then the locus of the wake spectrum in the Fourier spectrum of the image I is generally the same as in Z_w. There may be a trivial distortion if the image does not have the same resolution on both sides, but we will assume later on that the resolutions are identical.

The problem of detecting the Kelvin wake in the image is then equivalent to detecting the wake spectrum in the spectrum of the image. However, it is crucial to do this in a robust way since the wake spectrum will be embedded in the spectral components coming from other waves. The only approach we know so far, using the spectral approach, was proposed by Wu *et al.* [197]; to our knowledge, it is also the only document closely examining the exploitation of the Kelvin wake in high-resolution data. Wu's approach involves detecting pairs of points (P_{1i}, P_{2i}) present on the wake spectrum locus, by thresholding this spectrum, and then using these points to determine an estimate (V_i, θ_0^i) of the ship's speed and heading. The final estimate of V_b and θ_b is obtained by averaging the V_i and θ_b^i. We believe that this method is not very robust since only a small number of points detected in the wrong place are enough to corrupt the average. Even if a RANSAC[1]-like scheme [67]

[1] RANSAC stands for "Random Search And Consensus".

is used to reject bad points, it is better to try to go back to the basics of the method by improving wake detection.

7.3.2 The algorithm

In the following paragraphs, we will detail the steps implemented in the algorithm we propose to improve the detection of the wake spectrum. The input to the algorithm is an optical or radar image denoted I with geometric characteristics similar to those of a surface image seen from a "top-down" point of view (which may require correcting the perspective in optics and switching to ground resolution for radar). The algorithm itself is divided into three steps. First, a preprocessing step on the Fourier transform of the image is performed. Then, we perform a Generalized Radon Transform (GRT) on this Fourier transform. Finally, we threshold this transform to detect a peak corresponding to a wake. The output of the algorithm is information about the presence or absence of the wake, and in case of presence, it provides the speed and direction of the ship's trajectory.

7.3.2.1 Preprocessing

We start by computing the amplitude of the 2D Fourier transform of I. We then attenuate the low frequencies in the Fourier transform to limit false alarms later (in our implementation, the cutoff frequency was set to 10 cycles[2]). The contrast of the Fourier transform is then enhanced using a high-pass filter. We denote $F(K_x, K_y)$ the result of this preprocessing.

7.3.2.2 Generalized Radon Transform

To detect the wake, two things are desirable: first, we want to improve the signal-to-noise ratio of the spectral signature of the wake; then we want to reduce the spatial extent of this signature to detect it more easily. The general idea is to concentrate all the energy of the wake spectrum in as concentrated a peak as possible so that this peak can stand out from the rest of the spectral components, which are seen as noise. To do this, we will calculate the sum of the spectrum of F for all its possible locations, or for all possible pairs (V_b, θ_b), as these two parameters uniquely define a wake. If a wake is truly present in the image, then the sum will be very significant for the particular value of V_b and θ_b that corresponds to this wake, and low for all other values of V_b and θ_b. It is nothing more than the Generalized Radon Transform (GRT) of the image for a family of curve parameters (V_b, θ_b) with $g_{V_b,\theta_b}(K_x, K_y) = 0$ as an implicit equation. The transform R of F for a wake with parameters (V_b, θ_b) will be:

$$R(K_{V_b}, \theta_b) = \iint_{-\infty}^{+\infty} F(K_x, K_y)\delta\left(g_{V_b,\theta_b}(K_x, K_y)\right) dK_x dK_y \tag{7.23}$$

where δ is the Dirac distribution. Alternatively, we can note that a particular point of F located at coordinates (K_x, K_y) can intercept a whole family of wake locations with parameters (V, θ_b), or (K_b^0, θ_b), defined by the equation

$$K_b(\theta_b) = \sqrt{K_x^2 + K_y^2}\cos^2\left(\arctan(K_y/K_x) - \theta_b\right) \tag{7.24}$$

These curves are sinusoids in the plane of axes (K_b, θ_b). After calculating the GRT of F, the local mean is subtracted from the result R to give a function R', which improves the visibility of the peak that is present if a wake is in the image.

[2]For an image whose width n corresponds to one unit of length.

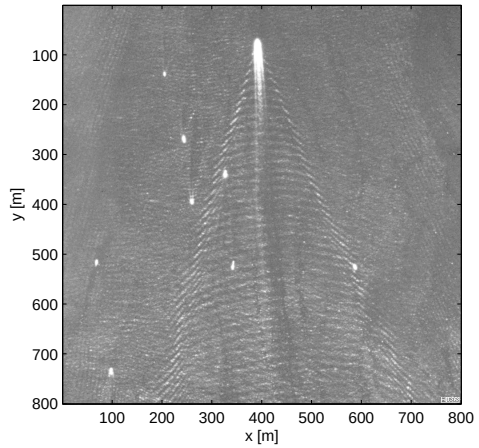

(a) Original optical image, side length L=800 m

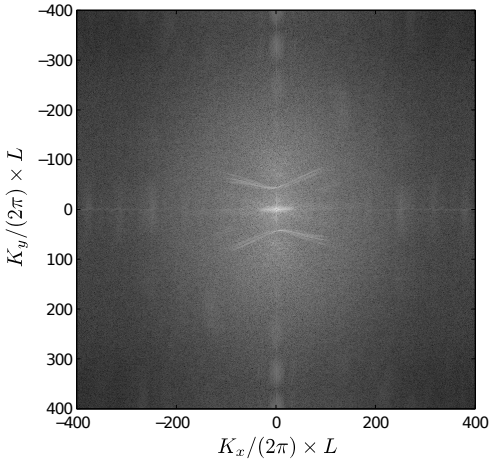

(b) 2D Fourier transform magnitude

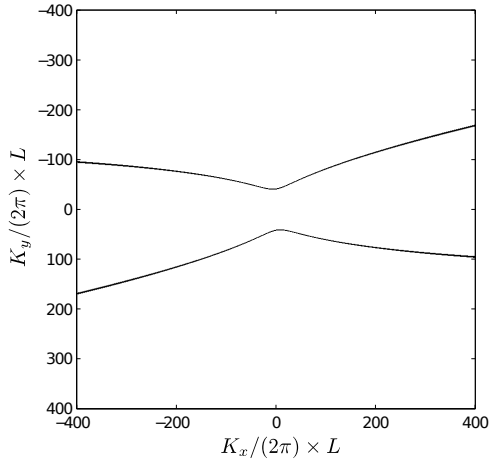

(c) Spectrum locus in the transform

Figure 7.1: *An optical image of a Kelvin wake (source: USGS) and the locus of the spectrum in the Fourier plane. We measure about 50 cycles over 800 m, corresponding to a wavelength of about 15 meters, as found in the original image a).*

7.3.2.3 Thresholding

The thresholding problem of the Radon transform is exactly the same as in the previous chapter. The position (K_b, θ_b) in the GRT of a detected peak gives the speed and direction of the ship. Therefore, we will not revisit the state of the art and the discussion that was conducted regarding thresholding in the previous chapter. However, as this is one of the most important steps of the algorithm, we will dedicate the following paragraph to improving the visibility of the peak through stochastic matched filtering. In the end, the algorithm follows the chain presented in Figure 7.2.

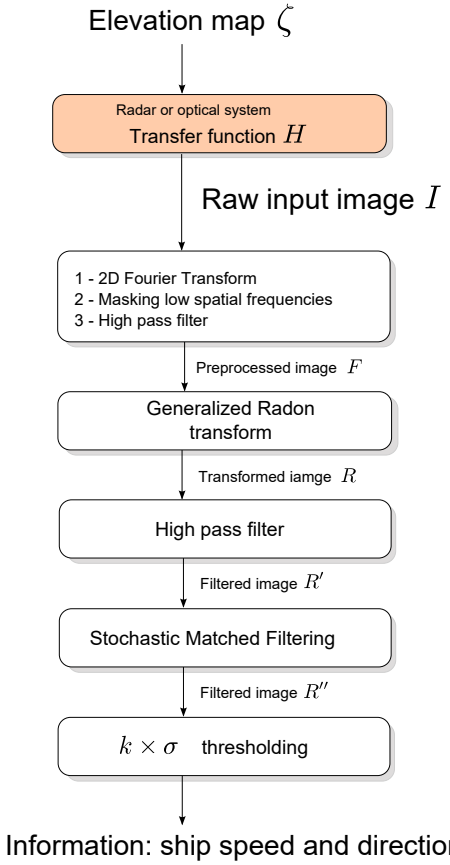

Figure 7.2: *Block diagram summarizing the acquisition and processing chain with our Kelvin wake detection and analysis algorithm. Note that we acquire not the height map but the raw image after the transfer function* H_{MTF}.

7.4 Improving thresholding with Stochastic Matched Filtering

We find ourselves, at the paragraph 7.3.2.3, in a situation very similar to that of chain 4 in Chapter 6, and within the theoretical framework defined in Appendix D, from which we take the notations. Here, the noise corresponds to the GRT of the wave spectrum in the image, while the signal corresponds to the signature of ship wakes, appearing as a peak whose shape can vary. Indeed, the shape of the signal fluctuates not only due to its position in the transform but also and especially due to the diversity in the shape of ship hulls, as well as the speed of the boats in the scene.

7.4.1 Construction of Stochastic Matched Filters

The construction of the battery of stochastic matched filters requires the estimation of the variance-covariance matrix of the signal and noise. This estimation can be done for a fixed-size window adapted to the size of the signal to be detected. We use simulation tools as well as real images for this. This process can be time-consuming (one day, in our case), but it can be done offline. Following Appendix D, we will denote `P` and `Q` as the variance-covariance matrices of the signal and noise, respectively.

First, it is necessary to estimate the typical size of the window adapted to the signal. This can be done through trial and error; in our case, we chose a square window of nine pixels wide (*i.e.*, $n = 9 \times 9 = 81$ entries). The window must capture the essential energy of the signal without being too large, so as not to demand too many samples for the estimation of the variance-covariance matrix. There must be at least n realizations of a signal window and noise window because for a smaller size, the estimated variance-covariance matrices would become singular. We can then calculate the stochastic matched filters $\{\mathbf{h}_i\}$ associated with the eigenvalues of the problem, $\{\lambda_i\}$, these eigenvalues allowing the thresholding of the signal (see Appendix D, paragraph D.6).

7.4.1.1 Estimation of `Q`

We apply the entire chain of preprocessing and Generalized Radon Transform to a set of real images that do not contain wakes. The images were taken in various sea conditions, different observation directions, and potentially with features such as the presence of internal waves or streak zones, locally disturbing the shape of the surface.

We worked with 64 optical images without wakes, sized 600×400 and with a resolution of 1 m (Figures 7.7 and 7.7), randomly taking several windows in the R' plane per image to sample the noise in the R' plane; in the end, we have 1000 pure noise windows. Note that the number of samples taken to generate pure signal and pure noise windows is relatively arbitrary; the essential thing is to find a compromise between diversity and a reasonable computation time.

For each image, we then chose a certain number of sub-windows in which we are certain that there is no noise. We then calculate the variance-covariance matrix C_n. This matrix has a dominant diagonal, showing that noise in the Radon transform is spatially uncorrelated.

7.4.1.2 Estimation of `P`

To estimate the signal, we must work in the absence of noise, forcing us to work with a model. We therefore considered nine classes $C_i, i \in [1..9]$ of "representative" hulls: pleasure sailboat, cruise ship, coastal patrol boat, frigate/destroyer, tanker, periscopic attack submarine, and Wigley-type parabolic hulls with different length/width ratios (4, 5, and 6). For each class C_i, we have a prototype hull model Y_0^i; for example, for the attack submarine class, it is a Los Angeles-class submarine (SSN 688); for the frigate/destroyer class, the chosen hull is the DTMB 5415; for the other classes, generic 3D models were used. Other ships $Y_j^i, j \geq 1$ are scaled versions of Y_0^i, with a length L_j^i and a speed V_j^i.

Here is how ships of each class are generated. We aim to vary the length and speed parameters (assuming that the width parameter is proportional to the length parameter, with the proportionality factor related to the class i; this is a somewhat arbitrary but significantly simplifying choice). The speeds V_b are chosen so that the associated wave numbers $K_b = g_0/V_b^2$ evolve with a step of one meter per second between 1 m/s and 13 m/s. For each speed, we generate (arbitrarily) 50 ships, making a total of 650 ships. The length of these ships is drawn from a normal distribution, with the mean being the

length of the class prototype, and the standard deviation $\sigma_i^{L_b}$ a parameter of the class chosen to be representative of the typical size of ships in that class. Similarly, the speed range for a class of ships is defined as a Gaussian centered at zero with standard deviation $\sigma_i^{V_b}$ (for negative speeds, a new value is drawn). Figure 7.3 shows the distribution of ships used here.

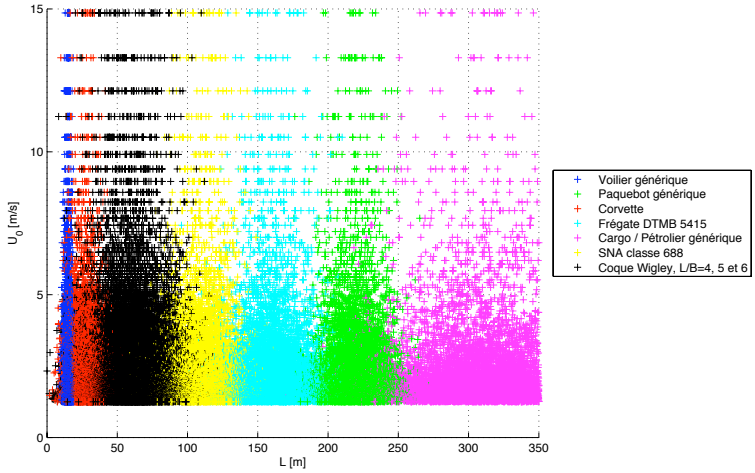

Figure 7.3: *Distribution of the 650 ships used to generate a bank of pure signals. The legend indicates the class of the ships.*

For each reference model Y_0^i, we can calculate the wake wave amplitude function $A_{Y_0^i}(V_b, \theta)$ (*cf.* 7.4) for all angles θ and a wide range of speeds V_b very finely sampled. We do this by integrating over the ship hull as explained in Chapter 3. This operation takes some time (about 40 s in our case), so we only do it for the class prototypes. Figure 7.4(a) shows the prototype of the periscopic attack submarine class, while Figure 7.4(b) shows the magnitude of its Kochin function $|A_{Y_0^i}(V_b, \theta)|$, with $\theta \in [-\pi/2, +\pi/2]$ and V_b between 0.3 and 12.8 m/s.

We can deduce the amplitude function $A_{Y_j^i}(V_b, \theta)$ for the ship Y_j^i from that of the class prototype Y_0^i. Indeed, two ships differing only in their scale and sharing the same Froude number $\mathrm{Fr} = V_b/\sqrt{g_0 L_b}$ will have the same wake with waves whose amplitude is proportional to the length of the ship. Therefore, if we have the input speed V_j^i, the length L_j^i of the i-th ship in the class j, and we know the length of the class prototype L_0^i, we can calculate the corresponding speed for the prototype V_0^i using the equality of Froude numbers, and the amplitude function of the ship hull Y_j^i becomes:

$$A_{Y_j^i}(V_j^i, \theta) = \frac{L_j^i}{L_0^i} A_{Y_0^i}\left(\sqrt{\frac{L_j^i}{L_0^j}} V_0^i, \theta\right) \tag{7.25}$$

By knowing the amplitude function $A_{Y_j^i}(V_j^i, \theta)$ and the location of the spectrum $g_{V_j^i}(K_x, K_y)$, we can simulate an image F as it would be obtained by the preprocessing obtained in paragraph 7.3.2.1; then we can calculate the generalized Radon transform R' of F; and then we can extract a window containing the peak of R' corresponding to the wake. We can then add this window to the set of noiseless signals that will be used to calculate the covariance matrix of the pure signal $\mathtt{P}$. Figure 7.5 shows an example of such an ideal signal.

The amplitude function $A_{Y_j^i}(V_j^i, \theta)$ alone is not sufficient to define the received image, as seen earlier; it is necessary to apply the transfer function specific to the sensor (*cf.*

paragraph 7.2). This also requires considering the incidence angle and the direction of the sensor (in optics) or the radar system (possibly bistatic) as random variables. Since we analytically have the Fourier transform of the wake, and it is located on a curve in complex space, it is much more advantageous to work with the "transfer function" approach, rather than generating a wake map ζ_w and working in natural space. We therefore directly generate the Fourier transform of the observed image without generating a wake map or calculating the rendering of that map.

Once these pure signals are obtained, we can also directly apply the processing of our detection chain in the Fourier plane, then calculate the generalized Radon transform, in order to ultimately obtain the signal in the R' plane. This signal forms a peak, of variable size and shape, but living in a low-dimensional space: a window `W` of 9×9 pixels at most. Figure 7.5 illustrates these ideas by showing the appearance of the generalized Radon transform of such a wake in the absence of noise.

7.4.2 Experiments on real optical images: protocol

Used Data We have two databases: one containing images of sea without wake (Figures 7.7 and 7.8), the other containing wake images (Figures 7.9 and 7.10). These images were obtained from `terraserver-usa.com`[3], and are of the same size and resolution: 600×400 pixels at 1 m resolution. There are 64 images in each database.

A limitation of the stochastic matched filtering test on real data Real images have the immense advantage of not being a simplified model. However, one does not always have all the desirable information, especially when working with data not explicitly acquired for testing purposes. In this case, there is a significant problem related to the overall gain of the signal simulation chain. On simulated data, calculating this gain is possible. On real data, such as those gathered on the Internet –the only ones easily available in quantity– a major drawback is that gain information is not available. The images are typically represented on 8 bits or 3×8 bits in color, and adjusted to be correctly exposed, with possibly a truncated histogram for extreme values (*clamping* or *histogram clipping*). This adjustment, or gain, is different from one image to another, and unknown. One cannot go back to the level of intrinsic signal or noise, *i.e.*, that obtained in an idealized acquisition without gain.

If the level of intrinsic noise were constant from one image to another, one could imagine normalizing the received images by the noise power, which is easy to estimate, and thus eliminate the gain (but not the histogram truncation). Indeed, globally the signal is made up of noise. The quantity of pixels corresponding to the signal is proportionally very small. Therefore, calculating a quantity such as the standard deviation will not be much biased by the presence of the signal and will correspond quite well to the threshold noise standard deviation. However, the level of intrinsic noise varies (with the sea state), while the signal level does not vary with the sea state: this asymmetric dependence on the sea state means that if one were to normalize the noise level, one would transfer the unknown to the signal level, which is not desirable. Overall, therefore, on real images acquired in an uncontrolled manner, we must work with an unknown gain in the end. This will not change the expression of the stochastic matched filters or the actual signal-to-noise ratio obtained, but only that of the *predicted* signal-to-noise ratio based on the eigenvalues $\{\lambda_i\}$, which no longer means anything.

Concretely, therefore, if such real data is used, one has only to calculate the filters $\{\mathbf{h}_i\}$ and try them out, keeping empirically only those that indeed improve the signal-to-noise

[3] As the images come from the U.S. Geographical Service, they are in the public domain.

ratio. We have therefore carried out this test by calculating the covariance matrix of the noise on our test base of 64 real images (Figures 7.7 and 7.8), by randomly taking several windows in the R' plane per image to sample the noise in the R' plane; we end up with a total of 1000 windows of pure noise. Note that the number of samples taken to generate the windows of pure signal and pure noise is relatively arbitrary, the main thing being to reach a compromise between diversity and reasonable computation time.

7.4.3 Result of tests on real optical images

Figure 7.6 presents the result of the processing on the image shown in Figure 7.1(a). The images are scaled so that the noise standard deviation is unity. It can be seen that the contrast in the image is better after using the stochastic matched filtering, and the spike corresponding to the ship wake is more visible. The signal-to-noise ratio is improved by 3.28 dB on this image, after using the stochastic matched filtering.

7.4.3.1 Processing time

The observed average processing time for 128 images, using Matlab[4], was 1.27 seconds for the entire processing, with 1.06 seconds in the Generalized Radon Transform (GRT). The input images had a size of 600×400 pixels; the output images were calculated for 180 angles with a one-degree step, and 360 pixels for the velocities, which is half the diagonal of the input image. The GRT was implemented in the C language using the naive algorithm[5], while taking care to precalculate elements as much as possible in the outermost loops, especially by tabulating trigonometric functions. This simple optimization gained us an 8x factor in computation time. The algorithmic complexity of the operation is $\mathcal{O}(n^2)$ where n is the size of the image side; this is the complexity of the Generalized Radon Transform, which cannot be computed by a Fourier transform like the Radon transform for lines. The complexity of the GRT dominates that of the Fourier transform in $\mathcal{O}(n \log n)$. It should be noted here that quadratic complexity becomes a concern for real-time applications.

7.5 Conclusion of this chapter

This chapter presented several considerations regarding the detection of Kelvin wake in high-resolution images, acquired either by radar or optical imaging.

In the first part, we briefly listed a number of parameters influencing the visibility of the Kelvin wake, which need to be optimized. The conclusions drawn from this analysis are as follows. First, it is desirable to have a sufficiently large incidence angle to increase the visibility of Kelvin wave patterns through shadows and minimize clutter. The use of HH polarization or cross-polarization is recommended. Finally, the ground resolution also influences the visibility of slow-moving ships: the higher the resolution, the more visible slow ships will be. The resolution requirement, along with the cost of the system, seems to favor airborne monostatic SAR systems or airborne BiSAR configurations with one of the two components (transmitter or receiver) on the ground, to the exclusion of any other bistatic configuration. However, the chosen bistatic configuration requires a cooperative transmitter, resulting in only marginal operational gain.

In the second part, we presented a new algorithm for Kelvin wake detection, designed to retrieve the speed and direction of the ship (*i.e.*, the heading with a π ambiguity). This

[4]Machine equipped with an Intel Core Duo processor, dual-core, clocked at 2.0 GHz, running MacOS X 10.5, 2 GB of RAM, with standard CPU load.

[5]It is not possible to optimize the GRT as in the linear case, where the Fourier slice theorem can be used, *cf.* the previous chapter.

algorithm is based on exploiting the locus of the wake spectrum, which depends only on the heading and speed, but not on the hull shape. The energy contained in the spectrum is then "compressed" into a peak in the plan of a generalized Radon transform adapted to the wake. We then tested the possibility of improving the visibility of this peak by using stochastic matched filtering. The construction of this stochastic matched filter involves building a reference wake database. To simplify the construction of this database, we work directly in the Fourier transform of the height map. We use a scheme that quickly generates a large number of different ship types from a small number of reference ship classes, whose wake amplitude function is known as a function of speed, using a parameterization by Froude number. We then show the influence of the transfer function to switch from the space of the height map to the received signal space. A transfer function in the optical case is presented, which is a generalization of the Kube and Pentland model modified by Chantler *et al.*, incorporating specular reflection (see Appendix E). The case of the radar transfer function is addressed by referring to the literature.

Regarding the validation of this method, we proposed an initial test on a real optical image database, showing the potential improvement brought by stochastic matched filtering. However, one can criticize the scope of this test, as the images used are not labeled in terms of ship type, sea state, or sensor configuration. Furthermore, it has been explained that it is not possible to use the by-product of stochastic matched filtering, which is the prediction of signal-to-noise ratio improvement. We are therefore reduced to setting the thresholds manually by trial and error. To test the algorithm more thoroughly, simulation is required. Similarly, we have not addressed an important question, which is to determine the minimum ratio between the amplitude of Kelvin wake waves and the amplitude of sea waves, allowing the detection of the Kelvin wake. This question is crucial as it determines up to what sea state and speed, for a given ship, it is possible to detect the wake.

We also discussed the computational time of the method, estimated at quadratic complexity in the number of pixels on the image side, for a computation time slightly over one second for a 600×400 pixel image (using Matlab). It should be noted that in theory, the application of the filtering scheme presented here should be applied to a sliding window, or at least to a large raw image partitioned into small images with overlap management in case the wake is at the edge of the image. All of this can make the computation time significant on a large image, but since the small images would be processed independently, it nevertheless opens the door to parallel processing. One could also imagine using the Kelvin wake analysis only after detecting a ship, which would likely be more robust. Finally, one could imagine using the filtering proposed here as a tool left to a human operator: the operator would draw a frame around a contact where the Kelvin wake is clearly visible, and the speed and heading information would be automatically calculated.

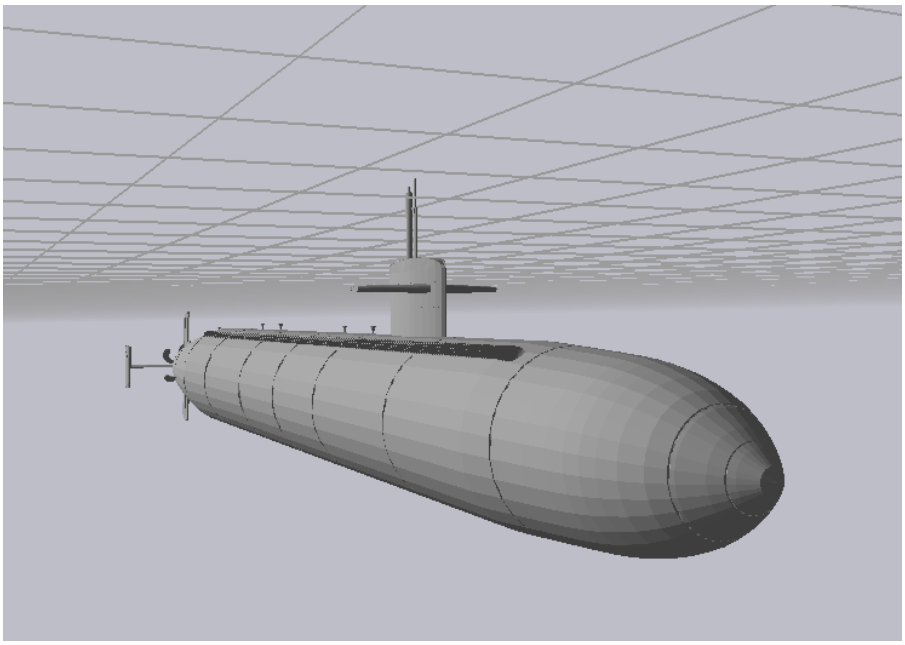

(a) Submarine in a situation in the MaRS graphical interface.

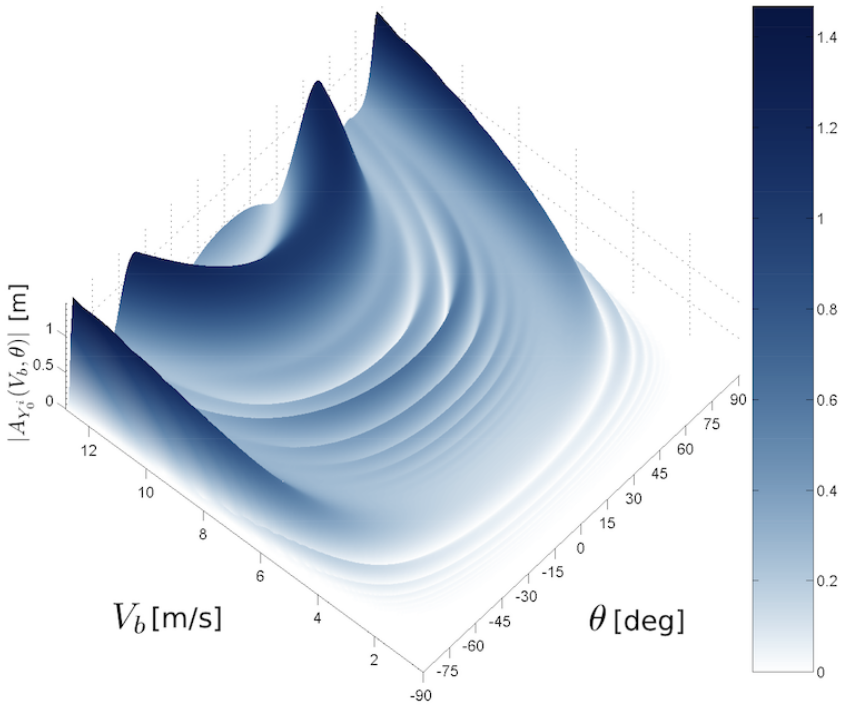

(b) Magnitude of the Kochin function $|A_{Y_0^i}(V_b, \theta)|$ of the submarine.

Figure 7.4: *Prototype of the periscopic attack submarine class 688 (length $L_b = 110$ m, width $B_b = 9.75$ m) and its amplitude function. The angle θ is taken in the ship's frame of reference $\mathcal{B}$.*

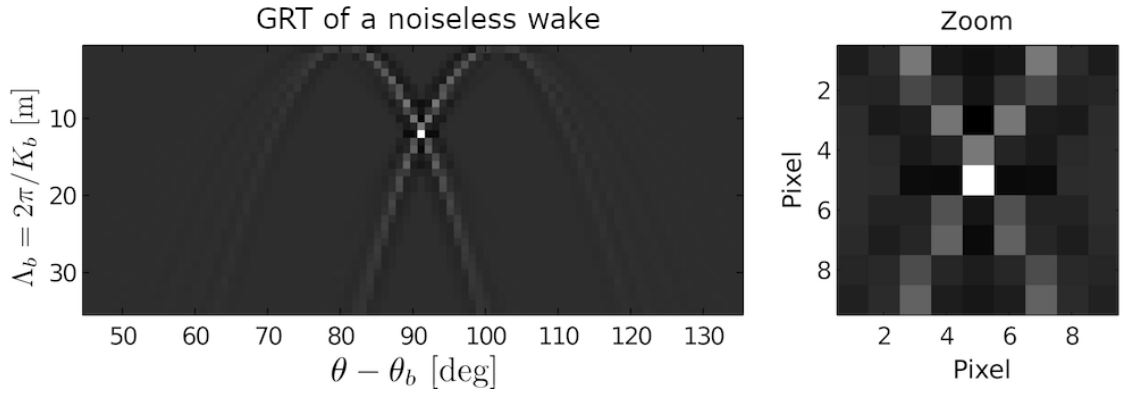

Figure 7.5: *Generalized Radon transform of a typical wake*

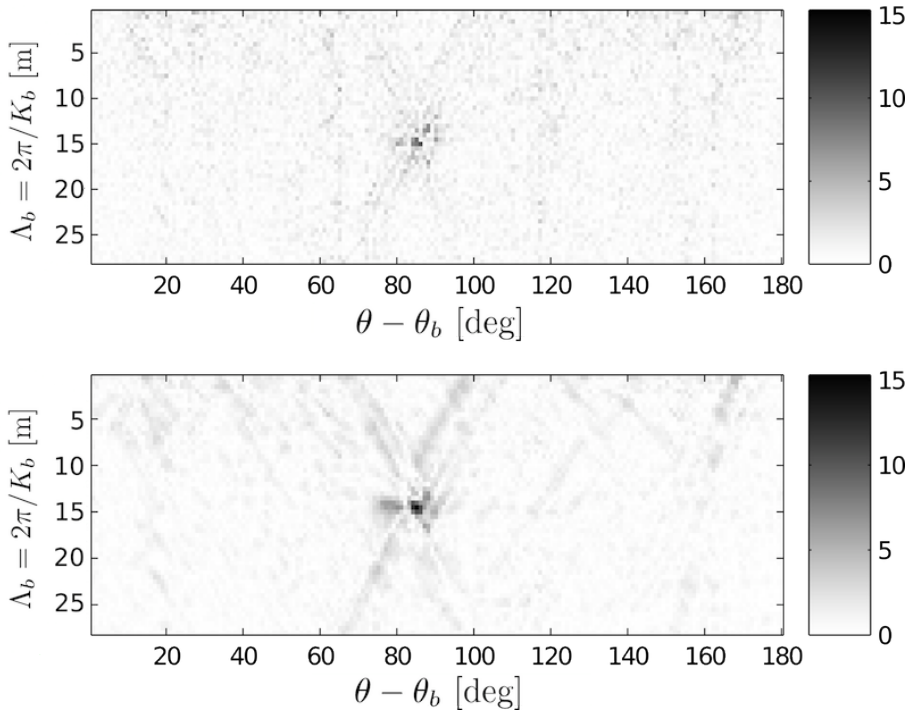

Figure 7.6: *Generalized Radon Transform of the elevation image shown in figure 7.1(a) (above) and result of the filtering by the best stochastic matched filter (below). Images are scaled so that the standard deviations be unit. The signal-to-noise ratio is improved by 3.28 dB on this image, after using the stochastic matched filtering. Along the ship's axis, the wake has a wavelength* $\Lambda_b = 15$ *m which is coherent with the measures in the original optical image: this corresponds to a realistic speed of 9.4 knots.*

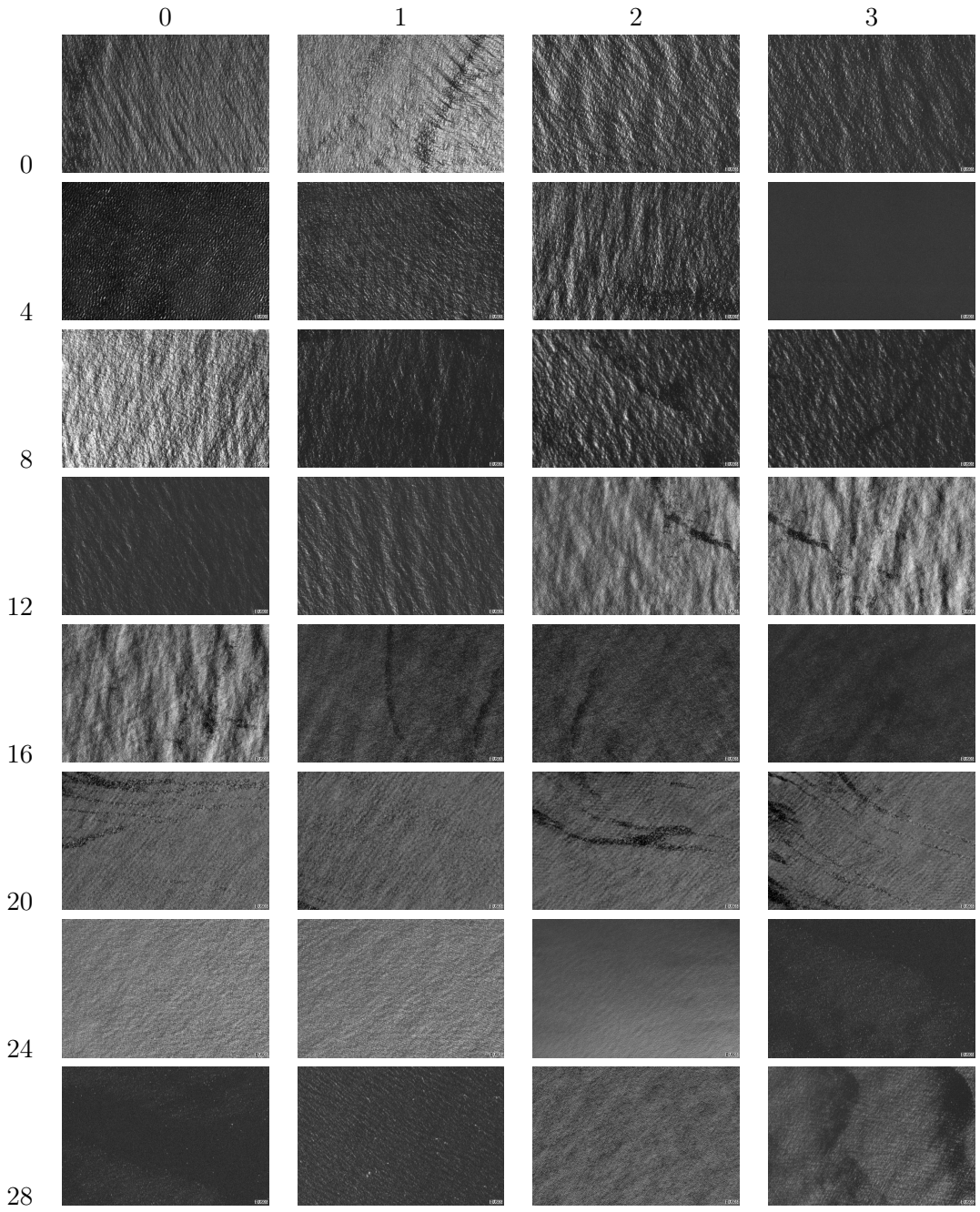

Figure 7.7: *The database of optical images of ocean surfaces without wakes*

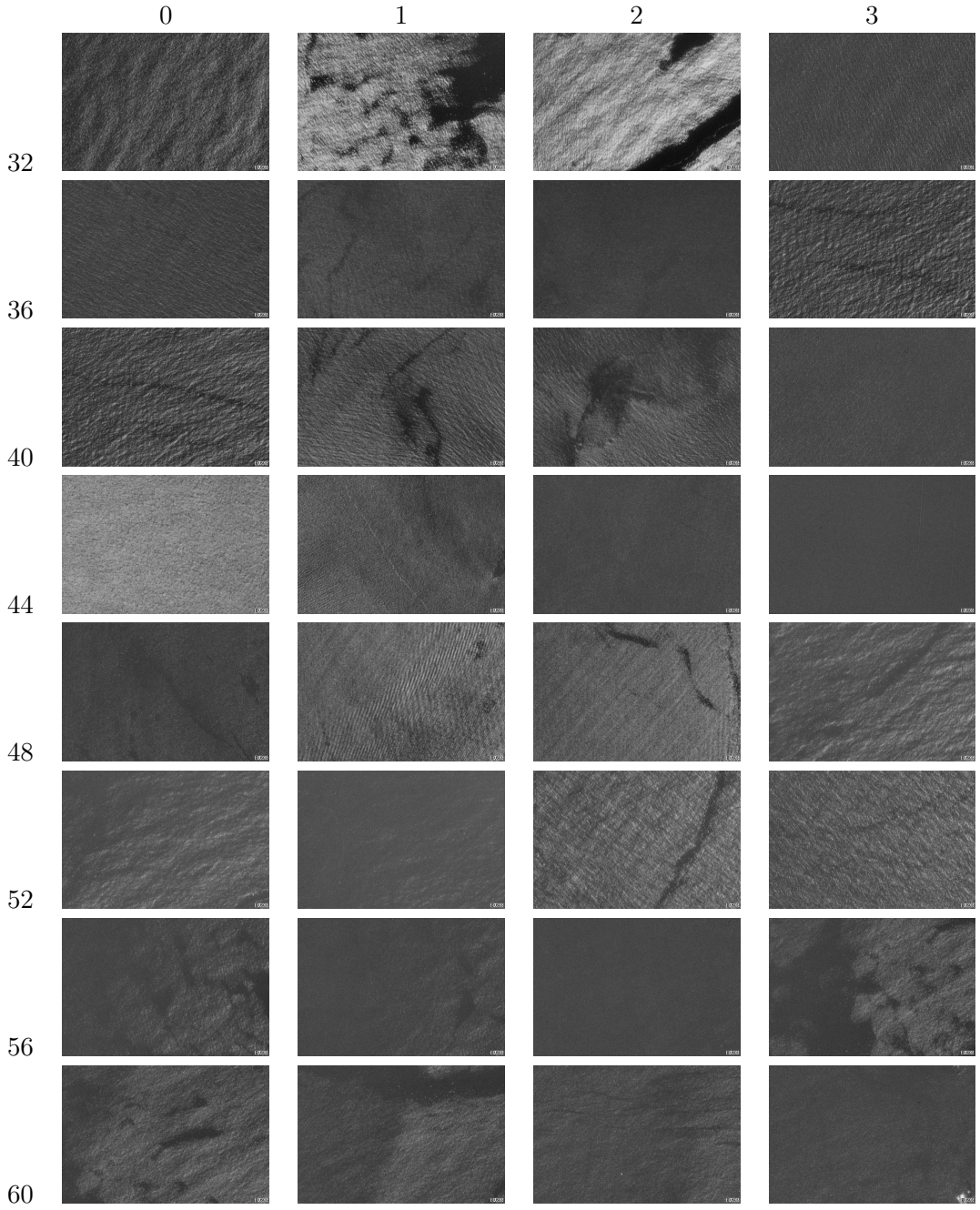

Figure 7.8: *The database of optical images of ocean surfaces without wakes (continued)*

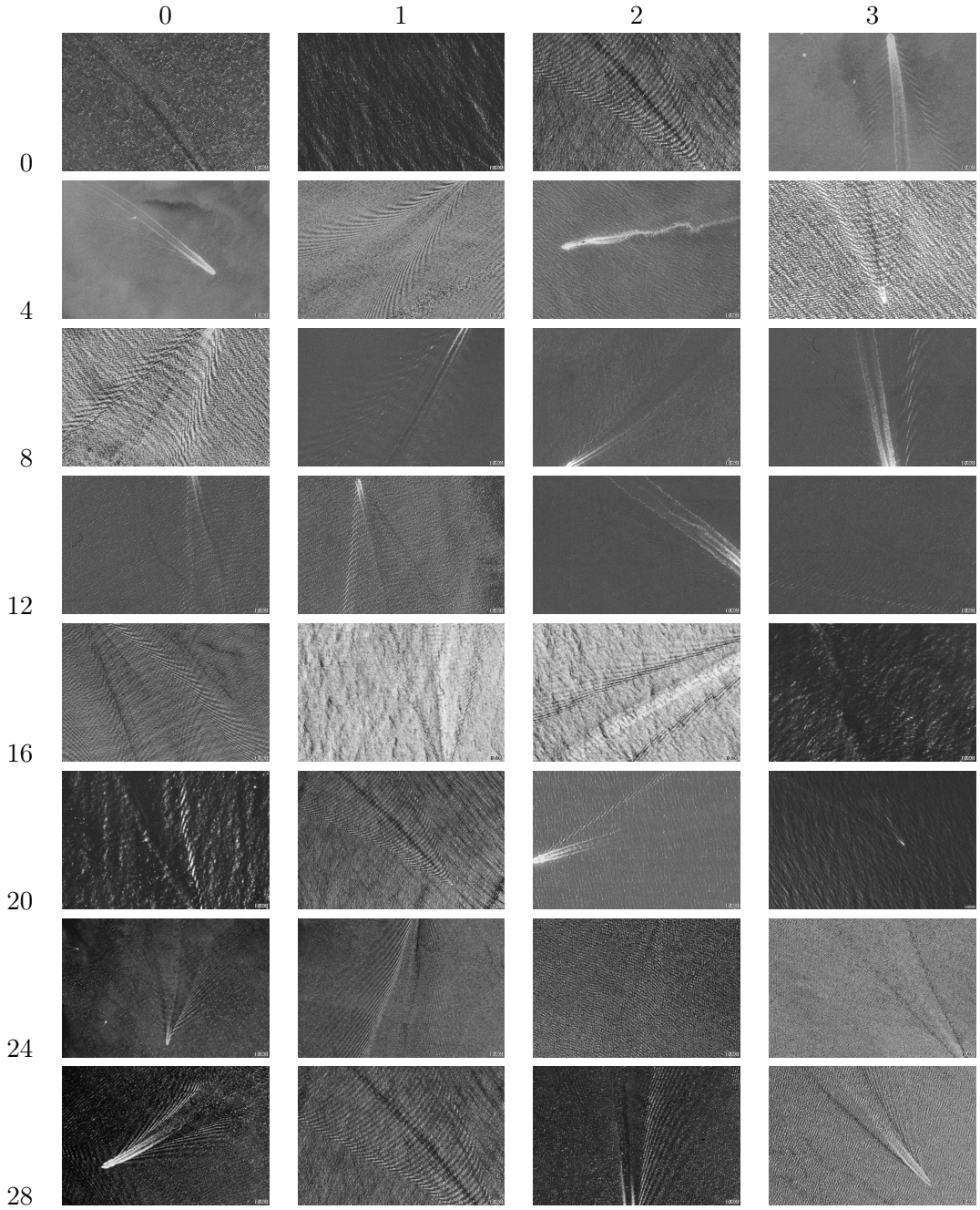

Figure 7.9: *The database of optical images of ocean surfaces with Kelvin wakes*

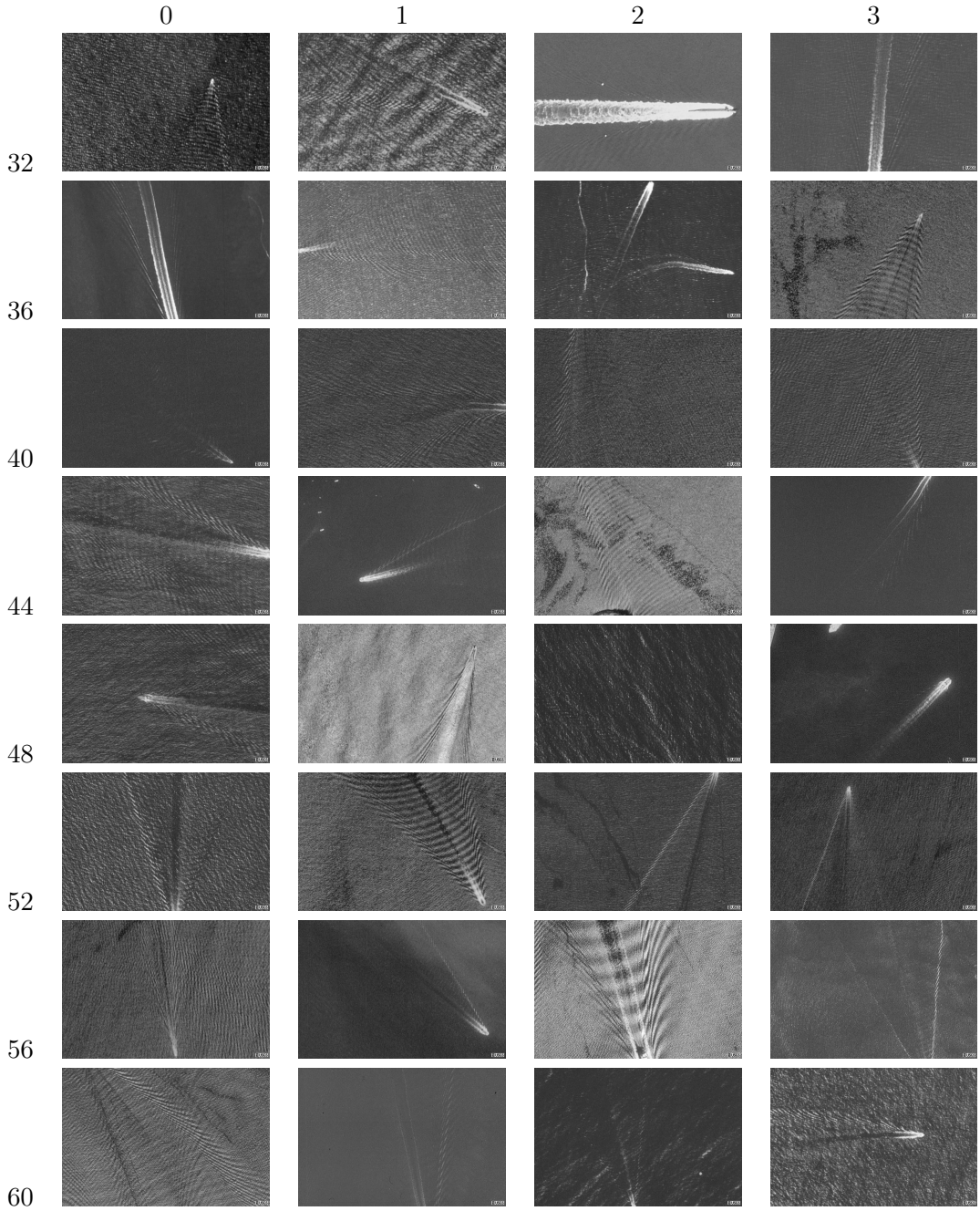

Figure 7.10: *The database of optical images of ocean surfaces with Kelvin wakes (continued)*

Conclusion of this thesis

Hardin remained silent for a short while. Then he said, 'When did Lameth write his book?'
'Oh – I should say about eight hundwed yeahs ago. Of cohse, he has based it lahgely on the pwevious wuhk of Gleen.'
'Then why rely on him? Why not go to Arcturus and study the remains for yourself?'
Lord Dorwin raised his eyebrows and took a pinch of snuff hurriedly. 'Why, whatevah foah, my deah fellow?'
'To get the information firsthand, of course.'
'But wheahs the necessity? It seems an uncommonly woundabout and jopelessly wigmawolish method of getting anywheahs. Look heah now, I've dot the wuhks of the mastahs – the gweat ahchaeologists of the past. I wigh them against each othah – balance of the disagweements – analyze the conflicting statements – decide which is pwobably cowwect – and come to a conclusion. That is the scientific method. At least' – patronizingly – 'as *I* see it. How insuffewably cwude it would be to go to Ahctuwus, oah to Sol, foah instance, and blundah about, when the old mastahs have covahed the gwound so much moah effectually than we could possibly hope to.'

– Isaac Asimov, *Foundation* 2, IV[a].

[a]Note at translation time: this dissertation was purely theoretical and simulation-based. Since I had no opportunity for experimental work. I had to rely on the observations made by others. This has always been a sore point for me.

In our work, we focused on the possibility of using the wake as a tool to assist maritime surveillance, in addition to ship detection. We also considered the case of bistatic imagery. These are two themes slightly on the sidelines of conventional maritime surveillance approaches. We found that the wake is merely a complement to ship detection, although it can provide very useful information when correctly detected. Moreover, maritime surveillance radars are, with few exceptions, all monostatic. Hence, it is interesting to explore what a discussion combining these two elements could bring.

The approach we used can be considered dual: the first part of the manuscript presented a direct path, starting from modeling the environment to deducing the received signal using a simulator. The second part is the indirect path, where we attempt to retrieve the ship's heading and speed parameters from radar data.

We began by individually presenting all the models and phenomena involved in the bistatic radar acquisition chain. This discussion was divided into four chapters. The first dealt with the radar system and data processing (e.g., for synthetic aperture integration) from a "signal processing" perspective. The second discussed the modeling of the sea sur-

face, particularly fluid mechanics models. The third addressed the wake and its modeling. The fourth finally addressed the reflection of radar signals from an electromagnetic point of view. This discussion, from our point of view, was necessary to understand the interdependence of various phenomena. It was also important to achieve the "unification" of these diverse domains within a single application, which we presented in the fifth chapter dedicated to the simulation of raw radar signals. We also believe that this "unification" has a certain didactic value.

The results of our simulation work are as follows. We demonstrated that the computation time for a raw signal simulator for a 500×500-meter scene is currently on the order of half an hour. As it stands, this computation time is very usable for a one-time simulation, which was not the case just a few years ago. However, this time is still too long for building a database of signals and exhaustive search for an optimal configuration. That said, the simulation mechanism is highly parallelizable. Parallelization and intensive use of graphics cards as co-processors are two avenues that must be explored to improve computation times. Moreover, if simulation has not been used intensively to build a database, it has nevertheless allowed the display of simulated radar images of the maritime surface in bistatic polarimetric SAR configuration, which has not yet been proposed to our knowledge. Our simulation is not limited to radar applications; for example, it has also been used to study the reflection of GPS-type signals on the sea surface (Coatanhay, Arnold-Bos, and Khenchaf [42, 41]).

The models (electromagnetic, fluid mechanics, etc.) we used were individually validated, ensuring that the simulated signal is correct from the standpoint of the average link budget. We also compared images with models and real data in the monostatic case, in terms of speckle noise characteristics. The result of this comparison is that we can recover the qualitative behavior of speckle noise models, especially the evolution of the shape of the speckle noise distribution with incidence, wind speed, and wind angle. However, we did not find perfect numerical agreement. We conjecture that this discrepancy could be explained either by not taking into account the non-linearities of the sea surface, or by the limitations of statistical models used when the simulated surface consists of very small facets. We emphasize the importance of comparing simulated data with real measurements and the need to investigate further the origin of the observed differences in the context of a "physical" simulation based on facetization. Simulation alone cannot replace field experience! Another important result of our study is the explicit consideration of specular reflection. In the literature, the emphasis is on diffuse reflection, which is correct for side-looking radar applications. However, in the general bistatic case, specular reflection cannot be ignored. Finally, we also paid special attention to the study of the discretization steps of the maritime surface used in the simulation. We believe that this discretization is a point often neglected in the literature.

As for the detection of the wake in radar images, here are the conclusions of our work. We started by comparing four typical reference chains for dead water wake detection. The result of this comparison is that the classical method of using a Radon transform (Rey *et al.* [150]) provides a very good balance between computation speed and results compared to other methods proposed later in the literature. It is possible to significantly increase the rate of good detections by improving the thresholding of the Radon transform. For this, the stochastic matched filtering method as proposed by Courmontagne [46] is an interesting alternative that does not significantly slow down the execution time compared to the basic method. However, it requires training on a base of real or simulated images. This training can be cumbersome to set up, but it can be done once and for all, offline. In any case, wake detection remains a computationally expensive operation. To limit computation time, it seems interesting to subordinate wake detection to ship detection in the image, i.e., to

trigger the use of the wake detection algorithm only upon detecting a ship. Finally, note that the issue of dark wake detection is similar to that of wild oil spill detection, opening up other interesting perspectives.

In the last chapter of the manuscript, we discussed the detectability of the Kelvin wake in high-resolution radar and optical images.

Firstly, we discussed the elements to consider for a *a priori* choice of a configuration to image the Kelvin wake in SAR (possibly bistatic). It emerged from this analysis that today, two types of configurations can be considered. One, already available, is that of airborne SAR, with good resolution (around a meter), in HH or cross-polarization. The other is a bistatic configuration with an airborne antenna and another placed at ground level. This configuration would use dedicated radar signals to achieve good resolution, excluding the use of opportunistic sources. Our simulator seems to suggest that this configuration allows reconciling the advantages of the low grazing angle configuration and synthetic aperture imaging, namely superior contrast and good resolution. However, both the transmitter and receiver must cooperate to synchronize the antenna directions. From our perspective, operational considerations should, however, take precedence over theoretical considerations. Therefore, considering the constraints it imposes, the contribution of this bistatic configuration seems extremely marginal in the context of maritime surveillance. It could, however, be interesting occasionally in the scientific context for wake studies, which could have repercussions in naval architecture. In such an experimental context, it is not certain that other systems[6] would not allow for such a study with even better performance and at a lower cost. However, these various systems would likely be complementary rather than redundant. Thus, radar still has its place in the field, despite implementation challenges.

Secondly, we proposed an algorithm for detecting Kelvin wakes, allowing for obtaining the direction of the ship's trajectory and its speed. The algorithm is based on utilizing the properties of the wake's spectrum locus in the Fourier transform of the received image, introducing a generalized Radon transform adapted to the wake. We also proposed to improve the visibility of this wake by using stochastic matched filtering. The proposed algorithm theoretically works on SAR, BiSAR, and optical spatial imagery. Initial tests on real optical images seem to confirm the feasibility of the method. As a perspective, we suggest further exploring the tests, at least in the optical domain, where images are easier to simulate. This would help determine the method's application domains (ship size and speed ranges, sea state, etc.). Also, note that the method we propose still requires significant computation time. Therefore, using it on a sliding window in an image is not feasible, and it is better to subordinate its use to ship detection. This algorithm can also be used as a tool provided to a human operator, who would manually select an area where a wake is present.

[6]Telemetry lidar, acoustic systems with a transducer array fixed at the bottom of the water targeting the surface, or optical imaging, could be considered.

Appendices

Appendix

A Frames and geometry

A.1 Transformations between frames

Considering two coordinate systems $\mathcal{R}_1(\mathrm{O}_1, \hat{\mathbf{x}}_1, \hat{\mathbf{y}}_1, \hat{\mathbf{z}}_1$ and $\mathcal{R}_2(\mathrm{O}_2, \hat{\mathbf{x}}_2, \hat{\mathbf{y}}_2, \hat{\mathbf{z}}_2)$, a frame change between these coordinates is defined as follows:

$$\{\mathbf{O_1A}\}_{\mathcal{R}_2} = \mathtt{R}_{1\to 2} \times \{\mathbf{O_1A} - \mathbf{O_1O_2}\}_{\mathcal{R}_1} \tag{A.1}$$

Rotation matrix $\mathtt{R}_{1\to 2}$ is defined as follows:

$$\mathtt{R}_{1\to 2} = \begin{pmatrix} 1 & 0 & 0 \\ 0 & \cos\check{x_1} & \sin\check{x_1} \\ 0 & -\sin\check{x_1} & \cos\check{x_1} \end{pmatrix} \begin{pmatrix} \cos\check{y_1} & 0 & \sin\check{y_1} \\ 0 & 1 & 0 \\ -\sin\check{y_1} & 0 & \cos\check{y_1} \end{pmatrix} \begin{pmatrix} \cos\check{z_1} & \sin\check{z_1} & 0 \\ -\sin\check{z_1} & \cos\check{z_1} & 0 \\ 0 & 0 & 1 \end{pmatrix} \tag{A.2}$$

Angles $\check{x_1}$, $\check{y_1}$, $\check{z_1}$ are the angles parametrizing the frame change. Thus, $\check{x_1}$ is a first rotation around vector $\hat{\mathbf{x}}_1$, the other angles being zero, *etc.*

A.2 Frames used in this dissertation

All frames used in the dissertation are orthonormal and direct. An illustration of most of the frames used in the thesis is given at figure A.2, page 223.

A.2.1 Global frame $\mathcal{W}(\mathrm{O}, \hat{\mathbf{x}}, \hat{\mathbf{y}}, \hat{\mathbf{z}})$

The origin O is placed at the mean sea level. Vector $\hat{\mathbf{z}}$ points to the sky. Vector $\hat{\mathbf{x}}$ points to the East, the vector $\hat{\mathbf{y}}$ to the North.

A.2.2 Wind frame $\mathcal{V}(\mathrm{O}, \hat{\mathbf{u}}, \hat{\mathbf{u}}_\perp, \hat{\mathbf{z}})$

Point O denotes a point on the average sea surface taken as reference. Vector $\hat{\mathbf{u}}$ points in the direction to which the wind blows (*downwind*). Vector $\hat{\mathbf{u}}_\perp$ points in the crosswind direction (*crosswind*). The third vector is the same as for the world frame. The wind direction is defined by angle $\psi_0 = (\hat{\mathbf{x}}, \hat{\mathbf{u}})$.

A.2.3 Local frame $\mathcal{L}(\mathrm{P}, \hat{\mathbf{x}}_l, \hat{\mathbf{y}}_l, \hat{\mathbf{z}}_l)$

The origin is a point P of the sea surface. Vector $\hat{\mathbf{z}}_l$ is along the local normal at the sea surface at P and points upwards to the sky. Vector $\hat{\mathbf{x}}_l$ is directed in the *downwind* direction, that is, $(\hat{\mathbf{x}}_l - \hat{\mathbf{z}}.\hat{\mathbf{x}}_l)/||\hat{\mathbf{x}}_l - \hat{\mathbf{z}}.\hat{\mathbf{x}}_l|| = \hat{\mathbf{z}}$ (assuming that the local surface is not vertical, which does not happen for non-breaking sea waves).

A.2.4 Transmitting antenna frame $\mathcal{X}(\mathrm{X}, \hat{\mathbf{x}}_x, \hat{\mathbf{y}}_x, \hat{\mathbf{z}}_x)$

The origin of the coordinate system is a reference point of the antenna, usually its center of symmetry if there is one. Vector $\hat{\mathbf{x}}_x$ gives the looking direction of the antenna. Vector $\hat{\mathbf{y}}_x$ is oriented to the largest dimension of the antenna.

A.2.5 Polarimetric frame of the transmitting antenna $\mathcal{P}_X(\mathrm{P}, \hat{\mathbf{v}}_x, \hat{\mathbf{h}}_x, \hat{\mathbf{r}}_x)$

This frame is defined with respect to an aribtrary point P of the space, which, relatively to the transmitting antenna frame $\mathcal{X}$, is located at a bearing angle $\check{z_x}$ and an elevation angle $\check{y_x}$. Vector $\hat{\mathbf{r}}_x$ is equal to $\mathbf{XP}/||\mathbf{XP}||$. Vector $\hat{\mathbf{v}}_x$ is in the plane defined by $\hat{\mathbf{r}}_x$ and $\hat{\mathbf{z}}_x$; it is equal to $-\hat{\mathbf{z}}_x$ if $\check{y_x} = 0$. Vector $\hat{\mathbf{h}}_x$ is such that $\mathcal{P}_x$ is direct and orthonormal.

A.2.6 Polarimetric frame of the incident radio wave $\mathcal{P}_I(\mathrm{P}, \hat{\mathbf{v}}_i, \hat{\mathbf{h}}_i, \hat{\mathbf{r}}_x)$

This frame has origin a point P of space, vector $\hat{\mathbf{h}}_i$ being equal to $\hat{\mathbf{r}}_x \times \hat{\mathbf{z}}_l$, and vector $\hat{\mathbf{v}}_i$ being normal to the two other vectors of the frame.

A.2.7 Polarimetric frame of the reflected radio wave, "*forward scattering alignment*" convention, $\mathcal{P}_S^F(\mathrm{P}, \hat{\mathbf{v}}_s^f, \hat{\mathbf{h}}_s^f, \hat{\mathbf{r}}_s^f)$

Vector $\hat{\mathbf{r}}_s^f$ is equal to $\mathbf{PR}/||\mathbf{PR}||$ where R is the origin of the polarimetric frame of the receiving antenna. Vector $\hat{\mathbf{h}}_s^f$ is equal to $\hat{\mathbf{z}}_l \times \hat{\mathbf{r}}_s^f$. Vector $\hat{\mathbf{v}}_s^f$ is normal to the two other vectors.

A.2.8 Polarimetric frame of the reflected radio wave, "*backscattering alignment*" convention, $\mathcal{P}_S^B(\mathrm{P}, \hat{\mathbf{v}}_s^b, \hat{\mathbf{h}}_s^b, \hat{\mathbf{r}}_r)$

Vector $\hat{\mathbf{r}}_r$ is equal to $-\hat{\mathbf{r}}_s^f$. Vector $\hat{\mathbf{h}}_s^b$ is equal to $\hat{\mathbf{z}}_l \times \hat{\mathbf{r}}_r$. Vector $\hat{\mathbf{v}}_s^b$ is normal to the two other vectors. The reason for this second frame, is that when $\mathrm{X} = \mathrm{R}$, then $\mathcal{P}_X$ and $\mathcal{P}_R^B$ are the same, which is easier to use in the monostatic case.

A.2.9 Polarimetric frame of the receiving antenna $\mathcal{P}_R(\mathrm{P}, \hat{\mathbf{v}}_r, \hat{\mathbf{h}}_r, \hat{\mathbf{r}}_r)$

This frame is defined for a point P of space, which, relatively to frame $\mathcal{R}$, has a bearing angle $\check{z_r}$ and an elevation angle $\check{y_r}$. Vector $\hat{\mathbf{r}}_r^b$ is equal to $\mathbf{RP}/||\mathbf{RP}||$. Vector $\hat{\mathbf{v}}_x$ is in the plane given by $\hat{\mathbf{n}}_r$ and $\hat{\mathbf{z}}_r$; it is equal to $-\hat{\mathbf{z}}_r$ if $\check{y_r} = 0$. Vector $\hat{\mathbf{h}}_r$ is such that $\mathcal{P}_r$ is orthonormal and direct.

A.2.10 Receiving antenna frame $\mathcal{R}(\mathrm{R}, \hat{\mathbf{x}}_r, \hat{\mathbf{y}}_r, \hat{\mathbf{z}}_r)$

The receiving antenna frame has its origin at point R, in general at its center of symmetry if it exists. Vector $\hat{\mathbf{x}}_r$ is the looking direction of the antenna. Vector $\hat{\mathbf{y}}_r$ is along the largest dimension of the antenna, and so that if the receiving antenna were co-located with the transmitting antenna (same position and looking direction), then $\hat{\mathbf{y}}_r$ would have the same direction as $\hat{\mathbf{y}}_x$.

A.2.11 Ship frame $\mathcal{B}(\mathrm{B}, \hat{\mathbf{x}}_b, \hat{\mathbf{y}}_b, \hat{\mathbf{z}}_b)$

The origin of the frame is at the fore, on the symmetry plane of the ship, at the waterline. Vector $\hat{\mathbf{x}}_b$ is along the longitudinal axis of the ship, on the symmetry plane and points at the aft. Vector $\hat{\mathbf{y}}_b$ pointe at starboard. Vector $\hat{\mathbf{z}}_b$ is the same as $\hat{\mathbf{z}}$. The ship frame is

illustrated at figure A.1. An elementary wake wave would propagate in direction θ which is measured in the mean sea level plane with reference to $\hat{\mathbf{x}}_b$.

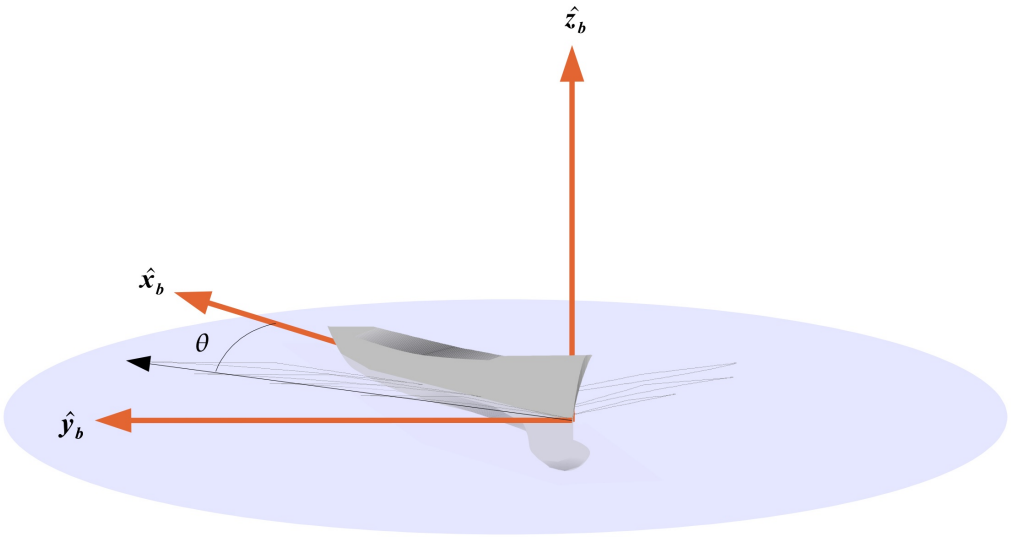

Figure A.1: *Definition of the ship frame $\mathcal{B}$.*

A.3 Bistatic angles

A.3.1 Généralités

Bistatic angles are used to define the geometry of the scattering. There are two series of bistatic angles: global and local. The global angles are defined with respect to the wind frame $\mathcal{V}$ which has for vertical vector $\hat{\mathbf{z}}$ and which is defined with respect to the mean sea level. We are therefore talking about global bistatic angles $(\theta_i^v, \phi_i^v, \theta_s^v, \phi_s^v)$. This series of angles is used for all statistical models such as the Kirchhoff approximation or the two-scale method. The other set of angles is defined relative to the local frame at a point, it is the one that is used for the small perturbations model. We are therefore talking about local bistatic angles $(\theta_i^l, \phi_i^l, \theta_s^l, \phi_s^l)$. Note that the two series of bistatic angles are equal if $\hat{\mathbf{z}}_l = \mathbf{z}$ and P is at the intersection of the "looking directions" of the two antennas. The reader is referred to the figure 4.2 of chapter 4, page 107, for a graphical illustration of both frames, and to figure A.2 for an illustration of local bistatic angles.

A.3.2 Définition

The global bistatic angles are defined by the direction of the antenna frames with respect to frame $\mathcal{V}$:

- θ_i^v is the incidence angle, meaning the angle going from $\hat{\mathbf{z}}$ to $\hat{\mathbf{x}}_x$ (note that sometimes the grazing angle $\pi/2 - \theta_i^v$ is considered);
- ϕ_i^v is the looking direction of the transmitter, meaning the angle from $-\hat{\mathbf{x}}$ to the projection $\hat{\mathbf{x}}_x - \hat{\mathbf{x}}_x.\hat{\mathbf{z}}$ of $\hat{\mathbf{x}}_x$ on the x-y plane of $\mathcal{V}$;
- θ_s^v is the emergence angle, meaning the angle from $\hat{\mathbf{z}}$ to $-\hat{\mathbf{x}}_r$;

- ϕ_s^v is the direction of the receiver, meaning the angle from $\hat{\mathbf{x}}$ to the projection $\hat{\mathbf{x}}_r - \hat{\mathbf{x}}_r.\hat{\mathbf{z}}$ of $\hat{\mathbf{x}}_r$ on the x-y plane of $\mathcal{V}$.

For local bitatic angles, one considers an arbitrary P which is not necessarily located at the intersection of the looking directions of the transmitting and receiving antennas, as well as the local frame $\mathcal{L}(\mathrm{P})$ at P which the locally tangent to the sea surface:

- θ_i^l is the local incidence angle, meaning the angle going from $\hat{\mathbf{z}}_l$ à $\hat{\mathbf{r}}_x(P)$ (the local grazing angle is $\pi/2 - \theta_i^l$);
- ϕ_i^l is the local looking direction of the transmitter, meaning the angle from $-\hat{\mathbf{x}}_l$ to the projection $\hat{\mathbf{r}}_x(\mathrm{P}) - \hat{\mathbf{r}}_x(\mathrm{P}).\hat{\mathbf{z}}$ of $\hat{\mathbf{r}}_x(\mathrm{P})$ on the x-y plane of $\mathcal{V}$;
- θ_s^l is the local emergence angle, meaning the angle from $\hat{\mathbf{z}}_l$ to $-\hat{\mathbf{r}}_r(\mathrm{P})$;
- ϕ_s^l gives the direction of the receiver from P, meaning the angle going from $\hat{\mathbf{x}}_l$ to projection $\hat{\mathbf{r}}_r(\mathrm{P}) - \hat{\mathbf{r}}_r(\mathrm{P}).\hat{\mathbf{z}}_l$ of $\hat{\mathbf{r}}_r(\mathrm{P})$ on the x-y plane of $\mathcal{L}(\mathrm{P})$.

A.3.3 Abuse of language

When demonstrating formulas relating to scattering with respect to the wind frame (using global bistatic angles), it will happen that we use the polarimetric frames for the incident radio wave and reflected radio wave although these are normally defined with respect to any point P of the surface. In this very specific case, the point being considered is the origin O of the wind frame.

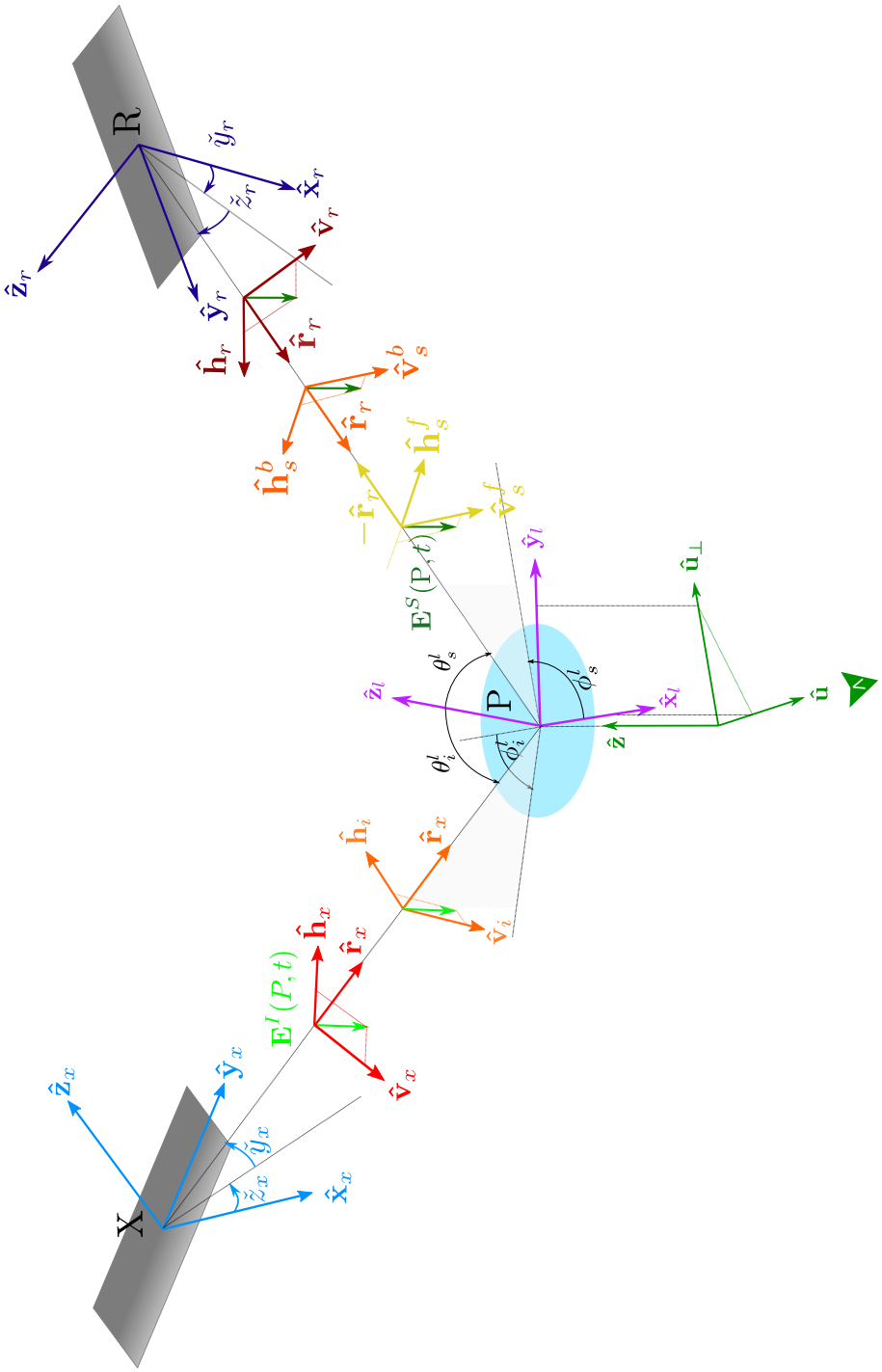

Figure A.2: *Frames* $\mathcal{V}$, $\mathcal{X}$, $\mathcal{P}_x$, $\mathcal{P}_I$, $\mathcal{L}$, $\mathcal{P}_S^F$, $\mathcal{P}_S^B$, $\mathcal{P}_r$, $\mathcal{R}$.

A.4 Intersection of the Fresnel ellipsoid with a plane

This part provides the parameters of the equidistance (Fresnel) ellipse, which is the intersection of the Fresnel ellipsoid with a plane. The notations are those of figure A.3, below. The interested reader may wish to turn to Norton and Omberg's article [134], which uses a different but nevertheless equivalent wording[1].

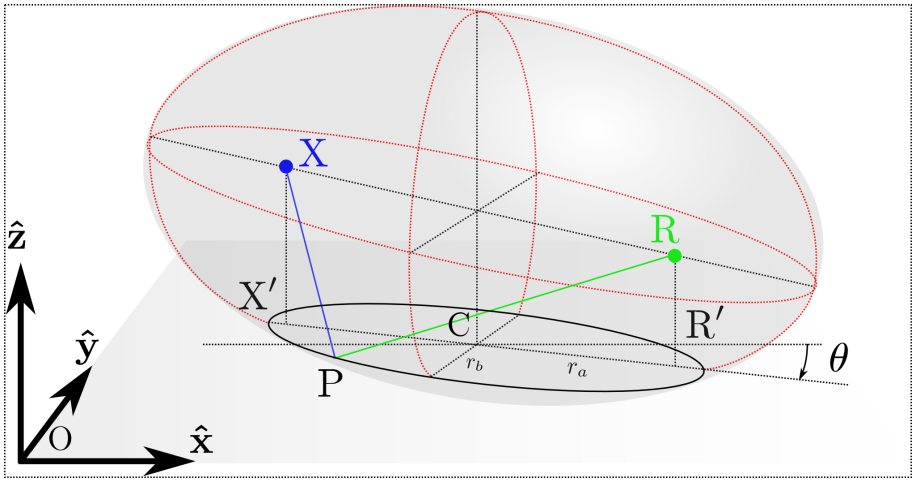

Figure A.3: *Fresnel ellipsoid for a distance r and its intersection with the plane such that $z = 0$.*

A.4.1 Problem statement

Let $\mathcal{P}$ be the plane of equation $z = 0$ in the world frame $\mathcal{W}(\hat{\mathbf{x}}, \hat{\mathbf{y}}, \hat{\mathbf{z}})$. In this frame, the transmitter X has coordinates (x_X, y_X, z_X) and the receiver R has coordinates (x_R, y_R, z_R). The problem is to find the intersection of $\mathcal{P}$ with the Fresnel ellispoid associated to the total path length r, defined as the set of points $\mathrm{P} \in \mathcal{P}$ such that:

$$XP + PR = r \tag{A.3}$$

A.4.2 Solution

It is known that the intersection of a plane with an ellipsoid, if it exists, is an ellipse, possibly degenerated into a point. The major axis of this ellipse is on the same line, as the projection of the major axis of Fresnel's ellipsoid. This ellipse is entirely defined by:

1. θ, between the x axis of the world frame and the major axis of the ellipse;
2. r_a and r_b, respectively the semi major and the semi minor axis length of the ellipse;
3. x_C and y_C, the coordinates of the center of the ellipse in $\mathcal{W}$

In the following paragraph, X' (resp. R'), denotes the projection of X (resp. R) onto the plane $z = 0$. First, let us perform a frame change from the world frame to an intermediate frame $\mathcal{I}(\mathrm{X}', \hat{\mathbf{x}}_i, \hat{\mathbf{y}}_i, \hat{\mathbf{z}}_i)$, with:

- $\hat{\mathbf{x}}_i = \mathbf{X}'\mathbf{R}'/X'R'$

[1]Note at translation time: see also P. Klein, "On the Ellipsoid and Plane Intersection Equation," Applied Mathematics, Vol. 3 No. 11, 2012, pp. 1634-1640

- $\hat{\mathbf{y}}_i = \hat{\mathbf{z}} \times \hat{\mathbf{x}}_i$;
- $\hat{\mathbf{z}}_i = \hat{\mathbf{z}}$;

The center of the ellipse is on segment [X'R']; its coordinates are $(x'_C, 0, 0)$ in $\mathcal{I}$ and $(x_C, y_C, 0)$ in $\mathcal{W}$. We have:

$$\theta = \angle(\hat{\mathbf{x}}, \hat{\mathbf{x}}_i) = \arctan \frac{y_R - y_X}{x_R - x_X} \tag{A.4}$$

In frame $\mathcal{I}$:

$$\begin{aligned} \{X'\}_{\mathcal{I}} &= \begin{pmatrix} x'_X \\ y'_X \\ z'_X \end{pmatrix} = \begin{pmatrix} 0 \\ 0 \\ 0 \end{pmatrix} \\ \{R'\}_{\mathcal{I}} &= \begin{pmatrix} x'_R \\ y'_R \\ z'_R \end{pmatrix} = \begin{pmatrix} (x_R - x_X)\cos\theta + (y_R - y_X)\sin\theta \\ -(x_R - x_X)\sin\theta + (y_R - y_X)\cos\theta \\ 0 \end{pmatrix} \end{aligned}$$

Let us introduce r_0, the length of the smallest path starting from X, hitting the $z = 0$ plane, then reaching R:

$$r_0 = \sqrt{(x'_X - x'_R)^2 + (y'_X - y'_R)^2 + (z'_X + z'_R)^2} \tag{A.5}$$

Three cases may occur:

Cas 1: $r < r_0$**:** In this case, there is no intersection with the plane.

Cas 2: $r = r_0$**:** The intersection is a point. This point is the specular reflection point, according to the Snell-Descartes law of reflection.

Cas 3: $r > r_0$**:** The intersection is an ellipse. In the intermediate frame $\mathcal{I}$, the equation of the ellipse is given by equation:

$$ax^2 + y^2 + cx = f \tag{A.6}$$

defined by:

$$\begin{aligned} a &= 1 - \left(\frac{x'_X - x'_R}{r}\right)^2 \\ c &= x'_R \left(1 + \frac{-x'^2_R + z^2_X - z^2_R}{r^2}\right) \\ f &= \frac{r^4 - 2\left(x'^2_R + z^2_X + z^2_R\right) r^2 + \left(-x'^2_R + z^2_X - z^2_R\right)^2}{4r^2} \end{aligned}$$

Equation A.6 can be put in the following form:

$$\frac{\left(x - \frac{c}{2a}\right)^2}{\left(\sqrt{\frac{\left(f + \frac{c^2}{4a}\right)}{a}}\right)^2} + \frac{y^2}{\left(\sqrt{f + \frac{c^2}{4a}}\right)^2} = 1 \tag{A.7}$$

where:

- $r_a = \sqrt{\frac{\left(f+\frac{c^2}{4a}\right)}{a}}$, is the semi major axis length;
- $r_b = \sqrt{f + c^2/(4a)}$, is the semi minor axis length;
- $x'_C = c/(2a)$, is the abscissa of the center of the ellipse in $\mathcal{I}$.

In the world frame $\mathcal{W}$, the centre of the ellipse has coordinates:

$$\begin{aligned} x_C &= x_X + \frac{c}{2a}\cos\theta \\ y_C &= y_X + \frac{c}{2a}\sin\theta \\ z_C &= 0 \end{aligned} \tag{A.8}$$

Appendix

B Characteristics of Common Radars

This appendix presents a selection of representative radar systems along with their main characteristics. These systems are all designed for maritime applications and, for the majority of them (except for the Seasat satellite), are currently in use. This selection provides an overview of the performance of current maritime surveillance radar systems, particularly in terms of antenna directivities, frequencies, and available bandwidths. It is worth noting that no bistatic radar is included in the list; as far as we know, such systems have never been implemented in the maritime domain and are therefore not commercially available.

B.1 Coastal maritime surveillance radars

B.1.1 FIKA

- Source: `www.mil.fi` (Finnish Defense Department);
- Peak power: 200 kW [sic];
- X-band;
- Antenna: 5 m $\times$ 0.8 m;
- Effective range: 50-70 km;
- Adjustable polarization.

B.1.2 Hyperion

- Manufacturer: Singapore Technologies Electronics (Satcom & Sensors Systems), `www.stee.stengg.com`;
- Peak power: 25 kW;
- Carrier frequency $f_0 = 9.410$ GHz, bandwidth $B = 60$ MHz;
- Range: 96 nautical miles / 178 km;
- Antenna: 6 to 12 feet long depending on versions;
- Accuracy: 10 in range, 0.3 degrees in azimuth.

B.1.3 Scanter 2001

- Manufacturer: Terma A/S, `www.terma.com`;
- Peak power: 25 kW (X-band), 30 kW (S-band);
- Carrier frequency f_0:
  - X-band: 9.170 or 9.375 or 9.410 or 9.438 or 9.4900 GHz
  - S-band: 3050 MHz
- Range: 96 nautical miles / 178 km;
- Antennas:
  - 7 feet: $\Phi_{\text{azimuth}} = 1.2$ degrees, $\Phi_{\text{elevation}} = 19$ degrees
  - 12 feet: $\Phi_{\text{azimuth}} = 0.6$ degrees, $\Phi_{\text{elevation}} = 19$ degrees
  - 18 feet: $\Phi_{\text{azimuth}} = 0.41$ degrees, $\Phi_{\text{elevation}} = 11$ degrees
- Pulse Repetition Frequency (PRF): 80 to 8000 Hz
- Bandwidth Modulation (B): 3, 8, or 20 MHz

B.2 Shipborne Radars

B.2.1 Furuno 1623: Entry-level Pleasure Boat Radar

- Manufacturer: Furuno, `www.furuno.com`;
- Maximum range: 16 nautical miles;
- Microstrip technology antenna in 388 mm diameter radome;
- Beamwidths $\Phi_{\text{azimuth}} = 6.2$ degrees, $\Phi_{\text{elevation}} = 25$ degrees;
- Carrier frequency $f_0 = 9.410$ GHz, bandwidth 60 MHz;
- T/PRF pairs: (0.08 μs, 3000 Hz), (0.3 μs, 1200 Hz), (0.8 μs, 600 Hz),
- Peak power: 2.2 kW

B.2.2 Furuno 1912 Mk 2: Mid-range Shipborne Radar

- Manufacturer: Furuno, `www.furuno.com`;
- 4-foot slotted antenna;
- Beamwidths $\Phi_{\text{azimuth}} = 1.9$ degrees, $\Phi_{\text{elevation}} = 22$ degrees;
- Carrier frequency $f_0 = 9.410$ GHz, bandwidth 60 MHz;
- T/PRF pairs: (0.08 μs, 2100 Hz), (0.3 μs, 1200 Hz), (0.8 μs, 600 Hz),
- Peak power: 6 kW

B.2.3 Furuno FAR2167DS: Shipborne Radar for Heavy Vessels

- Manufacturer: Furuno, `www.furuno.com`;
- Antennas:
  - X-band: 10 feet, $\Phi_{\text{azimuth}} = 0.75$ degrees, $\Phi_{\text{elevation}} = 20$ degrees;
  - S-band: 12 feet, $\Phi_{\text{azimuth}} = 1.8$ degrees, $\Phi_{\text{elevation}} = 25$ degrees;
- Carrier frequencies $f_0 = 9.410$ GHz, $B = 60$ MHz (X-band) or $f_0 = 3.050$ GHz $B = 60$ MHz (S-band);
- T/PRF pairs: (0.08 μs, 1900 Hz) to (1.2 μs, 500 Hz),
- Peak power: 60 kW

B.3 Airborne Maritime Surveillance Radars

B.3.1 AN/APS 134, Also Known as "SeaVue"

- Manufacturer: Raytheon, `www.raytheon.com`;
- Antenna: dimensions 124×65 cm (likely overall dimensions)
- X-band;
- Peak power: 8 kW, 15 kW, or 50 kW;
- SAR, ISAR, MTI (Moving Target Indicator) capabilities, chirp or more complex waveform emissions, with frequency agility
- Detection ranges: life raft 67 nautical miles; patrol ship: 119 nautical miles; cargo ship: 230 nautical miles.
- 360-degree scanning

B.3.2 Ocean Master

- Manufacturer: Thales Airborne Systems[1], `www.thalesgroup.com`;
- Antenna: bandwidth of 600 MHz, HH polarization;
- Precision: 0.5 degrees in azimuth, 100 m in range after Kalman tracking (200 possible tracks);
- X-band, modulation up to 70 MHz, adjustable carrier up to 1 GHz;
- Pulse Repetition Frequency (PRF) up to 60 kHz;
- Peak power: 8 kW, 15 kW, or 50 kW;
- SAR, ISAR, MTI capabilities, emission in chirp or more complex waveforms, with frequency agility;
- Maximum range: 200 nautical miles for significant targets, 60 nautical miles for small targets (periscopes, etc.);
- 360-degree scanning.

[1]Note at translation: now Thales DMS France.

B.3.3 High-Altitude, Long-Endurance Drone RQ-4A *Global Hawk* + HISAR Radar

- Manufacturer: Northrop Grumman (drone), Raytheon (radar)[2];
- Coverage: 37 km up to a range of 110 km;
- Resolution: 6×6 m in scanning SAR mode, 1.8×1.8 m in spotlight mode (imaged area in spotlight: 2.5 km^2);
- Altitude: 65,000 feet (20 km);
- Patrol speed: 343 knots (true speed);
- Endurance: 42 hours, 24 on-site with a transit of 3000 nautical miles.
- Covered area: 40,000 nautical square miles per day;

B.4 Radar-equipped satellites

Notes The *orbital period* is the time to complete one orbit. The *cycle* is the time for the satellite to pass exactly over the same point on Earth. The *sub-cycle* is the time for the satellite to pass closest to a considered point (within a few kilometers). As the orbit is heliosynchronous, a satellite will always be seen from the ground at the same local solar time.

B.4.1 Seasat (1978)

- Source: `http://southport.jpl.nasa.gov/scienceapps/seasat.html`
- Polarization: HH;
- Resolution: 30 m;
- Swath: 100 km;
- Antenna: 10.74×2.16 m
- Carrier frequency: 1.275 GHz (L-band);
- Peak power: 1 kW
- Pulse duration: 33.4 μs
- PRF: 1463-1640 Hz
- Heliosynchronous polar orbit, altitude approximately 800 km, inclination 108 degrees;
- Incidence angle at the Earth's surface: 23 degrees (±3 degrees).

Only 42 hours of data were recorded before the system failure.

[2]Data source: `http://www.airforce-technology.com/projects/global/specs.html` and `http://www.global-defence.com/1997/HughesHISAR.html`. The accuracy of the values should be taken with caution and as rough estimates only.

B.4.2 ERS 1 and 2 (1992-2000 and 1995-2011)

- Source: Attema [14]
- Polarization: VV;
- Resolution: 30 m;
- Swath: 100 km;
- Carrier frequency: 5.3 GHz (C-band);
- Pulse duration: 37.1 μs
- PRF: 98 Hz and 115 Hz, depending on incidence angle (multiple antennas)
- Incidence angles: 20-26 degrees;
- Heliosynchronous polar orbit, altitude 782 to 785 km, inclination 98.52 degrees, period 100 min, cycle 35 days, sub-cycle 3 days.

B.4.3 Radarsat 1 and 2 (1995-2013; 2007-present)

- Polarization: HH, VV, VH, HV;
- Antenna: 15 m by 1.5 m (Radarsat 2), with electronic scanning;
- Maximum resolution: 8 m at 100 m (Radarsat 1), 3 m (Radarsat 2); finest resolution is achieved in spotlight mode, normal scanning mode is at 50 or 100 m resolution.
- Swath: 50-500 km;
- Carrier frequency: 5.3 GHz (C-band);
- Incidence angles: 10 to 59 degrees (not necessarily the entire range simultaneously);
- Heliosynchronous polar orbit, altitude 791 to 793 km, inclination 98.6 degrees, period approximately 100 min, cycle 24 days, sub-cycle 3 days.
- Modulation: 11.6 MHz, 17.5 MHz, 30 MHz, 50 MHz, 100 MHz;
- PRF: 1257 Hz;

Appendix

C Some fundamental equations of electromagnetism

This appendix presents Maxwell's equations and, based on these, provides a demonstration of Kirchhoff's and Stratton and Chu's equations. These are fundamental equations used to calculate the field radiated by an antenna or the field scattered by any surface, especially the sea surface. The writing of all demonstrations owes much to Sophocles J. Orfanidis's work, *Electromagnetic Waves and Antennas*, available exclusively online[1], particularly Chapter 1 for sections C.1.1, C.1.2, and Chapter 17 for the rest. However, some demonstrations left as exercises to the reader in Orfanidis's work are detailed here, especially the transition from Kirchhoff's equation to Stratton and Chu's equation. Once Stratton and Chu's equations are demonstrated, the Kirchhoff approximation equations are established for the case of a maritime surface; these are the equations used in Chapter 4. The appendix concludes with the parameters of the small perturbation model for the maritime surface.

C.1 Maxwell's equations

C.1.1 General form

All classical electromagnetic phenomena are determined by the four Maxwell's equations, to which a certain number of boundary conditions are added to determine the behavior of the quantities when passing from one medium to another. Since these equations involve a time dependence, they are only valid for non-relativistic mechanics, which will, however, correspond to the use that will be made of them. These four equations are as follows:

$$div\,\mathbf{H} = 0 \qquad \text{(Conservation of flux)} \tag{C.1}$$

$$\mathbf{rot}\;\;\mathbf{H} = \mathbf{j} + \frac{\partial \mathbf{D}}{\partial t} \qquad \text{(Maxwell-Ampère)} \tag{C.2}$$

$$div\,\mathbf{D} = \rho_{EM} \qquad \text{(Maxwell-Gauss)} \tag{C.3}$$

$$\mathbf{rot}\;\;\mathbf{E} = -\frac{\partial \mathbf{B}}{\partial t} \qquad \text{(Maxwell-Faraday)} \tag{C.4}$$

where:

$\mathbf{E}$	[Volts/m]	electric field
$\mathbf{H}$	[Amperes/m]	magnetic field
$\mathbf{D}$	[Coulombs/m^2]	electric induction field
$\mathbf{B}$	[Webers/m^2]	magnetic induction field
ρ_{EM}	[Coulombs/m^3]	electric charge density
$\mathbf{j}$	[Amperes/m^3]	electric current density

[1] At the time of translating this manuscript (2024), the document is available at `http://www.ece.rutgers.edu/~orfanidi/ewa/`.

The fields can be related to the induction fields by the relations:

$$\mathbf{D} = \epsilon_{EM}\mathbf{E} \tag{C.5}$$
$$\mathbf{B} = \mu_{EM}\mathbf{H} \tag{C.6}$$

where ϵ_{EM} and μ_{EM} are respectively the permittivity (in Faradays/m) and permeability (in Henrys/m) of the considered medium.

$$div\,\mathbf{B} = 0 \tag{C.7}$$
$$\mathbf{rot}\ \ \mathbf{B} = \mu_{EM}\mathbf{j} + \mu_{EM}\epsilon_{EM}\frac{\partial \mathbf{E}}{\partial t} \tag{C.8}$$
$$div\,\mathbf{E} = \frac{\rho_{EM}}{\epsilon_{EM}} \tag{C.9}$$
$$\mathbf{rot}\ \ \mathbf{E} = -\frac{\partial \mathbf{B}}{\partial t} \tag{C.10}$$

C.1.2 Boundary conditions

The boundary conditions for electromagnetic fields crossing the boundary between two media are given below:

$$\mathbf{E}_{1t} - \mathbf{E}_{2t} = \mathbf{0} \tag{C.11}$$
$$\mathbf{H}_{1t} - \mathbf{H}_{2t} = \mathbf{j}_s \times \hat{\mathbf{n}} \tag{C.12}$$
$$\mathbf{E}_{1n} - \mathbf{E}_{2n} = \frac{\rho_{EM,s}}{\epsilon_{EM}} \tag{C.13}$$
$$\mathbf{H}_{1n} - \mathbf{H}_{2n} = 0 \tag{C.14}$$

The indices t and n denote respectively the tangential and normal components to the surface of the interface between medium 1 and medium 2. $\rho_{EM,s}$ and $\mathbf{j}_s$ are respectively the charge density and current density at the interface between the two media.

C.1.3 Duality theorem

The duality theorem is a mathematical artifice that makes Maxwell's equations invariant under a change of variables between electric and magnetic terms. To make Maxwell's equations symmetrical, it is possible to add purely fictitious (*i.e.*, zero) magnetic source terms: $\rho_{EM,m}$ and $\mathbf{j_m}$, called magnetic charge densities and magnetic current densities, respectively. The generalized form of Maxwell's equations is then as follows:

$$div\,\mathbf{H} = \frac{\rho_{EM,m}}{\mu_{EM}} \tag{C.15}$$
$$\mathbf{rot}\ \ \mathbf{H} = \mathbf{j} + \epsilon_{EM}\frac{\partial \mathbf{E}}{\partial t} \tag{C.16}$$
$$div\,\mathbf{E} = \frac{\rho_{EM}}{\epsilon_{EM}} \tag{C.17}$$
$$\mathbf{rot}\ \ \mathbf{E} = -\mathbf{j_m} - \mu_{EM}\frac{\partial \mathbf{H}}{\partial t} \tag{C.18}$$

Now, it is easy to see that the equations are invariant under the following change of variables:

$$\mathbf{E} \to \mathbf{H} \qquad \mathbf{H} \to -\mathbf{E} \tag{C.19}$$

$$\mathbf{j} \to \mathbf{j_m} \qquad \mathbf{j_m} \to -\mathbf{j} \tag{C.20}$$

$$\epsilon_{EM} \to \mu_{EM} \qquad \mu_{EM} \to \epsilon_{EM} \tag{C.21}$$

$$\rho_{EM,m} \to -\rho_{EM} \qquad \rho_{EM} \to \rho_{EM,m} \tag{C.22}$$

Indeed, after this change of variables, the first two Maxwell's equations are transformed into the other two, and vice versa. Similarly, any result obtained after manipulating the first version of the equations remains valid after the formal substitution of terms as given above. This important result is called the *duality theorem* of Maxwell's equations. This substitution allows, for example, to easily obtain relationships for $\mathbf{H}$ from relationships established for $\mathbf{E}$, and vice versa.

C.2 Wave equation

Taking the curl of the Maxwell-Faraday equation and applying the relation $\mathbf{rot}\ \mathbf{rot}\ \mathbf{V} = \mathbf{grad}\ \mathit{div}\,\mathbf{V} - \mathbf{\Delta V}$ (valid for any vector $\mathbf{V}$, the vector Laplacian $\mathbf{\Delta V}$ being obtained by calculating the scalar Laplacian on each component of $\mathbf{V}$), we get:

$$\mathbf{\Delta E} - \epsilon_{EM}\mu_{EM}\frac{\partial^2 \mathbf{E}}{\partial t^2} = \mu_{EM}\frac{\partial \mathbf{j}}{\partial t} + \frac{1}{\epsilon_{EM}}\mathbf{grad}\ \rho_{EM} + \mathbf{rot}\ \mathbf{j_m} \tag{C.23}$$

$$\mathbf{\Delta H} - \epsilon_{EM}\mu_{EM}\frac{\partial^2 \mathbf{H}}{\partial t^2} = \epsilon_{EM}\frac{\partial \mathbf{j_m}}{\partial t} + \frac{1}{\mu_{EM}}\mathbf{grad}\ \rho_{EM,m} - \mathbf{rot}\ \mathbf{j} \tag{C.24}$$

If we assume that the quantities vary in time with a frequency ω, we obtain (using complex notation) the following equation:

$$\mathbf{\Delta E} + \epsilon_{EM}\mu_{EM}\omega^2\mathbf{E} = \mu_{EM}\jmath\omega\mathbf{j} + \frac{1}{\epsilon_{EM}}\mathbf{grad}\ \rho_{EM} + \mathbf{rot}\ \mathbf{j_m} \tag{C.25}$$

$$\mathbf{\Delta H} + \epsilon_{EM}\mu_{EM}\omega^2\mathbf{H} = \epsilon_{EM}\jmath\omega\mathbf{j_m} + \frac{1}{\mu_{EM}}\mathbf{grad}\ \rho_{EM,m} - \mathbf{rot}\ \mathbf{j} \tag{C.26}$$

This is a inhomogeneous wave equation (or Helmholtz equation). This equation represents the field created at a point in space, produced by the current source $\mathbf{j}$ and the charge distribution ρ_{EM}.

Before solving the equation for an arbitrary source distribution, let's solve it in general for a point source:

$$\Delta G + k^2 G = -\delta_3(\mathbf{r} - \mathbf{r}') \tag{C.27}$$

where $k = \epsilon_{EM}\mu_{EM}\omega^2$, G is a scalar function, and δ_3 is the 3D Dirac distribution (equal to 1 if all three components of the argument are zero, 0 otherwise). This solution has several solutions. One, deterministic, is taken in the form:

$$G(\mathbf{r} - \mathbf{r}') = \frac{e^{\jmath\omega t - \jmath k|\mathbf{r}-\mathbf{r}'|}}{4\pi|\mathbf{r} - \mathbf{r}'|} \tag{C.28}$$

The solution physically reflects the disturbance occurring at point $\mathbf{r}$, created by a point charge at $\mathbf{r}'$. The disturbance varies at the same frequency, but with a phase shift $k|\mathbf{r}-\mathbf{r}'|$ (related to the wave travel time) and with a variation in amplitude inversely proportional to the distance traveled by the wave. The wave propagates isotropically, so we have a spherical wave. From now on, however, we will omit the carrier term $\jmath\omega t$ in the exponential to lighten the notations.

C.3 Kirchhoff and Stratton-Chu equations

Now we want to find the radiated field at a point in space for a more complex source distribution. It is possible to obtain several equivalent integral representations, all giving the electric (or magnetic, but this is equivalent, according to the duality principle stated above) field as a function of the source terms. We can then simplify these equations depending on the configuration of the problem to be solved.

C.3.1 Derivation of the equation

The derivation of these integral forms is done somewhat artificially by posing the following integral:

$$I(\mathbf{r}) = \int_V \left[G(\mathbf{r}-\mathbf{r}')\boldsymbol{\Delta}'\mathbf{E}(\mathbf{r}') - \mathbf{E}(\mathbf{r}')\boldsymbol{\Delta}'G(\mathbf{r}-\mathbf{r}')\right] dV' \tag{C.29}$$

The integral is taken over an *absolutely arbitrary* volume V. In this integral, the integration variable is the vector $\mathbf{r}'$, and the prime symbol means that the operator (Laplacian, gradient, *etc.*) is taken with respect to the integration variables. To simplify the writing of the integral, we will denote $G = G(\mathbf{r}-\mathbf{r}')$, $\mathbf{E} = \mathbf{E}(\mathbf{r}')$, etc. (except for G, all other quantities are evaluated at $\mathbf{r}'$ only). By adding and subtracting the term $k^2G(\mathbf{r}-\mathbf{r}')\mathbf{E}(\mathbf{r}')$, we get:

$$I = \int_V \left[G\left(\boldsymbol{\Delta}'\mathbf{E} + k^2\mathbf{E}\right) - \mathbf{E}\left(\Delta'G + k^2G\right)\right] dV' \tag{C.30}$$

If we use equation C.28, the second term in the integrand reduces to:

$$-\int_V \mathbf{E}\left(\Delta'G + k^2G\right) dV' = \int_V \mathbf{E}\delta(\mathbf{r}-\mathbf{r}')dV' = \mathbf{E}(\mathbf{r}) \tag{C.31}$$

hence:

$$I = \int_V G\left(\boldsymbol{\Delta}'\mathbf{E} + k^2\mathbf{E}\right) dV' + \mathbf{E}(\mathbf{r}) \tag{C.32}$$

Now, starting from the original integral C.29, let's apply the second Green's theorem to it:

$$I = -\oint_{S+S_\infty} \left[\mathbf{E}\frac{\partial G}{\partial \mathbf{n}'}(\mathbf{r}') - G\frac{\partial \mathbf{E}}{\partial \mathbf{n}'}(\mathbf{r}')\right] dS' \tag{C.33}$$

where the notation $\partial/\partial\mathbf{n}'$ is actually a shortcut for the notation $\mathbf{n}'.\mathbf{grad}'$, that is, the derivative in the direction $\mathbf{n}'$; we also note the presence of the minus sign, due to the fact that the normal points *into* the integration volume. The surfaces S and S_∞ are the outer envelopes of the considered volume. The notation S_∞ denotes a surface located infinitely far from the source terms. Since the field amplitude decreases as $1/r$, we can neglect the integral over S_∞; this term will not appear in the equation later.

By equating the two right-hand sides of C.32 and C.33, and then injecting C.25, we get *in fine*:

$$\mathbf{E}(\mathbf{r}) = -\int_V \left[\mu_{EM}\jmath\omega G\mathbf{j} + \frac{1}{\epsilon_{EM}} G\,\mathbf{grad}'\ \rho_{EM} - G\,\mathbf{rot}'\ \mathbf{j_m}\right] dV' \tag{C.34}$$

$$+ \oint_S \left[\mathbf{E}\frac{\partial G}{\partial \mathbf{n}'} - G\frac{\partial \mathbf{E}}{\partial \mathbf{n}'}\right] dS' \tag{C.35}$$

This equation is called the *Kirchhoff diffraction equation*. The name of this equation will be justified a little later. This equation is interesting but not very informative. We will need to make a little more effort to arrive at a more elegant form, known as the Stratton-Chu formula.

We have the vector identities:

$$\int_V \mathbf{rot}\ \mathbf{A}dV = \oint_S = \hat{\mathbf{n}} \times \mathbf{A}dS' \tag{C.36}$$

$$\int_V \mathbf{grad}\ \psi dV = \oint_S \psi\hat{\mathbf{n}}dS' \tag{C.37}$$

$$\mathbf{grad}\ (\phi\psi) = \phi\,\mathbf{grad}\ \psi + \psi\,\mathbf{grad}\ \phi \tag{C.38}$$

By applying these identities to the first integral of C.35, we get:

$$\int_V \left[\mu_{EM}\jmath\omega G\mathbf{j} + \frac{1}{\epsilon_{EM}} G\,\mathbf{grad}'\ \rho_{EM} + G\,\mathbf{rot}'\ \mathbf{j_m}\right] dV' \tag{C.39}$$

$$= \int_V \left[\mu_{EM}\jmath\omega G\mathbf{j} - \frac{\rho_{EM}}{\epsilon_{EM}}\,\mathbf{grad}'\ G + \mathbf{j_m} \times \mathbf{grad}'\ G\right] \tag{C.40}$$

$$- \oint_S \left[\frac{\rho_{EM}}{\epsilon_{EM}} G\hat{\mathbf{n}} + \hat{\mathbf{n}} \times \mathbf{j_m} G\right] dS' \tag{C.41}$$

We then use the following identity (actually valid for any function G and any vector field $\mathbf{E}$):

$$\oint_S \left[G\frac{\partial \mathbf{E}}{\mathbf{n}} - \mathbf{E}\frac{\partial G}{\partial \mathbf{n}}\right] dS' \tag{C.42}$$

$$= \oint_S \left[\hat{\mathbf{n}} G\, div'\ \mathbf{E} - (\hat{\mathbf{n}} \times \mathbf{E}) \times \mathbf{grad}'\ G - G\hat{\mathbf{n}} \times \mathbf{rot}'\ \mathbf{E} - (\hat{\mathbf{n}}\mathbf{E})\,\mathbf{grad}'\ G\right] dS' \tag{C.43}$$

If we then apply the following relations, which come directly from the Maxwell's equations:

$$\rho_{EM}/\epsilon_{EM} = div'\ \mathbf{E} \tag{C.44}$$

and:

$$\mathbf{rot}'\ \mathbf{E} + \mathbf{j_m} = -\mu_{EM}\jmath\omega\mathbf{H} \tag{C.45}$$

...we ultimately obtain the following result, first obtained by Stratton and Chu:

$$\mathbf{E}(\mathbf{r}) = \int_V \left[-\mu_{EM}\jmath\omega G\mathbf{j} + \frac{\rho_{EM}}{\epsilon_{EM}}\,\mathbf{grad}'\ G - \mathbf{j_m} \times \mathbf{grad}'\ G\right] dV' \tag{C.46}$$

$$+ \oint_S \left[-\mu_{EM}\jmath\omega G(\hat{\mathbf{n}} \times \mathbf{H}) - (\hat{\mathbf{n}}.\mathbf{E})\,\mathbf{grad}'\ G + (\hat{\mathbf{n}} \times \mathbf{E}) \times \mathbf{grad}'\ G\right] dS' \tag{C.47}$$

If we recall the duality principle stated above, we directly obtain:

$$\mathbf{H}(\mathbf{r}) = \int_V \left[-\mu_{EM}\jmath\omega G\mathbf{j_m} + \frac{\rho_{EM,m}}{\mu_{EM}}\,\mathbf{grad}'\ G + \mathbf{j}\times\mathbf{grad}'\ G\right] dV' \quad \text{(C.48)}$$

$$+ \oint_S \left[\mu_{EM}\jmath\omega G(\hat{\mathbf{n}}\times\mathbf{E}) + (\hat{\mathbf{n}}.\mathbf{H})\,\mathbf{grad}'\ G + (\hat{\mathbf{n}}\times\mathbf{H})\times\mathbf{grad}'\ G\right] dS' \quad \text{(C.49)}$$

C.3.2 Modification of Stratton-Chu equations for open surfaces

In fact, the equivalence between the Kirchhoff and Stratton-Chu equations is only true when the surface is closed (for example, the surface of a sphere). If, on the contrary, the surface is open, *i.e.*, bounded by a contour C, or if the charge distribution is nonzero only on a portion of the surface, it is necessary to add a line integral over C to the Stratton-Chu equations to maintain this equivalence. We obtain, for the electric field:

$$\mathbf{E}(\mathbf{r}) = \int_V \left[-\mu_{EM}\jmath\omega G\mathbf{j} + \frac{\rho_{EM}}{\epsilon_{EM}}\,\mathbf{grad}'\ G - \mathbf{j_m}\times\mathbf{grad}'\ G\right] dV' \quad \text{(C.50)}$$

$$+ \int_S \left[-\mu_{EM}\jmath\omega G(\hat{\mathbf{n}}\times\mathbf{H}) + (\hat{\mathbf{n}}.\mathbf{E})\,\mathbf{grad}'\ G + (\hat{\mathbf{n}}\times\mathbf{E})\times\mathbf{grad}'\ G\right] dS' \quad \text{(C.51)}$$

$$- \frac{1}{\jmath\omega\epsilon_{EM}}\oint_C (\mathbf{grad}'\ G)(\mathbf{H}.d\mathbf{l}) \quad \text{(C.52)}$$

...and for the magnetic field:

$$\mathbf{H}(\mathbf{r}) = \int_V \left[-\mu_{EM}\jmath\omega G\mathbf{j_m} + \frac{\rho_{EM,m}}{\mu_{EM}}\,\mathbf{grad}'\ G + \mathbf{j}\times\mathbf{grad}'\ G\right] dV' \quad \text{(C.53)}$$

$$+ \oint_S \left[\mu_{EM}\jmath\omega G(\hat{\mathbf{n}}\times\mathbf{E}) + (\hat{\mathbf{n}}.\mathbf{H})\,\mathbf{grad}'\ G + (\hat{\mathbf{n}}\times\mathbf{H})\times\mathbf{grad}'\ G\right] dS' \quad \text{(C.54)}$$

$$+ \frac{1}{\jmath\omega\mu_{EM}}\oint_C (\mathbf{grad}'\ G)(\mathbf{E}.d\mathbf{l}) \quad \text{(C.55)}$$

In practice, it turns out that the modification brought by this integral term is most often negligible, and it can therefore be ignored, unless it helps simplify the equations, as we will see later.

C.3.3 Interpretation of the Stratton-Chu equation

By identifying term by term the terms of the volume integral and the surface integral, we can note:

$$\mathbf{j_s} = \hat{\mathbf{n}}\times\mathbf{H} \quad \text{(C.56)}$$

$$\mathbf{j_{ms}} = -\hat{\mathbf{n}}\times\mathbf{E} \quad \text{(C.57)}$$

$$\rho_{EM,s} = \epsilon_{EM}(\hat{\mathbf{n}}.\mathbf{E}) \quad \text{(C.58)}$$

$$\rho_{EM,ms} = \mu_{EM}(\hat{\mathbf{n}}.\mathbf{H}) \quad \text{(C.59)}$$

where $\mathbf{j_s}$ and $\mathbf{j_{ms}}$ are on one hand the surface electric current density and the surface magnetic current density, and $\rho_{EM,s}$, $\rho_{EM,ms}$ are the surface electric and magnetic charge densities. We then arrive at a very elegant form that effectively highlights the equivalent role played by each term in the integral.

$$\mathbf{E}(\mathbf{r}) = \int_V \left[-\mu_{EM} \jmath\omega G \mathbf{j} + \frac{\rho_{EM}}{\epsilon_{EM}} \mathbf{grad}'\ G - \mathbf{j_m} \times \mathbf{grad}'\ G \right] dV' \quad \text{(C.60)}$$

$$+ \oint_S \left[-\mu_{EM} \jmath\omega G \mathbf{j_s} + \frac{\rho_{EM,s}}{\epsilon_{EM}} \mathbf{grad}'\ G - \mathbf{j_{ms}} \times \mathbf{grad}'\ G \right] dS' \quad \text{(C.61)}$$

$$\mathbf{H}(\mathbf{r}) = \int_V \left[-\mu_{EM} \jmath\omega G \mathbf{j_m} + \frac{\rho_{EM}}{\mu_{EM}} \mathbf{grad}'\ G + \mathbf{j} \times \mathbf{grad}'\ G \right] dV' \quad \text{(C.62)}$$

$$+ \oint_S \left[-\mu_{EM} \jmath\omega G \mathbf{j_{ms}} + \frac{\rho_{EM,ms}}{\mu_{EM}} \mathbf{grad}'\ G + \mathbf{j_s} \times \mathbf{grad}'\ G \right] dS' \quad \text{(C.63)}$$

At this point, let's recap the steps we've taken. We started with Maxwell's equations, and the only assumption we made is that the intensity of the source terms varies temporally with an angular frequency ω; thus, we consider a harmonic regime. Under this assumption, it is possible to relate the electric or magnetic field at a point $\mathbf{r}$ to the source terms (electric or magnetic) present in the considered space. These sources can be described by volume densities or surface densities, hence the presence of a volume integral and a surface integral. It is noteworthy, however, that each term in the integral plays an equivalent role.

In practice, one would choose V judiciously to simplify the equations. One can choose, in particular, to describe the entire space as the union of two volumes $V \cup V_1$ (these two volumes are not necessarily connected), with V_1 being the volume occupied by the sources, and V being the volume devoid of sources. In this case, if we work on volume V, only surface sources distributed on the surface S forming the interface between V and V_1 would remain (see Figure C.1). The volume integral can then be eliminated, and the Stratton-Chu equations become:

$$\mathbf{E}(\mathbf{r}) = \oint_S \left[-\mu_{EM} \jmath\omega G \mathbf{j_s} + \frac{\rho_{EM,s}}{\epsilon_{EM}} \mathbf{grad}'\ G - \mathbf{j_{ms}} \times \mathbf{grad}'\ G \right] dS' \quad \text{(C.64)}$$

$$\mathbf{H}(\mathbf{r}) = \oint_S \left[-\mu_{EM} \jmath\omega G \mathbf{j_{ms}} + \frac{\rho_{EM,ms}}{\mu_{EM}} \mathbf{grad}'\ G + \mathbf{j_s} \times \mathbf{grad}'\ G \right] dS' \quad \text{(C.65)}$$

Figure C.2 shows some possibilities for choosing surfaces S and integration contours C. When working under such conditions, the implicit choice of the integration volume is either the source-free space (cases a, c, and d) or the source-free half-space (case b, where the integration volume is the atmosphere, not the water volume).

C.3.4 Stratton-Chu equation in the far field regime

To simplify the Stratton and Chu equations, the far-field approximation is often employed, which assumes that the wave is plane. This leads to a form first proposed by Silver [157] (p. 161, eq. 103).

C.3.4.1 Fraunhofer zone

The spherical wave is approximated by a plane progressive wave following the Taylor expansion (with $\hat{\mathbf{r}} = \mathbf{r}/r$):

$$|\mathbf{r} - \mathbf{r}'| = r \times \left[1 - \frac{\hat{\mathbf{r}}.\mathbf{r}'}{r} + \frac{r'^2}{2r^2} - \frac{1}{8} \left(\frac{2\hat{\mathbf{r}}.\mathbf{r}'}{r} \right)^2 + \dots \right] \quad \text{(C.66)}$$

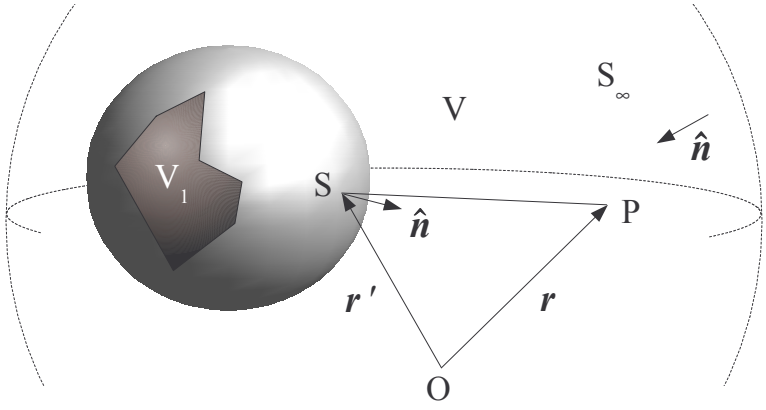

Figure C.1: *Description of the integration volumes. Electromagnetic sources are distributed in volume V_1 (which may not be connected), with an outer surface S. The volume V is source-free. Surface S_∞ is extended to infinity.*

...where terms up to order 2 are retained. Quadratic terms can be neglected as long as they do not contribute to a phase much greater than $\pi/2$ (some works use a limit of 2π). If the coordinate system's origin is placed at the center of the electromagnetic sources' distribution, and the diameter of this distribution is assumed to be D, then the phase shift induced by the quadratic part of the Taylor expansion can be considered equal to:

$$\Delta\phi = kr\left[\frac{r'^2}{2r^2} - \frac{1}{8}\left(\frac{2\hat{\mathbf{r}}.\mathbf{r}'}{r}\right)^2\right] \sim k\frac{r'^2}{2r} \tag{C.67}$$

with $k = 2\pi/\lambda$ being the electromagnetic wave number. Then:

$$\Delta\phi \ll \frac{\pi}{2} \Rightarrow r \gg \frac{D^2}{2\lambda} \tag{C.68}$$

and, with the other convention:

$$\Delta\phi \ll 2\pi \Rightarrow r \gg \frac{D^2}{8\lambda} \tag{C.69}$$

In the following, we will adhere to the first convention. Three working zones are then distinguished:

- *Rayleigh zone*, or near-field, if $r < \frac{D^2}{2\lambda}$. In this zone, an exact treatment taking into account edge effects will be required;
- *Fresnel zone*, or intermediate zone, if $\frac{D^2}{2\lambda} < r < \frac{2D^2}{\lambda}$;
- *Fraunhofer zone*, or far-field, if $\frac{2D^2}{\lambda} < r$

In the Fraunhofer zone, it is possible to approximate the electromagnetic wave by a progressive plane wave, *i.e.*,:

$$G(\mathbf{r}-\mathbf{r}') = \frac{e^{-\jmath k|\mathbf{r}-\mathbf{r}'|}}{4\pi|\mathbf{r}-\mathbf{r}'|} \sim \frac{e^{-\jmath kr}}{4\pi r}e^{\jmath k\hat{\mathbf{r}}.\mathbf{r}'} \tag{C.70}$$

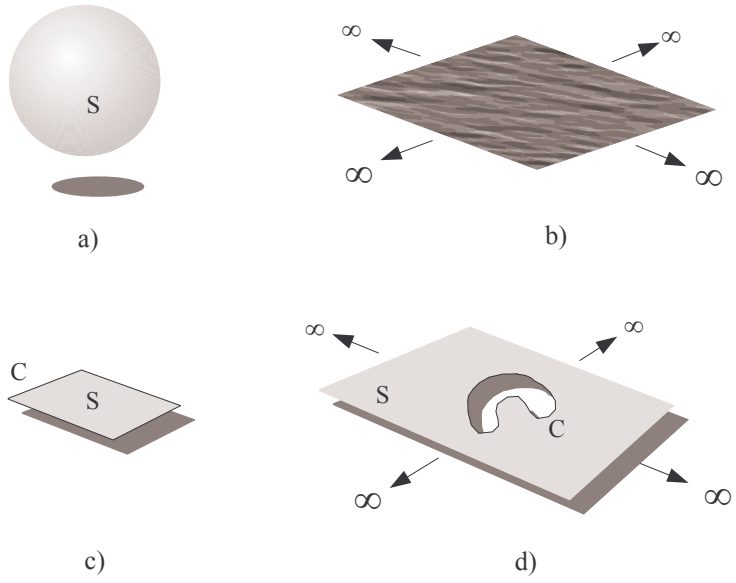

Figure C.2: *Some possible surfaces for integration.* a) *Finite open surface* b) *Infinite open surface (*e.g.*, the sea),* c) *Finite surface with an outer contour C,* d) *Infinite surface with an inner contour C. In reality, surfaces are not necessarily connected or flat.*

Under this approximation, we have:

$$\mathbf{grad}'\ G(\mathbf{r}-\mathbf{r}') = \jmath\mathbf{k}G(\mathbf{r}-\mathbf{r}') = \frac{j\mathbf{k}e^{-\jmath kr}}{4\pi r}e^{\jmath k\hat{\mathbf{r}}\mathbf{r}'} \tag{C.71}$$

...with $\mathbf{k} = k\hat{\mathbf{r}}$. It can also be shown that the curl operator can be approximated by a cross product:

$$\mathbf{rot}\ V \simeq -j\mathbf{k}\times V \tag{C.72}$$

C.3.4.2 Simplification of Stratton-Chu Equations

Applying the two approximations above to equation C.47, we obtain:

$$\mathbf{E}(\mathbf{r}) = \frac{\jmath e^{-\jmath kr}}{4\pi r}\oint_S \left[(\hat{\mathbf{n}}\times\mathbf{E})\times\mathbf{k} - \omega\mu_{EM}(\hat{\mathbf{n}}\times\mathbf{H}) + (\hat{\mathbf{n}}.\mathbf{E})\mathbf{k}\right]e^{j\mathbf{k}.\mathbf{r}'}dS' \tag{C.73}$$

If the surface is open, meaning it is bounded by a contour C, the line integral must be taken into account. Although this term can be practically neglected, retaining it is judicious as it leads to a simplification of the equation. Indeed, by applying Stokes' theorem:

$$\begin{aligned}
\oint_C(\mathbf{grad}'\ G)(\mathbf{H}.d\mathbf{l}) &= \frac{\jmath ke^{-\jmath kr}}{4\pi r}\int_S\left[\mathbf{rot}'\ (\mathbf{H}e^{\jmath kr'})\right]\hat{\mathbf{n}}dS' && \text{(C.74)}\\
&= \frac{\jmath ke^{-\jmath kr}}{4\pi r}\int_S\left[(\mathbf{grad}'\ e^{\jmath\mathbf{k}.\mathbf{r}'})\times\mathbf{H} + e^{\jmath kr'}\,\mathbf{rot}'\ \mathbf{H}\right]\hat{\mathbf{n}}dS' && \text{(C.75)}\\
&= \frac{\jmath ke^{-\jmath kr}}{4\pi r}\int_S\left[j\mathbf{k}\times\mathbf{H} + \jmath\omega\epsilon_{EM}\mathbf{E}\right]e^{\jmath kr'}\hat{\mathbf{n}}dS' && \text{(C.76)}\\
& && \text{(C.77)}
\end{aligned}$$

...the transition from the penultimate equation to the last is done using the Maxwell-Ampère equation in the absence of source terms. In the end, the line integral becomes:

$$-\frac{1}{\jmath\omega\epsilon_{EM}}\oint_C(\mathbf{grad}'\ G)(\mathbf{H}.d\mathbf{l})=\frac{je^{-\jmath kr}}{4\pi r}\int_S\left[\frac{((\mathbf{k}\times\mathbf{H})\hat{\mathbf{n}})\mathbf{k}}{\omega\epsilon_{EM}}+(\hat{\mathbf{n}}\mathbf{E})\mathbf{k}\right]e^{\jmath\mathbf{k}.\mathbf{r}'}dS' \quad \text{(C.78)}$$

and the Stratton-Chu equation in the far field for an open surface becomes[2]:

$$\begin{aligned}\mathbf{E}(\mathbf{r}) &= \frac{\jmath e^{-\jmath kr}}{4\pi r}\int_S\left[(\hat{\mathbf{n}}\times\mathbf{E})\times\mathbf{k}-\omega\mu_{EM}(\hat{\mathbf{n}}\times\mathbf{H})+\frac{((\mathbf{k}\times\mathbf{H})\hat{\mathbf{n}})\mathbf{k}}{\omega\epsilon_{EM}}\right]e^{\jmath\mathbf{k}.\mathbf{r}'}dS' \quad \text{(C.79)}\\ &= \frac{\jmath ke^{-\jmath kr}}{4\pi r}\left[\int_S\left[(\hat{\mathbf{n}}\times\mathbf{E})-\eta\hat{\mathbf{r}}\times(\hat{\mathbf{n}}\times\mathbf{H})\right]e^{\jmath\mathbf{k}.\mathbf{r}'}dS'\right]\times\hat{\mathbf{r}} \quad \text{(C.80)}\end{aligned}$$

In the particular case where the surface is flat, *i.e.*, where $\hat{\mathbf{n}}$ does not depend on $\mathbf{r}'$, this equation can also be written in the form:

$$\mathbf{E}(\mathbf{r})=\frac{\jmath ke^{-\jmath kr}}{4\pi r}\left[\hat{\mathbf{n}}\times\mathbf{F_E}-\eta\hat{\mathbf{r}}\times(\hat{\mathbf{n}}\times\mathbf{F_H})\right]\times\hat{\mathbf{r}} \quad \text{(C.81)}$$

which reveals the terms:

$$\begin{aligned}\mathbf{F_E} &= \int_S\mathbf{E}(\mathbf{r}')e^{\jmath\mathbf{k}.\mathbf{r}'}dS' \quad \text{(C.82)}\\ \mathbf{F_H} &= \int_S\mathbf{H}(\mathbf{r}')e^{\jmath\mathbf{k}.\mathbf{r}'}dS' \quad \text{(C.83)}\end{aligned}$$

Note that these two integrals are nothing but Fourier transforms.

C.3.4.3 Fraunhofer diffraction

In the case where the surface is electrically perfectly conductive, the electric field is obtained by removing the term $\mathbf{F_H}$ and doubling the term in $\mathbf{F_E}$ (for energy conservation reasons):

$$\mathbf{E}(\mathbf{r})=\frac{\jmath ke^{-\jmath kr}}{2\pi r}(\hat{\mathbf{n}}\times\mathbf{F_E})\times\hat{\mathbf{r}} \quad \text{(C.84)}$$

The opposite is done in the case of a magnetically perfectly conductive surface:

$$\mathbf{E}(\mathbf{r})=-\frac{\jmath ke^{-\jmath kr}}{2\pi r}\left[\eta\hat{\mathbf{r}}\times(\hat{\mathbf{n}}\times\mathbf{F_H})\right]\times\hat{\mathbf{r}} \quad \text{(C.85)}$$

In the first case, if we take the magnitude of $\mathbf{E}$, we find the classic formula giving the diffracted field at infinity by a surface of considerable size compared to the wavelength, by applying the Huygens-Fresnel principle (according to which any point on S can be considered as a point source having the phase and amplitude of the field on surface S):

$$||\mathbf{E}(\mathbf{k})||^2\propto I_0\int_S||\mathbf{E}(\mathbf{r}')||^2\exp[\jmath\mathbf{k}.\mathbf{r}']dS' \quad \text{(C.86)}$$

[2]The transition from equation C.79 to C.80 is done using a definition of the wave number: $k=c/\omega$ where c is the wave velocity in the medium, with $c=\frac{1}{\sqrt{\mu_{EM}\epsilon_{EM}}}$; and on the other hand, using the fact that $\eta=\sqrt{\mu_{EM}/\epsilon_{EM}}$ is the impedance of the considered medium. We then have $\omega\mu_{EM}=\eta k$ and $\frac{1}{\omega\eta}=\eta/k$. The vector relationship is then used: $\mathbf{A}\times(\mathbf{B}\times\mathbf{C})=\mathbf{B}(\mathbf{A}.\mathbf{C})-\mathbf{C}(\mathbf{A}.\mathbf{B})$, valid for any vectors $\mathbf{A}$, $\mathbf{B}$, $\mathbf{C}$, setting here $\mathbf{A}=\mathbf{k}$, $\mathbf{B}=\hat{\mathbf{r}}=\mathbf{k}/k$, and $\mathbf{C}=\mathbf{n}\times\mathbf{H}$.

C.4 The Kirchhoff Approximation

We start by writing the incident wave on a surface, which is considered to be a plane wave:

$$\mathbf{E}^i(\mathbf{r}) = E_0 \hat{\mathbf{e}}^i \exp \jmath(\omega t - \mathbf{k}_i.\mathbf{r}) \tag{C.87}$$

where E_0 is the amplitude of the incident wave near the surface, ω is its angular frequency, $\mathbf{k}_i$ is the incident wave vector, defined as $\mathbf{k}_i = k_0 \hat{\mathbf{r}}_x$ where k_0 is the wave number of the signal carrier (see also the definition of reference frames in Appendix A), $\mathbf{r}$ is the vector giving the position of the point where we evaluate the incident field, and $\hat{\mathbf{e}}^i$ is the vector giving the polarization of the electric field ($\hat{\mathbf{e}}^i$ is orthogonal to $\mathbf{k}_i$). The incident wave creates surface currents at the surface, generating a scattered wave denoted $\mathbf{E}^s$, propagating in the direction $\mathbf{k}_s = k_0 \hat{\mathbf{r}}_s^f$. It is possible to use the Stratton and Chu equation to evaluate the field $\mathbf{E}^s$ generated by these surface currents. We take these equations in their far-field form by adapting Equation C.80. We then have:

$$\mathbf{E}^s(\mathbf{r}) = \frac{\jmath k e^{-\jmath k r}}{4\pi r} \left[\int_S \left[(\hat{\mathbf{n}} \times \mathbf{E}) - \eta \hat{\mathbf{r}} \times (\hat{\mathbf{n}} \times \mathbf{H}) \right] e^{\jmath \mathbf{k}_s.\mathbf{r}'} dS' \right] \times \hat{\mathbf{r}} \tag{C.88}$$

The total electric field $\mathbf{E}(\mathbf{r})$ near and just above the surface (*i.e.*, in the air) is the sum of the incident field and the scattered field:

$$\mathbf{E}(\mathbf{r}) = \mathbf{E}^i(\mathbf{r}) + \mathbf{E}^s(\mathbf{r}). \tag{C.89}$$

It is this total field, at the water surface, that is used in the integral of Equation C.88. To evaluate this integral, we need to evaluate the components $\hat{\mathbf{n}} \times \mathbf{E}$ and $\hat{\mathbf{n}} \times \mathbf{H}$.

With this assumption, we can consider a local frame at the water surface $\mathcal{L}(\mathrm{P}, \hat{\mathbf{x}}_l, \hat{\mathbf{y}}_l, \hat{\mathbf{z}}_l)$ (see Appendix A). We assume that locally everything happens as if the surface were flat, *i.e.*, approximated by its tangent plane. We can then write the scattered field in terms of the incident field. To do this, we decompose the vector $\mathbf{E}^s$ into its polarization components in the polarization frame of the incident wave $\mathcal{P}_I(\mathrm{P}, \hat{\mathbf{v}}_i, \hat{\mathbf{h}}_i, \hat{\mathbf{r}}_x)$, namely the projection of $\mathbf{E}^i$ onto $\hat{\mathbf{h}}_i$ and $\hat{\mathbf{v}}_i$:

$$\mathbf{E}^i(\mathbf{r}) = E_0 e^{\jmath \mathbf{k}_i.\mathbf{r}} (\hat{\mathbf{e}}^i.\hat{\mathbf{h}}_i + \hat{\mathbf{e}}^i.\hat{\mathbf{v}}_i) \tag{C.90}$$

Similarly, for the reflected field, which involves the Fresnel coefficients R_h and R_v (see, for example, [136], Chapter 7, Eq. 7.4.4), written here in the case where the first medium is air and the second has a relative dielectric constant ϵ_r (defined in Chapter 2, Equation 2.3):

$$\mathbf{E}^s(\mathbf{r}) = E_0 e^{\jmath \mathbf{k}_r.\mathbf{r}} (R_h(\hat{\mathbf{e}}^i.\hat{\mathbf{h}}_i)\hat{\mathbf{h}}_i - R_v(\hat{\mathbf{e}}^i.\hat{\mathbf{v}}_i)\hat{\mathbf{v}}_i) \tag{C.91}$$

with:

$$R_h = \frac{cos\theta_i^l - \sqrt{\epsilon_r - \sin^2 \theta_i^l}}{cos\theta_i^l + \sqrt{\epsilon_r - \sin^2 \theta_i^l}} \tag{C.92}$$

$$R_v = \frac{\epsilon_r \cos\theta_i^l - \sqrt{\epsilon_r - \sin^2 \theta_i^l}}{\epsilon_r \cos\theta_i^l + \sqrt{\epsilon_r - \sin^2 \theta_i^l}} \tag{C.93}$$

We then have:

$$\mathbf{E}(\mathbf{r}) \times \hat{\mathbf{n}} = E_0 e^{\jmath \mathbf{k}_i.\mathbf{r}} ((1 + R_h)(\hat{\mathbf{e}}^i.\hat{\mathbf{h}}_i)\hat{\mathbf{n}} \times \hat{\mathbf{h}}_i - (1 - R_v)(\hat{\mathbf{n}}.\hat{\mathbf{r}}_x)(\hat{\mathbf{e}}^i.\hat{\mathbf{v}}_i)\hat{\mathbf{h}}_i) \tag{C.94}$$

Similarly, it can be shown that:

$$\eta\hat{\mathbf{n}}\times\mathbf{H}(\mathbf{r}) = -E_0 e^{\jmath\mathbf{k}_i.\mathbf{r}}((1-R_h)(\hat{\mathbf{e}}^i.\hat{\mathbf{h}}_i)(\hat{\mathbf{n}}.\hat{\mathbf{r}}_x)\hat{\mathbf{h}}_i + (1+R_v)(\hat{\mathbf{e}}^i.\hat{\mathbf{v}}_i)\hat{\mathbf{n}}\times\hat{\mathbf{h}}_i) \tag{C.95}$$

Setting the Stratton-Chu equation C.88 in the direction of diffusion ($\mathbf{r}\leftarrow\mathbf{r}_s = r\hat{\mathbf{r}}_s^f$), and setting $\mathbf{E}(\mathbf{r}) = \bar{\mathbf{E}}(\mathbf{r})e^{-\jmath\mathbf{k}_i.\mathbf{r}}$, $\mathbf{H}(\mathbf{r}) = \bar{\mathbf{H}}(\mathbf{r})e^{-\jmath\mathbf{k}_i.\mathbf{r}}$, we have:

$$\mathbf{E}^s(\mathbf{r}) = \frac{\jmath k_0 e^{-\jmath k_0 r}}{4\pi r}\left[\int_S \left[(\hat{\mathbf{n}}\times\bar{\mathbf{E}}) - \eta\hat{\mathbf{r}}_s\times(\hat{\mathbf{n}}\times\bar{\mathbf{H}})\right] e^{\jmath(\mathbf{k}_s-\mathbf{k}_i).\mathbf{r}'} dS'\right]\times\hat{\mathbf{r}}_s^f \tag{C.96}$$

At this point, several treatments are then possible. The first one follows from geometric optics. For this, we consider the phase term:

$$Q = (\mathbf{k}_s - \mathbf{k}_i).\mathbf{r}' \tag{C.97}$$

Where the phase Q evolves rapidly, the positive terms of the sum cancel out with the negative terms, and only points where this phase evolves slowly contribute to the sum: this is the stationary phase approximation. Physically, points where the phase evolves slowly are those that are specular with respect to the bistatic configuration considered. The second possible treatment comes from physical optics, which involves expanding Equation C.96 in a series around zero slope terms, a series that is truncated to the desired order. The result obtained has a slightly wider validity range, allowing for smaller radii of curvature compared to those supported by geometric optics [177]. In our work, only the first approach has been implemented, so it will be briefly detailed. In the wind frame $\mathcal{V}$:

$$Q = q_x x' + q_y y' + q_\zeta \zeta(x', y') \tag{C.98}$$

with $\{\mathbf{r}'\}_\mathcal{V} = [x', y', z']$, $\{\mathbf{k}_s - \mathbf{k}_i\}_\mathcal{V} = [q_x, q_y, q_\zeta]$, and $\zeta(x', y')$ the sea surface elevation function in the wind frame. The phase is stationary if:

$$\left\{\begin{array}{rcl} \frac{\partial Q}{\partial x} & = & 0 = q_x + q_\zeta\frac{\partial\zeta}{\partial x} = q_x - q_\zeta Z_u \\ \frac{\partial Q}{\partial y} & = & 0 = q_y + q_\zeta\frac{\partial\zeta}{\partial y} = q_y - q_\zeta Z_c \end{array}\right. \tag{C.99}$$

Note that the slope Z_u and Z_c have a negative sign; this is to facilitate the connection with the probabilistic slope model in Chapter 2, where the slopes are taken with respect to the upwind direction. With this stationarity assumption, the unit vectors $\hat{\mathbf{n}}$, $\hat{\mathbf{h}}_i$, and $\hat{\mathbf{v}}_i$ no longer depend on $\mathbf{r}$ but only on the specular direction; and therefore:

$$\left\{\begin{array}{rcl} \hat{\mathbf{n}} & = & \frac{k|q_\zeta|}{q^2 q_\zeta}(\hat{\mathbf{r}}_i - \hat{\mathbf{r}}_s^f) \\ \hat{\mathbf{h}}_i & = & \frac{|q_\zeta|}{Dq_\zeta}(\hat{\mathbf{r}}_i\times\hat{\mathbf{r}}_s^f) \\ \hat{\mathbf{v}}_i & = & \frac{|q_\zeta|}{Dq_\zeta}\left((\hat{\mathbf{r}}_i.\hat{\mathbf{r}}_s^f) - \hat{\mathbf{r}}_s^f\right) \end{array}\right. \tag{C.100}$$

with q being the norm of Q and $D = \sqrt{(\hat{\mathbf{r}}_i.\hat{\mathbf{v}}_s^f)^2 + (\hat{\mathbf{r}}_i.\hat{\mathbf{h}}_s^f)^2}$. We then have:

$$\mathbf{E}^s(\mathbf{r}) = \frac{\jmath k_0 e^{-\jmath k_0 r}}{4\pi r}\left[(\hat{\mathbf{n}}\times\mathbf{E}) - \eta\hat{\mathbf{r}}_s\times(\hat{\mathbf{n}}\times\mathbf{H})\right]\times\hat{\mathbf{r}}_s^f\int_S e^{\jmath Q} dS' \tag{C.101}$$

Expanding these equations, it can be shown that there is a relationship between the incident field, expressed in the "incident wave" polarimetric frame, and the scattered field, expressed in the "scattered wave" polarimetric frame in the so-called "forward scattering alignment" convention $\mathcal{P}_S^F(\mathrm{P}, \hat{\mathbf{v}}_r^f, \hat{\mathbf{h}}_r^f, \hat{\mathbf{r}}_s^f)$:

$$\left[\begin{array}{c} \mathbf{E}_v^s.\hat{\mathbf{v}}_i \\ \mathbf{E}_h^s.\hat{\mathbf{h}}_i \end{array}\right] = \underbrace{\frac{\jmath k_0 e^{-\jmath k_0 r}}{4\pi r} I E_0 \left(\begin{array}{cc} U_{vv} & U_{vh} \\ U_{hv} & U_{hh} \end{array}\right)}_{\text{polarimetric scattering matrix } \mathbf{S}} \left[\begin{array}{c} \mathbf{E}_v^s.\hat{\mathbf{v}}_s^f \\ \mathbf{E}_h^s.\hat{\mathbf{h}}_s^f \end{array}\right] \tag{C.102}$$

with:

$$I = \frac{q}{|q_\zeta|} \int_S \exp\left\{(\mathbf{k}_s - \mathbf{k}_i).\mathbf{r}'\right\} dS' \tag{C.103}$$

and:

$$U_{hh} = \frac{q \times \mathrm{sgn}(q_\zeta) \left\{ R_v(\hat{\mathbf{h}}_s^f.\hat{\mathbf{r}}_x)(\hat{\mathbf{h}}_i.\hat{\mathbf{r}}_s^f) + R_h(\hat{\mathbf{v}}_s^f.\hat{\mathbf{r}}_x)(\hat{\mathbf{v}}_i.\hat{\mathbf{r}}_s^f) \right\}}{kD^2} \tag{C.104}$$

$$U_{vh} = \frac{q \times \mathrm{sgn}(q_\zeta) \left\{ R_v(\hat{\mathbf{v}}_s^f.\hat{\mathbf{r}}_x)(\hat{\mathbf{h}}_i.\hat{\mathbf{r}}_s^f) - R_h(\hat{\mathbf{v}}_s^f.\hat{\mathbf{r}}_x)(\hat{\mathbf{v}}_i.\hat{\mathbf{r}}_s^f) \right\}}{kD^2} \tag{C.105}$$

$$U_{hv} = \frac{q \times \mathrm{sgn}(q_\zeta) \left\{ R_v(\hat{\mathbf{v}}_s^f.\hat{\mathbf{r}}_x)(\hat{\mathbf{v}}_i.\hat{\mathbf{r}}_s^f) + R_h(\hat{\mathbf{v}}_s^f.\hat{\mathbf{r}}_x)(\hat{\mathbf{h}}_i.\hat{\mathbf{r}}_s^f) \right\}}{kD^2} \tag{C.106}$$

$$U_{vv} = \frac{q \times \mathrm{sgn}(q_\zeta) \left\{ R_v(\hat{\mathbf{h}}_s^f.\hat{\mathbf{r}}_x)(\hat{\mathbf{v}}_i.\hat{\mathbf{r}}_s^f) - R_h(\hat{\mathbf{v}}_s^f.\hat{\mathbf{r}}_x)(\hat{\mathbf{h}}_i.\hat{\mathbf{r}}_s^f) \right\}}{kD^2} \tag{C.107}$$

We now calculate the *average* coefficients of the polarimetric scattering matrix in power Σ^0. By definition:

$$\sigma_{pq} = \frac{4\pi r_r^2}{A} \frac{\langle E_{pq}^s E_{pq}^{s\star} \rangle}{E_q^i E_q^{i\star}} \tag{C.108}$$

where $\star$ is the conjugation operator. We are thus led to calculate the mathematical expectation of $|I|^2$:

$$\langle |I|^2 \rangle = \frac{q^2}{q_\zeta^2} \iint_S e^{\jmath(q_x(x'-x'')+q_y(y'-y''))} \langle e^{\jmath(\zeta(x',y')-\zeta(x'',y''))} \rangle dS' dS'' \tag{C.109}$$

To proceed with the calculation, an assumption about the shape of the surface is needed. Historically (see, for example, Fung and Chan [77], cited by Khenchaf [103], p. 105), it is assumed that the surface follows a *Gaussian process*, *i.e.*, $\zeta(x, y)$ is a Gaussian variable drawn from a distribution with zero mean, a variance of σ^2, and a correlation function denoted by ρ_{EM}. Then:

$$\langle e^{\jmath(\zeta(x',y')-\zeta(x'',y''))} \rangle = e^{-q_\zeta \sigma^2 (1-\rho_{EM}(x'-x'',y'-y''))} \tag{C.110}$$

with $q_\zeta^2 \sigma^2 = (k_0\sigma)^2(\cos\theta_i^v + \cos\theta_s^v)^2$, where this parameter $q_\zeta \sigma$ characterizes the roughness of the considered surface. Under a certain number of assumptions:

1. stationarity of the process
2. finite size of the surface (area $A = 2a \times 2a$)
3. isotropic surface
4. a sufficiently large value of $q_\zeta^2 \sigma^2$ so that its contribution is significant only for small values of $x' - x''$ and $x' - x''$

... it can be shown that:

$$\langle |I|^2 \rangle = 2\pi \frac{q_\zeta^4 m^2}{q_\zeta} A e^{-\frac{q_x^2+q_y^2}{2m^2}} \tag{C.111}$$

with $m = \sigma\sqrt{|\rho''_{EM}(0)|}$ being the standard deviation of surface slopes. In the end, we obtain:

$$\sigma_{pq} = \frac{k_0^2 q^2 |U_{pq}|^2}{2q_\zeta^2 m^2} e^{-\frac{q_x^2+q_y^2}{2m^2}} \tag{C.112}$$

By identifying the Gaussian distribution that appears in this expression, we arrive at the form:

$$\sigma_{pq} = \frac{\pi k_0^2 q^2 |U_{pq}|^2}{q_\zeta^2} \mathrm{Pr}(Z_u, Z_c) \tag{C.113}$$

The function Pr is a probability of occurrence of slopes $Z_u = -\partial\zeta/\partial x = -q_x/q_\zeta$ and $Z_c = -\partial\zeta/\partial y = -q_y/q_\zeta$, for example, the Cox and Munk distribution (Chapter 2, p. 78). Equation C.113 is then used in Chapter 4.

C.5 Polarimetric coefficients of the Small Perturbation Method

In this section, we provide, without any demonstration, the values of the coefficients α_{pq} allowing the calculation of the scattered field by the Small Perturbation Method, using the formula 4.5 from Chapter 4, page 110. Interested readers may refer, for example, to Khenchaf [1, 103] for a complete demonstration. We first introduce two intermediate terms:

$$a_i = \sqrt{\epsilon_r \mu_r + \sin^2 \theta_i^v} \tag{C.114}$$

$$a_s = \sqrt{\epsilon_r \mu_r + \sin^2 \theta_s^v} \tag{C.115}$$

For the VV channel, we have:

$$n_1^{vv} = (\epsilon_r - 1)(\epsilon_r \sin\theta_i^v \sin\theta_s^v - a_i a_s \cos\phi_s^v) \tag{C.116}$$

$$n_2^{vv} = \epsilon_r^2 (\mu_r - 1)\cos\phi_s^v \tag{C.117}$$

$$d_1^{vv} = \epsilon_r \cos\theta_i^v + a_i \tag{C.118}$$

$$d_2^{vv} = \epsilon_r \cos\theta_s^v + a_s \tag{C.119}$$

$$\alpha_{vv} = \frac{n_1^{vv} + n_2^{vv}}{d_1^{vv} d_2^{vv}} \tag{C.120}$$

For the VH channel:

$$n_1^{vh} = (\mu_r - 1)\epsilon_r a_i \tag{C.121}$$

$$n_2^{vh} = (\epsilon_r - 1)\mu_r a_s \tag{C.122}$$

$$d_1^{vh} = a_i + \mu_r \cos\theta_i^v \tag{C.123}$$

$$d_2^{vh} = a_s + \epsilon_r \cos\theta_s^v \tag{C.124}$$

$$\alpha_{vh} = \frac{n_1^{vh} + n_2^{vh}}{d_1^{vh} d_2^{vh}} \sin\phi_s^v \tag{C.125}$$

For the HV channel:

$$n_1^{hv} = (\epsilon_r - 1)\mu_r a_i \tag{C.126}$$

$$n_2^{hv} = (\mu_r - 1)\epsilon_r a_s \tag{C.127}$$

$$d_1^{hv} = a_i + \epsilon_r \cos\theta_i^v \tag{C.128}$$

$$d_2^{hv} = a_s + \mu_r \cos\theta_s^v \tag{C.129}$$

$$\alpha_{hv} = \frac{n_1^{hv} + n_2^{hv}}{d_1^{hv} d_2^{hv}} \sin\phi_s^v \tag{C.130}$$

Finally, for the HH channel:

$$
\begin{aligned}
n_1^{hh} &= (\mu_r - 1)(a_i a_s \cos\phi_s^v - \mu_r \sin\theta_i^v \sin\theta_s^v) && \text{(C.131)}\\
n_2^{hh} &= \mu_r^2(\epsilon_r - 1)\cos\phi_s^v && \text{(C.132)}\\
d_1^{hh} &= a_i + \mu_r \cos\theta_i^v && \text{(C.133)}\\
d_2^{hh} &= a_s + \mu_r \cos\theta_s^v && \text{(C.134)}\\
\alpha_{hh} &= -\frac{n_1^{hh} + n_2^{hh}}{d_1^{hh} d_2^{hh}} && \text{(C.135)}
\end{aligned}
$$

In practice, in the case of interest (water-air interface), the constant μ_r is taken equal to 1. It should be noted that the bistatic angles used correspond to a flat surface. Also, when calculating the coefficients of the small perturbation model, care should be taken to use the bistatic angles in the local frame $\mathcal{L}$, associated with the facet, and which would only correspond to the wind frame $\mathcal{V}$ if the facet were completely coincident with the average sea surface.

Appendix

D Stochastic Matched Filtering

Stochastic Matched Filtering is a generalization of traditional matched filtering to the case where the signal to be detected is not deterministic. This appendix provides some basics regarding Stochastic Matched Filtering. These elements are a synthesis of several articles: [37], [47], [46], and the course on Stochastic Matched Filtering by Jean-François Cavassilas published on his personal webpage[1]. The theory is presented in the context of discrete signals only.

D.1 Problem statement and preliminary definitions

We consider representing a signal $\mathbf{z}$ measured by a sensor (an observation) in the form of an infinite-size vector:

$$\mathbf{z} = [z_0, z_1, z_2, \ldots, z_n, \ldots] \tag{D.1}$$

This signal represents the discretized version of a continuous signal z:

$$z_n = z(nT) \tag{D.2}$$

where T is the sampling period of the system. It is also assumed that the sampled signal is quantified on M levels of values v_0,..., v_{M-1} (not necessarily spaced uniformly). For each sample z_n, it is also assumed that one of the following two hypotheses is true:

- **Hypothesis H_1:** The sample contains only noise, i.e., unwanted information: $z_n = b_n$
- **Hypothesis H_2:** The sample contains desired information (signal), but this signal is corrupted by additive noise: $z_n = s_n + b_n$

In general, signal measurement is rarely done on a single sample. When a signal enters a measuring instrument, it has a certain duration that allows it to be measured over several consecutive samples. In the following, it is considered that the signal typically extends over $N = 2l+1$ consecutive samples centered around sample s_n. The window $\mathbf{w}(n)$ is then defined as the vector:

$$\mathbf{w}(n) = [z_{n-l}, z_{n-l+1}, \ldots, z_n, \ldots, z_{n+l-1}, z_{n+l}] \tag{D.3}$$

(the choice of an odd length N and a centered window is just a convenience). It will also be noted, later in the document:

$$\mathbf{w}(n) = [w_0, w_1, \ldots, w_n, \ldots, w_{N-2}, w_{N-1}] \tag{D.4}$$

According to the hypotheses, it can always be written as follows:

[1] `http://cava.univ-tln.fr/`

- **Hypothesis** H_1:

$$\mathbf{w}(n) = \mathbf{b}(n) \tag{D.5}$$

with:

$$\mathbf{b}(n) = [b_{n-l}, b_{n-l+1}, \ldots, b_n, \ldots, b_{n+l-1}, b_{n+l}] \tag{D.6}$$

- **Hypothesis** H_2:

$$\mathbf{w}(n) = \mathbf{s}(n) + \mathbf{b}(n) \tag{D.7}$$

with:

$$\mathbf{s}(n) = [s_{n-l}, s_{n-l+1}, \ldots, s_n, \ldots, s_{n+l-1}, s_{n+l}] \tag{D.8}$$

It is further assumed that the choice of hypothesis H_1 or H_2 does not affect the nature of $\mathbf{b}$.

D.1.1 Various figures associated to windows

The windows $\mathbf{w}(n)$ have a length of N. The signal is assumed to be sampled on M levels. For a given n, there are thus N^M different possible configurations of $\mathbf{w}(n)$ that can be observed. Let $\mathbf{w}_i$ denote the i-th window configuration, with $i \in \langle 1..N^M \rangle$. Each configuration has a certain probability of occurrence. Let r_i be the probability of occurrence of the i-th configuration (it follows that $r_0 + r_1 + \ldots + r_{N^M-1} = 1$). The i-th window is described as follows:

$$\mathbf{w}_i = [w_{i,1}, \ldots w_{i,N}] \tag{D.9}$$

There are also N^M possible constructions for $\mathbf{s}$ and for $\mathbf{b}$. Let p_i be the probability of occurrence of the i-th configuration $\mathbf{s}_i$ of $\mathbf{s}$ and q_i its counterpart for $\mathbf{b}$. The following functions and quantities are defined:

- the "power of $\mathbf{w}_i$" function, scalar:

$$\mathsf{P}_{\mathbf{w}}(i) = \sum_{j=1}^{j=N} w_{i,j}^2 = \mathbf{w}_i^t \mathbf{w}_i \tag{D.10}$$

- the "average of $\mathbf{w}_i$" function, scalar:

$$M_{\mathbf{w}}(i) = \frac{1}{N} \sum_{j=1}^{j=N} w_{i,j} \tag{D.11}$$

- the "average $\mathbf{w}$ vector":

$$\bar{\mathbf{w}} = \sum_{i=1}^{i=N^M} r_i \mathbf{w}_i = E(\mathbf{w}) \tag{D.12}$$

where E is the "expectation" operator. This vector has a length of N.

- the variance-covariance matrix of $\mathbf{w}$ whose entry (i, j) is:

$$\Sigma_{\mathbf{w}}(i, j) = [r_i(\mathbf{w}_i - \bar{\mathbf{w}})][r_j(\mathbf{w}_j - \bar{\mathbf{w}})]^t \tag{D.13}$$

where $'$ denotes the transpose-conjugate. This matrix is symmetric.

- and finally, the average power of $\mathbf{w}$, scalar:

$$\bar{\mathsf{P}}_{\mathbf{w}} = \sum_{i=1}^{i=N^M} r_i \mathbf{w}_i^2 = \sum_{i=1}^{i=N^M} r_i \mathsf{P}_{\mathbf{w}}(i) = E(\mathbf{w}\mathbf{w}^t) \tag{D.14}$$

The same can be done for $\mathbf{s}$ and $\mathbf{b}$. Finally, the signal-to-noise ratio ρ of $\mathbf{s}$ over $\mathbf{b}$ is defined as the ratio:

$$\rho = \frac{\bar{\mathsf{P}}_{\mathbf{s}}}{\bar{\mathsf{P}}_{\mathbf{b}}} \tag{D.15}$$

D.2 Stochastic Matched Filtering problem

Let $\mathbf{h}$ be a "filter" defined as the vector:

$$\mathbf{h} = [h_N^*, \ldots, h_1^*] \tag{D.16}$$

$\mathbf{w}$ can be filtered by $\mathbf{h}$, which is simply a scalar product: $\mathbf{h^t w} = \mathbf{w^t h}$.

Note: By calling $\mathbf{h}$ a filter and using the notion of a scalar product, we are making a language abuse. Strictly speaking, filtering is expressed by convolving a signal with an impulse response. However, this convolution is equivalent to the scalar product of the signal with the complex conjugate reversed response of the filter's impulse response. Therefore, $\mathbf{h}$ is called a "filter" here, although it is actually the complex conjugate reversed response of the filter's impulse response. Keep this abuse in mind when implementing filtering via the Fourier transform.

Stochastic Matched Filtering Problem The average power of windows $\mathbf{w}$ filtered by $\mathbf{h}$ is:

$$\bar{\mathsf{P}}_{\mathbf{w^t h}} = \sum_{i=1}^{i=N^M} r_i (\mathbf{w}_i^t \mathbf{h})^2 \tag{D.17}$$

The stochastic matched filtering problem is to find $\mathbf{h}$ such that:

$$\rho' = \frac{\bar{\mathsf{P}}_{\mathbf{s^t h}}}{\bar{\mathsf{P}}_{\mathbf{b^t h}}} > \rho \tag{D.18}$$

where $\bar{\mathsf{P}}_{\mathbf{s^t h}}$ and $\bar{\mathsf{P}}_{\mathbf{b^t h}}$ are defined as in equation D.17 with notation changes.

Lemma: The average power $\bar{\mathsf{P}}_{\mathbf{w^t h}}$ of windows $\mathbf{w}_i$ filtered by $\mathbf{h}$ is also equal to:

$$\bar{\mathsf{P}}_{\mathbf{h^t w}} = \mathbf{h}^t (\mathbf{\Sigma_w} + \bar{\mathbf{w}}^t \bar{\mathbf{w}}) \mathbf{h} \tag{D.19}$$

Proof:

$$\bar{\mathsf{P}}_{\mathbf{w^t h}} = \sum_{i=1}^{i=N^M} r_i [\mathbf{w}_i^t \mathbf{h}]^2 \tag{D.20}$$

$$= \sum_{i=1}^{i=N^M} r_i \mathbf{h}^t \mathbf{w}_i \mathbf{w}_i^t \mathbf{h} \tag{D.21}$$

$$\bar{\mathsf{P}}_{\mathbf{w^t h}} = \sum_{i=1}^{i=N^M} r_i \mathbf{h}^t (\mathbf{w}_i - \bar{\mathbf{w}} + \bar{\mathbf{w}})(\mathbf{w}_i - \bar{\mathbf{w}} + \bar{\mathbf{w}})^t \mathbf{h} \tag{D.22}$$

After expansion:

$$\bar{\mathsf{P}}_{\mathbf{w^t h}} = T_1 + T_2 + T_3 \tag{D.23}$$

with:

- Term T_1:

$$\begin{aligned} T_1 &= \sum_{i=1}^{i=N^M} r_i \mathbf{h}^t(\mathbf{w}_i - \bar{\mathbf{w}})(\mathbf{w}_i - \bar{\mathbf{w}})^t\mathbf{h} && \text{(D.24)} \\ &= \mathbf{h}^t \left(\sum_{i=1}^{i=N^M} r_i(\mathbf{w}_i - \bar{\mathbf{w}})(\mathbf{w}_i - \bar{\mathbf{w}})^t \right) \mathbf{h} && \text{(D.25)} \\ T_1 &= \mathbf{h^t}\Sigma_{\mathbf{w}}\mathbf{h} && \text{(D.26)} \end{aligned}$$

- Term T_2:

$$\begin{aligned} T_2 &= \sum_{i=1}^{i=N^M} r_i \mathbf{h}^t\bar{\mathbf{w}}\bar{\mathbf{w}}^t\mathbf{h} && \text{(D.27)} \\ &= \left(\sum_{i=1}^{i=N^M} r_i \right) \mathbf{h}^t\bar{\mathbf{w}}\bar{\mathbf{w}}^t\mathbf{h} && \text{(D.28)} \\ T_2 &= \mathbf{h}^t\bar{\mathbf{w}}\bar{\mathbf{w}}^t\mathbf{h} && \text{(D.29)} \end{aligned}$$

- Term T_3:

$$\begin{aligned} T_3 &= \sum_{i=1}^{i=N^M} r_i \mathbf{h}^t(\mathbf{w}_i - \bar{\mathbf{w}})\bar{\mathbf{w}}^t\mathbf{h} + r_i\mathbf{h}^t\bar{\mathbf{w}}(\mathbf{w}_i - \bar{\mathbf{w}})^t\mathbf{h} && \text{(D.30)} \\ &= 2\mathbf{h}^t\bar{\mathbf{w}} \left(\sum_{i=1}^{i=N^M} r_i\mathbf{w}_i \right) \mathbf{h}^t - 2(\bar{\mathbf{w}}^t\mathbf{h})^2 && \text{(D.31)} \\ &= 2(\bar{\mathbf{w}}^t\mathbf{h})^2 + 2(\bar{\mathbf{w}}^t\mathbf{h})^2 - 2(\bar{\mathbf{w}}^t\mathbf{h})^2 && \text{(D.32)} \\ T_3 &= 0 && \text{(D.33)} \end{aligned}$$

By factoring T_1 and T_2, we have what we set out to prove. □

Therefore, the stochastic matched filtering problem boils down to finding a vector $\mathbf{h}$ that maximizes the ratio:

$$\rho' = \frac{\mathbf{h}^t(\Sigma_{\mathbf{s}} + \bar{\mathbf{s}}\bar{\mathbf{s}}^t)\mathbf{h}}{\mathbf{h}^t(\Sigma_{\mathbf{b}} + \bar{\mathbf{b}}\bar{\mathbf{b}}^t)\mathbf{h}} \tag{D.34}$$

The solution to this problem is straightforward. First, we define:

$$\begin{aligned} \mathtt{P} &= \Sigma_{\mathbf{s}} + \bar{\mathbf{s}}\bar{\mathbf{s}}^t && \text{(D.35)} \\ \mathtt{Q} &= \Sigma_{\mathbf{b}} + \bar{\mathbf{b}}\bar{\mathbf{b}}^t && \text{(D.36)} \end{aligned}$$

(the ratio $\mathbf{h}^t\mathtt{P}\mathbf{h}/\mathbf{h}^t\mathtt{Q}\mathbf{h}$ is a so-called Rayleigh quotient). There is no obstacle to constrain the denominator to be 1; we will then maximize the numerator. This constraint is written as:

$$1 - \mathbf{h}^t\mathtt{Q}\mathbf{h} = 0 \tag{D.37}$$

The problem can be formulated as a Lagrangian:

$$\mathcal{L}(\mathbf{h}) = \mathbf{h}^t\mathtt{P}\mathbf{h} + \lambda(1 - \mathbf{h}^t\mathtt{Q}\mathbf{h}) \tag{D.38}$$

Taking the derivative of this Lagrangian with respect to $\mathbf{h}$ and finding where it equals zero:

$$\nabla\mathcal{L}(\mathbf{h}) = 2(\mathtt{P}\mathbf{h} + \lambda\mathtt{Q}\mathbf{h}) = 0 \tag{D.39}$$

This leads to a generalized eigenvalue problem:

$$\mathtt{P}\mathbf{h} = \lambda\mathtt{Q}\mathbf{h} \tag{D.40}$$

and we have:

$$\rho' = \frac{\mathbf{h}^t\mathtt{P}\mathbf{h}}{\mathbf{h}^t\mathtt{Q}\mathbf{h}} = \frac{\lambda\mathbf{h}^t\mathtt{Q}\mathbf{h}}{\mathbf{h}^t\mathtt{Q}\mathbf{h}} = \lambda \tag{D.41}$$

If $\mathtt{Q}$ is invertible (symmetric positive definite), the solutions to the generalized eigenvalue problem, i.e., the vectors $\mathbf{h}$ satisfying:

$$\begin{cases} \mathtt{Q}^{-1}\mathtt{P}\mathbf{h} = \lambda\mathbf{h} \\ \lambda > \rho \\ \mathbf{h}^t\mathtt{Q}\mathbf{h} = 1 \end{cases} \tag{D.42}$$

are N such vectors since $\mathtt{P}$ and $\mathtt{Q}$ are symmetric, so is $\mathtt{Q}^{-1}\mathtt{P}$, and this matrix is diagonalizable. Denoting $\mathtt{R} = \mathtt{Q}^{-1}\mathtt{P}$:

$$\mathtt{R} = \mathtt{H}\mathtt{D}\mathtt{H}^{-1} \tag{D.43}$$

The vectors $\mathbf{h}$ that are solutions to our problem are the columns of $\mathtt{H}$. Among the N solution vectors, there is a subset of N_f vectors ($N_f \leq N$) $\mathbf{h}_1 \dots \mathbf{h}_{n_f}$ associated with eigenvalues $\lambda_1 \dots \lambda_{N_f}$ greater than ρ (under the constraint: $\mathbf{h}^t\mathtt{Q}\mathbf{h} = 1$). These N_f vectors will increase the signal-to-noise ratio ρ' after filtering. These are the stochastic matched filters for the signal.

D.3 The "classical" matched filtering

Note: this section was much simplified during translation, making the derivation of the classical matched filter a much more natural sub-case of the stochastic matched filtering.

So far, it has been assumed in general that the signal could take N^M appearances $\mathbf{s}_1$, $\mathbf{s}_2 \dots$, $\mathbf{s}_{N^M}$, each occurring with probability p_1, $p_2, \dots$, p_{N^M}. If the signal is perfectly known, meaning that it only takes one appearance, then it is possible to write $\mathbf{s} = \mathbf{s}_1$, $p_1 = 1$, and $p_2, \dots, p_{N^M} = 0$. We also have $\bar{\mathbf{s}} = \mathbf{s}$. Under these conditions, the matrix $\mathtt{P}$ introduced earlier is: $\mathtt{P} = \mathbf{s}\mathbf{s}^t$. Therefore, we seek to maximize the Rayleigh quotient:

$$\rho' = \frac{\mathbf{h}^t\mathbf{s}\mathbf{s}^t\mathbf{h}}{\mathbf{h}^t\mathtt{Q}\mathbf{h}} \tag{D.44}$$

We can solve this problem in the same way as before. The matrix $\mathbf{s}\mathbf{s}^t$ has a unit rank, so there will be only one eigenvalue $\mathbf{h}$ for $\mathtt{Q}^{-1}\mathtt{P}$. This eigenvalue is called the matched filter. To get this filter, take the first line of equations system D.42, which now reads:

$$\lambda\hat{\mathbf{w}} = (Q^{-1}P)\hat{\mathbf{w}} = (Q^{-1}\bar{\mathbf{s}}.\bar{\mathbf{s}}^h).\hat{\mathbf{w}} = Q^{-1}\bar{\mathbf{s}}.(\bar{\mathbf{s}}^h.\hat{\mathbf{w}}) = Q^{-1}\bar{\mathbf{s}}(\mathbf{s}\cdot\hat{\mathbf{w}}) \tag{D.45}$$

Noting that $(\bar{\mathbf{s}}\cdot\hat{\mathbf{w}}) = \lambda$ is a scalar, so the only admissible eigenvector is $\hat{\mathbf{w}} = \alpha Q^{-1}\bar{\mathbf{s}}$ where α is an arbitrary coefficient. When normalizing the solution so that $\mathbf{h}^t\mathtt{Q}\mathbf{h} = 1$ as expected in the third line of D.42, it comes that:

$$\alpha = \frac{1}{\sqrt{\mathbf{s}^t\mathtt{Q}^{-1}\mathbf{s}}} \tag{D.46}$$

so that the matched filter is:

$$\mathbf{h} = \frac{1}{\sqrt{\mathbf{s}^t \mathtt{Q}^{-1}\mathbf{s}}}\mathtt{Q}^{-1}\mathbf{s} \tag{D.47}$$

Special Case of Gaussian White Noise If the noise is Gaussian white noise with variance σ_b^2:

$$\mathtt{Q}^{-1} = \frac{1}{\sigma_b^2}\mathtt{I} \tag{D.48}$$

Furthermore:

$$\mathbf{s}^t \mathtt{Q}^{-1}\mathbf{s} = \frac{\mathsf{P}_\mathbf{s}}{\sigma_b^2} \tag{D.49}$$

The impulse response of the matched filter is, up to a multiplicative constant, proportional to the conjugate of $\mathbf{s}$:

$$\mathbf{h} = \frac{1}{\sigma_b\sqrt{\mathsf{P}_\mathbf{s}}}\mathbf{s} \tag{D.50}$$

D.4 Additional properties of Stochastic Matched Filtering

Bases The eigenvectors $\mathbf{h}_1 \dots \mathbf{h}_{N_f}$ of the matrix $\mathtt{Q}^{-1}\mathtt{P}$ are by definition linearly independent and thus form a basis. This basis is not necessarily orthogonal (counterexamples are easily exhibited by taking random numerical values). The vectors $\mathbf{j}_i = \mathtt{Q}\mathbf{h}_i$ also form a basis. This property is easily demonstrated by the fact that $\det \mathtt{H} \neq 0$ since the $\mathbf{h}_i$ are linearly independent. Moreover, $\mathtt{Q}$ is assumed to be invertible, so $\det \mathtt{Q} \neq 0$. Therefore, $\det \mathtt{QH} \neq 0$ and the $\mathbf{j}_i$ are linearly independent.

Biorthogonality It can also be shown that the vectors $\mathbf{h}_i$ and the vectors $\mathbf{j}_i = \mathtt{Q}\mathbf{h}_i$ satisfy the property:

$$\mathbf{h}_i^t \mathbf{j}_j = \delta_{ij} \tag{D.51}$$

where δ_{ij} is the Kronecker symbol. It is said that the basis of $\mathbf{h}_i$ and the basis of $\mathbf{j}_i$ is biorthogonal. Indeed, we have:

$$\forall i \in \langle 1..N \rangle, \mathtt{Q}^{-1}\mathtt{P}\mathbf{h}_i = \lambda_i \mathbf{h}_i \tag{D.52}$$

By setting $\mathbf{j}_i = \mathtt{Q}\mathbf{h}_i$, we also have:

$$\forall i \in \langle 1..N \rangle, \mathtt{P}\mathtt{Q}^{-1}\mathbf{j}_i = \lambda_i \mathbf{j}_i \tag{D.53}$$

The matrices $\mathtt{P}$ and $\mathtt{Q}$ are symmetric: $\mathtt{P}^{-1} = \mathtt{P}'$, $\mathtt{Q}^{-1} = \mathtt{q}^t$. We have $\mathtt{R}^t = (\mathtt{Q}^{-1}\mathtt{P})^t = \mathtt{P}^t(\mathtt{Q}^{-1})^t = \mathtt{P}\mathtt{Q}^{-1}$. Then the relations D.52 and D.53 can be written as:

$$\begin{cases} \forall i \in \langle 1..N \rangle, \mathtt{R}\mathbf{h}_i = \lambda_i \mathbf{h}_i \\ \forall i \in \langle 1..N \rangle, \mathtt{R}'\mathbf{j}_i = \lambda_i \mathbf{j}_i \end{cases} \tag{D.54}$$

There is nothing preventing a change of variables in the second line:

$$\begin{cases} \forall i \in \langle 1..N \rangle, \mathtt{R}\mathbf{h}_i = \lambda_i \mathbf{h}_i \\ \forall j \in \langle 1..N \rangle, \mathtt{R}'\mathbf{j}_j = \lambda_j \mathbf{j}_j \end{cases} \tag{D.55}$$

Pre-multiply the first line of the system by $\mathbf{j}_j^t$ and the second by $\mathbf{h}_j^t$:

$$\begin{cases} \mathbf{j}_j^t \mathtt{R}\mathbf{h}_i = \lambda_i \mathbf{j}_j^t \mathbf{h}_i \\ \mathbf{h}_i^t \mathtt{R}'\mathbf{j}_j = \lambda_j \mathbf{h}_i^t \mathbf{j}_j \end{cases} \tag{D.56}$$

The left-hand sides of the two lines are equal, so we have, by subtracting the two lines:

$$\forall (i,j) \in \langle 1..N \rangle^2, (\lambda_i - \lambda_j)\mathbf{h}_i^t \mathbf{j}_j = 0 \tag{D.57}$$

And therefore:

$$\forall (i,j) \in \langle 1..N \rangle^2, \mathbf{h}_i^t \mathbf{j}_j = \delta_{ij} \tag{D.58}$$

which completes the demonstration. □

Joint Decomposition of Signal and Noise It is possible to decompose the signal on the basis of $\mathbf{h}_i$ and the noise on the basis of $\mathbf{j}_i$. A window $\mathbf{b}$ containing only noise can be written as a linear combination of $\mathbf{j}_i, i \in \langle 1..N \rangle$:

$$\mathbf{b} = \sum j = 1^N b'_j \mathbf{j}_j \tag{D.59}$$

The prime notation on the coefficients b'_j is used to clearly indicate that the coefficients correspond to the decomposition in a different basis than the original one. This window filtered by one of the $\mathbf{h}_i$ will be written as:

$$\mathbf{h}_i^t \mathbf{b} = \mathbf{h}_i^t \sum_{j=1}^{N} b'_j \mathbf{j}_j = \sum_{j=1}^{N} b'_j \mathbf{h}_i^t \mathbf{j}_j = \sum_{j=1}^{N} b'_i \delta_{ij} = b'_i \tag{D.60}$$

Hence the coefficients b'_i. Similarly, in this basis:

$$E(b'_j b'_i) = E(\mathbf{h}_j^t \mathtt{B}\mathtt{B}^t \mathbf{h}_i) = \mathbf{h}_j^t E(\mathtt{B}\mathtt{B}^t)\mathbf{h}_i = \mathbf{h}_j \mathtt{Q} \mathbf{h}_i = \delta_{i,j} \tag{D.61}$$

This means that the coefficients b'_i of the decomposition of $\mathbf{b}$ on the basis of $\mathbf{j}_i$ are uncorrelated random variables with unit power. In other words, the filtered noise is whitened and has unit power. Finally, a window $\mathbf{s}$ containing only signal can also be written as a linear combination of $\mathbf{j}_i, i \in \langle 1..N \rangle$:

$$\mathbf{s} = \sum_{j=1}^{N} s'_j \mathbf{j}_j \tag{D.62}$$

The filtered signal is then:

$$\mathbf{h}_i^t \mathbf{s} = \mathbf{h}_i^t \sum_{j=1}^{N} s'_j \mathbf{j}_j = \sum_{j=1}^{N} s'_j \mathbf{h}_i^t \mathbf{j}_j = \sum_{j=1}^{N} s'_i \delta_{ij} = s'_i \tag{D.63}$$

Hence the coefficients s_i^t. Similarly, in this basis:

$$E(s_j^t s_i^t) = E(\mathbf{h}'_j \mathbf{s}\mathbf{s}^t \mathbf{h}_i) = \mathbf{h}'_j E(\mathbf{s}\mathbf{s}^t)\mathbf{h}_i = \mathbf{h}_j \mathtt{P} \mathbf{h}_i = \lambda_i \mathbf{h}_j \mathtt{Q} \mathbf{h}_i = \lambda_i \delta_{i,j} \tag{D.64}$$

This means that the coefficients s_i^t of the decomposition of $\mathbf{s}$ on the basis of $\mathbf{j}_i$ are also uncorrelated random variables with power equal to λ_i. In other words, the filtered signal is also whitened.

D.5 Remarks

D.5.1 Concrete implementation of Stochastic Matched Filtering

We have observed that numerically, the eigenvector calculation scheme of the matrix $\mathtt{H}$ (equation D.43) could diverge (i.e., give incorrect solutions) in some cases where the mean vector of the noise is non-zero; meaning that in equation D.36: $\bar{\mathbf{b}}\bar{\mathbf{b}}^t \neq \mathbf{0}$. The problem is resolved when, on the contrary, the mean vector of the noise is zero. In practice, it is advisable to estimate the stochastic matched filters by taking:

$$\mathtt{P} = \Sigma_{\mathbf{s}} + \bar{\mathbf{s}}\bar{\mathbf{s}}^t \tag{D.65}$$

$$\mathtt{Q} = \Sigma_{\mathbf{b}} \tag{D.66}$$

then by filtering the signal by subtracting the mean vector of the noise first, meaning that the filtered version of $\mathbf{w}(n)$ is $\mathbf{h}^t.(\mathbf{w}(n) - \bar{\mathbf{b}})$. This process has the disadvantage of making the filtering non-linear, i.e., not computable using a Fourier transform.

D.5.2 Stochastic Matched Filtering on non-scalar signals

The notion of covariance matrix is more intricate for signals living in a space of dimensions greater than one:

$$\mathtt{Z} = [\mathbf{z}_0, \mathbf{z}_1, \mathbf{z}_2, ..., \mathbf{z}_n, ...] \tag{D.67}$$

where $\mathbf{z}_i$ are of dimension L. In this case, the observed window is a concatenation of vectors:

$$\mathtt{W} = [\mathbf{z}_{n-l}, \mathbf{z}_{n-l+1}, ..., \mathbf{z}_n, ..., \mathbf{z}_{n+l-1}, \mathbf{z}_{n+l}] \tag{D.68}$$

For example, if the signal is 2D, the observed window is no longer a vector but a matrix, of size $L \times (2l+1)$ in the previous case. One possibility to use the results demonstrated above is to "unfold" the window in order to make it one-dimensional, i.e., concatenate all the columns of $\mathtt{W}$:

$$\mathbf{w} = [\mathbf{W}_{n-l}, \mathbf{W}_{n-l+1}, ..., \mathbf{W}_i, ..., \mathbf{W}_{n+l-1}, \mathbf{W}_{n+l}] \tag{D.69}$$

with $-l \leq i \leq l$. For example, the following matrix:

$$\mathtt{W} = \left[\begin{array}{c|c|c} 1 & 4 & 7 \\ 2 & 5 & 8 \\ 3 & 6 & 9 \end{array}\right] \tag{D.70}$$

consists of three vectors $\mathbf{W}_0^t = [1,2,3]$, $\mathbf{W}_1^t = [4,5,6]$ and $\mathbf{W}_2^t = [7,8,9]$, and unfolds as follows:

$$\mathbf{w} = [1,2,3,4,5,6,7,8,9]^t \tag{D.71}$$

Then, one can calculate the filters and perform filtering in one dimension, or return to the original dimension by "folding" the filters by performing the inverse operation of equation D.69.

D.6 Use of Stochastic Matched Filtering for detection problems

Expressed in the basis of $\mathbf{j}_i$, the covariance matrix of the noise is the identity matrix:

$$\{\mathtt{Q}\}_{\mathbf{j}} = \begin{bmatrix} 1 & & & 0 \\ & 1 & & \\ & & \ddots & \\ 0 & & & 1 \end{bmatrix} \tag{D.72}$$

This is a direct consequence of relation D.51. Similarly, in the basis of $\mathbf{j}_i$, the covariance matrix of the signal is expressed as:

$$\{\mathtt{P}\}_{\mathbf{j}} = \begin{bmatrix} \lambda_1 & & & 0 \\ & \lambda_2 & & \\ & & \ddots & \\ 0 & & & \lambda_N \end{bmatrix} \tag{D.73}$$

The covariance matrix of the signal added to the noise is, assuming the two processes are independent:

$$\{\mathtt{R}\}_{\mathbf{j}} = \begin{bmatrix} 1+\lambda_1 & & & 0 \\ & 1+\lambda_2 & & \\ & & \ddots & \\ 0 & & & 1+\lambda_N \end{bmatrix} \tag{D.74}$$

Given a vector $\mathbf{w}$, we want to determine whether this vector has been drawn under hypothesis (H_1) (contains only noise):

$$\mathbf{w}(n) = \mathbf{b}(n) \tag{D.75}$$

or under hypothesis (H_2) (contains noise and signal). From here on, we assume that we approximate the distribution of $\mathbf{s}$ and $\mathbf{b}$ by a Gaussian distribution. In practice, this approximation is generally well satisfied. Under hypothesis (H_1), the signal then follows the density function:

$$f_1(W) = \frac{1}{(2\pi)^{N/2}} \exp\left(-\frac{1}{2}\mathbf{w}^t\mathbf{w}\right) \tag{D.76}$$

Under hypothesis H_2, it will be:

$$f_1(\mathbf{w}) = \frac{1}{(2\pi)^{N/2}\sqrt{\det \mathtt{R}}} \exp\left(-\frac{1}{2}\mathbf{w}^t\mathtt{R}\mathbf{w}\right) \tag{D.77}$$

We consider the likelihood ratio:

$$\Lambda(\mathbf{w}) = \frac{f_2(\mathbf{w})}{f_1(\mathbf{w})} \tag{D.78}$$

If $\Lambda(\mathbf{w}) > 1$, we consider that hypothesis 2 is true and that the observation $\mathbf{w}$ contains signal; otherwise, hypothesis 1 is true and the signal contains only noise. It is simpler to consider the functional $\log\Lambda$, i.e., the logarithmic domain of the likelihood ratio. It is easily shown that the criterion "$\log\Lambda(\mathbf{w}) > 1$" is equivalent to:

$$\sum_{i=1}^{i=N} w_i^2 \frac{\lambda_i}{1+\lambda_i} > \sum_{i=1}^{i=N} (1+\lambda_i) \tag{D.79}$$

To ensure that $\Lambda(\mathbf{w})$ is much greater than 1 under hypothesis 2, the series is truncated to order N_f. In this case, the hypothesis test will be on:

$$\sum_{i=1}^{i=N_f} w_i^2 \frac{\lambda_i}{1+\lambda_i} > \sum_{i=1}^{i=N_f} (1+\lambda_i) \tag{D.80}$$

D.7 Additional notes

Note: this section was added during translation.

The Stochastic Matched Filtering is nothing but the generalization of the Karhunen-Loève transform (KLT), as introduced in 1970 by Fukunaga and Koontz [213]. The Fukunaga-Koontz transform (FKT) and the Stochastic Matched Filtering both proceed to the optimization of a criterion expressed in terms of a Rayleigh quotient of the signal and noise covariance matrix; both transform result in the same eigenvectors (hence the equivalence). In the FKT approach, the signal and the noise are decomposed on a bi-orthogonal basis such that each vector is associated to an eigenvalue between 0 and 1. The eigenvalue is close to one when the eigenvector is associated to signal and close to zero when it is associated to noise. The idea of extending the KLT, but using a SNR maximization approach was made by Green *et al.* in 1988 [210], without mentioning the FKT which they probably did not know of. The result was called the *Maximum Noise Fraction* (in the original paper) or, more commonly today, the *Minimum Noise Fraction* [*sic*] or MNF. without mentioning the FKT which they probably did not know of. The application was to find a representation of multispectral images with an increasing noise fraction: this means that the vectors are built pixel-by-pixel, and n represents the number of channels per pixel. Each pixel is independent from the other. In this derivation, the signal and the noise were assumed to be with a zero average, an assumption which was not made in the original paper, so the MNF, and its associated properties, make it a strict subset of the FKT. The MNF was presented by Green *et al.* as an alternative to Principal Components Analysis (PCA) and is still known and used that way by the remote sensing community (with numerous variants). A strong hypothesis is that the images are of zero average, which is a sub-case of the derivation made in this appendix.

In 1993, independently from previous works, Cavassilas and Xerri [37] proposed the Stochastic Matched Filter, using an additive noise model with a zero-average signal and noise. Using a very similar approach, they came to the same conclusions as Green *et al.* and Lee *et al.*, but presented their results for signal processing on sliding windows instead of having dimensionality reduction in mind. In 1992 (with a publication in 1994), Mahalanobis (then working at Martin Marietta) and Singh published a similar method [207].

In the context of electro-encephalograms (EEG) processing, Koles *et al.* [211] presented in 1990, without naming it, the FKT under the zero-average hypothesis. In the field of EEG processing, the first paper to give that technique the name of Common Spatial Pattern was the article by Müeller, Gerkinga *et al.* [212] in 1999. Many interesting generalizations of the Common Spatial Pattern have been published in the meantime. For instance, Barachant *et al.* [218] showed a link between CSP and Riemannian geometry and showed that CSP spatial filtering and Log variance features extraction can be resumed as a computation of a Riemann distance in the space of covariances matrices. Another breakthrough is the extension of the CSP method to a multi-class situation, that is, more than just signal and noise, as proposed for instance by Domeghe *et al.* (2003) [208] and Grosse, Wentrup *et al.* [221] in 2008. Lotte *et al.* proposed a regularized version of the CSP to add robustness to the filtering scheme (2010) [219]. Finally, Yu *et al.* [220] proposed a non-parametric extension of the CSP where the hypothesis of Gaussian distributions for the signal and noise is relaxed; this method was also extended to a multi-class scenario.

In 2000, Caprari [209] discussed three generalizations of the matched filter:

1. the first filter is a generalization of the linear discriminant analysis framework, seeking a frame change maximizing the separation of the means of two classes of vectors

relative to the sum of their dispersions:

$$\max_{\mathbf{w}} \frac{\mathbf{w}^t(\bar{\mathbf{s}} - \bar{\mathbf{n}})((\bar{\mathbf{s}} - \bar{\mathbf{n}})\mathbf{w}}{\mathbf{w}^t(\Sigma_s + \Sigma_n)\mathbf{w}} \tag{D.81}$$

2. the second filter is the one maximizing the ratio of the energies of the two classes of vectors ("signal to noise ratio"), which is the stochastic matched filter mentioned until here:

$$\max_{\mathbf{w}} \frac{\mathbf{w}^t\mathtt{P}\mathbf{w}}{\mathbf{w}^t\mathtt{Q}\mathbf{w}} \tag{D.82}$$

3. the second filter is the one maximizing the inverse ratio of the energies of the two classes of vectors ("noise to signal ratio"):

$$\max_{\mathbf{w}} \frac{\mathbf{w}^t\mathtt{Q}\mathbf{w}}{\mathbf{w}^t\mathtt{P}\mathbf{w}} \tag{D.83}$$

Capari noted a similarity between filter 2 (which is the stochastic matched filter discussed in the appendix) and the FKT, without going as far as proving their equivalence. He also wrote the quadradtic detector rule in the general case, analogous to equation D.78 and following.

Specific cases of generalized matched filtering have also been found in the case of beamforming or direction-of-arrival (DoA) applications. It is possible[2] to identify the classical Bartlett beamformer [225] with the matched filter in the case of white noise, the Capon [214] beamformer with the matched filter in the case of coloured noise, and the MUSIC [217], [215], [216] algorithm conceptually using a similar approach as the original derivation of the FKT, assuming the noise to be white. There are immediate generalisations when the noise and/or the signal is coloured by using a minimum noise fraction-like approach.

In the image processing community, the classical correlation, that is, the solution of the general matched filtering problem when the noise is white (equation D.50), is still heavily used, with a great deal of derivatives and variants (see *e.g.* the work by Leonard [222] for a state of the art). It is only very recently that it came to the attention of some people in the Image Processing community, even in the Radar field, that it is possible to use the covariance of the noise to improve the correlation or template matching of a reference image with an input image. This approach is known as the General Inner Product detector. See for instance [223] for an eye detection application proposed in 2014 (where the method was qualified as "novel") and [224] in 2010 for an application in radar.

[2]The derivations are made in a Thales internal report. Publication in a proper article or communication is in project.

Appendix

E Transfer Function Linking Elevation Map to Optical Image

This appendix complements Chapter 7, Section 7.2.2. Its purpose is to present the calculation of the transfer function $\mathcal{F}[H_{\text{MTF}}]$ linking the Fourier transform of the ocean surface height map to the Fourier transform of an optical image typically acquired in the context of high-resolution satellite or airborne imaging. Here, we recall Equation 7.22 from Chapter 7:

$$\mathcal{F}\left[I\right](\kappa_i, \kappa_j) = \mathcal{F}[H_{\text{MTF}}](K_x, K_y)\mathcal{F}\left[\zeta\right](K_x, K_y) \tag{E.1}$$

where K_x, K_y are the wave numbers of the waves, ζ is the elevation function, I is the optical image, and κ_i, κ_j are the wave numbers of the spectral components of the image. Before constructing the modulation transfer function $\mathcal{F}[H_{\text{MTF}}]$, it is necessary to consider the geometry of the problem and the link budget. The most general optical vision chain model consists of several steps, which are philosophically similar to what is done in Radar: it starts with a link budget and ends with a projection that is specific to optical imaging. The link budget is done rigorously as in Radar since optics is nothing but high-frequency electromagnetism; but as most cameras do not use polarization, we will work with a scalar formalism. Also, we will use a simplified reflectivity model. Once the reflectivity model is constructed, we will linearize it, which will reveal the transfer function $\mathcal{F}[H_{\text{MTF}}]$.

E.1 Link budget and acquisition geometry in optical imaging

Here are the steps involved in the acquisition chain of the optical image:

1- Calculation of the Illumination Map This involves evaluating the incident luminous power density at each point on the height map. We will assume that the light source is located at infinity: in our case, it is the sun, so the assumption is reasonable. Its direction will be given by the unit vector $\hat{\mathbf{l}}$, pointing towards the source. It is also assumed that the illumination on the map is constant and equal to I_0 in $[\text{W/m}^2]$.

2- Calculation of the Reflected Intensity The reflected intensity is the product of the illuminance by the reflectance denoted R_f, which is dimensionless:

$$I_r(x, y) = I(x, y)R_f(x, y) \tag{E.2}$$

For this, a simple reflectivity model is used. We have chosen a classic model, the Phong model modified by Blinn. The Phong model [142], commonly used in real-time 3D computer graphics, is a semi-empirical model that works well for many materials. It breaks down into three additive components:

$$R_f(x, y) = R_a(x, y) + R_d(x, y) + R_s(x, y) \tag{E.3}$$

These components are:

- The "ambient" component is a constant term independent of the light direction, supposed to represent the contribution of secondary sources present in the scene and reflecting on the considered object:

$$R_a(x,y) = \rho_a \tag{E.4}$$

where ρ_a is a positive term.

- The "diffuse" component is modeled according to Lambert's law and involves the local normal to the surface at (x,y), denoted $\hat{\mathbf{n}}$:

$$R_d(x,y) = \rho_d \hat{\mathbf{n}}(x,y).\hat{\mathbf{l}}(x,y) \overset{\text{here}}{=} \rho_d \hat{\mathbf{n}}(x,y).\hat{\mathbf{l}} \tag{E.5}$$

where ρ_d is a positive term.

- The "specular" component is inspired by Lambert's law, but with a decrease in $\cos^{\gamma_s}$ around the direction $\hat{\mathbf{d}}$ given by Snell's law, which can be expressed in terms of $\hat{\mathbf{l}}$ and the local normal $\hat{\mathbf{n}}$:

$$\hat{\mathbf{d}}(x,y) = -\hat{\mathbf{l}}(x,y) + 2(\hat{\mathbf{l}}(x,y).\hat{\mathbf{n}}(x,y))\hat{\mathbf{n}}(x,y) \tag{E.6}$$

$$\overset{\text{here}}{=} -\hat{\mathbf{l}} + 2(\hat{\mathbf{l}}.\hat{\mathbf{n}}(x,y))\hat{\mathbf{n}}(x,y) \tag{E.7}$$

where ρ_a is a positive term. The specular reflection is, in the pure Phong model:

$$R_s(x,y) = \rho_s(\hat{\mathbf{d}}(x,y).\hat{\mathbf{v}}(x,y))^{\gamma_s} \tag{E.8}$$

with $\hat{\mathbf{v}}(x,y)$ the unit vector starting from $(x,y,\zeta(x,y))$ and pointing towards the camera. The term γ_s is the shininess term; the larger it is, the closer the specular reflection is to Snell's law. In the Blinn-Phong model [30], the specular reflection is approximated by:

$$R_s(x,y) \approx \rho_s(\hat{\mathbf{h}}.\hat{\mathbf{n}}(x,y))^{\gamma_s} \tag{E.9}$$

where the vector $\hat{\mathbf{h}}$ is defined as:

$$\hat{\mathbf{h}}(x,y) = \frac{\hat{\mathbf{l}} + \hat{\mathbf{v}}(x,y)}{||\hat{\mathbf{l}} + \hat{\mathbf{v}}(x,y)||} \tag{E.10}$$

This representation allows simplifying the calculation while giving very accurate results; in practice, this is the model that is implemented. Thus, by removing the constant terms, the Blinn-Phong model can always be written in the form:

$$R_f(x,y) = \rho_d \hat{\mathbf{n}}(x,y).\hat{\mathbf{l}} + \rho_s(\hat{\mathbf{h}}(x,y).\hat{\mathbf{n}}(x,y))^{\gamma_s} \tag{E.11}$$

Camera Model This is where the formalism notably diverges from radar imaging (in the general case). The main point is that an optical image acquired by a camera is fundamentally a projection. A classic model of an ideal optical camera is the pinhole model; it consists of considering all the light rays passing through the optical center C of the camera and intercepted by a planar sensor. A reference work in this field is the book *Computer Vision: Algorithms and Applications* by Richard Szeliski [19]. Now, consider a light source located at point P with coordinates $[x_c, y_c, z_c]$ in the camera frame $\mathcal{C}$ (see Figure E.1). The

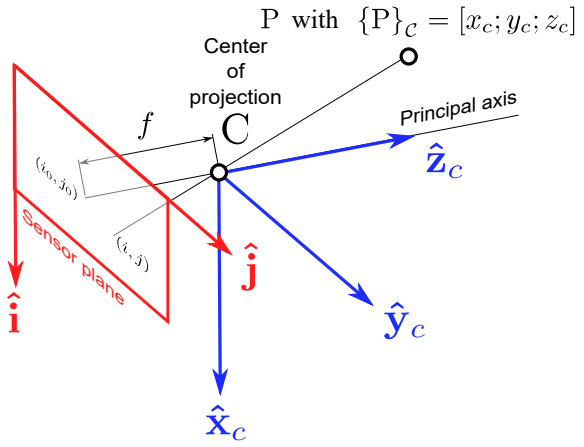

Figure E.1: *Notations used to define the camera frame $\mathcal{C}$ and the pinhole model's projective geometry.*

ray starting from P and passing through the camera's focal point C will hit the pixel with coordinates (i, j), given by the matrix relation:

$$\begin{pmatrix} si \\ sj \\ s \end{pmatrix} = \underbrace{\begin{pmatrix} -k_i f & 0 & i_0 & 0 \\ 0 & -k_j f & j_0 & 0 \\ 0 & 0 & 1 & 0 \end{pmatrix}}_{\mathtt{V}} \begin{pmatrix} x_c \\ y_c \\ z_c \\ 1 \end{pmatrix} \tag{E.12}$$

Here, $\mathtt{V}$ is the 3×4 matrix of the projection application; it is called the *intrinsic matrix* of the camera. The term s is a scale parameter, equal to z_c, which is lost by projection. The term f denotes the *focal length* of the camera, *i.e.*, the distance from the sensor plane to the optical center. The terms k_i and k_j are the pixel densities of the sensor, in pixels per meter[1]. Finally, the terms i_0 and j_0 represent the pixel coordinates of the camera's optical center; they are the coordinates of the line passing through the focal point and orthogonal to the sensor plane. Another camera model can also be used, namely, the affine model. The projection is in the form:

$$\begin{pmatrix} i \\ j \\ 1 \end{pmatrix} = \begin{pmatrix} a_{11} & a_{12} & a_{13} & i_0 \\ a_{21} & a_{22} & a_{23} & j_0 \\ 0 & 0 & 0 & 1 \end{pmatrix} \begin{pmatrix} x_c \\ y_c \\ z_c \\ 1 \end{pmatrix} \tag{E.13}$$

with the a_{ij} as camera parameters. The affine model is a good simplification of the pinhole model valid when the height variations of the observed surface are small compared to the camera's distance to the mean plane of the surface. This is typically true in the case of observing waves from an airplane or a satellite[2]. Therefore, we will now work with the affine model.

It is necessary to convert the scene's coordinates in the world frame $\mathcal{W}$ into coordinates in the camera frame $\mathcal{C}$. For a point P, the change of frame can be represented by the composition of a rotation and a translation, as follows (see also Appendix A):

$$\{\mathbf{OP}\}_{\mathcal{C}} = \mathtt{R}_{W \to C} \times \{\mathbf{OP} - \mathbf{OC}\}_{\mathcal{W}} \tag{E.14}$$

[1]Order of magnitude: for a 24×36 mm CCD sensor with a total of 20 million pixels (which corresponds to a current high-end digital single-lens reflex camera): $k_i = 1.52 \times 10^5$ pixels/m.

[2]On a satellite, acquisition is done by a linear sensor, and the scene scrolls under the satellite. But the final image can still be modeled by the affine model...

This can be represented in matrix form:

$$\begin{pmatrix} i \\ j \\ 1 \end{pmatrix} \{\mathbf{OP}\}_{\mathcal{C}} = \underbrace{\left(\begin{array}{ccc|c} & \mathtt{R}_{W\to C} & & -\mathtt{R}_{W\to C} \times \{\mathbf{OC}\}_{\mathcal{W}} \\ \hline 0 & 0 & 0 & 1 \end{array}\right)}_{\mathtt{E}} \left(\frac{\{\mathbf{OP}\}_{\mathcal{W}}}{1}\right) \tag{E.15}$$

The matrix $\mathtt{E}$ (dimension 4×4) obtained in this way for changing the frame is called the *extrinsic matrix*. Therefore, the entire projection operation can be coded as follows:

$$\left(\frac{\{\mathbf{OP}\}_{\mathcal{C}}}{1}\right) = \{\mathbf{OP}\}_{\mathcal{C}} = \mathtt{VE}\left(\frac{\{\mathbf{OP}\}_{\mathcal{W}}}{1}\right) \tag{E.16}$$

Then we can write the received light power at the pixel with coordinates (i, j):

$$I_r(i,j) = \iint_{x,y \in S(i,j)} I_0 R_f(x,y) dx dy \text{ [W]} \tag{E.17}$$

where $S(i, j)$ is the set of points in the solid angle originating from the optical center of the camera and formed by the pixel area (i, j). We add to the assumption of the affine model the hypothesis that the camera is looking in the vertical direction, in other words, $\hat{\mathbf{v}} = \hat{\mathbf{z}}$. In this case, we can see that the ground area of $S(i, j)$ is roughly the same everywhere and equal to a [m^2]. Assuming further that the reflectivity of the surface varies little over the domain $S(i, j)$, we can finally write:

$$I_r(i,j) = a I_0 R_f(x_i, y_i) \tag{E.18}$$

where (x_i, y_i) is the center of $S(i, j)$, its coordinates being obtained from the projection equation (E.16). In the following, we will additionally assume that the camera axes are the same as the axes of the world reference frame, which will simplify the treatment of the problem without losing generality.

E.2 Modulation transfer function in the optical case

Here, we consider an approach initially proposed by Kube and Pentland [139] for Lambertian diffusion, later adapted, simplified, and extended by Chantler *et al.* [39] (still in Lambertian diffusion). We modify this approach to incorporate specular reflection, resulting in the modulation transfer function corresponding to the Blinn-Phong model.

Diffuse Component We begin with the diffuse reflection framework, presenting the ideas of Chantler *et al.* [39] with our notations. From equation E.5, we have:

$$R_d(x,y) = \rho_d \hat{\mathbf{n}}(x,y).\hat{\mathbf{l}} \tag{E.19}$$

This equation can also be written as:

$$R_d(x,y) = \rho_d \frac{-p\cos\phi_i \sin\theta_i - q \sin\phi_i \sin\theta_i + \cos\theta_i}{\sqrt{p^2+q^2+1}} \tag{E.20}$$

where:

- $p = \left[\frac{\partial \zeta}{\partial x}\right]_{x,y}$

- $q = \left[\frac{\partial \zeta}{\partial y}\right]_{x,y}$
- $\left\{\hat{\mathbf{l}}\right\}_{\mathcal{W}} = [\cos\phi_i \sin\theta_i, \sin\phi_i \sin\theta_i, \cos\theta_i]^t$, using the notations from Chapter 4, assuming that the wind frame $\mathcal{V}$ is coincident with the world frame $\mathcal{W}$ here.

The partial derivatives are taken with respect to the axes of the world frame. However, we can consider a "light source" frame $\mathcal{L}$ with the abscissa axis parallel to the projection of $\mathbf{l}$ on the surface's mean plane. With (x', y') as coordinates in frame $\mathcal{L}$, we have a simpler expression:

$$R_d(x', y') = \rho_d \frac{-r \sin\theta_i + \cos\theta_i}{\sqrt{r^2 + t^2 + 1}} \tag{E.21}$$

with:

- $p = \left[\frac{\partial \zeta}{\partial x'}\right]_{x',y'}$
- $q = \left[\frac{\partial \zeta}{\partial y'}\right]_{x',y'}$

Using a Taylor expansion, we get:

$$R_d(x', y') = \rho_d(-r \sin\theta_i + \cos\theta_i)\left[1 - \frac{(r^2 + t^2)}{2!} + \frac{9(r^2 + t^2)}{4!} + \dots\right] \tag{E.22}$$

It is then shown that if the slopes are less than 15 degrees on the surface, then r^2 and t^2 are small compared to unity. Truncating all quadratic terms introduces no more than 3.5

$$R_d(x', y') \approx -\rho_d \left[\frac{\partial \zeta}{\partial x'}\right]_{x,y} \sin\theta + \cos\theta \tag{E.23}$$

We can calculate this slope in the Fourier domain. The derivative operator is a linear operator, allowing for a linear modulation transfer function. In frame $\mathcal{L}$, we have:

$$\mathcal{F}\left[\frac{\partial \zeta}{\partial x'}\right](K'_x, K'_y) = \rho_d \jmath K'_x \mathcal{F}[\zeta](K'_x, K'_y) \tag{E.24}$$

Returning to world frame $\mathcal{W}$, we can continue to represent it in the Fourier domain. However, to do so, we need to express K'_x in terms of the wavenumbers K_x and K_y in the Fourier domain associated with the world frame $\mathcal{W}$. We have:

$$K'_x = K_x \cos\phi_i + K_y \sin\phi_i = \sqrt{K_x^2 + K_y^2}\cos(\phi - \phi_i) \tag{E.25}$$

with ϕ being the generalized arctangent of K_y/K_x. Neglecting the constant term in equation E.23 and substituting the new Fourier transform, we ultimately have:

$$\mathcal{F}[R_d](K_x, K_y) \approx \rho_d \underbrace{[-\jmath K_x \cos(\phi - \phi_i)\sin\theta_i]}_{H_s(K_x, K_y, \theta_i, \phi_i)} \mathcal{F}[\zeta](K_x, K_y) \tag{E.26}$$

We conclude by recalling that we decided to take the camera axes parallel to the world axes. The frequencies in the image domain are then $\kappa_i = \alpha_i K_y$ and $\kappa_j = \alpha_j K_x$. Also, we have:

$$\phi = \arctan(\kappa_i/\kappa_j) = \arctan\frac{\alpha_i K_y}{\alpha_j K_x} \tag{E.27}$$

Specular Component We now extend the model to specular reflection, which was not done by Chantler *et al.* We start with the specular component of Blinn-Phong, given in equation E.9:

$$R_s(x,y) \approx \rho_s(\hat{\mathbf{h}}(x,y).\hat{\mathbf{n}}(x,y))^{\gamma_s} \tag{E.28}$$

where the vector $\mathbf{h}$ is $\hat{\mathbf{h}} = (\hat{\mathbf{l}} + \hat{\mathbf{v}}(x,y))/||\hat{\mathbf{l}} + \hat{\mathbf{n}}(x,y)||$, with $\hat{\mathbf{v}}$ pointing towards the camera. Since the camera is assumed to be at infinity (affine model), $\hat{\mathbf{l}}$ is constant and therefore $\hat{\mathbf{h}}$ is also! We then write the coordinates $\hat{\mathbf{h}}$ in $\mathcal{W}$ as follows: $[\cos\phi_i \sin\theta_i, \sin\phi_i \sin\theta_i, \cos\theta_i]'$. We can then repeat the entire previous demonstration, writing:

$$R_s(x',y') = \rho_s \left(\frac{-r\sin\theta_{is} + \cos\theta_{is}}{\sqrt{r^2+t^2+1}} \right)^{\gamma_s} \tag{E.29}$$

Expanding the denominator in a Taylor series:

$$\begin{aligned} R_s(x',y') &= (-r\sin\theta_i + \cos\theta_i)^{\gamma_s} \left[1 - \frac{\gamma_s(r^2+t^2)}{2} + \frac{(\gamma_s^2+2\gamma_s)(r^2+t^2)}{8} + \ldots \right] \\ &\approx (-r\sin\theta_i + \cos\theta_i)^{\gamma_s} \end{aligned} \tag{E.30}$$

...which corresponds to the numerator of E.29. We then expand E.30 in a Taylor series:

$$R_s(x',y') = -\rho_s\gamma_s \cos^{\gamma_s-1}\theta_{is} \sin\theta_{is} \left[\frac{\partial\zeta}{\partial x'} \right]_{x,y} + \cos^{\gamma_s}\theta_{is} \tag{E.31}$$

In the Fourier domain, neglecting the constant term, we have:

$$\mathcal{F}\left[R_s\right](\kappa_i,\kappa_j) \approx \rho_s \underbrace{\left[-\jmath K_x \gamma_s \cos^{\gamma_s-1}\theta_{is} \sin\theta_{is} \right]}_{\mathcal{F}[H_s](K_x,K_y,\theta_{is},\phi_{is})} \mathcal{F}\left[\zeta\right](K_x,K_y) \tag{E.32}$$

To conclude, we note that the Fourier transform of the received image –since it is proportional to the reflectance under our assumptions– can be linked to the Fourier transform of the elevation map. In the end, we have a relationship through a modulation transfer function as in equation 7.22, with:

$$\mathcal{F}[H_{\mathrm{MTF}}](K_x,K_y) = a[\mathcal{F}[H_d](K_x,K_y) + \mathcal{F}[H_s](K_x,K_y)] \tag{E.33}$$

Figure E.2 compares the approach based on the exact Blinn-Phong model with the rendering using the modulation transfer function for a simple mathematical surface and an oceanic surface. In both cases, the lighting is the same: $\phi_i = \pi/3$ and $\theta_i = \pi/4$. It is worth noting that in the second case, we are beyond the recommended 15-degree limit by Chantler *et al.* for the use of the modulation transfer function (and similarly, we are at the limit of wave breaking from a hydrodynamic point of view); however, the rendering remains correct.

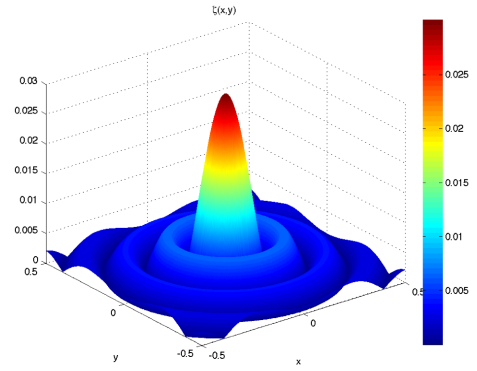

(a) Function $\zeta(x, y) = 0.03|\operatorname{sinc}(2\pi\sqrt{x^2 + y^2})|$, maximum slope 14.48 deg.

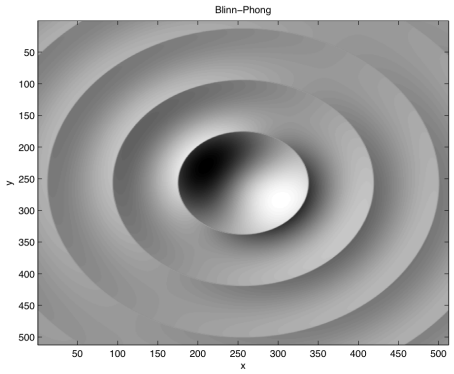

(b) Rendering with the Blinn-Phong model

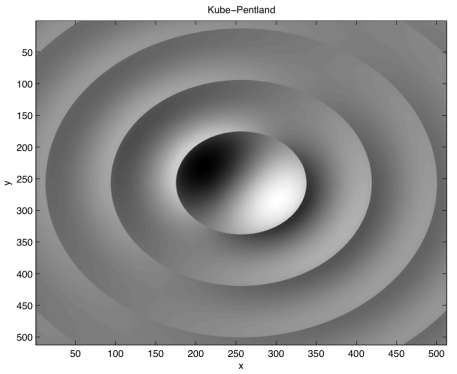

(c) Rendering with the Kube-Pentland model with specular component

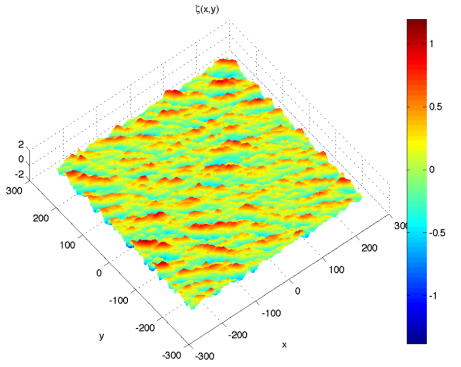

(d) Ocean, state 3, maximum slope 23.04 deg.

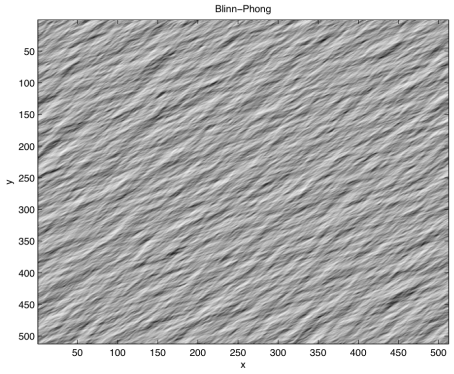

(e) Rendering with the Blinn-Phong model

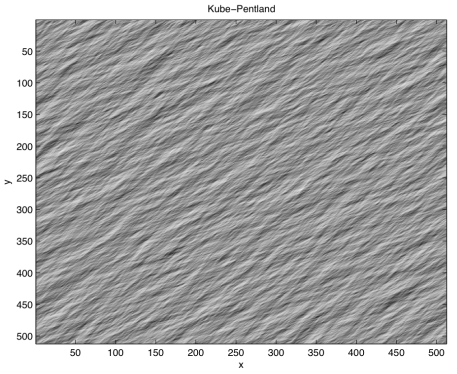

(f) Rendering with the Kube-Pentland model with specular component

Figure E.2: *Comparison between the Blinn-Phong model and the modified Kube-Pentland model with specular reflection presented in this chapter, on two surfaces. The direction to the light source is $\phi_i = \pi/3$ and $\theta_i = \pi/4$ from the center of the surface.*

References

[1] O. Airiau and A. Khenchaf, "A methodology for modeling and simulating target echoes with a moving polarimetric bistatic radar," *Radio Science*, vol. 35, no. 3, pp. 773–782, mai-juin 2000.

[2] E. I. Thorsos, "The validity of the Kirchhoff approximation for rough surface scattering using a Gaussian roughness spectrum," *Journal of the Acoustical Society of America*, vol. 83, no. 1, pp. 78–92, Jan. 1988.

[3] "Manuel des codes - codes internationaux, volume I.1 (annexe II du règlement technique de l'OMM), partie A - codes alphanumériques," Organisation Météorologique Mondiale, Genève, Suisse, Tech. Rep. OMM-No. 306, 2009.

[4] W. Alpers, *Satellite Microwave Remote Sensing*. Chichester, U.K.: Ellis Horwood, 1983, ch. Imaging ocean surface waves by synthetic aperture radar – A review, pp. 107–119.

[5] W. R. Alpers, D. B. Ross, and C. L. Rufenach, "On the detectability of ocean surface waves by real and synthetic aperture radar," *Journal of Geophysical Research*, vol. 86, pp. 6481–6498, 1981.

[6] I. Antipov, "Analysis of sea clutter data," Defence Science and Technology Organisation (Department of Defence, Australia), Tech. Rep. DSTO-TR-0647, Mar. 1998.

[7] J. I. Antonov, R. A. Locarnini, T. P. Boyer, A. V. Mishonov, and H. E. Garcia, *World Ocean Atlas 2005, Volume 2: Salinity*. U.S. Government Printing Office, Washington, D.C.: NOAA Atlas NESDIS 62, 2006.

[8] A.-S. Archambeau, *Les Océans*, ser. Que sais-je? Presses Universitaires de France, 2004, no. 92.

[9] A. Arnold-Bos, A. Khenchaf, and A. Martin, "Bistatic radar imaging of the marine environment. Part I: theoretical background," *IEEE Transactions on Geoscience and Remote Sensing, EUSAR '06 Special Issue*, vol. 45, no. 11, pp. 3372 – 3383, Nov. 2007.

[10] ——, "Investigating possible bistatic configurations for ship wake imaging through simulation," in *Proceedings of the IEE International Conference on Radar*, Edimbourg, Royaume Uni, Oct. 2007.

[11] ——, "An evaluation of current ship wake detection algorithms in SAR images," in *Caractérisation du Milieu Marin / Marine Environment Characterization, SeaTech-Week '06*, Brest, France, Nov. 2006.

[12] A. Arnold-Bos, A. Martin, and A. Khenchaf, "Obtaining a ship's speed and direction from its Kelvin wake spectrum using stochastic matched filtering," in *Proceedings of the International Geoscience and Remote Sensing Symposium (IGARSS)*, Barcelone, Espagne, July 2007.

[13] ——, "A versatile bistatic & polarimetric marine radar simulator," in *Proceedings of the IEEE Conference on Radars*, Verona, NY, Apr. 2006.

[14] E. Attema, "The active microwave instrument on-board the ERS-1 satellite," *Proceedings of the IEEE*, vol. 79, no. 6, pp. 791–799, jun 1991.

[15] A. Awada, M. Y. Ayari, A. Khenchaf, and A. Coatanhay, "Bistatic scattering from an anisotropic sea surface: Numerical comparison between the first-order SSA and the TSM models," *Waves in Random Media*, vol. 16, no. 3, pp. 383–394, Nov. 2006.

[16] M. Y. Ayari, "Détection électromagétique d'éléments polluants au dessus de la surface maritime," Ph.D. dissertation, Université de Bretagne Occidentale, Feb. 2006.

[17] D. H. Ballard, "Generalized Hough transform to detect arbitrary patterns," *IEEE Transactions on Pattern Analysis and Machine Intelligence*, vol. 13, no. 2, pp. 111–122, Apr. 1981.

[18] T. Balz, "Echtzeitvisualisierung von SAR-Effekten mittels programmierbarer Grafikhardware," Ph.D. dissertation, Universität Stuttgart, Dec. 2007.

[19] R. Szeliski, *Computer Vision - Algorithms and Applications*. Springer, 2010.

[20] P. J. Nahin, *Oliver Heaviside: the life, work, and times of an electrical genius of the Victorian age*. JHU Press, 2002.

[21] D. E. Barrick, "Rough surface scattering based on the specular point theory," *IEEE Transactions*, vol. AP-16, pp. 449–454, 1968.

[22] F. G. Bass and I. M. Fuks, *Wave Scattering from Statistically Rough Surfaces*. New York: Pergamon Press, 1979.

[23] P. Beckmann and A. Spizzichino, *The Scattering of Electromagnetic Waves from Rough Surfaces*. New York, NY: Macmillan Co., 1963.

[24] T. Beer, *Environmental Oceanography*. CRC Press, 1997, ISBN 0849384257.

[25] M. J. Ben Kassem, "SAR monostatique et bistatique - étude et analyse des méthodes de reconstruction d'imagerie radar," PhD thesis, Université de Nantes, 2004.

[26] B. Bender, "For US, a terror threat lurks in drug smuggling subs," the Boston Globe, 17 août 2008.

[27] D. Billon and F. Fohanno, "Two improved ping-to-ping cross-correlation methods for synthetic aperture sonar: theory and sea results," in *Proceedings of IEEE Oceans'02*, vol. 4, 2002, pp. 2284–2293.

[28] G. Birkhoff and E. Zarantello, *Jet, Wakes and Cavities*. Academic Press, 1957.

[29] Y. Blanchard, *Le radar 1904-2004*. Paris: Editions Ellipses, 2004.

[30] J. F. Blinn, "Models of light reflection for computer synthesized pictures," in *Proc. 4th annual conference on computer graphics and interactive techniques*, 1977.

[31] L. M. Brekovskikh, "Difrakciya voln na neronoj poverhnosti: 1. obschaya teoriya," *Zh. Eksp. Teor. Fiz.*, vol. 23, pp. 275–288, 1952.

[32] ——, "Difrakciya voln na neronoj poverhnosti: 2. prilosheniya obschej teorii," *Zh. Eksp. Teor. Fiz.*, vol. 23, pp. 289–304, 1952.

[33] W. J. Broad, "U.S. loses hold on submarine-exposing radar techniques," Mardi 11 mai 1999, The New York Times. [Online]. Available: http://www.nytimes.com/1999/05/11/world/us-loses-hold-on-submarine-exposing-radar-technique.html?pagewanted=1

[34] E. H. Buller and J. K. Tunaley, "The effect of the ships screws on the ship wakes and its implication for the radar image of the ship wake," in *Proceedings of the Internation Geoscience and Remote Sensing Symposium*, 1989.

[35] E. J. Candès and D. L. Donoho, "Ridgelets: a key to higher-dimensional intermittency?" *Philosophical Transactions of the Royal Society of London, Mathematical, physical and engineering sciences*, vol. 357, no. 1760, pp. 2495–2509, 1999.

[36] K. Case, R. Dashen, W. Munk, J. Vesecky, and K. Watson, "SEASAT report." MITRE Corporation, Tech. Rep., 1985.

[37] J.-F. Cavassilas and B. Xerri, "Extension de la notion de filtre adapté. Contribution à la détection de signaux courts en présence de termes perturbateurs." *Traitement du signal*, vol. 10, no. 3, pp. 215–221, 1993.

[38] H. Chan and A. K. Fung, "A theory of sea scatter at large incident angles," *Journal of Geophysical Research*, vol. 82, pp. 3439–3444, 1977.

[39] M. Chantler, G. Russell, and L. Linnett., "Illumination: a directional filter of texture?" in *Proceedings of the British Machine Vision Conference*, 1994.

[40] K. Chen, A. Fung, and D. E. Weissman, "A backscattering model for ocean surface," *IEEE Transactions on Geoscience and Remote Sensing*, vol. 30, no. 4, pp. 811–817, jul 1992.

[41] A. Coatanhay, A. Arnold-Bos, and A. Khenchaf, "Modeling of the GALILEO signals near a sea surface," in *European Navigation Conference - Global Navigation Satellite Systems*, Toulouse, France, 2008.

[42] ——, "Simulation of a GNSS signal for a receiver near a time-evolving sea surfaces," in *Proc. International Conference on Electromagnetics in Advanced Applications*, Turin, Italie, Sept. 2007.

[43] C. Cochin, T. Landeau, G. Delhommeau, and B. Alessandrini, "Simulator of ocean scenes observed by polarimetric SAR," in *Proceedings of the Comitee on Earth Observation Satellites SAR Workshop*, Toulouse, France, Oct. 1999.

[44] F. Comblet, M. Y. Ayari, F. Pellen, and A. Khenchaf, "Bistatic radar imaging system for sea surface target detection," in *Proceedings of the IEEE Conference on Oceans 2005 (Europe)*, Brest, France, June 2005.

[45] J. W. Cooley and J. W. Tukey, "An algorithm for the machine calculation of complex fourier series," *Math. Comput.*, vol. 19, pp. 297–301, 1965.

[46] P. Courmontagne, "An improvement of ship wake detection based on the Radon transform," *Signal Processing*, vol. 85, no. 8, pp. 1634–1654, 2005.

[47] ——, "Le filtrage adapté stochastique adaptatif appliqué aux images bruitées," *Traitement du Signal*, vol. 16, no. 4, pp. 303–318, 1999.

[48] C. Cox and W. Munk, "Statistics of the sea surface derived from sun glitter," *Journal of Marine Research*, vol. 13, pp. 198–227, 1954.

[49] D. J. Crisp, "The state-of-the-art in ship detection in synthetic aperture radar imagery," DSTO Australia, Intelligence, Surveillance and Reconnaissance Division, Information Sciences Laboratory, Rapport technique DSTO-RR-0272, 2004.

[50] C. Cuvilliez and R. Trégouët, "Rapport sur les conditions d'implantation d'un nouveau synchrotron et le rôle des très grands équipements dans la recherche publique ou privée, en France et en Europe - tome II : le rôle des très grands équipements dans la recherche publique ou privée en France et en Europe," Office parlementaire d'évalution des choix scientifiques et technologiques, Tech. Rep. 2821, Dec. 2000. [Online]. Available: http://www.assemblee-nationale.fr/11/dossiers/002821.asp

[51] F. Daout, "étude de la dépolarisation des ondes centimétriques par une surface rugueuse - application au domaine maritime," Ph.D. dissertation, Université de Nantes, Novembre 1996.

[52] G. Davidson, I. Cumming, and M. Ito, "A chirp scaling approach for processing squint mode SAR data," *IEEE Transactions on Aerospace and Electronic Systems*, vol. 32, no. 1, pp. 121–133, Jan. 1996.

[53] R. G. Dean and R. A. Dalrymple, *Water wave mechanics for engineers and scientists*, ser. Advanced Series on Ocean Engineering. World Scientific Publishing Co. Pte. Ltd., Jan. 1991, vol. 2, ISBN 981-02-0421-3.

[54] Z. Demirbilek and C. L. Vincent, *Coastal Engineering Manual, Part II, Chapter II-1: Water waves mechanics, Engineer Manual 1110-2-1100,.* Washigton, DC: U.S. Army Corps of Engineers, 2008, ch. II.

[55] R. Deriche, "Using Canny's criteria to derive a recursively implemented optimal edge detector," *International Journal of Computer Vision*, vol. 1, no. 2, pp. 167–187, May 1987.

[56] M. A. Donelan, J. Hamilton, W. H. Hui, and R. W. Stewart, "Directional spectra of wind-generated waves," *Philosophical transactions of the royal society of London, series A : mathematical and physical sciences*, vol. 315, no. 1534, pp. 509–562, 1985.

[57] Y. Dong, "Distribution of X-band high resolution and high grazing angle sea clutter," Defence Science and Technology Organisation (Department of Defence, Australia), Tech. Rep. DSTO-RR-0316, July 2006.

[58] P. Dubois-Fernandez, H. Cantalloube, O. R. du Plessis, M. Wendler, R. Horn, B. Vaizan, C. Coulombeix, D. Heuzé, and G. Krieger, "Analysis of bistatic scattering behavior of natural surfaces," in *Proceedings of the IEEE conference on Radars*, Toulouse, France, Oct. 2004.

[59] R. O. Duda and P. E. Hart, "Use of the Hough transform to detect lines and curves in pictures," *Communications of the ACM*, vol. 15, pp. 11–15, 1972.

[60] S. Q. Duntley, "Light in the sea," *Journal of the Optical Society of America*, vol. 53, no. 2, pp. 214–233, 1963.

[61] C. on Earth Observation Satellites, "Resources in earth observation 2000," CD-ROM, 2000, available online: http://ceos.cnes.fr:8100/html/cd00.htm.

[62] T. Elfouhaily and B. Chapron, "A comparison of wind wave spectra used in ocean remote sensing modeling," in *Proceedings of the International Geoscience and Remote Sensing Symposium*, 1996.

[63] T. Elfouhaily, B. Chapron, K. Katsaros, and D. Vandemark, "A unified directional spectrum for long and short wind-driven waves," *Journal of Geophysical Research*, vol. 102, no. C7, pp. 15 781–15 796, July 1997.

[64] T. M. Elfouhaily and C.-A. Guérin, "A critical survey of approximate scattering wave theories from random rough surfaces," *Waves in Random Media*, vol. 14, no. 4, pp. R1–R40(1), Oct. 2004.

[65] J. Ender, "Huelsmeyer memorial speech in the town hall of Cologne," in *Proceedings of the EUSAR conference*, 2002.

[66] D. Evans, "Spaceborne synthetic aperture radar: Current status and future directions," NASA - JPL, Tech. Rep. 4679, 1995.

[67] M. A. Fischler and R. C. Bolles, "Random sample consensus: A paradigm for model fitting with applications to image analysis and automated cartography," *Communications of the American Mathematical Society*, vol. 24, pp. 381–395, June 1981.

[68] ——, "SAR sensor trajectory deviations: Fourier domain formulation and extended scene simulation of raw signal," *IEEE Transactions on Geoscience and Remote Sensing*, vol. 44, pp. 2323– 2334, Sept. 2006.

[69] ——, "Efficient simulation of airborne SAR raw data of extended scenes," *IEEE Transactions on Geoscience and Remote Sensing*, vol. 44, pp. 2851–2860, Oct. 2006.

[70] G. Franceschetti, A. Iodice, D. Riccio, and G. Ruello, "Extended boundary condition method for scattering and emission for natural surfaces modeled by fractals," *IEEE Transactions on Geoscience and Remote Sensing*, vol. 43, no. 5, pp. 115–1125, May 2005.

[71] ——, "Fractal surfaces and electromagnetic extended boundary conditions," *IEEE Transactions on Geoscience and Remote Sensing*, vol. 40, no. 5, pp. 1018–1031, May 2002.

[72] G. Franceschetti, A. Iodice, D. Riccio, G. Ruello, and R. Siviero, "SAR raw signal simulation of oil slicks in ocean environments," *IEEE Transactions on Geoscience and Remote Sensing*, vol. 40, no. 9, pp. 1935–1949, Sept. 2002.

[73] G. Franceschetti, M. Migliaccio, and D. Riccio, "On ocean SAR raw signal simulation," *IEEE Transactions on Geoscience and Remote Sensing*, vol. 36, no. 1, pp. 84–100, Jan. 1998.

[74] G. Franceschetti, M. Migliaccio, D. Riccio, and G. Schirinzi, "SARAS: A Synthetic Aperture Radar (SAR) raw signal simulator," *IEEE Transactions on Geoscience and Remote Sensing*, vol. 30, no. 1, pp. 110–123, Jan. 1992.

[75] M. Frigo and S. G. Johnson, "The design and implementation of FFTW3," *Proceedings of the IEEE*, vol. 93, no. 2, pp. 216–231, 2005, special issue on "Program Generation, Optimization, and Platform Adaptation".

[76] V. Frost, J. Stiles, K. Shanmugan, and J. Holtzman, "A model for radar images and its application to adaptive digital filtering of multiplicative noise," *IEEE Trans. Pattern Analysis and Machine Intelligence*, vol. 4, no. 2, pp. 157–166, Mar. 1982.

[77] A. K. Fung and H. Chan, "Backscattering of waves by composite rough surfaces," *IEEE Transactions*, vol. AP-17, pp. 590–597, 1969.

[78] A. K. Fung and K. K. Lee, "A semi-empirical sea-spectrum model for scattering coefficient estimation," *IEEE Journal of Oceanic Engineering*, vol. 7, no. 4, pp. 166–176, 1982.

[79] F. Gérard, "La houle, théorie et prévision," *Met. Mar.*, vol. 117, pp. 5–23, 1982.

[80] J. H. Gart, "Electronics and aerospace industry in cold war arizona, 1945-1968: Motorola, hughes aircraft, goodyear aircraft." Ph.D. dissertation, Arizona State University, 2006.

[81] C. Gelpi and K. Norris, "Estimated surface-wave contributions to radar Doppler velocity measurements of the ocean surface," *Remote Sensing of Environment*, vol. 87, pp. 99–110, 2003.

[82] C. H. Gierull, "Bistatic synthetic aperture radar TIF - report (phase I)," Defence R&D Canada, Rapport technique DRDC Ottawa TR 2004-190, Nov. 2004.

[83] E. Girardeau, *Souvenirs de longue vie.* Berger-Levrault, 1968, chapitre 9.

[84] H. Greidanus, "Assessing the operationality of ship detection from space," in *Proceedings of the Symposium on New Space Services for Maritime Users: The Impact of Satellite Technology on Maritime Legislation.* UNESCO, 2005.

[85] O. Griffin, R. Skop, G. Keramidas, T. Swean, Jr., H. Wang, and Y. Leipold, "Ocean and ship wake modification by a surface wake flow pattern," in *Seventeenth Symposium on Naval Hydrodynamics: wakes, free surface effects – Office of Naval Research, United States*, 1989.

[86] A. Guissard, "Directional spectrum of the sea surface and wind scatterometry," *International Journal of Remote Sensing*, vol. 14, no. 8, pp. 1615–1633, 1993.

[87] L. Guo and Z. Wu, "Application of the extended boundary condition method to electromagnetic scattering from rough dielectric fractal sea surface," *Journal of Electromagnetic Waves and Applications*, vol. 18, no. 9, pp. 1219–1234, 2004.

[88] J.-P. Hardange, P. Lacomme, and J.-C. Marchais, *Radars Aéroportés et Spatiaux*, ser. Collection scientifique et technique Thomson-CSF. Paris: Masson, 1995.

[89] M. J. Harris, "Real-time cloud simulation and rendering," University of North Carolina, Tech. Rep. TR03-040, 2003.

[90] K. Hasselmann, T. P. Barnett, E. Bouws, H. Carlson, D. E. Cartwright, K. Enke, J. A. Ewing, H. Gienapp, D. E. Hasselmann, P. Kruseman, A. Meerburg, P. Müller, D. J. Olbers, K. Richter, W. Sell, and H. Walden, "Measurements of wind-wave growth and swell during the Joint North Sea Wave Project (JONSWAP)," *Deutsche Hydrographische Zeitung*, vol. 8, no. 12, pp. 1–95, 1973, suppl. A.

[91] K. Hasselmann and S. Hasselmann, "On the nonlinear mapping of an ocean wave spectrum into a synthetic aperture radar image spectrum and its inversion," *Journal of Geophysical Research*, vol. 96, no. C6, pp. 10,713–10,729, June 1991.

[92] A. Hein, *Processing of SAR Data: Fundamentals, Signal Processing, Interferometry.* Springer, 2004, ISBN 3-540-05043-4, pp. 38 à 44.

[93] I. Hennings, R. Romeiser, W. Alpers, and A. Viola, "Radar imaging of Kelvin arms of ship wakes," *International Journal of Remote Sensing*, vol. 20, no. 13, pp. 2519–2543, 1999.

[94] L. Henyey and J. L. Greenstein, "Diffuse radiation in the galaxy," *Astrophys. Journal*, vol. 93, pp. 70–83, 1941.

[95] S. A. Hovanessian, *Introduction to Synthetic Arrays and Imaging Radars.* Dedham, WA: Artech House, Inc, 1980.

[96] A. Isar, A. Quinquis, M. Legris, and D. Isar, "Débruitage des images SAR : applications de la TODDE (Transformée en ondelettes discrète à diversité enrichie)," *Revue Scientifique et Technique de la Défense*, vol. 64, pp. 139–148, 2004.

[97] A. Ishimaru, *Wave Propagation and Scattering In Random Media (Vol. 2).* Academic Press, 1978.

[98] C. R. Jackson and J. R. Apel, *Synthetic Aperture Radar Marine User's Manual.* Commerce Dept., NOAA, National Environmental Satellite, Data, and Information Service, Office of Research and Applications, 2005, ISBN 0-16-073214-X, available online: http://www.sarusersmanual.com/.

[99] A. C. Kak and M. Slaney, *Principles of Computerized Tomographic Imaging.* IEEE Press, 1988, available online: http://www.slaney.org/pct/index.html.

[100] M. Kalkuhl, P. Droste, W. Wiechert, H. Nies, O. Loffeld, and M. Lambers, "Parallel computation of synthetic SAR raw data," in *Proceedings of the International Geoscience and Remote Sensing Symposium*, Barcelona, Espagne, July 2007, pp. 536–539.

[101] G. Keramidas and W. Bauman, "FFSW: A computer code for far field ship wave calculations," Naval Research Laboratory, United States, Tech. Rep. NRL 6007, 1987.

[102] A. Khenchaf, "Bistatic scattering and depolarization by randomly rough surfaces: application to the natural rough surfaces in X-band," *Waves in Random Media*, vol. 11, pp. 61–89, 2001.

[103] ——, "Modélisation électromagnétique, radar bistatique et traitement de l'information," Habilitation à diriger des recherches, Université de Nantes, 2000.

[104] A. Khenchaf and O. Airiau, "Bistatic radar moving returns from sea surface," *IEICE Transactions on Electronics*, vol. E83-C, no. 12, pp. 1827–1835, Dec. 2000.

[105] B. Kinsman, *Wind waves.* Englewood Cliffs, N.J.: Prentice-Hall, Inc., 1965.

[106] S. A. Kitaigorodskii, *The Physics of Air-Sea Interaction.* Israel Program for Scientific Translations Ltd., 1973.

[107] L. A. Klein and C. T. Swift, "An improved model for the dielectric constant of sea water at microwave frequencies," *IEEE Transactions on Antennas and Propagation*, vol. AP-25, no. 1, pp. 104–111, 1977.

[108] G. J. Komen, L. Cavaleri, M. Donelan, K. Hasselmann, S. Hasselmann, and P. A. E. M. Janssen, *Dynamics and modelling of ocean waves.* Cambrige University Press, 1994.

[109] ——, "Symmetry and asymmetry from local phase," in *Proc. AI'97, Tenth Australian Joint Conference on Artificial Intelligence.*, Dec. 1997.

[110] H. E. Krogstad, "A simple derivation of Hasselmann's nonlinear ocean-synthetic aperture radar transform," *J. Geophys. Res.,*, vol. 97, no. C2, pp. 2421–2425, 1992.

[111] H. E. Krogstad and H. Schyberg, "On Hasselmann's nonlinear ocean-SAR transformation," in *Proc. IGARSS '91*, 1991.

[112] D. Kuan, A. Sawchuk, T. Strand, and P. Chavel, "Adaptive restoration of images with speckle," *IEEE Transactions on Acoustics, Speech and Signal Processing*, vol. 35, no. 3, pp. 373–383, Mar. 1987.

[113] J. M. Kuo and K.-S. Chen, "The application of wavelets correlator for ship wake detection in SAR images," *IEEE Transactions on Geoscience and Remote Sensing*, vol. 41, no. 6, pp. 1506–1511, June 2003.

[114] M. Labarrere, J. Krief, and B. Gimonet, *Le filtrage et ses applications*, ser. Collection SUPAERO. Cepadues éditions, 1988.

[115] H. Lamb, *Hydrodynamics (6th ed.).* Cambridge University Press., 1994, ISBN 9780521458689.

[116] F. Le Chevalier, *Principles of radar and sonar processing.* Artech House, 2002, ISBN 1-58053-338-8.

[117] J.-S. Lee, "Digital image enhancement and noise filtering by use of local statistics," *IEEE Journal on Pattern Recognition*, vol. PAMI-2, no. 2, pp. 165–168, 1980.

[118] G. Li, J. Xu, P. Ying-Ning, and X. Xiang-Gen, "Bistatic linear antenna array SAR for moving target detection, location, and imaging with two passive airborne radars," *IEEE transactions on geoscience and remote sensing*, vol. 45, no. 3, pp. 554–565, 2007.

[119] J. Lighthill, *Waves in Fluids.* Cambridge University Press, 1978.

[120] R. A. Locarnini, A. V. Mishonov, J. I. Antonov, T. P. Boyer, and H. E. Garcia, *World Ocean Atlas 2005, Volume 1: Temperature.* U.S. Government Printing Office, Washington, D.C.: NOAA Atlas NESDIS 61, 2006.

[121] M. W. Long, *Radar Reflectivity of Land and Sea*, 3rd ed. Artech House, 2001, ch. 6, p. 353.

[122] D. Luebke, "Full day GPU course (introduction)," in *SIGGRAPH conference*, 2005.

[123] J. Lyden, "Synthetic aperture radar imaging of surface ship wakes," *Journal of Geophysical Research*, vol. 93, no. 12, pp. 12,293–12,303, 1988.

[124] M. S. Longuet-Higgins et al., *Ocean Wave Spectra*. Prentice-Hall, Inc., 1963, ch. Observations of the Directional Spectrum of Sea Waves Using the Motions of a Floating Buoy, pp. 111–136.

[125] B. L. Méhauté, *Introduction to Hydrodynamics and Water Waves*. Springer Verlag, Jan. 1976.

[126] A. Martin, H. Laanya, and A. Arnold-Bos, "Evaluation for uncertain image classification and segmentation," *Pattern Recognition*, vol. 39, no. 11, pp. 1987–1995, Nov. 2006.

[127] G. A. Mastin, P. Watterberg, and J. Mareda, "Fourier synthesis of ocean scenes," *IEEE Computer Graphics and Applications Magazine*, vol. 7, no. 3, pp. 16–23, Mar. 1987.

[128] C. Melsheimer, H. Lim, and C. Shen, "Observation and analysis of ship wakes in ERS SAR and SPOT images," in *Proceedings of the 20th Asian Conference on Remote Sensing*, Hong Kong, China, 1999, pp. 554–559.

[129] J. H. Michell, "The wave-resistance of a ship," *Philosophical Magazine, Series 5*, vol. 45, pp. 106–123, 1898.

[130] H. Mitsuyasu, F. Tasai, T. Suhara, S. Misuno, M. Ohkuso, T. Honda, and K. Rindishi, "Observation of the directional spectrum of ocean waves using a cloverleaf buoy," *Journal of Physical Oceanography*, vol. 5, pp. 750–760, 1975.

[131] R. K. Moore and A. K. Fung, "Radar determination of winds at sea," *Proceedings of the IEEE*, vol. 67, no. 11, pp. 1504– 1521, Nov. 1979.

[132] A. Mori and F. D. Vita, "A time-domain raw signal simulator for interferometric SAR," *IEEE Geoscience and Remote Sensing*, vol. 42, no. 9, pp. 1811–1817, Sept. 2004.

[133] W. Munk, P. Scully-Power, and P. Zachariasen, "Ships from space," *Proceedings of the Royal Society of London A*, vol. 412, pp. 231–254, 1987.

[134] K. Norton and A. Omberg, "The maximum range of a radar set," *Proceedings of the IRE*, vol. 35, no. 1, pp. 4–24, Jan. 1947.

[135] F. O'Gorman and M. Clowes, "Finding picture edges through collinearity of feature points," *IEEE Transactions on Computers*, vol. C-25, no. 4, pp. 449–456, Apr. 1976.

[136] S. J. Orfanidis, "Electromagnetic waves and antennas," http://www.ece.rutgers.edu/ orfanidi/ewa/.

[137] K. Oumansour, "Modélisation de la rétrodiffusion des sillages de navire en imagerie radar polarimétrique," Ph.D. dissertation, Université de Nantes, July 1996.

[138] K. Oumansour, Y. Wang, and J. Saillard, "Multifrequency SAR observation of a ship wake," *Radar, Sonar and Navigation, IEE Proceedings*, vol. 143, no. 4, pp. 275–280, Aug. 1996.

[139] P. P. Kube and A. Pentland, "On the imaging of fractal surfaces," *IEEE Transactions on Pattern Analysis and Machine Intelligence*, vol. 10, no. 5, pp. 704–707, Sept. 1988.

[140] J. Pedersen, T.Bauna, L. Seljelv, L. Steinbakk, and R.T.Enoksen, "The ERS contribution to oil spill monitoring - from R&D towards an operational service," in *Proceedings of the ESA-ENVISAT Symposium: "Looking down to Earth in the new Millenium"*, Gothenburg, Suède, 2000.

[141] ——, "Scale-space and edge detection using anisotropic diffusion," *IEEE Transactions on Pattern Analysis and Maching Intellignce*, vol. 12, no. 7, pp. 629–639, July 1990.

[142] B. Phong, "Illumination for computer generated pictures," *Comm. ACM*, vol. 18, no. 6, pp. 311–317, juin 1975.

[143] W. J. Pierson and L. Moskowitz, "A proposed spectral form of fully developped wind seas based on the similarity theory of S. A. Kitaigorodskii," *Journal of Geophysical Reasearch*, vol. 69, no. 64, pp. 5181–5190, 1964.

[144] T. Radko, "Ship waves in a stratified fluid," *Journal of ship research*, vol. 45, no. 1, pp. 1–12, Mar. 2001.

[145] E. Radoi, A. Quinquis, and P. Saulais, "Analysis and simulation of sea clutter at high range resolution and low grazing angles," in *Proceedings of the International Geoscience and Remote Sensing Symposium (IGARSS)*, Toulouse, France, July 2003.

[146] J. H. Radon, "Über die Bestimmng von Funktionen durch Ihre Integralwerte längs gewisser Mannigfaltigkeiten," *Berichte über die Verhandlungen der Sächsische Akademie der Wissenschaften*, vol. 69, pp. 262–277, 1917.

[147] J. H. Radon and P. C. Parks (traducteur), "On the determination of functions from their integral values along certain manifolds," *IEEE Transactions on Medical Imaging*, vol. 5, no. 4, pp. 170–176, 1986.

[148] R. K. Raney, H. Runge, R. Blamer, I. Cumming, and F. Wong, "Precision SAR processing using chirp scaling," *IEEE Transactions on Geoscience and Remote Sensing*, vol. 32, no. 4, pp. 786–799, 1994.

[149] A. M. Reed and J. H. Milgram, "Ship wakes and their radar images," *Annual Review of Fluid Mechanics*, vol. 34, no. 34, pp. 469–502, 2002.

[150] M. T. Rey, J. K. Tunaley, J. T. Folinsbee, P. A. Jahans, J. A. Dixon, and M. R. Vant, "Application of Radon transform techniques to wake detection in Seasat-A SAR images," *IEEE Transactions on Geoscience and Remote Sensing*, vol. 28, no. 4, pp. 553–560, July 1990.

[151] S. O. Rice, "Reflection of electromagnetic waves from slightly rough surfaces," *Comm. Pure Appl. Math.*, vol. 4, no. 4, pp. 351–378, 1951.

[152] J. C. Russ, *The image processing handbook*, 5th ed. CRC Press, 2007.

[153] M. Saillard, P. Forget, G. Soriano, M. Joelson, P. Broche, and P. Currier, "Sea surface probing with L-band Doppler radar : experiment and theory," *C. R. Physique*, vol. 6, no. 6, pp. 675–682, 2005.

[154] W. J. Saucier, *Principles of Meteorological Analysis*. Dover Phoenix Editions, 2003, ISBN: 0486495418, reproduction identique de l'édition de 1955.

[155] O. Shemdin, "Synthetic aperture radar imaging of ship wakes in the gulf of Alaska," *Journal of Geophysical Research*, vol. 95, no. C9, pp. 16 319–16 338, 1990.

[156] J. Shen and S. Castan, "An optimal linear operator for step edge detection," *CVGIP: Graphical Models and Image Processing*, vol. 54, no. 2, pp. 112–133, Mar. 1992.

[157] S. Silver, *Microwave Antenna Theory and Design*, 1st ed. McGraw-Hill Book Company, Inc, 1949.

[158] M. I. Skolnik, *Radar Handbook*, 2nd ed. New York: McGraw-Hill Publishing Company, 1990.

[159] E. Smith and S. Weintraub, "The constants in the equation for atmospheric refractive index at the radio frequencies." *Proc. IRE*, vol. 41, pp. 1035–1037, 1953.

[160] N. Sochen, R. Kimmel, and R. Malladi, "A geometrical framework for low-level vision," *IEEE Transactions on Image Processing, Special Issue on PDE-based Image Processing*, vol. 7, no. 3, pp. 310–318, Mar. 1998.

[161] G. Soriano, C.-A. Guérin, and M. Saillard, "Scattering by two-dimensional rough surfaces: comparison between the method of moments, the Kirchhoff and the small-slope approximation," *Waves in Random Media*, vol. 12, no. 1, pp. 63–83, Jan. 2002.

[162] G. Soriano and M. Saillard, "Modelization of the scattering of electromagnetic waves from the ocean surface," *Progress in Electromagnetics Research*, vol. X, chapitre 4, pp. 102–128, 2003.

[163] N. Stacy, D. Crisp, A. Goh, D. Badger, and M. Preiss, "Polarimetric analysis of fine resolution X-band SAR sea clutter data," in *Proceedings of the International Geoscience and Remote Sensing Symposium (IGARSS)*, July 2005, pp. 2787– 2790.

[164] N. R. Stapleton, "Ship wakes in radar imagery," *International Journal of Remote Sensing*, vol. 18, no. 6, pp. 1381–1386, 1997.

[165] R. H. Stewart, "Introduction to physical oceanography," Cours. Department of Oceanography, Texas A&M University, 2008, available online: http://oceanworld.tamu.edu/home/course_book.htm.

[166] ——, "Seasat: results of the mission," *Bulletin of the American Meteorological Society*, vol. 69, no. 12, pp. 1441–1447, 1988.

[167] J. A. Stratton, *Electromagnetic Theory*, 1st ed., ser. International Series in Physics. McGraw-Hill Book Company, Inc, 1941.

[168] J. T.F. Swean, "Numerical simulations of the wake downstream of a twin-screw destroyer model," Naval Research Laboratory, Tech. Rep. NRL 6131, 1987.

[169] R. Timman, A. J. Hermans, and G. C. Hsiaco, *Water waves and ship hydrodynamics*, ser. Mechanics of Fluids & Transport processes. Martins Njihoff Publishers & Delft University Press, 1985.

[170] ——, "Numerical simulations of scattering from time-varying, randomly rough surfaces," *IEEE Transactions on Geoscience and Remote Sensing*, vol. 38, no. 4, pp. 1616 – 1625, July 2000.

[171] L. Tsang and J. Kong, *Scattering of Electromagnetic Waves, Vol. 3: Advanced Topics*. Wiley Interscience, 2001.

[172] E. O. Tuck, "The wave resistance formula of J. H. Michell (1898) and its significance to recent research in ship hydrodynamics," *J. Austral. Math. Soc. Ser. B*, vol. 30, pp. 365–377, 1989.

[173] E. O. Tuck, J. I. Collins, and W. H. Wells, "On ship wave patterns and their spectra," *Journal of Ship Research*, vol. 15, pp. 11–21, Mar. 1971.

[174] E. O. Tuck, L. Lazauskas, and D. C. Scullen, "Sea wave pattern evaluation, part I report, primary code and test results (surface vessels)," Applied Mathematics Department, The University of Adelaide, Tech. Rep., Apr. 1999.

[175] M. P. Tulin and M. Landrini, "Breaking waves in the ocean and around ships," in *Proceedings of the Twenty-Third Symposium on Naval Hydrodynamics*, 2001.

[176] J. K. E. Tunaley, E. H. Buller, K. H. Wu, and M. T. Rey, "The simulation of the SAR image of a ship wake," *IEEE Transactions on Geoscience and Remote Sensing*, vol. 29, no. 1, pp. 149–155, Jan. 1991.

[177] F. T. Ulaby, R. K. Moore, and A. K. Fung, *Microwave Remote Sensing: Active and Passive, vol. II.* Artech House, 1986.

[178] L. M. H. Ulander, H. Hellsten, and G. Stenstrom, "SAR processing using fast factorized backprojection," *IEEE Trans. on Aerospace and Electron. Syst.*, vol. 39, pp. 760–776, 2003.

[179] F. Ursell, "The long-wave paradox in the theory of gravity waves," *Proc. Cambridge. Phil. Soc.*, vol. 49, pp. 685–694, 1953.

[180] G. R. Valenzuela, "Theories for the interactions of electromagnetic and oceanic waves – a review," *Boundary-Layer Meteorology*, vol. 13, pp. 61–85, 1978.

[181] A. Vidal-Pantaleoni and M. Ferrando, "SPECAN techniques for range and azimuth ScanSAR processing," *Proceedings of SPIE, the International Society for Optical Engineering*, vol. 4173, pp. 54–63, 2000.

[182] A. G. Voronovich, "Small-slope approximation for electromagnetic wave scattering at a rough interface of two dielectric interfaces," *Waves in Random Media*, vol. 4, pp. 337–367, 1994.

[183] A. G. Voronovitch and V. U. Zavorotni, "Theoretical model for scattering of radar signals in Ku- and C-bands from a rough sea surface with breaking waves," *Waves in Random Media*, vol. 11, no. 3, pp. 247–269, 2001.

[184] E. J. Walsh, M. L. Banner, J. H. Churnside, J. A. Straw, D. C. Vandemark, C. W. Wright, J. B. Jensen, and S. Lee, "Visual demonstration of three scales sea-surface roughness under light wind conditions," *IEEE Transactions on Geoscience and Remote Sensing*, vol. 43, no. 8, pp. 1751 – 1762, Aug. 2005.

[185] X. Wang, Y. Yu, Y. Chen, J. Xiao, and M. Zhu, "Bistatic SAR raw data simulation for ocean," in *Proceedings of the International Geoscience and Remote Sensing Symposium*, Barcelone, Espagne, July 2007, pp. 871–874.

[186] K. D. Ward, "Compound representation of high resolution sea clutter," *Electron. Lett.*, vol. 17, no. 16, pp. 561–563, 1981.

[187] K. D. Ward, C. Baker, and S. Watts, "Maritime surveillance radar. Part 1: Radar scattering from the ocean surface," *IEE Proceedings*, vol. 137, Pt. F, no. 2, pp. 51–62, Apr. 1990.

[188] K. D. Ward, R. J. Tough, and S. Watts, *Sea Clutter: scattering, the K-distribution and radar performance.* The Institution of Engineering and Technology, 2006.

[189] R. Rapp and W. Melville, "Laboratory measurements of deep water breaking waves," *Philos. Trans. R. Soc. London*, vol. A, no. 331, pp. 735–780, 1990.

[190] R. Watson-Watt, *Three steps to victory.* Odhams Press, 1958.

[191] S. Watts and D. C. Wicks, "Empirical models for prediction in K-distribution radar sea clutter," in *IEEE International Radar Conference*, 1990, pp. 189–194.

[192] D. R. Wilkinson, "Efficient image reconstruction techniques for a multiple receiver synthetic aperture sonar," Master's thesis, University of Canterbury, 2001.

[193] N. J. Willis, *Bistatic Radar*, 2nd ed. SciTech Publishing Inc., 2005, ISBN 978-1891121456.

[194] F. H. Wong, I. G. Cumming, and L. N. Yew, "Focusing bistatic SAR data using the nonlinear chirp scaling algorithm," *IEEE transactions on geoscience and remote sensing*, vol. 46, no. 9, pp. 2493–2505, 2008.

[195] J. W. Wright, "A new model for sea clutter," *IEEE Transactions*, vol. AP-16, pp. 217–223, 1968.

[196] ——, "Backscattering from capillary waves with application to sea clutter," *IEEE Transactions*, vol. AP-14, pp. 749–754, 1966.

[197] Z. Wu, "On the estimation of a moving ship's velocity and hull geometry information from its wave spectra," Ph.D. dissertation, The University of Michigan, 1991.

[198] L. N. Yew, F. H. Wong, and I. G. Cumming, "Processing of azimuth-invariant bistatic SAR data using the range Doppler algorithm," *IEEE transactions on geoscience and remote sensing*, vol. 46, no. 1, pp. 14–21, 2008.

[199] Z. Zavorotny, A. Voronovich, S. Katzberg, J. Garrison, and A. Komjathy, "Extraction of sea state and wind speed from reflected GPS signals: modeling and aircraft measurements," in *Proc. IEEE 2000 International Geoscience and Remote Sensing Symposium IGARSS 2000*, vol. 4, 2000, pp. 1507–1509 vol. 4.

[200] G. Zilman and T. Miloh, "Kelvin and V-like ship wakes affected by surfactants," *Journal of Ship Research*, vol. 45, no. 2, pp. 150–163, June 2001.

[201] ——, "Radar backscatter of a V-like ship wake from a sea surface covered by surfactants," in *Proceedings of the Twenty-First Symposium on Naval Hydrodynamics*, 1997, pp. 235–248.

[202] G. Zilman, A. Zapolski, and M. Marom, "The speed and beam of a ship from its wake's SAR images," *IEEE Transactions on Geoscience and Remote Sensing*, vol. 42, no. 10, pp. 2335– 2343, Oct. 2004.

[203] L. M. Zurk and W. Plant, "Comparison of actual and simulated synthetic aperture radar image spectra of ocean waves," *Journal of Geophysical Research*, vol. 101, no. C4, pp. 8913–8931, 1996.

[204] "Tracking down drug smugglers in the Mediterranean," Broadcast, France 24, 12 décembre 2008, 19 h 34.

[205] "APL-UW high-frequency ocean environmental acoustic models handbook," Advanced Physics Laboratory, University of Washington, Tech. Rep. TR 9407, Oct. 1994.

[206] "Report of the Seasat failure review board," NASA, Tech. Rep., 1978, http://klabs.org/richcontent/Reports/Failure_Reports/seasat/seasat.pdf.

[207] A. Mahalanobis and H. Singh, "Application of correlation filters for texture registration," *Applied Optics*, vol. 33, no. 11, pp. 2173–2179, 1994.

[208] G. Doemeghe, B. Blankertz, G. Curio, and K.-R. Müller, "Increase information transfer rates in BCI by CSP extension to multi-class." in *Proceedings of the 16th international conference on neural information processing systems (NIPS'03)*, 2003.

[209] R. Caprari, "Generalized matched filters and univariate neyman-pearson detectors for image target detection," *IEEE Transactions on Information Theory*, vol. 46, no. 5, pp. 1932–1937, 2000.

[210] A. Green, M. Berman, P. Switzer, and M. Craig, "A transform for ordering multispectral data in terms of image quality with implications for noise removal," *IEEE transactions on Geoscience and Remote Sensing*, vol. 16, no. 1, pp. 65–74, Jan. 1988.

[211] Z. J. Koles, M. S. Lazaret, and S. Z. Zhou, "Spatial patterns underlying population differences in the background EEG," *Brain topography*, vol. 2, no. 4, pp. 275–284, 1990.

[212] M.-G. Johannes, P. Gert, and F. Henrik, "Designing optimal spatial filters for single-trial EEG classification in a movement task," *Clinical Neurophysiology*, vol. 110, no. 5, pp. 787–798, 1999.

[213] K. Fukunaga and W. L. G. Koontz, "Application of the Karhunen-Loève expansion to feature selection and ordering," *IEEE Transactions on Computers*, vol. C-19, no. 4, pp. 311–318, Apr. 1970.

[214] J. Capon, "High-resolution frequency-wavenumber spectrum analysis," *Proceedings of the IEEE*, vol. 57, pp. 1408–1418, 1969.

[215] G. Bienvenu and L. Kopp, "Optimality of high resolution array processing using the eigensystem approach," *IEEE Transactions on Acoustics, Speech and Signal Processing*, vol. ASSP-31, pp. 1234–1248, Oct. 1983.

[216] R. Schmidt, "Multiple emitter location and signal parameter estimation," *IEEE Transactions on Antennas and Propagation*, vol. 34, no. 3, pp. 276–280, 1986.

[217] ——, "Multiple emitter location and signal parameter estimation," in *Proceedings of RADC spectrum estimation workshop, Saxpy Computer Corporation, USA*, 1979, pp. 243–258.

[218] A. Barachant, S. Bonnet, M. Congedo, and C. Jutten, "Common spatial pattern revisited by riemannian geometry," 2010.

[219] F. Lotte and C. Guan, "Regularizing common spatial patterns to improve bci designs: Unified theory and new algorithms," *IEEE Transactions on Biomedical Engineering*, vol. 58, no. 2, pp. 355–362, 2011.

[220] H. Yu, H. Lu, S. Wang, K. Xia, Y. Jiang, and P. Qian, "A general common spatial patterns for eeg analysis with applications to vigilance detection," *IEEE Access*, vol. 7, pp. 111 102–111 114, 2019.

[221] M. Grosse-Wentrup and M. Buss, "Multiclass common spatial patterns and information theoretic feature extraction," *IEEE Transactions on Biomedical Engineering*, vol. 55, no. 8, pp. 1991–2000, 2008.

[222] I. Léonard, "Reconnaissance des objets manufacturés dans des vidéos sous-marines, thèse de doctorat, université de bretagne occidentale," 2012.

[223] G. M. Araujo, F. M. L. Ribeiro, E. A. B. Silva, and S. K. Goldenstein, "Fast eye localization without a face model using inner product detectors," in *2014 IEEE International Conference on Image Processing (ICIP)*, 2014, pp. 1366–1370.

[224] M. C. Wicks, Y. Zhang, and R. Schneible, "A generalized inner product based algorithm for improved detection and discrimination of over resolved targets in mimo radar," in *8th European Conference on Synthetic Aperture Radar*, 2010, pp. 1–4.

[225] M. S. Bartlett, "Periodogram Analysis and Continuous Spectra," *Biometrika*, vol. 37, no. 1-2, pp. 1–16, 06 1950. [Online]. Available: https://doi.org/10.1093/biomet/37.1-2.1

Publications

Journal papers

[A1] **A. Arnold-Bos**, A. Khenchaf, and A. Martin, "Bistatic radar imaging of the marine environment. Part I: theoretical background," *IEEE Transactions on Geoscience and Remote Sensing*, vol. 45, no. 11, pp. 3372 – 3383, Nov. 2007.

[A2] ——, "Bistatic radar imaging of the marine environment. Part II: simulation and results analysis," *IEEE Transactions on Geoscience and Remote Sensing*, vol. 45, no. 11, pp. 3372 – 3383, Nov. 2007.

[A3] A. Martin, H. Laanya, and **A. Arnold-Bos**, "Evaluation for uncertain image classification and segmentation," *Pattern Recognition*, vol. 39, no. 11, pp. 1987–1995, Nov. 2006.

[A4] G. Soares, **A. Arnold-Bos**, L. Jaulin, J. A. Vasconcelos, and C. A. Maia, "An interval-based target tracking approach for range-only multistatic radar," *IEEE Transactions on Magnetics*, vol. 44, no. 6, pp. 1350–1353, June 2008.

Conference papers

[A5] **A. Arnold-Bos**, A. Khenchaf, and A. Martin, "Investigating possible bistatic configurations for ship wake imaging through simulation," in *Proceedings of the IEE International Conference on Radar*, Edimbourg, Royaume Uni, Oct. 2007.

[A6] ——, "An evaluation of current ship wake detection algorithms in SAR images," in *Proceedings of the Caractérisation du Milieu Marin / Marine Environment Characterization conference, "SeaTechWeek '06"*, Brest, France, Nov. 2006.

[A7] **A. Arnold-Bos**, A. Martin, and A. Khenchaf, "Obtaining a ship's speed and direction from its Kelvin wake spectrum using stochastic matched filtering," in *Proceedings of the International Geoscience and Remote Sensing Symposium (IGARSS)*, Barcelone, Espagne, July 2007.

[A8] ——, "A versatile bistatic & polarimetric marine radar simulator," in *Proceedings of the IEEE Conference on Radars*, Verona, NY, États Unis, Apr. 2006.

[A9] A. Coatanhay, **A**. **Arnold-Bos**, and A. Khenchaf, "Modeling of the GALILEO signals near a sea surface," in *Proceedings of the European Navigation Conference - Global Navigation Satellite Systems*, Toulouse, France, Apr. 2008.

[A10] ——, "Simulation of a GNSS signal for a receiver near a time-evolving sea surface," in *Proceedings of the International Conference on Electromagnetics in Advanced Applications*, Turin, Italie, Sept. 2007.

Scientific workshops

[A11] **A**. **Arnold-Bos**, A. Khenchaf, and A. Martin, "Investigating possible bistatic configurations for ship wake imaging through simulation," in *4th MATHERON workshop on Airborne and Spatial Imaging*, Thales Research and Technology, Palaiseau, France, Nov. 2007.

[A12] ——, "Surveillance maritime et suivi de navires en multistatique," in *Manifestation scientifique 2006 du métier détection électromagnétique*, ENSTA, Paris, France, Nov. 2006.

Marine surveillance with bistatic radar: theory, simulation, contribution to computer-aided ship wakes detection.

We study the feasability of ship wake detection in monostatic or bistatic radar images to get parameters such as the ship's heading and speed. We begin by describing the bistatic radar acquisition chain in the marine environment, in particular the electromagnetic wave scattering models applied to ocean surfaces and how to obtain an elevation map of the Kelvin ship wake. Then we describe a raw radar signal simulator able to tackle bistatic configurations, and we compare our results with data obtained from literature.

The second part of the thesis is a study on ship wake detectability in radar images. First we consider the case of the so-called "dead water" wake, by benchmarking four typical reference chains. Then we study the detectability of Kelvin ship wakes in high resolution radar images: we discuss the choice of a radar configuration to optimize the visibility of the wake, and then we present an algorithm able to obtain the ship's heading and speed from the images. The algorithm is based on the stochastic matched filtering theory, and it also operates on high resolution optical images acquired from space.

Keywords: Marine surveillance, bistatic synthetic aperture radar, raw radar signal simulation, Kelvin ship wake, dead water ship wake, stochastic matched filtering, computer-aided detection.

La surveillance maritime en imagerie radar bistatique: théorie, simulation, contribution à la détection automatique du sillage de navires.

Nous étudions la faisabilité de la détection du sillage de navires en imagerie radar, éventuellement bistatique, afin d'obtenir des paramètres tels que le cap et la vitesse du navire. Dans un premier temps, on décrit la chaîne d'acquisition radar bistatique ainsi que l'environnement maritime, en particulier les modèles de diffusion des ondes électromagnétiques sur des surfaces océaniques et la manière d'obtenir une carte des hauteurs des vagues de sillage de Kelvin d'un navire. On décrit ensuite un simulateur de signaux radars bruts en configuration bistatique, en validant les résultats obtenus avec des données radar monostatiques disponibles dans la littérature.

La seconde partie de la thèse est dédiée à l'étude de la détectabilité du sillage de navires. On traite tout d'abord du cas de la détection du sillage d'eau morte, en réalisant un test comparatif de quatre chaînes de référence représentatives. On traite ensuite la détectabilité du sillage de Kelvin dans des images radar de haute résolution, en commençant par discuter le choix d'une configuration radar optimisant la visibilité du sillage, puis en présentant un algorithme de détection et de traitement basé sur la théorie du filtrage adapté stochastique. Cet algorithme fonctionne également sur des données d'imagerie spatiale optiques haute résolution.

Mots-clés: Surveillance maritime, radar à synthèse d'ouverture bistatique, simulation de signaux radar bruts, sillage de Kelvin, sillage d'eau morte, filtrage adapté stochastique, détection assistée par ordinateur.